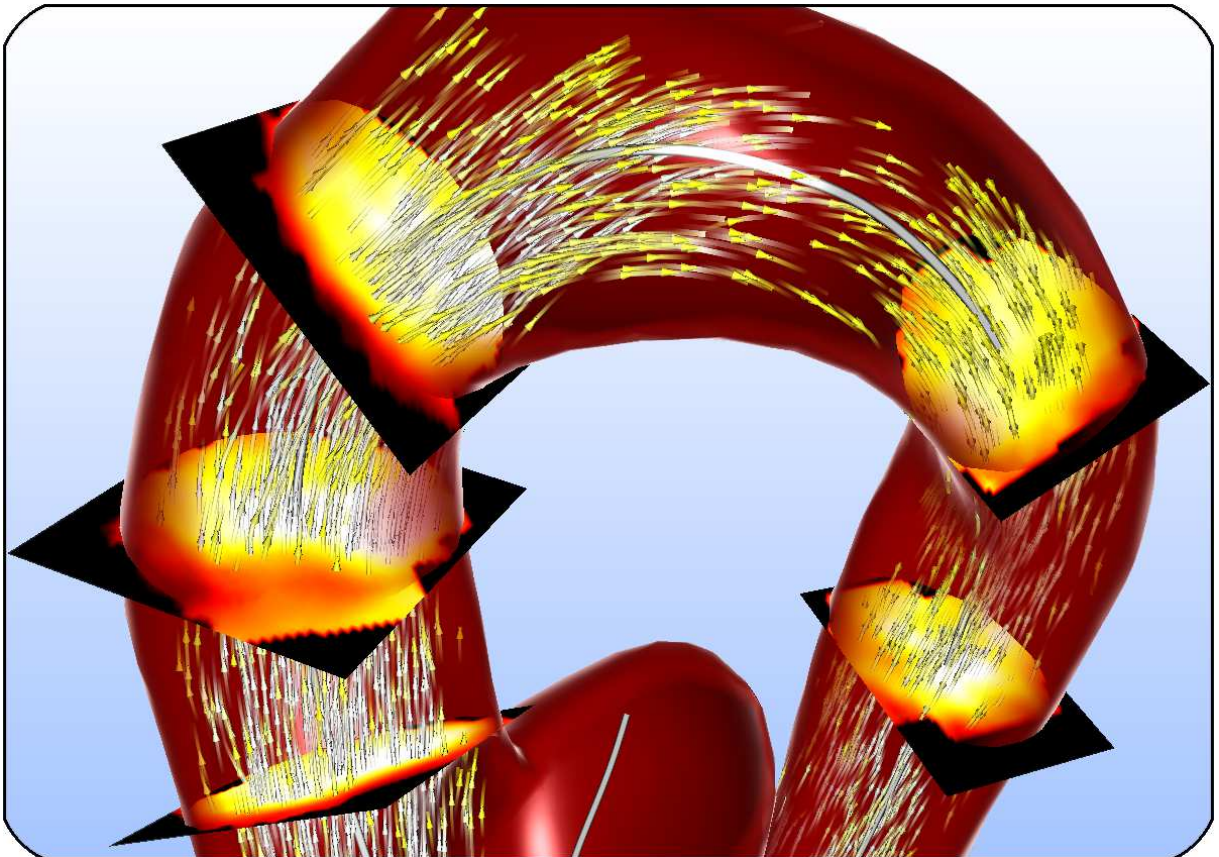


BENJAMIN KÖHLER

**GUIDED QUALITATIVE AND QUANTITATIVE
ANALYSIS OF CARDIAC 4D PC-MRI BLOOD
FLOW DATA**





GUIDED QUALITATIVE AND QUANTITATIVE ANALYSIS OF CARDIAC 4D PC-MRI BLOOD FLOW DATA

DISSERTATION

zur Erlangung des akademischen Grades

Doktoringenieur (Dr.-Ing.)

angenommen durch die Fakultät für Informatik
der Otto-von-Guericke-Universität Magdeburg

von **M.SC. BENJAMIN KÖHLER**

geb. am 04.03.1988 in Meiningen

Gutachterinnen / Gutachter:

Prof. Dr.-Ing. Bernhard Preim
Prof. Dr. Geric Scheuermann
Prof. Dr. Anna Vilanova

Magdeburg, den 14.04.2016

Benjamin Köhler:
Guided qualitative and quantitative analysis of cardiac 4D PC-MRI blood flow data
Dissertation, Otto-von-Guericke-Universität Magdeburg
(submitted: 14.04.2016, defended: 26.09.2016, printed: 10.10.2016)
© 10.10.2016

A PRELIMINARIES	1
SUMMARY	3
ZUSAMMENFASSUNG	5
1 INTRODUCTION	7
1.1 STRUCTURE AND CONTRIBUTIONS OF THIS THESIS	8
1.2 NOTATIONS	10
B BACKGROUND	11
2 THE CARDIOVASCULAR SYSTEM	13
2.1 HEART ANATOMY AND BLOOD CIRCULATION	13
2.2 CARDIOVASCULAR DISEASES	14
2.2.1 ALTERATIONS OF THE VESSEL WALL	14
2.2.2 VALVE PATHOLOGIES	16
2.2.3 COMPLEX CONGENITAL PATHOLOGIES	17
2.2.4 COLLECTIVE TERMS	18
2.3 SUMMARY	19
3 CARDIAC BLOOD FLOW MEASUREMENTS	21
3.1 4D PHASE-CONTRAST MRI	21
3.1.1 MRI BASICS	21
3.1.2 FLOW MEASUREMENT	25
3.1.3 DATASET DESCRIPTION	26
3.2 ECHOCARDIOGRAPHY	28
3.2.1 DOPPLER ECHOCARDIOGRAPHY	28
3.2.2 ECHO PARTICLE IMAGE VELOCIMETRY	29
3.3 COMPARISON	30
3.4 SUMMARY	30
4 DATA PRE-PROCESSING	33
4.1 CORRECTION OF IMAGE ARTIFACTS	33
4.1.1 PHASE UNWRAPPING	33
4.1.2 VELOCITY OFFSET CORRECTION	34
4.1.3 NOISE MASKING	35
4.1.4 DIVERGENCE FILTERING AND REGULARIZATION	36
4.2 VESSEL SEGMENTATION	37
4.2.1 PC-MRI-BASED ANGIOGRAPHIES	37
4.2.2 LUMEN SEGMENTATION - 3D	38
4.2.3 LUMEN SEGMENTATION - 4D	39
4.2.4 CROSS-SECTION SEGMENTATION	40
4.3 SUMMARY	41
5 QUALITATIVE DATA ANALYSIS	43
5.1 ANATOMICAL CONTEXT VISUALIZATION	43
5.1.1 GEOMETRIC SURFACE MESHES	43
5.1.2 DIRECT VOLUME RENDERING	44

5.2	FLOW VISUALIZATION	46
5.2.1	DIRECT METHODS	46
5.2.2	GEOMETRY-BASED METHODS	47
5.2.3	FEATURE-BASED METHODS	52
5.3	CLINICAL VALUE OF INVESTIGATING FLOW CHARACTERISTICS	56
5.3.1	CARDIOVASCULAR VORTEX FLOW	56
5.4	SUMMARY	62
6	QUANTITATIVE FLOW ANALYSIS	65
6.1	CROSS-SECTIONAL METHODS	65
6.1.1	FLOW RATE	66
6.1.2	PULSE WAVE VELOCITY	67
6.1.3	FLOW DISPLACEMENT	69
6.1.4	AORTIC VALVE AREA	70
6.2	SURFACE-BASED METHODS	71
6.2.1	WALL SHEAR STRESS	71
6.3	GRID-BASED METHODS	73
6.3.1	PRESSURE GRADIENTS	73
6.3.2	TURBULENT KINETIC ENERGY	75
6.3.3	VORTEX STRENGTH	76
6.3.4	LAGRANGIAN COHERENT STRUCTURES	77
6.3.5	CONNECTIVITY	78
6.4	SUMMARY	78
C	GUIDED DATA EVALUATION	81
7	BLOODLINE	83
7.1	WORKFLOW	83
7.1.1	VESSEL SEGMENTATION	84
7.1.2	SURFACE MESH AND CENTERLINE EXTRACTION	85
7.1.3	QUALITATIVE ANALYSIS	86
7.1.4	QUANTITATIVE ANALYSIS	88
7.2	IMPLEMENTATION DETAILS	89
7.3	APPLICATION	90
7.4	ALTERNATIVE SOFTWARE	91
7.5	CONCLUSION AND FUTURE WORK	94
8	ENHANCED ASSESSMENT OF VORTEX FLOW	95
8.1	SEMI-AUTOMATIC VORTEX EXTRACTION USING LINE PREDICATES	95
8.1.1	REQUIREMENT ANALYSIS	96
8.1.2	EXTENSION OF LINE PREDICATES	97
8.1.3	SUCCESSIVE VORTEX EXTRACTION	98
8.1.4	COMPARISON OF LOCAL VORTEX CRITERIA	99
8.1.5	RESULTS AND INFORMAL EVALUATION	103
8.1.6	CONCLUSION	107
8.2	2D PLOT VISUALIZATION OF AORTIC VORTEX FLOW	108
8.2.1	METHOD	109
8.2.2	RESULTS	111
8.2.3	DISCUSSION	112
8.3	ADAPTIVE ANIMATIONS OF EXTRACTED VORTEX FLOW	112
8.3.1	METHOD	112
8.3.2	RESULTS	115
8.3.3	DISCUSSION	116

8.4	VORTEX CHARACTERIZATION IN THE AORTA	116
8.4.1	CLUSTERING	117
8.4.2	CLASSIFICATION	121
9	ENHANCED FLOW RATE QUANTIFICATION	135
9.1	ROBUST CARDIAC FUNCTION ASSESSMENT	135
9.1.1	REQUIREMENT ANALYSIS	136
9.1.2	METHOD	136
9.1.3	RESULTS	143
9.1.4	CONCLUSION AND FUTURE WORK	147
9.2	MOTION-AWARE STROKE VOLUME QUANTIFICATION	148
9.2.1	METHOD	148
9.2.2	RESULTS	152
9.2.3	DISCUSSION	157
9.2.4	CONCLUSION AND FUTURE WORK	158
10	SUMMARY AND OUTLOOK	159
10.1	SUMMARY OF CONTRIBUTIONS	159
10.2	FUTURE WORK	159
10.3	4D PC-MRI POTENTIAL	162
D	APPENDIX	163
	LITERATURE	165
	ABBREVIATIONS	195
	SYMBOLS	197
	FIGURES	199
	TABLES	203
	PUBLICATIONS	205
	PHD PORTFOLIO	209
	CURRICULUM VITAE	211
	EHRENERKLÄRUNG	213
	DANKSAGUNG	215

A

PRELIMINARIES

The genesis and progression of cardiovascular diseases (CVDs) depend on various factors. A better comprehension of patient-specific blood flow hemodynamics has great potential to increase their diagnosis, support treatment decision-making and provide a realistic forecast of such pathologies, facilitating a better implementation of preventative measures. Four-dimensional phase-contrast magnetic resonance imaging (4D PC-MRI) gained increasing importance and clinical attention in recent years. It is a non-invasive imaging modality that allows for time-resolved, three-dimensional measurement of blood flow information. The resulting 4D grid data, which contain vectors that represent the blood flow direction and velocity, are of limited spatio-temporal resolution and suffer from multiple artifacts, making complex image processing methods a prerequisite. Qualitative data analysis aims to depict the course of the blood flow with emphasis on specific flow patterns, such as vortex flow, which can be an indicator for different cardiovascular diseases. For this purpose, flow visualization techniques can be adapted to the cardiac context. Quantitative data analysis facilitates assessment of, e.g., the cardiac function by evaluating stroke volumes, heart valve performances by evaluating percentaged back flows, and fluid-vessel wall interactions by evaluating wall shear stress.

This thesis proposes both qualitative and quantitative data evaluation methods, embedded in a developed software prototype with a guided workflow. A semi-automatic extraction of vortex flow is presented that is based on the line predicates methodology and preserves visually appealing path lines with long and continuous courses. It was tailored towards our targeted user group: Radiologists focused on the cardiovascular system and cardiologists. The extracted path lines were used to establish an overview visualization of aortic vortex flow and to adapt the speed of videos so that the display vortical flow behavior is enhanced. Vortices were grouped into single entities (clustering) and subsequently analyzed according to different criteria that describe properties, such as their rotation direction and elongation. Based on this classification, a simplifying glyph visualization was established.

Moreover, this thesis addresses an improved quantification of the flow rate-based measures, such as stroke volumes, which are prone to errors especially in case of pathologic vortex flow. A robust procedure is presented that analyzes multiple, systematically generated configurations of required measuring planes and evaluates the resulting sample distributions. Additionally, the flow rate calculation is influenced by the dynamic morphology. Therefore, a semi-automatic extraction of corresponding motion information was established and incorporated in an adapted quantification.

Der Ursprung und Verlauf kardiovaskulärer Erkrankungen hängt von einer Vielzahl von Faktoren ab. Ein besseres Verständnis der Patienten-spezifischen Hämodynamik hat großes Potential, deren Diagnose zu verbessern, Therapieentscheidungen zu unterstützen und anhand von genaueren Prognosen eventuelle Präventivmaßnahmen einzuleiten. Vierdimensionale Phasenkontrast Magnetresonanztomographie (4D PC-MRI) erlangte in den vergangenen Jahren verstärkt Aufmerksamkeit von Seiten der Kliniker. Es ist eine nicht-invasive Bildmodalität, die es erlaubt, zeitaufgelöste, dreidimensionale Messungen von Blutflussinformationen durchzuführen. Das resultierende 4D Gitter enthält Vektoren, welche die Blutflussrichtung und Geschwindigkeit darstellen. Vorhandene Bildartefakte und die geringe räumlich / zeitliche Auflösung machen eine komplexe Vorverarbeitung notwendig. Eine qualitative Datenanalyse zielt darauf ab, die Verläufe des Blutes darzustellen und dabei insbesondere abnormale Flussmuster wie Verwirbelungen hervorzuheben, welche ein Indikator für verschiedene kardiovaskuläre Erkrankungen sein können. Dafür können entsprechende Flussvisualisierungstechniken für den kardialen Kontext angepasst werden. Eine quantitative Datenanalyse ermöglicht es, die Herz- sowie Herzklappenfunktion zu beurteilen und die Wechselwirkung zwischen Blut und Gefäßwand genauer zu evaluieren. Dafür kommen Maße wie das Schlagvolumen, der prozentuale Rückfluss und der Wall Shear Stress zum Einsatz.

In der vorliegenden Dissertation werden sowohl qualitative als auch quantitative Methoden vorgestellt. Eine semi-automatische Extraktion von Verwirbelungen basierend auf Linienprädikaten wird vorgestellt, welche visuell hochqualitative (lang und unterbrechungsfrei) Pfadlinien erhält. Es wurde auf die entsprechende Zielgruppe an Benutzern zugeschnitten: Radiologen mit Fokus auf das kardiovaskuläre System und Kardiologen. Die extrahierten Pfadlinien wurden außerdem dazu verwendet, um eine Überblickvisualisierung über Verwirbelungen in der Aorta zu erstellen und um Videos mit adaptiver Geschwindigkeit zu generieren, welche den Wirbelfluss hervorheben. Die Verwirbelungen wurden in einzelne Entitäten gruppiert (geclustert) und im Anschluss gemäß verschiedener Kriterien analysiert, die deren Charakteristiken wie Drehrichtung und Ausdehnung beschreiben. Basierend auf dieser Klassifikation wurde eine vereinfachende Visualisierung durch Glyphen realisiert.

Des Weiteren wird in dieser Arbeit eine verbesserte Quantifizierung von Maßen wie dem Schlagvolumen vorgestellt, die auf der Flussrate basieren. Deren Berechnung ist, insbesondere im Bereich von Verwirbelungen, sehr fehleranfällig. Ein robustes Verfahren, das systematisch verschiedene Konfigurationen von benötigten Messebenen auswertet und die entstehende Verteilung von Stichproben analysiert, wird präsentiert. Die Berechnung der Flussrate hängt zudem von der eigentlich dynamischen Gefäßmorphologie ab. Daher wird ein weiteres Verfahren präsentiert, was semi-automatisch Bewegungsinformationen extrahiert und diese in die Quantifizierung mit einbezieht.

THIS SECTION IS BASED ON:

- [270, SECTION 1]: **B. KÖHLER**, R. GASTEIGER, U. PREIM, H. THEISEL, M. GUTBERLET, AND B. PREIM. “SEMI-AUTOMATIC VORTEX EXTRACTION IN 4D PC-MRI CARDIAC BLOOD FLOW DATA USING LINE PREDICATES”. IN: *IEEE Transactions on Visualization and Computer Graphics* 19.12 (2013), PP. 2773–82. DOI: [10.1109/TVCG.2013.189](https://doi.org/10.1109/TVCG.2013.189)
- [275, SECTION 1]: **B. KÖHLER**, S. BORN, R. F. P. VAN PELT, A. HENNEMUTH, U. PREIM, AND B. PREIM. “A SURVEY OF CARDIAC 4D PC-MRI DATA PROCESSING”. IN: *Computer Graphics Forum* (2016), EPUB. DOI: [10.1111/CGF.12803](https://doi.org/10.1111/CGF.12803)

SEE SECTION [PUBLICATIONS](#) IN THE APPENDIX FOR THE DIVISION OF WORK.

Cardiovascular diseases (CVDs) – the number one cause of death in the world [357] – are of great clinical interest. Their initiation and evolution depends on many different variables, such as genetic predispositions, the vessel morphology and the blood hemodynamics. Blood flow in the heart and its surrounding vessels, such as the aorta and pulmonary artery, have been investigated for many decades [403, 466]. Derived information have great potential to improve the diagnosis of CVDs, assess their severity, monitor as well as predict their progression, and support the corresponding treatment decision-making.

2D PC-MRI: Two-dimensional phase-contrast magnetic resonance imaging (2D PC-MRI) [268] was established in the 1980s based on advances in MR velocity mapping [74, 513] using the echo rephasing sequence [323, 376, 402]. It is a non-invasive imaging modality with a decent spatial resolution that provides time-resolved (cine), quantitative 2D data with blood flow velocity information in a plane, which is angulated prior to the scan. The facilitated quantification of different measures related to the cardiovascular function made 2D PC-MRI a useful tool in the clinical routine. The flow rate describes passing blood for each time of the cardiac cycle. Among others, this allows to assess the amount of pumped blood per heart beat – the stroke volume (SV) – and the percentage of blood that flows back into the ventricle – the regurgitation fraction (RF). The latter is increased in case of a malfunctioning aortic (AV) or pulmonary valve (PV). Wall shear stress (WSS) relates to shear forces on the vessel wall induced by nearby blood flow. It is suspected to play an important role in the development of pathologic vessel dilations (ectasia / aneurysm). High pressure gradients can occur in pathologically narrowed (stenotic) valves or vessels, which typically also increases peak flow velocities, since the same amount of blood has to pass a smaller cross-sectional area. The pulse wave velocity denotes the speed of the flow rate curve through a vessel. It may be higher and lower in stiff and elastic vessels, respectively.

4D PC-MRI: Technical progress in the field of MRI nowadays enables four-dimensional (4D) PC-MRI, which was introduced by Wigström et al. [556] in 1996. It is also known as flow-sensitive MRI, MR velocity mapping or 4D flow cardiovascular MR (CMR). This modality is able to provide time-resolved, three-dimensional velocity fields. These data allow for an extensive quantitative analysis, since they contain the full spatio-temporal blood flow information and, e.g., an infinite number of measuring planes can be placed *after* the scan – in contrast to 2D PC-MRI, where a new scan is required in case of placement errors or the need of information about further locations. Another major advantage is that a qualitative analysis of the three-dimensional, pulsatile blood flow becomes possible. Characteristic flow aspects facilitate a deeper understanding of a patient’s situation, since specific patterns, such as vortex flow, are correlated to different pathologies. There is, e.g., a high probability of emerging systolic vortex flow in the ascending aorta if the aortic valve is *bicuspid*, i.e., two of the three leaflets are fused [472]. This affects the valve’s opening characteristics [40, 325]. Vortex flow close to the vessel wall may induce high shear forces [197, 520] that increase the risk of aneurysm development [79]. Further

understanding this mutual influence of hemodynamics and vessel morphology can support treatment decision-making and the corresponding risk assessment. Advances towards higher resolutions and faster acquisitions, as well as studies proving the clinical impact, yielded an increasing interest in 4D PC-MRI in recent years [4].

For the evaluation of 4D PC-MRI data, flow visualization techniques, such as integral lines, can be adapted to the cardiac context. However, the enormous data complexity makes the exploration and analysis a time-consuming, tedious and highly subjective task. There is a need for standardized and fast techniques as well as software with guided workflows in order to make 4D PC-MRI viable for the clinical routine [342]. Standardized methods do not only save time, but also decrease the inter-observer variability, which helps to objectively evaluate larger studies. Fully automatic approaches are often not suitable due to the large variety of anatomical situations. Semi-automation allows to incorporate the expert knowledge of the targeted user group: Radiologists focused on the cardiovascular system and cardiologists.

Overviews about 4D PC-MRI and related clinical studies were provided by: Hope and Herfkens [227], Hope et al. [226], Srichai et al. [483], Ebbers [136], Markl et al. [341, 343], Calkoen et al. [83], Stankovic et al. [488] and Nayak et al. [375]. Sengupta et al. [468] performed an extensive comparison between *phase-encoded MRI*, *echocardiography particle image velocimetry* and *color Doppler echocardiography* for cardiovascular flow visualization. They considered multiple aspects, such as spatio-temporal resolutions, scan time, low- and high-velocity accuracy, and the need for breath-holding. Dyverfeldt et al. [135] – a group of physicists, physicians and biomedical engineers – recently published a 4D PC-MRI consensus paper consisting of shared experiences and ideas. They described the potential clinical and research utility of 4D PC-MRI flow, as well as achieved and open development goals.

1.1. STRUCTURE AND CONTRIBUTIONS OF THIS THESIS

The work presented in this thesis aims to support users from the clinical area in evaluating 4D PC-MRI data of the aorta and pulmonary artery. The established methods were integrated in the developed software prototype named *Bloodline*, which benefits from feedback by our clinical collaborators who have access to the tool for research purposes:

- Matthias Gutberlet, Matthias Grothoff, Franziska Reinhold, Barbara Brenneis, Huong Luu Thi Thanh and Daniel Gräfe from the Department of Diagnostics and Interventional Radiology in the Heart Center in Leipzig, Germany,
- Katharina Fischbach from the Department of Radiology and Nuclear Medicine in the university hospital in Magdeburg, Germany, and
- Uta Preim from the Department of Diagnostic Radiology in the municipal hospital in Magdeburg, Germany.

The background part of the thesis is structured as follows:

- Chapter 2 provides information on the cardiovascular system. This comprises an overview about the heart's anatomy, the circulatory system as well as selected CVDs that are relevant for the further understanding.
- Chapter 3 explains the basic principle of MRI-based measurements. It proceeds with 4D flow acquisitions and characterizes the obtained image data. A brief comparison to alternative flow imaging modalities is provided.
- Chapter 4 is about artifacts in 4D PC-MRI data and available correction procedures.
- Chapter 5 describes the combined anatomical context and flow visualization and the corresponding qualitative assessment. Emphasis is put on physiological and pathological occurrences of characteristic flow patterns, such as vortex flow.
- Chapter 6 is about the clinical significance and calculation of various quantitative measures.

The following main contributions were made:

- **GUIDED EVALUATION:** Until now, 4D PC-MRI is primarily used for research purposes. A major reason is the lack of standardized and easy-to-use evaluation software with guided workflows and an automated report generation. Also, data evaluation is challenging for larger studies due to the high manual effort.

The research prototype *Bloodline* [273] was constantly developed in collaboration with our clinical partners. A detailed description of the workflow is presented in Chapter 7. *Bloodline* allows to process datasets within 10 min. It integrates a full pre-processing pipeline as well as a quantitative and qualitative data analysis. The use of (semi-)automatic methods enables a fluent workflow. Carefully selected defaults strongly reduce the necessity to adjust parameters. State-of-the-art visualizations can easily be created and saved in order to share results. *Bloodline* was used to evaluate more than 60 datasets of healthy volunteers as well as patients with various CVDs.

Summarized experiences in the 4D PC-MRI data processing were published as a survey paper [275] to provide other researchers with a good starting point. This can be found in the background Chapters 3–6.

- **VORTEX FLOW:** One interest of clinicians is vortex flow, which can be an indicator for various pathologic alterations of the cardiovascular system. It is usually assessed manually by evaluating animations of the full flow. Here, due to the high complexity of the 4D flow data, visual clutter is a relevant problem. Especially smaller structures can easily be missed. For example a centrally located helix, which is surrounded by near-wall laminar flow, can be hidden. Vortices are further classified according to criteria that describe their shape, temporal occurrence and behavior, such as the turning direction. The employed criteria are often imperfect, imprecise, oversimplified (binary graduation), and not standardized. Moreover, their assessment is highly subjective. All together, the comparison of different datasets is challenging.

Several methods for the enhanced evaluation of vortex flow are presented in Chapter 8, starting with a GPU-implemented extraction of vortex-representing path lines to reduce visual clutter. This method was excessively used by our clinical collaborators and has been proved as very helpful. Based on this, an overview 2D polar plot visualization of aortic vortex flow was established, which allows a quick comparison of datasets within a study regarding the existence of vortex flow. Rendered videos were modified using time lapse and slow motion to emphasize the temporal visibility of vortex flow. This is a convenient tool for offline evaluations (case discussions) or presentations. A suitable clustering method for the vortex-representing path lines was determined. On top of this, a semi-automatic classification was established, which complements and extends clinical classifiers. This helps to decrease inter-observer variability and to make datasets more objectively comparable.

- **FLOW RATE AND STROKE VOLUME QUANTIFICATION:** The flow rate forms the basis for some essential measures to assess the cardiac function, such as the stroke volume (SV). 4D flow MRI scans suffer from various artifacts, e.g., due to inhomogeneous magnetic fields, critical a priori scan parameters, limited spatio-temporal resolution with related partial volume effects, and respiratory motion. The quantification of flow rates often requires a repeated modification of the employed measuring planes and a result estimation based on experience and plausibility. Furthermore, a 3D approximation of the actually dynamic vessel is usually employed, which introduces additional quantification errors.

Chapter 9 starts with an automation of physicians' manual approach. Measuring plane configurations were systematically evaluated. Plausible results were suggested, based on an analysis of the obtained samples distribution, and an estimation of the result uncertainty was conveyed. The method provides reliable and reproducible results and is suitable to be integrated in an automated data evaluation. The chapter proceeds with an approach to automatically extract the time-varying vessel morphology solely from the 4D PC-MRI data. Motion information were extracted, processed, incorporated in the SV quantification, and deviations to the approach using static vessels were investigated.

Chapter 10 summarizes this thesis and discusses potential future research topics as well as the potential that lies in 4D PC-MRI.

1.2. NOTATIONS

There is an ambiguity regarding the term *velocity*. It either represents a vectorial flow direction or the scalar length of the flow direction. In this thesis, velocity $\|\vec{v}\|$ consistently denotes a scalar value – the magnitude of the corresponding velocity vector $\vec{v} \in \mathbb{R}^3$. Therefore, velocity is equivalent to the term *speed*. Vectorial values are explicitly named *vector* or *direction*, e.g., flow direction or velocity vector. A vector field is denoted as \mathbf{V} , spatial positions as $\vec{p} = (x, y, z)$ and spatio-temporal positions as $\vec{p}_t = (\vec{p}, t) = (x, y, z, t)$.

In this thesis, the common terms 2D PC-MRI and 4D PC-MRI are adopted, which actually denote time-resolved (cine) 2D (2D + time) PC-MRI and cine 3D (3D + time) PC-MRI, respectively.

Citations are normally blue [556]. Red citations [275] refer to works where the author of this thesis contributed.

OB

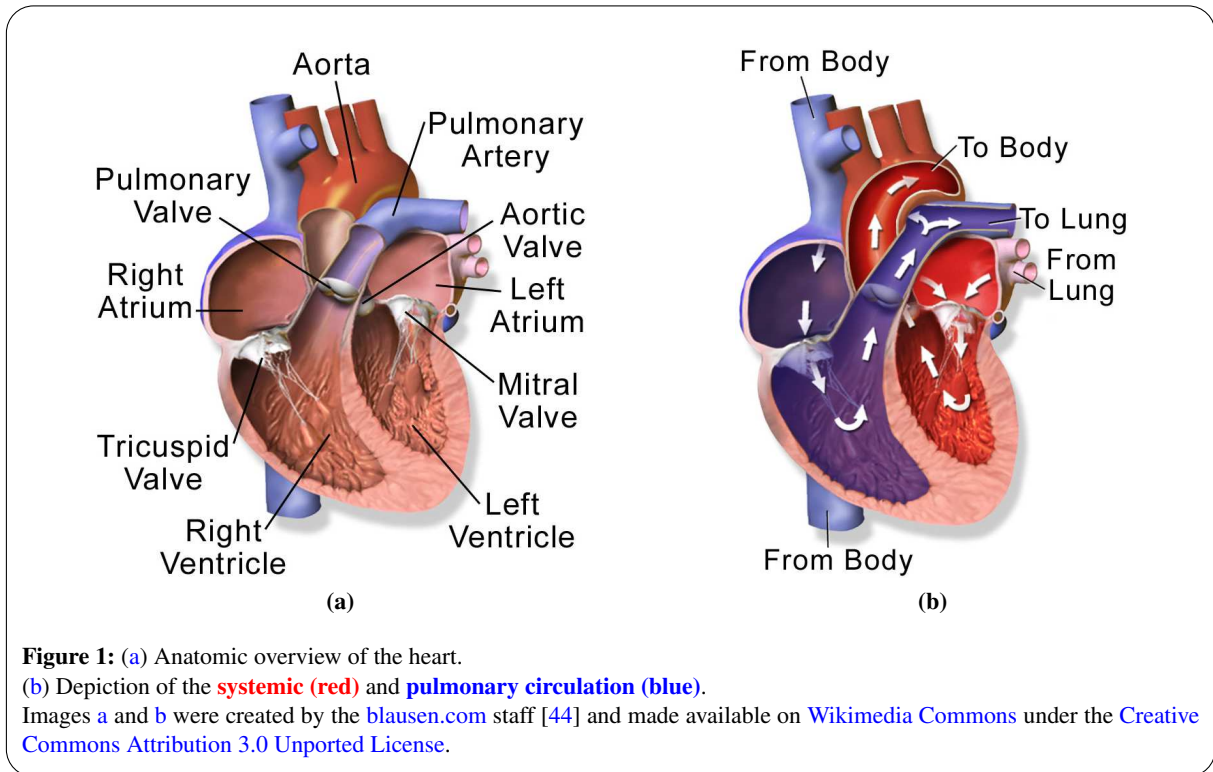
BACKGROUND

2. THE CARDIOVASCULAR SYSTEM

This chapter provides an anatomical overview of the heart, the circulatory system, and selected cardiovascular diseases (CVDs) with emphasis on the aorta and pulmonary artery.

2.1. HEART ANATOMY AND BLOOD CIRCULATION

Both heart halves consist of an *atrium* and *ventricle*, which are connected through a valve (see Figure 1a). This is the tricuspid and mitral valve in the *right* (RV) and *left* ventricle (LV), respectively. The *aorta* (Ao) is attached to the LV, separated through the tricuspid *aortic valve* (AV). Tricuspid means that it consists of three leaflets. The crooked aorta is the largest artery in the body with a diameter of about 2.5–3.5 cm and 30–40 cm length [447]. Its vessel sections are commonly divided into the *aortic root*, located at the AV, the *ascending aorta* (AAo) behind the AV, the *aortic arch* and the *descending aorta* (DAo). The *pulmonary artery* (PA) is connected to the RV and separated through the *pulmonary valve* (PV). The *main PA* (also: *pulmonary trunk*), directly behind the PV, splits into the *left* (LPA) and *right pulmonary artery* (RPA), which reach to the left and right half of lung, respectively.



The main purpose of the cardiovascular system is to control the blood flow to various parts of the body [427]. A heart beat consists of two phases: *Systole* and *diastole*. During systole, oxygenated blood is pumped from the left ventricle into the aorta (see Figure 1b). The otherwise closed aortic valve is open at this point. Smaller arteries branch off the aorta and supply the blood to all body regions. The blood is transported back to the right atrium through veins. This part of the circulatory system is called *systemic circulation*. Also during systole, deoxygenated blood is pumped from the right ventricle into the pulmonary artery through the opened pulmonary valve. The blood is enriched with oxygen in the left and right half of lung and then transported to the left atrium. This process is referred to as *pulmonary circulation*. The ventricles are refilled during diastole with blood coming from the left and right atrium through the opened tricuspid and mitral valve, respectively. The next heart beat begins.

The heart's shape facilitates efficient blood supply to the lung [264]. However, the blood flow leads to shear forces on the vessel walls, which causes a continuous remodeling of the heart morphology and vessel tissue [147].

2.2. CARDIOVASCULAR DISEASES

Cardiovascular diseases (CVDs) are the number one cause of death worldwide [357]. The World Health Organization (WHO) reports:

- "In 2012, an estimated 52 % of all deaths under age 70 was due to noncommunicable diseases (NCDs), and two thirds of those deaths were caused by cardiovascular diseases (CVD), cancer, diabetes and chronic respiratory disease. Premature mortality rates due to NCDs declined globally by 15 % between 2000 and 2012. A major factor is the decrease in CVD mortality, driven by population-level blood pressure improvements, declines in tobacco use and advances in medical treatment. Declines have been greater in high-income countries than in the low- and middle-income countries." (Boerma et al. [49, page 133])
- "The leading risk factor for CVD is high blood pressure." (Boerma et al. [49, page 135])
- "More people die annually from CVDs than from any other cause, with an estimated 17.5 million deaths in 2012 (46 % of all noncommunicable disease deaths) [564]. Of these deaths, an estimated 7.4 million were due to coronary heart disease and 6.7 million were due to stroke. Around one third of these CVD deaths occur in adults age 30–70, which are the focus of the global NCD and sustainable development goals (SDG) targets." (Boerma et al. [49, page 140])

Besides the death toll itself, this represents an enormous cost factor for the health systems. For example, the direct and indirect cost of CVDs and stroke in the United States in 2011 were [373]:

- 215.6 billion USD for heart disease,
- 46.4 billion USD for hypertension,
- 33.6 billion USD for stroke, and
- 24.6 billion USD for other CVDs.

In the European Union, about 196 billion Euro are spent annually. Of this total cost "around 54 % is due to health care costs, 24 % due to productivity losses and 22 % due to the informal care of people with CVDs." (Nichols et al. [382])

In the following, an overview of selected CVDs is given, which are relevant for the further understanding of this thesis. Conventional diagnostic methods and treatments are explained as well.

PARTS OF THIS OVERVIEW ARE BASED ON:

- [270, SECTION 3.1]: **B. KÖHLER, R. GASTEIGER, U. PREIM, H. THEISEL, M. GUTBERLET, AND B. PREIM.** "SEMI-AUTOMATIC VORTEX EXTRACTION IN 4D PC-MRI CARDIAC BLOOD FLOW DATA USING LINE PREDICATES". IN: *IEEE Transactions on Visualization and Computer Graphics* 19.12 (2013), PP. 2773–82. DOI: [10.1109/TVCG.2013.189](https://doi.org/10.1109/TVCG.2013.189)
- [278, SECTION 3.2]: **B. KÖHLER, U. PREIM, M. GROTHOFF, M. GUTBERLET, K. FISCHBACH, AND B. PREIM.** "ROBUST CARDIAC FUNCTION ASSESSMENT IN 4D PC-MRI DATA OF THE AORTA AND PULMONARY ARTERY". IN: *Computer Graphics Forum* 35.1 (2016), PP. 32–43. DOI: [10.1111/CGF.12669](https://doi.org/10.1111/CGF.12669)
- [277, SECTION 3]: **B. KÖHLER, U. PREIM, M. GROTHOFF, M. GUTBERLET, K. FISCHBACH, AND B. PREIM.** "MOTION-AWARE STROKE VOLUME QUANTIFICATION IN 4D PC-MRI DATA OF THE HUMAN AORTA". IN: *International Journal for Computer Assisted Radiology and Surgery* 11.2 (2016), PP. 169–79. DOI: [10.1007/s11548-015-1256-4](https://doi.org/10.1007/s11548-015-1256-4)

SEE SECTION [PUBLICATIONS](#) IN THE APPENDIX FOR THE DIVISION OF WORK.

2.2.1. ALTERATIONS OF THE VESSEL WALL

This group of CVDs refers to changes of the vessel wall due to different causes, e.g., inflammatory processes.

ECTASIA AND ANEURYSM: A pathologic vessel dilation up to $1.5\times$ the original vessel diameter is referred to as *ectasia*. Above a factor of 1.5 the term *aneurysm* is applied (see Figure 2a). Aneurysms bear the risk of rupture, which is fatal in most cases for heart vessels.

STENOSIS AND COARCTATION: On the contrary, a pathologic narrowing of the vessel is named *stenosis*. If the aortic arch is affected, it is referred to as *coarctation* (see Figure 2a). A stenosis can cause increased flow velocities and raised pressure before the narrowed region. The severity is graded by the percentaged area of the vessel's cross-section that is blocked. Depending on whether the vessel is blocked equally from all sides or primarily from one side, a stenosis is *concentric* or *eccentric*. A potential cause for eccentric stenoses is *plaque* [240] (see Figure 2b). Moreover the length of the stenotic vessel section is of interest for the classification.

AORTIC DISSECTION: A tear in the inner layer of the aortic wall allows blood to flow between the inner and outer wall layer, which causes their separation (see Figure 2c). The outer layer is widened pathologically and bears a high risk of rupture, which is fatal in most cases. Lansman et al. [298] described different subtypes of *aortic dissection*.

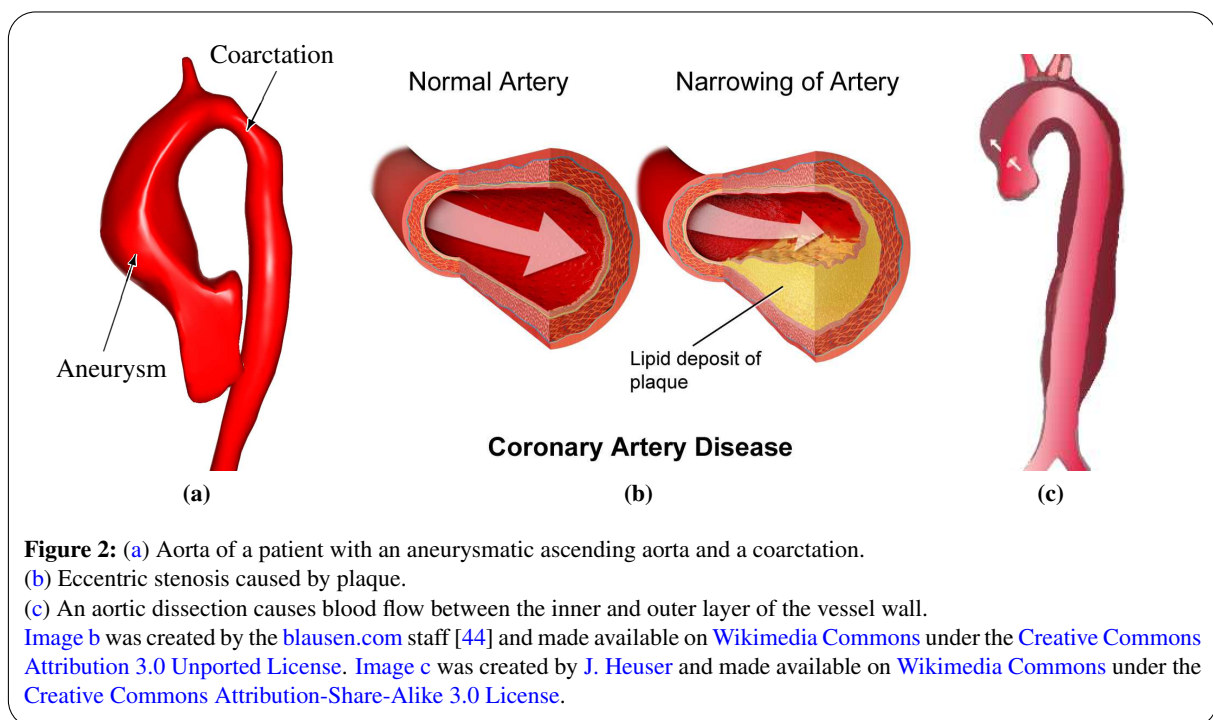


Figure 2: (a) Aorta of a patient with an aneurysmatic ascending aorta and a coarctation.

(b) Eccentric stenosis caused by plaque.

(c) An aortic dissection causes blood flow between the inner and outer layer of the vessel wall.

Image b was created by the [blausen.com](#) staff [44] and made available on [Wikimedia Commons](#) under the [Creative Commons Attribution 3.0 Unported License](#). Image c was created by [J. Heuser](#) and made available on [Wikimedia Commons](#) under the [Creative Commons Attribution-Share-Alike 3.0 License](#).

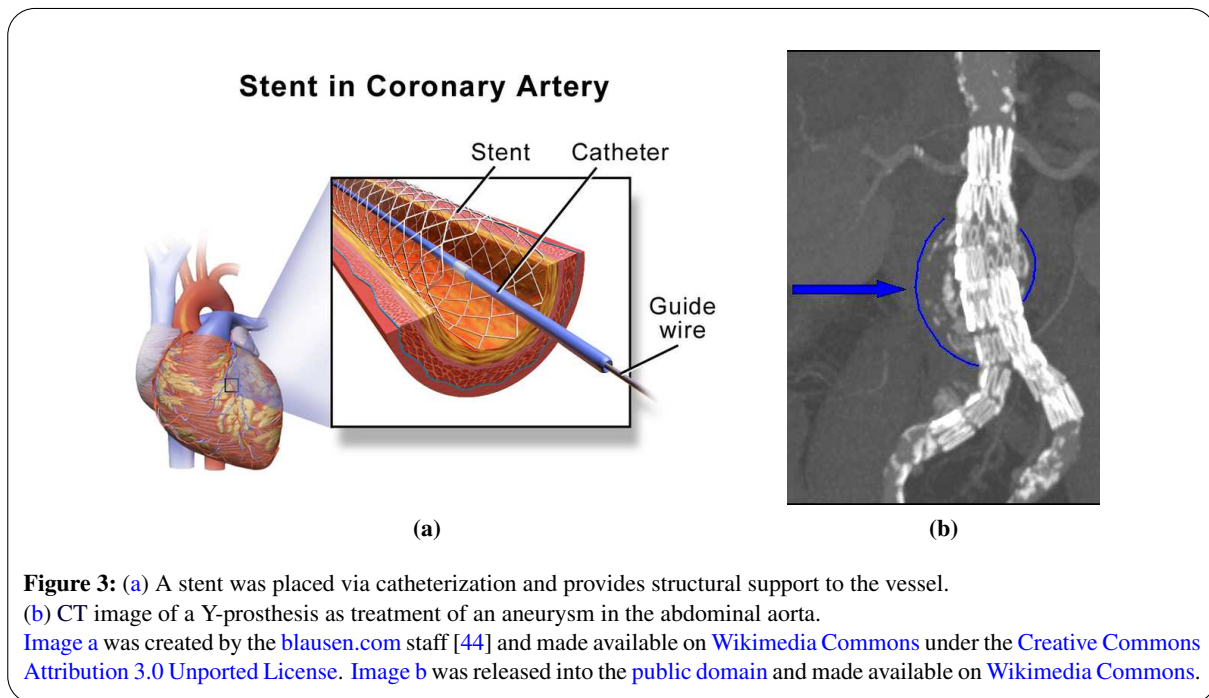
PULMONARY HYPERTENSION: *Pulmonary hypertension* [350, 477] (PAH) begins with an inflammation of pulmonary arteries' (PA) vessel wall cells. Here, small PAs and capillaries in the lung are meant. These PAs become blocked, narrowed or even destroyed, which complicates blood transport. The (right) heart's workload increases, resulting in raised blood pressure. In the long run, PAH causes a weakening of the heart muscle and eventually its failing.

DIAGNOSIS AND TREATMENT: Shape alterations can be diagnosis with *morphological scans* from multislice spiral CT or MRI. In combination with contrast agent it is referred to as MR or CT angiography. For example, the latter can be used to assess plaques [186]. Unfortunately, the image resolution of MR or CT is too coarse to obtain information on the vessel wall, e.g., the thickness. *Cardiac catheterization* in combination with contrast agent and X-rays facilitates the detection of narrowed or blocked vessels. Interventions, such as balloon dilatation, can be performed to widen a narrowed vessel and stents can be placed to provide structural support to the vessel (see Figure 3a). However, catheters are usually inserted in the arm or groin. Navigation to the heart requires in-depth knowledge of the circulatory system and much experience, since the toxic contrast agent in combination with X-ray

imaging can only be used scarcely. Severe stenoses can be treated with a *bypass surgery*, which is a highly invasive and risky procedure. A possible treatment for pathologic vessel dilations is to insert a vascular prosthesis as an artificial vessel course (see Figure 3b). This detains blood from flowing close to the weakened vessel wall and decreases the chance of further dilation or rupture. An *aortic valve-sparing surgery* [112] is an advanced procedure where the, e.g., aneurysmatic, aortic root can be replaced while preserving the native aortic valve.

Aortic dissection typically causes a severe pain in the chest, back or between the shoulder blades. Other symptoms comprise clammy skin and an elevated heart rate. Since these could also be caused by other, more common conditions, a dissection might be difficult to diagnose without initial suspicion. However, a quick diagnosis is important to increase the chance of survival in case of rupture [145, 260, 505]. The widened outer layer of the aortic wall can be assessed using X-ray, CT or an MR angiography. As a treatment the aorta can be reconstructed using a *stent-graft* [139]. If the aortic valve took damage as well, it can be replaced. It has been shown that hemodynamics play an important role in the evolution of aortic dissection [5].

Symptoms like shortness of breath, chest pain and tiredness, which may limit physical activity, are typical for pulmonary hypertension [170]. PAH can be diagnosed by anamnesis or physical examination. Both echocardiography and catheterization are employed to assess right heart pressure and function. Unfortunately, there is no cure for PAH. Corresponding treatments aim at reducing symptoms and increasing the quality of life.



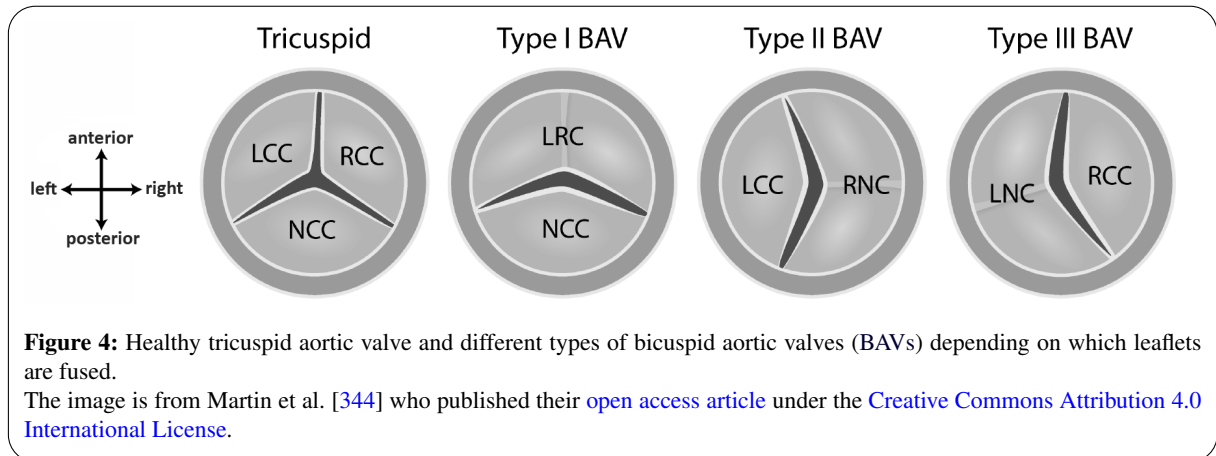
2.2.2. VALVE PATHOLOGIES

Pathological valve alterations comprise morphological changes as well as malfunctions [383].

STENOSIS: Similar to vessels, a *stenotic* valve is abnormally narrowed. This is the most frequent valvular heart disease in Europe and North America [27]. The valve orifice area is used to grade the severity of the stenosis [171]. "The aortic valve area (AVA) must be reduced to roughly one-fourth its normal size before any significant changes occur in hemodynamics [57]." (Garcia and Kadem [171])

INSUFFICIENCY: If a valve does not close properly to prevent blood from flowing back, e.g. to the ventricle, it is *insufficient*, which negatively affects the cardiac function. The percentage of blood that flows back is called *regurgitation fraction* (RF). It is used as a measure of severity.

BICUSPID AORTIC VALVE: The most common aortic valve malformation, with a prevalence¹ of 1–2 % [155], is the *bicuspid aortic valve* (BAV). In this case, two of the normally three valvular leaflets are fused (see Figure 4). In the majority of cases this is inherited, but it also can develop during the lifetime. The constant hemodynamic dysfunction due to the valve’s altered opening characteristics can lead to an aortic valve stenosis and / or insufficiency. ”BAV may account for more morbidity and mortality than all other congenital cardiac malformations combined.” (Hope et al. [220])



DIAGNOSIS AND TREATMENT: *Cardiac catheterization* allows to assess a valve’s function and to determine the blood flow and pressure in the heart chambers (atria, ventricles) as well as the vessels. Besides MRI, BAVs can be diagnosed using an *echocardiogram*, which is an ultrasound of the heart (see Section 3.2). Valve replacement is a possible treatment of valve pathologies. However, this is highly invasive and should only be performed when a positive benefit-risk ratio is likely. Current medical research investigates less invasive methods, such as *transcatheter aortic-valve implantation* [430] (TAVI), where a heart valve can be replaced via catheterization.

2.2.3. COMPLEX CONGENITAL PATHOLOGIES

This category refers to hereditary diseases that are often characterized by a multitude of conditions.

TETRALOGY OF FALLOT: *Tetralogy of Fallot*² (ToF) is the most common, inherited, cyanotic heart disease. This complex condition consists of four components (see Figure 5):

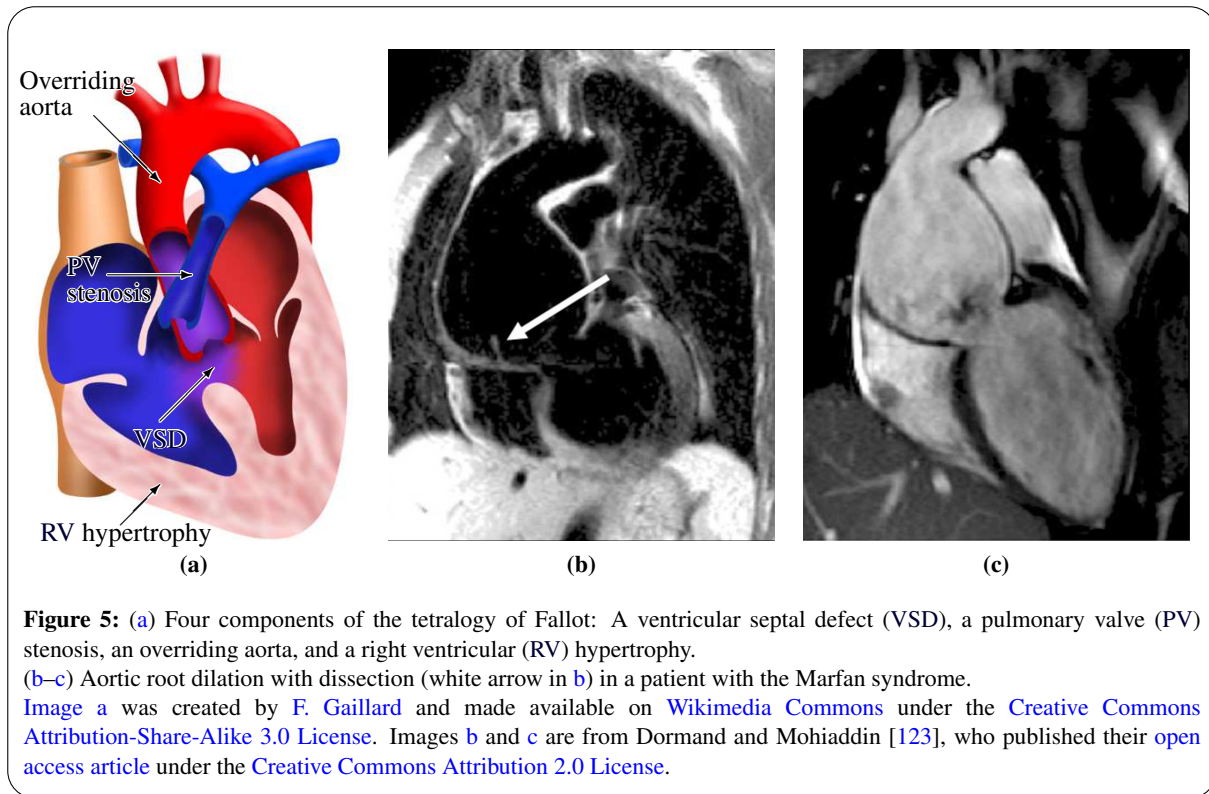
- A *ventricular septal defect* (VSD) is a hole in the wall (septum) between the left and right ventricle, which causes a mixture of oxygenated and deoxygenated blood in the left ventricle.
- Due to a pulmonary valve stenosis, the mixed blood from both ventricles is preferably pumped through the aorta. This behavior is called *right-to-left shunt*.
- The constantly increased resistance due to the PV stenosis promotes the development of a *right ventricular hypertrophy* – an enlargement of the heart muscle.
- An *overriding aorta* names a special malpositioning where the aorta is directly positioned over the VSD instead of the left ventricle.

MARFAN SYNDROME: The *Marfan syndrome*³ is a genetic disorder of the connective tissue. Marfan patients show an increased susceptibility to developing aneurysms due to ”*altered mechanical properties of the aortic wall related to the decreased aortic elasticity*.” (Geiger et al. [181]) This strongly increases the risk of aortic dissection (see Figures 5b–c). Dormand and Mohiaddin [123] provided a corresponding overview.

¹Prevalence is the percentage of a population that has a specific condition.

²Named after the French physician Étienne-Louis Arthur Fallot.

³Named after the French pediatrician Antoine Marfan.



DIAGNOSIS AND TREATMENT: ToF is a cyanotic disease, where the blood oxygen levels are low. Thus, suspicion is raised if a baby has blueish skin. Other symptoms comprise enlarged skin or bones around the fingernails, a poor overall development and occasional dizziness due to the oxygen deficiency. Nowadays ToF is surgically corrected within months after birth [548]. The VSD is closed and the PV stenosis is treated. However, ToF patients are highly vulnerable to developing a post-operative pulmonary valve insufficiency.

Marfan syndrome can be diagnosed using an echocardiogram of the heart, an eye examination to see if the lenses are out of place, and a CT or MRI of the lower back to check if the sac around the spinal column is swollen. The Marfan syndrome itself cannot be cured. Thus, the treatments depend on the developing secondary diseases.

2.2.4. COLLECTIVE TERMS

This section defines umbrella terms for heart conditions with similar symptoms and outcomes.

CONGESTIVE HEART FAILURE: *Congestive heart failure* (CHF) denotes the inability of the heart to supply enough blood to the body. This can be caused by a limited pumping capacity of the heart due to a damaged heart muscle (*cardiomyopathy*), e.g., from drug abuse or infection. Also, the heart muscle can be damaged during a heart attack, where the coronary arteries, which supply oxygen to the heart muscle, are blocked. This can promote the forming of improperly functioning scar tissue. Other causes are valve-related. Regurgitation fractions up to 5 % are considered as physiological and unproblematic [560], whereas higher values can indicate CHF.

CONGENITAL HEART DISEASE: *Congenital heart diseases* [335] (CHDs) refer to inherited pathologies in general. These can be valve defects, problems with the heart muscle, the vessel walls or conditions of specific blood vessels – for example tetralogy of Fallot or aortic coarctation [530].

DIAGNOSIS AND TREATMENT: Besides physical examination, angiographies and blood tests, the individual patient history is important to diagnose CHF or CHD. A gold standard does not exist. Also, treatments depend on the patient-specific symptoms and causes. Modifications of the lifestyle might be appropriate, e.g., in case of a self-induced cardiomyopathy.

2.3. SUMMARY

CIRCULATORY SYSTEM: The *aorta* (Ao) is attached to the *left ventricle* (LV), the *pulmonary artery* (PA) to the *right ventricle* (RV). A heart beat consists of *systole*, where blood is ejected from the LV and RV to the body and lung, respectively, and *diastole*, where both ventricles are refilled.

CARDIOVASCULAR DISEASES: CVDs are the number one cause of death in the world and a cost burden to the health systems. Vessel morphology alterations comprise pathologic dilations (*ectasia*, *aneurysm*), narrowings (*stenosis*, *coarctation*) as well as obstructions (due to *plaque* or vessel wall *inflammation*, e.g., of lung capillaries in *pulmonary hypertension* (PAH)), and tears (*aortic dissection*, *aneurysm rupture*). Valve pathologies comprise *stenosis* (reduced orifice area), *insufficiency* (no proper closing, blood flows back), and altered morphology (*bicuspid aortic valve* (BAV)). Congenital diseases (*tetralogy of Fallot* (ToF), *Marfan syndrome*) consist of multiple components. Marfan patients are prone to aneurysm development. *Congestive heart failure* (CHF) and *congenital heart disease* (CHD) are collective terms for pathologies that affect the sufficient blood supply or that are inherited, respectively.

Conventional diagnostic tools comprise *morphological scans* (CT, MRI), *angiographies* (CT and MRI with intravascular contrast agent), patient *anamnesis* or *echocardiography* (ECG, ultrasound-based imaging). *Cardiac catheterization* allows to determine various cardiac function parameters, such as pressure, but is invasive, causes patient stress, and requires highly skilled performing physicians.

Vessel dilations can be treated with *vessel prostheses* (artificial vessel courses, often supported with a *stent*) or replacement of the corresponding vessel section, e.g., aortic root replacement. A *bypass surgery* can be performed in case of severe narrowings. Mild cases can be widened via *balloon dilatation*, where a subsequently placed *stent* provides structural support to the vessel. Malfunctioning valves can be replaced (highly invasive surgery) or reconstructed (repaired via catheterization, less invasive). ToF is corrected within months after birth, though, later development of pulmonary insufficiency is likely.

CRITICISM: Blood flow and its interaction with the vessel wall is considered insufficiently with current methods. A fully comprehensive picture of the patient situation might not be obtained.

3. CARDIAC BLOOD FLOW MEASUREMENTS

This chapter explains the ideas behind four-dimensional phase-contrast magnetic resonance imaging (4D PC-MRI) blood flow measurements, characterizes the resulting datasets, and considers selected alternatives based on ultrasound. A basic understanding of the data is essential for the comprehension of existing and development of new analysis methods.

3.1. 4D PHASE-CONTRAST MRI

This section starts with an explanation of general MRI measurements [230], followed by an adaption of this principle that facilitates the measurement of instationary blood.

3.1.1. MRI BASICS

INTRODUCTION: *Magnetic resonance imaging* (MRI) [202] is a non-invasive imaging modality that allows the acquisition of slice images. For a historical overview, please consider Rinck [429]. MR scanners are available in most hospitals. Different *scan sequences* enable a wide variety of possible applications, e.g.:

- T_1 and T_2 are standard sequences that provide a decent contrast in soft tissue and fluids.
- *Functional MRI* (fMRI) [163, 321] facilitates the measurement of neuronal activity.
- *Diffusion tensor imaging* (DTI) [372] allows to obtain directions of fiber bundles in the brain.
- *Phase-contrast MRI* (PC-MRI) – the central topic of this thesis – enables the measurement of blood flow directions and velocities in, e.g., the heart, the head [20] and the liver [487].

Strong magnetic fields are the basic tool of MRI. Exposure to such fields has no known side-effects. This is a great advantage over other modalities, such as computerized tomography (CT), where ionizing radiation is used that is not always applicable, e.g., in case of pregnancy. Though, MRI has its own restrictions. For instance, it is not applicable for patients with technical gadgets, such as cardiac pacemakers, or if there is metal inside the body. Moreover, it is often more costly in terms of time than other imaging modalities and has a higher consumption of electricity.

The physical principle depicted in this thesis is the classic one, excluding quantum mechanical properties [201]. The goal is to provide only a basic understanding of MRI as well as 4D PC-MRI.

SPINNING PROTONS: MRI exploits a physical property of some atomic nuclei called *spin* [308]. This type of angular momentum can be seen as rotation around an arbitrary, internal axis (see Figure 6). Hydrogen atoms (H), consisting of a *proton* and an *electron*, are most relevant for biomedical applications since the human body consists to approximately two third of water (H₂O) [544]. This allows to distinguish water from fat tissue, but also to encode fluid movement.

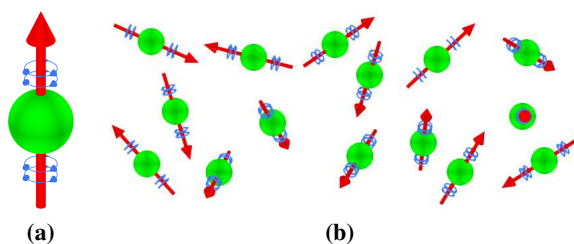


Figure 6: Protons (green) in their natural state.
(a) Each one rotates (blue) around an individual spin axis (red).
(b) Countless protons in the body with arbitrary spin axes.

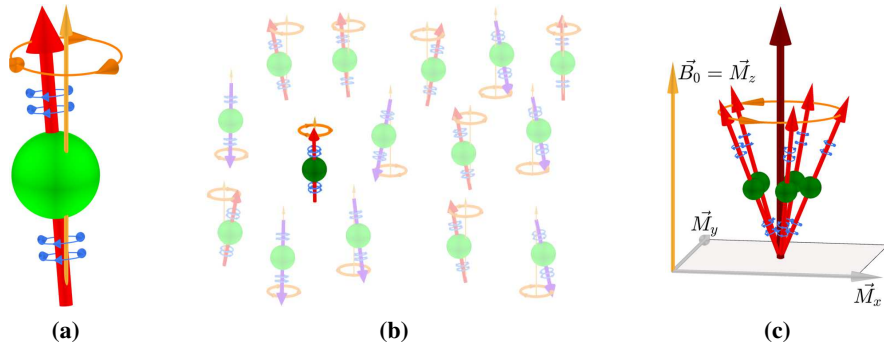


Figure 7: Protons in an active B_0 magnetic field.

(a) The **proton's (green) spin axis (red)** is not fully aligned with the B_0 **direction \vec{B}_0 (orange)**. Instead, a **precession (orange)** like a gyroscope is performed.

(b) A spin axis aligns either parallel or antiparallel to \vec{B}_0 . Pairs of parallel and antiparallel protons (transparent) erase their contribution to an *net (overall) magnetization*. However, as the parallel alignment is energetically more favorable, there are slightly more protons in this state, yielding some **unmatched protons (dark green)**. This configuration is called *equilibrium*.

(c) The sum of **their** magnetic moments provides a **net magnetization \vec{M} (dark red)**, which solely consists of a *longitudinal* part \vec{M}_z , parallel to \vec{B}_0 , at this moment.

SPIN ALIGNMENT: Application of an external magnetic field – the B_0 main magnetic field – causes a proton's spin axis to align either parallel or antiparallel with the B_0 direction \vec{B}_0 , where the parallel alignment is energetically more favorable. Consequently, more protons are in this state with a ratio of 1.000.007 : 1.000.000. This configuration of protons, where solely B_0 is active, is referred to as *equilibrium*.

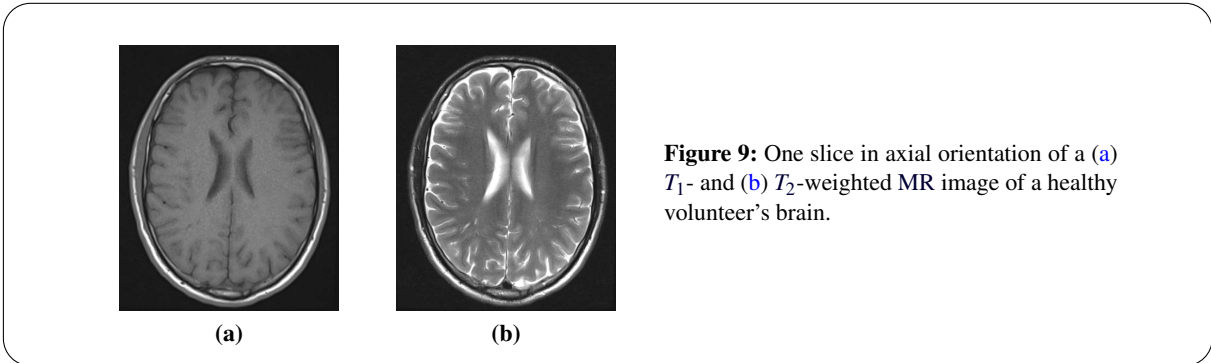
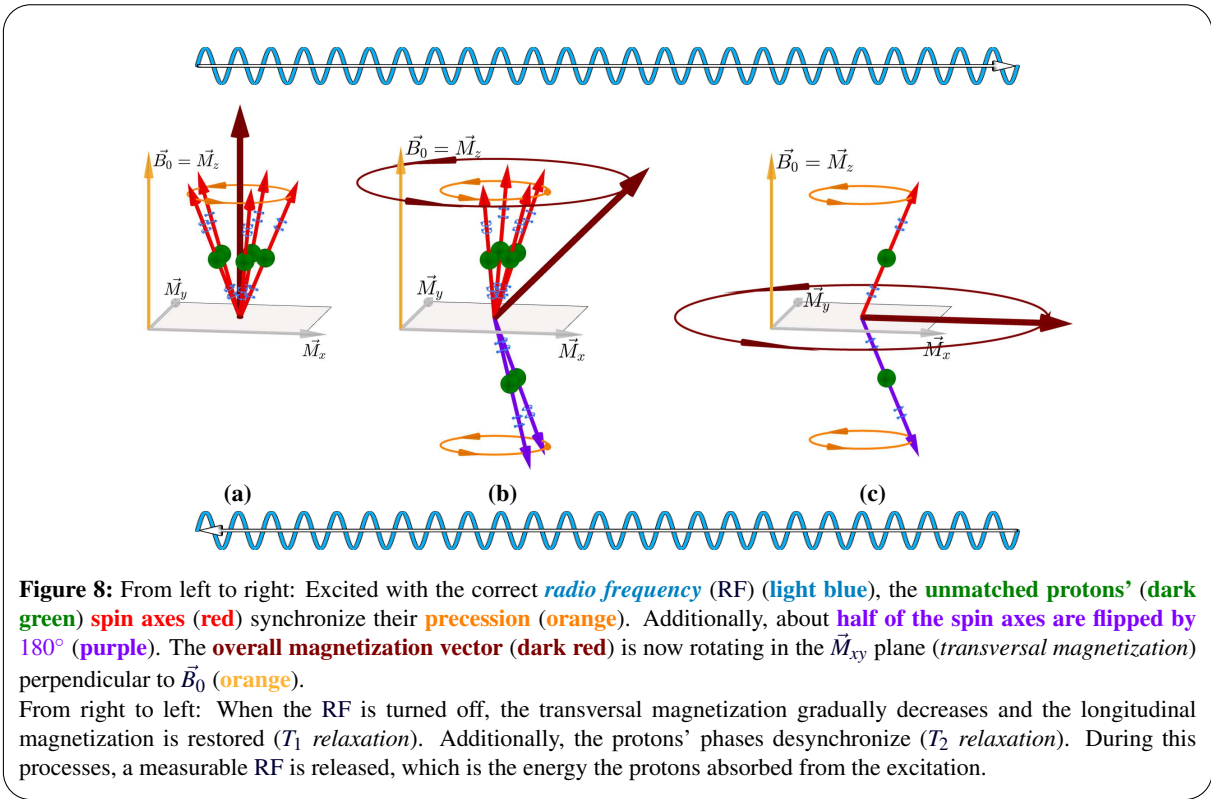
The spin directions are not fully aligned with / parallel to the B_0 direction. Instead, they *precess* around \vec{B}_0 like gyroscopes (see Figure 7a), where the individual precessions are out of *phase* (unaligned, not synchronized). The precession frequency, named *Larmor frequency*⁴, is directly proportional to the magnetic field strength and varies for different nuclei. The Larmor frequency of hydrogen nuclei at 1 T field strength is 42.58 MHz. Typical scanners available in clinics achieve 1.5 or 3 T. Some special productions for research purposes achieve even 7 T. For comparison, the earth's magnetic field strength is about 3.2×10^{-5} T at 0° latitude and 0° longitude.

The sum of all protons' magnetic moments yields a *net (also: overall) magnetization \vec{M}* , which increases with higher magnetic field strengths. However, a pair of parallel and antiparallel protons cancel each other out in their effect. Nevertheless, due to the unequal distribution of parallel and antiparallel alignments, there are a few unmatched protons (see Figure 7b). The number of such protons is sufficient for MR imaging due to the vast amount of overall protons in the body, which is approximately $4.7 \cdot 10^{27}$. In the following, the term proton solely refers to unmatched protons. \vec{M} is composed of a *longitudinal* part \vec{M}_z , parallel to \vec{B}_0 , and a *transversal* component \vec{M}_{xy} , orthogonal to \vec{M}_z . The latter is 0 in the equilibrium (see Figure 7c).

EXCITATION AND RELAXATION: When the protons are excited with a *radio frequency (RF)* equal to their Larmor frequency from a direction perpendicular to \vec{B}_0 , about half of the protons spin axes flip by 180° . As a result, the transversal magnetization component \vec{M}_{xy} increases until \vec{M} rotates in a plane perpendicular to \vec{B}_0 (see Figure 8). Additionally, the individual precessions synchronize. During this *phase coherence*, \vec{M} is maximally amplified.

When the RF signal is turned off, the *relaxation* begins. The protons *dephase (spin-spin relaxation)* within the constant time T_2 . It denotes when the transversal magnetization *reduced by* about 63 %. Also, the spin axes recover from the flipping, causing a stepwise restoration of the longitudinal magnetization

⁴Named after the British physicist [Joseph Larmor](#).



\vec{M}_z while the transversal component \vec{M}_{xy} decays. This *spin-lattice relaxation* happens within the constant time T_1 , which is longer than T_2 . It denotes when about 63 % of the longitudinal magnetization are *restored*. Both the T_1 and T_2 relaxation are independent from one another and happen simultaneously.

RESONANCE: An electromagnetic current is induced in a receiver coil by the rotating transverse magnetization during the relaxation. In other words, the protons release the energy that was absorbed from the RF excitation [353]. This provides a measurable RF signal that depends on the amount of hydrogen nuclei in the corresponding tissue (*proton density*), the B_0 magnetic field strength and the T_1 as well as T_2 relaxation times.

A repeated excitation and measurement of the magnetic resonance is necessary to acquire an MR image. Thus, the RF excitation is done as a pulse sequence [33], where the signal is rapidly switched on and off again. The time between two excitations (a scan parameter), during which the longitudinal magnetization can recover, is called *repetition time* (TR). If a low value is chosen, tissue with a short and long T_1 time provides a strong and weak signal, respectively. For example, fat appears bright and water dark in a T_1 -weighted image (see Figure 9a). The time between the excitation and the measurement of the signal is called *echo time* (TE) and is another scan parameter. Small values focus tissue with short T_2 times, such as water, which appears bright in T_2 -weighted images, whereas fat appears dark [424] (see Figure 9b).

SPATIAL ENCODING: In order to create a volumetric image, spatial positions within the body must be distinguishable during the acquisition. The idea is to employ three linear magnetic field gradients for this purpose, i.e., spatially varying magnetic fields that are superimposed on the B_0 field. The direction of each gradient is perpendicular to the other two:

1. As mentioned before, the Larmor frequency is directly proportional to the magnetic field strength. The z -gradient is oriented from head to feet and, therefore, encodes the image slice. *Slice distances* are a result of the steps in which the RF for excitation is incremented during the scan.
2. The y -gradient facilitates the selection of a specific column within a slice. It is turned on and off for a short period of time, directly after the RF, and causes a phase shift of the precessing spin axes. Therefore, it is also called *phase-encoding gradient*.
3. The *frequency-encoding x -gradient* is active together with the z -gradient when the signal is received. It encodes the row by causing a shift in the precession frequencies within the column.

Finally, each image position is uniquely identifiable (see Figure 10). An often employed sequence of RF and gradients pulses is the *spin echo sequence*, as described by Hahn [198].

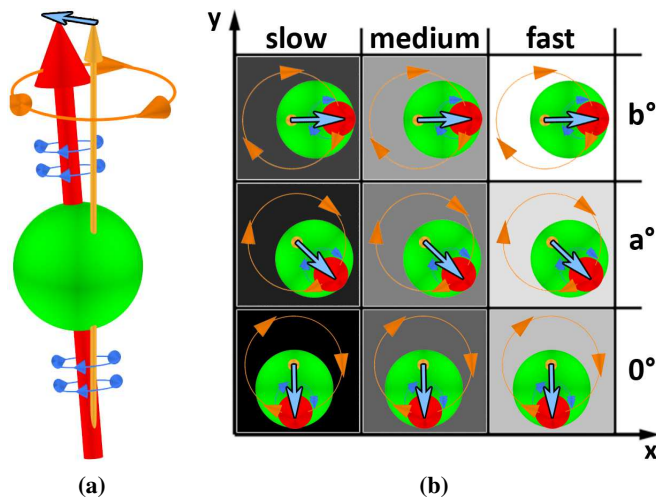


Figure 10: Spatial encoding within a slice.

(a) The phase of a proton's precession is illustrated as **blue vector**.

(b) The *phase-encoding y -gradient* causes a different **phase shift (blue)** for each row ($0^\circ, a^\circ, b^\circ$), whereas the *frequency-encoding x -gradient* alters the speed of the individual precessions (slow, medium, fast). Together they facilitate the selection of a specific position, as indicated by the grayscale background colors.

Image **b** is based on a [learning script for physicians about MRI basics](#) by Dr. med. Christoph Pabst from the [University Hospital Giessen and Marburg](#).

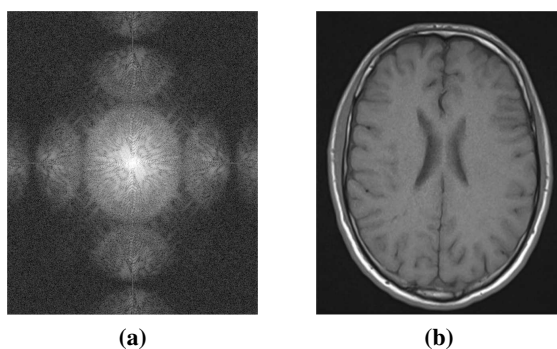


Figure 11: The images show a slice in axial orientation of a T_1 -weighted MR image of a healthy volunteer's brain.

(a) Acquired k -space data matrix, which encodes phase and frequency.

(b) Image reconstruction via inverse Fourier transform.

IMAGE RECONSTRUCTION: If each position was processed individually, an enormous amount of time would be necessary to obtain a slice image. For example, if a slice's grid resolution is 256×256 and each of the 65536 positions takes 10 ms to process, scanning this one slice alone would take nearly 11 min. Therefore, no single points are considered. Instead, row by row is read with a special sequence and composed into a raw data matrix, which is referred to as k -space and encodes both the measured phases and frequencies. An inverse Fourier transform allows to convert this data matrix into an image (see Figure 11). In the example above, this reduces the expenditure of time by a factor of 256 to 2.56 s.

3.1.2. FLOW MEASUREMENT

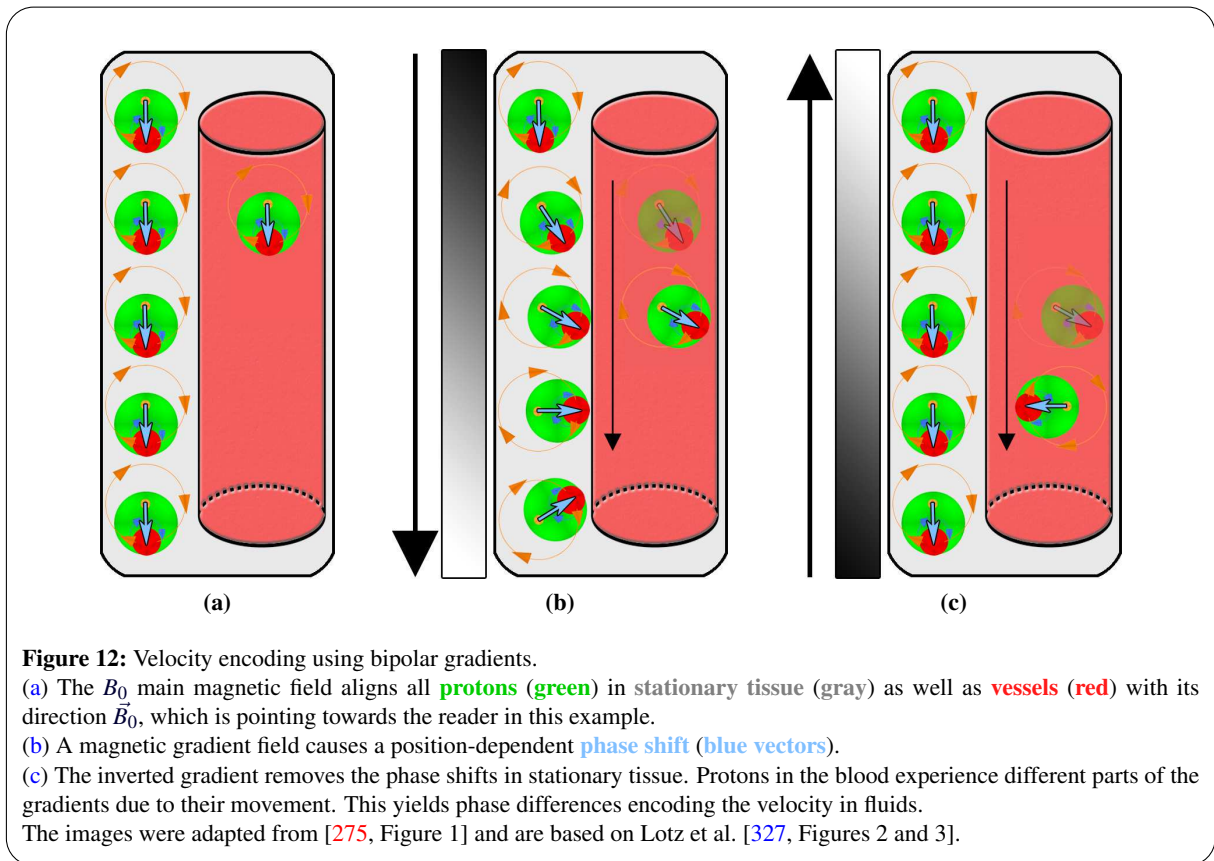
Besides the vessel morphology, information about the direction and velocity of the intravascular blood flow are of interest in the cardiac context.

THIS SECTION IS PARTIALLY BASED ON:

- [275, SECTION 2.1]: **B. KÖHLER**, S. BORN, R. F. P. VAN PELT, A. HENNEMUTH, U. PREIM, AND B. PREIM. “A SURVEY OF CARDIAC 4D PC-MRI DATA PROCESSING”. IN: *Computer Graphics Forum* (2016), EPUB. DOI: [10.1111/cgf.12803](https://doi.org/10.1111/cgf.12803)

SEE SECTION [PUBLICATIONS](#) IN THE APPENDIX FOR THE DIVISION OF WORK.

IDEA: An assumption made in standard MRI acquisitions is that the protons remain stationary. This is not always the case due to various movements within the body, such as the respiratory motion (breathing), the heart contraction, vessel pulsations, swallowing, and flow (moving fluids). This causes phase differences during the acquisitions, resulting in image artifacts like unwanted blurring or ghosting, which denotes displaced image duplications in direction of the phase encoding. However, exactly this motion sensitivity of MRI is exploited for flow measurements. While *magnitude images* are the ones reconstructed from the k-space, an additional possibility is to generate specific *phase images*. This is the central idea of blood flow measurements: Encode velocity using phase information.



BIPOLAR GRADIENTS: For this purpose, the MRI sequence is slightly modified. After application of the slice-selecting z-gradient and before the phase- as well as frequency-encoding, two *bipolar gradients* are superimposed on the B_0 field. Bipolar means that the gradients have the same strength but opposite directions.

The protons' spin axes are aligned with the B_0 direction and the protons were excited with the RF, which causes phase coherence (see Figure 12a). Now, a new magnetic field gradient (the first of the bipolar gradients) is applied. It causes a position-dependent phase shift in both stationary tissue as well as in

fluids (see Figure 12b). Application of the same gradient in opposite direction removes this phase shift in stationary tissue. Protons in the blood flow, however, have moved a certain distance. Consequently, they experience a different part of the gradient. Two acquisitions are performed – one with the first and one with the second of the bipolar gradients active. The rest of the sequence is unaltered. Afterwards, both images are subtracted. The resulting *phase difference* is directly related to the flow velocity (see Figure 12c). For a more detailed explanation, please see Lotz et al. [327], Markl et al. [342], or Stankovic et al. [488].

THE V_{ENC} PARAMETER: The two bipolar magnetic field gradients are adjusted so that the maximum phase shifts of $\pm 180^\circ$ correspond to the *velocity encoding* (V_{ENC}). This essential scan parameter describes the maximum measurable blood flow velocity between $\pm V_{ENC}$ [m/s] per dimension. Exploiting the full range by setting the V_{ENC} to the highest expected velocity is desired to obtain higher phase differences, resulting in increased image contrast and quantitative precision. Unfortunately, the V_{ENC} has to be estimated based on experience, especially for pathologic cases. A common choice for aortic blood flow is $V_{ENC} = 1.5$ m/s [336, 342]. Flow velocities in the ventricles or pathologically narrowed vessels may differ greatly from this value. It has been shown that the achieved signal-to-noise ratio (SNR) is inversely proportional to the chosen V_{ENC} . Thus, adjusting the scan to the blood flow in a specific region is crucial for a successful acquisition.

Buonocore [75] used a modified MR sequence that allows the usage of two V_{ENC} values. He used 2 and 0.3 m/s during systole and diastole, respectively, leading to significantly improved ascending aortic flow measurements. However, this has not been used for clinical routine so far [327]. Nett et al. [379] also described a dual V_{ENC} approach. They combined flow images with different V_{ENC} to cover a wide range of velocities (high V_{ENC}) and still obtain a decent contrast (low V_{ENC}). However, acquisition times increase and an image composition scheme is required.

ACCELERATION TECHNIQUES: Acquisition times are a crucial factor for the applicability of 4D PC-MRI in the clinical routine. Advances in recent years reduced scan times from more than 30 min to about 8–12 min for the aorta and 10–20 min for the whole heart [488]. Nayak et al. [375] provided an overview of corresponding techniques, such as the *broad-use linear speed-up technique* (k-t BLAST) [510], *sensitive encoding* (k-t SENSE) [422], and *generalized autocalibrating partially parallel acquisitions* (k-t GRAPPA) [190]. Schnell et al. [458] reduced scan times by 28–68 % using k-t GRAPPA. Hess et al. [215] demonstrated an increased SNR at 7 T field strength, compared to flow acquisitions using 1.5 T and 3 T, which can be utilized to accelerate the scans or improve image resolutions.

REPEATABILITY: Greil et al. [189] examined different sets of scan parameters using a pulsatile flow phantom with properties similar to aortic tissue. They concluded that 4D PC-MRI is both accurate and reproducible. The selected *field of view* (FOV) had the biggest influence on the results, since larger FOVs produce lower spatial resolutions. This enhances partial volume effects and results in higher measured flow velocities. Wentland et al. [552] found a strong repeatability of 4D PC-MRI measurements in a study with ten healthy volunteers where each individual was scanned twice. The reproducibility of systolic flow velocities and wall shear stress (see Section 6.2.1) in healthy volunteers was confirmed by Van Ooij et al. [521].

3.1.3. DATASET DESCRIPTION

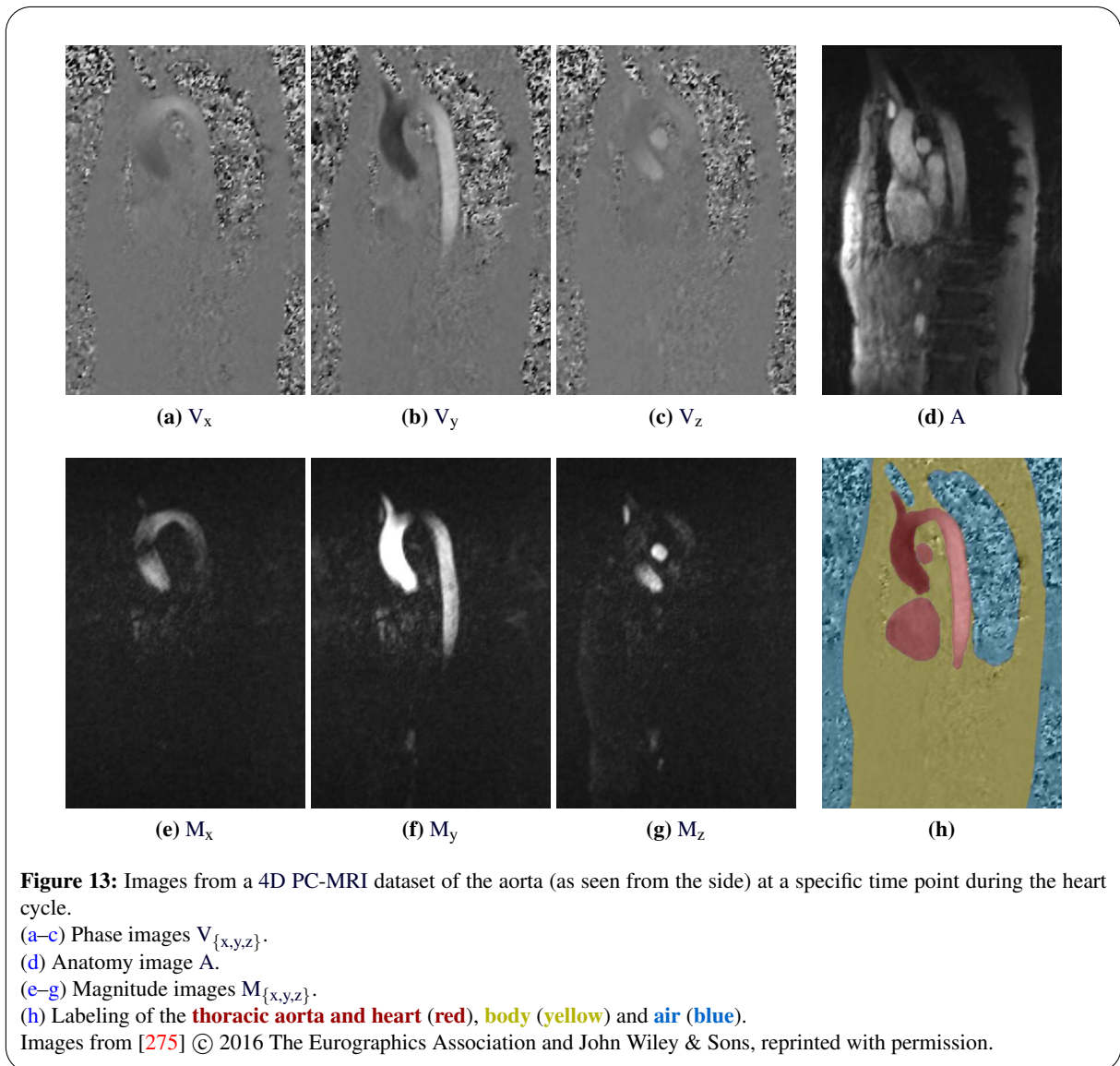
THIS SECTION IS BASED ON:

- [275, SECTION 2.1]: **B. KÖHLER, S. BORN, R. F. P. VAN PELT, A. HENNEMUTH, U. PREIM, AND B. PREIM.** “A SURVEY OF CARDIAC 4D PC-MRI DATA PROCESSING”. IN: *Computer Graphics Forum* (2016), EPUB. DOI: [10.1111/cgf.12803](https://doi.org/10.1111/cgf.12803)

SEE SECTION [PUBLICATIONS](#) IN THE APPENDIX FOR THE DIVISION OF WORK.

Three *phase* (also: *gradient* or *velocity*) images $V_{\{x,y,z\}}$ are reconstructed by calculating all phase differences. Each image contains the velocity values in one of the spatial directions x , y and z (see Figures 13a–c). From these three components, a 3D velocity vector field V is reconstructed, which forms the basis of all further flow analyses. Another reconstruction process yields undirected flow strengths into three *magnitude* images $M_{\{x,y,z\}}$. These data are less error-prone to uncorrelated noise (see Figures 13e–g). In an analogous manner, one combined magnitude image M is generated. However, this is not suitable for the calculation of quantitative measures. An *anatomy* image A is derived from averaging signal intensities (see Figure 13d). There is an ambiguity, as some papers refer to this as magnitude image instead.

A dataset contains a full heart beat, which is the average of multiple cardiac cycles during several minutes. Typical resolutions are 1.5–2.5 mm between data points in a slice, with slice distances of 2–4 mm and 20–50 ms between subsequent time steps, often abbreviated as, e.g., $2 \times 2 \times 3.5 \text{ mm} / 40 \text{ ms}$. This yields a grid with about 150×200 voxels in each of the 20–50 slices and 15–40 temporal positions. The data are usually stored in a 12 bit unsigned integer. Values range from 0 to 4095, where 2048 corresponds to zero velocity, and values below and above 2048 correspond to negative and positive velocities along the current spatial dimension, respectively.



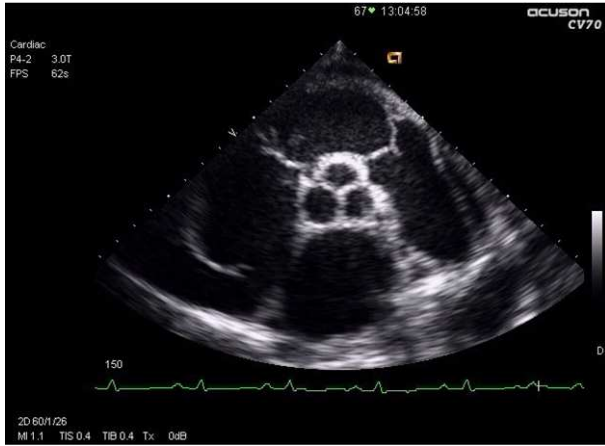


Figure 14: Ultrasound examination of the tricuspid aortic valve.

The image is in the [public domain](#) and was made available on [Wikimedia Commons](#).

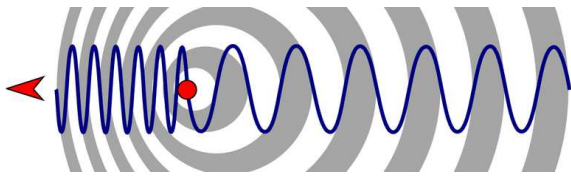


Figure 15: The *Doppler effect*. Sound waves (dark blue) are of different frequency depending on the sound source (red).

The image is in the [public domain](#) and was made available on [Wikimedia Commons](#).

3.2. ECHOCARDIOGRAPHY

Echocardiography (ECG) is based on *ultrasound waves* [184] – in the medical context with 1–40 MHz [125]. The sound waves travel through different tissues with different velocities, e.g., fat with 1460 m/s, blood with 1570 m/s, and bone with 3500 m/s. When passing tissue, a part of the waves is reflected (*echo*). The higher the tissue density is, the stronger is the reflection. An analysis of the *transit time* allows a calculation of the tissue depth. The *echo intensity* is mapped to grayscale. The main applications of echocardiography are assessment of the anatomy, ventricular function, and stenotic or insufficient valves (see Figure 14).

3.2.1. DOPPLER ECHOCARDIOGRAPHY

Doppler ECG (also: *Doppler Ultrasound* [204]) exploits the *Doppler effect*⁵ (also: *Doppler shift*), which describes a frequency change of sound waves when the sound source is moving, depending on the direction of this movement. If the sound source comes closer, the frequency increases, and if the sound source moves further away, the frequency decreases (see Figure 15).

Like in common ultrasound examinations, the sound waves are reflected – in this case by blood cells. Due to their movement inside the vessel, the sound waves experience a frequency change directly related to the blood flow velocity $\|\vec{v}\|$ [369]:

$$\Delta F = \frac{2 \cdot F_0 \cdot \|\vec{v}\| \cdot \cos(\alpha)}{C} \quad \rightarrow \quad \|\vec{v}\| = \frac{\Delta F \cdot C}{2 \cdot F_0 \cdot \cos(\alpha)} \quad (1)$$

ΔF is the frequency shift due to the Doppler effect, F_0 is the emitted frequency, α is the angle between the blood flow and sound waves, and C is the velocity of the sound waves in the corresponding tissue. It can be seen that the angle of the emitted sound waves by the ultrasound probe is critical. Since $\cos(0) = +1 \hat{=} 0^\circ$ and $\cos(\pm\pi) = -1 \hat{=} \pm 180^\circ$, sound waves aligned parallelly with the flow direction provide the best results. The opposing signs allow to distinguish between blood receding from and approaching the transducer (see Figure 16). No velocities can be obtained for perpendicular

⁵Named after the Austrian mathematician and physicist [Christian Andreas Doppler](#).

alignments, since Equation 1 is not defined for $\cos(\pm\pi/2) = \cos(\pm 3/2 \cdot \pi) = 0$. As a consequence, the resulting image quality strongly depends on the performing physician. Also, this lowers the reproducibility. Attempts have been made to use multiple transducers from different angles in order to obtain true flow vectors. Fox et al. [158] employed two transmitting and one receiving transducer(s) simultaneously. The method was used successfully for phantoms, but has not been established in the clinical routine. Swillens et al. [495] revisited this approach (*vector Doppler*) in comparison with others. Grothoff et al. [191] investigated the quantification of pulmonary insufficiency in patients with surgically repaired tetralogy of Fallot. They found that acceptable results can be achieved with Doppler echocardiography compared to 4D PC-MRI.

3.2.2. ECHO PARTICLE IMAGE VELOCIMETRY

Particle image velocimetry (PIV) [2, 508, 558] is an optical method to obtain two-dimensional velocity fields for optically opaque fluids. Tracer particles are seeded, which are then illuminated by a pulsed laser. The now visible particles are recorded by a camera, and the single images are analyzed for the particle patterns (globally, not of individual particles). This yields the flow velocity and direction.

Ultrasound-based PIV [108] uses ultrasound beams as imaging source. This principle is nowadays known as *Echo-PIV* and allows the visualization of blood flow within the cardiac chambers. It facilitates the assessment of blood flow directions and, thus, to generate arrow plots (see Figure 17) or to integrate path lines as depiction of flow patterns. Echo-PIV was successfully used in the clinical practice, e.g., by Hong et al. [218] to analyze left ventricular vortex flow patterns.



Figure 16: Doppler echocardiography of anomalous pulmonary veins. The blood flow directions are color-coded relative to the ultrasound probe in a scale from blue to red, which is a common choice in this context. The image was provided by Nepomuceno et al. [377] on [Wikimedia Commons](#) under the [Creative Commons Attribution 2.0 Generic License](#).



Figure 17: Intraventricular flow evaluation using *echo particle image velocimetry* (Echo-PIV). Flow patterns are shown as arrow plot in real-time. The image is a screenshot taken from a video provided by Lampropoulos et al. [294] on [Wikimedia Commons](#) under the [Creative Commons Attribution 2.0 Generic License](#).

3.3. COMPARISON

THE FOLLOWING COMPARISON OF 4D PC-MRI, DOPPLER ECG AND ECHO-PIV WAS INSPIRED BY TABLE 1 FROM SENGUPTA ET AL. [468], WHO RECENTLY PUBLISHED A CORRESPONDING OVERVIEW OF THESE IMAGING MODALITIES. THEY CONSIDERED MULTIPLE ASPECTS, SUCH AS SPATIO-TEMPORAL RESOLUTIONS, SCAN TIME, LOW- AND HIGH-VELOCITY ACCURACY, AND THE NEED FOR BREATH-HOLDING.

4D PC-MRI: 4D PC-MRI provides a good spatial, three-dimensional resolution and captures all flow directions accurately. The achieved temporal resolution is typically about 20–50 ms between subsequent phases. Advances in recent years reduced the scan times from more than 30 min to about 8–12 min for the aorta and 10–20 min for the whole heart [488]. Each flow-representing phase image is the average of many cardiac cycles. Thus, small scale features, visible only once every heart beat, might be missing in the data. The data evaluation is performed offline. An infinite number of arbitrarily configured measuring planes can be placed after the scan, since the complete spatio-temporal information are available. This also facilitates a large variety of qualitative and quantitative evaluation methods. The maximum measurable flow velocity (the V_{ENC}) is a scan parameter. Exceeding this value leads to image artifacts that can be corrected afterwards – to a certain extent. Breathing control can be used to reduce motion artifacts, but this increases scan times and causes additional patient stress. However, the image quality can also be preserved without it [258]. MRI is not suitable for patients with cardiac pacemakers. Metal stents or implanted artificial valve rings cause local artifacts. 4D PC-MRI is employed to scan large vessels, such as the aorta, pulmonary artery, as well as the cardiac chambers.

DOPPLER ECG: In 2D, Doppler ECG achieves a high spatial and temporal (4–20 ms) resolution. In 3D, the spatial resolution is still good, but the temporal one is rather low. It has rapid scan times, facilitating an evaluation in real-time. This allows the depiction of small scales features that are only present for short periods of time. However, in clinical settings, only one velocity direction parallel to the transducer can be obtained. High velocities are well-resolved within a certain aliasing limit, but lower velocities are often underestimated or their acquisition suffers from noise. Breathing control is not required. Doppler ECG is mainly used to analyze the heart chambers and aortic flow. The latter may require the use of transesophageal echocardiography, i.e., a small transducer that emits ultrasound waves from the patient’s esophagus [545]. In contrast to 4D PC-MRI, pacemakers and other implanted devices are no limit. Moreover, ultrasound-based examinations are at low cost, which increases the applicability in the clinical routine.

ECHO-PIV: Echo-PIV achieves a good spatial 2D resolution – if required even for multiple planes. The temporal resolution of 4–20 ms is comparable to Doppler ECG. An acquisition requires a few heart beats and the evaluation can be performed during the scan or later offline. Echo-PIV provides two in-plane flow directions, but the one through-plane is missing. High velocities may be underestimated, low velocities are captured well. Breathing control is not necessarily needed, since a scan can be performed during one breath-hold. The applications of Echo-PIV are similar to the ones of Doppler ECG: The heart chambers and aortic flow. The costs are similarly low and pacemakers as well as other implants are also no limit.

3.4. SUMMARY

MAGNETIC RESONANCE IMAGING: MRI builds upon proton excitation with magnetic fields and measuring resonance during relaxation phases. Positions are encoded using magnetic field gradients. There are various scan sequences for MRI that provide decent contrast in soft tissue and fluids or that facilitate the determination of, e.g., neuronal activity and fiber directions in the white brain matter.

4D PHASE-CONTRAST MRI: 4D PC-MRI allows to determine directional blood flow information. It is exploited that moving protons in the blood are surrounded by stationary protons in static tissue. The V_{ENC} parameter has to be adjusted prior to the scan. It describes the maximum measurable flow velocity, which varies in different vessels. Datasets are 3D + time vector fields in a regular grid. They contain one cyclic heart beat. Spatio-temporal resolutions are about $1.5\text{--}2.5 \times 1.5\text{--}2.5 \times 2\text{--}4$ mm / 20–50 ms. *Phase images* $V_{\{x,y,z\}}$ contain flow strengths and directions. They are used for the subsequent flow analysis and quantification. *Magnitude images* $M_{\{x,y,z\}}$ result from another reconstruction. They contain undirected flow strengths and are less noisy. An *anatomy image* A depicts averaged signal intensities.

ALTERNATIVES: *Doppler ECG* and *Echo-PIV* are ultrasound-based modalities. They are cheaper and faster than 4D PC-MRI, but obtained data are less comprehensive. 4D PC-MRI has the highest potential to provide the possibility for a complete qualitative and quantitative flow analysis. Therefore, this modality is the focus of this thesis.

4D PC-MRI acquisitions suffer from various artifacts that alter the measured flow directions. This negatively affects both the qualitative as well as quantitative data evaluation and makes a careful pre-processing a prerequisite. Section 4.1 explains the most important artifacts and corresponding correction steps that can be applied.

Vessel masks are useful in many different ways. They allow to restrict flow integration to the lumen (cavity within the vessel) and establish a morphology visualization. Moreover, they are required for many quantitative analyses. Section 4.2 describes corresponding segmentation approaches for 4D PC-MRI data.

THIS CHAPTER IS BASED ON:

- [275, SECTION 2.2]: B. KÖHLER, S. BORN, R. F. P. VAN PELT, A. HENNEMUTH, U. PREIM, AND B. PREIM. “A SURVEY OF CARDIAC 4D PC-MRI DATA PROCESSING”. IN: *Computer Graphics Forum* (2016), EPUB. DOI: [10.1111/CGF.12803](https://doi.org/10.1111/CGF.12803)

SEE SECTION PUBLICATIONS IN THE APPENDIX FOR THE DIVISION OF WORK.

4.1. CORRECTION OF IMAGE ARTIFACTS

Chest MRI suffers from motion artifacts due to the beating heart and respiratory motion (breathing). Bakker et al. [19] described general sources of errors particularly for 2D PC-MRI flow measurements that also occur in its 4D counterpart. Among others, this comprises *phase wraps* (also: *aliasing*) and *velocity offsets* due to various causes. *Partial volume effects* [561] are especially critical for small vessels [13]. Many artifacts can be corrected in a post-processing step. This is necessary to increase the precision of quantitative results and the quality of flow visualizations.

4.1.1. PHASE UNWRAPPING

If the blood flow velocity exceeds the V_{ENC} (recall Section 3.1.2), it appears as a flipped value in the image data, which means that the measured flow seemingly runs in the opposite direction. Assuming that velocities of spatio-temporally adjacent voxels should not differ by more than V_{ENC} , such *phase wraps* can be identified and corrected [46] (see Figure 18). Phase wraps may occur in various MRI-based measurements. Corresponding correction procedures are commonly referred to as *phase unwrapping*. This thesis follows a classification of phase unwrapping methods by Loecher et al. [320]. A shared weakness of all mentioned methods is that they are not capable of correcting multiple phase wraps, when a pixel is wrapped at least twice.

METHODS FOR MRI: General phase unwrapping methods are not specifically tailored towards the phase-contrast MRI context. Cusack and Papadakis [111] described a robust, iterative, 3D phase unwrapping that estimates the noise per voxel and processes voxels with low noise first. The unwrapping is performed in adjacent voxels of a specified seed point, and a manually initialized noise threshold is gradually increased in each iteration. Jenkinson [245] described *PRELUDE* – a fully automatic method suitable for N -dimensional images that was applied to fMRI data. It is based on a cost-function optimization using a best-pair-first region merging approach. The processing time is about 20 min for larger 3D datasets and might scale unacceptably if applied to 4D PC-MRI data. The employed *greedy optimization* can get stuck in local minima, but is faster than suggested alternatives like *simulated annealing*. Langley and Zhao [296] proposed a method based on *Chebyshev polynomials*, which was tested on phantom as well as human brain datasets, and achieved nearly identical results compared to *PRELUDE*. Bioucas-Dias and Valadao [39] utilized *graph cuts* in their proposed *PUMA* method to

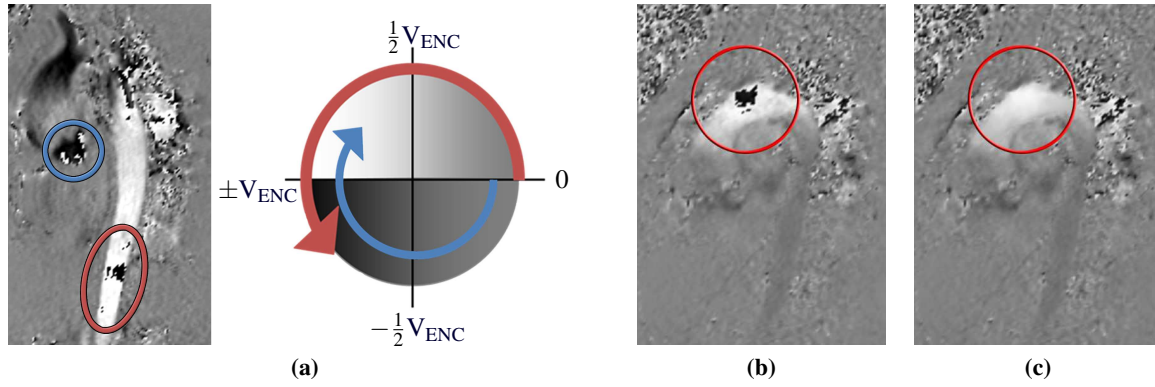


Figure 18: Phase unwrapping.

(a) The wrapped velocities are $+\frac{3}{4} \cdot V_{ENC}$ (blue) and $-\frac{3}{4} \cdot V_{ENC}$ (red encirclement). The corrected velocities are $\frac{5}{4} \cdot V_{ENC}$ of opposite sign.

(b-c) Phase image before and after (red) phase unwrapping.

Images from [275] © 2016 The Eurographics Association and John Wiley & Sons, reprinted with permission.

perform an energy minimization based on first-order *Markov random fields*. *PUMA* was applied solely to artificial data.

METHODS FOR PC-MRI: Other methods were specifically designed for PC-MRI data. They often exploit spatial continuity and phase singularity [12, 34]. Song et al. [480] assumed that phase changes between pixels are less than V_{ENC} . A least-squares problem was formulated of which the solution equals the solution of a Poisson equation, allowing the usage of fast Poisson solvers. Though, the success of their algorithm strongly depends on an incorporated sequence of thresholds, which has to be chosen carefully.

METHODS FOR CINE PC-MRI: Methods for time-resolved PC-MRI data often consider temporal continuity. Xiang [567] proposed a 1D *temporal phase unwrapping* where *differential velocity maps* (DVMs) between adjacent time steps are calculated. Due to lower absolute velocities and temporal continuity of the velocity field, which makes abrupt changes in subsequent time frames impossible, the DVMs are free of aliasing artifacts. A *reference velocity map* (RVM) is calculated as integration of the DVMs. The DVMs are then used as bridges to connect the RVM with the temporal positions and perform the phase unwrapping. Yang et al. [570] used the anatomy image *A* to estimate the pixelwise motion between subsequent time steps, which ensures that unwrapped pixels represent the same flow region. Salfity et al. [439] compared the performance of phase unwrapping algorithms that consider one, three and four dimensions. Loecher et al. [318] used a probabilistic measure in a 4D gradient-based approach to decide if a voxel is phase wrapped. Untenberger et al. [514] employed spatial constraints by using a region of interest (ROI) and temporal constraints by demanding temporal continuity in forward and backward direction. The ROI is automatically propagated to all time steps. Schofield and Zhu [459] described a method based on *Laplacian operators*, which was used for 2D interferometry data and has been shown to be useful for MRI [18, 313, 535]. Loecher et al. [320] combined spatio-temporal continuity in all four dimensions with the Laplacian-based approach and proposed a fully automatic, single-step method.⁶

4.1.2. VELOCITY OFFSET CORRECTION

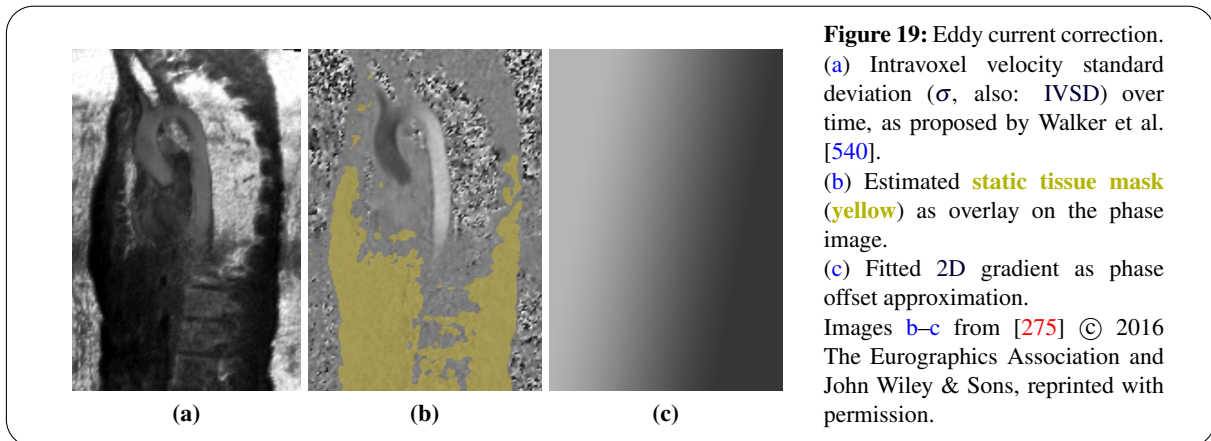
Measurement errors can cause a shift (an *offset*) of the true flow velocities. There are three major causes [326]:

⁶Loecher et al. provide the data and MATLAB code at <https://github.com/mloecher/4dflow-lapunwrap> (accessed 02/2016)

1. *Eddy currents* [102, 540] in the magnetic field are caused by rapidly switching the velocity encoding gradients.
2. *Concomitant gradient* (also: *Maxwell*) terms [32] are related to terms of the Maxwell equation for the curl and divergence of a magnetic field. A nonlinear, spatially dependent magnetic field, which produces phase errors, is always generated.
3. *Gradient field nonlinearity* [337, 405] denotes that the magnetic field coils are not able to produce a perfectly accurate field. Thus, there is always an inhomogeneous distribution.

Cause 2 and 3 can be corrected during the image reconstruction without user interaction [488]. Bernstein et al. [32] proposed modifications to the phase contrast pulse sequence and an adapted reconstruction method to minimize the effects of Cause 2. Markl et al. [337] showed that measurement errors due to Cause 3 are directly related to model-based predictions, which can be used to correct the gradient field distortion, and presented a corresponding generalized reconstruction.

EDDY CURRENT CORRECTION: However, an *eddy current* (also: *velocity offset*, *phase offset*) correction is required during the data processing. This systematic, non-constant error, which affects both the stationary tissue and the vessels, can be subtracted from the image. For this purpose, Walker et al. [540] calculated the standard deviation (σ) for each voxel in the phase image along the temporal dimension (see Figure 19a). The temporal σ is highest for air and lowest for static tissue. Vessels are in between. Based on the assumption that obtained flow velocities in static tissue are erroneous, an approximate static tissue mask (see Figure 19b) is created via interactive thresholding on the temporal σ image. One plane per phase image slice per temporal position is fitted to the velocity values of the static tissue mask (see Figure 19c) and then subtracted from the corresponding phase image slice. Bock et al. [45, 46] suggested to fit only one plane to slices from the late diastole and use this for the correction of all time steps. This is because here the aorta and pulmonary artery have the least motion, Lankhaar et al. [297] and Chernobelsky et al. [102] showed that such corrections improve quantification results. Fair et al. [154] investigated improvements when using data with a higher signal-to-noise ratio. Lotz et al. [327] pointed out that phase offset corrections can also introduce new errors and have to be applied carefully. They suggested to process only the local surroundings of the target vessel. Lorenz et al. [326] underlined the importance of velocity offset corrections to substantially improve flow visualizations.



4.1.3. NOISE MASKING

Bock [45] proposed a masking of noisy flow values in the phase images, mostly present in the lungs or in the surroundings of the patient. Their removal can be important to enhance the quality of anatomical context rendering (see Section 5.1.2) or to improve particle system-based flow visualizations (see Section 5.2.2.1) by diminishing random movements if a particle leaves the vessel. To select air-filled regions, they performed a thresholding on either the anatomical image A or on the temporal σ image proposed by Walker et al. [540]. The threshold is either set interactively or using a heuristic, e.g., use

the top 15 % values in the temporal σ image or use the bottom 15 % values in A . The resulting binary mask (see Figure 20b) is then multiplied with the flow image V (see Figures 20c–d). For this purpose, the velocity values in each phase image $V_{\{x,y,z\}}$ should be scaled to $[-V_{ENC}, +V_{ENC}]$ so that zero means no flow. However, a careful application is recommended, as parts of the vessel and intravascular flow can inadvertently be removed.

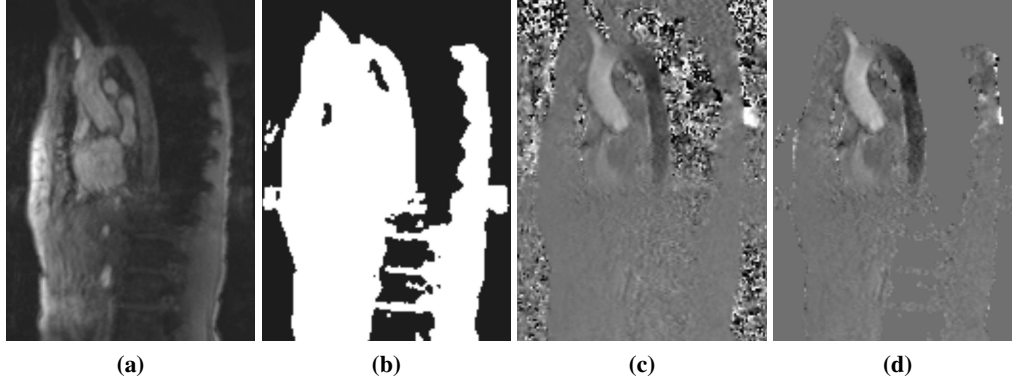


Figure 20: Noise masking.

(a) Anatomical image A .

(b) User-adjusted threshold on A .

Original (c) and masked (d) flow image V . One slice and temporal position of V_y is shown as an example.

Images from [275] © 2016 The Eurographics Association and John Wiley & Sons, reprinted with permission.

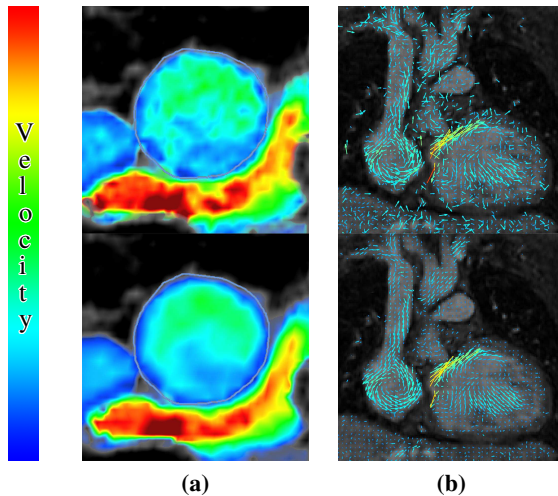


Figure 21: Flow profile in the ascending aorta's cross-section (a) and flow vectors \vec{v} of one slice through the heart (b) before (top) and after (bottom) divergence filtering [389]. Flow velocities are color-coded.

Images kindly provided by F. Ong and used in [275] © 2016 The Eurographics Association and John Wiley & Sons, reprinted with permission.

4.1.4. DIVERGENCE FILTERING AND REGULARIZATION

Blood, as an incompressible fluid, should be divergence-free, which might not be the case in the acquired data due to measurement errors. *Divergence filters* suppress these divergent components. Tafti et al. [496, 497] proposed a variational reconstruction method that employs total-variation regularization and incorporates the flow curl and divergence. Loecher et al. [319] described positive effects of divergence-free filters on the integration of stream lines. They evaluated connectivity by counting stream lines, seeded on an emitter plane, that reach another plane inside the vessel before leaving the vessel due to flow field inaccuracies. Bostan et al. [64] additionally incorporated conditions about the flow's rotational behavior and assumed that flow varies smoothly over time. They introduced a flow field regularization that improved the visualization of swirling patterns in 4D PC-MRI data of the

aorta. However, a quantitative comparison was not performed. Thus, it is not clear if the calculation of quantitative measures remains reliable. For the calculation of pressure differences from measured 4D flow (see Section 6.3.1), divergence filtering did not change the results significantly [355]. Later, Bostan et al. [65] described a regularization based on the nuclear norm, which is the sum of singular values, of the flow field's Jacobian matrix J . A better SNR performance was shown for phantom data and an improved stream line visualization was established for 4D PC-MRI data. Santelli et al. [446] penalized divergence in flow fields, measured with undersampled 4D PC-MRI, using divergence-free wavelets or a finite difference method based on the ℓ_1 -norm of divergence and curl. Ong et al. [389] described a technique based on a wavelet transform that is robust to segmentation errors and improves visualization while preserving quantification results (see Figure 21).

4.2. VESSEL SEGMENTATION

For many analysis and visualization tasks, a vessel segmentation or approximation is required. There are various 3D vessel segmentation techniques for angiography data from MRI or CT. Therefore, one approach is to generate an image similar to MR angiography from the 4D PC-MRI data and then use well-established algorithms. Lesage et al. [310] provided a corresponding overview of methods that are not tailored to cardiac vessels. Mirzaee and Hennemuth [365] fused flow images with additional anatomical data to improve the segmentation of, e.g., stenotic vessels. In this section, selected approaches are explained that solely use 4D PC-MRI data.

4.2.1. PC-MRI-BASED ANGIOGRAPHIES

An automatic 4D segmentation is challenging, since image contrast depends on the time-varying blood flow velocities that are typically lower during diastole. Manual 4D segmentation of the whole vessel is not feasible in clinical practice due to the enormous expenditure of time. A common approach is to derive a 3D contrast-enhanced image, which resembles MR angiography [128], but no longer has temporal information.

TMIP: A *temporal maximum intensity projection* (TMIP) obtains the maximum velocity per voxel along the temporal dimension of size T . Usually, this technique is applied to the magnitude image M [524]:

$$\mathbf{TMIP}(\vec{p}) = \max_t \left(\| M(\vec{p}_t) \| \right) \quad (2)$$

The TMIP is bright at positions $\vec{p} \in \mathbb{R}^3$, where fast blood flow was present at some time $t = 0 \dots T - 1$ during the cardiac cycle (see Figure 22a). Inflow jets may appear prominently. Distant vessel sections can lose contrast due to decreasing velocities. Further contrast variations might be caused by the typically parabolic flow profile, which means that the highest velocities are located in the center. This profile can be disturbed in case of vortex flow.

PCMRA: A *phase-contrast magnetic resonance angiography* (PCMRA) image [213] combines the anatomy image A with the phase image V . Both have a high vessel contrast, but an opposing high and low contrast for static tissue and noise regions. A PCMRA can be calculated using:

$$\mathbf{PCMRA}(\vec{p}) = \sqrt{\frac{1}{T} \cdot \sum_{t=0}^{T-1} A^2(\vec{p}_t) \cdot \| V(\vec{p}_t) \|^2} \quad (3)$$

or similar formulae [47]. A temporal average instead of the maximum is calculated (see Figure 22b).

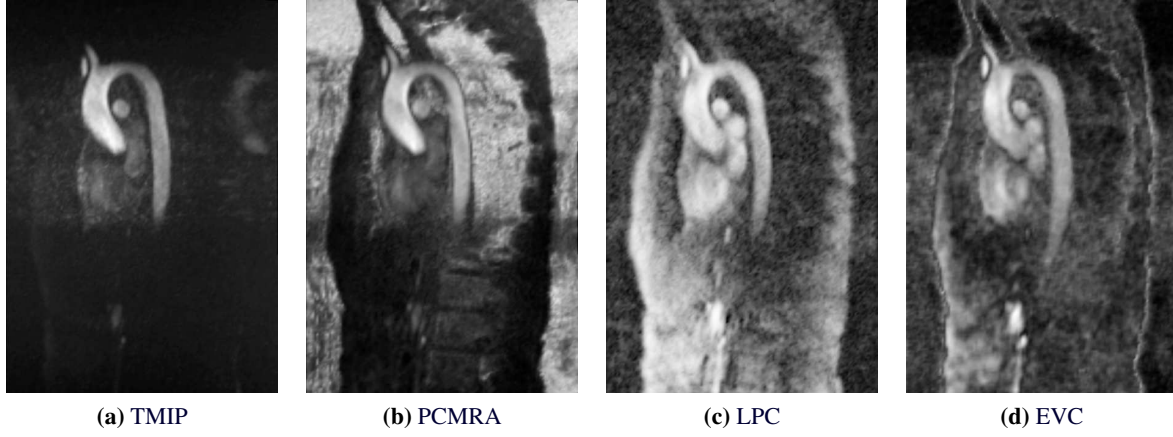


Figure 22: 3D images with enhanced vessel contrast.

(a) Temporal maximum intensity projection of the magnitude image.

(b) Phase-contrast magnetic resonance angiography image.

Time-averaged local phase coherence (c) and eigenvalue coherence (d).

Images from [275] © 2016 The Eurographics Association and John Wiley & Sons, reprinted with permission.

LPC: Chung et al. [103] defined *local phase coherence* (LPC) (see Figure 22c) as the average angle between a normalized velocity vector and its normalized neighboring velocity vectors at \vec{p}_t^n :

$$\text{LPC}(\vec{p}_t) = \frac{1}{26} \cdot \sum_{\forall \vec{p}_t^n} \frac{\mathbf{V}(\vec{p}_t) \cdot \mathbf{V}(\vec{p}_t^n)}{\|\mathbf{V}(\vec{p}_t)\| \cdot \|\mathbf{V}(\vec{p}_t^n)\|} \quad (4)$$

The normalization causes insensitivity towards the actual velocities, which might be advantageous in vessels with slower blood flow or if the image contrast is poor due to a V_{ENC} chosen too high.

EVC: Similar to the LPC, Persson et al. [407] and Solem et al. [479] described *eigenvalue coherence* (EVC, also *eigenvalue divergence*) (see Figure 22d), which is based on an eigenvalue analysis of a local velocity tensor:

$$\text{EVC}(\vec{p}_t) = \frac{4 \cdot \lambda_0 \cdot \lambda_1}{(\lambda_0 + \lambda_1)^2} \quad \text{with} \quad (5)$$

$$\{\lambda_0 \geq \lambda_1 \geq \lambda_2\} = \text{eig} \left(\frac{1}{26} \cdot \sum_{\forall \vec{p}_t^n} \mathbf{V}(\vec{p}_t) \cdot \mathbf{V}(\vec{p}_t^n)^T \right)$$

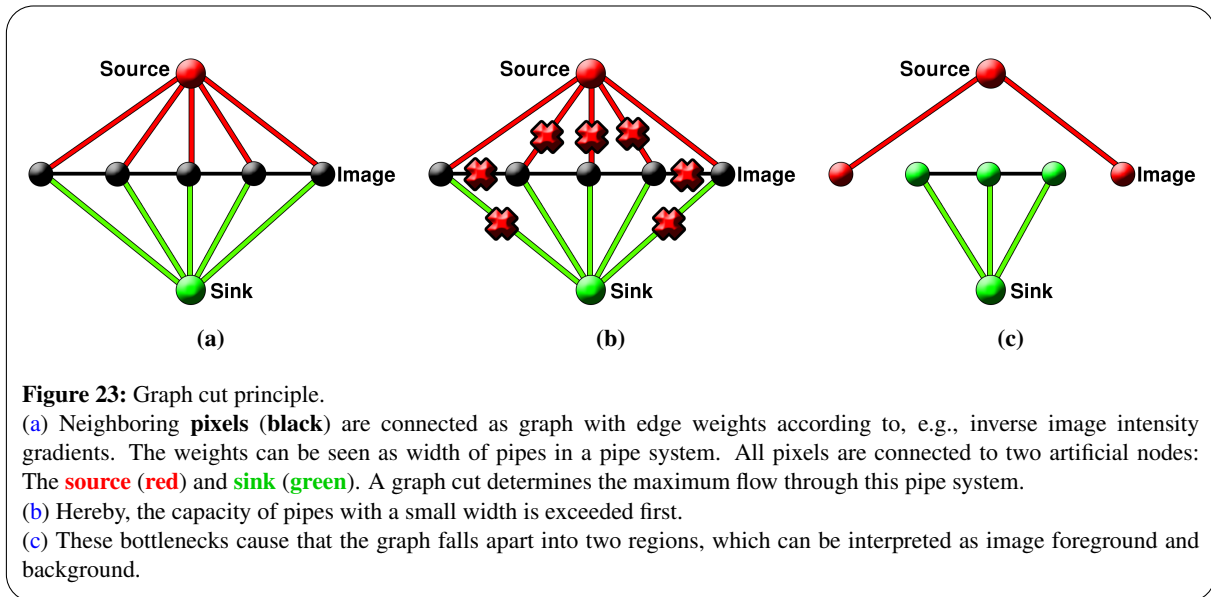
LPC and EVC both preserve temporal information, which enables the subsequent application of either temporal averaging, as the PCMRA does (see Equation 3), or a TMIP (see Equation 2), where M is substituted accordingly. Temporal averaging produces better results, since the LPC and EVC images tend to be noisy.

4.2.2. LUMEN SEGMENTATION - 3D

A 3D vessel mask is an approximation of the dynamic vessel morphology and can be used for the subsequent anatomical context visualization, for quantification purposes, or for the extraction of a centerline. Tagliasacchi [498] provided an overview of centerline extraction methods. The *Vascular Modeling Toolkit* (VMTK) [410] provides corresponding functionality specifically for vascular structures [10].

REGION-BASED APPROACHES: Hennemuth et al. [213] used a *watershed transformation* on a PCMRA image, where the user specifies include and exclude points. Stalder et al. [486] clustered the temporal σ image [540] (recall Section 4.1.2) into air, static tissue and vessels using "a maximum-likelihood estimation of the Gaussian mixture model by expectation maximization (EM clustering [196])." The method is fully automatic, but does not allow to distinguish between different vessels.

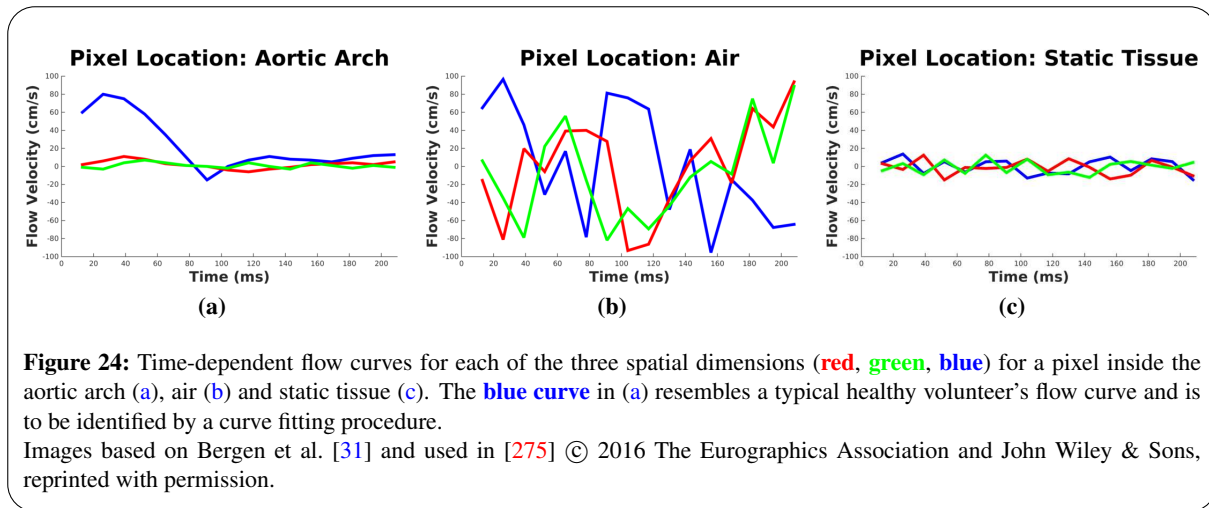
GRAPH-BASED APPROACHES: Gülsün and Tek [193] computed a centerline based on a *medialness map* between user-specified seeds on a PCMRA image and extracted the vessel lumen using a graph cut with the centerline as input. *Graph cuts* [68, 244, 315] (see Figure 23) on the TMIP are used in Bloodline (see Chapter 7), where regions inside and outside the vessel are user-provided via drawing.



MODEL-BASED APPROACHES: Van Pelt et al. [526] used an *active surface model* on the TMIP, where three parameters $\in [0, 1]$ for internal and external forces of the energy minimization can be adjusted. Default values are not given. The computation is done within a few seconds. However, a separation of single vessels is not possible. The method was validated using four datasets of healthy volunteers. Volonghi et al. [536] estimated the vessel via thresholding on a PCMRA image that was filtered with anisotropic diffusion. An initial surface is extracted using marching cubes [324] and a corresponding centerline is approximated. This is used as initialization for an automatic *level set* segmentation [390, 391]. Bergen et al. [31] analyzed each voxel in $V_{\{x,y,z\}}$ along the temporal dimension. When plotted, one curve should resemble a typical flow curve, whereas outside voxels produce noise curves (see Figure 24). A GPU-based curve fitting is performed to find the mean and standard deviation of the assumed normal distribution. Subsequent interval thresholding generates an approximate segmentation that is used as input for a *geodesic active contour* [95] (GAC) on the temporal position of the anatomy image A , where the contrast is highest (typically during peak-systole).

4.2.3. LUMEN SEGMENTATION - 4D

A 4D vessel segmentation facilitates the depiction of the vessel movement. It can be employed for quantification with increased accuracy and is crucial to calculate measures that interact with the vessel wall, such as wall shear stress.



GRAPH-BASED APPROACHES: Section 9.2 describes a procedure to automatically segment the aorta in each temporal position. The user performs an initial 3D graph cut-based segmentation on a TMIP image as basis. The resulting mesh, which is extracted via marching cubes, represents the maximum vessel extent. Based on the assumption that the vessel diameter does not shrink more than 50 % during diastole, the 3D graph cut is automatically set up for each time step of the anatomy image A. Intravascular regions are initialized using a dilated centerline, regions outside are initialized with a dilated contour of the mesh.

MODEL-BASED APPROACHES: Kainmüller et al. [257] presented a level set approach where multiple sources of information are integrated. A 3D surface is used as a priori shape knowledge, edge information are derived from a *Canny edge detector* [86], curvature information from *mean iso surface curvatures* in local 2-neighborhood, and measured flow is incorporated using local phase (LPC) or eigenvalue coherence (EVC). The model was evaluated by segmenting the left ventricle and atrium in each one dataset of a healthy pig and human with 25 and 30 temporal positions, respectively. Segmentation of the first time step took 30 min, whereas each further one required 2 min.

Bustamante et al. [81] created an *atlas* from the dataset of a healthy volunteer, where multiple vessels were segmented on a PC-MRA image. The atlas also contains standardized measuring planes. It was employed to obtain time-resolved segmentations of other datasets using robust *affine registrations* as initialization, followed by *non-rigid registrations* as fine-tuning. The net flow volume (see Section 6.1.1) was automatically obtained for each defined measuring plane. Their method requires datasets that were scanned with an equal orientation. Thus, a possible application is the evaluation of studies. However, pathologic cases with vessel morphologies that strongly differ from the atlas are problematic.

4.2.4. CROSS-SECTION SEGMENTATION

Quantification methods often require an *accurate* definition of the lumen in a measuring plane orthogonal to the vessel. Obtaining this from a 3D segmentation without temporal information might introduce errors, since the vessel pulsation is neglected. Also, in contrast to the voxels of the 3D segmentation, measuring planes are not necessarily parallel to the image axes. Consequently, 2D cross-section segmentations that are sampled from a 3D lumen segmentation might have a square-edged boundary.

Instead, manual contour drawing can be carried out by the user. However, this might be tedious if multiple evaluations are performed or if time-resolved cross-section segmentations are required. The problem is well-known from the 2D PC-MRI context. There, many tools let the user create one contour that is then automatically propagated over time and readjusted in each temporal position based on the image intensity gradients (edges).

REGION-BASED APPROACHES: Van Pelt et al. [524] detected cross-sections in the TMIP based on an *eigendecomposition* of a local structure tensor for user-given query positions. The results were used as seeding planes for the subsequent blood flow visualization.

MODEL-BASED APPROACHES: Goel et al. [187] described an automatic method to find vessel cross-sections in the anatomy image. They performed an edge detection on 2D image slices and used a *Hough transform* [231] to determine the most circular objects in each temporal position. The ascending and descending aorta are highly circular in axial planes. Thus, it is likely that they achieve large values.

4.3. SUMMARY

ARTIFACTS: *Phase wraps* denote seemingly flipped flow in the phase images. They occur if measured flow exceeds the specified V_{ENC} parameter. *Phase unwrapping* is often able to correct these erroneous regions if they are sufficiently enclosed by correct flow values.

Velocity offsets are caused by gradient field inhomogeneities. Assuming that flow should be zero in static tissue, these erroneous flow values can be approximated as gradients and subtracted from the phase images. Carefulness is recommended, since new errors can be introduced.

Air produces extreme noise in the phase images outside the body and in the lungs. These regions can be approximated by analyzing intravoxel standard deviations (IVSD) over time. A rough segmentation, derived via thresholding, can be used to mask the phase images. Caution is advised, since higher thresholds remove parts of the vessels.

Complex divergence filters recreate flow fields with enforced model assumptions. Zero-divergence is demanded, since the incompressible blood should be divergence-free. Such filters can improve the qualitative flow analysis. However, it is not clear to what extent quantification results are preserved.

SEGMENTATION: 3D approximations of the dynamic vessels are commonly employed. For this purpose, special images are calculated that provide high vessel contrast at the cost of temporal information. A *temporal maximum intensity projection* (TMIP) of the magnitude images is most relevant for this thesis.

Segmentation approaches comprise *region-based methods* (*watershed*), *graph-based methods* (*graph cut*) and *model-based methods* (*active surface*, *level set*, *atlas-based registration*). 2D cross-sectional segmentations are performed for quantification purposes. 3D segmentations are performed on a 3D high contrast image, e.g., a TMIP, and adapt methods that were originally made for MR angiography. 3D segmentations can be used to derive arbitrary cross-sectional masks. Moreover, they facilitate the quantification of wall-related measures. 4D segmentations are challenging to obtain due to limited 4D PC-MRI data quality.

Qualitative analysis refers to the visual examination of the acquired cardiac 4D PC-MRI blood flow data. Radiologists are well trained in the slice-based evaluation of medical image data. This allows them to quickly assess vascular morphology changes and create a 3D image in their mind. Thus, visualization of the anatomy mainly serves as context in a comprehensive flow visualization. A requirement, though, is the (semi-)transparent depiction of the vessel front, as seen from the viewer, so that intravascular flow becomes visible.

What is difficult even for medical experts, is to obtain an impression of the time-varying flow using solely the grayscale phase difference images. This issue can be tackled by adapting techniques from the flow visualization community to the cardiovascular context, since 4D PC-MRI data are discrete, time-varying (also: unsteady), 3D vector fields. However, the high data complexity makes additional effort necessary to enhance specific flow characteristics that are interesting for physicians. Also, due to low spatio-temporal data resolutions and a limited signal-to-noise ratio (SNR), a certain robustness of employed methods is also required.

This chapter briefly addresses different approaches to depict the anatomical context and then proceeds with the calculation, rendering and filtering of blood flow representing path lines. Afterwards, the clinical value of visual blood flow evaluation is emphasized by presenting the results of selected medical studies.

THIS CHAPTER IS BASED ON:

- [275, SECTION 5]: **B. KÖHLER**, S. BORN, R. F. P. VAN PELT, A. HENNEMUTH, U. PREIM, AND B. PREIM. “A SURVEY OF CARDIAC 4D PC-MRI DATA PROCESSING”. IN: *Computer Graphics Forum* (2016), EPUB. DOI: [10.1111/CGF.12803](https://doi.org/10.1111/CGF.12803)

SEE SECTION [PUBLICATIONS](#) IN THE APPENDIX FOR THE DIVISION OF WORK.

5.1. ANATOMICAL CONTEXT VISUALIZATION

When the complete intravascular flow is shown, one can already get a good impression of the vessel shape. In this case, an additional depiction of the vessels would be no critical requirement. However, this might not work when exclusively specific flow features, such as vortices, are shown. Here, the vessel anatomy can be displayed as orientation and contextual information.

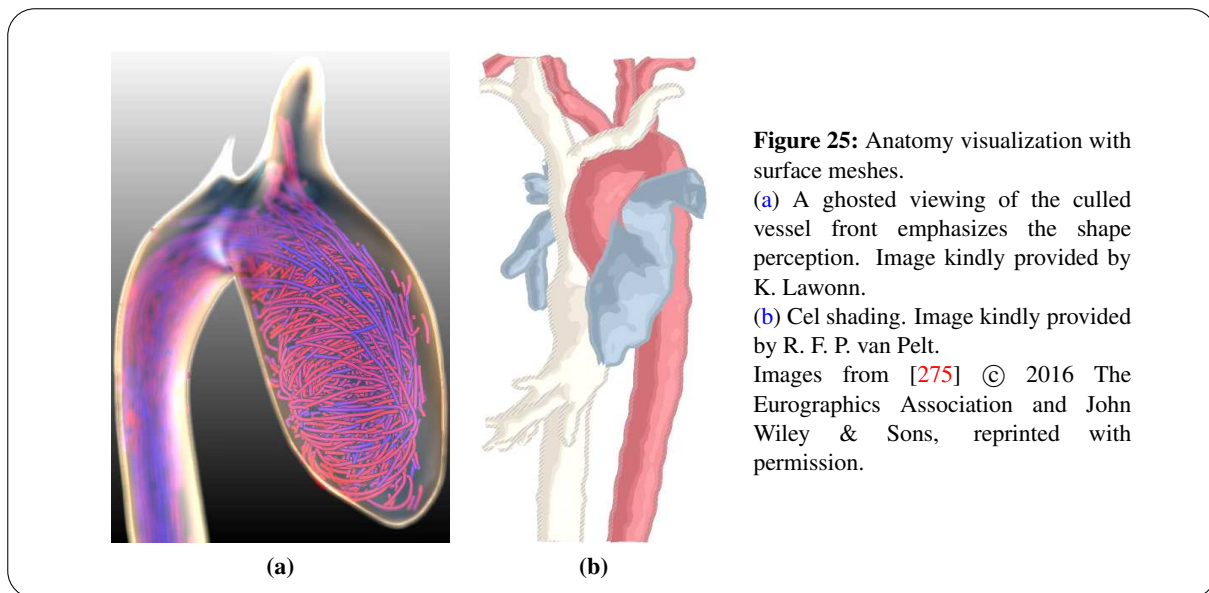
There are two basic approaches to visualize the the vessels. Vessels are either extracted from 3D lumen segmentations or depicted via direct volume rendering of a 3D high contrast image (recall Section 4.2). Both approaches are outlined in the following. In addition, approaches to extract and visualize time-varying surface meshes are briefly described.

5.1.1. GEOMETRIC SURFACE MESHES

If different vascular structures have separate meshes, single vessels can easily be hidden to focus the evaluation or reduce visual clutter. In addition, the assessment of vascular diameters and cross-sectional areas becomes possible. Furthermore, a segmentation or surface mesh facilitates the extraction of a centerline, which can be used, e.g., for the placement of measuring planes.

5.1.1.1. STATIC VESSELS

To extract triangular surface meshes from 3D segmentations, *marching cubes* [324] or *constrained elastic surface nets* [185] can be employed. Mesh-based rendering techniques, such as *Phong shading* [409],



can be applied to create appealing visualizations. A common way to make intravascular flow visible is to render only the vessel's back side, as seen from the viewer's position. Gasteiger et al. [177, 178] used a *Fresnel-reflection model* [455] to show parts of the culled front faces in order to increase the spatial shape perception: The smaller the angle between a surface normal and the view vector is, the higher the transparency gets. Lawonn et al. [306] additionally emphasized convex and concave regions with an illustrative technique that was inspired by *suggestive contours* [115] (see Figure 25a). The method is applicable to arbitrary surfaces and thus suitable for the cardiac anatomy. Van Pelt et al. [522, 524] abstracted the surface depiction using a *cel shading* (see Figure 25b). This denotes a cartoon-like rendering of 3D scenes [116]. Preim and Botha [421] provided an overview of the visualization of vascular structures.

5.1.1.2. DYNAMIC VESSELS

A depiction of the vessel motion might support the understanding of interdependencies between the pulsatile flow and the dynamic morphology. Furthermore, the increased realism can support patient education and inspire discussions among treating physicians. Lantz et al. [300] performed manual segmentations for each temporal position on additional *balanced steady-state free precession* images using the freely available software *Segment* by Heiberg et al. and *Medviso* [209]. They created an initial mesh that was then stretched to match the geometries of every time step. Consequently, the topology was preserved, which also minimized the computational effort in a subsequently performed CFD simulation. We use a graph cut-based 4D segmentation (recall Section 4.2.3) to obtain meshes of each temporal position, as well as a base mesh representing an upper boundary [277]. Projections from the base mesh onto the time-dependent meshes are then used to obtain a list of displacement vectors for each vertex. This facilitates a constant topology (the base mesh), which allows a spatio-temporal smoothing of the motion information (the displacement vectors). A dynamic visualization is established using an OpenGL geometry shader, where normal vectors are recalculated in every frame to ensure correct lighting. A detailed description can be found in Section 9.2.

5.1.2. DIRECT VOLUME RENDERING

A *direct volume rendering* (DVR) can be realized with *raycasting*, which is a common choice nowadays since it is highly parallelizable and thus suitable for GPU computing [288, 450]. The TMIP turns out very suitable, since it shows the least noise. Unfortunately, viewing the intravascular flow is limited in standard DVR, since it is not simply possible to make solely the back side of the vessel opaque and the front as well as inner regions transparent. Methods that simulate iso surface visualizations by

emphasizing boundaries could use gradients to approximate front face culling. In a work by Behrendt et al. [29], where the author of this thesis contributed, a DVR front face culling was proposed, where the vessel's back sides are determined during the raycasting (see Figure 26).

Instead, a common approach is to employ a *maximum intensity projection* (MIP). This avoids unnecessary algorithm complexity and the specification of a transfer function. Due to the 2D nature of MIP, spatial relations get lost. However, when intravascular flow is shown, the user gets a reasonable impression of the vessel shape (see Figure 27a). Venkataraman [531] implemented such an approach as technical demo. A MIP is also suitable for the combination with a geometric mesh, since it can be used as background for the vessel surface rendering (see Figure 27b).

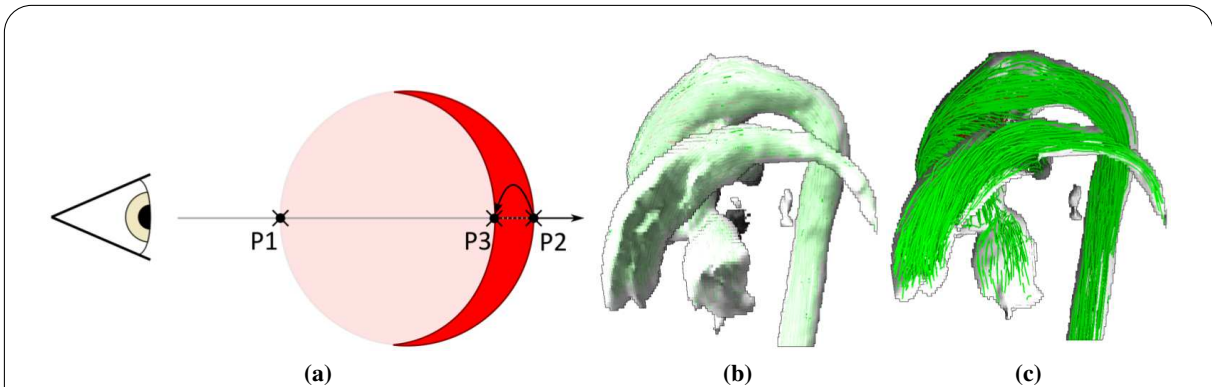


Figure 26: DVR front face culling by Behrendt et al. [29].

(a) Two Boolean values are stored for each ray during the raycasting procedure. The first defines if a vessel has been entered (at P1) and the second if the vessel has been left again (at P2). Both are determined using an underlying binary segmentation, which was automatically approximated with a threshold on the TMIP. If the vessel is left the ray position is set back by a certain amount, which is a parameter, to P3. Then, only the segment between P2 and P3 is processed by the volume rendering, whereas the rest of the ray does not contribute. This yields a rendering of the vessel's back side.

(b) Intravascular flow is hidden when standard DVR is used.

(c) Results of the proposed method.

Images from [29] © 2016 Springer-Verlag Berlin Heidelberg, reprinted with permission.

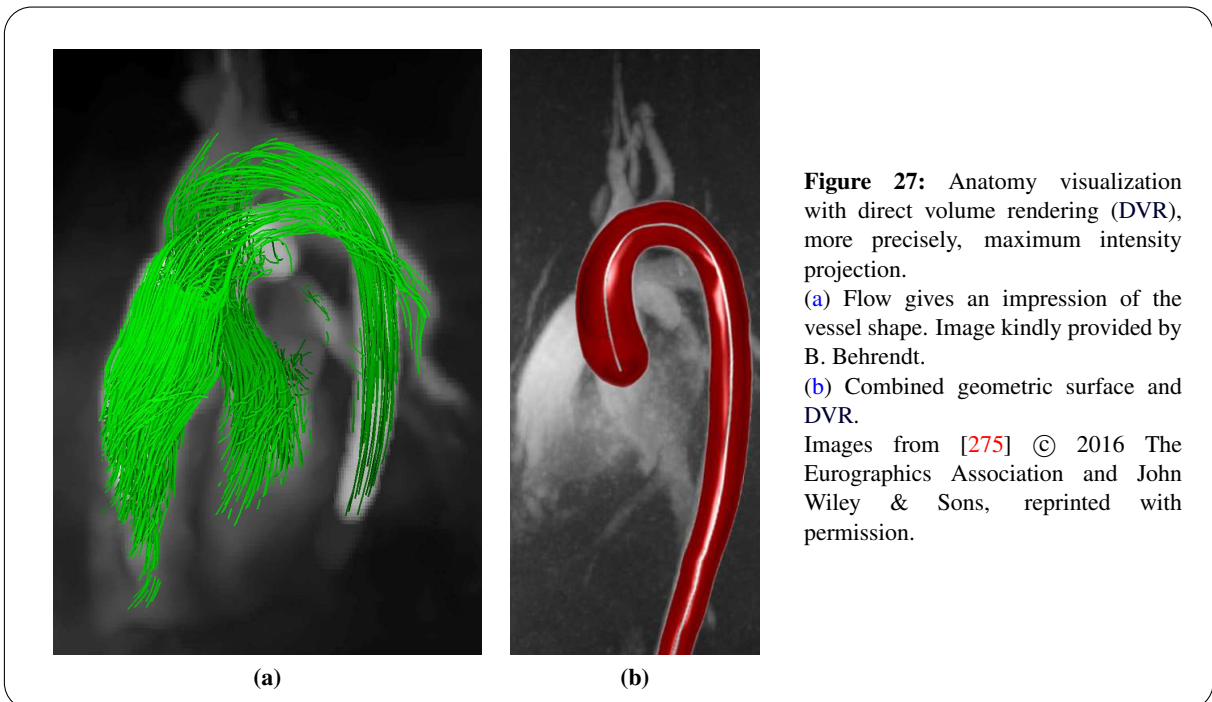


Figure 27: Anatomy visualization with direct volume rendering (DVR), more precisely, maximum intensity projection.

(a) Flow gives an impression of the vessel shape. Image kindly provided by B. Behrendt.

(b) Combined geometric surface and DVR.

Images from [275] © 2016 The Eurographics Association and John Wiley & Sons, reprinted with permission.

5.2. FLOW VISUALIZATION

Analysis of the vessel shape helps to assess morphology-related pathologies, such as dilations or narrowings. However, the investigation of blood flow characteristics facilitates a deeper understanding of a patient's situation. Segmentations – accurate or approximate – are commonly used to restrict the flow calculation to the inside of the vessel.

Inspired by Post et al. [416], direct as well as geometry- and feature-based flow visualization techniques are explained in the following. Texture-based methods, such as *line integral convolution* [82], are difficult to adapt to time-varying 3D data. Thus, they are rather uncommon in the cardiovascular context and will not be considered.

5.2.1. DIRECT METHODS

Direct flow visualization techniques are suitable to illustrate basic flow characteristics in a vessel cross-section, whereas 3D and 4D visualizations are rapidly dominated by visual clutter.

5.2.1.1. VELOCITY PROFILES

Blood flow through a cross-section is often color-coded according to the velocities. Rainbow scales are widely used in the medical context, although they might be confusing, obscuring, misleading [59], and should be avoided. Yet, they are used as default in most commercial medical image viewers. Other colormaps, such as red-blue, are often used to depict the flow direction regarding the centerline tangent or the viewing direction. Silva et al. [476] provided an overview of color scales including important guidelines.

HEIGHT FIELDS: The temporal development of the flow profile might be shown in an animation or as a height field (see Figure 28a). This allows to draw conclusions on the distribution of high velocities. Height field visualizations were established early on by Paulsen and Hasenkam [403], who depicted time-varying velocity profiles of canine ascending aortas using data from a hot-film anemometer. The latter *“is used to measure the instantaneous velocities of fluid flows [and] is based on the dependence of the sensor (gauge) heat transfer on the fluid velocity, temperature, and composition.”* (Shekhter [470])

CROSS-SECTIONAL PATTERNS: Line or arrow *glyphs* can be helpful to analyze flow patterns in a cross-section (see Figure 28b). Laidlaw et al. [292] performed a comparison of six different 2D vector field visualizations. Yang et al. [568] suggested animated arrow maps to depict pulsatile flow.

5.2.1.2. DIRECT VOLUME RENDERING OF FLOW VELOCITIES

A DVR of flow velocities in one time step illustrates the distribution of fast and slow blood (see Figure 28c). Masking the phase images is recommended to exclude surrounding noise from the visualization (recall Section 4.2.2). However, the visualization includes no directional information, a transfer function has to be specified, and one has to either find a suitable temporal position to show, such as peak systole, or establish a time-varying DVR.

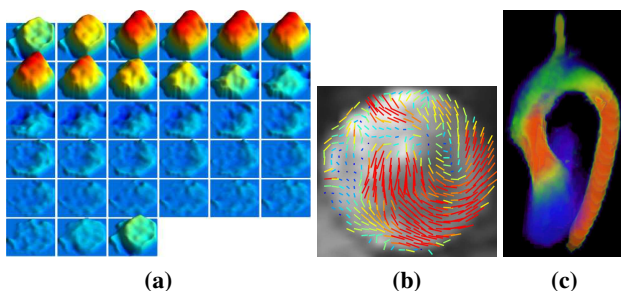


Figure 28: Direct visualization techniques. (a) The time-dependent flow through a measuring plane is shown as height fields, where height and color represent the velocity. (b) Flow pattern in a cross-section depicted via line glyphs. (c) DVR (raycasting) of systolic flow velocities. Image a based on Heiberg et al. [209]. All images from [275] © 2016 The Eurographics Association and John Wiley & Sons, reprinted with permission.

5.2.2. GEOMETRY-BASED METHODS

Geometry-based flow visualization techniques depict the course of flow trajectories by means of geometric objects, such as lines, particles, or surfaces. Surfaces can depict enclosures of regions with similar properties. However, they are rather uncommon in the blood flow context and therefore only briefly described in the following.

Buonocore [76] described the visualization of blood flow patterns using *paths* (stream lines, path lines) and linked abnormal flow patterns to atherosclerosis. This concept of flow trajectories has been widely adopted for the visualization of 4D PC-MRI blood flow. Wigström et al. [557] proposed the simultaneous display of particle traces and morphologic slices to increase the comprehension of intracardiac flow patterns.

5.2.2.1. FLOW TRAJECTORIES

SEEDING: A flow trajectory is the solution to an *initial value problem* of an *ordinary differential equation*. Each initial value, which is a 4D *seed point* in the flow field V , will produce one particle path. A *seeding strategy* is a specific scheme to place seed points within the flow domain (here: the vessel). The goal is to minimize visual clutter, while including salient features in the resulting set of trajectories. Jobard and Lefer [252] and Turk and Banks [511] proposed common techniques for evenly-spaced stream line placement in 2D that resemble appearances from hand-drawn sketches. However, in the 4D cardiac context the situation is more complex.

A *uniform distribution* places 4D seed points at random spatio-temporal positions within the vessel. To ensure that characteristic flow features, such as vortices, are captured, one seed can be placed in *every* voxel in *each* time step, using either the voxel center or another intravoxel random position. A less time- and memory-consuming approach is to guarantee that every voxel is *visited at least once* per temporal position. This can be done by alternating seeding plus integration and then checking which voxels were visited. The density of the resulting line set depends on the dataset's grid resolution. *Entropy-based methods* place seeds in proximity to features, which can be determined by thresholding a corresponding measure like a vortex criterion.

An *emitter plane*, preferably lying in the vessel's cross-section, facilitates interactive flow exploration. Again, uniform distribution or a specific scheme on the plane can be used. Van Pelt et al. [522, 525] proposed a probing tool, which is a truncated cone that fits the vessel at a user-specified location. It is as trade-off between planar and volumetric seeding.

Ye et al. [572] described a 3D stream line seeding based on a flow field analysis regarding critical points. This was used to identify important flow patterns that need to be presented. Wu et al. [566] proposed an evenly spaced stream line placement that was also based on a topological feature analysis (singularities, separatrices) of the flow field. Chen et al. [100] presented an adaptive seeding approach for 2D and 3D vector fields based on stream line similarity. Such approaches might be challenging to adapt to the cardiac context due to the amount of noise in the data and the impeded extraction of the flow topology. For a further overview on the seeding problematic, please consider McLoughlin et al. [351].

CALCULATION: The common approach to calculate blood flow trajectories is to use an integration scheme from the *Runge-Kutta* family, such as the *Dormand-Prince method* (DOPRI5(4)) [124]. In combination with hardware-accelerated 3D texture look-ups this is suitable for fast GPU computing, as described by Kipfer et al. [266] and Krüger et al. [289]. If only one temporal position is considered, the integration yields a 3D *stream line*, representing a snapshot of the dynamic flow (see Figure 29). Vortex cores of stream lines and path lines do not necessarily coincide. Thus, only a 4D (3D + time) *path line* (also: *particle path*) represents true blood flow trajectories in the cardiac cycle. Path lines can be precalculated in an initialization step, which increases the performance during the visualization (or animation). Another approach is to perform the flow integration in real-time as particle system, where each particle stores a series of recent positions.

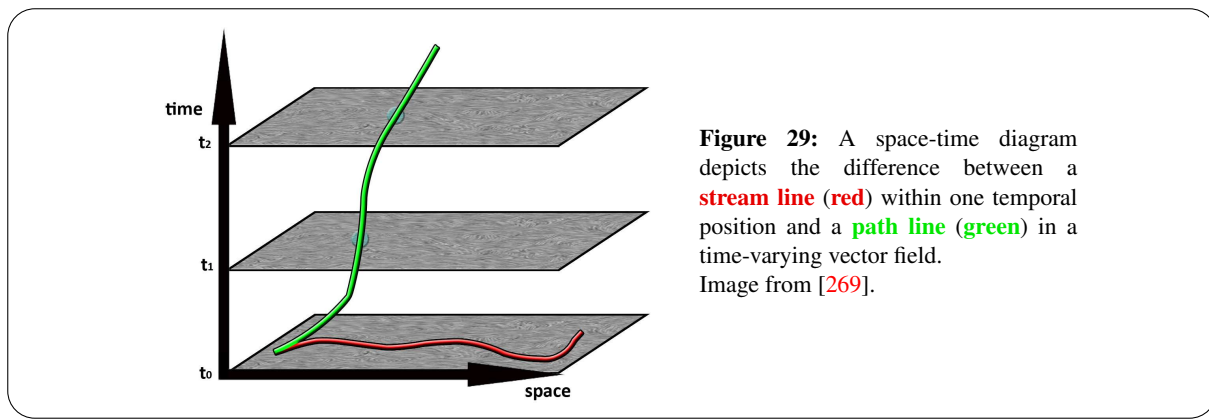


Figure 29: A space-time diagram depicts the difference between a **stream line** (red) within one temporal position and a **path line** (green) in a time-varying vector field. Image from [269].

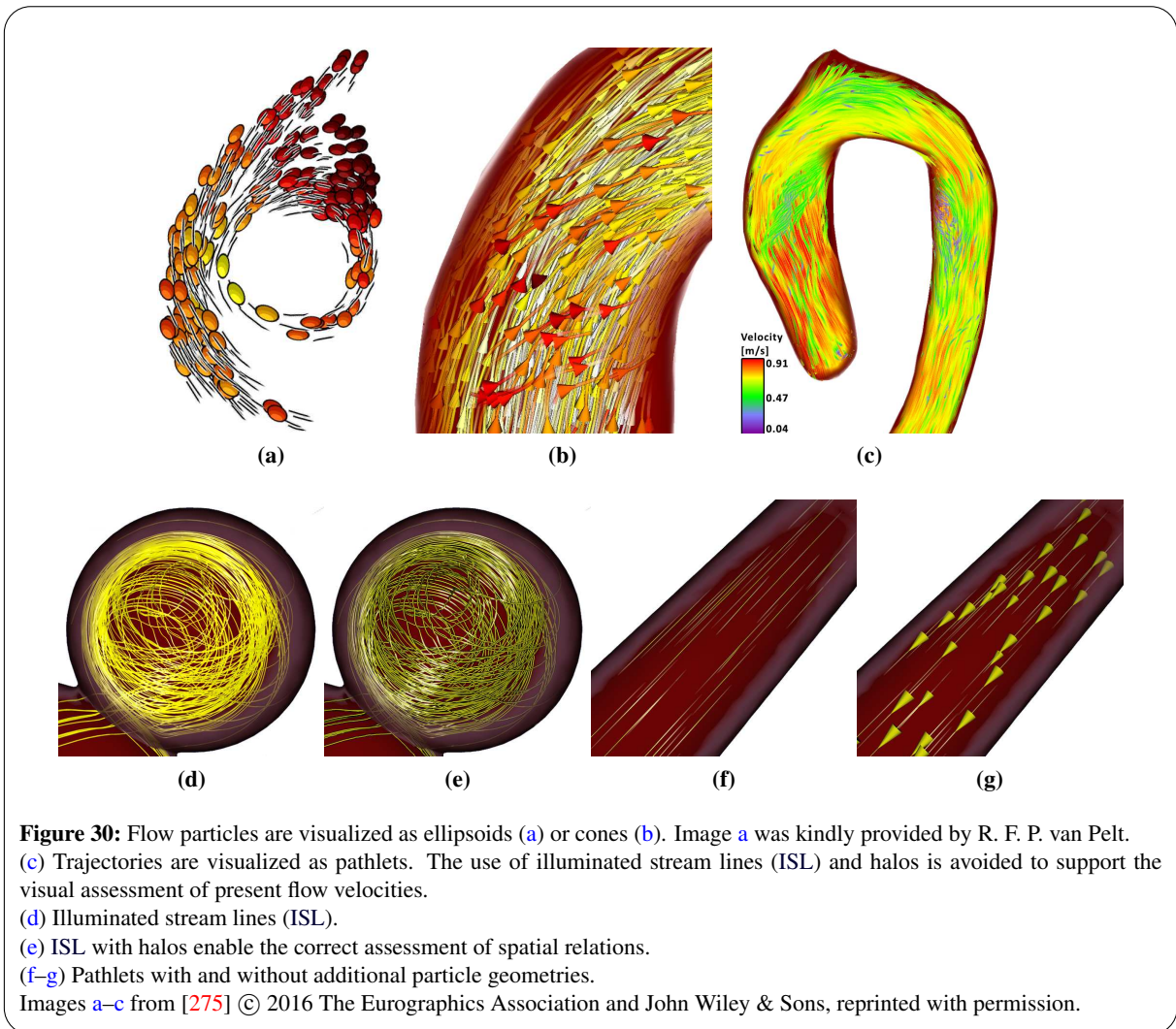
VISUALIZATION: Particles may be visualized as glyphs, such as arrows, spheres, cones [270], or ellipsoids that are stretched according to the flow velocities [522, 525] (see Figures 30a–b). *Pathlets* (also: *trails*) emphasize the development of a trajectory. Temporal information can be mapped to transparency, so that the opacity is decreased for older positions. In this case, *order-independent transparency* (OIT) [571] is recommended to ensure correct *alpha blending*.

The path lines can be shown all at once without employing the temporal information. Techniques such as *illuminated stream lines* (ISL) [334, 579] and *halos* [11, 151, 152, 241, 347] (see Figures 30d–e) are suitable to enhance the flow visualization. A halo is a contour around the line, as seen from the viewer’s perspective. In case of overlapping lines, the contour of a distant line is interrupted, whereas the nearby contour is continuous. This allows to correctly assess occlusion and enhances depth perception. ISL employ a scheme to consistently select one of the infinite normal vectors of a 3D line segment using the tangent of the line and the direction of the light source. This facilitates the application of Phong illumination [409], which normally would require the use of planar geometric primitives (triangles or quads) that allow the calculation of a needed normal vector. However, if lines are rendered as geometric tubes, the GPU’s workload is vastly increased – especially for dense line sets. A trade-off is to use *view-aligned quads* in combination with the normal vectors provided by ISL. This means to render the lines as quad primitives that always remain orthogonal to the viewer’s direction. A real-time capable implementation can be achieved with the OpenGL geometry shader.

McLoughlin et al. [351] established a corresponding overview of flow visualization techniques. Stoll and Gumhold [490] provided a variety of methods for the enhancement of line primitives, such as mapping information about the flow rotation as texture. If (semi-)quantitative assessment is the focus, a careful use of line visualization techniques is recommended to avoid distractions (see Figure 30c). Illustrative techniques [153, 235] might be adapted to the blood flow context as well, as done by Born [60]. Brambilla et al. [70] provided an overview of illustrative flow visualization techniques.

UNCERTAINTY: Numerical approximations in the trajectory calculation cause errors that accumulate for longer lines. Lodha et al. [317] described a corresponding visualization of such uncertainties. However, “the value of uncertainty visualization is severely limited by the quality and scope of uncertainty data, by the limited confidence in the data itself, and by the perceptual and cognitive confusion that the depiction of this data can generate.” (Boukhelifa and Duke [66]) Uncertainty glyph visualizations, as established by Hlawatsch et al. [217] and Wittenbrink et al. [559], might be challenging to adapt to the highly complex 4D cardiac context. Otto [394] proposed several uncertainty techniques for general 2D and 3D vector fields.

PERCEPTION: Ware [542] has shown that long and continuous flow courses can be interpreted efficiently. Forsberg et al. [157] performed a comparison between four 3D integral line renderings: Lines and tubes on monoscopic and stereoscopic monitors. The study participants had to answer five questions regarding the occurrences and characterization of critical points as well as the overall swirling



and flow behavior. They concluded that the best method is task-dependent, but lean towards lines on stereoscopic monitors as an overall favorite.

Günther et al. [194, 195] presented an opacity optimization for 3D stream line sets that was, among others, applied to blood flow in cerebral aneurysms from simulated (CFD) data. An adaption to the cardiac 4D PC-MRI context would require the incorporation of the temporal component and an elaborate handling of noise.

ANIMATION: A pathlet visualization can also be achieved with precalculated path lines. Particles (the glyphs) are placed at positions where the current time of the running animation matches the temporal component of the path line. In addition, only a small time frame around the particle position is shown, i.e., all path line points with a temporal distance higher than a threshold are hidden (see Figures 30f–g). An advantage of precalculated path lines over on-the-fly-integrated particles is that the exact same paths can be evaluated multiple times. *Vortex animations with adaptive speed (VAAS)* [276] are presented in Section 8.3. The technique can be described as view-dependent histogram equalization of feature (vortex) visibility in videos by using time lapse and slow motion. Feature visibility is analyzed for each individual video frame by rendering both the vessel mesh and extracted path lines, which represent the feature of interest, as binary masks, and then forming the ratio of foreground pixels.

INTERACTION: Manipulation of the current animation time is possible with a slider or simply via pause, stop and play. Line predicates (see Section 5.2.3.1) allow a threshold-based filtering of particular flow properties of interest, such as high velocities [60, 63]. Van Pelt et al. [522, 525] provided a probing tool suitable for a vessel depiction via DVR. The method facilitates an interactive, qualitative exploration

of intravascular flow without a segmentation. Created measuring planes for cross-sectional quantification methods (see Section 6.1) are initially placed perpendicularly to the centerline and scaled according to the vessel's extent. The user can adjust the position by dragging the plane along the centerline. More general flow analysis techniques comprise, among others, the use of focus-context approaches [105], such as *magic lenses* [36, 169, 347, 533]. Gasteiger et al. [179] presented the *FlowLens*, which is an adaption of this concept to the enhanced exploration of cerebral aneurysms. Vilanova et al. [534] established an overview of further exploration tools for measured and simulated, cerebral and cardiac data. Alternative focus-and-context approaches, as proposed by Jones and Ma [253], allow the selection of a specific particle path, calculate the correlation to the surrounding area, and display it in a non-intrusive way. Bürger et al. [77] described an interactive exploration of large 3D+time datasets using asynchronous data streaming. While this is feasible for data on uniform grids, the handling of irregular grids is challenging [80, 351, 454].

5.2.2.2. FLOW SURFACES

In contrast to line-based visualization, flow surfaces do not depict a single particle course. Instead, multiple integral lines are calculated, starting from a seed line. Their courses are then triangulated, which yields a surface. Depending on the type of integral lines, this can be, e.g., a stream surface, as introduced by Hultquist [237], or a path surface.

USAGE IN ARTIFICIAL DATA: Research was mainly performed in the field of simulated (CFD) or artificial flow data. Corresponding works investigated the depiction of vortices [174], the adaption to time-varying vector fields [176, 284, 448], the improvement of performance [448], accuracy [453, 456] and topological correctness [386, 406, 457], and the automatic selection of appropriate stream surfaces [69, 345]. Illustrative techniques were applied to enhance the surface visualization [60, 61, 93, 238].

USAGE IN MEASURED 4D PC-MRI DATA: Stalder et al. [485] extracted unconnected points within vortex regions using the λ_2 criterion (see Section 5.2.3.2) and visualized them as spheres that were scaled according to the vortex strength. Section 8.4.2 describes the generation of a glyph that encloses aortic vortex flow and conveys specific characteristics like the rotational direction.

5.2.2.3. FLOW SIMPLIFICATION AND CLUSTERING

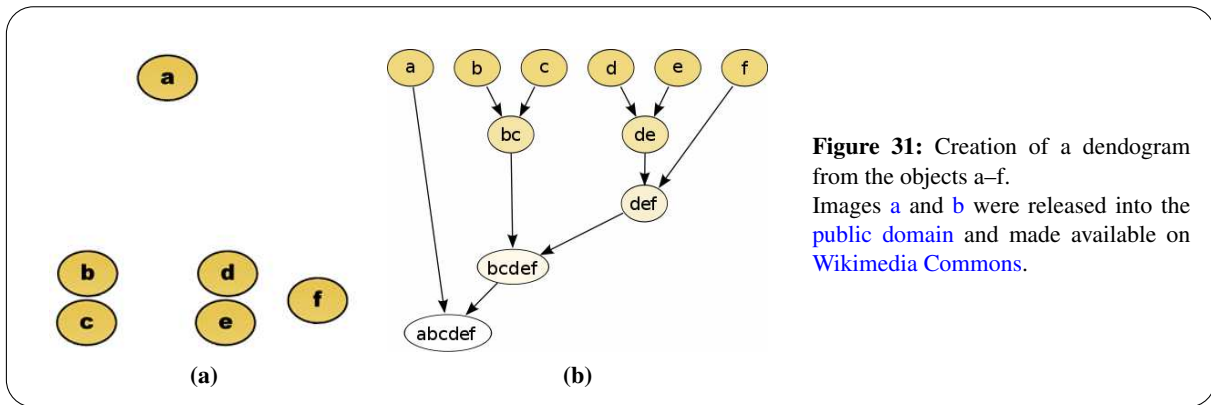
REDUCTION OF VISUAL CLUTTER: Visual clutter is a problem for dense line sets. Angelelli and Hauser [8] described a vessel straightening to simplify side-by-side visualizations of integral lines of different temporal positions. In Section 8.2 a polar plot [274] is presented that conveys vortex flow in the aorta as an overview. The temporal component is mapped to the plot's angle, analogous to a clock, and the course of the centerline is mapped to the radius, starting at the aortic valve location in the center.

THE NEXT PARAGRAPH IS PARTLY BASED ON:

- [360, SECTION 4.2]: M. MEUSCHKE. "COMPUTERGESTÜTZTE ANALYSE VON VERWIRBELUNGEN IN 4D PC-MRI BLUTFLUSSDATEN DER AORTA". MA THESIS. OTTO-VON-GUERICKE-UNIVERSITY, MAGDEBURG, GERMANY, 2015

SEE SECTION PUBLICATIONS IN THE APPENDIX FOR THE DIVISION OF WORK.

FLOW FIELD AND TRAJECTORY CLUSTERING: Salzbrunn et al. [445] introduced partition-based clustering techniques for general vector fields as a new class that employs the actual vectors, calculated integral lines or topological properties of the flow field. Telea and Van Wijk [501] presented a vector field-based *agglomerative hierarchical clustering* (AHC) for 2D and 3D data without a temporal component. In AHC every object starts as an individual cluster. Based on similarity, they are merged iteratively until only one cluster remains. The hierarchy, often represented as a tree (*dendrogram*, see Figure 31), conveys the merging process and allows to select an intermediate result with the desired number of clusters. Their (Telea and Van Wijk) proposed *elliptical dissimilarity* measure is a linear combination of velocity vectorial and positional distances. Ellipses are employed in the process to



derive deviations. Kuhn et al. [290] described a hierarchical method for steady 3D vector fields where a scalar field is calculated that represents the vector fields curvature. Individual cluster surfaces are then generated via *marching cubes* [324] and color-coded according to an eigenvalue analysis of the Jacobian matrix. The method was applied to simulated (CFD) data of cerebral aneurysms. McLoughlin et al. [352] established an AHC for stream and path lines. Their employed distance matrix describes the pairwise line similarity and was composed of the lines' curvature, torsion and tortuosity. Rössl and Theisel [432] proposed a spectral clustering for stream lines based on their geometries using pairwise *Hausdorff distances*⁷ [206]. The number of desired clusters is a parameter. Their method was applied to a simulated dataset with three cerebral aneurysms. A clustering that is suitable for vortex-representing path lines in 4D PC-MRI data [362] is determined in Section 8.4.1.

REPRESENTATIVE LINES: Yu et al. [573] subdivided time-varying 4D vector fields with an adaptive *octree*, where each octant stores the average of the contained vectors. The subdivision stops when the resulting octants are too similar. Afterwards, they applied the clustering method by Telea and Van Wijk [501] and calculated representative path lines for each cluster.

Van Pelt et al. [522, 527] performed a hierarchical clustering on the 4D PC-MRI phase image. Average velocities were not considered as a suitable measure to determine clusters, since they do not respect different flow directions. Average velocity vectors were not considered as appropriate, since they do not incorporate the cluster positions. Therefore, two more complex dissimilarity measures were used:

1. The *elliptical dissimilarity* by Telea and Van Wijk [501], as described in the previous paragraph.
2. The *local linear expansion* by Carmo et al. [92], which employs linear models to estimate the flow velocities and derives squared errors per cluster. The dissimilarity is the cost to merge two clusters.

Van Pelt et al. discussed performance bottlenecks during hierarchical clustering. They are, to large parts, a result of the repeated search for minimal dissimilarities. To circumvent this problem, they introduced *coarse hierarchical clustering*, where multiple clusters are merged in each step – all below a certain similarity threshold, for which a reasonable default value was suggested. The number of clusters, i.e., the desired level in the hierarchy, is selected by the user. Finally, an exemplary path line for each cluster is generated as representative. Cluster centers (in 3D or 4D) were chosen as seed points and the line integration was performed for two temporal positions both forward and backward in time.

Instead of clustering, the approach by Born et al. [60, 62] is based on voxelization and skeletonization of line bundles. They first use line predicates (see Section 5.2.3.1) to extract flow lines with a specific property, such as high velocities. The lines are smoothed to decrease the complexity while preserving the main information. Then, the line bundle is voxelized, and a skeleton is extracted using a thinning approach by Palàgyi and Kuba [399]. Additionally, they add voxelized vortex core lines to the skeleton that were extracted with a previous approach [63]. A minimal subset of representative lines is determined that visits each skeleton voxel. Typical results contain 1–5 lines. The visualization of the representatives is done in an illustrative way. 3D stream tapes with arrowheads are employed, where similar courses

⁷Named after the German mathematician [Felix Hausdorff](#).

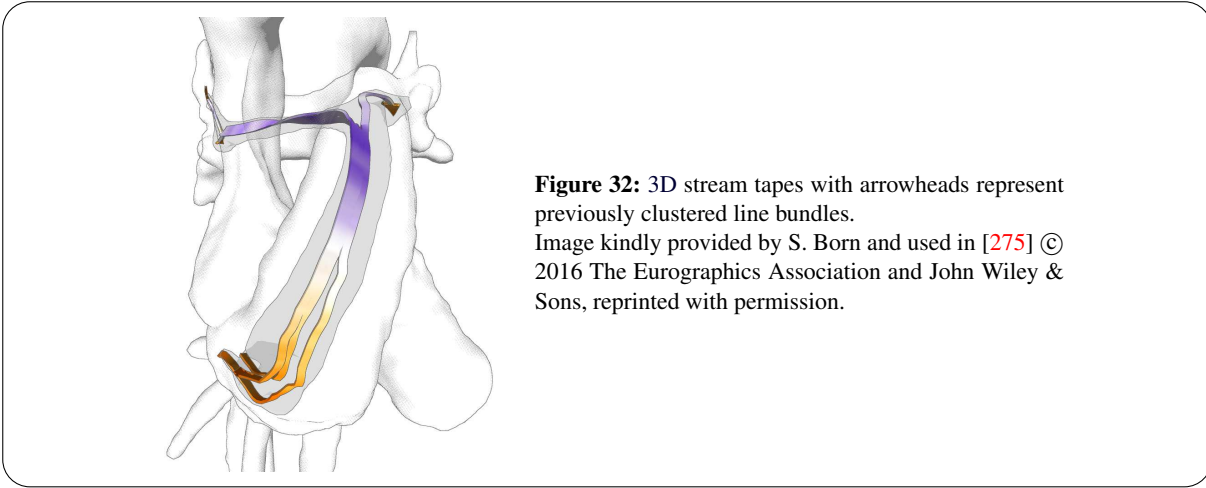


Figure 32: 3D stream tapes with arrowheads represent previously clustered line bundles. Image kindly provided by S. Born and used in [275] © 2016 The Eurographics Association and John Wiley & Sons, reprinted with permission.

are fused (see Figure 32). Feedback by two radiologists confirmed the intuitiveness of their method. Neglecting small-scale features was not considered as a disadvantage. The facilitated easier comparison of pre- and post-operative patient data was seen as a clinical benefit.

Oeltze et al. [387] pursued a similar approach of selecting stream line representatives for simulated (CFD) data of cerebral, aneurysmatic vessels. Stream lines are clustered according to different attributes that either describe the flow field (e.g. velocity, vorticity, pressure), the line geometry (e.g. curvature, torsion and adapted *mean of closest point distances* [106]) or the domain (e.g. vessel wall distance). They compared AHC, *k-means* [203, 329, 499] as well as *spectral clustering* (SC) [200, 538] and determined SC as most suitable, closely followed by AHC. One stream line representative was then selected per cluster to establish an overview visualization of the flow behavior. In a subsequent work, Oeltze-Jafra et al. [388] focused on the in-depth analysis of vortex flow in cerebral aneurysms. Besides the depiction of topological properties, such as sources and sinks [212], they map additional properties like the normalized helicity (see Section 5.2.3.2) to the representatives.

5.2.3. FEATURE-BASED METHODS

Feature extraction is used to simplify visualizations or to investigate specific macroscopic blood flow properties. Therefore, the term *feature* refers to specific flow characteristic, such as high-velocity jets in cardiac vessels. In this section, emphasis is put on salient patterns, since prominent vortical flow behavior is considered as indicator for different cardiovascular pathologies and thus is of great clinical interest. Pobitzer et al. [413] provided an overview of topology-based visualization methods for general, unsteady flow.

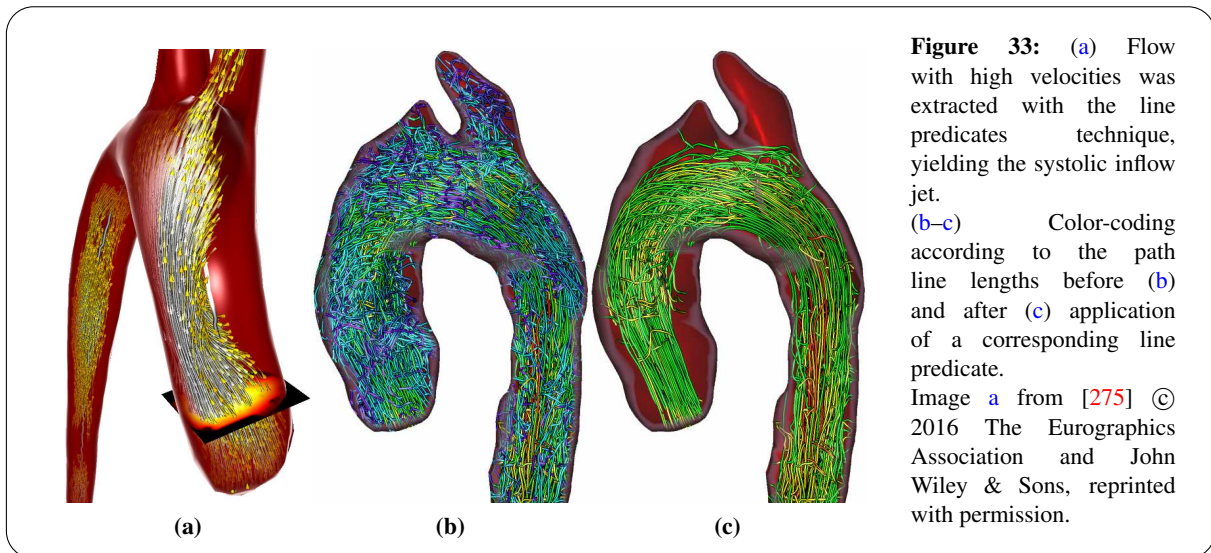
5.2.3.1. LINE PREDICATES

Salzbrunn and Scheuermann [442–444] introduced *stream* and *path line predicates* as Boolean functions that encode if certain properties of interest are fulfilled or not. A line predicate Π maps a point \vec{p}_t of a path line \mathbb{P} to *true* or *false*:

$$\begin{aligned} \Pi : \mathbb{P} &\rightarrow \{true, false\} \\ \vec{p}_t &\mapsto \Pi(\vec{p}_t) \end{aligned} \quad (6)$$

Criteria are based on line geometries or the underlying flow field V . These classes are extended in Section 8.1.2. Shi et al. [471] described various attributes especially for path lines. A predicate filters all points that do not lie within a certain value interval. It can be applied to whole lines or to the single points of it. In the latter case, lines can be split into fragments. All points that are mapped to *true*, are called the *characteristic set* C_Π :

$$C_\Pi = \{(\vec{p}_t \in D \times T \mid \Pi(\vec{p}_t) = true)\}, \quad \vec{p} \in D, \quad t \in T \quad (7)$$



D is the \mathbb{R}^3 domain of the flow field and T is the set of all temporal positions. Common set operations like union and difference provide the possibility to connect different characteristic sets and combine multiple line predicates. This allows to formulate complex queries. Born et al. [60, 63] used line predicates to extract different features, such as specific flow paths, jets (see Figure 33) or blood with high *residence times*. Furthermore, they extracted vortices and used predicates to display involved integral lines. Hennemuth et al. [213] filtered by source and target regions, which yielded a connectivity visualization. Gasteiger et al. [177, 180] determined *inflow jets* and *impingement zones* in simulated (CFD) blood flow data of cerebral aneurysms, which shows the high flexibility of line predicates. They demanded that stream lines of the inflow jet should contain points where the distance to the vessel wall is minimal, the flow direction changes rapidly and there is a strong deceleration due to the impingement on the wall.

5.2.3.2. VORTEX CORES AND REGIONS

THIS SECTION IS BASED ON:

- [269, SECTION 4.2]: **B. KÖHLER**. “WIRBELEXTRAKTION IN 4D PC-MRI BLUTFLUSSDATEN DER AORTA”. MA THESIS. OTTO-VON-GUERICKE-UNIVERSITY, MAGDEBURG, GERMANY, 2012. LINK: [VISMD.DE](http://vismd.de) (ACCESSED AT 02/2016)

SEE SECTION [PUBLICATIONS](#) IN THE APPENDIX FOR THE DIVISION OF WORK.

COMMON METHODS: Vortex extraction in 2D and 3D vector fields is a well-known problem from the fluid dynamics community. Jiang et al. [250] provided an overview of extraction methods up to 2005, Kolář [280] up to 2007, and Van Gelder [517] up to 2012 plus a discussion of different vortex definitions. Corresponding methods are divided into *local* and *global* techniques. Local methods operate mainly on the velocity vectors and their partial derivatives [99], whereas global methods incorporate larger parts of the dataset and, thus, are often more complex as well as computationally expensive. As an example, the analysis of stream and path line geometries is global, since the full set of such integral lines encodes the major flow behavior [60, 63].

Vortex extraction methods either produce core lines (as point sets, line segments or actual lines) or they extract regions with vortex flow behavior. There are various approaches, such as *combinatorial methods* [248, 249], *predictor-corrector schemes* [21], the construction of *feature flow fields* [438, 503], the *parallel vectors operator* [168, 434], *winding angle-based methods* [398, 415, 436, 437], and *Poincaré-index-based methods* [175]. Selected local methods are briefly explained in the following list, as they are relevant for this thesis:

- The **vorticity** $\vec{\omega}$ (also: **curl**) of a vector field \mathbf{V} describes the local rotation direction of particles in the flow:

$$\vec{\omega} = \nabla \times \mathbf{V} = \begin{pmatrix} \frac{\partial V_z}{\partial y} - \frac{\partial V_y}{\partial z} \\ \frac{\partial V_x}{\partial z} - \frac{\partial V_z}{\partial x} \\ \frac{\partial V_y}{\partial x} - \frac{\partial V_x}{\partial y} \end{pmatrix} \quad (8)$$

The **vorticity magnitude** $\|\vec{\omega}\|$ describes the strength of this rotation. Corresponding vortex extraction is based on the assumption that there is a high $\|\vec{\omega}\|$ along the vortex core. Depending on the assigned threshold, a smaller or larger vortex region is extracted. Adapted methods were introduced to obtain core lines [491]. A known problem is that the vorticity is high at boundaries, even if there are no vortical structures [127].

- The **normalized helicity** H_n by Levy et al. [311] is based on the assumption that the direction of the velocity vector \vec{v} and the vorticity vector $\vec{\omega}$ are aligned at the vortex core. Thus, it is defined as:

$$H_n = \frac{\vec{\omega} \cdot \vec{v}}{\|\vec{\omega}\| \cdot \|\vec{v}\|} \quad (9)$$

H_n is the cosine $\in [-1, +1]$ of \vec{v} and $\vec{\omega}$. The sign provides information on the turning direction of the flow. Vortex core lines are where \vec{v} and $\vec{\omega}$ are parallel, i.e., $H_n = \pm 1$. Compared to vorticity, the helicity does not produce false-positives at boundaries. However, the results may still contain other false-positives [433].

- The λ_2 **criterion** by Jeong and Hussain [247] and the **Q criterion** by Hunt [239] both are based on the assumption that there is a pressure minimum along the vortex core line. The Jacobian matrix J is decomposed into its symmetric and anti-symmetric part S and Ω , respectively:

$$S = \frac{1}{2} \cdot (J + J^T) \quad \text{and} \quad \Omega = \frac{1}{2} \cdot (J - J^T) \quad (10)$$

The idea of the λ_2 criterion is to find these pressure minima inside the vortex. From the *Navier-Stokes*, *vorticity transport* and *strain-rate transport equation*, a formula is derived that, in addition to S and Ω , contains a tensor with information on local pressure extrema. A local minimum is where this tensor has two positive eigenvalues. If the strain-rate transport equation is adapted for incompressible fluids, such as blood, local minima are present where the second eigenvalue λ_2 of the matrix $S^2 + \Omega^2$ is negative (with $\lambda_1 \geq \lambda_2 \geq \lambda_3$). However, the existence of local pressure minima is neither a sufficient nor necessary criterion for the existence of a vortex. The mathematical derivation for incompressible fluids including the simplifications is seen as main cause for arising inaccuracies [280, 565]. For example, the λ_2 criterion has problems with differentiating very close vortices [250]. Though, it is commonly considered as effective and reliable [449].

The Q criterion requires the second invariant Q of the Jacobian matrix to be positive. Q is defined as $\frac{1}{2} \cdot (\|\Omega\|^2 - \|S\|^2)$. This is the case where the vorticity is greater than the strain-rate. Additionally, it is required that the pressure is smaller than the pressure of the surrounding. Both the λ_2 and Q criterion provide vortex regions and have an implicitly given threshold of 0.

- Sujudi and Haines [493] proposed a method to extract vortex core lines based on an eigenvalue analysis of the Jacobian matrix. Two complex eigenvalues are a necessary condition, whereas the third one λ_R – with the corresponding eigenvector \vec{e}_R – is real-valued. \vec{e}_R describes the direction of the vortex core and is required to be parallel to the velocity vector \vec{v} . Sujudi and Haines defined the term **reduced velocity** \vec{v}_r as:

$$\vec{v}_r = \vec{v} - (\vec{v} \cdot \vec{e}_R) \cdot \vec{e}_R \quad (11)$$

Thus, \vec{v} is projected onto the plane perpendicular to \vec{e}_R . If \vec{e}_R and \vec{v} are parallel, the length of $\|\vec{e}_R\|$ is 0.

The original method operates on tetrahedral meshes. For each (triangular) side of a tetrahedron it is determined if there is a point where $\|\vec{e}_R\| = 0$. If there are exactly two sides with such a point, they are connected to a line segment that represents a part of the vortex core line. Although the method works well [250], the extracted core line is likely to have discontinuities, especially in case of curved vortex cores. This is due to the piecewise linear determination of the Jacobian matrix within the tetrahedrons. Weinkauff et al. [549, 550] introduced *cores of swirling particle motion* (COSPM) as a direct extension of the reduced velocity to 4D vector fields.

- The **torsion** τ is a measure for 3D lines that describes how sharply a curve $C(t)$ is twisting out of the plane. It is calculated as:

$$\tau = \frac{(C'(t) \times C''(t)) \cdot C'''(t)}{\|C'(t) \times C''(t)\|^2} \quad (12)$$

Biswas et al. [42] proposed a consensus-based uncertainty model, where the results of four point-based vortex extraction methods are combined in a voting scheme. This facilitates the identification of vortex regions with higher confidence.

APPLICATION TO 4D PC-MRI: The majority of methods from the flow analysis community is made for 2D or 3D vector fields and is therefore not directly applicable to 4D PC-MRI data, since flow is inherently time-varying. Evaluating each temporal position independently with a 3D method might introduce errors, since it is not guaranteed that vortices of stream and path lines coincide. Nevertheless, many 3D techniques have been shown to produce reasonable approximations. Stalder et al. [485] used a combination of the λ_2 criterion and the reduced velocity to identify independent points that represent vortex cores mainly in the aorta. Stream lines were seeded in the close surrounding to provide a visual impression of the vortices.

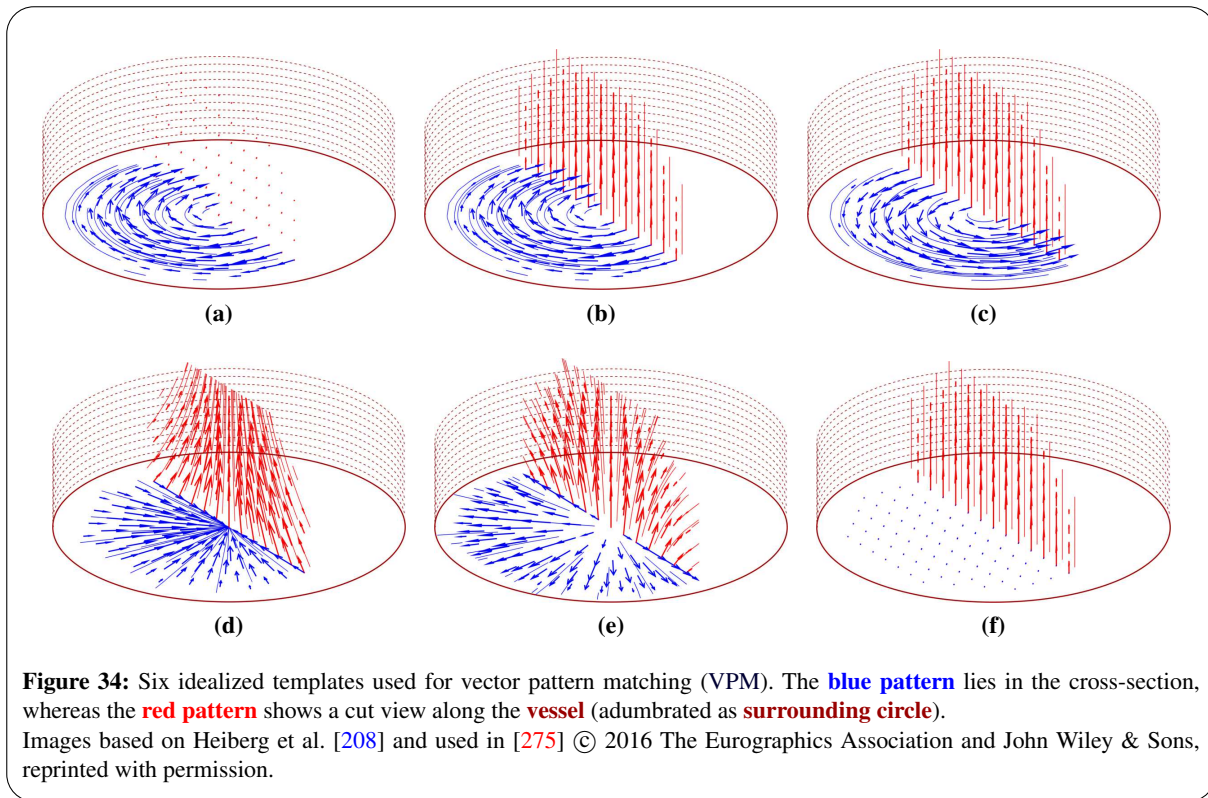
We observed that clinicians are often more interested in the characteristic of a vortex than topological properties such as core lines [270]. Consequently, we aimed at extracting visually appealing path lines with long, continuous, and smooth courses that can be interpreted efficiently [542]. Different local vortex criteria were incorporated in the line predicates technique and the λ_2 criterion was determined as most suitable. Chapter 8 describes this enhanced extraction and assessment of vortex flow.

Elbaz et al. [142, 144] employed the λ_2 criterion to extract vortex core rings, which are a blood transport mechanism in the left and right ventricle. They created a λ_2 scalar field and computed a reference *shape signature* from a training set using *Euclidean distance shape distributions*. The best fitting iso value and thus shape of the vortex ring is determined using an iterative search for the best shape distribution match with the reference signature, which is facilitated by a hierarchical clustering. However, vortex core extraction is challenging due to noise in the measured data.

5.2.3.3. PATTERN MATCHING

Vector pattern matching (VPM) analyzes the similarity of normalized flow vectors in a plane to idealized flow templates via convolution. It was described by Heiberg et al. [208] in order to locate and identify specific 3D flow structures. Each template consists of a pattern, such as right-handedly swirling flow, describing the structure's cross-section and a second perpendicular pattern that is oriented in direction of the structure (see Figure 34). The largest eigenvalue of a resulting structure tensor per voxel is used as similarity measure. The computational effort is high, since different rotations of the patterns are used to find the maximum similarity. Furthermore, specification of the templates requires a priori knowledge, e.g., about the forward movement along the vortex core (axial velocity).

ADAPTIVE VPM: Drexler et al. [127] proposed an adaptive VPM. Here, candidate voxels are identified using a threshold on the vorticity magnitude $\|\vec{\omega}\|$. The vortex core orientation is then estimated with the vorticity vector $\vec{\omega}$, and templates are rotated accordingly. Adaptive VPM is 50 % faster than VPM, shows increased robustness, and has a simplified template specification, since it needs only one template for the detection. Among others, they used the dataset of an aneurysmatic aorta in the evaluation and showed the capability of their method to extract vortex cores.



PATTERN PARAMETRIZATION: Van Pelt et al. [528] proposed a VPM-based blood flow characterization. They defined a single parameter $\in [0, 1]$ that is sufficient to describe patterns in the plane and, thus, to characterize helical and vortical flow behavior.

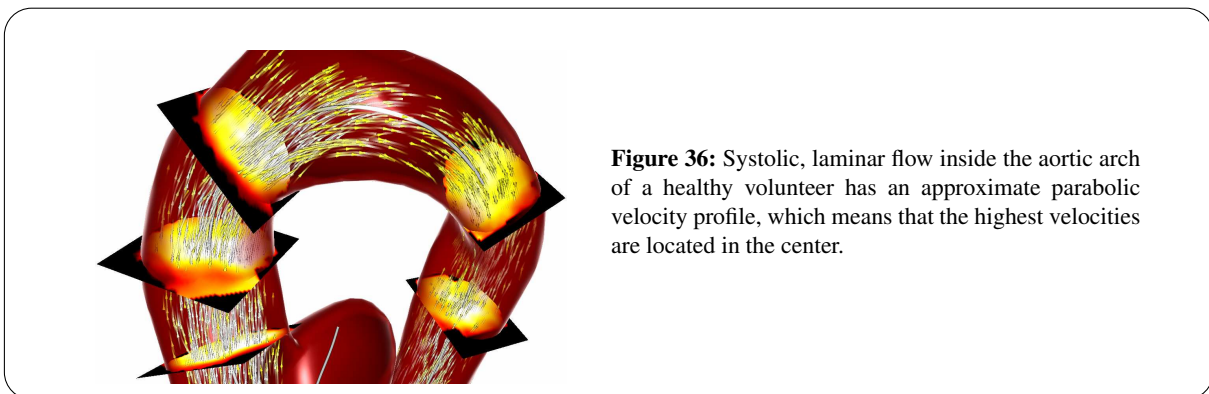
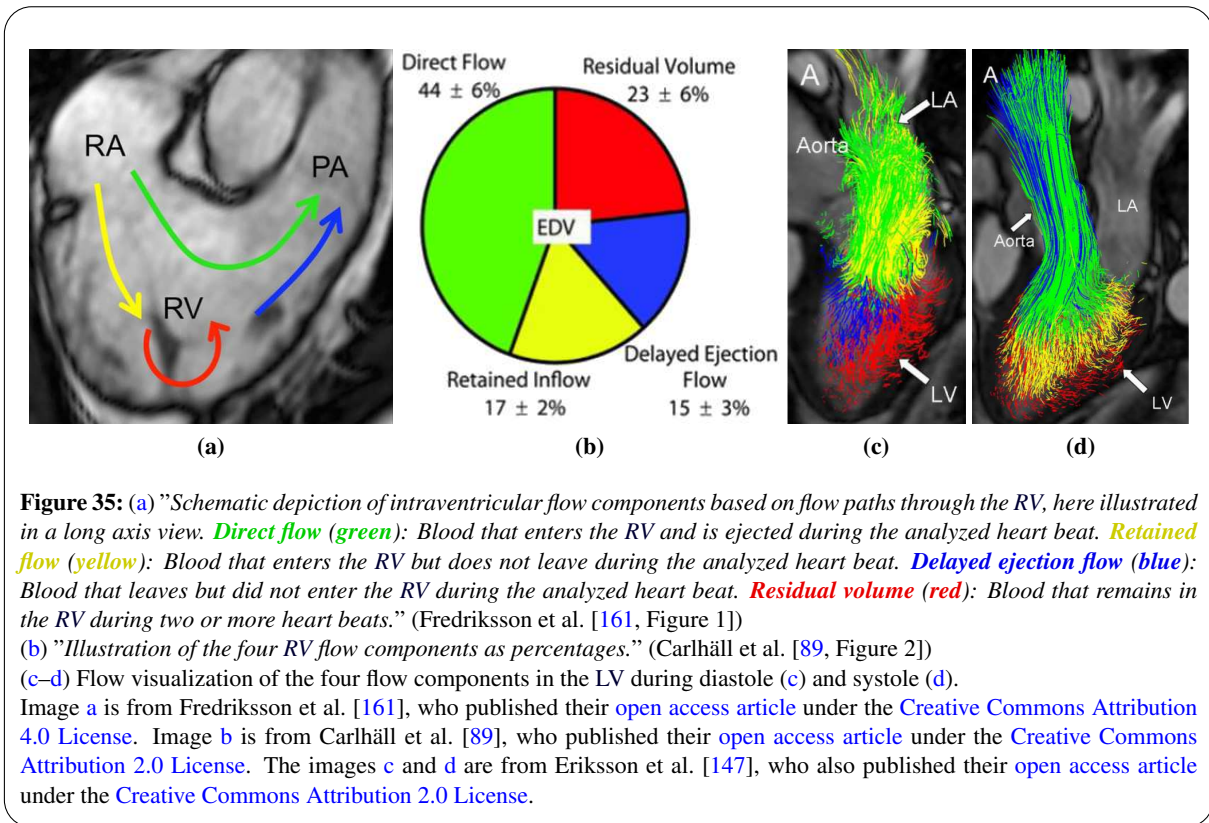
5.3. CLINICAL VALUE OF INVESTIGATING FLOW CHARACTERISTICS

The visualization of blood flow courses provides various useful information. For example, Calkoen et al. [85] investigated intraventricular flow. Among others, they visualized the left ventricular inflow using stream lines that were integrated on 4D PC-MRI data, and used this information to re-position measuring planes so that they capture peak velocities better by being perpendicular to the main flow jet [84]. The pursued quantification of flow volumes was more reliable after this correction. Dyverfeldt et al. [131] described challenges in the qualitative evaluation of the right ventricle (RV), such as the minimization of background phase offsets (recall Section 4.1.2) and the simultaneous left and right heart measurement due to greatly differing flow velocities (recall V_{ENC} , Section 3.1.2). A corresponding RV flow analysis, as performed, e.g., by Eriksson et al. [147] and Fredriksson et al. [161], provides a better insight regarding the blood transport, which is composed of four main components (see Figure 35). A similar behavior can be observed in the left ventricle (LV). Carlhäll and Bolger [88] described the alteration of this distribution in the failing LV.

Qualitative analysis of such data facilitates a deeper comprehension pathologies by inspecting blood flow courses. Especially vortex flow raised clinical interest, since this is considered as strong indicator for different diseases. This section presents selected clinical studies.

5.3.1. CARDIOVASCULAR VORTEX FLOW

Flow in the aorta (Ao) and pulmonary artery (PA) is typically laminar with a parabolic velocity profile. This means that the flow is parallel to the vessel course and the highest velocities are in the center (see Figure 36). In case of vortex flow, this laminar flow behavior can be disturbed. Fundamental research is performed to understand the correlation between flow patterns and various cardiovascular pathologies [53]. In the long term, this could facilitate a better demarcation of physiological [423] and pathological flow characteristics.

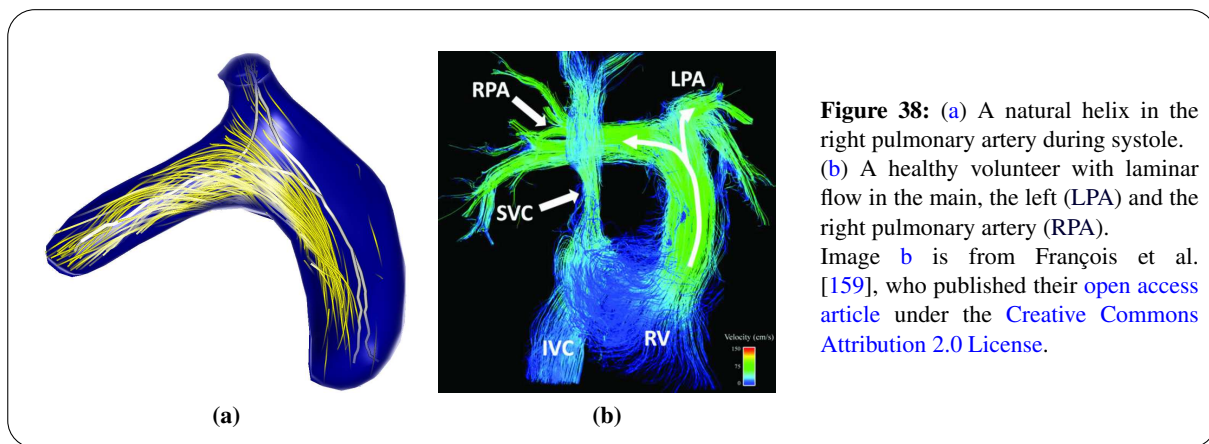
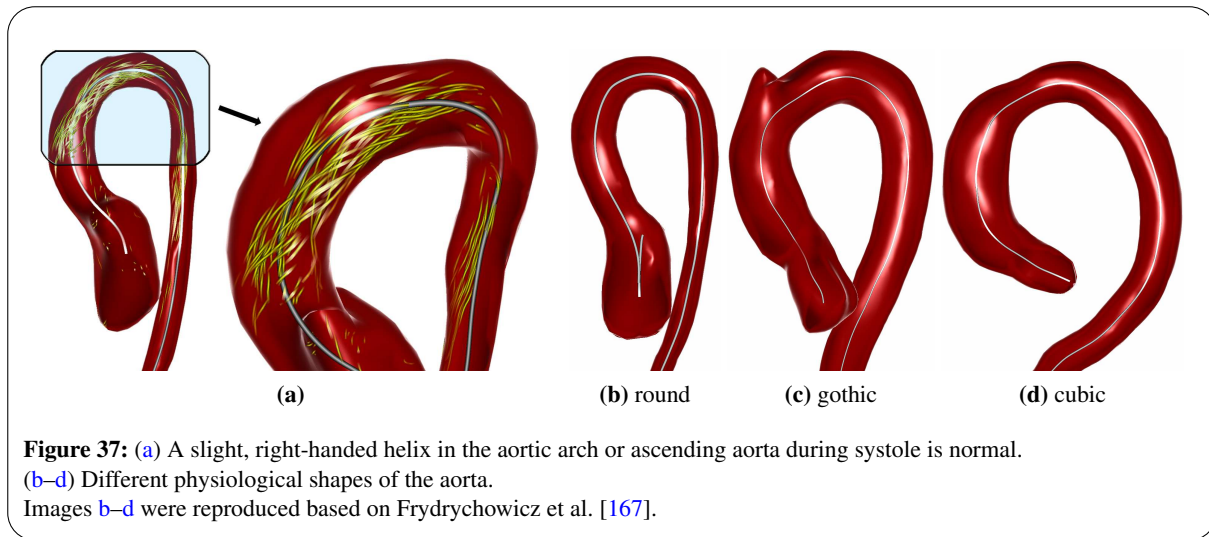


5.3.1.1. PHYSIOLOGICAL OCCURRENCES

There are some natural occurrences of vortices in the great heart vessels. Slight helical flow behavior in the aorta and pulmonary artery is physiological as well as pronounced swirling flow in the ventricles.

AORTA: Kilner et al. [263] observed helical flow in the aortic arch or ascending aorta during systole (see Figure 37a) in a study with 10 healthy volunteers. They consider them as a result of the shaped aortic geometry. Bogren et al. [56] described a similar clockwise-rotating flow behavior. However, they stated that it is not perfectly helical or spiral. In another study with 16 healthy volunteers of different age, Bogren and Buonocore [52] confirmed the observations of a right-handed helix in the ascending aorta and aortic arch. Moreover, a slight left-handed helix could be observed in the descending aortas of all participants. Both amplified in older subjects, which was explained with an increase of age-related vessel wall stiffness. According to Jin et al. [251], the wall motion also plays a role in the formation of these physiological patterns. Liu et al. [316] and Morbiducci et al. [371] supposed that helical flow in the aorta could protect from the development of arteriosclerosis.

Frydrychowicz et al. [167] investigated the influence of age and aortic morphology (shape, radius and

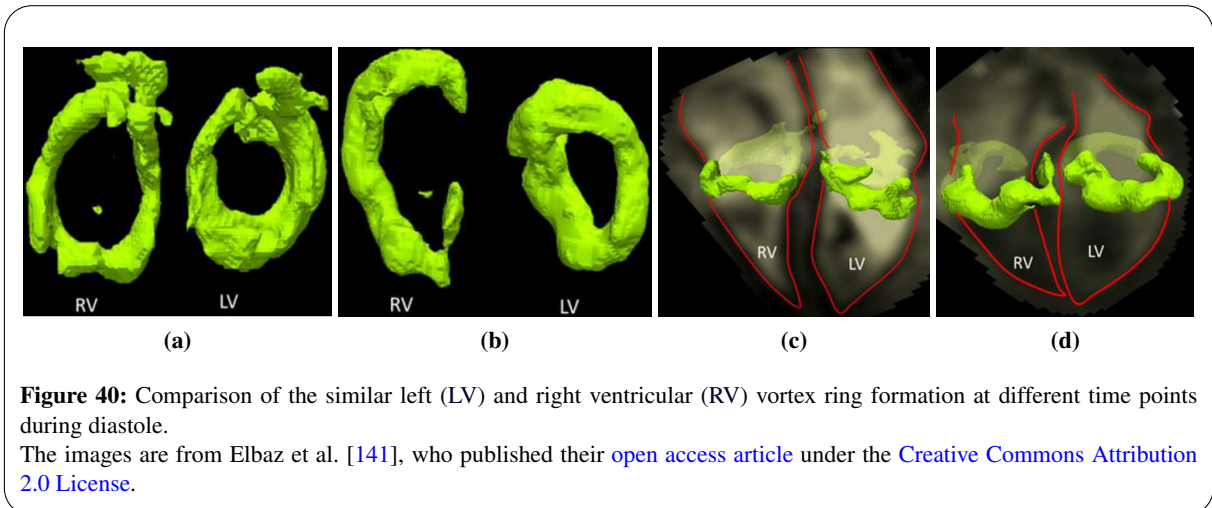
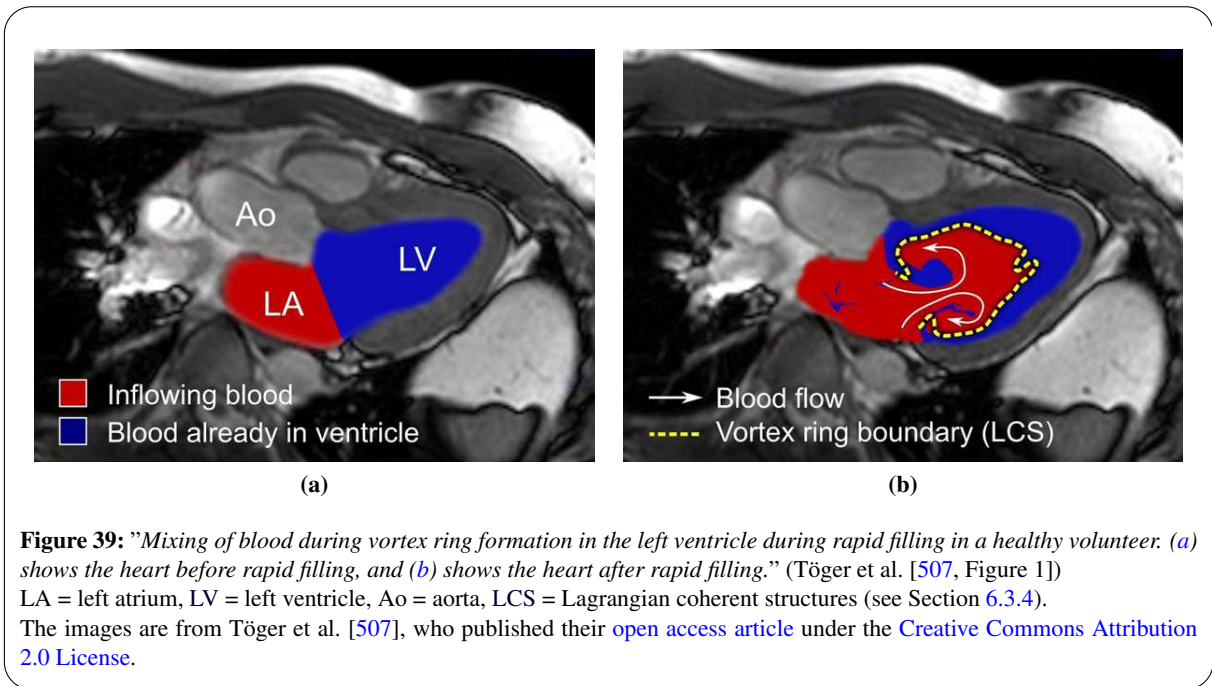


angle) on the formation of vortex flow in the thoracic aorta in a study with 64 healthy volunteers. They distinguished between a round, gothic and cubic appearance (see Figures 37b–d). Vortex flow was determined in 75 % of the cases, preferably right-handed helices in roundly shaped aortas. Furthermore, the probability of vortex flow formation was positively correlated with the age of participants and their aortic diameter.

PULMONARY ARTERY: Bogren et al. [56] detected helical flow in the right pulmonary arteries of healthy subjects (see Figure 38a). Bächler et al. [16] observed counter-rotating helices in the main PA. They were not sure about the cause, but suggested specific contraction patterns of the right ventricular outflow tract. This confirms previous findings by Bogren et al. [54] and Sloth et al. [478], who also indicated that the curvature of the PA might play a role in the helix formation. Those assumptions were later confirmed by François et al. [159] and Sundareswaran et al. [494]. However, flow can also be laminar in the whole pulmonary artery (see Figure 38b).

LEFT VENTRICLE: A 3D ring-shaped vortex (*vortex ring*) forms in the left ventricle during diastole and is an optimized blood transport mechanism (see Figure 39). The corresponding hypothesis about their existence was confirmed by Kim et al. [265]. Schenkel et al. [452] performed a validation using computational fluid dynamics (CFD). Töger et al. [506] and Elbaz et al. [142, 144] confirmed and analyzed this flow behavior using 4D PC-MRI.

RIGHT VENTRICLE: Elbaz et al. [141] also determined vortex rings in the right ventricle, where they are also a physiological flow behavior during diastole. Figure 40 shows results of their comparison with the left ventricle.



5.3.1.2. PATHOLOGICAL OCCURRENCES

AORTA: François et al. [160] investigated blood flow in patients with aortic dissection. The alteration of the flow patterns was in accordance with the disease severity. Future studies might help to "establish prognostic indicators for development of complications or aneurysm growth in patients."

A potential cause for aberrant blood flow patterns in the aorta are morphologic alterations, i.e., narrowings or dilations (see Figure 41). Frydrychowicz et al. [166] performed a study with 28 patients with a coarctation that was surgically corrected in 24 cases. In comparison to 19 healthy volunteers, 25 patients had additional vortex flow, especially in the post-stenotic vessel section. Hope et al. [222] confirmed these findings in a similar study. Prominent vortex flow was detected in 9 of 13 patients with a strongly bent aortic arch after the coarctation was corrected. Frydrychowicz et al. [165] established a link between aneurysm development in the post-stenotic vessel section and the repair of coarctation. Vortex flow was considered as potential cause by Crook and Hope [110] and Hope et al. [225].

Markl et al. [342] considered aneurysms in the thoracic aorta as potential cause for the formation of vortex flow. In a study with 13 aneurysm patients compared to 19 healthy volunteers, Hope et al. [228] found strong, right-handed, helical flow in the ascending aorta in 80 % of the patients. Similar studies

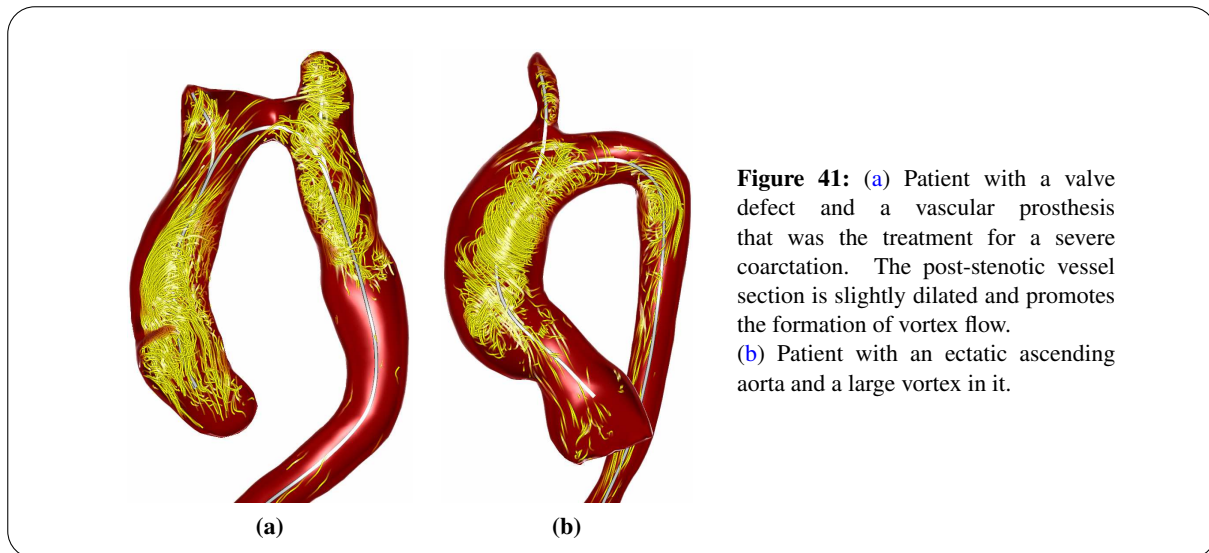


Figure 41: (a) Patient with a valve defect and a vascular prosthesis that was the treatment for a severe coarctation. The post-stenotic vessel section is slightly dilated and promotes the formation of vortex flow. (b) Patient with an ectatic ascending aorta and a large vortex in it.

with similar results were performed by Bürk et al. [78], Frydrychowicz et al. [164], Landgraf et al. [295], Markl et al. [338], and Weigang et al. [546].

Examining 26 patients with the Marfan syndrome, Markl et al. [340] found that they have a 3–25 % larger aortic diameter. As a result, they had increased helical flow in the descending aorta and in the vessels branching off from the aortic arch. A similar result was determined by Geiger et al. [181].

Kozerke et al. [282] examined flow in patients with bi-leaflet aortic valve prostheses. They found altered flow patterns in close proximity to the valve during early systole as well as adjacent retrograde flow. Kvitting et al. [291] compared six healthy volunteers to two Marfan patients six months after an aortic valve-sparing surgery (recall Section 2.2.1). They described a loss of natural vortex flow after peak systole in the replaced aortic root region. Von Knobelsdorff-Brenkenhoff et al. [537] investigated flow patterns in patients after aortic valve replacement. They determined flow characteristics that are different from healthy volunteers, depending on the concrete valve replacement type.

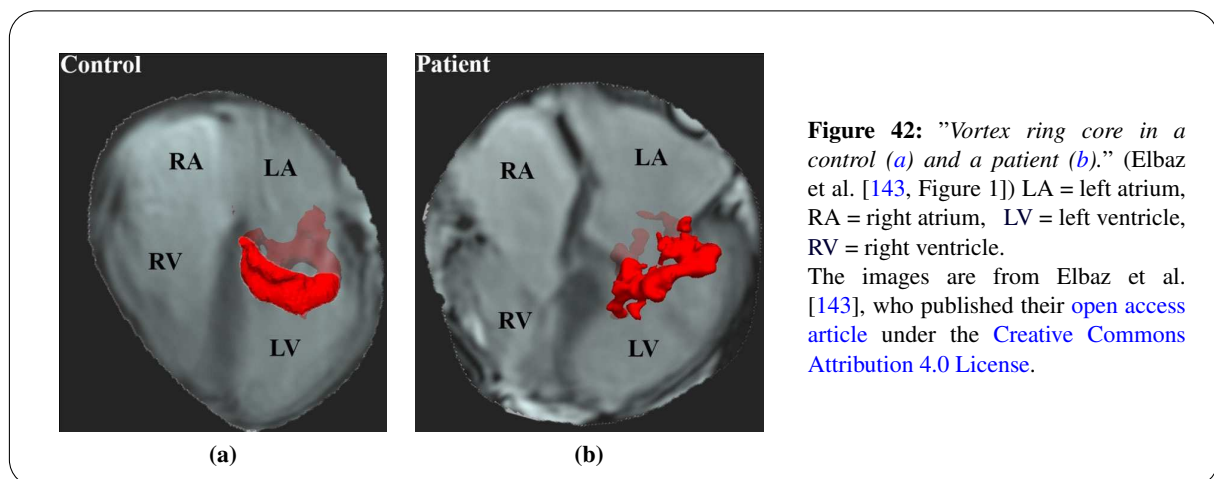
There are different types of bicuspid aortic valves (BAVs), depending on which cusps are fused. Sievers and Schmidtke [472] provided a corresponding classification as a result of 304 surgeries. Hope et al. [221] found helical flow in the ascending aortas of 75 % of their examined 20 BAV patients. These findings were confirmed by Meierhofer et al. [356] in a similar study where 85 % of the 18 patients had such flow patterns. Barker et al. [25] and Bissell et al. [40] described a dependency of occurring flow patterns and the BAV fusion type, which allows a prediction of the severity of the flow abnormalities [41]. In a more general study with various aortic valve malformations, Entezari et al. [146] confirmed the influence on the resulting flow in the ascending aorta. BAV patients are prone to aneurysm development, as stated by Barker and Markl [22]. There is increasing evidence that the resulting vortex flow induces altered shear forces on the vessel wall (*wall shear stress* (WSS), see Section 6.2.1) [24, 223]. The flow eccentricity was linked to aneurysm growth rates by Hope et al. [224], whereas the valve morphology (fusion type) has been shown to produce different WSS distributions by Mahadevia et al. [331]. These might be the cause for these secondary pathologies. A better understanding of the vessel wall-fluid interdependencies may lead to improved clinical guidelines for the treatment of corresponding diseases in the future.

PULMONARY ARTERY: In tetralogy of Fallot patients, MRI-based flow parameters are incorporated in the decision for a re-operation or intervention [312, 504].

Reiter et al. [425, 426] used qualitative flow analysis to assess pulmonary hypertension by evaluating vortex flow in the main pulmonary artery. They showed that the period of vortex existence facilitates the measurement of elevated mean arterial pressure. This is a great success, since an extremely dangerous right-heart catheterization, which is normally used to evaluate the pressure [211], is replaced with

non-invasive 4D PC-MRI. Additionally, they observed that larger vessels promote the formation of vortex flow.

LEFT VENTRICLE: A disturbance of the left ventricular (LV) vortex ring formation due to various diseases might affect the diastolic function and the overall cardiac health, as stated by Gharib et al. [183] (see Figure 42). Töger et al. [506] determined the ring volume in healthy volunteers and patients with *ischemic cardiomyopathy* – a defect of the heart muscle due to narrowed coronary arteries. The volume was smaller in the patients, implying a loss of efficiency of the blood transport mechanism. In a similar study with 107 subjects, Kheradvar et al. [262] confirmed a different filling behavior in the LV in patients with diastolic dysfunction. Moreover, the vortex formation time might be a useful parameter for the diagnosis and prognosis of heart failure, as suggested by Poh et al. [414] and Belohlavek [30]. Pedrizzetti et al. [404] underlined that LV flow analysis provides new insight in addition to the analysis of conventional function parameters.



5.3.1.3. CLASSIFICATION

Clinical studies focus on more than the pure existence of vortex flow, since some pathologies cause characteristic patterns. A classification aims to describe these characteristics by defining specific properties [55]. So far, this is done completely manually and since there is a smooth transition between some properties, the classification can suffer from a high inter-observer variability. Commonly used criteria are briefly described in the following:

- The **shape** refers to the stretching and forward movement within the vessel. Swirling flow with a rather roundish appearance and a small forward movement is called *vortex* or *vortical flow*. Such flow keeps rotating in the same vessel section. Elongated flow with a strong forward movement is called a *helix* or *helical flow*. In other words by Geiger et al. [181]: "Vortex flow was defined as revolving particles around a point within the vessel with a rotation direction deviating by more than 90° from the physiological flow direction. They resemble recirculating areas within the vessel. Helix flow was considered a movement around an axis with some net forward flow along the flow direction creating some kind of a corkscrew-like motion." They further distinguished between a *global helix*, encompassing the whole vessel, and a *local helix* that occurs only in a specific vessel section.
- The **size** of a vortex describes how much of the vessel's cross-section is occupied by swirling flow. *Minor* and *major* describe less and more than 50 %, respectively.
- A spatial characterization of the vortex occurrence is given by the **vessel section**. For the aorta (Ao) there is the aortic root, ascending aorta (AAo), aortic arch and descending aorta (DAo). For the pulmonary artery (PA) there is the pulmonary trunk (also: main PA) and the left (LPA) as well as right PA (RPA). In the ventricles, the proximity to a specific valve can be used as descriptor.

- The **time** is the temporal occurrence of the vortex. Usually, it is only distinguished between *systole* and *diastole*. Persistent vortices are present during the full cardiac cycle.
- The **rotational strength** refers to the accumulated angle of swirling flow. Meierhofer et al. [356] used a grading from 0 to 3. Grade 0 was defined as laminar flow. The grades 1, 2 and 3 describe helical flow with maximum a half turn (below 180°), maximum one turn (between 180° and 360°), and more than one turn (above 360°). Geiger et al. [181] had a similar approach with 3 grades: No rotation, below 360°, and above 360°. The term *pronounced helical flow* was employed for the highest grade.
- The **turning direction** distinguishes the direction of rotation between *left-* and *right-handed*. Since the centerline tangent is used as reference axis, the turning direction describes a clockwise or counterclockwise flow rotation in the vessel's cross-section [228].
- **Nested helical flow** is defined as "*greater than 180° curvature of the majority of high velocity peak systolic stream lines around slower central helical flow in the ascending thoracic aorta.*" (Hope et al. [221])

Section 8.4 describes an approach to cluster vortex entities and automatically obtain an objective classification based on an adaption of the listed criteria.

5.4. SUMMARY

ANATOMICAL CONTEXT: Vessels are displayed as contextual information. They are either extracted as a geometric surface from an underlying (3D) segmentation or visualized directly using volume rendering (DVR). Geometric surfaces can be employed for various quantifications, and single vessels can easily be hidden to focus the analysis. Both approaches require front face culling to make the intravascular flow visible.

FLOW VISUALIZATION: *Direct methods* are the simplest group of techniques. *Arrow plots* depict velocity vectors and *height fields* show time-dependent flow strengths in the vessel's cross-section. *Texture-based* methods are uncommon in the blood flow context. Instead, *geometry-based methods* have been widely adopted, as they are intuitive and easy to interpret. Calculated blood flow *trajectories* (*path lines*) are depicted using well-known flow visualization techniques, such as *illuminated stream lines* (ISL) and *halos*. *Pathlets* and *particles* are employed in the *animation* of the 4D path lines. The problem of visual clutter was addressed by establishing *simplified visualizations*. A prerequisite is the *clustering* of similar line bundles. Selected *cluster representatives* can be displayed or *illustrative arrows* as the average course of a cluster. *Feature-based methods* aim at an extraction of specific flow characteristics. *Line predicates* are a suitable filtering technique. Among others, they were employed to extract high-velocity *inflow jets*. A relevant feature is vortex flow. A wide range of global and local vortex core and region extraction methods (for general vector fields) was described in the last decades. An often employed local measure is the λ_2 criterion. Other feature-based approaches analyze similarities to pre-defined flow patterns via template matching.

HEALTHY AND PATHOLOGICAL FLOW BEHAVIOR: Physiological flow in the aorta and pulmonary artery is mostly laminar with a parabolic velocity profile, i.e., the highest velocities are in the center. Flow in the left and right ventricle naturally forms vortex rings during diastole, which are an optimized blood transport mechanism. Typical vortex flow patterns are caused by specific pathologies, e.g.:

- Bicuspid aortic valves (BAVs) are likely to produce systolic vortex flow in the ascending aorta. This is associated with increased shear forces (WSS) on the vessel wall and aneurysm development.
- Vortices often occur in post-stenotic vessel sections, which also tend to be dilated.
- The persistence of pulmonary artery vortex flow in patients with pulmonary hypertension (PAH) gradually increases with the mean arterial pressure.

- Ventricular diseases can disturb the vortex ring formation, which decreases the transport efficiency and increases the heart's workload.

Medical publications classify vortices according to their *shape* (elongated helix or roundish vortex), *rotational strength* (e.g. 180° or 360° turn), *temporal occurrence* (systole, diastole or both), *vessel section* of occurrence, *size* (occupancy of the vessel's cross-section) and *turning direction* (left- or right-handedly swirling). Employed criteria are mostly binary and would benefit from a revision.

6. QUANTITATIVE FLOW ANALYSIS

Quantitative measures are essential to assess the severity of pathologies or to support treatment decisions. They allow to derive the cardiac function, vessel wall interaction and intrinsic properties of the blood flow, such as kinetic energy. For example, the *stroke volume* helps to assess the heart's pumping capacity. Pathologically low values might indicate heart failure. Stenotic vessels typically show a *pressure drop*, i.e., there is a high and low pressure before and after the narrowed region, respectively. The re-evaluation of *pressure gradients*, e.g., after a balloon dilatation (widening of the vessel), may improve the judgment of a patient's post-treatment situation. Nordmeyer et al. [385] pointed out the benefit of 4D PC-MRI data, where multiple vessels can be evaluated *after* the scan, since the full spatio-temporal flow information are available. Moreover, quantitative measures facilitate the establishment of comprehensive visualizations of a patient's situation. Hope et al. [226] provided an overview of such measures with emphasis on the clinical importance.

THIS CHAPTER IS BASED ON:

- [275, SECTION 6]: B. KÖHLER, S. BORN, R. F. P. VAN PELT, A. HENNEMUTH, U. PREIM, AND B. PREIM. "A SURVEY OF CARDIAC 4D PC-MRI DATA PROCESSING". IN: *Computer Graphics Forum* (2016), EPUB. DOI: [10.1111/CGF.12803](https://doi.org/10.1111/CGF.12803)

SEE SECTION [PUBLICATIONS](#) IN THE APPENDIX FOR THE DIVISION OF WORK.

6

6.1. CROSS-SECTIONAL METHODS

Measuring planes that are modeled as discrete grids are the basis for many quantifications. An accurate determination of the lumen pixels – the pixels inside the vessel – is required (recall Section 4.2.4). A plane can be aligned orthogonally to the vessel using time-averaged flow vectors, analysis of local structure tensors [524] as estimation of the vessel course, or, if available, the centerline direction.

MEASURING PLANE PLACEMENT: Measuring planes can be evaluated at arbitrary positions, which might impede result comparison between different datasets. Therefore, Schulz-Menger et al. [460] proposed a standardization of the post-processing and data evaluation. Among others, they suggested measuring plane locations in the aorta based on anatomical landmarks (see Figure 43).

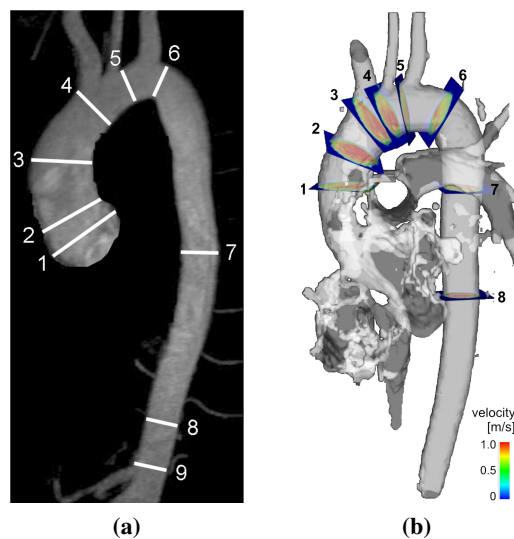


Figure 43: (a–b) Standardized measuring plane placements in the thoracic aorta based on anatomical landmarks.

Image a is from the [open access article](#) by Schulz-Menger et al. [460]. Image b is from the [open access article](#) by Bürk et al. [78]. Both were published under the [Creative Commons Attribution 2.0 License](#).

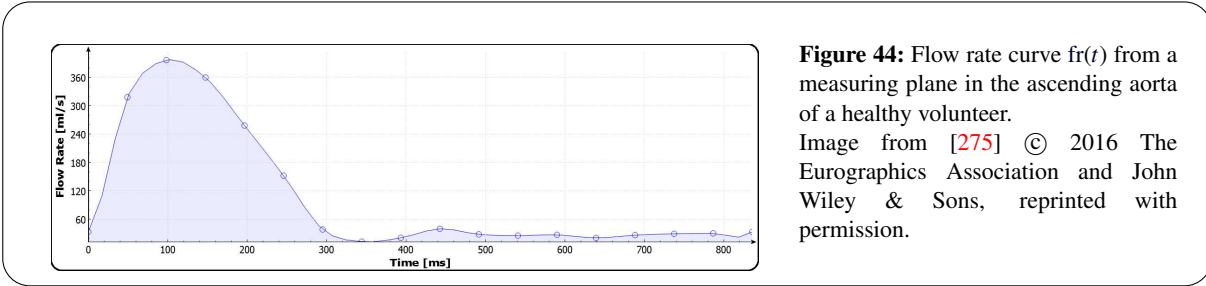
6.1.1. FLOW RATE

The *time-dependent flow rate* $fr(t)$ [ml/s] describes the orthogonally passing blood flow through a plane P with the normal vector $\vec{n} \in \mathbb{R}^3$, scale $\vec{s} = (s_x, s_y)$ [mm] per cell, and grid size $\vec{g} = (g_x, g_y)$:

$$fr(t) = s_x \cdot s_y \cdot \vec{n} \cdot \sum_{x=0}^{g_x-1} \sum_{y=0}^{g_y-1} S(P(x,y), t) \cdot \mathbf{V}(P(x,y), t) \quad (13)$$

with $S(P(x,y), t) = \begin{cases} 1, & (P(x,y), t) \text{ inside vessel} \\ 0, & \text{else} \end{cases}$

$P(x,y) = \vec{p}$ is a position on the plane transformed to 3D world coordinates. $\mathbf{V}(P(x,y), t)$ [m/s] yields velocity vectors \vec{v} from the phase image \mathbf{V} . If calculated for each temporal position, $fr(t)$ is periodic, since it represents one full heart beat (see Figure 44).



6

FLOW VOLUMES: The *forward flow volume* (FFV) [ml] and *backward flow volume* (BFV) [ml] is the area of the $fr(t)$ curve above and below 0, respectively, scaled with 10^{-3} to obtain [ml]. Thus, the FFV is the blood volume during the whole cardiac cycle through the plane in one direction, which points towards the main blood flow jet, whereas the BFV is the corresponding blood volume through the plane in the opposite direction. The *net flow volume* (NFV) [ml] is $FFV - BFV$ or simply the integral of $fr(t)$. Thus, the NFV is the amount of blood that effectively passes the plane. It can be positive or negative, depending on whether forward or backward flow is predominant [51, 268]. The *stroke volume* (SV) [ml] describes the pumped blood per heart beat. It is a special case of the NFV, where the measuring plane is located directly above the aortic or pulmonary valve (both values should coincide). The SV can be used as marker for the cardiac function [431], as abnormally low values might indicate the inability of the heart to supply a sufficient amount of blood to the body. The *cardiac output* (CO) [l/min] is the pumped blood volume per unit time. The *cardiac index* (CI) [l/min/m²] additionally incorporates the *body surface area* [m²], which is approximated with a formula that contains a person's height [cm] and mass [kg].

NFVs can also be used to quantify the severity of *shunt flows*. For example, a *right-to-left shunt* allows blood to flow between the right and left ventricle due to a hole in the ventricular septum – the wall between the ventricles. Mauritz et al. [348] quantified the SV above the pulmonary valve in patients with pulmonary hypertension (PAH), which is considered as a standard procedure. However, they showed a limited accuracy of the obtained SVs and suggested to prefer measurements above the aortic valve instead. Eriksson et al. [148] examined the SV in patients with heart failure and in healthy volunteers. They found that the patients' hearts had a higher workload, although the SVs were equal. Westenberg et al. [554] presented a method for the improved measurement of flow volumes through the mitral valve (MV). They manually defined a MV plane in each temporal position that was used for the corresponding through-flow calculation. Hsiao et al. [234] used SVs to verify an accelerated 4D flow measurement technique that facilitates data acquisition in under 10 min.

The *percentaged back flow volume* (PBFV) [%] is the ratio $BFV / (FFV + BFV)$. The *regurgitation* (also: *regurgitant*) *fraction* (RF) [%] is the PBFV measured directly above the aortic or pulmonary valve and thus describes the percentage of blood flowing back when the corresponding valve should be closed. RFs below 5 % can also occur in healthy persons and are considered as physiological [560].

INACCURACIES: Hoogeveen et al. [219] pointed out the susceptibility of the flow rate calculation to different imaging artifacts. They suggested a model-based approach that is applicable to small, straight, and cylindrical arteries with a parabolic velocity profile. Therefore, this is not suitable for the cardiac context. Bakker et al. [19] summarized potential sources of errors in 2D PC-MRI acquisitions, such as aliasing (phase wraps).

We determined vortex flow as a main cause for quantification uncertainties [278]. Section 9.1 describes a systematic evaluation of measuring planes with slightly different angulations that yields a distribution of NFVs. A box plot-based graph then illustrates the result variations, which can be seen as uncertainty. Section 9.2 investigates the incorporation of motion information in the SV quantification.

6.1.2. PULSE WAVE VELOCITY

The *pulse wave velocity* (PWV) [m/s] [71, 349] refers to the “rate of transmission of the systolic pulse through a vessel.” (Hope et al. [226]) It is an indicator for arterial stiffness, since it is lower and higher in elastic and stiff vessels, respectively. Stiffness increases with age [134] as well as various physiological, genetic, and cardiovascular risk factors [226]. “The measurement of PWV is generally accepted as the most simple, non-invasive, robust, and reproducible method to determine arterial stiffness.” (Laurent et al. [305]) Kröner et al. [287] examined patients with aortic aneurysms and found a strong correlation between the vascular diameter and the PWV. The latter was most reliable in the descending aorta (DAo) and of moderate accuracy in the ascending aorta (AAo). PWV was associated with the mass of left ventricle by Brandts et al. [72]. Amaral et al. [6] found an inverse association of PWV with the total lung capacity. Blacher et al. [43] determined PWV as a marker for the presence of atherosclerosis and a predictor of cardiovascular risk in patients with hypertension. Laurent et al. [304] performed a similar study and showed that PWV is a predictor of cardiovascular mortality in patients with hypertension. Van Elderen et al. [516] examined type 1 diabetes mellitus patients and found PWV plus the related aortic stiffness to be a predictor for white matter brain atrophy.

The description in this section follows Wentland et al. [553] and Dyverfeldt et al. [134], who both provided overviews of MRI-based PWV measurements. They were first discussed by Mohiaddin and Longmore [367]. Markl et al. [339] focused directly on 4D PC-MRI in their overview. Originally, PWV is computed using the *Moens-Korteweg* equation:

$$\text{PWV} = \sqrt{\frac{E \cdot h}{2 \cdot r \cdot \rho}}, \quad (14)$$

where E [kg/(m · s²)] is the vessel’s *elastic* (also: *Young’s modulus*), h [m] is the wall *thickness*, r [m] is the vessel *radius* and ρ [kg/m³] is the blood *density*.

PWV FOR MRI: The MRI-based calculation directly relates to the development of the flow curve (also: *wave* due to its typical appearance) along the vessel’s course:

$$\text{PWV} = \frac{\Delta d}{\Delta t} \quad (15)$$

Δd [m] describes the intravascular distance (length of the centerline) between two measuring planes and Δt [s] is the temporal offset of the flow rate $fr(t)$ curves (see Figures 45a–b). The offset between two waves can be obtained using specific landmarks (see Figure 45c) or by comparing whole curves:

- *Time-to-peak* (TTP) uses the curves’ global peak as landmark. This is prone to errors, since the actual peak can easily be missed due to the limited temporal data resolution.
- *Time-to-foot* (TTF) (also: *zero crossing*) [50, 368, 574] fits a regression line to the upstroke of the waveform and then determines its intersection with either the baseline ($fr(t) = 0$) or another regression line prior to the upstroke. Often, only data points between 20 % and 80 % of the maximum value are considered [553]. A variation of TTF is to use the time on the fitted line where the velocity corresponds to, e.g., 20 % or 50 % of the peak velocity (*threshold method* (TH)).

- *Time-to-upstroke (TTU)* (also: *derivative method*) uses the time of the wave's first derivative peak value as landmark [15].
- *Sigmoid fitting* approximates a sigmoid function describing the wave's upstroke [119]. The temporal distance between the sigmoid functions is determined by comparing the positions with the highest curvature.
- *Cross-correlation (XCorr or just XC)* [156] performs incremental temporal shifts of one waveform and uses the temporal offset as result where two curves' correlation was highest.
- The *Fourier analysis (FA) method* is used to determine two waves' phase shift by fitting a line to low frequency components of the Fourier transformed waves [303]. The temporal distance is derived from the slope of this regression line.
- The *center of mass (COM)* [134] is calculated as weighted average of points on the curve that are located between 20 % of the peak flow rate on the upslope and 20 % of the peak flow rate on the downslope of the wave.

PERFORMANCE: Methods that operate on the upslope (TTP, TTF, TH, TTU, sigmoid fitting) tend to produce lower values than methods that incorporate global wave information (XCorr, FA, COM). Thus, Dyverfeldt et al. [134] suggested a careful interpretation of PWV values depending on the employed technique. Comparing TH, TTF and TTU, Mirzaee et al. [366] determined TH as most robust. Wentland et al. [551] reported similarly reliable results of TTU, TTF, and XCorr compared to TTP as well as a good agreement of PWV obtained with 2D and 4D PC-MRI.

ROBUSTNESS: Often, the PWV is obtained using more than two planes. In this case, Δd and Δt are calculated between each plane sample and the first plane. The inverse slope of a fitted regression line yields the PWV. Drexler et al. [126] described a PWV calculation, where the user simply defines a start and end position on the centerline and equidistant planes are generated and evaluated automatically (see Figure 46b). Spottiswoode et al. [482] and Magrath et al. [330] achieved increased robustness by fitting second order polynomial planes to a series of flow curves' upstrokes (see Figure 46a).

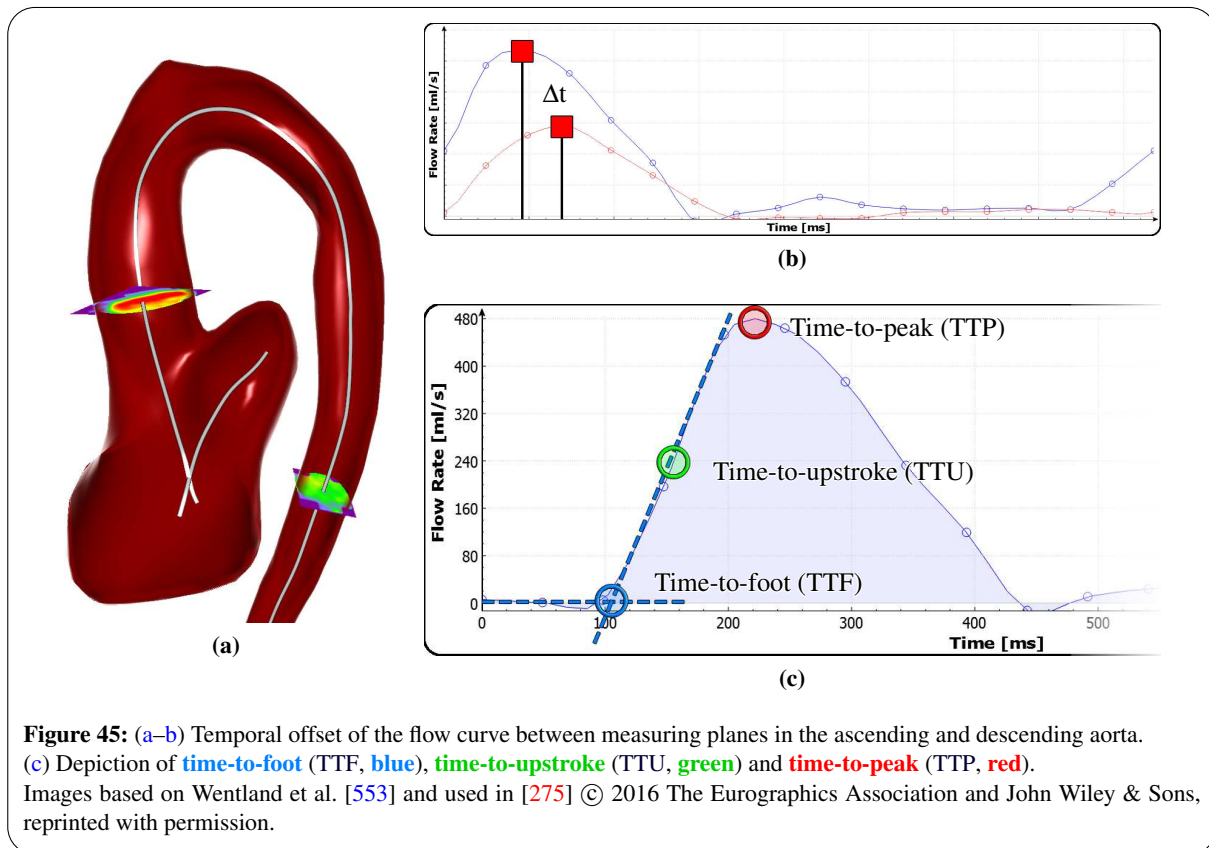
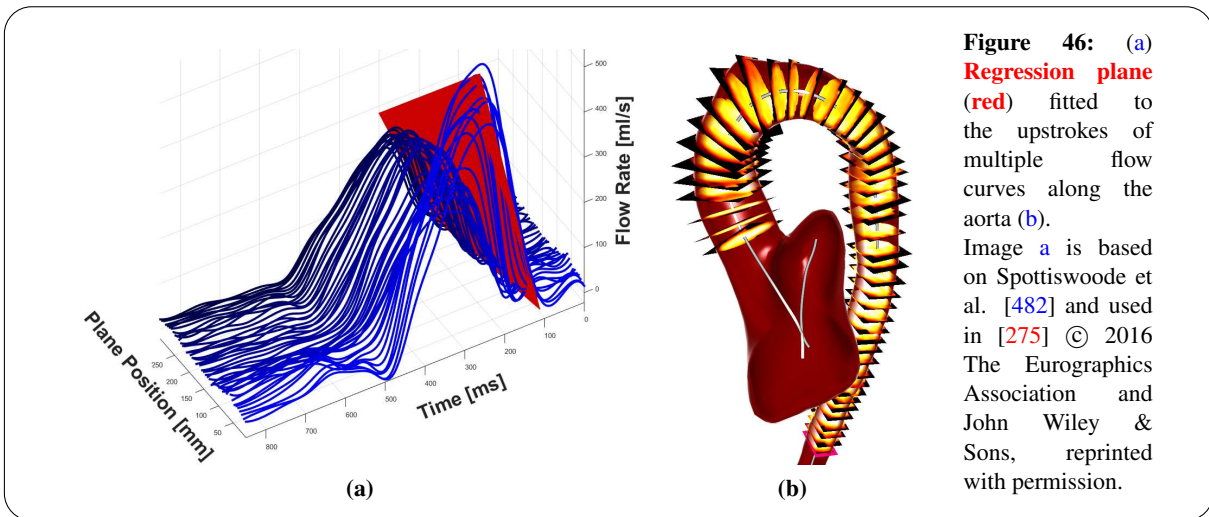


Figure 45: (a–b) Temporal offset of the flow curve between measuring planes in the ascending and descending aorta. (c) Depiction of **time-to-foot** (TTF, blue), **time-to-upstroke** (TTU, green) and **time-to-peak** (TTP, red).

Images based on Wentland et al. [553] and used in [275] © 2016 The Eurographics Association and John Wiley & Sons, reprinted with permission.



DRAWBACKS: A general problem of the PWV quantification is its strong dependency on typically shaped, noise-free flow rate curves (see Figure 45b). Noise or an ambiguous peak value can lead to implausible results. Especially pathologic cases with vortex flow are likely to produce aberrant flow rate curves depending on the respective measuring plane configurations [278]. Dyverfeldt et al. [134] restrict the PWV quantification to the descending aorta, since the flow rate calculation is more reliable there.

6.1.3. FLOW DISPLACEMENT

Flow in the great arteries typically has an approximate parabolic velocity profile, so that the highest velocities are in the vessel center (see Figure 47a). This pattern can be disturbed by various diseases, causing a *displacement* of the peak velocities or *eccentric flow* (see Figure 47b). High velocities close to the vessel wall may induce increased shear forces (wall shear stress), which can initiate a permanent, pathologic dilation.

To quantify *eccentric flow jets*, Sigovan et al. [473, 475] defined *flow displacement* $\in [0, 1]$ in a cross-section as distance between the center position and the *center of velocities*, which is the velocity-weighted average of all positions in the plane, normalized with the vessel diameter (see Figure 47c). Kari et al. [259] defined the *flow compression index* $\in [0, 1]$ as fraction of the area of mid-systolic high velocity flow and the total area of the aorta's cross-section (see Figures 47d–e).

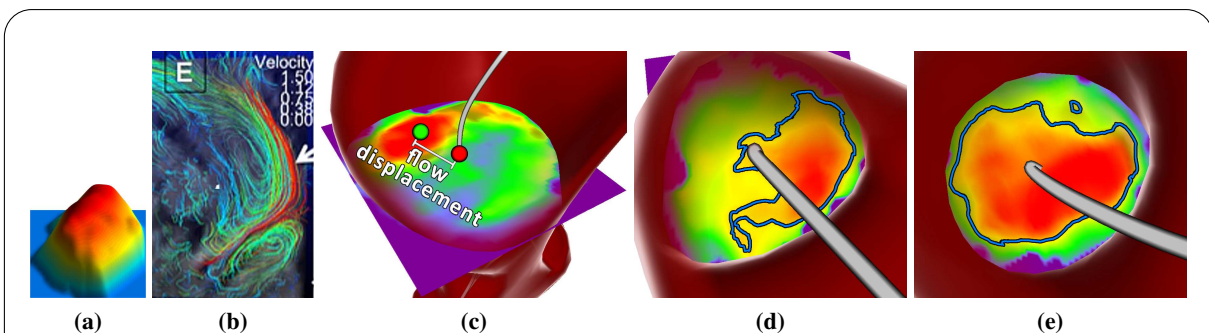


Figure 47: (a) An approximate parabolic velocity profile, which is a typical pattern in great arteries, such as the aorta and pulmonary artery.

(b) Eccentric flow jet in a patient's ascending aorta.

(c) Flow displacement in a cross-section as difference between the **center position** (red) to the **"center of velocities"** (green).

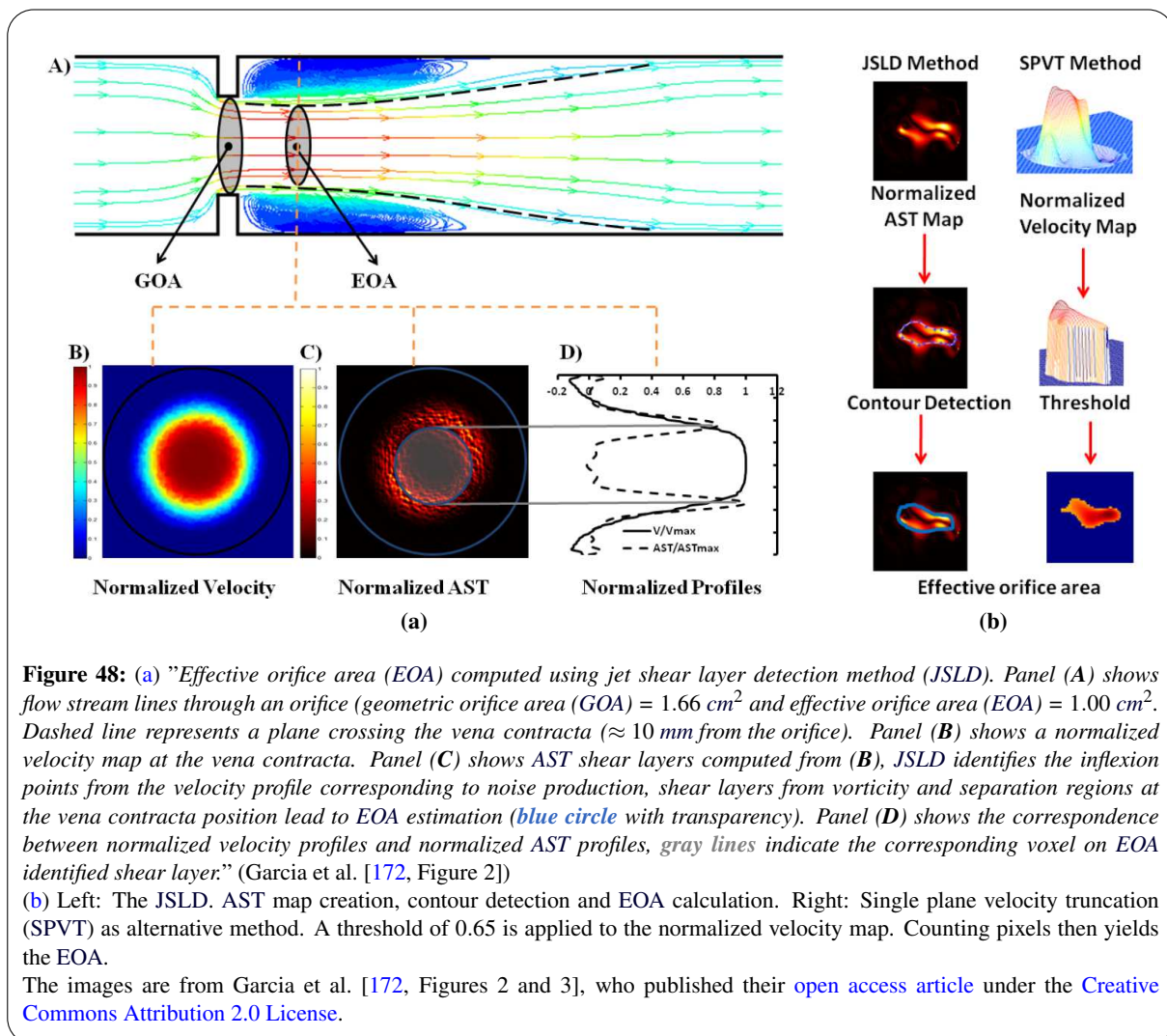
(d–e) More (d) and less compressed (e) distribution of high systolic flow velocities (framed in blue).

Image b is from Sigovan et al. [474], who published their [open access article](#) under the [Creative Commons Attribution 2.0 License](#). Images c–e from [275] © 2016 The Eurographics Association and John Wiley & Sons, reprinted with permission.

Flow displacement can alternatively be determined as angle between the velocity vector of the main (eccentric) flow jet and the direction of the left ventricular outflow tract (LVOT), as done by den Reijer et al. [117]. Dyverfeldt et al. [133] used the latter to grade the reproducibility of flow quantification in the aorta.

6.1.4. AORTIC VALVE AREA

The *aortic valve area* (AVA) [171] is an indicator for the severity of an aortic valve stenosis. One has to distinguish between the *geometric orifice area* (GOA) and the *effective orifice area* (EOA) (see Figure 48a). GOA is "the anatomical area of the aortic valve orifice", whereas EOA is "the minimal cross-sectional area of the flow jet downstream of the aortic valve." (Garcia and Kadem [171]) The latter is usually the measure of interest. From MRI data it can be obtained via planimetry, i.e., size quantification on a cross-sectional plane. However, Donal et al. [120] showed that such an assessment overestimates the EOA in stenotic BAV patients, which was confirmed by House et al. [232]. In a letter to the editor, Seaman and Sucosky [464] corresponded to this and underlined the mechanical complexity of BAVs, as described in their own article [465]. Especially the degree of valve calcification and pressure recovery are two important factors for the deviation of GOA and EOA. Alternatively, the EOA can be measured using Doppler echocardiography and the *continuity equation*.



Inspired by vortex sound theory [233, 314, 420], Garcia et al. [172] introduced the *jet shear layer detection method* (JSLD) (see Figure 48). Flow downstream of an aortic stenosis produces high vorticity, which is responsible for sound generation [58]. JSLD employs the *acoustical source term* (AST), which

can be computed using the velocity vector \vec{v} and vorticity vector $\vec{\omega}$ of the flow [255, 256]. It is defined as $\nabla(\vec{\omega} \wedge \vec{v})$, where \wedge is the *exterior (also: wedge) product*. Thus, the AST “is an amplification of [the] vorticity map by local velocity magnitude.” (Garcia et al. [172]) Finding a contour on the AST map that connects the local maxima allows to derive the EOA as the enclosed area. The feasibility of JSLD was subsequently shown in a study with aortic valve stenosis patients [173].

6.2. SURFACE-BASED METHODS

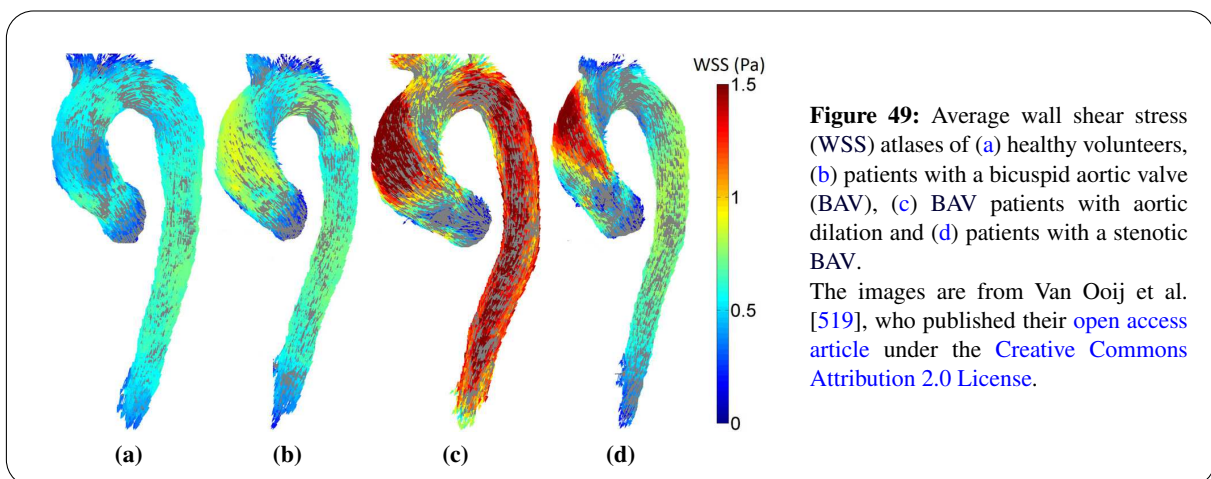
Surface-based measures describe fluid-vessel wall-interactions and the resulting effects on the vascular wall. Research on this mutual influence can increase the understanding of the initiation and progression of related vascular diseases. Corresponding calculations typically depend on an accurate vessel segmentation and geometry.

6.2.1. WALL SHEAR STRESS

Wall shear stress (WSS) [Pa] represents the force tangential to the inner layer of the vessel wall caused by nearby, complex blood flow. A WSS vector $\vec{\tau}_{\text{WSS}}$ describes the corresponding direction of the shear force (*shear stress*). Exposure to increased shear forces over a long period of time promotes pathologic vessel dilations [79]. For example, significantly increased WSS was detected in the ascending aortas of BAV patients by Van Ooij et al. [519] (see Figure 49). Geiger et al. [182] determined increased WSS in patients with the Marfan syndrome, although the aortic dimensions were comparable to healthy volunteers. Truong et al. [509] examined WSS in patients with pulmonary hypertension (PAH) compared to healthy volunteers. They showed that pathologic dilations are more likely in PAH patients, while net flow volumes were similar to healthy volunteers. As consequence of the same amount of flow passing a larger cross-sectional area, the WSS decreases. This might influence the cellular function.

WSS is a *time-resolved* measure, calculated as the product of the *shear rate* $\dot{\gamma}$ [1/s] and the *dynamic viscosity* μ [Pa · s]. The latter describes the blood’s resistance to gradual deformation by shear stress and is often chosen as $10^{-3} \cdot 3.5$ [400] or $10^{-3} \cdot 3.2$ Pa · s [555] for large arteries. However, $\dot{\gamma}$ has to be derived from the measured flow. In some applications, WSS is *time-averaged*, calculated at only one specific temporal position, such as peak systole, or the *maximum* WSS during the cardiac cycle is projected.

Papaioannou and Stefanadis [400] provided an overview of basic principles of and methods for vascular WSS. While WSS can be obtained from CFD blood flow simulations with a very fine grid in near-wall vessel regions, it is more challenging to reliably compute it based on measured flow data. The description in this section follows Potters et al. [418] who specifically described different MRI-based calculations. In addition to reliable flow measurements, especially in proximity to the wall, all WSS methods require an accurate segmentation of the vessel lumen or, more precisely, the vessel wall.



WSS APPROXIMATION ON A BOUNDARY CURVE: If a single slice is evaluated, WSS is obtained for the cross-section's boundary curve that equals a ring on the vessel surface. Simple approximations determine a mean WSS value WSS_{avg} for the whole curve using the *Poiseuille* formula [333]:

$$WSS_{avg} = \mu \cdot \dot{\gamma} = \mu \cdot \frac{4 \cdot Q}{\pi \cdot r^3} \quad (16)$$

or similar velocity-based formulae, such as:

$$WSS_{avg} = \mu \cdot \frac{4 \cdot \|\vec{v}\|_{avg}}{r} \quad \text{or} \quad (17)$$

$$WSS_{avg} = \mu \cdot \|\vec{v}\|_{max} \cdot \sqrt{\frac{2 \cdot \pi \cdot \|\vec{v}\|_{max}}{Q}}, \quad (18)$$

where Q [m³/s] is the mean *volumetric flow rate*, r [m] is the radius and $\|\vec{v}\|_{avg}$ [m/s] and $\|\vec{v}\|_{max}$ [m/s] is the average and maximum velocity, respectively. Such methods assume that the flow is steady and laminar and the vessel is straight, cylindrical, and inelastic [400]. This is especially problematic for pathologic cases.

More sophisticated approaches incorporate the actual measured flow profiles in the WSS calculation. Oshinski et al. [392] plotted sampled velocities in the plane against the distance of the corresponding pixels to the vessel wall. The slope of a linear regression line yields the required shear rate $\dot{\gamma}$. The use of a parabolic instead of linear function for the fitting might increase the accuracy [346]. Oyre et al. [395–397] derived the WSS from a 3D paraboloid fitted to large parts of the velocity profile. They excluded pixels close to the wall and in the center. Cheng et al. [101] employed analytical velocity derivatives along the inward pointing normal. They were established by local velocity profile approximations via *Lagrangian base functions*.

WSS VECTORS $\vec{\tau}_{WSS}$ ON A BOUNDARY CURVE: Newer WSS methods incorporate the additional information provided by 4D PC-MRI data (see Figure 50b). Köhler et al. [279] and Papathanasopoulou et al. [401] fitted a fifth order polynomial to the whole 3D velocity profile of subsequent slices in a bifurcation phantom in order to derive $\vec{\tau}_{WSS}$. Stalder et al. [484] manually defined measuring planes inside the aorta and performed cross-section segmentations. $\vec{\tau}_{WSS}$ were derived from B-splines that were fitted to the velocity values on the segmentation boundary, which represents the vessel wall. Sotelo et al. [481] proposed a method based on finite elements where $\vec{\tau}_{WSS}$ were obtained from a global least-squares stress-projection. Their technique is suitable for arbitrary plane sections of the thoracic aorta.

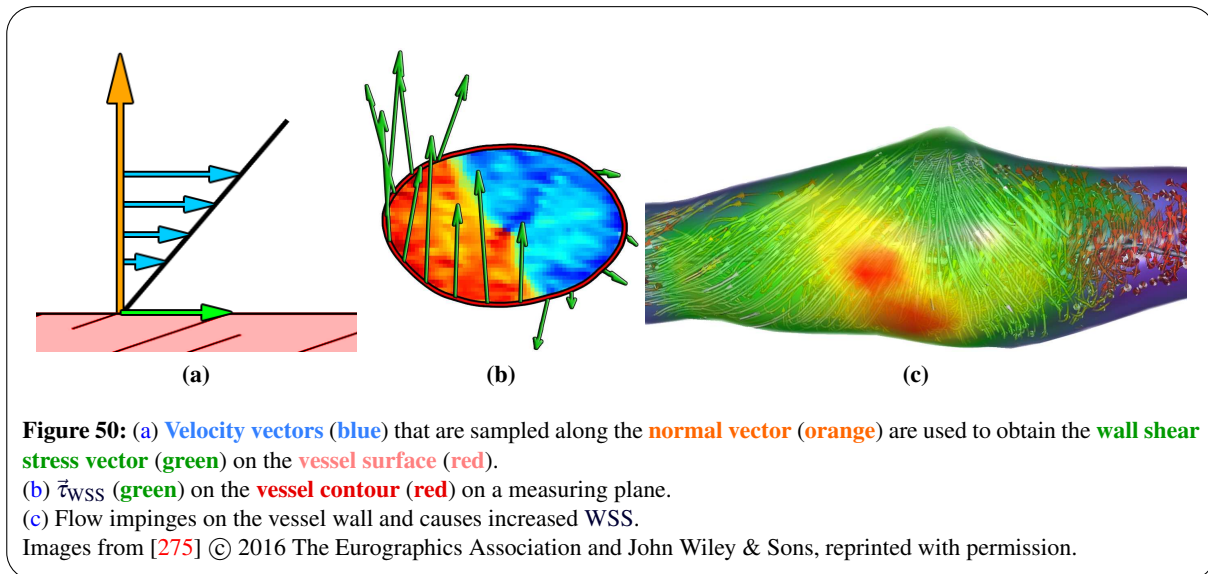


Figure 50: (a) Velocity vectors (blue) that are sampled along the normal vector (orange) are used to obtain the wall shear stress vector (green) on the vessel surface (red).

(b) $\vec{\tau}_{WSS}$ (green) on the vessel contour (red) on a measuring plane.

(c) Flow impinges on the vessel wall and causes increased WSS.

Images from [275] © 2016 The Eurographics Association and John Wiley & Sons, reprinted with permission.

WSS VECTORS $\vec{\tau}_{\text{WSS}}$ ON THE WHOLE SURFACE: Biegung et al. [35] introduced a method to obtain $\vec{\tau}_{\text{WSS}}$ on each position of a geometric vessel surface. Consequently, a segmentation of the whole dynamic vessel instead of just a cross-section is required. 3D approximations from a TMIP or similar images with high vessel contrast are often used for convenience (recall Section 4.2.2). Potters et al. [417, 418] used the term *vectorial* or *volumetric* WSS. This is defined as:

$$\text{WSS} = \|\vec{\tau}_{\text{WSS}}\| \quad \text{with} \quad \vec{\tau}_{\text{WSS}} = \mu \cdot \dot{\gamma} = \mu \cdot \frac{\partial \vec{v}_{\parallel}}{\partial \vec{n}}, \quad (19)$$

where \vec{n} is the normal vector of the corresponding surface mesh position and $\vec{\tau}_{\text{WSS}}$ represents the *shear stress* [Pa]. Velocity vectors $V(\vec{p}_t) = \vec{v}$ are obtained along the inward pointing normal $-\vec{n}$ with the number of samples as well as the maximum distance from the surface point as parameters [419]. An orthonormal basis $\{\vec{n}, \vec{n}_x, \vec{n}_y\}$ is used to obtain vectors \vec{v}_{\parallel} that are parallel to the surface's tangential plane:

$$\vec{v}_{\parallel} = \vec{v} - (\vec{v} \cdot \vec{n}) \cdot \vec{n} \quad (20)$$

The first derivatives of the \vec{v}_{\parallel} samples are calculated analytically and evaluated at the vessel wall [518] (see Figure 50a). One-dimensional, interpolating, cubic B-splines with natural boundary conditions can be fitted to the x and y component of \vec{v}_{\parallel} for this purpose.

SIMILARITY TO CEREBRAL ANEURYSMS: Extensive research on WSS has been done in the field of cerebral aneurysms [96]. Elevated pressure in combination with increased flow velocities and resulting high WSS have been shown as initiator for local vessel wall dilations by causing a degeneration of elastin as well as smooth muscles of the vessel and an increased production of collagen [97, 359]. However, there are two theories about the role of WSS in the progression and rupture of cerebral aneurysms [67, 358, 469]:

- Theory 1: Exposure to *high WSS* causes an increased production of nitric oxide. This causes the death (*apoptosis*) of smooth muscle cells as well as the gradual destruction of endothelial cells, resulting in a lower arterial tone.
- Theory 2: Abnormally *low WSS* causes inflammation of the vessel wall, which leads to its progressive degeneration.

Guzzardi et al. [197] determined an increased regional WSS in BAV patients as well as a degeneration of elastic fibers and elastin degradation [87]. Clearly, the process of aneurysm development in the aorta has similarities to cerebral vessels. From a clinical standpoint this is interesting, as aortic aneurysms above a certain diameter bear the risk of rupture, which is lethal in most of the cases. Thus, an estimation of the risk level of aneurysm development and rupture by evaluating low and high shear forces has the potential to guide therapeutic decisions in the future.

6.3. GRID-BASED METHODS

Grid-based techniques operate directly on the acquired image data or solve *differential equations* in *finite elements*.

6.3.1. PRESSURE GRADIENTS

Pressure gradients are employed as a measure to assess the severity of obstruction, e.g., due to a stenotic valve or vessel. In such cases, blood has to pass a smaller cross-sectional area or valve orifice. Increased flow velocities and intravascular pressure are the consequence. The current gold standard for pressure measurements is catheterization, which is invasive and stress for patients. However, recent advances facilitate the calculation of pressure information from MRI blood flow data.

Riesenkampff et al. [428] derived pressure fields in patients with aortic coarctation. The promising results suggest that 4D PC-MRI measurements might be a reasonable alternative to invasive catheterizations in

the future. Thus, the blood's *relative pressure* p [mmHg] is an important factor to grade the degree of stenosis (see Figure 51). Nett et al. [380] found a good agreement of pressure gradients obtained from Doppler ultrasound and 4D PC-MRI in patients with aortic stenosis. Pitcher et al. [412] demonstrated the calculation of different pressure components in healthy volunteers and patients (see Figure 52a). Eriksson et al. [150] found a spatially heterogeneous relative pressure in the left ventricle of healthy volunteers (see Figure 52b).

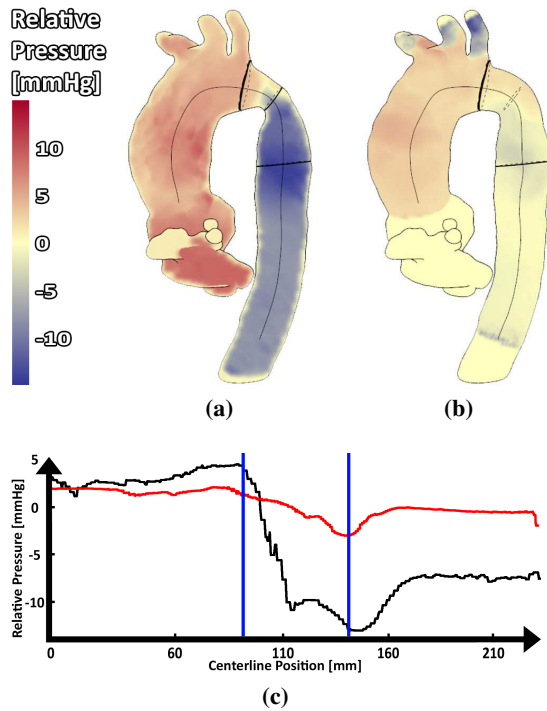


Figure 51: Relative pressure in a patient with aortic coarctation.

(a) Pressure drop derived from 4D PC-MRI data.

(b) Simulated patient situation after treatment.

(c) Pressure along the centerline. The **black** and **red curve** show (a) and (b), respectively. The **blue enclosure** is the aortic arch region, marked with **black cross-sections** in (a) and (b).

Images kindly provided by M. Neugebauer and used in [275] © 2016 The Eurographics Association and John Wiley & Sons, reprinted with permission. Image data are courtesy of Prof. Dr. Titus Kühne, German Heart Center. The pressure visualization technique was established by Schumann and Hennemuth [462].

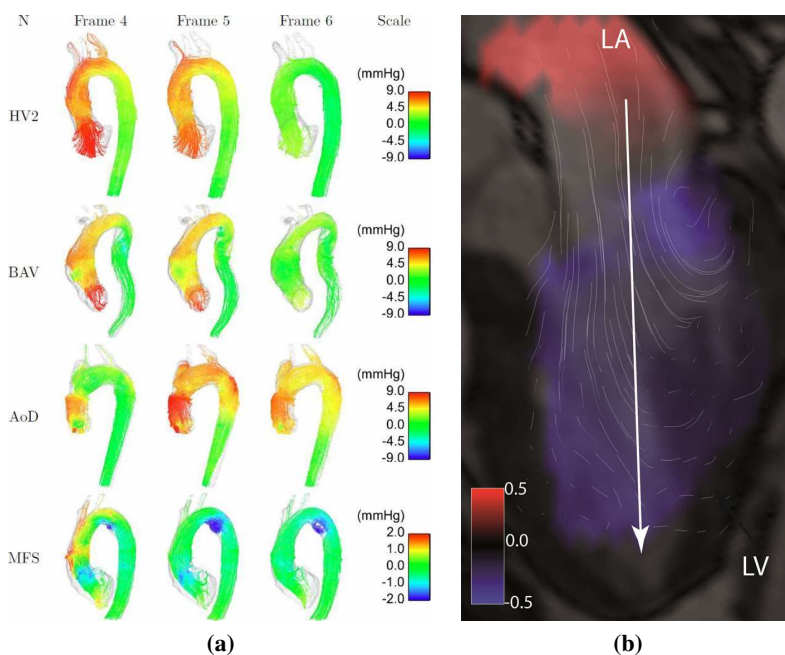


Figure 52: (a) Aortic pressure in a healthy volunteer (HV2) and three patients with a bicuspid aortic valve (BAV), aortic dissection (AoD), or Marfan syndrome (MFS).

(b) Relative pressure gradient between the left atrium (LA) and ventricle (LV) in a healthy volunteer.

Image a is from the [open access article](#) by Pitcher et al. [412]. Image b is from the [open access article](#) by Eriksson et al. [149]. Both were published under the [Creative Commons Attribution 2.0 License](#).

BERNOULLI: The *simplified Bernoulli equation* allows to estimate *pressure gradients* Δp based on the maximum velocity $\|\vec{v}\|_{\max}$ [205]:

$$\Delta p = 4 \cdot \|\vec{v}\|_{\max}^2 \quad (21)$$

Due to the quadrature, this is highly sensitive to measurement errors. Oshinski et al. [393] discussed further drawbacks, such as not considering the vessel shape.

NAVIER STOKES / POISSON: For blood, as a viscous, incompressible, laminar, Newtonian fluid, Δp can be derived using the *pressure Poisson equation* (PPE, see Equation 22), which is based on the *Navier-Stokes equation* [138, 569]:

$$-\Delta p = \nabla \cdot \left(\rho \cdot \frac{\partial \vec{v}}{\partial t} + \rho \cdot (\vec{v} \cdot \nabla) \cdot \vec{v} - \mu \cdot \nabla^2 \vec{v} \right) \quad (22)$$

The divergence-free condition must be met due to the fluid incompressibility, where $\nabla \cdot \vec{v} = 0$. $\rho = 1060 \text{ kg/m}^3$ is the fluid *density* [48], $\mu = 10^{-3} \cdot 3.2$ or $10^{-3} \cdot 3.5 \text{ Pa} \cdot \text{s}$ is the *dynamic viscosity*, \vec{v} [m/s] are velocity vectors from the flow field V and t [s] is the time. Gravitational forces can be neglected due to the horizontal patient positioning in the scanner.

Tyszka et al. [512] described an iterative PPE solver that has been shown to produce a good agreement with expected values in phantoms and with values of healthy volunteers from the literature [48]. Ebbers and Farnebäck [137] proposed a *multi-grid finite-difference scheme* to solve the PPE directly in the segmented vessel. Meier et al. [354, 355] exploited properties of hexahedral voxel grid elements to simplify the incorporation of these boundary conditions and being able to use efficient conjugate solvers due to a symmetric system matrix. Itu et al. [243] solved a 1D Navier-Stokes equation numerically with patient-specific boundary conditions to obtain the pressure distribution along the vessel's centerline. Mihalef et al. [364] described a method that uses enhanced geometric models, which provide better accuracy than voxel masks of the vessel. Physiologically meaningful boundary conditions are established via tagging of inlets and outlets. Lamata et al. [293] described a separate evaluation of the transient $\rho \cdot \frac{\partial \vec{v}}{\partial t}$, convective $\rho \cdot (\vec{v} \cdot \nabla) \cdot \vec{v}$ and viscous component $-\mu \cdot \nabla^2 \vec{v}$ (see Equation 22), which is based on the finite-element method by Krittian et al. [286]. They identified transient effects, originating from the acceleration of the blood, as main cause for relative pressure in the aorta. Donati et al. [121] paid special attention to the viscous component. They automatically fit a tubular mesh in near-wall regions, where the signal-to-noise ratios are lowest, and reconstructed the vector field there. This improved the computation of the required second order derivatives. In other work, Donati et al. [122] derived pressure differences using the *work-energy equation* for Newtonian fluids.

6.3.2. TURBULENT KINETIC ENERGY

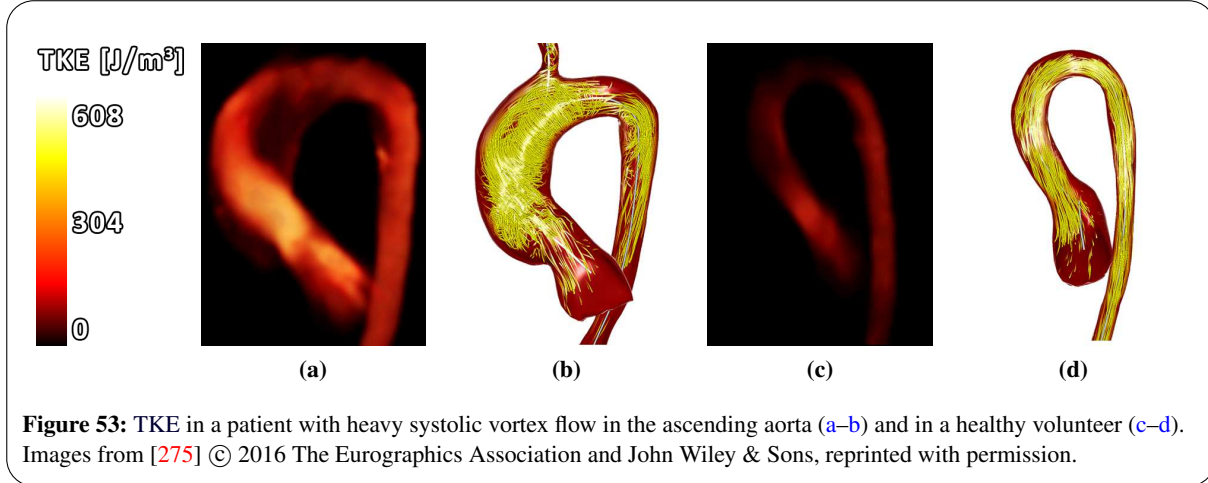
Parts of the blood's kinetic energy is irreversibly converted into heat due to viscous friction. An elevated level of lost energy increases the heart's workload and might enhance the risk of ventricular hypertrophy (enlargement). Thus, quantification of the energy loss might be a marker for disease severity [3, 26].

TURBULENT FLOW: Flow turbulences are irregularities and velocity fluctuations of the blood flow. After turbulences were studied in the aorta with a hot-film anemometer [378, 489], they were considered as potential cause for such energy losses [104]. Dyverfeldt et al. [129] described *intravoxel velocity standard deviations* (IVSD). They are the basis for *turbulent kinetic energy* (TKE) [J/m^3], which is a direction-independent measure of turbulence intensities [130] (see Figure 53). It was exploited that turbulent flow attenuates the signal in the 4D flow measurements. A *Reynolds decomposition* of the velocity field V , which is given by the phase images $V_{\{x,y,z\}}$, yields a separation into a mean \bar{V} and fluctuating velocity field V' , so that $V = \bar{V} + V'$. Assuming a Gaussian distribution, the kinetic energy of the velocity fluctuations (the TKE) corresponds to:

$$\text{TKE} = \frac{\rho}{2} \cdot \left(\sigma_x^2 + \sigma_y^2 + \sigma_z^2 \right), \quad (23)$$

where $\sigma_{\{x,y,z\}}^2$ [m^2/s^2] is the variance of velocities in $V_{\{x,y,z\}}$ and ρ [kg/m^3] is the fluid density [37]. Binter et al. [38] showed that TKE calculation has a relatively low sensitivity to the spatial data resolution.

Loudon et al. [328] found significantly higher peak TKE in patients with bicuspid aortic valve stenosis compared to patients with tricuspid aortic valve stenosis. Zajac et al. [575] determined overall low TKE values in the left ventricles of healthy volunteers. It was increased in patients with cardiomyopathy. Dyverfeldt et al. [132] used TKE to assess the severity of mitral regurgitation. They correlated the degree of flow distortion in the left atrium (LA) to the average LA TKE of one cardiac cycle.



Carlsson et al. [90, 91] quantified kinetic energy (KE) [mJ/ml] in a similar way:

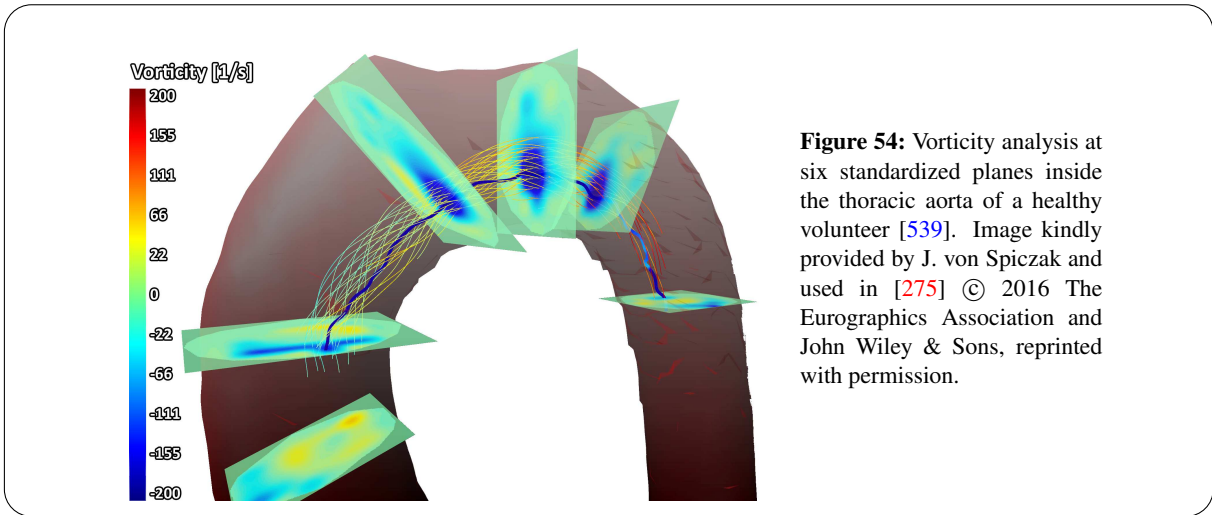
$$\text{KE} = \frac{\|\vec{v}\|^2}{2} \cdot m \quad (24)$$

The mass m of blood in the voxel is calculated as volume of the voxel multiplied with the blood density ρ , which was set to 1.05 g/ml. They found a higher peak KE during early diastole in the LV compared to the RV and explained this behavior with a possibly higher suction of blood in the LV. Lee et al. [309] examined a patient with surgically repaired congenital heart disease (CHD), which often leads to post-operative pulmonary regurgitation and obstruction. They found that the amount of energy loss was considerably increased compared to a healthy volunteer. In the future, KE could serve as non-invasively assessable biomarker for the disease severity. Jeong et al. [246] performed a similar study in patients with repaired tetralogy of Fallot and found higher KE in both the left and right ventricle compared to healthy volunteers.

6.3.3. VORTEX STRENGTH

The vorticity $\vec{\omega}$ (also: *curl*) of a vector field $\nabla \times \mathbf{V}$ describes local spinning vectors and the vorticity magnitude $\|\vec{\omega}\|$ [$1/\text{s}$] is a measure for rotational strength (recall Section 5.2.3.2). Wong et al. [562] visualized slices through the heart chambers using stream line plots colored by the flow velocities, and vector as well as contour maps depicting the vorticity magnitudes. They analyzed the mean vorticity and / or vorticity for each temporal position and depicted the results in a histogram. In addition, they defined a circulation measure as line integral of the tangential velocity along a circuit enclosing a point of interest [563]. Hess et al. [214] described *circulation* as fraction of the integral of vorticity magnitudes in an intra-aortic cross-section and the corresponding cross-sectional area. Bächler et al. [16] plotted maximum absolute vorticity magnitudes over time for measuring planes inside a vessel.

2D and 3D metrics to quantify vortex flow in the thoracic aorta were presented by von Spiczak et al. [539]. Six standardized ROIs throughout the aorta were analyzed for minimum, maximum, and average vorticity magnitudes (see Figure 54). An adapted predictor-corrector method [21] in combination with



the λ_2 vortex criterion was used to extract vortex core lines. The cores were evaluated regarding their strength and elongation over time. Additionally, surrounding vorticity magnitudes were radially sampled for each core line position using eight lines perpendicular to the core. The sampling stops when $\|\vec{\omega}\|$ falls below a given threshold. They defined a vortex' *radial expansion* as the circle's area with a radius equal to the average length of the eight lines.

HELICITY: Lorenz et al. [325] calculated averaged *helicity density* H_d and *relative helicity* H_r , which is the helicity before and after normalization (recall Section 5.2.3.2), for equidistant measuring planes inside the aorta as:

$$H_d = \vec{\omega} \cdot \vec{v} \quad \text{and} \quad H_r = \frac{H_d}{\|\vec{\omega}\| \cdot \|\vec{v}\|} \quad (25)$$

Morbiducci et al. [370] proposed a *helical flow index* as the average of *local normalized helicity* along path lines. This is equal to H_r from Equation 25. Averaging the values of all path lines yields a global assessment of present helicity in the dataset.

6.3.4. LAGRANGIAN COHERENT STRUCTURES

Lagrangian coherent structures (LCS) [199] facilitate the creation of surfaces, e.g., at vortex boundaries, that divide flow into regions with different characteristics. Based on this, Töger et al. [506] established a volume quantification of vortex rings (recall Section 5.2.3), which are a blood transport mechanism in the left and right ventricle.

FTLE: LCS are based on *finite-time Lyapunov exponents* (FTLE) [261, 301] that describe the rate of separation of nearby particles when integrated for a certain time frame Δt . A *flow map* [73] contains the end positions of particles that started at the spatio-temporal positions \vec{p}_t and were integrated for Δt . It usually has a higher resolution than the acquired image data. The concrete upsampling factor is a parameter. The FTLE is defined as:

$$\text{FTLE}(\vec{p}_t) = \frac{1}{\Delta t} \cdot \log(\lambda(\vec{p}_t)) \quad (26)$$

$$\text{with } \lambda(\vec{p}_t) = \sqrt{\lambda_{\max}[J(\vec{p}_t)^T \cdot J(\vec{p}_t)]}$$

J is the Jacobian matrix and λ_{\max} the maximum eigenvalue.

Krishnan et al. [285] directly employed the FTLE as a stop criterion for particle path calculations (recall Section 5.2.2). If the FTLE is determined close to the vessel boundaries, some of the nearby particles will be seeded inside and some will be placed outside the vessel. Thus, some particles follow the intravascular

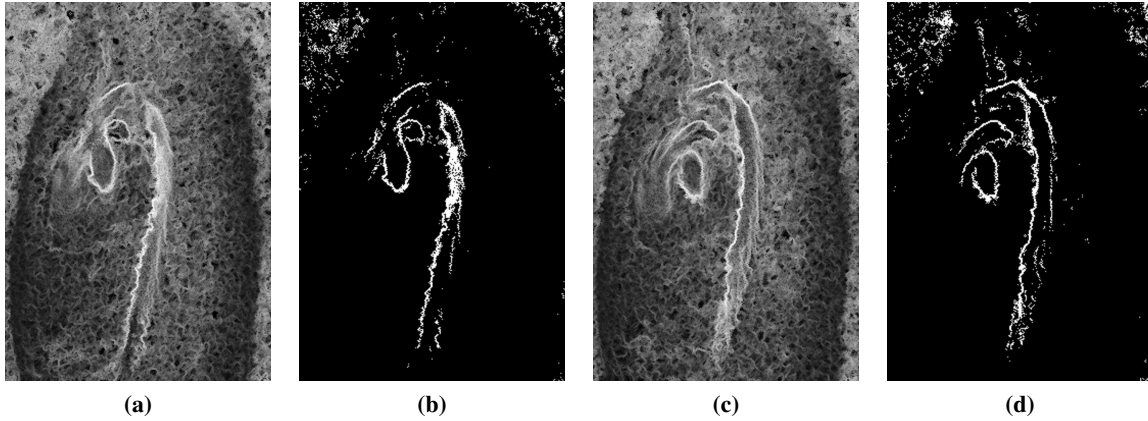


Figure 55: The application of a threshold (b,d) on FTLE images (a,c) provides an estimation of the vessel boundaries. Image from [275] © 2016 The Eurographics Association and John Wiley & Sons, reprinted with permission.

flow and some will experience a more or less random movement due to low velocities and / or arbitrary directions outside the vessel. The resulting high separation allows to estimate the vessel boundaries via thresholding (see Figure 55). Unfortunately, the boundaries' FTLE values depend on the flow velocities and thus may vary for different vessels.

6

6.3.5. CONNECTIVITY

The *connectivity* is calculated as the number of path lines that pass two specific ROIs [213]. Problems may arise if the integral lines represent wrong paths due to noise, offset errors or partial volume effects. There is a strong similarity to *diffusion tensor imaging* (DTI) [372] and the related *fiber tracking*, where probabilistic approaches are employed to calculate paths in uncertain crossings of two or more fiber bundles.

UNCERTAINTY: The connectivity is also used to establish an uncertainty quantification of the integration. Friman et al. [162] introduced a probabilistic approach that employs a sequential *Monte Carlo* sampling. They showed that each component of a velocity vector \vec{v} can be approximated by a *Gaussian* (also: *normal*) *distribution* (GD) around the true velocity vector \vec{u} :

$$\vec{v} \in GD(\vec{u}, \sigma) \quad \text{with} \quad \sigma = \frac{V_{\text{ENC}} \cdot \sqrt{2}}{\pi \cdot \text{SNR}} \quad (27)$$

Schwenke et al. [463] incorporated this estimated uncertainty into a *fast marching* method and calculated blood flow trajectories as minimal paths.

6.4. SUMMARY

Quantification results can suffer from the low spatio-temporal 4D PC-MRI data resolution and MRI-related imaging artifacts. Some methods require an accurate segmentation of cross-sections or the whole vessel.

CROSS-SECTIONAL METHODS: Cross-sectional methods employ measuring planes that are perpendicular to the vessel course and thus lie in the cross-section. Standardized placements were proposed, based on anatomical landmarks. *Flow rates* are usually shown as time-dependent flow curves. They form the basis for essential measures to assess the cardiac function:

- The *stroke volume* (SV) is the amount of pumped blood per heart beat. Too low values can indicate an insufficient blood supply to the body.

- *Regurgitation fraction* (RF) denotes the percentaged amount of blood that flows back in case of an improperly closing valve. Increased values (above 5 %) can indicate heart insufficiency.

The evaluation of these measures is highly sensitive to the specific plane configuration, i.e., location and angulation. *Pulse wave velocities* (PWV) describe the speed of transmission of flow curves through the vessel. They are higher than the actual flow velocities. PWV values are lower and higher in elastic and stiff vessels, respectively. There are multiple evaluation methods that differ in their results. *Flow displacement* refers to the position of the main flow jet. Eccentric flow jets can be a side effect of various pathologies. The *aortic valve orifice area* (AVA) is used to grade the severity of aortic valve stenosis.

SURFACE-BASED METHODS: Surface-based methods describe fluid-vessel wall interactions. *Wall shear stress* (WSS) refers to shear forces on the vessel wall caused by nearby, complex blood flow. Exposure to increased WSS over a longer period of time is linked to aneurysm growth. 4D PC-MRI-based calculations often underestimate absolute WSS values. Though, relative information can be obtained, e.g., regions with locally increased WSS.

GRID-BASED METHODS: Grid-based methods operate directly on the grid data structure, e.g., as *finite-element* techniques. *Pressure gradients* are used to evaluate stenoses. Pressure drop after a stenotic vessel section is a typical behavior. *Turbulent kinetic energy* (TKE) is based on *intravoxel velocity standard deviations* (IVSD). It describes flow fluctuations that cause energy loss and increase the heart's workload. A quantification of *vortex strengths* using *vorticity* $\vec{\omega}$ or *normalized helicity* H_n is pursued to further assess vortex flow. *Lagrangian coherent structures* (LCS) are based on *finite-time Lyapunov exponents* (FTLE). They emphasize regions with a high rate of blood flow separation, e.g., vortex boundaries. Among others, LCS were employed to approximate vessel boundaries. *Probabilistic trajectory* calculation can be employed in a *connectivity analysis*, which also enables an estimation of line integration uncertainties.

C

GUIDED DATA EVALUATION

4D PC-MRI datasets contain the full spatio-temporal blood flow information and allow a more flexible analysis than data from its 2D counterpart. Recent advances greatly reduced acquisition times to levels that are feasible for the clinical routine. Although it has the potential to replace 2D PC-MRI, 4D flow scans are mainly performed for research purposes at the moment. This points out the need for standardized and guided techniques to analyze these highly complex data. Software solutions that integrate such methods into easy-to-use workflows are of equal importance.

In this chapter, the developed software *Bloodline* is described in detail. It facilitates data analysis within ten minutes. The analysis comprises an automated data pre-processing, a graph cut-assisted vessel segmentation, semi-automatic vortex flow extraction, and analysis of the stroke volume as well as percentaged backflow. This workflow is described in Section 7.1. Resulting visualizations can easily be saved and shared using the provided one-click solutions for videos of the animated flow and screenshots of the 3D view or GUI. Section 7.2 provides background information on the code design. Section 7.3 and 7.4 characterize Bloodline’s application and alternative software, respectively.

THIS CHAPTER IS BASED ON:

- [270, SECTION 5.2]: **B. KÖHLER**, R. GASTEIGER, U. PREIM, H. THEISEL, M. GUTBERLET, AND B. PREIM. “SEMI-AUTOMATIC VORTEX EXTRACTION IN 4D PC-MRI CARDIAC BLOOD FLOW DATA USING LINE PREDICATES”. IN: *IEEE Transactions on Visualization and Computer Graphics* 19.12 (2013), PP. 2773–82. DOI: [10.1109/TVCG.2013.189](https://doi.org/10.1109/TVCG.2013.189)
- [273]: **B. KÖHLER**, U. PREIM, M. GROTHOFF, M. GUTBERLET, K. FISCHBACH, AND B. PREIM. “GUIDED ANALYSIS OF CARDIAC 4D PC-MRI BLOOD FLOW DATA”. IN: *Proceedings: Eurographics Short Papers and Medical Prize Awards*. 2015, EPUB. DOI: [10.2312/EGM.20151029](https://doi.org/10.2312/EGM.20151029)
- [278, SECTION 3.3]: **B. KÖHLER**, U. PREIM, M. GROTHOFF, M. GUTBERLET, K. FISCHBACH, AND B. PREIM. “ROBUST CARDIAC FUNCTION ASSESSMENT IN 4D PC-MRI DATA OF THE AORTA AND PULMONARY ARTERY”. IN: *Computer Graphics Forum* 35.1 (2016), PP. 32–43. DOI: [10.1111/CGF.12669](https://doi.org/10.1111/CGF.12669)
- [277, SECTION 3.2]: **B. KÖHLER**, U. PREIM, M. GROTHOFF, M. GUTBERLET, K. FISCHBACH, AND B. PREIM. “MOTION-AWARE STROKE VOLUME QUANTIFICATION IN 4D PC-MRI DATA OF THE HUMAN AORTA”. IN: *International Journal for Computer Assisted Radiology and Surgery* 11.2 (2016), PP. 169–79. DOI: [10.1007/s11548-015-1256-4](https://doi.org/10.1007/s11548-015-1256-4)

SEE SECTION [PUBLICATIONS](#) IN THE APPENDIX FOR THE DIVISION OF WORK.

7.1. WORKFLOW

This section summarizes the established processing pipeline, which partially implements methods from the Chapters 4–6. A primary concern during the development of Bloodline was to provide a guided workflow. This was established on the main screen. Processing screens are successively enabled from left to right during the analysis of a dataset. If the software is started for the first time and no datasets were imported yet, there is only one clickable button *Import Data* (see Figure 56). We received raw 4D PC-MRI data as folder with DICOM files, where every slice in each temporal position is a separate file. They are scanned and converted to 4D images in the *Import Data* part using information from the DICOM headers. A velocity offset correction (recall Section 4.1.2) is then applied to the flow images using the method by Walker et al. [540] with their suggested default parameters. Back on the start screen, the dataset now appears in the list of available datasets with a short summary on the spatio-temporal resolution and the V_{ENC} . The enumeration of already extracted vessels is empty at this time. However, the second part named *Vessel Segmentation* is now enabled (see Figure 57).

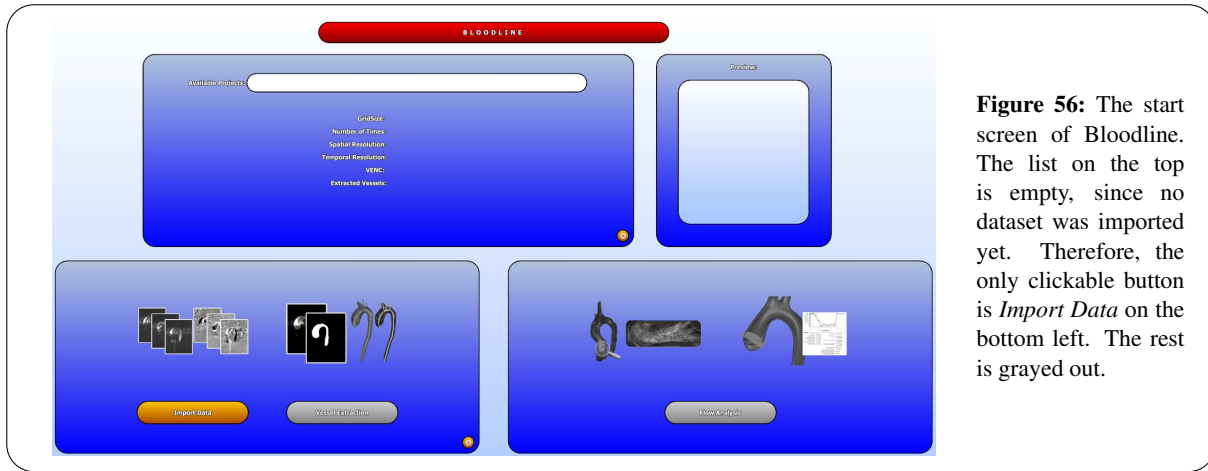


Figure 56: The start screen of Bloodline. The list on the top is empty, since no dataset was imported yet. Therefore, the only clickable button is *Import Data* on the bottom left. The rest is grayed out.

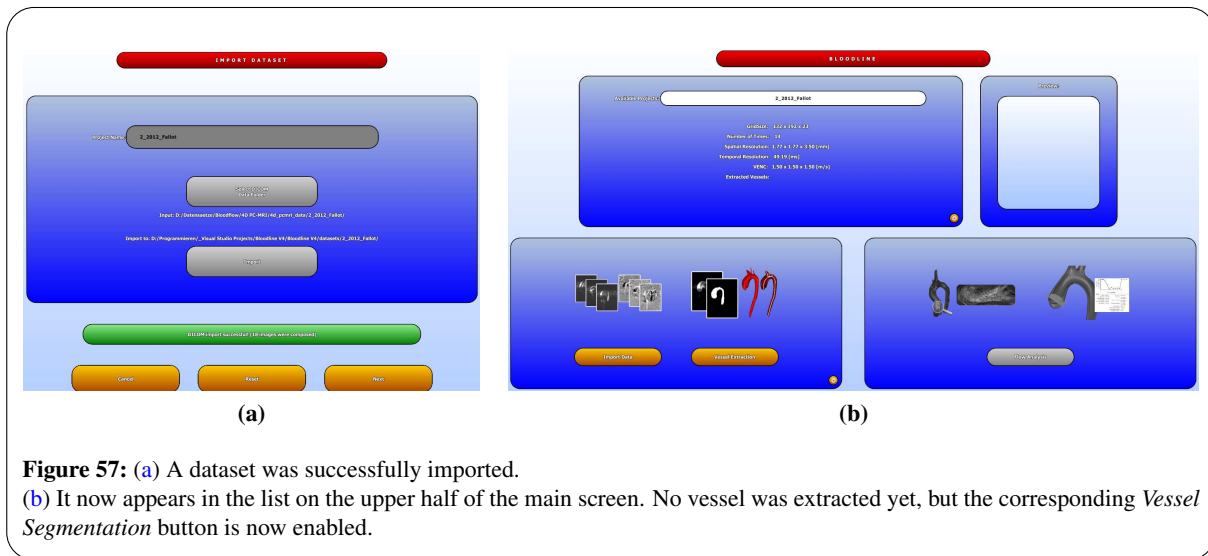


Figure 57: (a) A dataset was successfully imported.

(b) It now appears in the list on the upper half of the main screen. No vessel was extracted yet, but the corresponding *Vessel Segmentation* button is now enabled.

7.1.1. VESSEL SEGMENTATION

A temporal maximum intensity projection (TMIP) of the magnitude images and a time-averaged local phase coherence (LPC) are computed. Both yield a high-contrast 3D image and facilitate a static 3D approximation of the dynamic vessel (recall Section 4.2).

The TMIP, which we use by default, emphasizes regions with high velocity magnitudes in at least one time point. Since flow in the aorta is fast, it is clearly visible. However, the normally centrally located main blood flow jet appears prominently, while near-wall regions and vessel sections with greater valve distance may lack contrast. Therefore, the use of a non-automatic segmentation method that allows user corrections seems appropriate. Threshold-based methods, such as region growing, might not handle the varying contrasts, whereas model-based methods, such as active contours, have to compromise between high flexibility in order to capture pathologic vessel shapes and noise robustness. *LiveWire* [451] would be convenient if one finds a suitable cost function and is willing to process each image slice individually.

We decided to employ a graph cut [68, 244, 315]. For our research purposes, we employ the free (for academic purposes) version of *GridCut*. Graph cuts require the specification of regions in- and outside the target structure, which is intuitive for medical doctors. The user provides these information by drawing on the slices (see Figure 58). The better the image quality is, the less input is necessary to achieve satisfactory results. Though, detail corrections can be performed if the segmentation includes unwanted or excludes wanted parts.

The graph cut is 3D and operates in a 26-neighborhood per voxel. Thus, input is not required on every

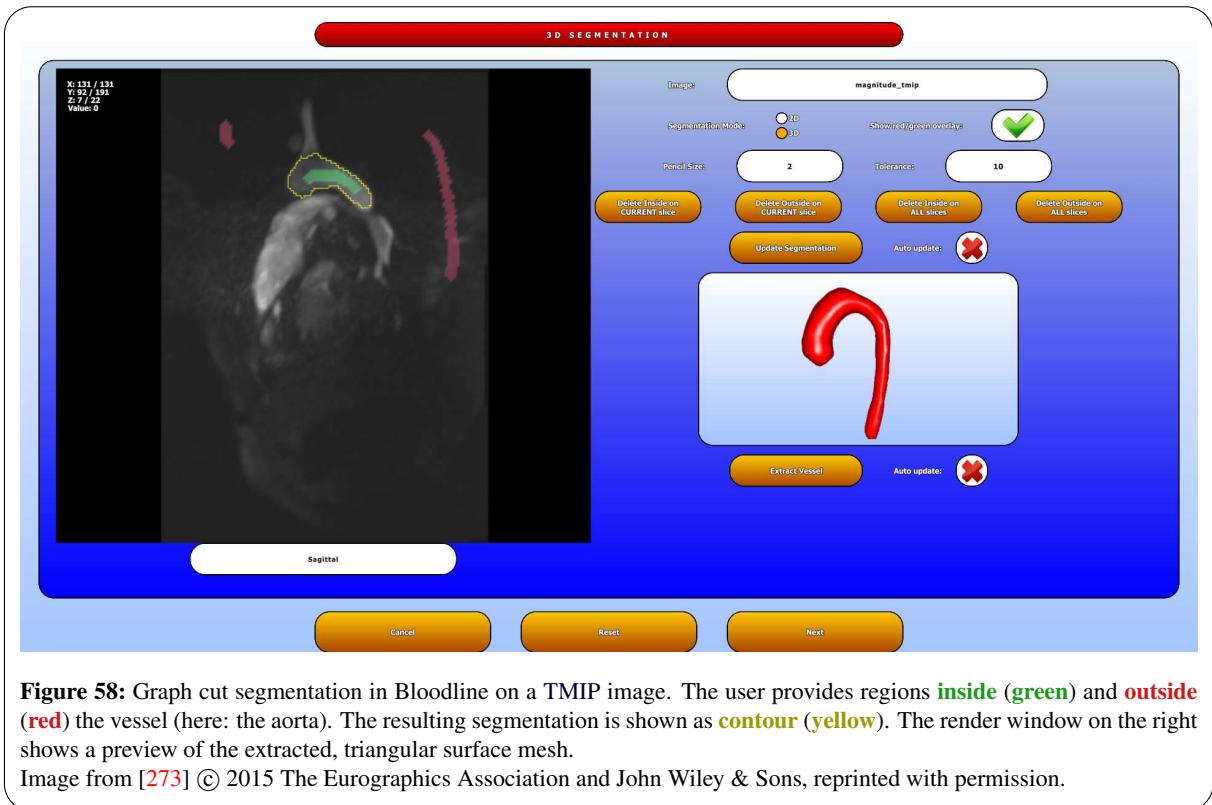


Figure 58: Graph cut segmentation in Bloodline on a TMIP image. The user provides regions **inside (green)** and **outside (red)** the vessel (here: the aorta). The resulting segmentation is shown as **contour (yellow)**. The render window on the right shows a preview of the extracted, triangular surface mesh.

Image from [273] © 2015 The Eurographics Association and John Wiley & Sons, reprinted with permission.

slice. Edge weights between nodes in the graph are set to:

$$\exp(-\alpha \cdot \|\nabla I\|^2), \quad (28)$$

where I are the $[0, 1]$ -scaled image intensities and the tolerance parameter $\alpha = 1000$ (our default) was experimentally determined. The higher α is, the larger the segmented region becomes. Gradients are calculated via finite differences. Noise in the resulting segmentation is reduced with a $3 \times 3 \times 3$ morphological opening and closing. Phase wraps (recall Section 4.1.1) are corrected within the obtained segmentations [118]. The rest of the flow image is not processed to save time.

7.1.2. SURFACE MESH AND CENTERLINE EXTRACTION

Marching cubes [324] is employed to automatically extract the vessel surface from the binary segmentation. We apply a *low-pass filter* by Taubin et al. [500] and reduce the mesh via *quadric decimation* by Hoppe [229] to minimize discontinuities in of the surface. We currently use implementations from the *Visualization Toolkit* (VTK):

- `vtkMarchingCubes` with `iso = 0.5`,
- `vtkWindowedSincPolyDataFilter` with 50 iterations and `passband = 0.1`, and
- `vtkQuadricDecimation` with topology-preserving enabled and `target reduction = 0.8`.

The parameters are experimentally determined default values. The low-pass filter was chosen since a comparison of mesh smoothing algorithms [17] revealed its quality for medical surface models.

An aorta is, on average, represented by 2500–3000 equilateral triangles with an edge length of about 5 mm and a mean area of 10–11 mm². For comparison, a voxel diagonal is 4.3 mm long. This mesh resolution is sufficient because of the non-complex shape of the aorta and pulmonary artery.

The subsequent *centerline extraction* (see Figure 59a) by Antiga et al. [10] calculates minimum arc length paths that follow local maxima on a distance map, which is based on the Voronoi diagram of the surface points. A robust implementation is provided by the *Vascular Modeling ToolKit* [410] (VMTK, `vmtkcenterlines`). The user specifies a start and one or multiple end points and thus can indirectly

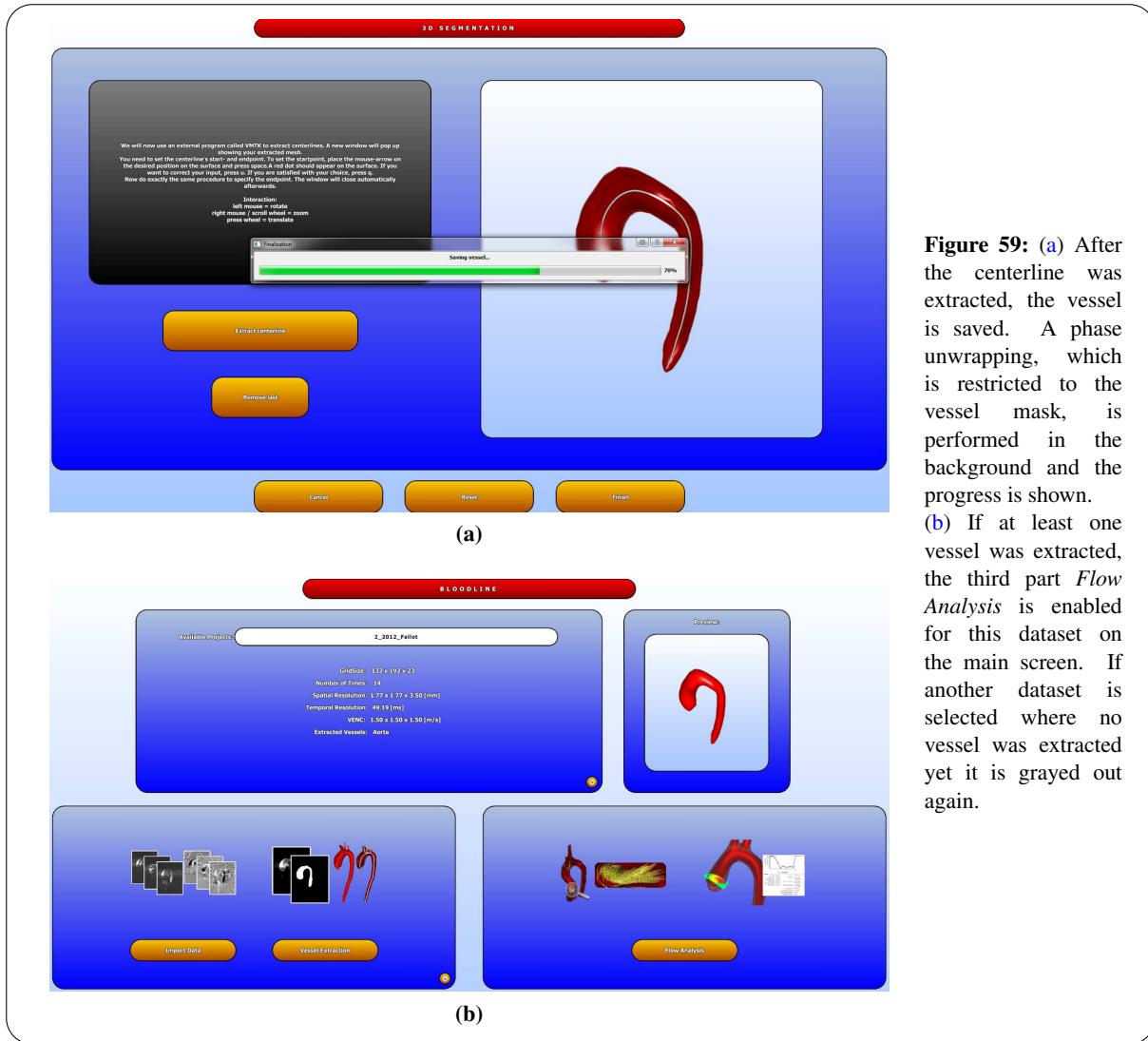


Figure 59: (a) After the centerline was extracted, the vessel is saved. A phase unwrapping, which is restricted to the vessel mask, is performed in the background and the progress is shown. (b) If at least one vessel was extracted, the third part *Flow Analysis* is enabled for this dataset on the main screen. If another dataset is selected where no vessel was extracted yet it is grayed out again.

exclude undesired vessel branches from the centerline topology. Further parameters are not required. Multiple end points are allowed to create centerlines in branching vessels, such as the pulmonary artery. A [branch splitting](#) by Antiga and Steinman [9] is employed to distinguish between the left and right pulmonary artery. We resample centerlines from an [interpolating cubic spline \(ALGLIB\)](#) to guarantee equal distances of 0.5 mm (our default) between successive points. After the mesh(es) and centerline(s) are extracted, the next part *Flow Analysis* is enabled on the main screen (see Figure 59b).

7.1.3. QUALITATIVE ANALYSIS

VECTOR INTERPOLATION AND PATH LINE INTEGRATION: Path lines are integrated entirely on the GPU using an adaptive step size Runge-Kutta-4 (RK4) method [124]. A velocity vector $\vec{v} \in \mathbb{R}^3$ in the 3D flow field / phase image V_t of one temporal position t is obtained by hardware-accelerated trilinear interpolation. To interpolate a vector at the spatio-temporal position $\vec{p}_t = (x, y, z, t)$, the two temporally adjacent positions $t_0 = \lfloor t \rfloor$ and $t_1 = \lceil t \rceil$ are determined (the cyclic nature of the data has to be considered when ceiling). The vectors \vec{v}_{t_0} and \vec{v}_{t_1} are calculated in the corresponding flow fields V_{t_0} and V_{t_1} . Afterwards, \vec{v}_{t_0} and \vec{v}_{t_1} are interpolated linearly, weighted by the inverse temporal distances $1 - \|t - t_0\|$ and $1 - \|t - t_1\|$. In other words, we apply quadrilinear interpolation by using the GPU's fast trilinear interpolation twice and doing the last linear interpolation manually. Because of the rather small dataset resolutions, we are able to store all flow fields of all temporal positions in the GPU's memory at once. Larger datasets would make an asynchronous data streaming necessary, as shown by, e.g., Venkataraman [531].

We ensure that each voxel of the segmentation is visited at least once in every temporal position. For this purpose, we seed one path line at a random position inside each segmentation voxel at the first temporal position. For each remaining time step, in succession, we determine the voxels that were not visited, create new seeds and integrate the path lines. This approach directly depends on the dataset resolution and can lead to a vast amount of path lines. To alleviate this problem, the binary *visited map*, which keeps track of the spatio-temporal voxel visits, uses an individual resolution. Our experimentally determined default is $2 \times 2 \times 2$ mm/50 ms. A post-processing to exclude unwanted lines is performed in the following order:

- We assume that flow with velocities less than 0.05 m/s is not interesting.
- We filter lines that are shorter than a half voxel diagonal.
- During the path line integration on the GPU the voxel-based segmentation is used to restrict the calculations to the vessel. Since the vessel mesh runs through voxels, path lines can slightly protrude. These parts are identified and cropped.
- We perform a line reduction so that subsequent points have a minimum distance of 0.25 mm (our experimentally determined default).

All in all, this results in approximately 15000–40000 path lines per vessel.

VORTEX EXTRACTION: During the full flow integration, we also calculate the λ_2 vortex criterion for each path line point. To alleviate the impact of the low data resolution and noise, we smooth the values along each path line using a 1D binomial filter with kernel size 3. Contrary to our previous work [270], which is comprehensively described in Section 8.1, we do not crop away parts of the path lines. Instead, we provide the option to flexibly hide all non-vortex parts using a slider that adjusts the λ_2 threshold (see Figure 60). Filtering flow velocities is possible in the same way. If desired, a 2D polar plot can be generated as overview of present vortices in the aorta [274] (see Section 8.2).

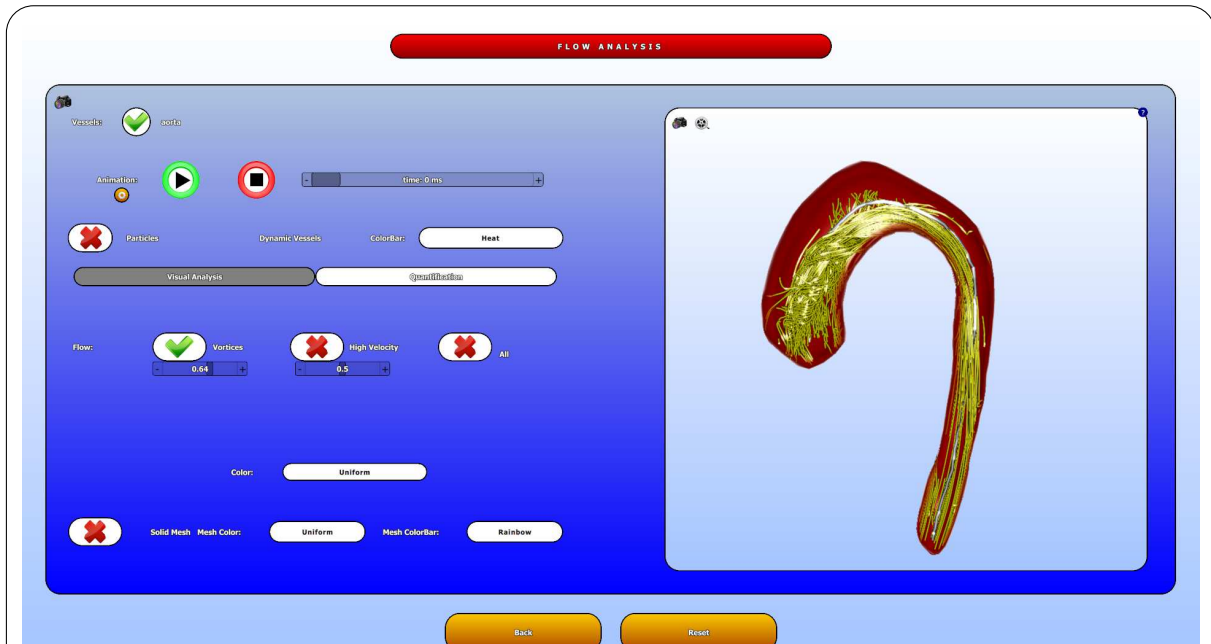
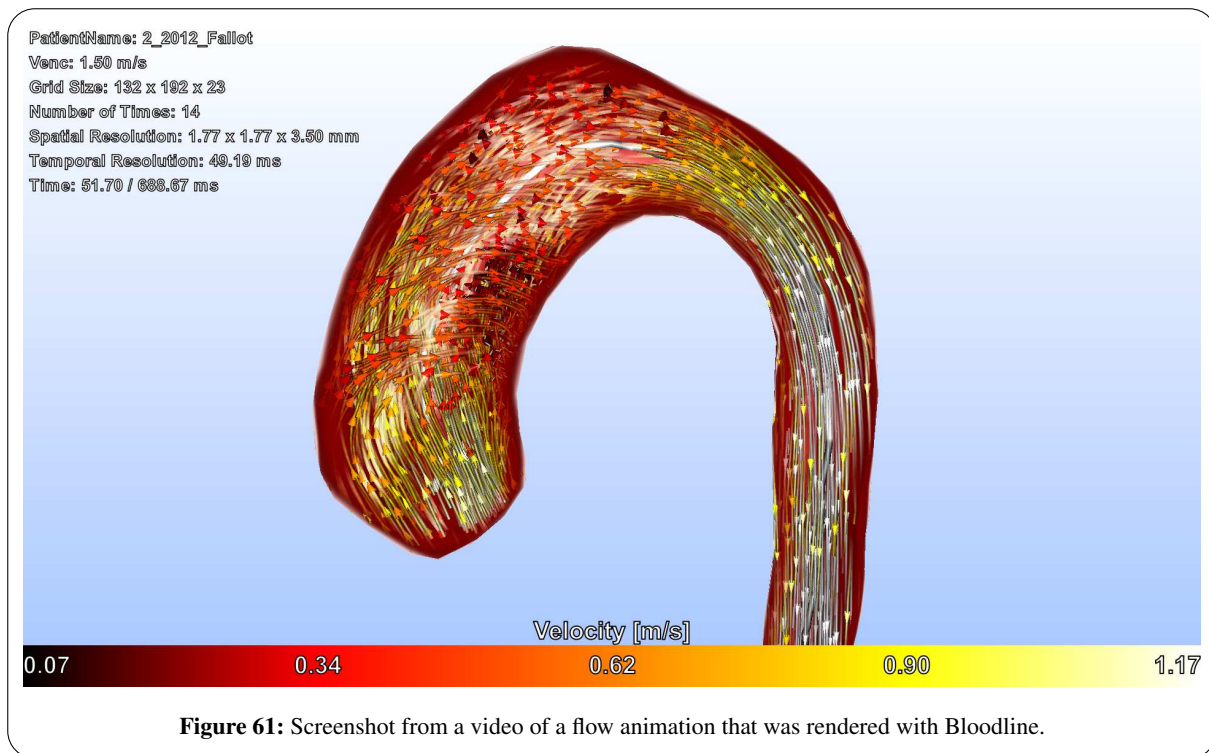


Figure 60: Qualitative flow analysis in Bloodline allows to filter vortex as well as high-velocity flow and to run an animation. The path lines as well as the vessel surface mesh can be colored according to different properties. The employed color scales can flexibly be adjusted.

Image from [273] © 2015 The Eurographics Association and John Wiley & Sons, reprinted with permission.

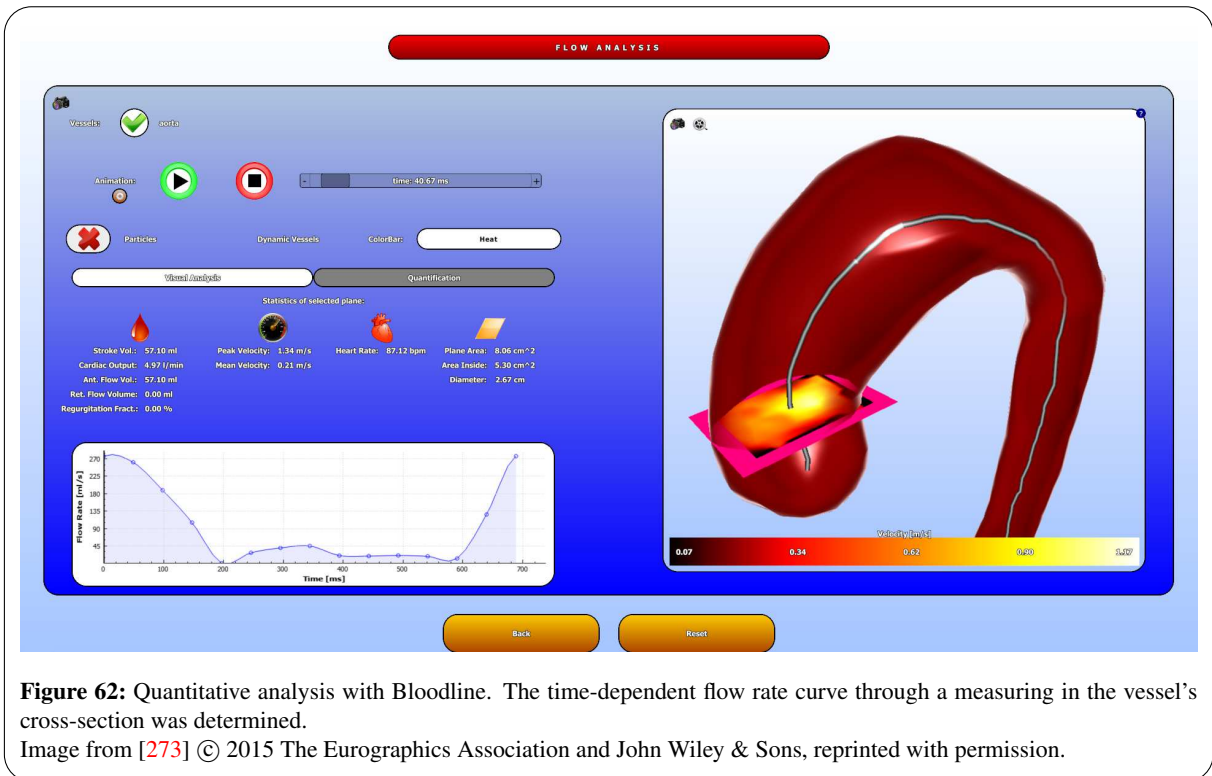


VISUALIZATION: The vessel front is culled and only hinted at with a ghosted viewing, as proposed by Gasteiger et al. [178]. The back faces are rendered with Phong illumination [409]. Path line visualization is enhanced with illuminated stream lines (ISL) and halos to improve spatial and depth perception. Path lines with halos are created in the OpenGL geometry shader as view-aligned quads. Illuminated stream lines (ISL) are implemented in the subsequent fragment shader. In the animation mode, cone-shaped particles with trails are optionally drawn on every position where the current animation time matches a path line's temporal component. Order-independent transparency (OIT) ensures correct alpha blending. The default line width, particle width, and particle length depend on the dataset's voxel diagonal. The standard trail length depends on the temporal resolution and number of time steps. Real-time adjustment of all visualization parameters is possible via sliders.

MEDIA GENERATION: Results can easily be shared by taking a high-resolution screenshot of the GUI or the render window. The animated flow can be exported to a 1080p video with a single click. An option to create videos with adaptive speed that enhance extracted vortex flow is provided (VAAS, see Section 8.3). Patient and dataset information from corresponding DICOM tags are automatically added to the top left corner. They are basically the same that are shown on the main screen. The employed color scale for the flow is included on the bottom. If the mesh shows a property, another color bar is rendered on the top. Figure 61 shows one frame of an exported video of a flow animation.

7.1.4. QUANTITATIVE ANALYSIS

Measuring planes are automatically oriented orthogonal to the centerline and their size is automatically determined so that they fit the vessel (see Figure 62). The user can drag a plane along the centerline or adjust the angulation, i.e., rotate it. Standardized measuring plane positions, as proposed by, e.g., Schulz-Menger et al. [460], are not yet implemented. A diagram shows the time-dependent flow rate determined for this plane configuration. Additionally, the stroke volume, cardiac output, regurgitation fraction, mean as well as peak velocity, and the vessel diameter are provided. Unfortunately, the calculations are highly sensitive towards the plane's angulation. Therefore, a robust stroke volume and regurgitation fraction analysis can be performed [278] (see Section 9.1). Another quantifiable measure on the vessel surface is vectorial wall shear stress (recall Section 6.2.1).



7.2. IMPLEMENTATION DETAILS

Bloodline is written in C++ and uses OpenGL for rendering, embedded in a Qt/QML-based GUI. This section gives a rough insight into the code design.

The code is organized in the *model-view-controller* [283] (MVC) architectural pattern. The *model*, which is the logical core of the software and contains the data, builds upon BLIB – a library that has been developed for personal use by the author of this thesis. The *view* employs Qt/QML. Each GUI screen is defined in a separate QML file. The link between QML and C++ is established with each one *EventHandler* class per screen. The *controller* is realized as set of controller classes. They are called from the *EventHandlers* with corresponding parameters that were set on the GUI and invoke corresponding tasks that are executed by the model. The MVC facilitates an easy replacement of the GUI, if necessary, and a general structuring of the code into separated, logical areas.

BLIB: BLIB is a header-only, heavily templated C++ library: It provides:

- *N-dimensional* (ND) *vectors* with specialized functionality for specific dimensions, such as cross-product for 3D.
- *ND images* with multivariate entries of an arbitrary arithmetic type. They provide functionality like ND linear interpolation and resampling. Derived types are, e.g., binary segmentations, which enable in-out checks, and flow fields, which facilitate line integration. There are various isotropic and anisotropic *image filters*. Global filters operate on the whole image (e.g. histogram equalization). Neighborhood filters consider the surrounding data elements (e.g. median). Convolution filters inherit from neighborhood filters and apply a mask (e.g. binomial smoothing). Specialized filters for binary images (e.g. morphological operators) and 4D PC-MRI images (e.g. artifact corrections and TMIP) are available.
- *Meshes* with ND vertices and *M* indices per cell. Static and dynamic 3D triangular meshes are derived that provide functionality like VTK import and export, extraction from an image (e.g. binary segmentation) via marching cubes, calculation of and access to normal vectors, smoothing, decimation, voxelization, inside / outside checks, and centerline extraction. A kDTree is generated on demand for optimized closest point queries.

- *Discrete ND curves* as basis for integral lines (stream and path lines). Among others, they allow filtering via line predicates (recall Section 5.2.3.1).
- *Measuring planes* extend an image with a spatial position (center of the plane) and a local coordinate system. They are available in a static and dynamic version.
- Miscellaneous functionality: DICOM processing, colors and color bars, kDTrees, Singleton, trackball using quaternions, general file I/O, sampling geometric objects with different distributions (e.g. uniform or Poisson-distributed on a sphere), and export to VTK and MATLAB for prototyping purposes.

BLOODLINE: Bloodline builds upon BLIB. The following list summarizes extended functionality:

- A *dataset* holds the image data and additional parameters, such as the V_{ENC} , patient name, and a list of vessels that were extracted from the data. The currently loaded dataset is realized as a singleton, so that is accessible from everywhere in the code. A *dataset importer* processes the raw DICOM files, manages their classification, and reads relevant tags.
- Various OpenGL GUI elements are defined. The default 3D viewer renders static and dynamic meshes as well as path lines, facilitates measuring plane placement as well as interaction, and runs animations. A standard slice viewer enables the analysis of slice-based image data. The graph cut segmenter, as a slice viewer extension, allows to draw on the slices to provide regions inside and outside the target structure (vessel). The input is forwarded to a graph cut solver and the resulting segmentation is depicted as contour.
- The *integrator* implements adaptive RK4 on the GPU and provides real-time quantification of flow rates for measuring planes. Different *seeding strategies* can be employed for line integration, such as N random in the whole vessel, N random per voxel, N random per voxel per time, N visits per voxel, or N visits per voxel per time.

7.3. APPLICATION

Bloodline is available for research purposes on each one computer in the Heart Center in Leipzig, Germany, where also a Siemens prototype is used, in the University Hospital in Magdeburg, Germany, and on the private computer of Uta Preim who works in the municipal hospital in Magdeburg, Germany. However, the software is not publicly available in a free or commercial manner.

Meanwhile, more than 64 datasets were evaluated in close collaboration with cardiologists and radiologists specialized in the cardiovascular system. Besides 36 healthy volunteers, the following pathologies were present:

- 1 aneurysm in the left subclavian artery,
- 3 aortic insufficiencies,
- 3 ectasias / aneurysms in the ascending aorta,
- 15 bicuspid aortic valves (BAV), some of them with ectatic ascending aortas,
- 1 tetralogy of Fallot with pulmonary insufficiency,
- 3 vascular prostheses, and
- 2 coarctations.

DATASET ACQUISITION: A 3 T Magnetom Verio (Siemens Healthcare, Erlangen, Germany) with a dedicated 32-channel cardiac coil was used for data acquisition. The imaging parameters were as follows: slice thickness 3.5 mm, flip angle 15° , field of view 340 mm, echo time 3.2 ms, repetition time 6.1 ms, temporal resolution 49 ms, sampling bandwidth 491 Hz/pixel, 10–20 reconstructed phases, one acquisition. The maximum expected velocity (V_{ENC}) was set to 1.5 m/s per dimension. A sagittal oblique 3D slab was positioned to include the aorta. Heart and wall motion artifacts were minimized using prospective ECG gating. The spatial resolution is $1.77 \times 1.77 \times 3.5$ mm in a 132×192 grid with 15–23 slices. Isotropic resolution and respiratory control were not used to achieve shorter acquisition

times. The number of time steps varies from 14–21 with a temporal resolution of about 50 ms. Recall Section 3.1.3 for available image data in 4D PC-MRI datasets.

USAGE: After familiarization, physicians are able to perform a standard evaluation, i.e., vortex flow extraction and stroke volume as well as regurgitation fraction analysis, in less than ten minutes, which was rated as feasible for the clinical routine. The graph cut-assisted segmentation shows high acceptance due to the exploitation of the physicians' anatomy knowledge. The option to hide vessels in order to reduce occlusions and the independence of specific MRI scanners were appreciated. A suggestion was to let the program perform pending automatic operations, such as path line integrations, for all new datasets at once. This way, the concentrated waiting time could be used for other things.

7.4. ALTERNATIVE SOFTWARE

Various free or commercial tools are being developed or were already established, such as *FourFlow* by Heiberg et al. [210], *Quantitative Flow Explorer* by Van Pelt et al. [524], *MeVisFlow* by Hennemuth et al. [213], *QFlow ES* by Medis, *CMR 42* by Circle CVI, *Arterys*, *4D Flow Demonstrator* by Siemens [23, 467] (see Figure 63a), *EnSight* by CEI (see Figure 63b), *GTFLOW* by GyroTools (see Figure 63c), an *OsiriX* plugin by Hüllebrand et al. [236], and *Velomap* by Bock et al.⁸ Table 1 shows a rough comparison of selected software.

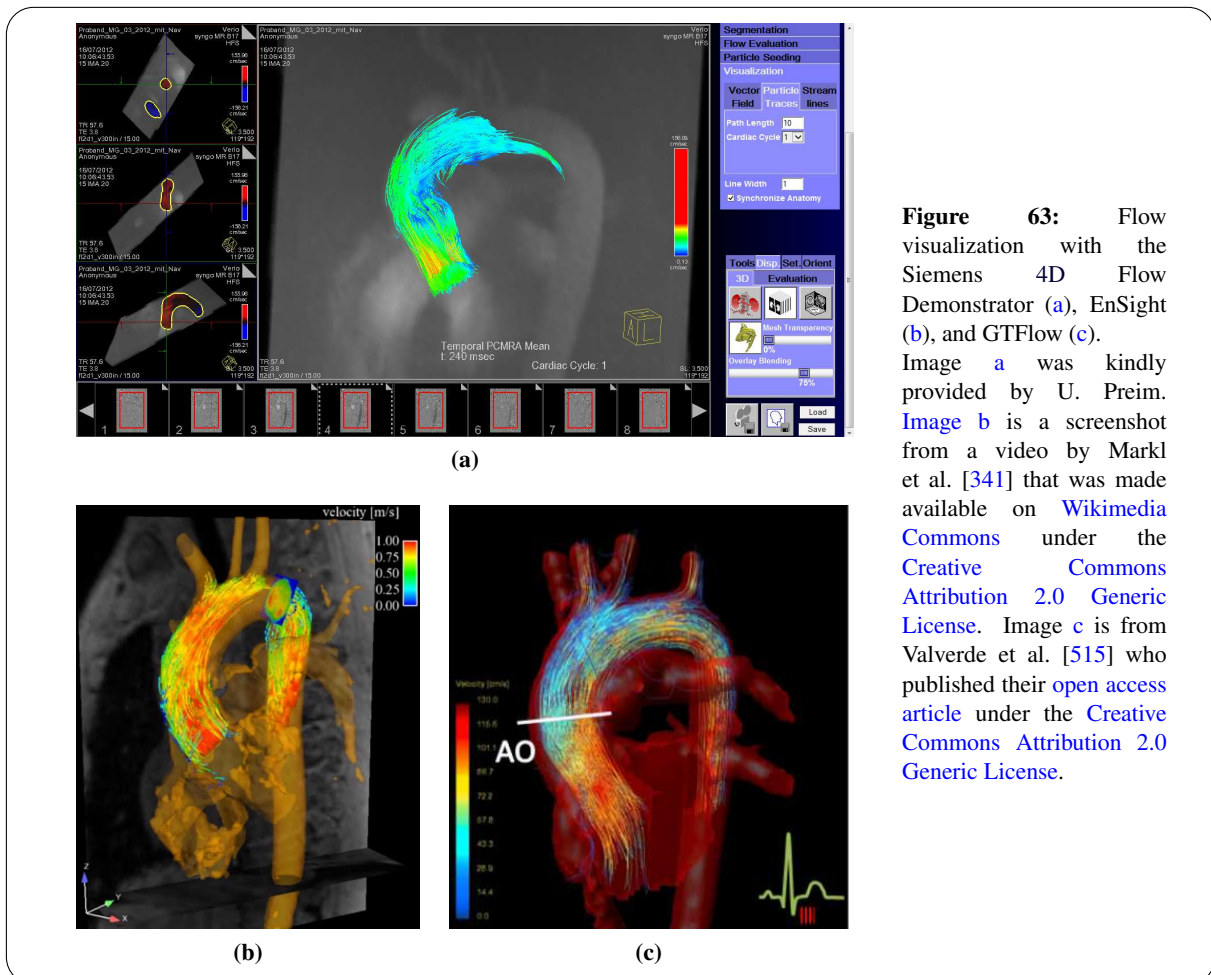


Figure 63: Flow visualization with the Siemens 4D Flow Demonstrator (a), EnSight (b), and GTFLOW (c).

Image a was kindly provided by U. Preim. Image b is a screenshot from a video by Markl et al. [341] that was made available on [Wikimedia Commons](#) under the [Creative Commons Attribution 2.0 Generic License](#). Image c is from Valverde et al. [515] who published their [open access article](#) under the [Creative Commons Attribution 2.0 Generic License](#).

⁸Links accessed 03/2016

	Pre-processing	Anatomical context	Qualitative flow analysis	Quantification	Miscellaneous
FourFlow	<ul style="list-style-type: none"> - phase wraps - velocity offsets 	<ul style="list-style-type: none"> - external segmentation via <i>Segment [209]</i> (open source software) - 3D vessel surface rendering 	<ul style="list-style-type: none"> - path line integration, animation, color-coding (velocity) 	<ul style="list-style-type: none"> - flow velocities, rates, volumes, regurgitation - KE, TKE 	<ul style="list-style-type: none"> - open source software based on ParaView - clipping planes
Quantitative Flow Explorer	<ul style="list-style-type: none"> - 	<ul style="list-style-type: none"> - marching cubes iso surface on TMIP (needs iso value) - segmentation with active surface model on TMIP + LPC + EVC (needs weights) - 3D vessel surface rendering or DVR 	<ul style="list-style-type: none"> - real-time particle and pathlet animation, color-coding (velocity) - special exploration tools (e.g. probing) 	<ul style="list-style-type: none"> - 	<ul style="list-style-type: none"> - proprietary research prototype for internal use
MeVisFlow	<ul style="list-style-type: none"> - phase wraps - velocity offsets 	<ul style="list-style-type: none"> - watershed segmentation on PCMRA image (needs in- and exclude points) - 3D vessel surface rendering 	<ul style="list-style-type: none"> - path line integration, animation, color-coding (velocity, direction, curvature, emitter region) 	<ul style="list-style-type: none"> - flow velocities, rates, volumes, regurgitation - pressure difference maps - WSS on surface - connectivity and derived uncertainty 	<ul style="list-style-type: none"> - proprietary - studies: good accordance with Doppler ECG and pressure catheters; time savings over conventional tools
QFlow	<ul style="list-style-type: none"> - phase wraps - velocity offsets 	<ul style="list-style-type: none"> - automatic detection of vessel borders in cross-sections (<i>no details available</i>) 	<ul style="list-style-type: none"> - color-coding (velocity) in cross-sections 	<ul style="list-style-type: none"> - flow velocities, rates, volumes, regurgitation - pressure gradients 	<ul style="list-style-type: none"> - commercial - restricted to cine 2D flow - result export as PDF, HTML, XML
VeloMap	<ul style="list-style-type: none"> - phase wraps - velocity offsets - noise masking - PCMRA export for external segmentation 	<ul style="list-style-type: none"> - 	<ul style="list-style-type: none"> - 	<ul style="list-style-type: none"> - 	<ul style="list-style-type: none"> - proprietary, in-house developed MATLAB script for data pre-processing

<p>Siemens 4D Flow Demonstrator</p>	<ul style="list-style-type: none"> - phase wraps - velocity offsets - motion 	<ul style="list-style-type: none"> - centerline computation based on medialness map (between 2 specified points), then automatic graph cut; no manual correction - 3D vessel surface rendering with image slice in the background 	<ul style="list-style-type: none"> - path line integration (seeded on specified cross-sections), animation, color-coding (velocity) 	<ul style="list-style-type: none"> - flow velocities, rates, volumes, regurgitation 	<ul style="list-style-type: none"> - proprietary research prototype
<p>Ensignt</p>	<p>(no details available)</p>	<ul style="list-style-type: none"> - surface estimation (no details available) - 3D vessel surface rendering with image slice in the background 	<ul style="list-style-type: none"> - path line integration, animation, color-coding (velocity) 	<ul style="list-style-type: none"> - flow velocities, rates, volumes, regurgitation - WSS on cross-section boundary curves - pressure 	<ul style="list-style-type: none"> - general flow evaluation (e.g. also CFD data) - commercial - multiplanar reformatting views of anatomical image
<p>GTFlow</p>	<ul style="list-style-type: none"> - phase wraps - velocity offsets - noise clipping 	<ul style="list-style-type: none"> - semi-automatic or manual segmentation (no details available) - 3D vessel surface rendering with image slice in the background (cine mode available) - ROI contours for quantification via freehand / B-spline / polygon / circle / rectangle drawing - automatic contour propagation 	<ul style="list-style-type: none"> - path line integration, animation, color-coding (velocity), quantification (length, time of arrival, particle count) 	<ul style="list-style-type: none"> - flow velocities, rates, volumes, regurgitation - WSS - pressure maps - TKE 	<ul style="list-style-type: none"> - commercial (for research purposes only) - session save & restore - key-frame editor and movie generator - DICOM anonymization
<p>Bloodline</p>	<ul style="list-style-type: none"> - phase wraps - velocity offsets 	<ul style="list-style-type: none"> - graph cut segmentation on TMIP or LPC (needs in- and outside regions) - centerline via VMTK (needs 1 start and 1-N end points) - 3D vessel surface rendering - prototype: automatic 4D vessel extraction 	<ul style="list-style-type: none"> - path line integration (full coverage guaranteed), animation, color-coding (velocity) - vortex extraction - vortex analysis with other, in-house software prototype - 2D polar plot (aortic vortex flow) 	<ul style="list-style-type: none"> - flow velocities, rates, volumes, regurgitation (robust estimation) - WSS 	<ul style="list-style-type: none"> - one-click export of screenshots and videos (optionally with adaptive speed) - proprietary

Table 1: Comparison of selected 4D PC-MRI evaluation software. Since it is based on publicly available information, completeness and in-depth details might be missing.

7.5. CONCLUSION AND FUTURE WORK

We presented the cardiac 4D PC-MRI data evaluation software *Bloodline* that allows to process datasets within ten minutes. It integrates a full pre-processing pipeline as well as a quantitative and qualitative data analysis. The workflow was developed in close collaboration with the clinical partners. However, the employed GUI design was made as an initial suggestion and leaves room for future improvements. For instance, the GUI elements take up lots of space, which should be optimized.

The use of (semi-)automatic methods enables a fluent workflow. Carefully selected defaults strongly reduce the necessity to adjust parameters. State-of-the-art visualizations can easily be created and saved in order to share results. A unique feature of *Bloodline*, compared to other free or commercial tools that are being developed or were already established, is the comprehensive analysis of vortex flow.

OUTLOOK: In the future, the quantification of further measures shall be facilitated, such as pulse wave velocities (PWV), turbulent kinetic energy (TKE), or flow displacements (recall Chapter 6). Another goal is to automatically generate clinical reports. Hence, larger studies can be better evaluated and gender- and age-specific norm values may be determined. This could benefit from the implementation of standardized measuring planes [460]. Moreover, special functionality for the ventricles shall be provided in the future, such as the analysis of vortex rings. Until now, *Bloodline* is a proprietary research prototype. A distribution in free or commercial form is planned for the future. A connection to the *Picture Archiving and Communication System* (PACS) would be a useful addition for the use in a clinical environment.

8. ENHANCED ASSESSMENT OF VORTEX FLOW

Vortical flow behavior is of great clinical interest, since it can be an indicator for various cardiovascular diseases (CVDs). The qualitative evaluation of vortex flow can be challenging due to the high complexity of the acquired 4D PC-MRI data. This leads to potentially high visual clutter in animations of the path lines as well as in static visualizations where their temporal component is simply ignored. Section 8.1 presents a semi-automatic extraction of vortex flow-representing path lines using the line predicates technique (recall Section 5.2.3.1). This facilitates an enhanced exploration of vortical flow behavior using a single threshold, which is adapted in real-time.

In some cases, medical studies determine the pure existence of vortex flow regardless of further characteristics like the turning direction. This means to evaluate the blood flow of every single case, typically by viewing an animation. In order to support this process, an overview plot visualization for aortic vortex flow is presented in Section 8.2.

A further enhancement of the actual flow animations, preferably of extracted vortex flow, is presented in Section 8.3. The idea was to adaptively employ time lapse and slow motion to emphasize interesting parts of the cardiac cycle.

A more detailed comprehension of cardiovascular vortex flow requires an in-depth analysis of vortex characteristics. Being able to grade single vortex entities requires a clustering as a prerequisite. A corresponding approach that works on the extracted, vortex-representing path lines is explained in Section 8.4.1. Section 8.4.2 proceeds with a mathematical description of employed criteria, which are based on clinicians' descriptions. They are evaluated for each vortex entity, yielding an objective characterization. An established glyph visualization conveys the main properties.

8.1. SEMI-AUTOMATIC VORTEX EXTRACTION USING LINE PREDICATES

THIS SECTION IS BASED ON:

- [270]: **B. KÖHLER**, R. GASTEIGER, U. PREIM, H. THEISEL, M. GUTBERLET, AND B. PREIM. "SEMI-AUTOMATIC VORTEX EXTRACTION IN 4D PC-MRI CARDIAC BLOOD FLOW DATA USING LINE PREDICATES". IN: *IEEE Transactions on Visualization and Computer Graphics* 19.12 (2013), PP. 2773–82. DOI: [10.1109/TVCG.2013.189](https://doi.org/10.1109/TVCG.2013.189)
- [269]: **B. KÖHLER**. "WIRBELEXTRAKTION IN 4D PC-MRI BLUTFLUSSDATEN DER AORTA". MA THESIS. OTTO-VON-GUERICKE-UNIVERSITY, MAGDEBURG, GERMANY, 2012. LINK: [VISMD.DE](http://vismd.de) (ACCESSED AT 02/2016)

SEE SECTION [PUBLICATIONS](#) IN THE APPENDIX FOR THE DIVISION OF WORK.

This work is a continuation of my Master's thesis [269]. The following results were already presented there:

- Section 8.1.2: An introduction of new line predicate classes and a formal extension.
- Section 8.1.4: A comparison of local vortex criteria where the λ_2 criterion was determined as most suitable for the cardiac context.

The following extensions were made as PhD student:

- Sections 8.1.3–8.1.4: The proposed step-by-step vortex extraction procedure was adapted. A GPU implementation increases the clinical feasibility. Instead of seeding N uniformly distributed path lines, it is now ensured that each voxel is visited at least once in every temporal position. This guarantees that no small flow structures are missed. The path line integration, Jacobian matrix estimation, and λ_2 calculation are performed on the GPU. *Cardano's method* [281] was used to solve the arising cubic equation from the eigenvalue analysis. The extraction procedure was adapted so that now a single slider facilitates the vortex filtering.
- Section 8.1.5: A detailed, qualitative case evaluation was performed in collaboration with the clinical partners.

Further comments of this kind are included in the single subsections to provide maximum transparency regarding the reuse of existing results.

Discussions with our collaborating experts – radiologists specialized on the cardiovascular system and cardiologists – revealed that they are often more interested in the characteristic of a vortex than topological properties, such as core lines. Consequently, the aim of this work was to support the blood flow analysis for vortex patterns. This was done by extracting path lines that represent vortex flow (see Figure 64). First, the requirements are analyzed, followed by an extension of the line predicates technique. Then, we describe the generic vortex extraction scheme, where different vortex criteria with particular thresholds are employed. This is followed by comparing the results achieved with different vortex criteria in collaboration with domain experts. Thereby, we define key questions to enable a qualitative comparison.

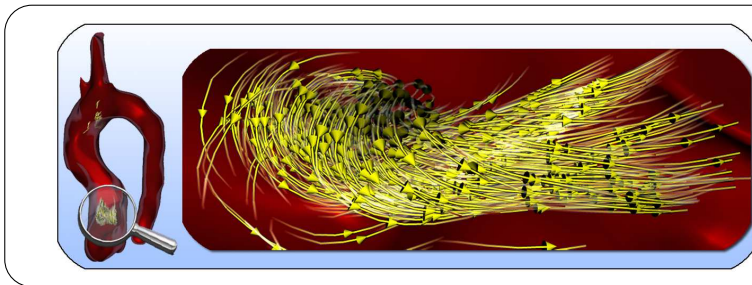


Figure 64: Physiological vortex in the left ventricle during diastole in this patient with tetralogy of Fallot. Image from [270] © 2013 IEEE Computer Society, reprinted with permission.

8.1.1. REQUIREMENT ANALYSIS

The majority of vortex extraction methods is designed for 3D steady flow fields, whereas methods for 3D unsteady flow, such as cores of swirling particle motion (COSPM) [550], are rare. Although the vortex cores of stream lines and path lines can be similar when the flow changes only slightly, there is no guarantee that they match.

The identification of the most suitable local vortex criterion in combination with line predicates requires an extensive evaluation. Considered aspects are mainly not precise enough to put them into a mathematical description and, since there is no ground truth, we have to rely on subjective evaluations of domain experts.

To make the characteristics of a vortex easy to interpret, it is necessary to preserve path lines of high quality. Ware [542] described that long lines are well-interpretable at the neuronal level *“because a continuous contour will produce stronger mutual excitation [of neurons] than broken but aligned contours.”* Thus, we have to avoid their fragmentation during the filtering process and instead maintain continuous and smooth courses. In order to achieve the desired high computational performances, the GPU’s potential has to be utilized.

Summarizing, our discussion with domain experts suggests to focus on the following requirements:

- Find the local vortex criterion that provides the best results combined with our extraction procedure.
- Assess the suitability of 3D vortex criteria applied to the 4D blood flow.
- Ensure independent calculations to make our approach easy to implement on the GPU.
- Maintain easy to interpret high-quality path lines during the subsequent filtering.
- Be able to derive clinically relevant information from the results provided by our approach.

8.1.2. EXTENSION OF LINE PREDICATES

THE CONTENT OF THIS SECTION IS COMPLETELY BASED ON:

- [269]: **B. KÖHLER**. “WIRBELEXTRAKTION IN 4D PC-MRI BLUTFLUSSDATEN DER AORTA”. MA THESIS. OTTO-VON-GUERICKE-UNIVERSITY, MAGDEBURG, GERMANY, 2012. LINK: VISMD.DE (ACCESSED AT 02/2016)

SEE SECTION [PUBLICATIONS](#) IN THE APPENDIX FOR THE DIVISION OF WORK.

A line predicate Π assigns a value \hat{p} to each point \vec{p} of an integral line (or \vec{p}_t of a path line). Born et al. [63] suggested a classification of line predicates according to the necessary data for the calculation: *Line-based predicates* depend solely on the path lines' geometry, and *derived predicates* use the underlying flow field. We renamed these two classes as *geometry* and *flow field predicates*, Π_Γ and Π_V , respectively. Moreover, we proposed three further groups in [269]:

- *Mesh predicates* Π_M utilize the explicit vessel representation. An example is the minimal distance of a point to the surface.
- *Stream predicates* Π_Ω depend on surrounding path lines. For instance, the number of path lines weighted by their distance to each other can be used as a density value.
- To modify the values of one integral line in different ways, we created *meta predicates* Π_{meta} as a superclass:
 - The *sum predicate* Π_Σ adds up all calculated values \hat{p}_i along an integral line weighted by the corresponding segment lengths $L(\cdot)$ and assigns this value to each of the N points:

$$\Pi_\Sigma = \frac{\sum_{i=0}^{N-1} (\hat{p}_i \cdot L(p_i))}{\sum_{k=0}^{N-1} L(p_k)} \quad (29)$$

By applying this meta predicate, longer path lines implicitly score higher than shorter ones.

- The *mean predicate* Π_\circ assigns the average value to each point. It is calculated as the sum predicate divided by N .
- The *smoothing predicate* $\Pi_{\sigma,n}$ applies a one-dimensional binomial filter with a kernel size of 3 in n iterations to the values along an integral line.

We use a simplified notation to describe the application of a series of line predicates to all existing path lines. A characteristic set C_Π results in:

$$C_\Pi = \Pi_1, t_1 \rightarrow \Pi_2, t_2 \rightarrow \dots \rightarrow \Pi_n, t_n, \quad (30)$$

where Π_i are the subsequently applied line predicates with the corresponding thresholds t_i . A threshold can be one of the following:

- $\hat{p} \lesseqgtr v$: All values below or above v are valid.
- $v_0 \leq \hat{p} \leq v_1$: All values between v_0 and v_1 are valid.
- $\overline{v\%} = \hat{p} \geq \hat{p}_{\min} + \frac{v}{100} \cdot (\hat{p}_{\max} - \hat{p}_{\min})$: The upper $v\%$ of the values are valid.
- $\underline{v\%} = \hat{p} \leq \hat{p}_{\min} + \frac{v}{100} \cdot (\hat{p}_{\max} - \hat{p}_{\min})$: The lower $v\%$ of the values are valid.

The application of a meta predicate is denoted as $\Pi_{\text{meta}}(\Pi)$, where $\Pi_{\text{meta}} \in \{\Pi_\Sigma, \Pi_\circ, \Pi_{\sigma,n}\}$ and $\Pi \in \{\Pi_V, \Pi_\Gamma, \Pi_M, \Pi_\Omega\}$. The following characteristic set is an example for a better understanding of the procedure:

$$C_\Pi = \Pi_{\sigma,n}(\Pi_V^{\text{velocity}}), \overline{v_0\%} \rightarrow \Pi_\Gamma^{\text{length}}, \hat{p} \geq v_1 \text{ mm} \quad (31)$$

After the first step, C_Π contains all points that represent the upper $v_0\%$ of the velocity domain after applying a smoothing predicate with n iterations. From this result, all path lines shorter than v_1 mm are removed in the second step.

8.1.3. SUCCESSIVE VORTEX EXTRACTION

THE CONTENT OF THIS SECTION IS PRIMARILY BASED ON:

- [269]: **B. KÖHLER**. “WIRBELEXTRAKTION IN 4D PC-MRI BLUTFLUSSDATEN DER AORTA”. MA THESIS. OTTO-VON-GUERICKE-UNIVERSITY, MAGDEBURG, GERMANY, 2012. LINK: VISMD.DE (ACCESSED AT 02/2016)

SEE SECTION [PUBLICATIONS](#) IN THE APPENDIX FOR THE DIVISION OF WORK.

Paragraph [INITIALIZATION](#) contains a later established extension.

INITIALIZATION: First, the whole dataset inside the segmentation mask is covered with path lines. 25000–35000 spatially and temporally uniformly distributed path lines were used, depending on the data resolution and the flow field’s changes over time. This produced the desired rather high line density.

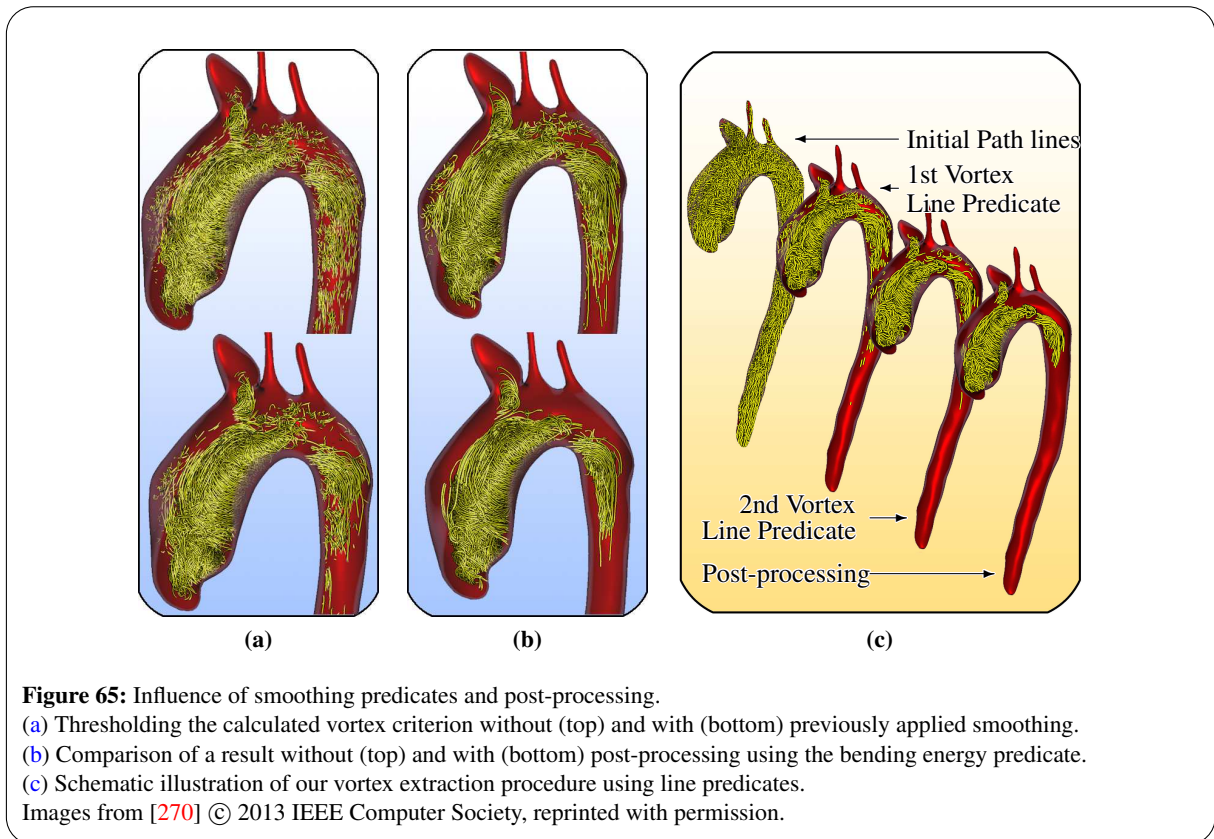
In a later version, which was established after the appearance of this paper [270], it is ensured that each voxel is visited at least once in every temporal position. This usually yields more path lines, but increases the chance that smaller flow structures are not missed. The computational effort of the path line integration was reduced by implementing a method on the GPU (recall Section 7.1.3).

JACOBIAN MATRIX ESTIMATION: Local vortex criteria are in many cases based on an analysis of the Jacobian matrix or a derived matrix based on the Jacobian. So, its robust estimation increases the chance for proper results considerably. The calculation of one single Jacobian matrix for a whole voxel will deliver discontinuities at the voxel boundaries and affect the quality of the results negatively. Instead, we use central differences of the interpolated vectors $\vec{v} \in \mathbb{R}^3$ at the exact query positions $\vec{p}_i \in \mathbb{R}^4$ and the displacements $\pm\Delta\{x, y, z\}$. The offset in each direction is set to one corresponding voxel dimension and decreased successively if one of the shifted positions is not within the segmentation mask. Based on the assumption that central differences ensure better results than forward and backward differences, they are used even near the segmentation mask boundaries. The multiple vector interpolations enable the smooth capturing of changes of the Jacobian matrix.

LINE PREDICATE 1 – FINDING VORTICES: To extract vortex structures via line predicates, the following procedure is used. First, a local vortex criterion is calculated as flow field predicate Π_V^{vortex} . Since the result tends to be noisy, a smoothing predicate $\Pi_{\sigma,25}$ is applied before thresholding: $\Pi_{\sigma,25}(\Pi_V^{\text{vortex}}), t_0^{\text{vortex}}$. On the one hand, line segments with values that indicate swirling behavior are extended. Consequently, longer segments remain after applying the threshold. On the other hand, outliers, i.e., single values indicating non-swirling-regions within a segment of swirling-values, diminish. Hence, thresholding does not interrupt the corresponding segments. As a result, the average filtered path line length increases. The application of a smoothing predicate reduces the fragmentation problem. We recommend to choose a very low threshold, just enough to crop certain non-swirling parts of the path lines. Figure 65a shows a comparison without (top) and with (bottom) the application of a smoothing predicate. The noise reduction and increased average path line length is especially noticeable in the right vortex in the distal aortic arch in this example. Due to their local nature, some of the vortex criteria are suitable for parallel calculation on the GPU.

LINE PREDICATE 2 – REFINING THE VORTEX SHAPES: Sum and mean predicates apply the same value to every point of a path line. As a consequence, path lines can be removed or kept as a whole when thresholding, but further fragmentation is impossible. Therefore, it is continued with the application of a mean predicate of the local vortex criterion: $\Pi_{\circ}(\Pi_V^{\text{vortex}}), t_1^{\text{vortex}}$.

LINE PREDICATE 3 – POST-PROCESSING: Despite the application of the smoothing predicate, it is likely that some short path line fragments will occur, which decrease the visual quality. Thus, an additional post-processing step is applied to remove these fragments properly. A bending energy predicate is employed, which is the sum predicate of curvature values: $\Pi_{\Gamma}^{\text{bendingEnergy}}, t_2 = \Pi_{\Sigma}(\Pi_{\Gamma}^{\text{curvature}}), t_2$. Based on this measure, a subsequent thresholding preserves long curved path lines. Figure 65b shows the comparison of a result without (top) and with (bottom)



the application of a bending energy predicate for post-processing. The successive vortex extraction is illustrated in Figure 65c.

VISUALIZATION: Color-coding by velocity is de-facto a standard in the cardiac context. Mapping other attributes like directions to color might be misleading for physicians. Since velocities are not relevant for this work, it was decided to employ uniformly colored path lines to avoid distractions.

8.1.4. COMPARISON OF LOCAL VORTEX CRITERIA

THE CONTENT OF THIS SECTION IS PRIMARILY BASED ON:

- [269]: **B. KÖHLER**. “WIRBELEXTRAKTION IN 4D PC-MRI BLUTFLUSSDATEN DER AORTA”. MA THESIS. OTTO-VON-GUERICKE-UNIVERSITY, MAGDEBURG, GERMANY, 2012. LINK: VISMD.DE (ACCESSED AT 02/2016)

SEE SECTION [PUBLICATIONS](#) IN THE APPENDIX FOR THE DIVISION OF WORK.

Section 8.1.4.3: [SUMMARY](#) contains a paragraph with later established [EXTENSIONS](#).

In the following, it is investigated which vortex criterion P_V^{vortex} provides the best results, i.e., path lines that reliably describe vortex structures in 4D PC-MRI data. The λ_2 criterion by Jeong and Hussain [247] and Q criterion by Hunt [239], reduced velocity by Sujudi and Haines [493], cores of swirling particle motion (COSPM) by Weinkauff et al. [550], normalized helicity by Levy et al. [311], vorticity, and torsion are considered (recall Section 5.2.3.2). Afterwards, reasonable thresholds for the placeholders t_0^{vortex} , t_1^{vortex} , and t_2 are suggested.

We applied our procedure to ten datasets. Since the results are consistent, for sake of simplicity, the comparison for one representative case is demonstrated (see Figure 66). The patient has an ectasia in the ascending aorta. The manual exploration revealed three vortices: One large vortex in the ascending aorta that is present during the complete heart cycle and two smaller ones in the distal aortic arch that occur only during the systole.

8.1.4.1. DEFINITION OF QUALITY CRITERIA

A quantitative comparison will be challenging due to the missing ground truth. Thus, we rely on subjective impressions and formulate key questions for the vortex criteria in collaboration with the medical experts. They put great emphasis on the correctness of the results and the capability of our procedure to extract and present different vortex types with expressive path lines. We complemented their expectations with considerations about the vortex criterias' value domains and the possibility to use universal thresholds. In summary, the evaluation was performed considering the following key aspects:

- **Fixed minimum and maximum:** Is there a fixed minimum and / or maximum of the calculated value domain? This facilitates the identification of a generally applicable threshold for all datasets.
- **Implicit threshold:** Is there an implicit threshold to distinguish between vortex and non-vortex regions? This would make the previous question superfluous.
- **Constant vortex core values:** Are the values of the criterion constant along vortex cores? This aspect influences the filtering behavior. If the values are constant, vortices are filtered from the outside to the inside when the threshold is increased.
- **Correctness:** Is the extraction procedure able to find at least every vortex that was discovered by the physicians' previously performed manual exploration of the datasets?
- **Helical and vortical flow:** Vortices can be classified according to their appearance: Swirling path lines with a strong movement along the vortex core are helical, whereas path lines that tend to swirl in the plane are vortical. Is the employed vortex criterion able to determine both?
- **Vortex shape:** Is the shape of a vortex pointed out sufficiently? Its swirling characteristic should be comprehensibly presented by the path lines.
- **Path line quality:** The extracted vortices should be presented by path lines with long and continuous courses. False-positive results as well as short path line fragments are unwanted.

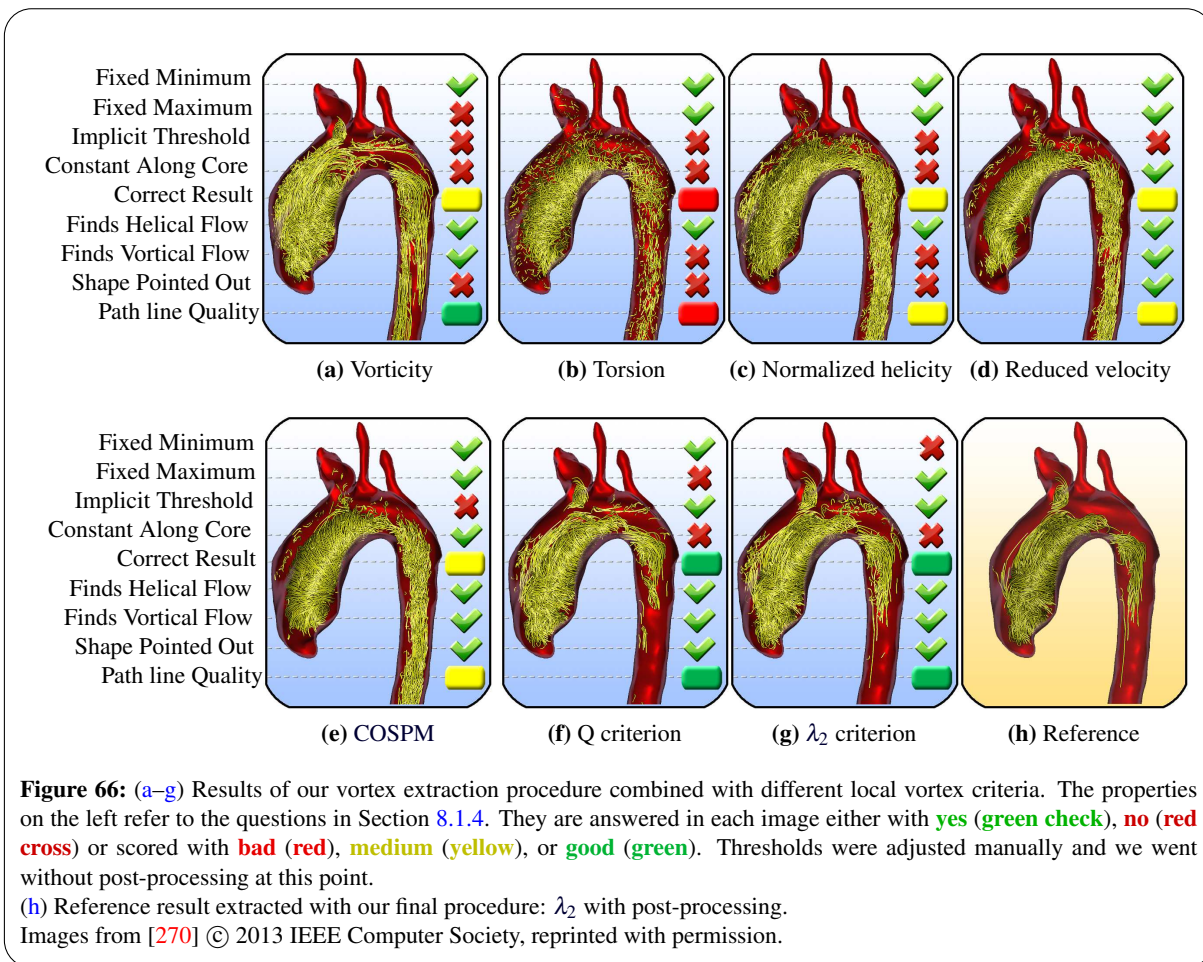
All thresholds were manually adjusted at this point to achieve the best possible findings. In addition, it was decided to not use the bending energy line predicate 3 for post-processing in order to emphasize the actual differences between the results.

8.1.4.2. OBSERVATIONS

In the following, the main outcomes of the discussion with the domain experts about the results of each vortex criterion are described. The key questions are also answered in short in the Figures 66a–g. A green check or red cross answers yes / no questions and a green, yellow, or red bar stands for a good, medium, or bad rating of a property. Figure 66h is an anticipation of a result achieved with the final procedure described in Section 8.1.4.3 and provided as a reference. For that reason, this is the only result with applied post-processing.

VORTICITY: The vorticity (see Figure 66a) preserves helical and vortical path lines, but exhibits a high false-positive rate especially near the vessel boundaries. The quality of the path lines is appropriate. There is a fix minimum value of 0, but the maximum depends directly on the derivatives of the occurring velocities. Thus, there is no fixed peak value among different vortices. The same yields for a general threshold. A small vortex often vanishes before the shape of a larger one is pointed out sufficiently. This can even happen within a single vortex since the criterion is not constant along vortex cores or within vortex regions.

TORSION: By using the torsion (see Figure 66b), it is hardly possible to extract satisfactory path lines that meet the expectations. Though the path line density is higher in vortex regions, they are highly fragmented. Not all vortices are captured correctly, and a large amount of false-positive path lines is present. Helical flow is extracted rather than vortical flow, since the torsion describes the twisting of a curve out of the plane. The minimum of 0 and maximum of 1 are fixed values, but a generally applicable threshold could not be determined.



NORMALIZED HELICITY: The results of the normalized helicity (see Figure 66c) are very similar to the ones achieved by using the torsion. Especially vortical flow is extracted insufficiently. A unique characteristic of the helicity is its sign that helps to characterize the orientation of a vortex into left- and right-handed. The value domain ranges from -1 to $+1$, where 0 is no helicity and ± 1 is the maximum left- or right-handed swirling strength.

REDUCED VELOCITY: The reduced velocity (see Figure 66d) is a projection of the velocity vector onto a plane orthogonal to the vortex core direction. If the angle between the velocity vector and the vortex core direction is small, the length of the projected vector, the reduced velocity, is 0 . This minimum value is constant along the vortex cores of all vortices. Applying a threshold results in progressively removing off the path lines from the outer regions to the vortex core. This is suitable for cases where the path lines swirl helically along the vortex core direction. Path lines that represent vortical flow tend to swirl in a plane with increasing distance. These path lines are filtered away early when increasing the threshold and, consequently, the extracted vortices may appear thinly. In addition, this problem can lead to the unwanted interruption of path lines. Also, smaller regions of vortical flow are not always captured correctly. An implicit threshold is not given for the reduced velocity, but reasonable values should be close to 0 .

CORES OF SWIRLING PARTICLE MOTION: COSPM (see Figure 66e) is the extension of the reduced velocity from steady to unsteady 3D flow. The results are very similar, which might be an indication that the flow alteration over time is rather small in the cardiac 4D PC-MRI datasets. This fact increases the reliability of steady flow vortex criteria applied to the unsteady blood flow. The minimum of 0 and maximum of 1 are fixed values. As before, a value of 0 means that a position is directly on the vortex core.

Q CRITERION: The Q criterion (see Figure 66f) was able to extract every single vortex in the datasets. The path line quality meets the requirements and there is an implicit threshold of $Q > 0$. The criterion is neither constant along the vortex core nor has a behavior like the reduced velocity or COSPM regarding the distance to the vortex core. Therefore, increasing the threshold should be avoided, since it cannot be reliably predicted which path lines will be maintained or filtered.

λ_2 **CRITERION:** Like the Q criterion, the λ_2 criterion (see Figure 66g) was able to detect all vortices. Their results are nearly identical. Using the λ_2 criterion made it likewise possible to extract all vortices correctly with the same path line quality. The only difference to the Q criterion is that 0 is the maximum value and the implicit threshold is given by $\lambda_2 < 0$.

8.1.4.3. SUMMARY

Based on the previous comparison, the λ_2 and Q criterion have shown the best results. In accordance with the domain experts, a significant difference cannot be seen. Thus, the usage of both criteria is recommended for the extraction of vortices in blood flow. For detailed differences between the λ_2 and the Q criterion, please consider Sahner et al. [438].

A possible explanation for their robust results is that, in contrast to all other criteria, λ_2 and Q solely analyze the derivatives of the velocity vectors (the Jacobian matrix). The reduced velocity, for instance, uses the Jacobian matrix *and* the velocity vectors. This might amplify noise in the data and introduce further errors. It was decided to use the λ_2 criterion, since it seems to be more established among blood flow-specific works [63, 449, 485].

The implicit threshold of $\lambda_2 < 0$ will be used for the first vortex line predicate. For the second (mean) vortex predicate, the removal of points representing the lower 10 % of the value margin is recommended. Post-processing via the bending energy predicate carries the risk of removing short path lines representing very small vortices, especially when other comparatively large vortices exist. Therefore, the user's judgment is incorporated and this last step is offered as optional, manual post-processing.

Since no vortex was found that was exclusively detected by another vortex criterion and not by λ_2 , it was decided not to combine different vortex criteria. In summary, the final procedure is to cover the whole dataset (inside the vessel segmentation) with path lines and then calculate the characteristic set C_{Π}^{vortex} as:

$$\begin{aligned} C_{\Pi}^{\text{vortex}} &= \Pi_{\sigma,25}(\Pi_V^{\lambda_2}), \hat{p} < 0 \\ &\rightarrow \Pi_{\circlearrowleft}(\Pi_V^{\lambda_2}), \underline{90\%} \\ &\rightarrow \Pi_{\Gamma}^{\text{bendingEnergy}}, t_{\text{manual}} \end{aligned} \quad (32)$$

On the average taken over all datasets, the mean path line length, measured after application of the first and last line predicate, becomes three times larger. This supports the claim that path lines of increased quality are obtained.

The only necessary user interaction is to adjust the bending energy threshold for the optional post-processing. Furthermore, if the aforementioned standard parameters are not used, the required input extends to choosing the number of seed points as well as adjusting three successive thresholds.

EXTENSIONS: In the most recent version of *Bloodline*, the necessary determination of the Jacobian matrix as well as its eigenvalue analysis is done on the GPU using *Cardano's method* [281]. Moreover, the extraction procedure was modified. The first step of the procedure remains approximately the same. The λ_2 calculation is performed on the GPU and the smoothing on the CPU. Contrary to the initial approach, path lines are no longer cropped. Instead, the mean λ_2 calculation of the second step ($\Pi_{\circlearrowleft}(\Pi_V^{\lambda_2})$) is only performed on line segments that fulfilled the first predicate. As a result, path lines now consist of zero-valued non-vortex segments or λ_2 -averaged segments. This facilitates the usage of a single value to hide path line segments that are below the user-given mean λ_2 threshold, which can

be modified interactively with one slider. The originally proposed bending energy predicate is not used anymore, since there is always a risk to exclude smaller vortices with shorter path lines. The slightly increased visual clutter is tolerable, especially during animations.

8.1.5. RESULTS AND INFORMAL EVALUATION

THIS SECTION IS NEW CONTENT (NOT CONTAINED IN THE MASTER'S THESIS [269]) BASED ON:

- [270]: B. KÖHLER, R. GASTEIGER, U. PREIM, H. THEISEL, M. GUTBERLET, AND B. PREIM. "SEMI-AUTOMATIC VORTEX EXTRACTION IN 4D PC-MRI CARDIAC BLOOD FLOW DATA USING LINE PREDICATES". IN: *IEEE Transactions on Visualization and Computer Graphics* 19.12 (2013), PP. 2773–82. DOI: [10.1109/TVCG.2013.189](https://doi.org/10.1109/TVCG.2013.189)

SEE SECTION [PUBLICATIONS](#) IN THE APPENDIX FOR THE DIVISION OF WORK.

The vortex extraction method was applied to ten 4D PC-MRI datasets of the aorta and pulmonary artery. In the following, two clinical cases are described in detail, whereas the other ones are presented as an overview. The results of our extraction procedure were shown to one cardiologist as well as two radiologists. They were asked to relate occurring vortex patterns to the present pathologies. The evaluation was performed informally and the domain experts were not required to solve specific tasks.

The integration of 30000 path lines and calculation of the λ_2 criterion is performed in less than 10 ms on a GeForce GTX 680. The data transfer between GPU and CPU takes another 1.7 s. The presented images are directly captured from the animation.⁹ In addition to the static path line visualization, freely scalable arrowheads are added at positions where a path line's time matches the animation time to make the current flow directions easier recognizable.

8.1.5.1. TETRALOGY OF FALLOT WITH PULMONARY REGURGITATION

The first case has tetralogy of Fallot. A VSD surgery has been performed about 20 years ago at the age of one. The patient mentions a fast exhaustion with dyspnea during physical activities, nausea, a pulling pain into the legs, and regularly occurring palpitations. The absence of anginous pain suggests that there is no coronary heart disease. Nocturia, one of many possible symptoms for congestive heart failure, was also not present.

Ultrasonography revealed the existence of distinct diastolic retrograde flow in the pulmonary artery. A closer examination of the heart showed a mild hypertrophy of the right ventricle, although a significant narrowing of the pulmonary artery was not present. There is still a minimal right-to-left shunt, but rather small and therefore clinically irrelevant. According to the admission note, the regurgitation fraction is about 30 % from the pulmonary artery back into the right ventricle. This characterizes a severe pulmonary insufficiency. The hypertrophic right ventricle may be encouraged by the increased blood pressure due to the pulmonary regurgitation.

For clinical research, a 4D PC-MRI measurement was performed. The qualitative analysis of the complete flow in the pulmonary artery shows a clearly visible retrograde flow even without the enhancement of certain data aspects or features. A vortex occurs during diastole when the blood flows back into the ventricles through a small gap, which is caused by an improperly closing valve (see Figure 67).

The quantification results verify the regurgitation fraction of 30 %. Clearly, the situation in the pulmonary artery is pathologic and explains the vortex near the valve. However, the mere existence of such a vortex should not be seen as sufficient evidence, but rather lead to further investigations. All necessary information and explanations of the symptoms for the case are present in this dataset and the domain experts were able to diagnose the same pathology in the pulmonary artery.

⁹A video is available at <https://www.youtube.com/watch?v=y3xf5WAFo2M> (accessed 03/2016)

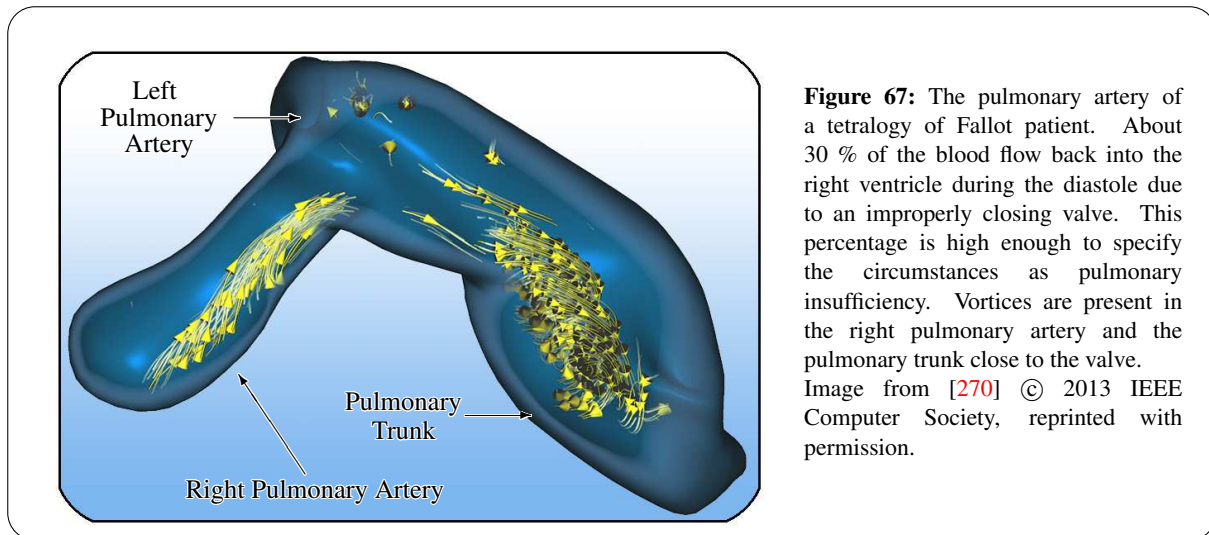


Figure 67: The pulmonary artery of a tetralogy of Fallot patient. About 30 % of the blood flow back into the right ventricle during the diastole due to an improperly closing valve. This percentage is high enough to specify the circumstances as pulmonary insufficiency. Vortices are present in the right pulmonary artery and the pulmonary trunk close to the valve. Image from [270] © 2013 IEEE Computer Society, reprinted with permission.

8.1.5.2. ANEURYSM AND BAV WITH FORMER COARCTATION

The primary disease of the second case was a coarctation, which was widened via balloon dilatation. Based on a suspicion for a re-coarctation nine years later, a new examination was performed combined with the acquisition of a 4D PC-MRI dataset. The patient has no physical limitations, but describes a casually occurring tingling in the left arm, headaches near the temples, dizziness in the morning, and often cold and sweaty hands.

The re-coarctation could be excluded with a cardiac catheterization. An MRI of the heart showed a large aneurysm in the left subclavian artery and an ectatic distal aortic arch. The aneurysm in an early stage was already known from the first examination, but has grown progressively since then. Such an aneurysmatic dilation of the subclavian artery is very rare. Further typical symptoms, such as chest pain, did not occur.

The first look at the overall flow revealed a huge vortex during the full systole and diastole ranging from the dilated left subclavian artery to the descending aorta (see Figure 68). Our vortex extraction procedure reveals no pathological findings in the pulmonary artery, but an abnormal vortex structure near the aortic valve during systole. Hope et al. [221] found swirling flow in the ascending aorta during the systole in 75 % of their 20 BAV cases *“but in none of the healthy volunteers or patients with a tricuspid aortic valve.”* Considering these results, it is likely that the BAV causes this vortex in our dataset as well. This assumption, however, could not be confirmed with certainty by the domain experts, but such a flow behavior could indicate a valve defect and lead to further investigations.

Further discussions about the aneurysmatic left subclavian artery revealed another important flow behavior: Blood passes the area of the former coarctation and then, due to the altered vessel shape, keeps flowing straight ahead instead of following the distal aortic arch leading into the descending aorta. The flow impinges on the surface and then starts swirling upwards into the subclavian artery and downwards along the descending aorta. Recent works observed an increased wall shear stress in regions where high velocity flow impinges on the vessel’s surface. They agree that abnormally high wall shear stress is one main cause for the initial development of aneurysms [384, 469]. As a consequence, the permanent stress caused by the swirling flow could be one important factor for the patient’s progressively dilating vessel.

Again, the 4D PC-MRI data complemented the diagnostic information, helped to explain the symptoms and supported the understanding of the case. The aneurysmatic subclavian artery as well as the ectatic distal aortic arch could be determined easily and the systolic vortex near the aortic valve gave a clear hint towards the BAV.

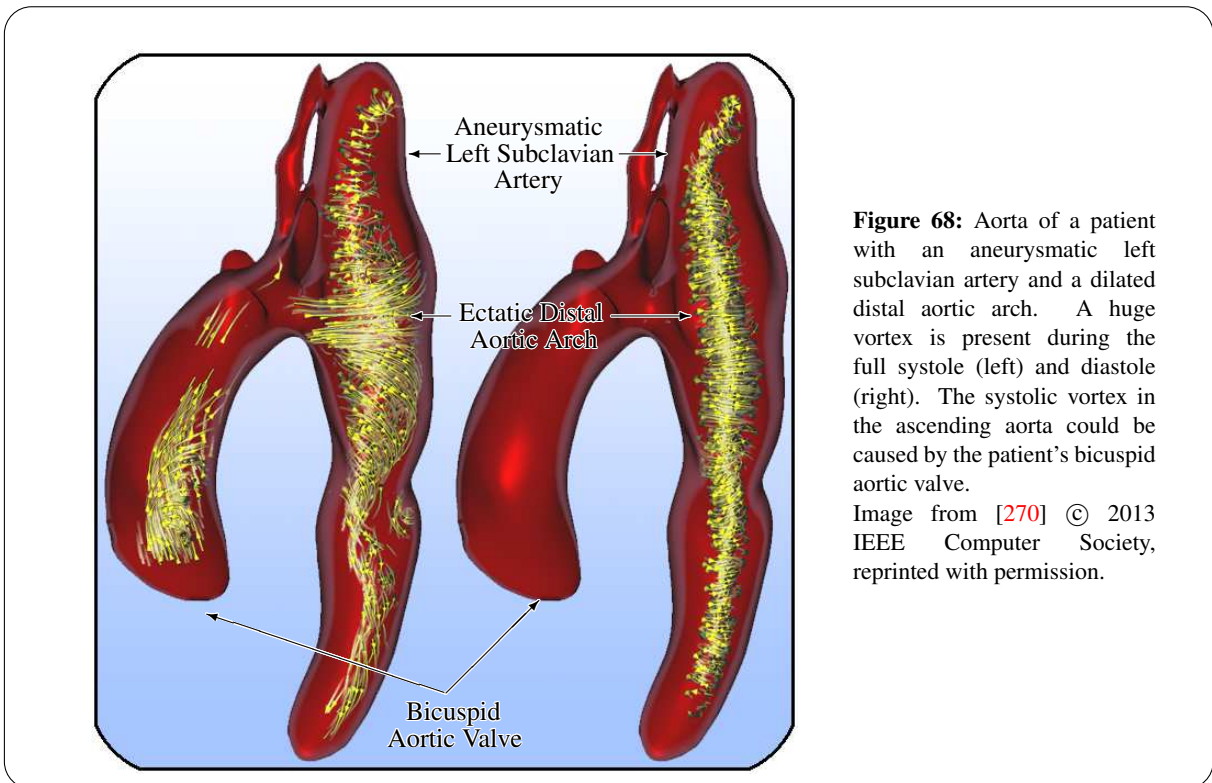


Figure 68: Aorta of a patient with an aneurysmatic left subclavian artery and a dilated distal aortic arch. A huge vortex is present during the full systole (left) and diastole (right). The systolic vortex in the ascending aorta could be caused by the patient's bicuspid aortic valve.

Image from [270] © 2013 IEEE Computer Society, reprinted with permission.

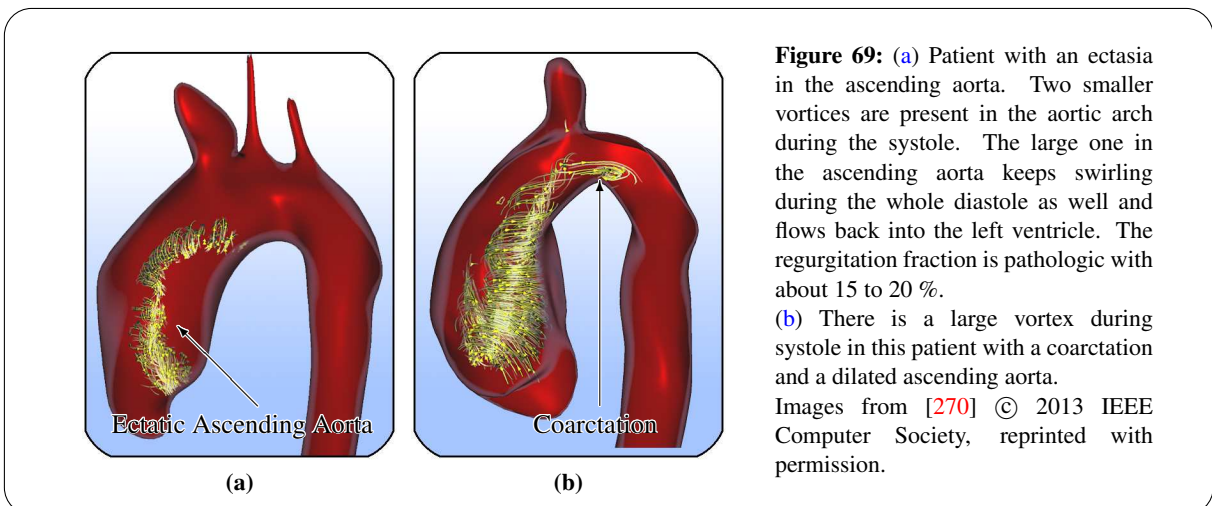


Figure 69: (a) Patient with an ectasia in the ascending aorta. Two smaller vortices are present in the aortic arch during the systole. The large one in the ascending aorta keeps swirling during the whole diastole as well and flows back into the left ventricle. The regurgitation fraction is pathologic with about 15 to 20 %.

(b) There is a large vortex during systole in this patient with a coarctation and a dilated ascending aorta. Images from [270] © 2013 IEEE Computer Society, reprinted with permission.

8.1.5.3. OVERVIEW OF OTHER CASES

Figure 69a shows the patient we presented previously for the vortex criteria comparison. The large vortex in the ascending aorta keeps swirling during the diastole and flows back through the aortic valve into the left ventricle. Further quantification shows a pathologic regurgitation fraction of about 15–20 %. According to our experts, this fact can support the decision whether or not to implant an artificial valve.

The patient shown in Figure 69b has a coarctation and a slightly dilated ascending aorta. Analogous to all our other datasets with dilated ascending aortas, a large vortex is present in this part of the vessel.

A similar case is shown in Figures 70a–b. The patient has an ectatic ascending aorta and one large vortex is present during the systole. In contrast to the first example, the vortex disappears in the diastole and no significant retrograde flow is determinable. The pulmonary artery shows a slight vortex in the pulmonary trunk near the valve during the systole. Considering the results regarding aortic valve defects, this could indicate a bicuspid pulmonary valve. Assuming that vortex flow promotes the development of

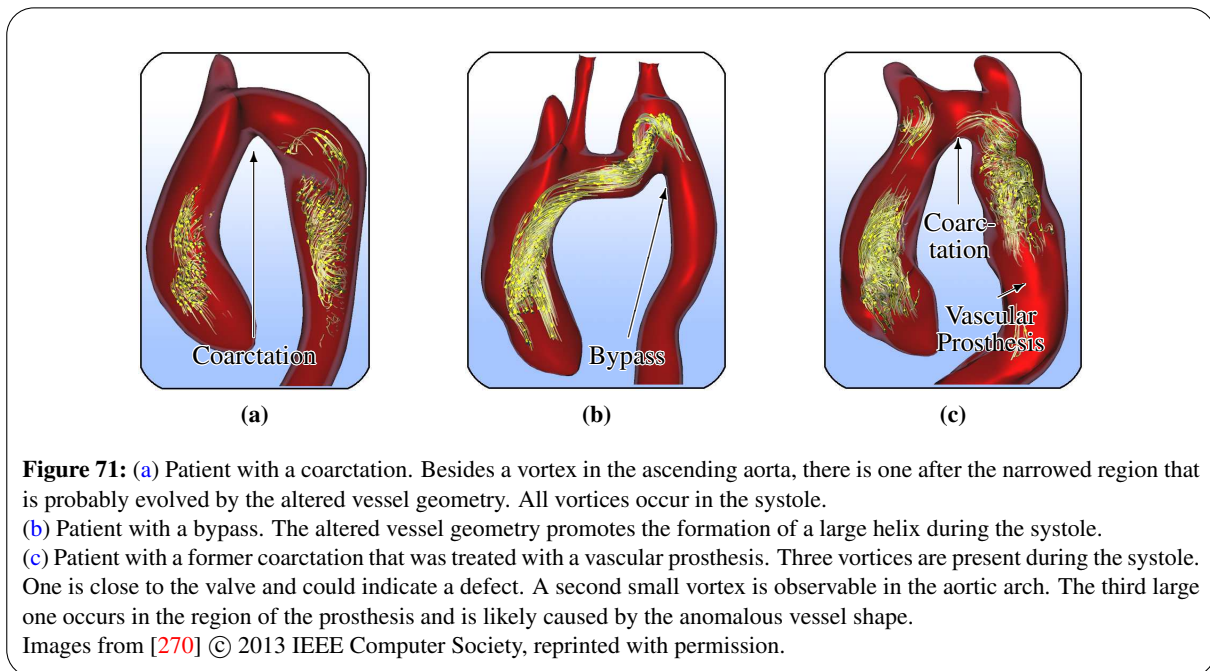
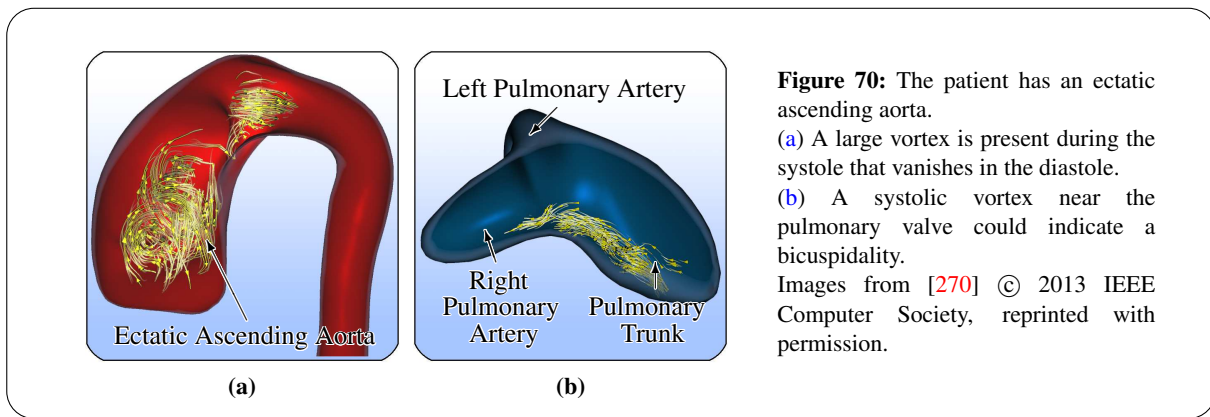
vessel dilations and, in turn, bicuspid valves encourage vortex flow, the conclusion could be drawn that bicuspidalities increase the risk of an ectasia development.

Figure 71a shows a patient with a coarctation. The narrowed vessel geometry seems to cause the vortex from the distal aortic arch into the descending aorta. Again, we can observe a vortex in the ascending aorta during the systole that could indicate a BAV.

The case shown in Figure 71b had undergone a bypass operation. There is one large helix present during the systole that is likely promoted by the altered course of the vessel.

The last example in Figure 71c shows a similar case. The patient has a vascular prosthesis implant as treatment of a former, severe coarctation.. The occurring vortex patterns are comparable to the ones in Figure 71a and were possibly caused by the same reasons. An additional small vortex is present in the aortic arch. All vortices occur in the systole.

Our two healthy volunteers were, as expected, without pathologic findings. The same yields for the pulmonary arteries of all cases except for the two we showed in Figures 70b and 67.



8.1.5.4. BAV IN A PORCINE MODEL

THE SECTION IS BASED ON:

- [192]: M. GROTHOFF, C. D. ETZ, B. PREIM, B. KÖHLER, AND M. GUTBERLET. “PHASE CONTRAST 4D FLOW IN BICUSPID AORTIC VALVE IN A PORCINE MODEL”. IN: *Journal of Cardiovascular Magnetic Resonance* 17.SUPPL 1 (2015), P416. DOI: [10.1186/1532-429X-17-S1-P416](https://doi.org/10.1186/1532-429X-17-S1-P416)

SEE SECTION [PUBLICATIONS](#) IN THE APPENDIX FOR THE DIVISION OF WORK.

The influence of aortic valve bicuspidalization (BAV, recall Section 2.2.2) was investigated in a study with pigs. Pigs are often used for such purposes, since their cardiac anatomy is similar to human hearts and they are readily available [109]. Three mongrel swines were scanned with 4D flow MRI. Then BAV surgeries were performed:

- The right and left-coronary leaflet (R-L) were fused in swine one.
- The right and the non-coronary leaflet (R-N) were fused in swine two.
- In swine three, it was discovered that it already had an inherited BAV (also R-L type).

Please consider Sievers and Schmidtke [472] or Martin et al. [344] for an explanation of the BAV fusion types. A post-operative scan was performed of swine one and two. Subsequently, vortex flow patterns before and after were compared. Before the surgery both pig one and two had mostly laminar flow during systole. Post-op they had, same as swine three, prominent vortex flow in the ascending aorta or aortic arch (see Figure 72). The study could successfully demonstrate the influence of bicuspidalization of the aortic valve to blood flow patterns.

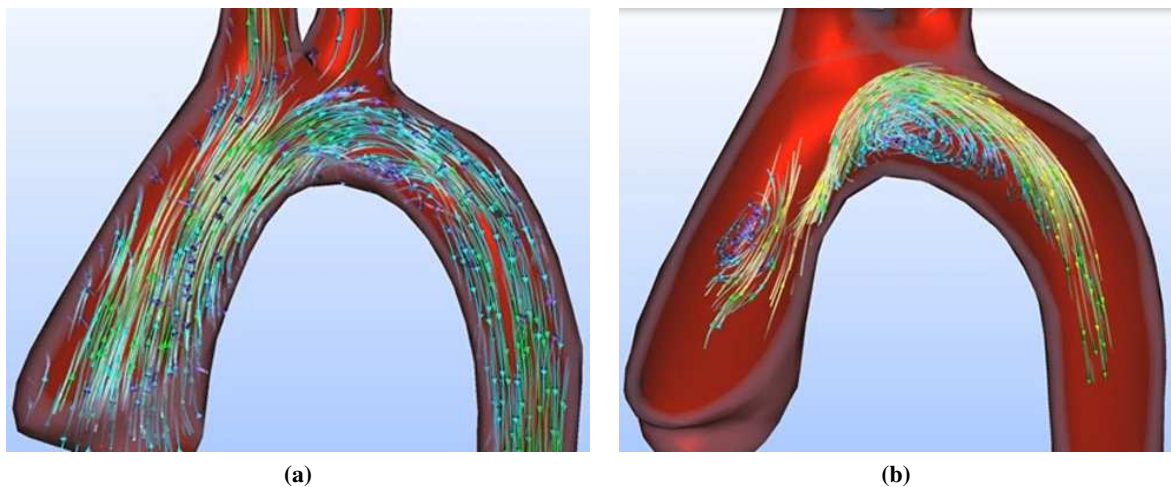


Figure 72: (a) Swine one with a tricuspid aortic valve has mainly laminar systolic flow. Path lines are color-coded by velocity.

(b) Prominent vortex flow emerges after a surgical bicuspidalization.

The images are from our [open source article](#) [192], which is available under the [Creative Commons 4.0 Attribution License](#).

8.1.6. CONCLUSION

It was shown that the approach reliably extracts vortices in the aorta and pulmonary artery based on 4D PC-MRI measured flow information. A result was considered as correct if at least all vortices were extracted that experts were able to discover manually. The extraction achieves real-time capability due to its entire computation on the GPU. A detailed investigation of several vortex criteria was performed in [269] where the λ_2 criterion was identified as the most appropriate local vortex criterion for cardiac 4D PC-MRI datasets. Yet, the limited diversity of the datasets might alleviate the generality of this result.

As a follow-up to this work, Carnecky et al. [94] further increased the noise robustness of λ_2 calculation in 4D PC-MRI data by suggesting an orthogonal decomposition of the phase images.

Line predicates were incorporated to extract meaningful path lines that describe vortex flow structures. Their quality is high and meets the domain experts' and our requirements. The experts came to similar conclusions regarding the relation of present pathologies and occurring vortices for the presented cases. Thus, the straight forward and semi-automatic extraction pipeline in combination with reasonable default parameters ensures the ease of use of our method and minimizes the inter-observer variability.

The results allow a more precise diagnosis, support treatment decisions, and facilitate the understanding of the progression of cardiovascular diseases, such as ectasias and aneurysms. Vortices are a strong indicator for certain pathologies of the cardiovascular system and complement other features like velocities, flow rates, and the amount of retrograde flow. However, the correlation between pathologies and vortex flow patterns is an ongoing research topic. The clinical collaborators indicate that with more confidence in the developed tools, they may replace the standard 2D blood flow measurements in the future. This would be a big step forward, since 4D blood flow measurements would leave the stage of an experimental modality only used for selected cases. An important requirement for future work will be to optimize the workflow and usability of tools.

The line predicate technique is flexible enough to be extended, so that more flow characteristics can be determined (see Born et al. [63]). Possible targets are laminar flow, high velocity flow during the diastole, the separation of antegrade and retrograde flow, flow that impinges on the vessel walls with high velocities, and flow that causes high WSS.

8.2. 2D PLOT VISUALIZATION OF AORTIC VORTEX FLOW

THIS SECTION IS BASED ON:

- [274]: B. KÖHLER, M. MEUSCHKE, U. PREIM, K. FISCHBACH, M. GUTBERLET, AND B. PREIM. "TWO-DIMENSIONAL PLOT VISUALIZATION OF AORTIC VORTEX FLOW IN CARDIAC 4D PC-MRI DATA". IN: *Proceedings: Bildverarbeitung für die Medizin*. 2015, pp. 257–61. DOI: [10.1007/978-3-662-46224-9_45](https://doi.org/10.1007/978-3-662-46224-9_45)

SEE SECTION [PUBLICATIONS](#) IN THE APPENDIX FOR THE DIVISION OF WORK.

Vortex flow in the great mediastinal vessels, such as the aorta, is presumed to be a strong indication of several pathologies. Therefore, studies with homogeneous patient groups are performed to quantify the probability of vortex occurrence in specific vessel sections during the cardiac cycle. Common path line visualizations of the highly complex 4D PC-MRI datasets allow a qualitative analysis. In the previous section, an adapted line predicates technique to semi-automatically filter vortex flow was established. Such methods are essential to make 4D PC-MRI viable for the clinical routine. Nevertheless, when the path lines are displayed all at once by ignoring their temporal component, heavy visual clutter remains. Particle animations alleviate this problem, but increase the required evaluation time per dataset.

Different works established simplified visualizations of the cardiovascular morphology. Cerqueira et al. [98] proposed the nowadays widely used 2D bull's eye plot (BEP) of the left ventricle that is based on a standardized segmentation. The plot is simple, unambiguous, and thus a convincing reduction of the 3D information. Based on this, Termeer et al. [502] described a plot visualization of coronary artery disease. Angelelli and Hauser [8] introduced a straightening of tubular structures and applied it to the aorta in order to enhance flow analysis with reference to the main flow direction, which usually is the centerline. Yet, when the whole cardiac cycle is to be analyzed, numerous such visualizations with different temporal positions are required.

In this work, a circular 2D plot is introduced that is adaptable to various flow characteristics. The focus lies on vortex flow due to the strong correlation to cardiovascular pathologies. The plot provides detailed information about the temporal position and approximates the corresponding vessel section. A grid view of different datasets enables the fast assessment of vortex behavior in a user-defined database. A scalar parameter controls the plots' sensitivity towards vortex flow. The possibility to set already analyzed

datasets as references enhances the evaluation of new cases. After a brief training, our collaborating cardiologists and radiologists were able to reliably find pathologic cases in the grid view.

8.2.1. METHOD

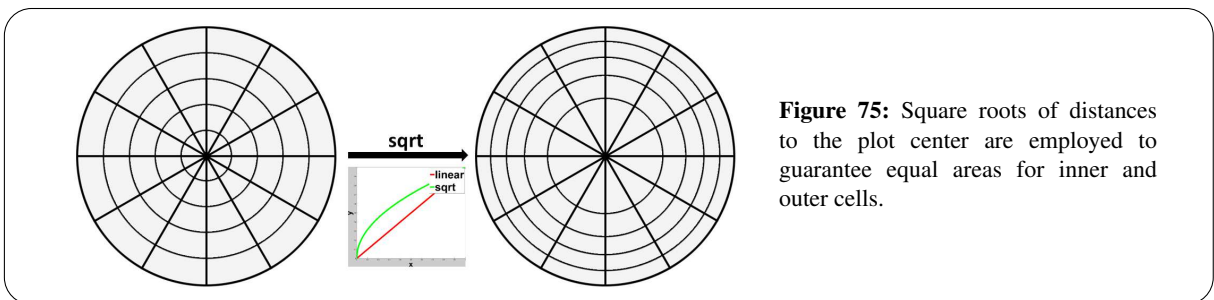
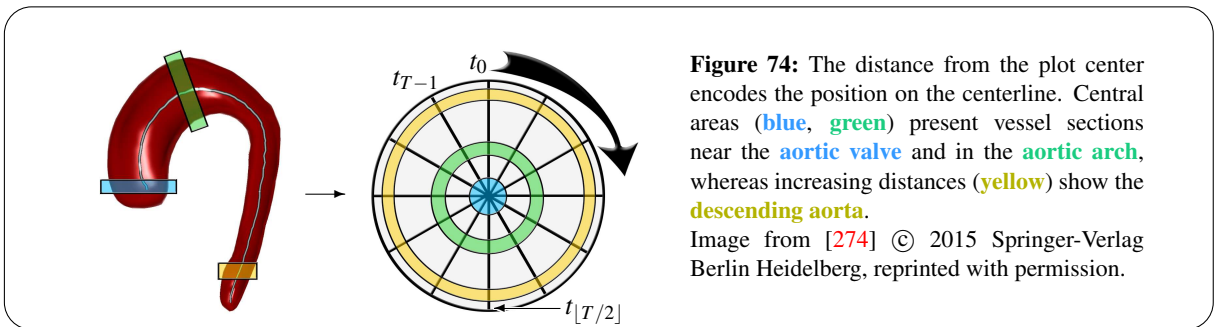
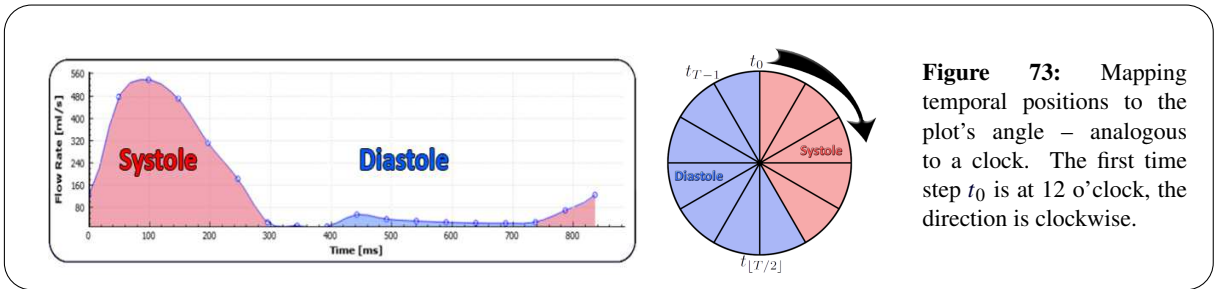
MAPPING: Intravascular positions $\vec{p}_t = (x, y, z, t)$ in the 4D PC-MRI dataset consist of a three-dimensional spatial and a one-dimensional temporal component. The circular plot visualization, however, offers merely an angle ϕ and a distance d to the center as degrees of freedom.

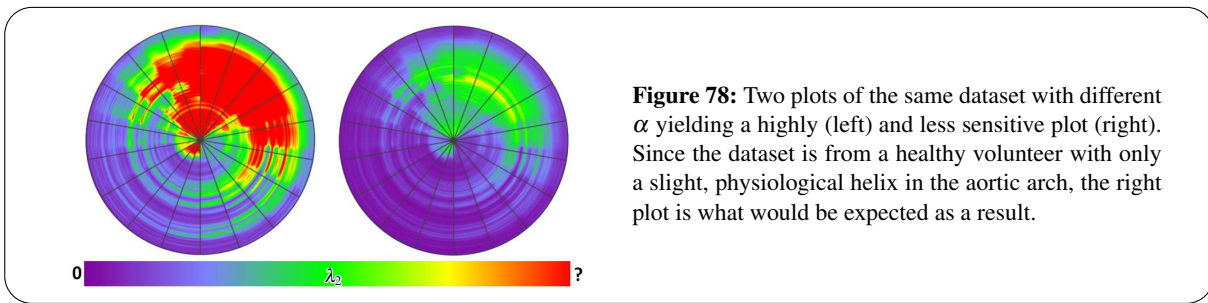
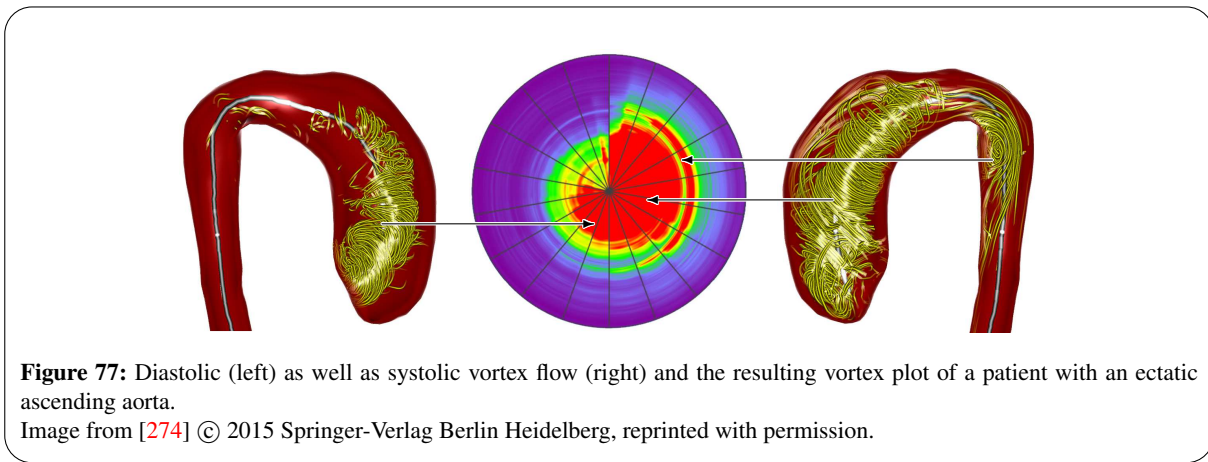
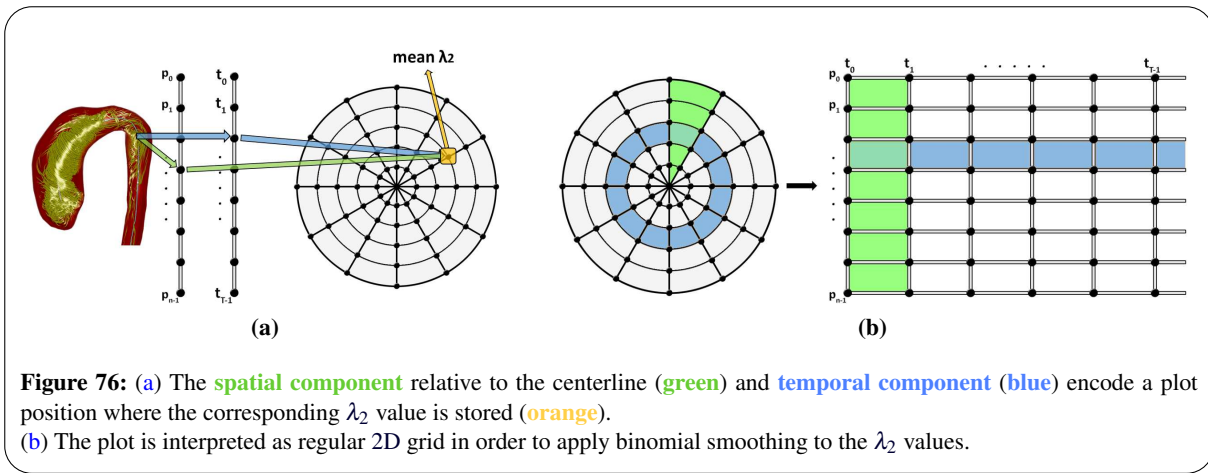
Medical research papers that correlate the presence of vortex flow patterns to specific pathologies have two central questions: *When* (during the cardiac cycle) does the vortex occur and in *what vessel section*? We decided to map a vortex' temporal position to the plot's angle as an analogy to a clock and due to the cyclic nature of the data (see Figure 73).

Now there is only the center distance d left to map the spatial position. The idea is to employ the centerline for this purpose. The projection \vec{q} of a spatial position in the vessel onto the centerline is determined and used to obtain $d \in [0, 1]$ as:

$$d = \sqrt{\text{length}(\text{centerline until } \vec{q}) / \text{length}(\text{centerline})} \tag{33}$$

Thus, the plot center corresponds to the approximate aortic valve location where the centerline starts. Increasing d encode positions in the aortic arch and descending aorta (see Figure 74). The square root is used to ensure that inner and outer parts of the plot are represented with equally large areas (see Figure 75).





VORTEX PROCESSING: Each centerline point stores T values, where T is the number of time steps in the dataset. These buckets are used to accumulate a quantitative measure, in our case the λ_2 criterion since it is well suited for vortex extraction in the cardiac 4D PC-MRI context [270]. As a pre-processing, the centerline is equidistantly resampled in 0.5 mm steps via cubic spline interpolation in order to have the same distances in different datasets and a sufficient amount of buckets. Since the employed path line integration uses adaptive step sizes, the vortex-representing path lines are resampled as well in the same manner. Afterwards, every point of each path line is processed. The closest spatio-temporal projection onto the centerline is determined and the λ_2 value of the path line vertex is split among the two neighboring centerline buckets weighted by their inverse distance to the projection. After evaluating all path lines the mean λ_2 value is calculated for each bucket (see Figure 76a). A binomial smoothing of the accumulated values is performed as post-processing (see Figure 76b).

Vortices are present where $\lambda_2 < 0$. The smaller λ_2 is, the stronger is the vortex flow. Unfortunately, the criterion has no fixed minimum, which negatively affects the comparability between different datasets.

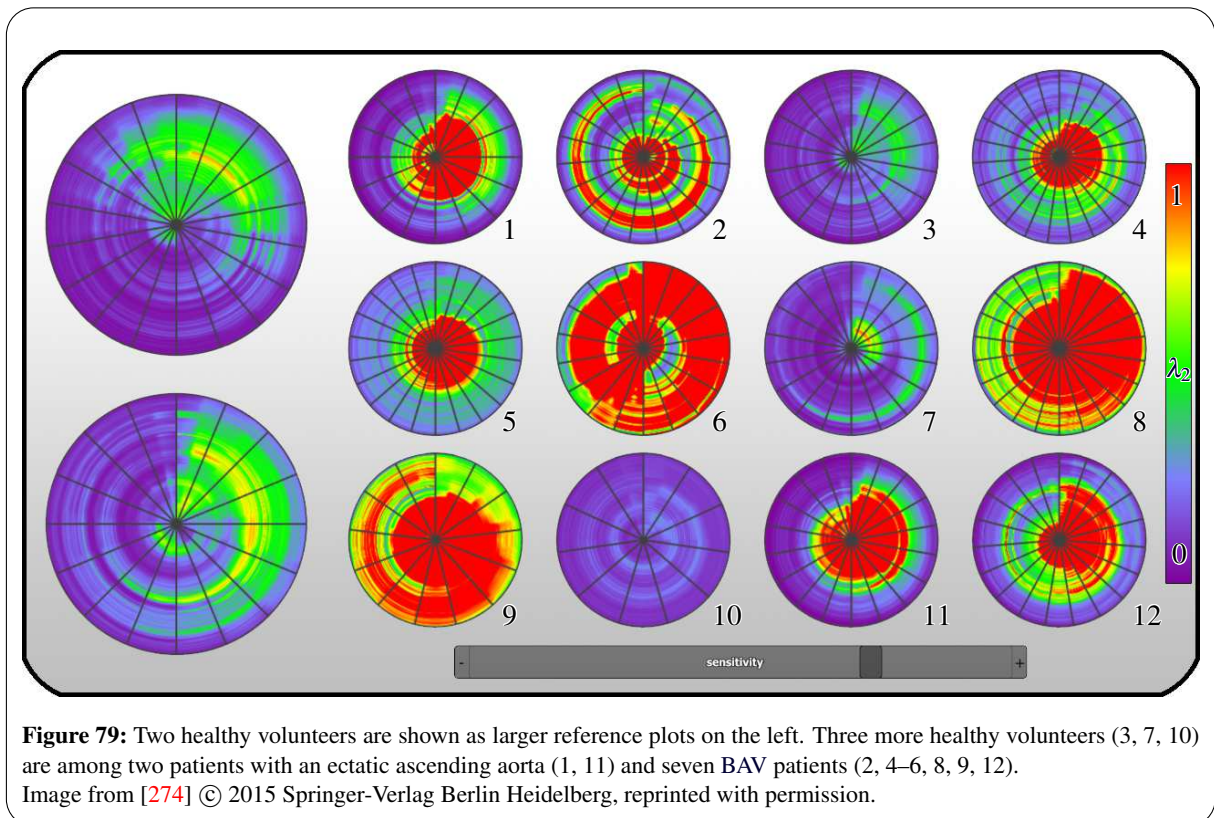
As a remedy, we let the user define a minimum λ_2 value as parameter α within 0 and the minimal occurring λ_2 value. The closer α is to 0, the more sensitive the visualization is towards vortex flow. The parameter is used to scale as well as clamp the λ_2 values to $[0, 1]$. The scaled values are then mapped to an arbitrary color scale. We employ the rainbow scale despite their perceptual problems, since this a common choice in the clinical context (see Figure 77).

DATASET COMPARISON: The expressiveness of a single plot might be limited, since an appropriate choice of α is not always clear – especially for pathologic datasets. This problem further increases if there are λ_2 outlier values. Figure 78 shows two α settings, each one close to 0 and the λ_2 minimum, for a healthy volunteer. Incorporating a priori knowledge, one would expect a plot that shows almost no critical regions (vortex flow), as only a slight, systolic helix in the aortic arch is expected.

To tackle this problem, a grid view is provided that enables the efficient comparison of multiple datasets. Here, the sensitivity parameter α is used globally for all plots. Additionally, the user has the option to choose known cases as reference plots in addition to the actual cases that are selected for evaluation.

8.2.2. RESULTS

We used 14 datasets for the evaluation: Five healthy volunteers, two patients with an ectatic ascending aorta, and seven BAV patients. Each patient has prominent systolic vortex flow in the ascending aorta. The computation time per case is between 2 and 5 s on an Intel i7-3930K depending on the amount of path lines. Figure 77 shows one of the patients with a dilated ascending aorta and depicts the relation between occurring vortex flow and the resulting plot. Figure 79 shows the proposed grid view with all datasets. The two larger plots on the left represent healthy volunteers that were selected as references. The sensitivity parameter α was interactively adjusted so that these two plots merely indicate the slight physiologic helix in the aortic arch during systole. In an informal evaluation, our collaborating radiologists and cardiologists were easily able to spot the remaining three healthy volunteers without pathologic vortex flow.



8.2.3. DISCUSSION

We presented a two-dimensional circular plot visualization of aortic vortex flow. Domain experts were able to quickly assess whether or not pathologic vortices are present in a dataset and could estimate their positions and temporal extents. Presenting the temporal position based on a clock analogy was considered as intuitive, whereas the mapping of spatial positions using the centerline required a short briefing. A possible application of our method is to get a quick overview of datasets in larger studies. Tasks like counting the BAV patients with systolic vortex flow in the ascending aorta can be performed comfortably. In addition, our method could support the clinical report generation and serve as a summary of a patient's vortex flow behavior. Our method provides no information about a vortex' wall closeness, which might be interesting due to the association with high shear forces [96]. However, a visualization or integration of other measures in the plot, derived from arbitrary flow properties or line predicates, is conceivable. The comparability of datasets acquired with different scanners and / or MR sequences has to be analyzed in a future work. Potential problems may arise due to differently scaled λ_2 values. Our proposed plot uses exactly one centerline to project the spatial intravascular positions. Another future topic could be the adaption for branching vessels, such as the pulmonary artery.

8.3. ADAPTIVE ANIMATIONS OF EXTRACTED VORTEX FLOW

THIS SECTION IS BASED ON:

- [276]: B. KÖHLER, U. PREIM, M. GROTHOFF, M. GUTBERLET, AND B. PREIM. "ADAPTIVE ANIMATIONS OF VORTEX FLOW EXTRACTED FROM CARDIAC 4D PC-MRI DATA". IN: *Proceedings: Bildverarbeitung für die Medizin*. 2016, pp. 194–9

SEE SECTION [PUBLICATIONS](#) IN THE APPENDIX FOR THE DIVISION OF WORK.

While quantitative data analysis allows to assess the cardiac function and monitor disease progression, qualitative methods support the identification of characteristic flow patterns. Flow animations commonly employ pathlets or particles [351]. The extraction of vortex flow facilitates an easier comprehension of the highly complex 4D data [270]. Though, vortices are mostly not present during the full cardiac cycle. An interactive manipulation of the animation time is possible in flow analysis software, but rendered videos typically use a constant speed. As a consequence, many seconds of the video are potentially wasted by displaying an empty vessel or flow outside the focus. There are other works that established flow simplifications or abstractions [275]. However, a great advantage of flow animations is their intuitiveness. Therefore, we enhance this technique by describing view-dependent *vortex animations with adaptive speed* (VAAS). Here, time-spending is concentrated on flow characteristics of interest, whereas the rest is time-lapsed.

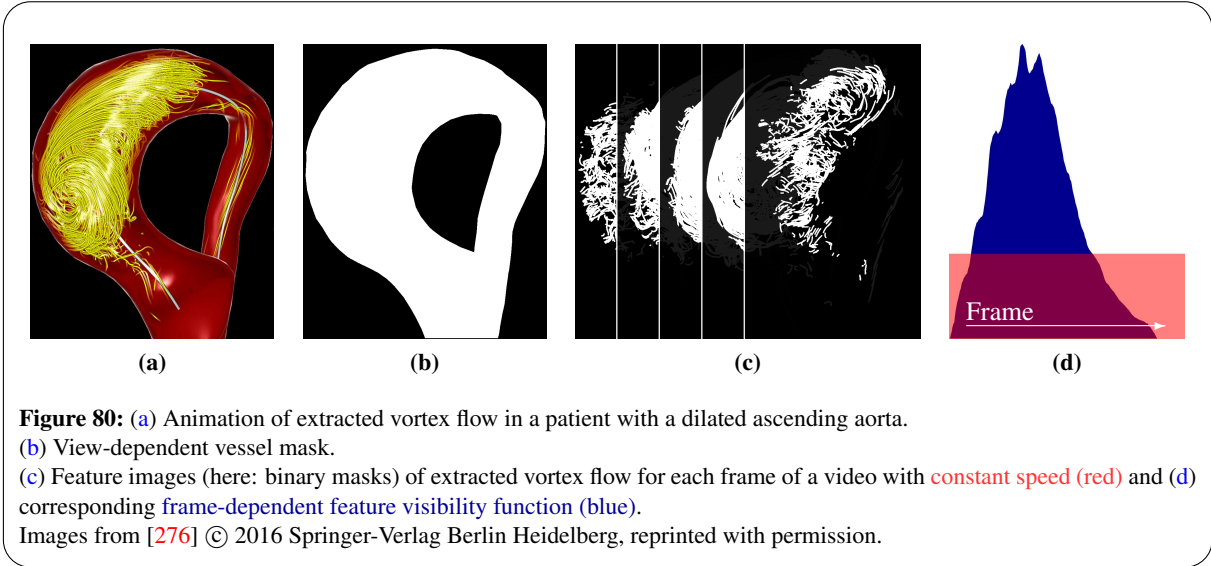
Our collaborating radiologists and cardiologists appreciate the easier vortex analysis from videos and see the principal application in presentations, case discussions, or documentations. We present four diverse datasets in an informal evaluation.

8.3.1. METHOD

This section describes our work, which can be seen as a histogram equalization for the temporal vortex visibility. 4D PC-MRI data were pre-processed as described in Section 7.1.

VIDEO SETTINGS: A video with the target length S seconds and FPS frames per second consists of $N = S \cdot FPS$ single images. The cyclic 4D PC-MRI dataset has T temporal positions. For standard videos, the temporal offset between successive frames is a constant function:

$$\Delta t(i) = \frac{T}{N-1} \quad \text{with} \quad i = 0 \dots N-1 \quad (34)$$



VESSEL MASK: The number of pixels in the current viewing direction that show the vessel mesh is required (see Figure 80a). This can be counted on a binary vessel mask that is rendered with disabled shading and disabled depth testing into the stencil buffer (see Figure 80b). Only front face culling should be enabled, as it normally is when intravascular flow is shown.

FEATURE MASKS: *Feature images* (see Figure 80c) of the extracted vortex flow are created for each frame of the video with constant speed. The pathlets are rendered without illumination or halos, but with depth testing against the front face culled vessel. The animation's current time t as well as a user-given parameter l that controls the pathlets' length are used to calculate the visibility $\alpha_{01}(t, \vec{p}_t, t, l)$ for each path line position \vec{p}_t with its temporal component $\vec{p}_t.t$:

$$\alpha_{01}(t, \vec{p}_t, t, l) = \begin{cases} 1, & \text{if } t - l < \vec{p}_t.t < t + l \\ 0, & \text{else.} \end{cases} \quad (35)$$

When checking $t - l < \vec{p}_t.t < t + l$, it is important to consider the cyclic nature of the data.

FEATURE VISIBILITY FUNCTION: Every value of the discrete, frame-dependent *feature visibility function* $f(i)$ (see Figure 80d) represents the ratio of number of foreground (white) pixels in the feature (vortex) mask of that frame and the vessel mask. Each $f(i)$ is set to $\max(f(i), h)$ as a correction, where the parameter h indirectly controls the maximum value in the adaptive speed function $\Delta t_{\text{ad}}(i)$. If not restricted, $\Delta t_{\text{ad}}(i)$ can skip very large parts of the cardiac cycle if no vortices are visible. We use $h = 0.05 \cdot \max(f(i))$ as experimentally determined default. $f(i)$ is resampled to $g(k)$, $k = 0 \dots 100 \cdot N - 1$ using a periodic spline (Catmull-Rom from ALGLIB). Each value of $g(k)$ is divided by the spline's integral as a normalization.

ADAPTIVE SPEED FUNCTION: To maintain the target video length S , the integral of the *adaptive speed function* $\Delta t_{\text{ad}}(i)$ has to equal the dataset's number of temporal positions T , as $\int_0^{N-1} \Delta t(i) di$ does. Each frame of a video with constant speed shows $p = 1/N$ % information of the cardiac cycle. In the video with adaptive speed, we equate information with vortex visibility. This is used to transform $g(k)$ to $\Delta t_{\text{ad}}(i)$ via Algorithm 1. If enough information are gathered ($\text{info} \geq p$) from $g(k)$ after $k - k_{\text{old}}$ steps, $\Delta t_{\text{ad}}(i)$ is set to the corresponding portion of the cardiac cycle (see Figure 81). To avoid irritating sudden speed changes, $\Delta t_{\text{ad}}(i)$ is smoothed in two iterations with a 1D binomial filter with kernel size 3 (experimentally determined default). A subsequent correction is applied to ensure that:

$$\int_0^{N-1} \Delta t_{\text{ad}}(i) di \approx \sum_{i=0}^{N-1} \Delta t_{\text{ad}}(i) = T \quad (36)$$

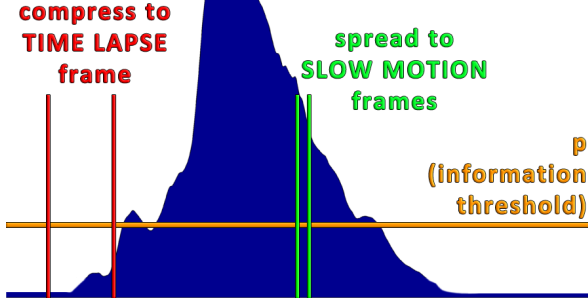


Figure 81: Additional visual explanation of Algorithm 1. Depending on the information (vortex visibility), time lapse or slow motion is applied to different time segments.

```

p ← 1/N // information threshold
info ← 0 // gathered information
kold ← 0
i ← 0 // Δtad index

```

```

for k = 0 to 100 · N - 1 do
  info ← info + g(k) // gather information

```

```

if info ≥ p then
  // enough information gathered
  Δtad(i) ← T · (k - kold) / (100 · N)
  i ← i + 1
  info ← info - p
  kold ← k
end if

```

```

end for

```

Algorithm 1. Construction of the adaptive speed function $\Delta t_{ad}(i)$ from the resampled feature visibility function $g(k)$.

```

p ← T/N // adaptive speed threshold
temp ← 0 // gathered adaptive speed
iold ← 0
cnt ← 0 // Δtrel index

```

```

for i = 0 to N - 1 do
  temp ← temp + Δtad(i) // gather adaptive speed

```

```

if temp ≥ p then
  // enough adaptive speed gathered
  m ← round(temp/p)
  d ← m / (1 + i - iold)

```

```

for n = 0 to m - 1 do
  Δtrel(cnt) ← d
  cnt ← cnt + 1
end for

```

```

temp ← temp - (p * m)
iold ← i + 1
end if

```

```

end for

```

Algorithm 2. Construction of the relative video speed $\Delta t_{rel}(i)$ from $\Delta t_{ad}(i)$, which is shown in the diagrams (red).

While this integral is smaller than T , a value c is added to each $\Delta t_{ad}(i)$. Afterwards, while the integral is greater than T , c is subtracted from each $\Delta t_{ad}(i)$. As default we use:

$$c = \frac{0.01}{100 \cdot N} \quad (37)$$

This allows to alter the integral by 0.01 in each iteration. Finally, we set:

$$\Delta t_{ad}(100 \cdot N - 1) += T - \int_0^{N-1} \Delta t_{ad}(i) di \quad (38)$$

This is done to achieve the exact target video length S . In all diagrams we show the relative video speed $\Delta t_{rel}(i)$ (see Algorithm 2) instead of $\Delta t_{ad}(i)$. This is more expressive, since it displays the speed level of the video at each time step.

For the final video rendering, we employ $\alpha(t, \vec{p}_t, t, l)$ (see Equation 39) as path line opacity function. Order-independent transparency (OIT) [571] ensures correct alpha blending of the semi-transparent

pathlets.

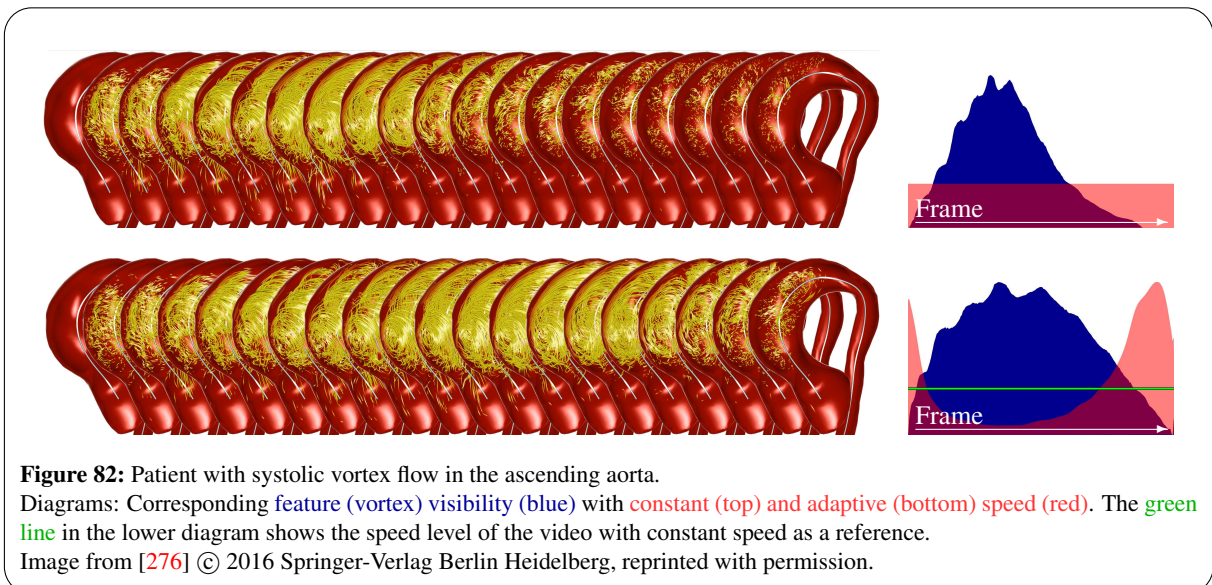
$$\alpha(t, \vec{p}_t, l) = \begin{cases} \sqrt{1 - |t - \vec{p}_t| / (2 \cdot l)}, & \text{if } t - l < p_t < t + l \\ 0, & \text{else.} \end{cases} \quad (39)$$

EXTENSIONS: Our procedure is directly applicable to a region of interest. In case of simultaneously occurring vortices, this allows to emphasize one of them. In addition, another flow property, such as the path lines' velocity, can be mapped to gray scale. The feature images (previously binary masks) then store color values between 0 and 1 that serve as an implicit weighting. Instead of counting foreground pixels, these color values are accumulated, while the remaining procedure is the same as before. This could also be used to emphasize near-wall vortex flow, which is associated with increased shear forces (wall shear stress). However, disabling line illumination is required to avoid false-positive high feature values.

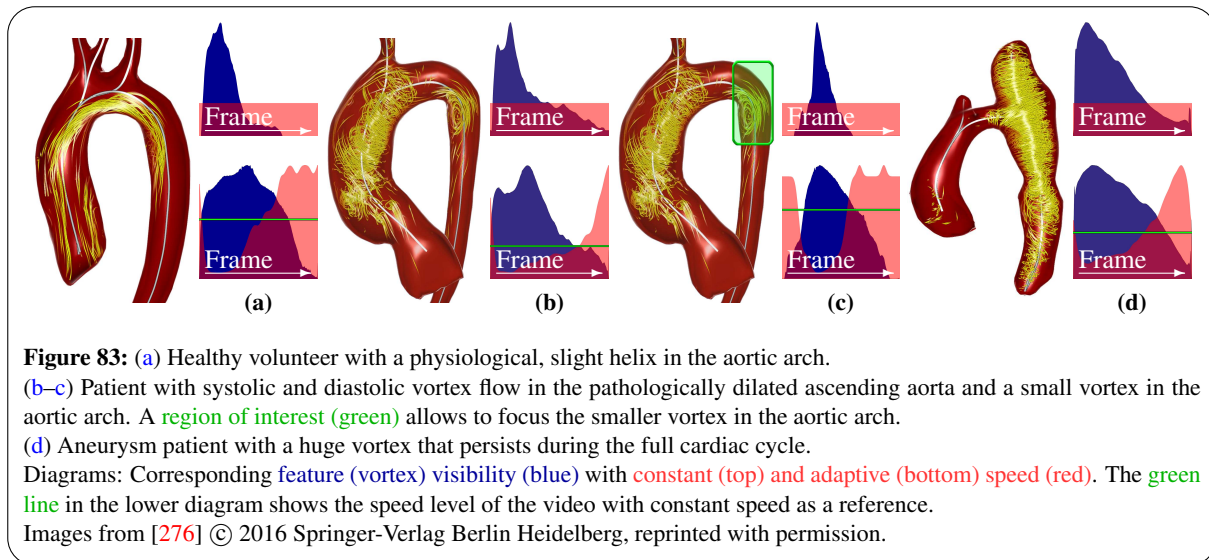
8.3.2. RESULTS

We applied our method to four datasets.¹⁰ The first patient has systolic vortex flow in the dilated ascending aorta (see Figure 82). The adaptive video speed ranged from 19–315 % compared to the constant version. A healthy volunteer with a physiological helix in the aortic arch is shown in Figure 83a. In the adaptive video, time lapse is applied to the diastole, where almost none of the extracted vortex flow is visible. Figure 83b shows a patient with pathologic vessel dilation, heavy systolic as well as diastolic vortex flow in it, and an additional systolic vortex in the aortic arch. A slight speed increase during diastole is achieved when our method is applied to the whole vessel, since vortex flow is visible during the whole cardiac cycle. Figure 83c shows the same patient with a focus (region of interest) on the smaller vortex in the aortic arch. Due to a shorter overall feature visibility, our method has an increased effect in this case. Figure 83d shows an aneurysm patient with a prominent vortex that is present during the full cardiac cycle. The result is similar to Figure 83b.

The employed test system has an Intel Core i7-2600K and a GeForce GTX 680. Our default video setup with 5 s and 50 FPS takes about 50 s to create and analyze the visibility function, and another 45 s to render the actual video. The performance directly scales with the desired FPS and the target video length.



¹⁰A video is available at <https://www.youtube.com/watch?v=6k9DTCvYXD8> (accessed 03/2016)



8.3.3. DISCUSSION

We presented *vortex animations with adaptive speed* (VAAS) to support the evaluation of cardiac vortex flow patterns. In a figurative sense, the technique is a histogram equalization for vortex visibility. While histogram equalization aims at an optimal use of the available gray values, VAAS aims at an optimal use of given presentation time. The effect, i.e., the use of time lapse and slow motion, is higher the more squeezed the initial feature visibility function is. The results of our method could slightly vary with different line width and pathlet lengths. Also, fast path lines might be favored implicitly, since they produce longer pathlets and thus occupy more pixels in the feature images. The computational effort could be decreased by not analyzing every video frame to create the visibility function. But, features that are visible for only a short time could be missed this way.

Our method processes only the mesh and path line geometry and thus is independent from the underlying image data. An application to simulated CFD data or other vessels is conceivable. Our clinical collaborators appreciate the reduced downtimes, where an empty vessel or uninteresting flow was shown. This was considered as helpful during case discussions, presentations, and for documentation purposes. It was required that the user should explicitly need to enable our method in the software to avoid confusion. Integrating a speedometer was a further idea raised by our clinical collaborators. This would support the recognition of time lapse and slow motion. Additionally, a reference to the current temporal position within the heart cycle should be shown, e.g., as a bar in a flow curve diagram.

8.4. VORTEX CHARACTERIZATION IN THE AORTA

Recent medical works are not only interested in the pure existence of vortex flow, but also in specific characteristics of the vortices. Especially bicuspid aortic valves (BAVs) have been shown to produce different systolic flow patterns [25, 40, 41] in the ascending aorta [221, 356], depending on the valve's cusp fusion type [472] (recall Sections 2.2 and 5.3.1).

A prerequisite to analyze single vortex entities is their separation by means of clustering. A corresponding approach is described in Section 8.4.1. Afterwards, different criteria for vortex characterization are discussed and evaluated in Section 8.4.2.

8.4.1. CLUSTERING

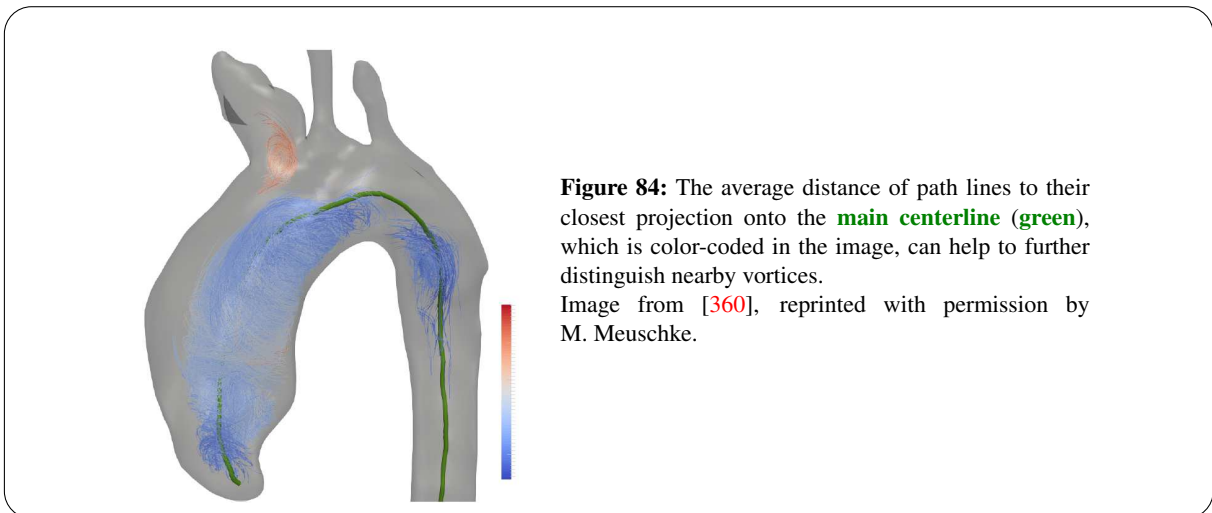
THIS SECTION IS BASED ON:

- [362]: M. MEUSCHKE, K. LAWONN, B. KÖHLER, U. PREIM, AND B. PREIM. “CLUSTERING OF AORTIC VORTEX FLOW IN CARDIAC 4D PC-MRI DATA”. IN: *Proceedings: Bildverarbeitung für die Medizin*. 2016, PP. 182–7
- [360]: M. MEUSCHKE. “COMPUTERGESTÜTZTE ANALYSE VON VERWIRBELUNGEN IN 4D PC-MRI BLUTFLUSSDATEN DER AORTA”. MA THESIS. OTTO-VON-GUERICKE-UNIVERSITY, MAGDEBURG, GERMANY, 2015

SEE SECTION [PUBLICATIONS](#) IN THE APPENDIX FOR THE DIVISION OF WORK.

There are different types of clustering techniques, depending on what they take into account (recall Section 5.2.2.3). Since we focus on cardiac 4D PC-MRI data, two major classes are relevant:

- *Vector field-based methods*, e.g., the hierarchical clustering by Van Pelt et al. [527], that operate directly on the voxel grid of the acquired image data, and
- *Integral curve-based methods*, e.g., the generation of representatives by Born et al. [62], that analyze similarities of calculated flow curves.



8.4.1.1. DISSIMILARITY FUNCTION

This work builds upon the previously described extraction of vortex flow-representing path lines with line predicates (recall Section 8.1). Therefore, we pursued the integral curve-based approach and established a pairwise dissimilarity function for path lines.

Assuming continuous path lines from the extraction, a single vortex is connected in space and time. Thus, the first employed measure analyzes the pairwise spatio-temporal distances of the extracted path lines. We further assume that two path lines of the same cluster start and end at similar spatio-temporal positions. Therefore, instead of computing pairwise distances for the whole path lines, only the start and end points are considered. This simplification was mainly made to speedup calculations.

As an additional measure, the distance of a path line to the centerline was incorporated. It is calculated as average of the distances of each path line point to its closest projection onto the centerline. This can be useful to further distinguish nearby vortices (see Figure 84).

This yields five measures that describe the pairwise path line dissimilarity:

1. The Euclidean distance of the start points,
2. the Euclidean distance of the end points,
3. the temporal distance of the start points,

4. the temporal distance of the end points, and
5. the difference of the average centerline distances.

Each measure is normalized to $[0, 1]$ using corresponding maximum values. For Euclidean distances, this is approximately the length of the centerline. The maximum distance in time is derived from the cyclic dataset's temporal resolution. The maximum occurring vessel radius, which is determined in the centerline construction based on maximum inscribed spheres [10] and provided by VMTK [410], is used to normalize the average centerline distances. A matrix M is composed with entries M_{ij} that describe the dissimilarity of the path lines i and j . Consequently, the main diagonal is composed of zeros and M is symmetric.

More elaborate measures, but with higher computational effort, could be employed as well. For instance, geometry- or flow field-based properties could be incorporated, as done by, e.g., Oeltze et al. [387].

8.4.1.2. CLUSTERING METHODS

The number of vortices in a dataset often is between 0 and 4. However, the concrete value is unknown. Therefore, we focused on clustering methods that do not require the expected cluster number as a parameter. The following three approaches were tested:

1. *Agglomerative hierarchical clustering* (AHC).
2. *Spectral clustering* (SC).
3. *Density-based spatial clustering of application with noise* (DBSCAN).

AHC initializes each path line as a separate cluster and then recursively merges the two closest clusters until only a single cluster remains. This yields a hierarchy (*dendrogram*, recall Section 5.2.2.3), which facilitates the quick comparison of results with different cluster numbers. Four proximity measures were compared [113]:

1. *Single link* determines the minimum distance of (single objects from) two clusters.
2. *Complete link* determines the maximum distance of (single objects from) two clusters.
3. *Average link* (also: *centroid method*) determines the distance of two clusters' (objects') mean values.
4. *Ward's method* [541] finds minimal values of an arbitrary objective function. The sum of squared distances is often employed, which yields *Ward's minimum variance method*.

Besides the dissimilarity matrix M and the employed proximity measure, AHC has no further parameters. An automatic suggestion for the optimal number of clusters was derived from the *L-method* by Salvador and Chan [441], which finds the knee in a graph of different cluster numbers (x-axis) and cluster merge distances (y-axis).

SC generates a lower dimensional feature space based on an eigenvalue decomposition of the dissimilarity matrix M . In this space, each path line is represented as a single point, facilitating the use of *k-means* clustering. Required parameters are the number of desired clusters and a control for the cluster similarity. Both can be estimated automatically with the self-tuning SC method by Zelnik-Manor and Perona [576].

DBSCAN identifies dense regions and requires two parameters:

1. ε defines the maximum allowed distance for grouping objects into one cluster.
2. *minObjects* defines necessary minimum number of objects that form a valid cluster.

Objects with less than *minObjects* neighbors in their ε -neighborhood are considered as outliers. *minObjects* was set to 1 in our tests, so that each path line can be a cluster. ε was set to 10 % of the maximum occurring value in the dissimilarity matrix M (experimentally determined). Smaller and larger values led to smaller and larger clusters, respectively, that did not reproduce the ground truth from manual classification.

Name	Num. Vort.	AHC SL	AHC AL	AHC CL	AHC WM	DBSCAN	SC
Aortenbypass_1_2011	2	all (6)	all (3)	all (3)	all (3)	all (4)	all (3)
Aortenektasie_04_2011	3	all (3)	all (6)	all (3)	all (6)	all (3)	all (4)
Aortenektasie_09_2012	2	all (3)	all (3)	all (3)	all (3)	all (2)	all (2)
Flow_AortaAneurysm	4	2 (3)	all (4)	2 (5)	2 (3)	all (7)	2 (2)
ISTA_06_2012	3	1 (3)	all (3)	all (5)	all (3)	all (6)	all (2)
ISTA_08_2012	2	all (7)	all (3)	0 (3)	all (4)	all (2)	all (3)
ISTA_12_2012	3	1 (9)	all (6)	all (3)	1 (3)	2 (7)	all (2)
Flow_MD_1_2014	1	all (3)	all (4)	all (3)	all (4)		
Flow_MD_2_2014	1	all (3)	all (10)	all (3)	all (4)		
Flow_MD_3_2014	1	all (9)	all (3)	all (3)	all (3)		
Flow_MD_4_2014	1	0 (3)	all (3)	all (3)	all (3)		
Flow_MD_7_2014	1	0 (3)	all (3)	all (3)	all (3)		
UP	1	all (5)	all (3)	all (3)	all (3)		
2_2012_Fallot	1	0 (10)	all (6)	all (7)	0 (3)		
ProtheseISTA_11_2012	4	0 (4)	all (7)	3 (3)	all (3)		

Table 2: Clustering results using strongly (first seven) and coarsely (last eight) filtered path line sets. *Num. Vort.* is the manually determined number of clusters. *AHC {SL, AL, CL, WM}* is AHC in combination with single, average, and complete link as well as Ward’s method. If *all* vortices could be clustered correctly, the number of applied post-processing steps (interactions) is color-coded as **zero (green)**, **up to three (orange)** and **more than three (red)**. In brackets are the number of clusters that the methods determined automatically as initial solution. AHC with average link was the only method capable of resembling all manual results.

8.4.1.3. RESULTS

In the first part of the evaluation, the most suitable clustering method is determined. We used seven datasets of patients with various diseases (first seven datasets of Table 2). The extracted path lines in these datasets were post-processed manually with a bending energy predicate, as described in Section 8.1. Each patient has at least one pathologic vortex inside the aorta. The maximum number of occurring vortices in a patient is 4. A manual separation (definition of vortex entities) that was employed as a ground truth was performed by the co-author Uta Preim – a radiologist specialized on the cardiovascular system.

The user is allowed to interactively change the number of clusters if the automatic suggestion is not appropriate. Also, clusters can be merged or excluded manually as a post-processing. Up to three interactions were considered as feasible.

AHC with average link was the only method that could reproduce all manual results correctly with up to three interactions each. Therefore, this is considered as most suitable method. The computational effort depends directly on the number of extracted path lines. Between 2 and 9 s were required on an Intel Core i7 with 2 GHz. AHC with single link sometimes connects dissimilar objects through a series of similar objects. Complete link and Ward’s method work better, but still not as good as average link. DBSCAN produces a fixed cluster configuration instead of a hierarchy. It also tends to connect close clusters, and it is difficult to find generally applicable parameters. SC could not separate the vortices correctly in one case and required more than three post-processing interactions in three cases.

In the second part of the evaluation, eight further datasets are examined where the path lines were filtered without the bending energy post-processing (last eight datasets of Table 2). Therefore, the line sets might contain more noise and laminar flow. This test is only performed with AHC – the previously detected winner. Figure 85 exemplary depicts five results. Again, AHC was most reliable in combination with average link, although more than three post-processing interactions were required in four cases.

All path lines are shown in a static view, i.e., the temporal component is ignored so that they are visible all at once with full opacity. Each cluster is visualized in an individual color. Pastel colors are used, as they were appraised as professionally looking by our clinical collaborators.

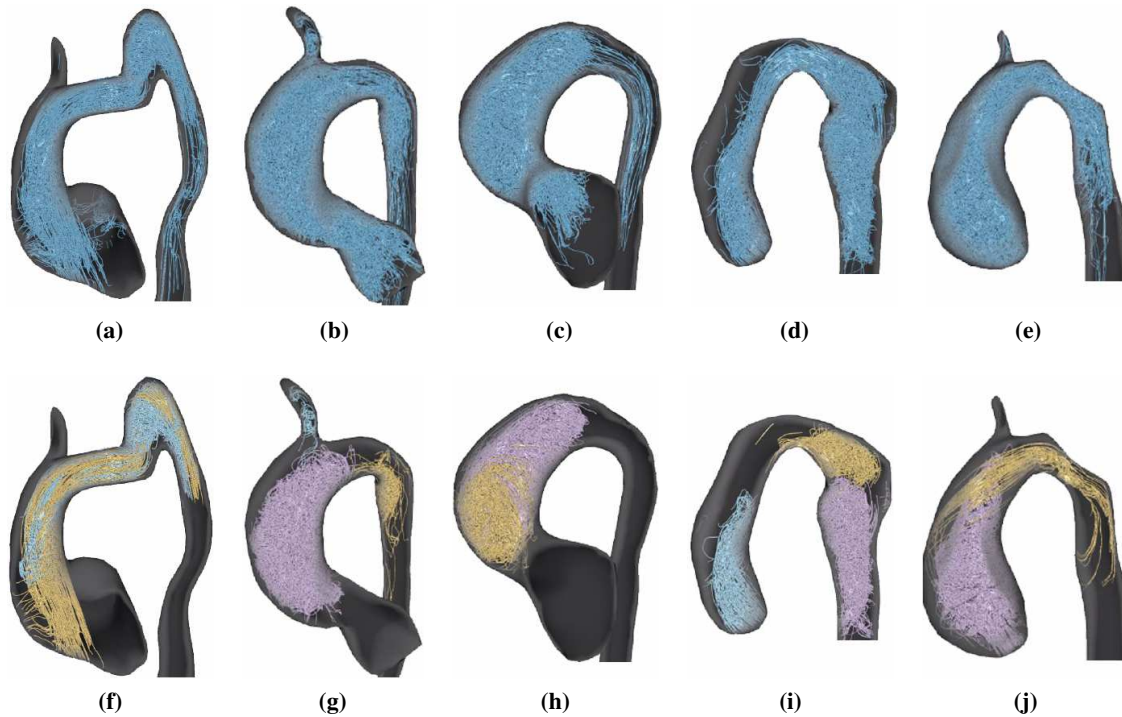


Figure 85: (a–e) Five exemplary clustering results with extracted, vortex-representing path lines without bending energy post-processing.

(f–j) Results of AHC with average link .

Patients column-wise from left to right: (a, f) Aortenbypass_1_2011, (b, g) Aortenektasie_04_2011, (c, h) Aortenektasie_09_2012, (d, i) ISTA_06_2012, (e, j) ISTA_08_2012.

Images from [360], reprinted with permission by M. Meuschke.

8.4.1.4. DISCUSSION

We presented an integral line-based clustering method for vortex flow-representing path lines that were extracted from 4D PC-MRI data of the aorta. The technique facilitates the subsequent analysis of single vortex entities, which is described in Section 8.4.2. A comparison of three different clustering methods was carried out. Agglomerative hierarchical clustering (AHC) in combination with average link was most reliable for both strongly and coarsely filtered path line sets. The amount of necessary interactions for post-processing the determined clusters increased for coarse filtering, but was still below or equal three in many cases.

FUTURE WORK: An adaption of the clustering to branching vessels, such as the pulmonary artery, is a future topic. Here, the measure regarding the average centerline distance is not directly applicable. Furthermore, the straight use of Euclidean distances introduces errors, e.g., if the distance from the aortic valve to the descending aorta is evaluated. Instead, the real intravascular distance (following the centerline) should be considered. Alternatively, distances could be measured in a straightened vessel [8]. *Cluster ensembles*, as proposed by Strehl and Ghosh [492], could be used to combine and optimize different clustering results. However, this would increase the computational effort significantly.

8.4.2. CLASSIFICATION

THIS SECTION IS BASED ON:

- [363]: M. MEUSCHKE, B. KÖHLER, U. PREIM, B. PREIM, AND K. LAWONN. “SEMI-AUTOMATIC VORTEX FLOW CLASSIFICATION IN 4D PC-MRI DATA OF THE AORTA”. IN: *Computer Graphics Forum* 35.3 (2016), PP. 351–60. DOI: [10.1111/CGF.12911](https://doi.org/10.1111/CGF.12911)
- [360]: M. MEUSCHKE. “COMPUTERGESTÜTZTE ANALYSE VON VERWIRBELUNGEN IN 4D PC-MRI BLUTFLUSSDATEN DER AORTA”. MA THESIS. OTTO-VON-GUERICKE-UNIVERSITY, MAGDEBURG, GERMANY, 2015

SEE SECTION [PUBLICATIONS](#) IN THE APPENDIX FOR THE DIVISION OF WORK.

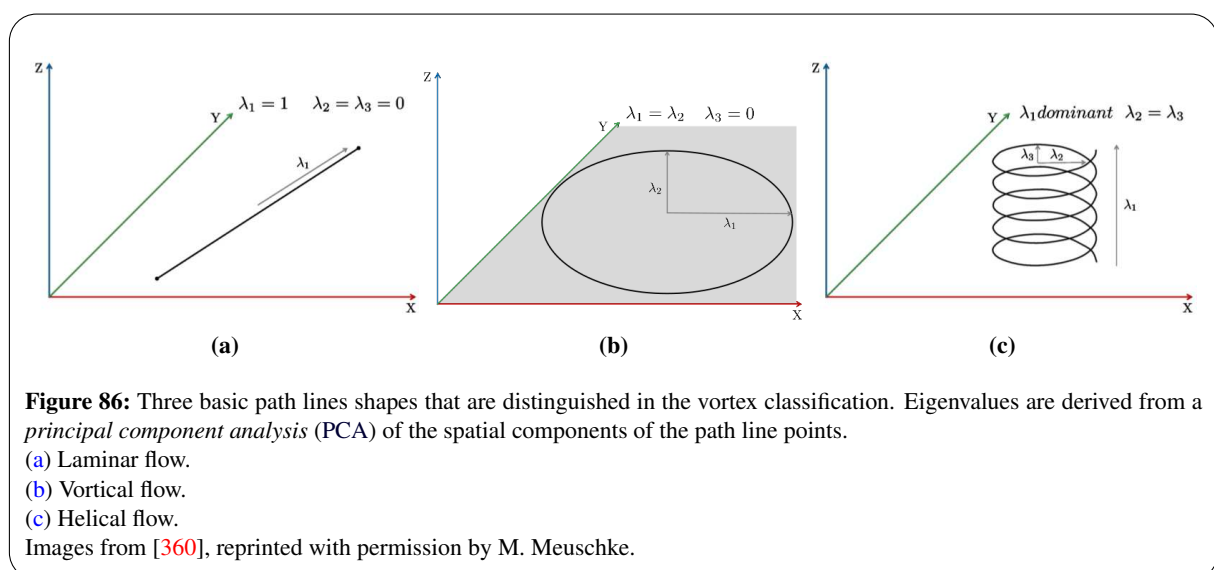
Manual classification approaches for cardiovascular vortex flow, as performed by recent medical works, were described in Section 5.3.1.3. The aim of this work is to provide a semi-automatic method for this task. This does not only speedup the classification process itself, but also increases the result reproducibility.

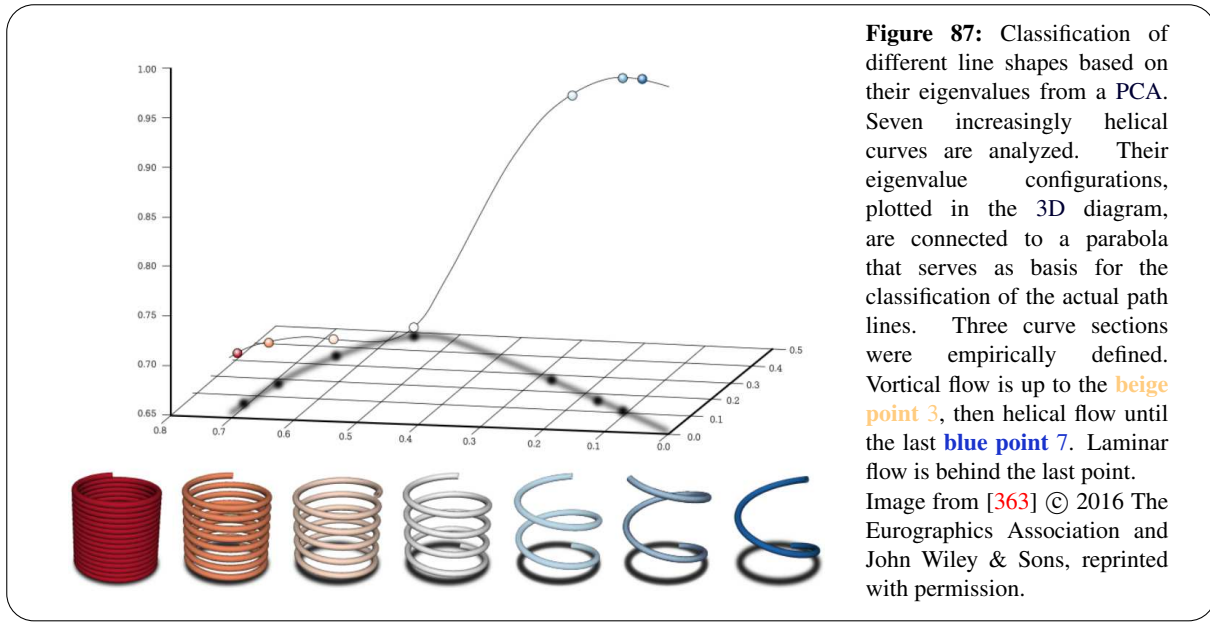
8.4.2.1. REQUIREMENT ANALYSIS

The classification of single vortex entities, based on extracted path lines, requires a reliable clustering that is able to separate vortices with low spatio-temporal distances correctly and to exclude laminar flow as well as noise. Such an approach, which forms the basis for this work, was described in the previous section.

The employed criteria for the classification should resemble the ideas of already established measures. A drawback of some proposed criteria is their binary nature, even if the described characteristic shows a continuous behavior. For example vortex shapes, which refer to the forward movement, are separated strictly into helical and vortical. The threshold is subjective, leading to potentially high inter-observer variability. However, the underlying property, which might be represented by the average angle between the vortex flow and the centerline direction, provides continuous values. This should be exploited to increase the expressiveness of vortex descriptors. Due to the large diversity of anatomic situations and intravascular flow behaviors, the user should be able to correct results if necessary.

Besides a tabular summary, an overview visualization will be established. For this purpose, the previously introduced vortex plot (recall Section 8.2) will be reused. In addition, a new glyph representation is proposed.





8.4.2.2. CRITERIA

VORTEX SHAPE: The path lines of a cluster are analyzed individually for their shape via *principal component analysis* (PCA). Therefore, the covariance matrix of the spatial positions of one path line’s points is calculated (the temporal component is ignored), and an eigenvalue analysis is performed. The three eigenvalues $\lambda_{\{1,2,3\}}$ are sorted descendingly by their absolutes, so that $|\lambda_1| \geq |\lambda_2| \geq |\lambda_3|$. The eigenvalues are real-valued, since the covariance matrix is symmetric. A path line shape can be (see Figure 86):

- *Laminar:* A straight line. Here, two eigenvalues are 0 and the third is 1.
- *Vortical:* Rotating in the plane with low to no forward movement. Here, two eigenvalues are equal and the third is 0.
- *Helical:* Rotating with stronger forward movement. Here, two eigenvalues are equal and the third one is not 0.

However, path lines will not take one of these idealized shapes. Instead, they will be intermediate shapes that can be described as a compression or stretching of a perfect helix:

$$C(t) = \begin{pmatrix} r \cdot \cos(2 \cdot \pi \cdot t) \\ r \cdot \sin(2 \cdot \pi \cdot t) \\ h \cdot t \end{pmatrix} \tag{40}$$

t is the number of turns of the helix and r is the radius. The influence of h , which refers to the elongation, is depicted in Figure 87. Seven different helix shapes, resulting from successively increasing h , and the corresponding eigenvalues, which are connected as a parabolic curve, are shown. The parabola is separated into three sections (empirically determined):

1. Vortical flow is until point 3 (beige).
2. Helical flow is from point 3 (beige) to point 7 (last point, blue).
3. Laminar flow is behind point 7 (last point, blue).

The shape analysis identifies the closest point on the parabola and derives the path line classification. However, the mere eigenvalue analysis is not reliable in every case, since the shape behavior of a path line can change along its course. A line that starts vortically and then proceeds laminarily is false-positively classified as helical. As a remedy, the torsion is calculated for all points of path lines that were classified as helical. False-positive helices have a low torsion, whereas true-positive ones have a high torsion. A

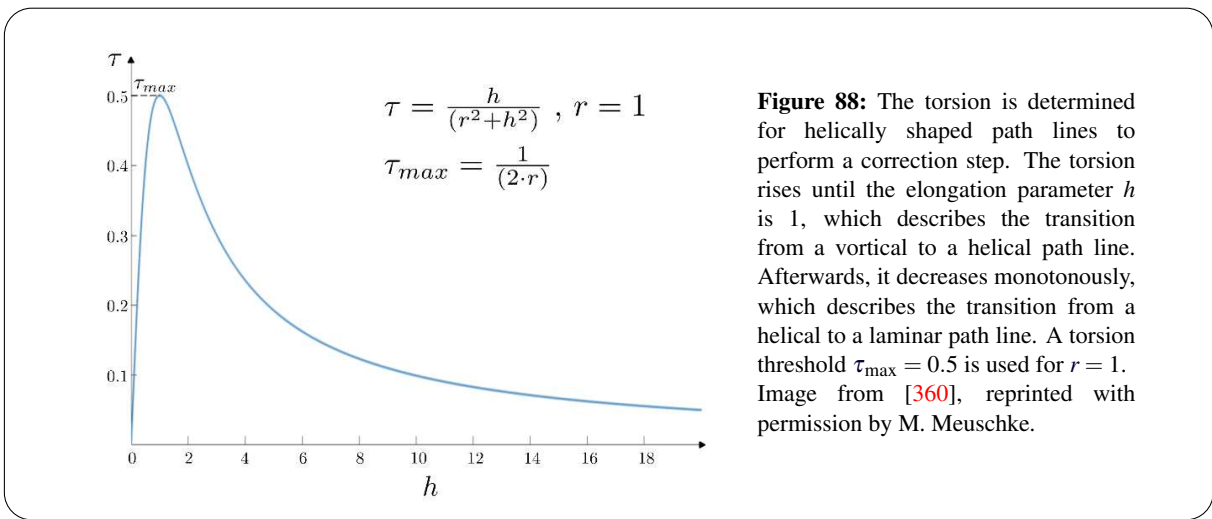
threshold is required to separate the two. The torsion τ of the curve from Equation 40 is given by:

$$\tau = \frac{h}{r^2 + h^2} \quad (41)$$

Figure 88 shows the relationship of the torsion τ and the elongation parameter h for $r = 1$. τ increases for $h < 1$, which represents the transition from a vortical to a helical line. It reaches its maximum of $\tau_{\max} = 0.5$ at $h = 1$ and then decreases monotonously, which is the transition from a helix to a straight line (laminar flow). We set the threshold τ_{thresh} to $c \cdot \tau_{\max}$, where c is an empirically determined constant depending on the average vessel radius r_{avg} , which was 7–13 mm in the available datasets:

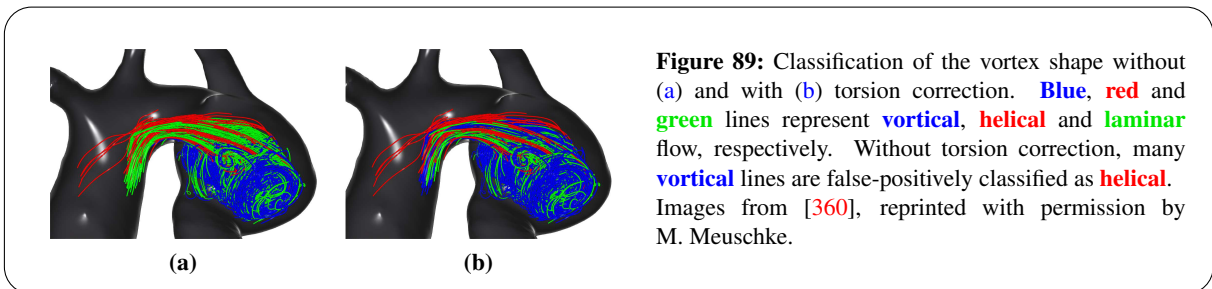
$$c(r_{\text{avg}}) = \frac{1}{2} \cdot (r_{\text{avg}} - 13) + 3 \quad (42)$$

Equation 42 was derived from a manual categorization of the correction term c , as shown in Table 3. Figure 89 depicts an example of the effect of the employed torsion correction.



Mean vessel radius r	c
7–9 mm	1
9–11 mm	1.5
11–12 mm	2
12–13 mm	2.5
13 mm	3

Table 3: Manual specification of the correction term c for the torsion threshold τ_{thresh} , depending on the mean vessel radius r . Table from [360], reprinted with permission by M. Meuschke.



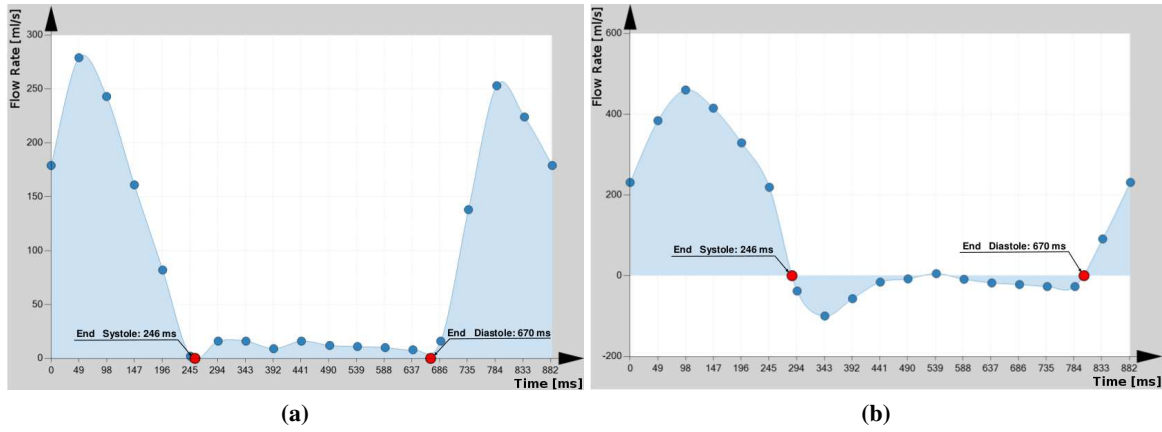


Figure 90: Systole and diastole are distinguished for the temporal occurrence of vortices. Both are separated by the **red points**. They are automatically determined, but can be corrected by the user if necessary.
 (a) Healthy volunteer with out back flow (negative flow rates).
 (b) Patient with slightly increased regurgitation fraction.
 Images from [360], reprinted with permission by M. Meuschke.

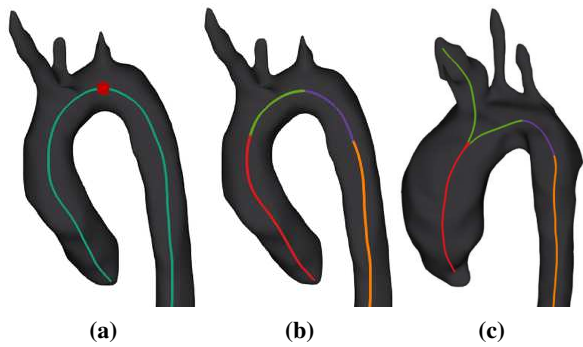


Figure 91: (a) Automatic **cusp point** (red) detection. (b–c) Definition of the **ascending aorta** (red), **ascending aortic arch** (green), **descending aortic arch** (purple) and **descending aorta** (orange).
 Images from [360], reprinted with permission by M. Meuschke.

TEMPORAL OCCURRENCE: We decided to keep the classification from medical works, so that a vortex can occur during systole, diastole, or both. This requires the definition of two temporal positions: The end of the systole, which is also the begin of the diastole, and the end of the diastole, which corresponds to the beginning of the systole (see Figure 90). A flow rate curve (recall Section 6.1.1), obtained in the ascending aorta, is used for this purpose. The required measuring plane was placed manually once for each dataset.

If there are no negative flow rates, the first local minimum is used as systolic end point (see Figure 90a). Otherwise, the first zero crossing is used (see Figure 90b). Analogously, the last local minimum or last zero crossing marks the diastolic end point. Automatic suggestions are made, but the user is allowed to perform a manual correction with a simple drag and drop interaction.

VESSEL SECTION: To automatically define vessel sections in the aorta, we rely on that there is usually a centerline cusp in the aortic arch (see Figure 91a). In the internal coordinate system, the cusp is simply the centerline point with the minimum y-coordinate. Then, the centerline length L between the first and the cusp point is determined. It is assumed that the centerline starts at the approximate aortic valve location. One third of L is used to separate the ascending aorta from the aortic arch ($cusp - L/3$) and the aortic arch from the descending aorta ($cusp + L/3$). For this work, the aortic arch was separated into ascending and descending aortic arch (see Figures 91b–c).

Again, manual corrections are possible via dragging and dropping the suggested cusp point along the centerline. From discussions with domain experts, we derived that a path line is considered as *in* a specific vessel section when at least 30 % of its points lie in the vessel section.

VORTEX SIZE: Medical publications define minor and major vortex flow for vortices that occupy less and more than 50 % of the vessel, respectively. They do not take into account that the size can vary along the course of the vortex.

Vortex core lines can be challenging to compute in 4D PC-MRI data due to low SNR in the image data and other artifacts. Therefore, we calculate a 3D curve $C(u)$ per vortex as approximation of its centerline. This is done via least-squares spline approximation (ALGLIB) of all corresponding path line points of the (clustered) vortex. This yields a piecewise polynomial curve of degree k with l sections. Based on our experiments, $l = k = 4$ was determined as a suitable parameter set. Higher values incorporated outliers too much and lower values did not properly capture the vortex courses. $C(u)$ has three dimensions:

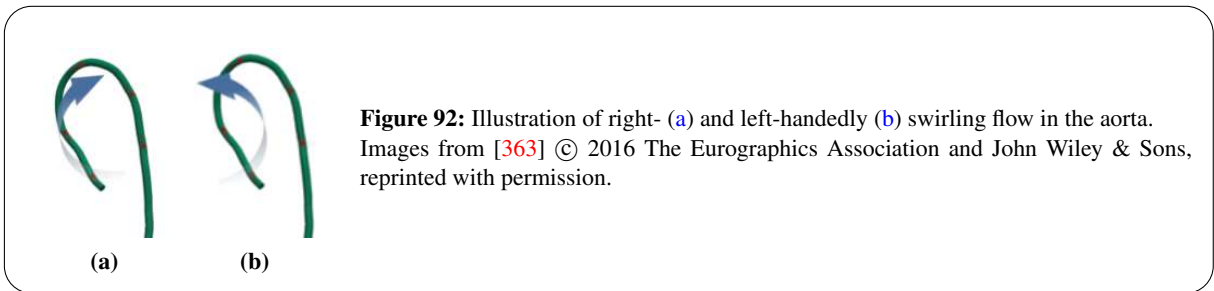
$$C(u) = \begin{pmatrix} f_1(u) \\ f_2(u) \\ f_3(u) \end{pmatrix} \quad (43)$$

A 1D spline is calculated for each component $f_{\{1,2,3\}}$, which first requires an ordering of all path line points. For this, the (normalized) eigenvector \vec{e} , corresponding to the largest eigenvalue from the PCA shape analysis, is used. Every path line point \vec{p}_i is projected onto \vec{e} , yielding a scalar:

$$d_i = \vec{p}_i \cdot \vec{e} \quad (44)$$

All d_i are sorted ascendingly afterwards. The index i serves as x-component in the spline fitting and the actual point coordinates of \vec{p}_i , belonging to d_i , are used as y-component. The resulting spline is then sampled in equidistant steps, yielding points c_i with 2 mm distances.

A local coordinate system (LoCoSys) is generated for each c_i where the z-axis corresponds to the centerline tangent. The orientation of subsequent LoCoSys is consistent (see Section 9.1.2.3). The x- and y-axis span a plane in the cross-section. For each path line point, the closest projection onto one of these planes is determined and stored. Then, for each plane with the projected points, a 95 % confidence ellipse is calculated. Thus, 5 % are declared as outliers. This is based on the assumption that the points are normal distributed. The ratio of the ellipse area and the area of the cross-section yields the percentage that is occupied by the vortex in this cross-section. The cross-sectional area is estimated as circle with the vessel radius that was derived from the centerline extraction based on maximum inscribed spheres [10, 410]. To resemble the physicians' global minor / major classification, the average over all analyzed cross-sections can be calculated.



ROTATION DIRECTION: We distinguish right-handed (clockwise) and left-handed (counterclockwise) vortex movements (see Figure 92). Each spatial path line segment (the temporal component is ignored) with its points \vec{p}_k and \vec{p}_{k+1} is projected onto the closest cross-sectional plane belonging to c_i (see previous paragraph). This yields the projected points q_k and q_{k+1} in xy-coordinates of the LoCoSys. The atan2 of the projected points provides an angle α_k and α_{k+1} for each that allows to determine in which quadrant the points are in. We consider three quadrant configurations and propose different solutions (see Algorithm 3 and Figure 93):

1. Both points are on the top or bottom half. Here, a simple comparison of α_k and α_{k+1} allows to determine the rotation direction.
2. Both points are on the right or left half. Here, the order of the first and second points' quadrants are compared.
3. The points are in diagonal quadrants. Here, it is first determined, which point is in the right and left half. Then, the intersection of the y-axis and a line connecting q_k and q_{k+1} is determined and evaluated.

A path line is classified as right- or left-handedly swirling, depending on the majority of rotation directions of the single segments. In the same manner, a vortex is classified as right- or left-handed according to the majority of path line rotation directions. Additionally, this allows to derive percentages of present rotation directions, which can be used instead of the binary classification.

```

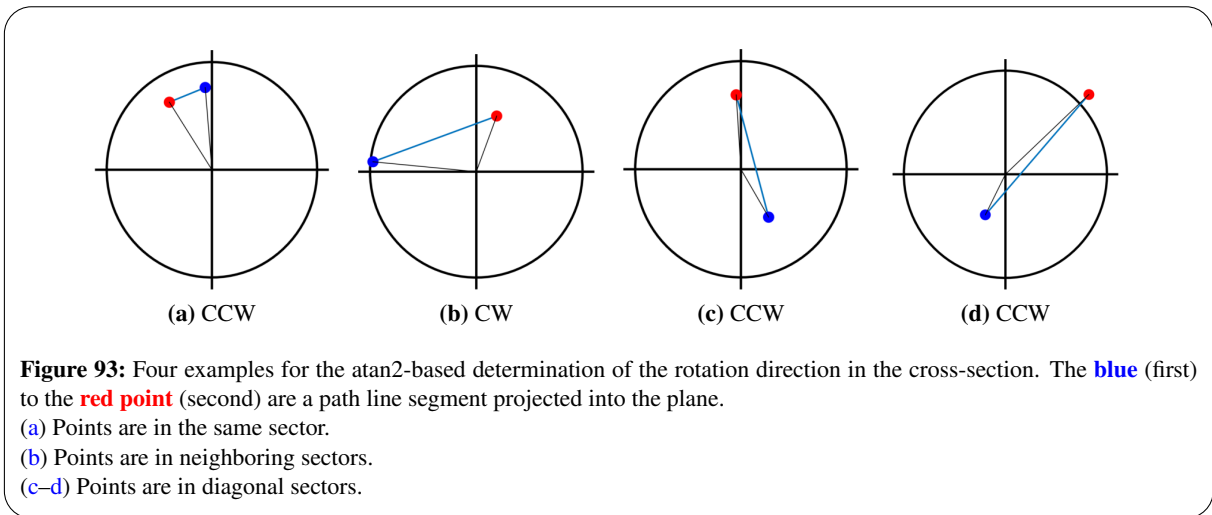
 $q_k \leftarrow 2D \text{ projection of } \vec{p}_k$ 
 $q_{k+1} \leftarrow 2D \text{ projection of } \vec{p}_{k+1}$ 
 $\alpha_k \leftarrow \text{atan2}(q_k.y, q_k.x)$ 
 $\alpha_{k+1} \leftarrow \text{atan2}(q_{k+1}.y, q_{k+1}.x)$ 

// both on top or bottom half
if ( $\alpha_k > 0 \ \&\& \ \alpha_{k+1} > 0$ ) || ( $\alpha_k < 0 \ \&\& \ \alpha_{k+1} < 0$ ) then
  return ( $\alpha_k < \alpha_{k+1}$ ) ? CCW : CW
else
  //both on left or right half
  if ( $\alpha_k > 0 \ \&\& \ \alpha_k \leq \pi/2 \ \&\& \ \alpha_{k+1} < 0 \ \&\& \ \alpha_{k+1} \geq -\pi/2$ ) then
    return CW // top right to bottom right quadrant
  else if ( $\alpha_{k+1} > 0 \ \&\& \ \alpha_{k+1} \leq \pi/2 \ \&\& \ \alpha_k < 0 \ \&\& \ \alpha_k \geq -\pi/2$ ) then
    return CCW // bottom right to top right quadrant
  else if ( $\alpha_k > \pi/2 \ \&\& \ \alpha_k \leq \pi \ \&\& \ \alpha_{k+1} < -\pi/2 \ \&\& \ \alpha_{k+1} \geq -\pi$ ) then
    return CCW // top left to bottom left quadrant
  else if ( $\alpha_{k+1} > \pi/2 \ \&\& \ \alpha_{k+1} \leq \pi \ \&\& \ \alpha_k < -\pi/2 \ \&\& \ \alpha_k \geq -\pi$ ) then
    return CW // bottom left to top left quadrant
  else
    //diagonal quadrants: evaluate y-axis intersection
     $d \leftarrow q_k - q_{k+1}$ 
     $l \leftarrow -q_{k+1}.x/d.x$ 
     $s \leftarrow q_{k+1}.y + l \cdot d.y$ 

    if ( $(\alpha_k > 0 \ \&\& \ \alpha_k \leq \pi/2) \ || \ (\alpha_k \leq 0 \ \&\& \ \alpha_k > -\pi/2)$ ) then
      return ( $s > 0$ ) ? CCW : CW //  $q_k$  on right half
    else
      return ( $s > 0$ ) ? CW : CCW //  $q_k$  on left half
    end if
  end if
end if

```

Algorithm 3: RotDir_CrossSection(): Determination of the turning direction of a line segment in a cross-section.



8.4.2.3. VISUALIZATION

We provide a simultaneous 2D and 3D visualization to interpret the results.

2D VISUALIZATION: For the 2D visualization, the previously proposed polar overview plot for aortic vortex flow (recall Section 8.2) is adapted. The plot angle still represents the temporal component and the distance from the plot center maps the centerline course. Positions close to the center correspond to the approximate aortic valve location and positions on the outside represent the descending aorta. Instead of continuous distance values, we use four discrete sections for this work, which refer to the four vessel sections:

1. Ascending aorta,
2. ascending aortic arch,
3. descending aortic arch, and
4. descending aorta.

Each plot segment is colored according to the portions of vortex clusters that lie in the corresponding vessel section. We demand that at least 30 % of the path line points of a cluster lie in the vessel section. Otherwise, the corresponding plot segment is not colored. The threshold was derived from discussions with domain experts.

3D VISUALIZATION: The 3D visualization is intended to convey the vortex size and turning direction. First, a vortex hull is determined. For this purpose, the confidence ellipses from the previous section are reused (see Figure 94c). Each ellipse is sampled with a fixed number of points that are then transformed back from the local coordinate system (LoCoSys) into world coordinates. Since all LoCoSys have a consistent orientation and the ellipse sampling always starts at the same angle, correspondence of the sampled points of neighboring contours can easily be derived via the points' indices. This is used to establish a triangulation (see Figure 94d). The vortex size is mapped to the surface color of the glyph (see Figure 94e). A linear blue-to-red color scale was used to emphasize if more than 50 % of the vessel are occupied. The rotation direction is depicted as quadstrip around the vortex hull, using an approach by Lawonn et al. [307]. Arrows on the quadstrip are depicted in the original cluster color to establish a link to the 2D visualization.

8.4.2.4. CLASSIFICATION RESULTS

We performed a comparison of 15 datasets against a manually generated ground truth. There were 2 healthy volunteers and 13 patients with various diseases, such as a dilated ascending aorta, coarctation, or bicuspidality of the aortic valve. Each patient has at least one non-physiological vortex somewhere in the aorta.

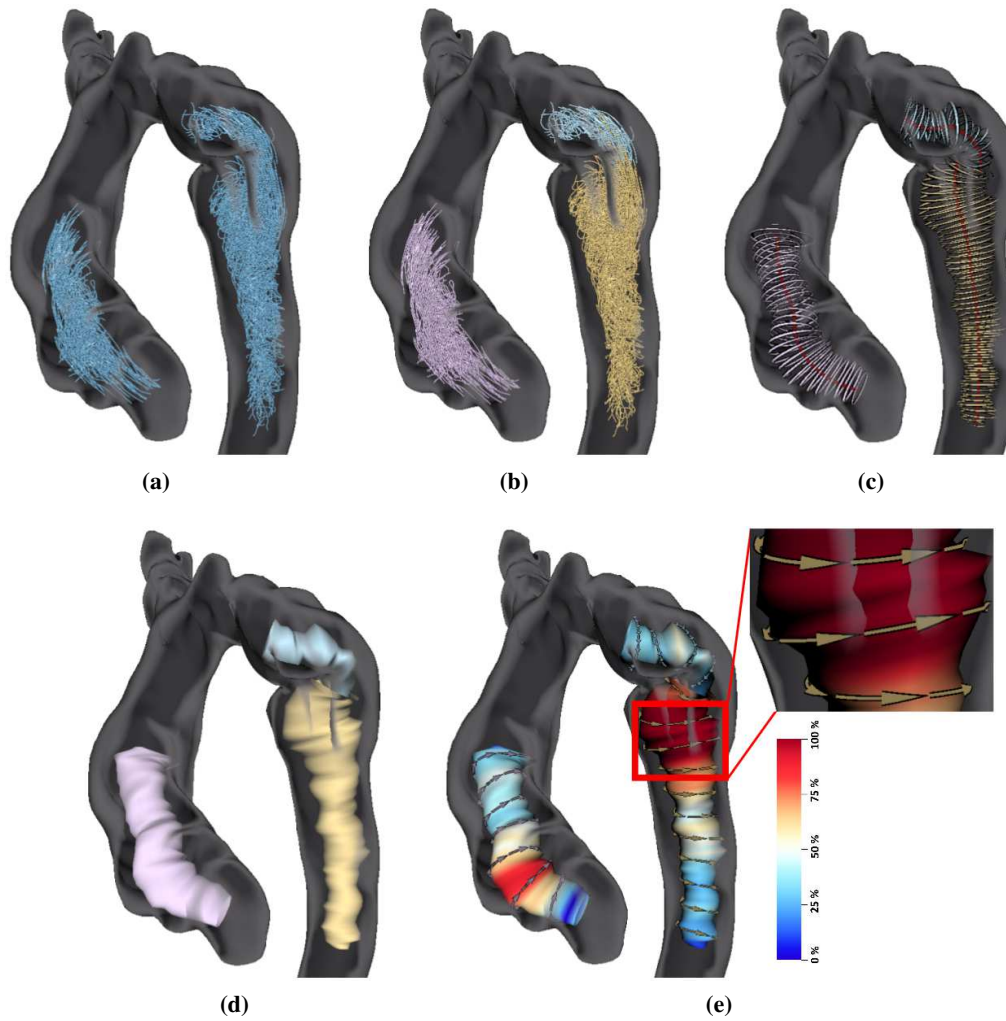


Figure 94: 3D glyph visualization of clustered vortex flow.

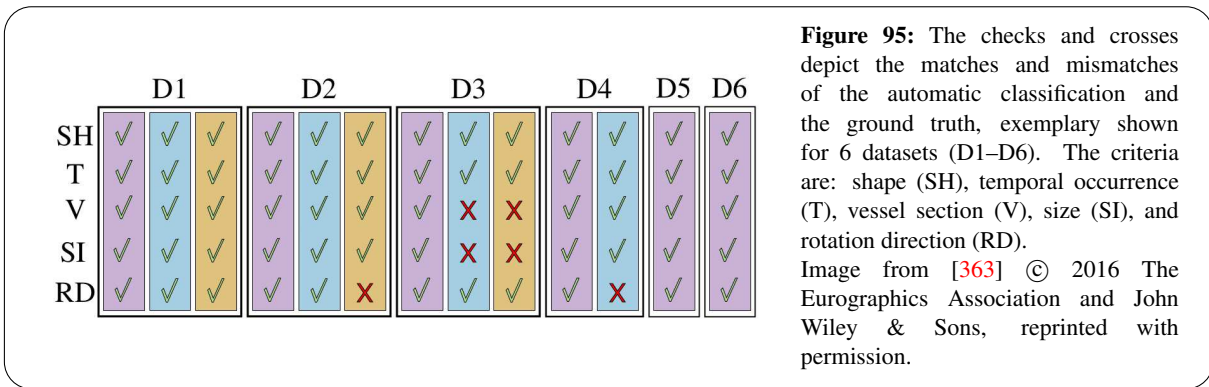
- (a) Extracted, vortex-representing path lines.
- (b) Path lines grouped into three clusters.
- (c) Vortex course and extent approximation.
- (d) Triangulated vortex surfaces.
- (e) Vortex size mapped to the color of the surfaces. A band of arrows in the original cluster color depicts the rotation direction.

Images from [363] © 2016 The Eurographics Association and John Wiley & Sons, reprinted with permission.

The ground truth comprises clustering and classification. It was generated manually in collaboration with Uta Preim – one of the coauthors of this work. A standard flow animation with pathlets as well as static visualization of the extracted vortices were used for this purpose. Especially the vortex size was difficult to assess, so that the overall process took 3 h

The maximum number of vortices in one patient was four. Ten different colors were used to depict the results of the agglomerative hierarchical clustering (recall Section 8.4.1). The six extra colors show laminar flow or noise. Overall, there were 30 vortices in all datasets.

The test computer was an Intel Core i7 with 2 GHz, 12 Gb RAM, and a GeForce GT540M. The implementation is completely CPU-based. The overall computation time for the clustering and the classification was 12–20 s per case, depending on the number of extracted path lines. Figures 95 and 96 exemplary show the results for six cases.



Manual classification	Helical flow [%]	Vortical flow [%]
Vortex (5×)	max. 38 %	min. 62 %
Helix (4×)	min. 64.6 %	max. 35.4 %
Intermediate shape (rest)	min. 41.8 %	min. 54.6 %

Table 4: Manual vs. automatic vortex shape classification.
Table from [363] © 2016 The Eurographics Association and John Wiley & Sons, reprinted with permission.

VORTEX SHAPE: All vortex shapes were correctly classified as helix or vortex. Table 4 shows the manual vortex classification and the percentaged amount of helical and vortical path lines that was determined by our approach.

TEMPORAL OCCURRENCE: The systolic and diastolic end points were determined correctly for all datasets. This facilitated the subsequent, accurate classification of each vortex. Systolic vortices were, on average, present during systole by 90.7 % and during diastole by 9.3 %. Vortices that occurred in both cardiac phases were by 68 % systolic flow and by 32 % diastolic flow.

VESSEL SECTION: Five out of ten cases had to be corrected manually by the user. Patients with vessel morphologies that differ strongly from healthy volunteers can be problematic, e.g., if a bypass surgery was performed. The subsequent determination of the vessel sections of each vortex cluster coincided with the ground truth.

VORTEX SIZE: Minor vortex flow was manually classified in eight cases. Here, our approach determined sizes of 16.8–37.1 %, which matches well. Six cases could not be classified manually with certainty. The automatic classification provided sizes slightly below 50 % for three cases (46.9–48.3 %) and sizes slightly above 50 % for the other three cases (50.9–53.6 %). The rest was classified as major vortex flow both manually and automatically.

One vortex (D2 brown) with 37.1 % was overestimated by our method. Here, the assumption that the projected points in the cross-section are normally distributed did not hold. The overestimated size may cause the glyph surface to protrude out of the vessel. In two cases (D2 brown, D3 blue and brown), the employed 95 % confidence ellipses in the cross-section excluded too many path line points from the calculation. The extracted path lines in this dataset had fewer outliers than in other datasets.

ROTATION DIRECTION: The rotation direction was determined correctly 28 times. Two vortices are neither left- nor right-handed. Instead, their core is aligned perpendicularly to the vessel’s centerline. We call this *roll over rotation*. This is not considered in our current approach and, thus, cannot be classified correctly.

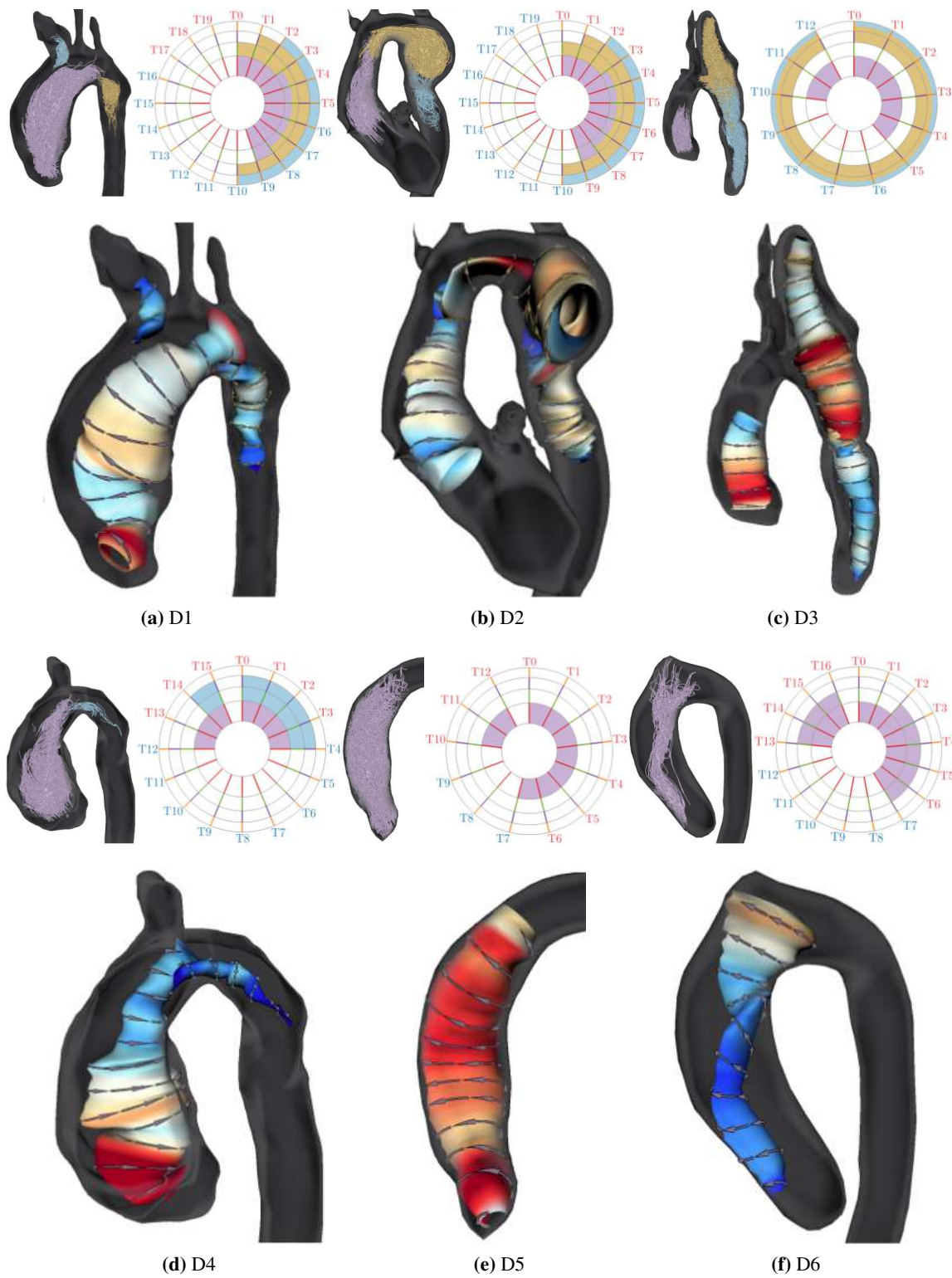


Figure 96: Resulting 2D plot and 3D glyph visualization for six patients (D1–D6, same as in Figure 95) that was derived from the clustered vortex-representing path lines.
 Image from [363] © 2016 The Eurographics Association and John Wiley & Sons, reprinted with permission.

8.4.2.5. USER STUDY RESULTS

A user study was performed with 12 participants (*P*): 1 physician and 11 researchers with background in medical visualization. Our proposed visualization of clustering and classification results was compared

to a static visualization of the path lines (temporal component is ignored) and animations.

SETUP: The participants had to assess:

1. The vessel section (ascending / descending aorta or aortic arch).
2. The temporal occurrence (systole, diastole, or both).
3. The rotation direction (left- or right-handed).
4. The vortex size (fills on average below (minor) or above (major) 50 % of the vessel diameter).

The test setup was as follows. Four datasets were used for each task. Two were visualized with both our proposed methods. The 2D plot was used for Task 1 and 2, the 3D glyph for Task 3 and 4. The other two datasets were depicted with the standard path line visualization.

The participants were divided into two groups: *A* and *B*. Both groups assessed the same datasets. *A* always started with the standard visualization, whereas *B* started with our methods. Thus, each vortex was evaluated with both the standard and our method. The goal of changing the techniques was to reduce learning effects.

The results were compared to the ground truth, and verbal comments from the participants were noted. During evaluation, a questionnaire with two questions was answered with a five-point Likert scale (–, –, 0, +, ++):

1. How difficult was it to solve the task based on the particular visualization method? (In the following tables referred to as *Simplicity*)
2. How certain are you with your assessment? (In the following tables referred to as *Certainty*)

For the interpretation of the Likert scale we provide two values in the following:

1. *m* is the most frequently given answer.
2. *P* is the number of participants that answered with + or ++.

TASK 1 – VESSEL SECTIONS: Each four vortices (V1–V4) had to be assessed with the 2D plot and the standard path line visualization by every participant. V1 lies in one vessel section and was correctly assessed by all participants with both techniques. V2–V4 occupy multiple sections. All 36 classifications (12 participants × 3 vortices) of V2–V4 were done correctly using the 2D plot. Additional vessel sections were determined in 8 cases with the standard visualization. The other 28 were assessed correctly. Estimating the percentages of vortices in vessel sections was described as difficult using the standard visualization, which leads to uncertainties. Table 5 shows the answered questionnaire.

	Simplicity		Certainty	
	<i>m</i>	<i>P</i>	<i>m</i>	<i>P</i>
2D plot	++	12/12	++	12/12
Path line visualization	+	10/12	++	11/12

Table 5: Questionnaire results regarding the assessment of the vessel sections.

Table from [363] © 2016 The Eurographics Association and John Wiley & Sons, reprinted with permission.

TASK 2 – TEMPORAL ASSESSMENT: The classification of the cardiac phase, systole and / or diastole, was done for three vortices (V1–V3) per technique. V1 is systolic; V2 and V3 occur during both systole and diastole. All vortices were classified correctly with the 2D plot. With the standard path line visualization, two participants classified V2 as systolic only. Table 6 shows the answered questionnaire.

	Simplicity		Certainty	
	<i>m</i>	<i>P</i>	<i>m</i>	<i>P</i>
2D plot	++	12/12	++	10/12
Path line visualization	+	10/12	+	11/12

Table 6: Questionnaire results regarding the temporal assessment.

Table from [363] © 2016 The Eurographics Association and John Wiley & Sons, reprinted with permission.

TASK 3 – ROTATION DIRECTION: Three vortices (V1–V3) per technique (3D glyph and standard path line visualization) were assessed in Task 3. About 90 % of V1, located in the ascending aorta, have the same rotation direction. This was classified correctly with both techniques. V2 has a rotation direction distribution of about 70 % : 30 %, which is challenging. V3 lies in the descending aorta. With the standard visualization, V2 and V3 were classified correctly 11 of 18 times. Both were assessed correctly with the 3D glyph. In contrast to the standard visualization, it abstracts the flow, making the analysis less dependent on the local flow complexity. This is reflected in a higher simplicity and certainty in the questionnaire (see Table 7).

	Simplicity		Certainty	
	<i>m</i>	<i>P</i>	<i>m</i>	<i>P</i>
3D glyph	++	12/12	++	12/12
Path line visualization	–	1/12	<i>o</i>	4/12

Table 7: Questionnaire results regarding the assessment of the rotation direction.

Table from [363] © 2016 The Eurographics Association and John Wiley & Sons, reprinted with permission.

TASK 4 – VORTEX SIZE: Three vortices (V1–V3) per technique were classified according to their size. V1 was minor (below 40 %) or major (above 60 %). This was correctly assessed with the 3D glyph and 3× wrong with the standard path line visualization. V2 and V3 were both rather minor or rather major (50 ± 10 %). One participant wrongly classified a rather major vortex, whereas 18 classifications were wrong using the standard visualization. The problems with the standard visualization coincide well with the answered questionnaire (see Table 8). Using the standard visualization, a high degree of interaction (scene rotation) was necessary to assess the sizes. This was not required with the color-coded glyph.

	Simplicity		Certainty	
	<i>m</i>	<i>P</i>	<i>m</i>	<i>P</i>
3D glyph	+	10/12	<i>o</i>	6/12
Path line visualization	–	1/12	–	0/12

Table 8: Questionnaire results regarding the assessment of the vortex size.

Table from [363] © 2016 The Eurographics Association and John Wiley & Sons, reprinted with permission.

8.4.2.6. DISCUSSION AND CONCLUSION

We presented an approach for the semi-automatic classification of extracted, vortex flow-representing path lines. A previously described clustering method was used to group single vortex entities (recall Section 8.4.1). The considered vortex criteria are in accordance with recent medical publications. These are: The vortex size, shape, rotation direction, and its spatial (vessel section) as well as temporal occurrence. Manual classification has a high inter-observer variability. Among others, this is due to a lack of clear and objective definitions of the criteria.

Our approach facilitates a reproducible classification. The analysis is based on the path lines' geometries as well as their relation to the vessel surface. User corrections can be performed prior to the analysis if necessary. This allows experts to incorporate their specialized knowledge. Since the approach is independent from the underlying 4D PC-MRI data, it is also applicable to other contexts, such as measured or simulated flow in cerebral aneurysms.

The results are presented with a 2D plot that was adapted from a previous work (recall Section 8.2). The plot conveys the temporal occurrence and the occupied vessel sections of the clustered vortices without occlusion. A 3D glyph was designed to present the vortex hull, size in the cross-sections, and the turning direction. The performed user study shows the benefit of our method compared to standard path line visualization and animation.

FUTURE IMPROVEMENTS: Eigenvalue analysis of a path line course is error-prone due to the curved vessel shape. For example, a laminar path line that follows the aortic arch is bent instead of straight. The problem could be alleviated if vessel straightening [8] is used prior to the analysis. However, this

increases the algorithm complexity. The size of a vortex is actually a time-dependent measure. A thin vortex with a centerline that is rotating over time like a rope would be classified as major, since it appears as if the whole vessel is occupied in the static visualization. This should be considered in the glyph design and calculation. The current glyph does not directly allow to distinguish between helical and vortical shapes. The forward movement of a vortex could be incorporated in the calculation of the band that shows the rotation direction. Another interesting property, which might be considered in a future work, is the proximity of a vortex to the vessel wall. The assumption of the vessel cusp detection was not always met. A more general approach could perform a PCA of the centerline, find the largest eigenvalue as well as eigenvector, and find the cusp in this local coordinate system. Right now, only vortex flow in the aorta can be assessed. An adaption for, e.g., the pulmonary artery, requires mainly an adaption of the vessel section determination.

9. ENHANCED FLOW RATE QUANTIFICATION

The genesis and evolution of cardiovascular diseases (CVDs) depends on various factors. Recent works have shown that atypical flow patterns, such as vortices, can be found in many pathologies of the cardiovascular system [159, 221]. Yet, when it comes to assessing the severity, quantitative measures are essential. However, quantitative analyses need to be reliable, reproducible, and sufficiently accurate.

It was pointed out that the assessment of flow rates suffers from various inaccuracies in the acquired 4D PC-MRI data (recall Section 6.1.1). Thus, two contributions are presented in this chapter. In Section 9.1 a method is presented that puts emphasis on robustness and physiological plausibility. Net flow volumes (NFVs) are determined automatically, the quantification uncertainty is emphasized, and the development of the NFV along the vessel is reconstructed. Section 9.2 describes an approach to automatically obtain 4D segmentations of the dynamic vessels, which is typically not done due to the high expenditure of time. The segmentations are used to establish a dynamic vessel surface that is visualized on the one hand and incorporated into the quantification of stroke volumes (SVs) on the other hand.

9.1. ROBUST CARDIAC FUNCTION ASSESSMENT

THIS SECTION IS BASED ON:

- [278]: B. KÖHLER, U. PREIM, M. GROTHOFF, M. GUTBERLET, K. FISCHBACH, AND B. PREIM. “ROBUST CARDIAC FUNCTION ASSESSMENT IN 4D PC-MRI DATA OF THE AORTA AND PULMONARY ARTERY”. IN: *Computer Graphics Forum* 35.1 (2016), PP. 32–43. DOI: [10.1111/CGF.12669](https://doi.org/10.1111/CGF.12669)

SEE SECTION PUBLICATIONS IN THE APPENDIX FOR THE DIVISION OF WORK.

Two of the most important quantitative measures to assess the cardiac function are the *stroke volume* (SV) and *regurgitation fraction* (RF). The first describes the volume of pumped blood per heart beat and is the *net flow volume* (NFV) above the aortic or pulmonary valve. The second characterizes the *percentaged backward flow volume* (PBFV) into the corresponding ventricle during diastole. Both quantifications require the *flow rate* in forward and backward direction through a plane that is usually aligned orthogonally to the vessel’s centerline (recall Section 6.1.1). Unfortunately, the calculations are highly dependent on the plane’s configuration. Unlike 2D PC-MRI, where unsatisfying results make a whole new acquisition necessary, 4D PC-MRI datasets contain the patient’s full four-dimensional flow information. This allows to evaluate multiple planes with different positions and angulations *after* the scan.

In this work, various healthy volunteer and patient datasets were analyzed in close collaboration with radiologists and cardiologists. We carefully observed their manual approach to estimate SVs and RFs while anticipating the high sensitivity towards the plane angulation. From this, we derived an automatic procedure which systematically analyzes multiple angulations for one position on the vessel’s centerline. The obtained statistical information facilitate the robust quantification of the measures and the visualization of uncertainties.

The collaborating experts expect the SV, i.e., the highest NFV, directly above the aortic or pulmonary valve. From there, a continuous decrease along the vessel course is assumed due to smaller vessels that branch off and supply blood to certain body regions. However, noise and a low spatio-temporal data resolution often lead to physiologically implausible results, i.e., the NFV development is not monotonous. We employed these two expectations as heuristics to establish a procedure that fits a function which guarantees the desired behavior. In addition, we adapted this method for the use in branching vessels, such as the pulmonary artery.

9.1.1. REQUIREMENT ANALYSIS

All necessary interactions should fit to the clinicians' mental model and utilize their in-depth understanding of anatomical shapes including occurring variations, e.g., due to pathologies. Therefore, we have to avoid parameter settings that do not correlate to such medical knowledge and provide reasonable default values for numerical input whenever possible.

The automatic evaluation of different plane angulations should need only a small number of angulation samples in order to limit the computational effort. Thus, an adequate sample distribution is required. The obtained information about the NFV deviation shall be utilized to provide insight into uncertainties.

A proper function has to be determined that represents the expected continuous NFV decrease along the vessel course after a peak value (the SV) above the valve. To ensure that the NFV is properly preserved in case of branching vessels, a comparison and, if necessary, correction of the NFV before and after the junction is required.

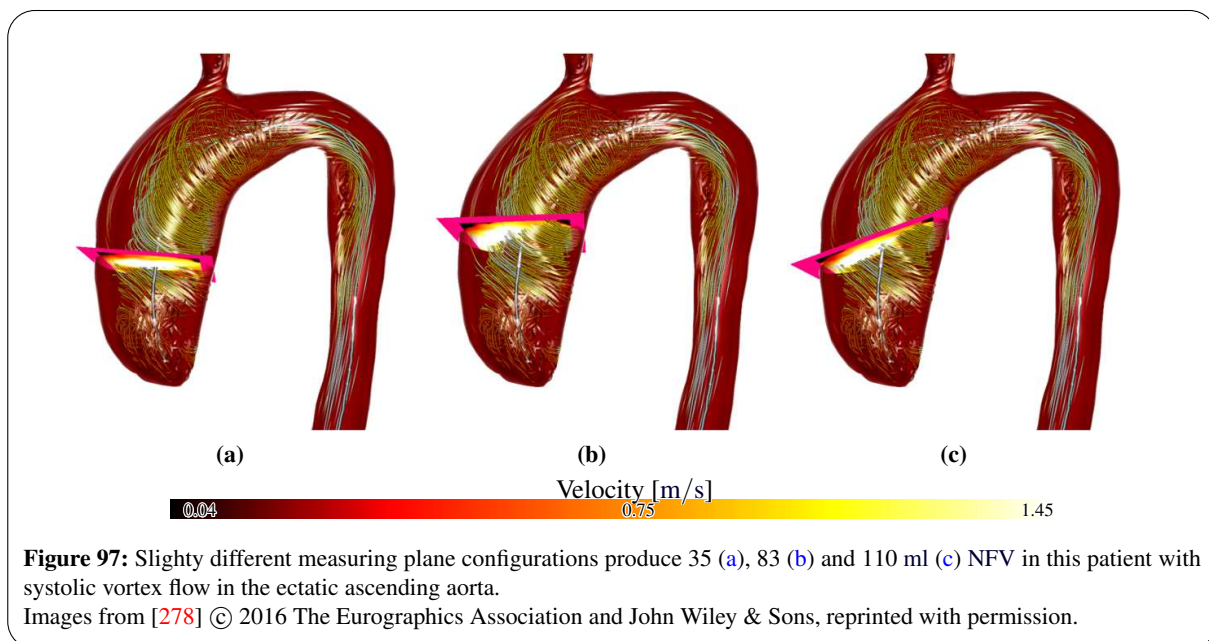
To exploit the high computational power of the GPU, algorithm parallelization as well as an appropriate data structure for the measuring planes are required.

9.1.2. METHOD

In the following, we describe the NFV as well as PBFV evaluation with increased robustness for one measuring plane at a specific position on the centerline. Afterwards, we employ this procedure to determine a physiologically plausible NFV development along the vessel course and derive the SV as well as the RF. The last part is about necessary adjustments to facilitate usage in branching vessels.

9.1.2.1. OBSERVATIONS

Figure 97 shows the typical situation in a patient dataset with pathologic vortex flow where three slightly different measuring planes produce SVs of 35, 83 and 110 ml. Carefully observing our collaborating cardiologists and radiologists in such unsatisfying situations gave insight into their usual approach. They evaluate multiple measuring planes with slightly different positions as well as angulations and estimate a plausible SV based on their experience. We assume that this value is the mean or median of the samples. We also observed that the problem of uncertain quantification is reduced in healthy volunteer datasets.



9.1.2.2. EVALUATION OF A SINGLE POSITION ON THE CENTERLINE

In this section, we present the robust NFV quantification method which is an automation of the observed manual approach. We start with a detailed description of the employed measuring plane model and provide basic information about the NFV calculation. Then, we proceed with the systematic angulation sample generation, summarize our GPU-supported evaluation procedure, and apply this principle to the PBFV quantification.

PLANE MODEL: Hoogeveen et al. [219] focused on small arteries. They made the simplifying model assumptions that a vessel is cylindrical, straight, and has a parabolic velocity profile. However, the aorta and pulmonary artery are the largest arteries in the body, curved, and the parabolic velocity profile can be disturbed in case of vortex flow. Therefore, their approach might not be suitable for the cardiac context.

We model a measuring plane as grid with the following components:

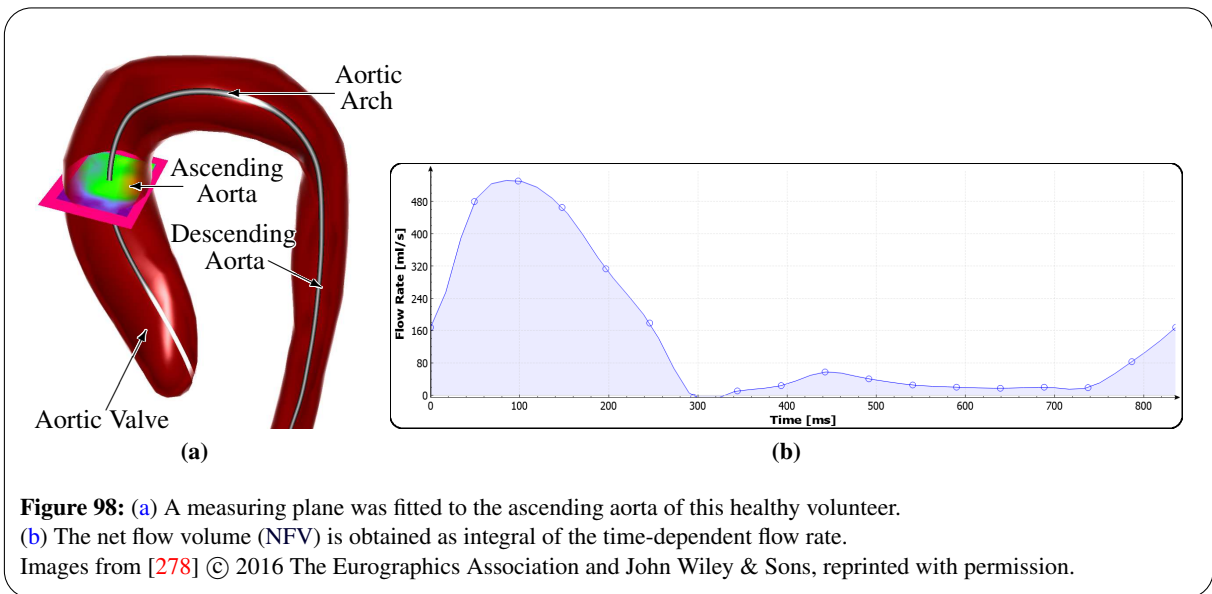
- $\vec{g} = (g_x, g_y)^T$, $g_{\{x,y\}} \in \mathbb{N}$ is a parameter that describes the number of rectangles in x- and y-dimension,
- $\vec{s} = (s_x, s_y)^T$, $s_{\{x,y\}} \in \mathbb{R}$ is the size per rectangle,
- $\vec{c} \in \mathbb{R}^3$ is a center position close to or on the vessel's centerline,
- $\vec{n} \in \mathbb{R}^3$ is the plane's normal vector, i.e., angulation, that is commonly set to the corresponding normalized centerline tangent, and
- \vec{n}_x and $\vec{n}_y \in \mathbb{R}^3$ form a local orthonormal system with \vec{n} . \vec{n}_x is determined via cross product of \vec{n} with the x-axis $(1, 0, 0)^T$. If $\|\vec{n}_x\| = 0$, the cross product is performed with the y-axis. If the length of \vec{n}_x is still 0, the z-axis is used. \vec{n}_y is obtained as $\vec{n}_x \times \vec{n}$.

These information are sufficient to calculate world coordinates $\vec{w} \in \mathbb{R}^3$ for every grid position (x, y) :

$$\vec{w} = \vec{c} + \left(s_x \cdot \vec{n}_x \cdot \left(x - \frac{g_x}{2} \right) \right) + \left(s_y \cdot \vec{n}_y \cdot \left(y - \frac{g_y}{2} \right) \right) \quad (45)$$

The low memory requirements are advantageous for GPU computation.

FITTING A PLANE TO THE VESSEL: The size per rectangle $\vec{s} \in \mathbb{R}^2$ has to be determined by fitting the plane P to the vessel. For this purpose, the plane's intersection curve with the triangular vessel mesh is determined. Then, the maximum extents in \vec{n}_x and \vec{n}_y dimension are analyzed and \vec{s} is set accordingly so that P is the minimum axis-aligned bounding rectangle (AABR) of the vessel cross-section. \vec{c} is set to the AABR's center. Figure 98a shows an example of a plane fitted to the ascending aorta.



BASIC NET FLOW VOLUME QUANTIFICATION: The time-dependent flow rate $fr(t)$, $t \in [0, T-1]$, where T is the number of temporal positions in the dataset, is required to calculate the NFV for the plane P :

$$fr(t) = s_x \cdot s_y \cdot \vec{n} \cdot \sum_{x=0}^{g_x-1} \sum_{y=0}^{g_y-1} S_3(P(x,y)) \cdot \mathbf{V}(P(x,y), t)$$

$$\text{with } S_3(P(x,y)) = \begin{cases} 1, & (P(x,y)) \text{ inside vessel} \\ 0, & \text{else} \end{cases} \quad (46)$$

$P(x,y)$ is the grid position (x,y) transformed to world coordinates \vec{w} (see Equation 45). $\mathbf{V}(P(x,y), t)$ are velocity vectors \vec{v} in the flow field \mathbf{V} , which is given by the phase images. The product $s_x \cdot s_y$ is the area per rectangular grid element. Since a 4D PC-MRI dataset contains one full heart beat, $fr(t)$ is periodic. The integral of $fr(t)$ provides the NFV, depicted in Figure 98b. A [periodic spline fitting \(ALGLIB\)](#) is utilized in the implementation. The vessel segmentation is employed to realize $S_3(P(x,y))$. This allows to exploit hardware-accelerated 3D texture lookups on the GPU.

PLANE ANGULATION SAMPLE GENERATION: The automatic evaluation of different plane angulation samples \vec{a} , i.e., normal vectors, requires their systematic generation. All possible angulations form a half sphere, where the plane's original normal vector \vec{n} points to the top. The maximum angle between \vec{n} and \vec{a} is $\alpha = \pi/2 \hat{=} 90^\circ$. Lower α values restrict the angulation to a smaller sphere section. Thus, α describes an angulation tolerance.

The inverse cumulative distribution function (CDF) method allows to generate uniformly distributed samples on a sphere within $[\theta_1, \theta_2]$ and $[\phi_1, \phi_2]$, where θ and ϕ are longitude and latitude, respectively:

$$\theta = \arccos\left(\cos(\theta_1) + u \cdot (\cos(\theta_2) - \cos(\theta_1))\right)$$

$$\phi = \phi_1 + v \cdot (\phi_2 - \phi_1) \quad (47)$$

u and $v \in [0, 1]$ are uniformly distributed random numbers. For $\vec{n} = (0, 0, 1)^T$, the sphere section is described by $\phi_1 = 0$, $\phi_2 = 2\pi$, $\theta_1 = 0$, and $\theta_2 = \alpha \in [0, \pi/2]$. The samples are transformed from spherical coordinates $(1, \theta, \phi)$ to Cartesian coordinates (x, y, z) and used to obtain the angulation sample $\vec{a} = x \cdot \vec{n}_x + y \cdot \vec{n}_y + z \cdot \vec{n}$, where \vec{n}_x and \vec{n}_y are part of the plane's local orthonormal system (LoCoSys).

We generate Poisson-distributed angulations [254] to ensure that the whole sphere section is covered with a small number of samples, which limits computational effort. The parameter d_{\min} describes the minimum distance of two angulations on the unit sphere surface. A new distribution is calculated for each plane evaluation to avoid bias. Figure 99 depicts the angulation samples.

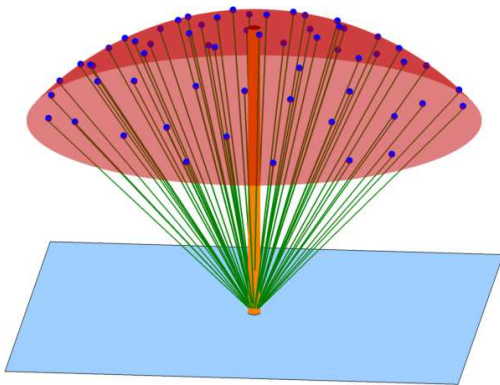


Figure 99: Poisson-distributed **angulation samples (green)** were generated on a $\alpha = \pi/4 \hat{=} 45^\circ$ **sphere section (red)** around the **plane's (blue) normal vector (orange)**.

Image from [278] © 2016 The Eurographics Association and John Wiley & Sons, reprinted with permission.

```

P ← measuring plane
A ← angulation samples

```

```

for i ← 0 to size(A)−1 do
  /*normal*/ P.n̄ ← Ai
  P.n̄x, P.n̄y ← orthonormal system construction
  /*scale*/ P.s̄ ← fit P to vessel mesh
  GPU buffer ← add parameters of current P
end for

```

```

F ← FlowRates_GPU() // one thread per angulation
NFV ← net flow volumes

```

```

for i ← 0 to size(A)−1 do
  f ← time-resolved flow rates Fi for Ai
  S ← periodic spline fitted to f
  NFVi ← integral of S (Fig. 98b)
end for

return NFV

```

Algorithm 4: Robust_NFV()

```

P ← current measuring plane configuration
V ← flow field
T ← number of temporal positions
fr ← flow rate vector of size T

```

```

for x ← 0 to /*grid size x*/ P.gx−1 do
  for y ← 0 to /*grid size y*/ P.gy−1 do
    w̄ ← (x, y) to world coordinates
    if w̄ in binary vessel segmentation then
      for t ← 0 to T−1 do
        ū ← V(w̄, t)
        frt ← frt + ū · P.n̄
      end for
    end if
  end for
end for

```

```

for t ← 0 to T−1 do
  frt ← frt · (P.sx · P.sy) // area per rectangle in grid
end for

```

```

return fr

```

Algorithm 5: FlowRates_GPU()

ROBUST NET FLOW VOLUME QUANTIFICATION: The NFV determination for one plane is summarized in Algorithms 4 and 5. The evaluation of all angulations provides a range of NFVs with an unknown distribution and possible outliers. Thus, the median of these samples is used as robust result.

ROBUST PERCENTAGED BACKWARD FLOW VOLUME QUANTIFICATION: The NFV determination is directly applicable for the PBFV quantification. This requires the forward (FFV) and backward flow volume (BFV). They are calculated as integral of the positive and negative part of the flow rate $fr(t)$, i.e., they are the curve's area above and below 0, respectively. For this purpose, the integral in the ROBUST_NFV procedure (see Algorithm 4) is adapted accordingly. Analogous to the NFV, the FFV/BFV distributions' median values are used as result. The PBFV for one position on the centerline is then obtained as $BFV / (FFV + BFV)$.

9.1.2.3. EVALUATION OF A JUNCTION-FREE CENTERLINE

In the following, we explain how to obtain the SV as well as RF, and a process to fit a physiologically plausible function to the NFV development along the vessel course. The resulting function represents our collaborators' expectations.

DENOISING PLANE SIZES: The fitting of planes to the vessel's cross-section might produce degenerated sizes if the segmentation contains perpendicularly branching vessels. The scales $s̄$ per rectangular grid element will be too large which negatively affects the NFV quantification. Therefore, we perform a smoothing of scales along the centerline as a pre-processing step. For this purpose, a consistent alignment of the planes' local coordinate systems (LoCoSys) is required. Unfortunately, if the LoCoSys of each plane is constructed independently using cross products with the x-, y- and z-axis (recall Section 9.1.2.2), there will be a twist, as shown in Figure 100a. Therefore, only the first plane's LCS $\vec{n}^0, \vec{n}_x^0, \vec{n}_y^0$ is determined this way. Consistent orientation of $\vec{n}^i, \vec{n}_x^i, \vec{n}_y^i, i > 0$ with its predecessor

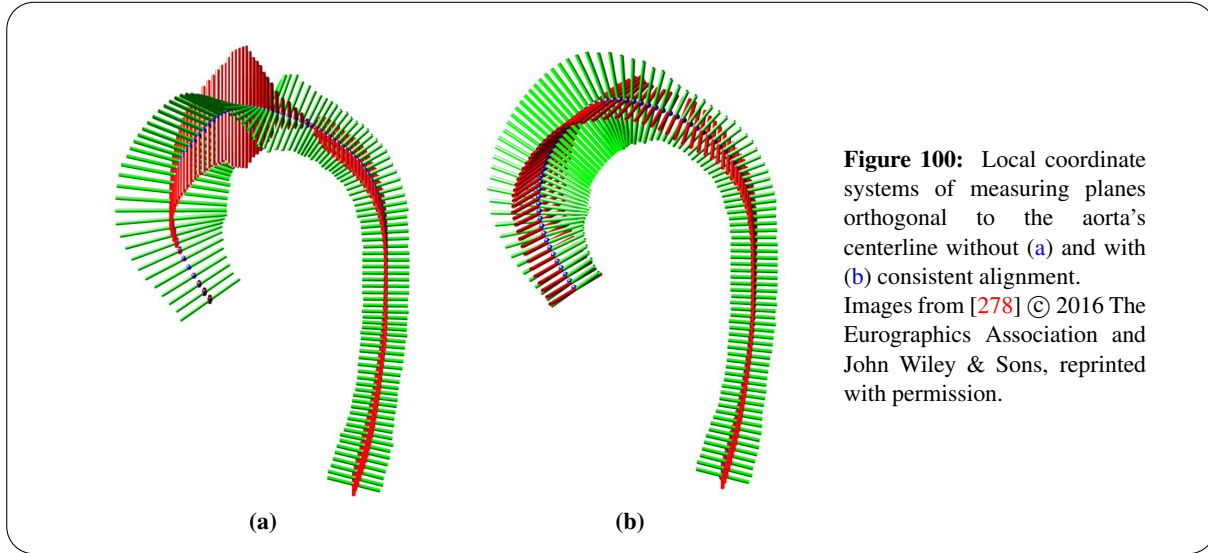
$\vec{n}^{i-1}, \vec{n}_x^{i-1}, \vec{n}_y^{i-1}$ is achieved by employing the angle θ and rotation axis $\vec{r}^i = (r_x^i, r_y^i, r_z^i)^T$ between \vec{n}^i and \vec{n}^{i-1} :

$$\theta = \arccos(\vec{n}^i \cdot \vec{n}^{i-1}), \quad \vec{r}^i = \vec{n}^i \times \vec{n}^{i-1} \quad (48)$$

If $\|\vec{r}^i\| = 0$, i.e., the normal vectors point in the same direction, then $\vec{n}_x^i = \vec{n}_x^{i-1}$ and $\vec{n}_y^i = \vec{n}_y^{i-1}$. Otherwise, $\vec{n}_x^i = R \cdot \vec{n}_x^{i-1}$ and $\vec{n}_y^i = R \cdot \vec{n}_y^{i-1}$, where R is the general rotation matrix around \vec{r}^i :

$$R = \cos \theta \cdot I + \sin \theta \cdot \begin{bmatrix} 0 & -r_z^i & r_y^i \\ r_z^i & 0 & -r_x^i \\ -r_y^i & r_x^i & 0 \end{bmatrix} + (1 - \cos \theta) \cdot (\vec{r}^i \cdot \vec{r}^{i T}) \quad (49)$$

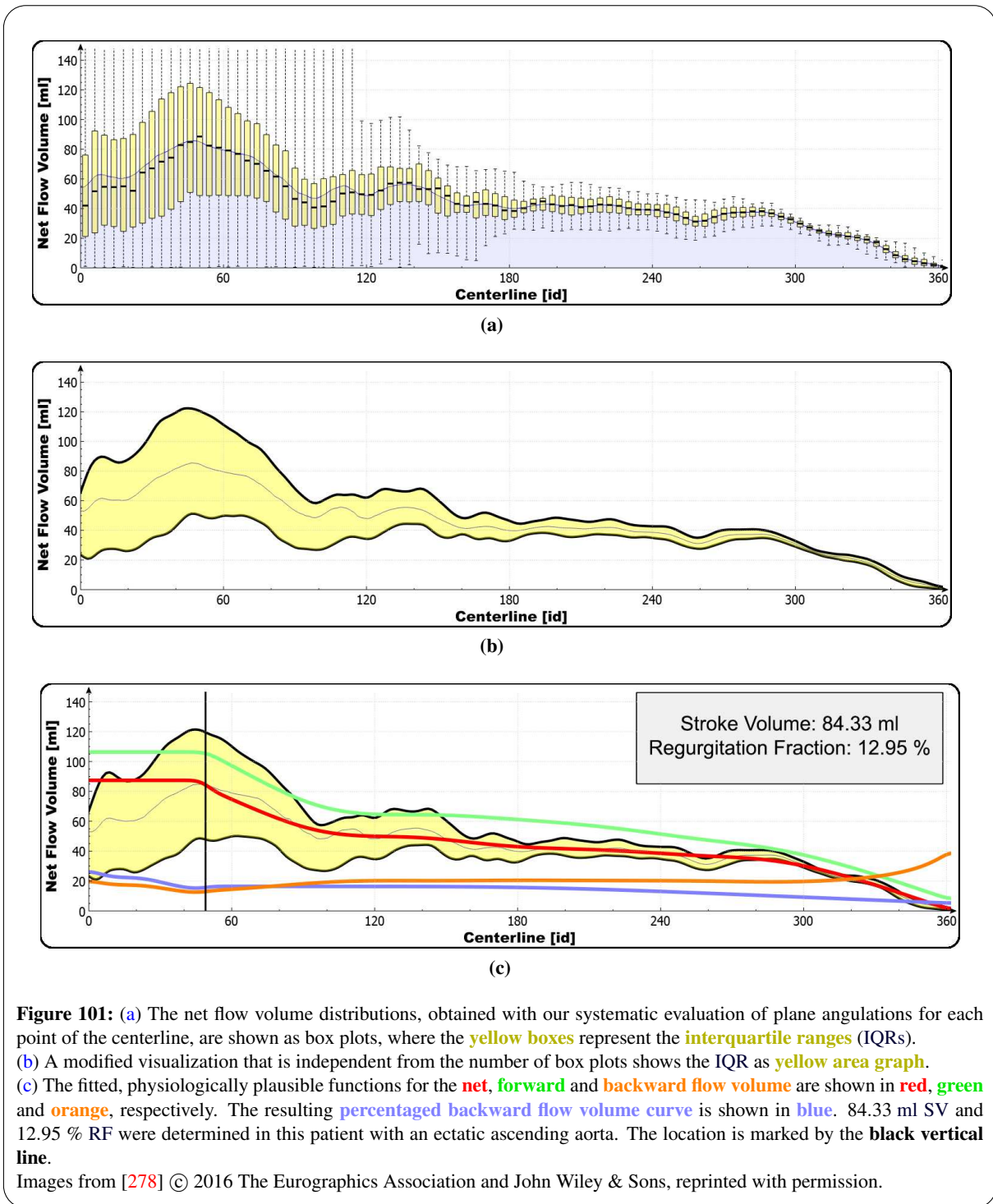
I is the 3×3 identity matrix. Figure 100b shows \vec{n}_x and \vec{n}_y of the aligned LoCoSys after resampling from a cubic spline (ALGLIB), where the parameter $\rho \in [-15, 15]$ controls a non-linearity penalization. $\rho = 2$ is used as default value which, according to the library developers, corresponds to a moderate amount of non-linearity.



STROKE VOLUME DETERMINATION: The robust NFV determination (see Algorithm 4) is performed for each of the equidistant centerline points. The x-axis in Figure 101 describes the centerline points in flow direction so that the left part of the plot corresponds to the approximate valve location. The yellow boxes in Figure 101a show the interquartile ranges (IQRs), which are the middle 50% of the sorted NFV samples. Large ranges indicate high sensitivity to the angulation and thus uncertainty in the corresponding vessel section. The thin blue curve interpolates the median NFVs. The SV is obtained as maximum value of this curve. In the following, by NFV and NFV deviations we refer to the median and the IQR of the NFV samples at one centerline position, respectively.

We observed that the IQRs are the most interesting part of the box plots, since outliers, especially behind the valve, may reach unrealistic values, such as 10 or 200 ml, and thus barely provide further insight. Therefore, we modified the visualization by changing the box plots to a continuous area and removing the whiskers for the minimum and maximum. In addition, this visualization is independent from the centerline length, since no number of box plots needs to be specified. Figures 101a–b show a comparison.

The user has the option to limit the evaluation to a part of the centerline in between two specified planes. This can be useful, e.g., if the segmentation contains parts of the ventricles that shall be excluded from the calculation. Additionally, if only the SV and RF are of interest, a restriction to the ascending aorta or pulmonary trunk considerably reduces the computational effort.



PLAUSIBLE NET FLOW VOLUME DEVELOPMENT: Our collaborating cardiologists and radiologists expect a continuous decrease of the NfV after the SV. This is due to smaller vessels that branch off the main vessel and supply blood to certain regions of the body. Yet, even our robust quantification is often not able to produce this behavior. Instead, physiologically implausible local minima and maxima occur. Therefore, we describe a method to enforce this behavior by fitting a monotonous function to the partial NfV function (thin blue curve in Figure 101) right of the SV. In our implementation, this non-trivial task is realized with an iterative **cubic, non-linearity penalizing spline fitting (ALGLIB)**. High and low penalization parameters ρ lead to linear least squares approximation and interpolation, respectively. Our procedure is initialized with $\rho = -5$. After the spline is fitted, its monotonicity is

determined by evaluating the signs of all first derivatives. If it is not monotonous, ρ is slightly increased by 0.1, otherwise the loop stops.

All NFVs between the valve and SV location cannot be lower than the SV and thus are set to the SV as a correction. Unfortunately, C^0 continuity of the fitted monotonous function right and corrected function left of the SV is not guaranteed. As a remedy, both functions are concatenated and smoothed in 15 iterations using a one-dimensional binomial filter with kernel size 5. This is solely performed to increase the visual quality of the diagrams. Therefore, no further parameter analysis is necessary at this point. Figure 101c shows the resulting function in red.

The NFV only decreases due to branching vessels and is constant in vessel sections between two junctions. Following this, the question may arise why no step function is employed as model. This approach would require the locations of all branches and, more critical, a guarantee that all branches are present in the segmentation. The latter is problematic because of limited data resolution and low contrast in smaller vessels due to typically lower flow velocities.

REGURGITATION FRACTION DETERMINATION: The RF is obtained as PBFV at the SV location. If desired, monotonous functions for the FFV, BFV, and PBFV can be fitted in the same manner as for the NFV. An example is depicted in Figure 101c. The tasks are independent from one another and thus can be performed in parallel threads on the CPU.

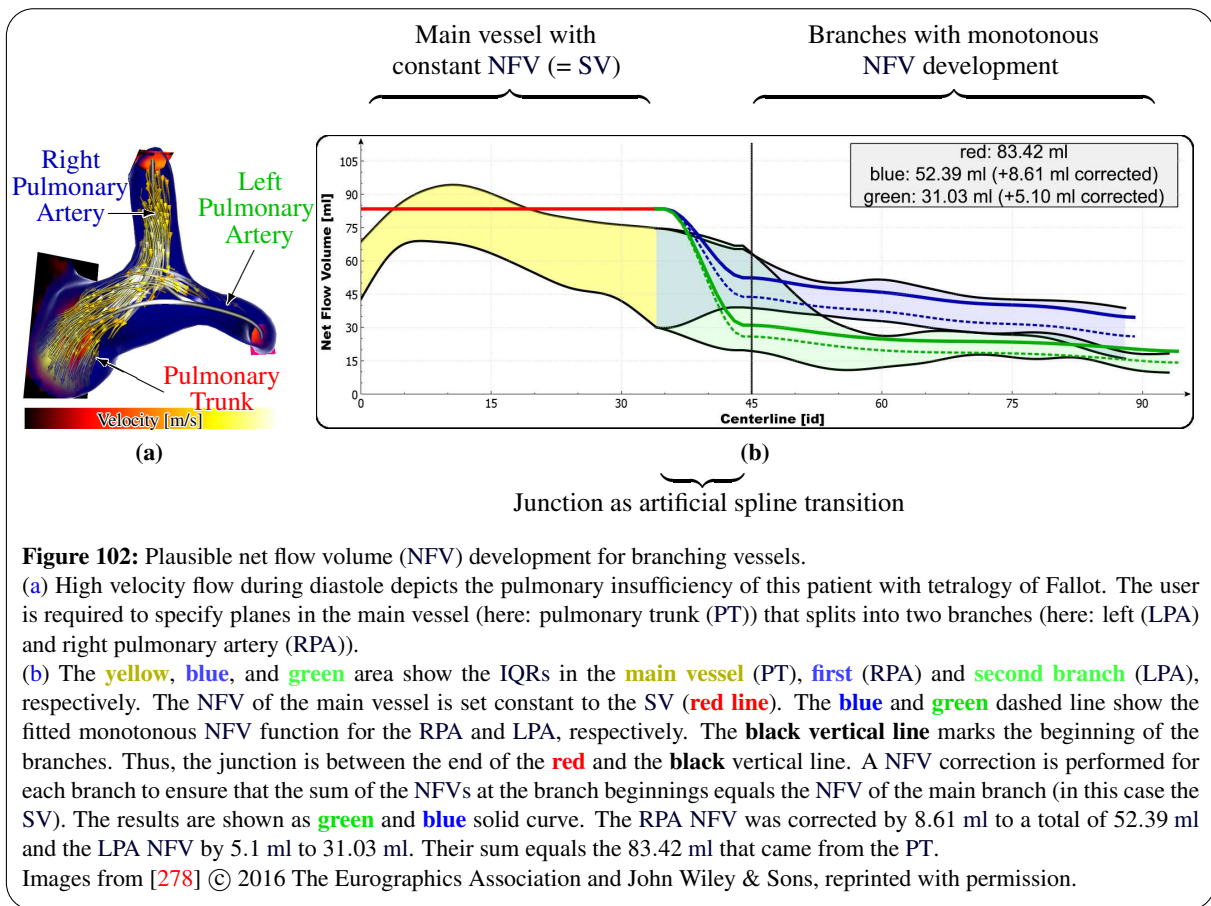
9.1.2.4. EVALUATION OF BIFURCATIONS

In the following, the extension of our method for branching vessels, such as the pulmonary artery (PA), is described. The user is required to specify three planes as an initialization. The first one is located at the beginning of the main vessel V_{main} , the second and third are located at the end of the branches B_0 and B_1 . Figure 102a shows an example where V_{main} is the pulmonary trunk that splits into the left and right PA which is B_0 and B_1 , respectively. A new branching centerline is calculated that starts at the closest point on the vessel surface to the center of the first plane and ends at the corresponding points from the second and third plane. Afterwards, the centerline is split into V_{main} , B_0 , B_1 , and the junction using a branch splitting [9] provided by VMTK. Our method for junction-free centerlines is then applied to each part separately (recall Section 9.1.2.3). However, monotonous NFV functions are only fitted for B_0 and B_1 . We assume that they are the only branching vessels from V_{main} . In case of the PA this is a fact. Therefore, we set the NFV in V_{main} constant to the SV. Artificial transitions that connect the constant NFV / SV from V_{main} with the monotonous NFV curves of B_0 and B_1 in the plot are created using cubic Hermite splines (ALGLIB). They represent the junction. The same is performed for the upper and lower boundaries of the IQR area visualizations.

Based on physiologic considerations, we may assume that the sum of the NFVs at the beginning of the branches (NFV(B_0) and NFV(B_1)) equals the NFV (SV in case of the PA) from V_{main} (NFV(V_{main})). Despite using our proposed quantification with increased robustness, this is not always the case. Thus, a correction step is performed:

$$\begin{aligned} \text{NFV}_{\text{diff}} &= \text{NFV}(V_{\text{main}}) - (\text{NFV}(B_0) + \text{NFV}(B_1)) \\ \text{NFV}(B_0) + &= \frac{\text{NFV}_{\text{diff}} \cdot \text{NFV}(B_0)}{\text{NFV}(B_0) + \text{NFV}(B_1)} \\ \text{NFV}(B_1) + &= \frac{\text{NFV}_{\text{diff}} \cdot \text{NFV}(B_1)}{\text{NFV}(B_0) + \text{NFV}(B_1)} \end{aligned} \quad (50)$$

The plot includes both the fitted monotonous NFV functions before and after correction. Additionally, the IQR, which can be considered as uncertainty, of B_0 and B_1 is increased by the values of the corresponding NFV corrections. The upper IQR boundary is increased in case of a positive correction, otherwise the lower IQR boundary is decreased. However, the ratio of NFV(B_0) and NFV(B_1) before and after correction is the same. Figure 102b shows an example.



9.1.3. RESULTS

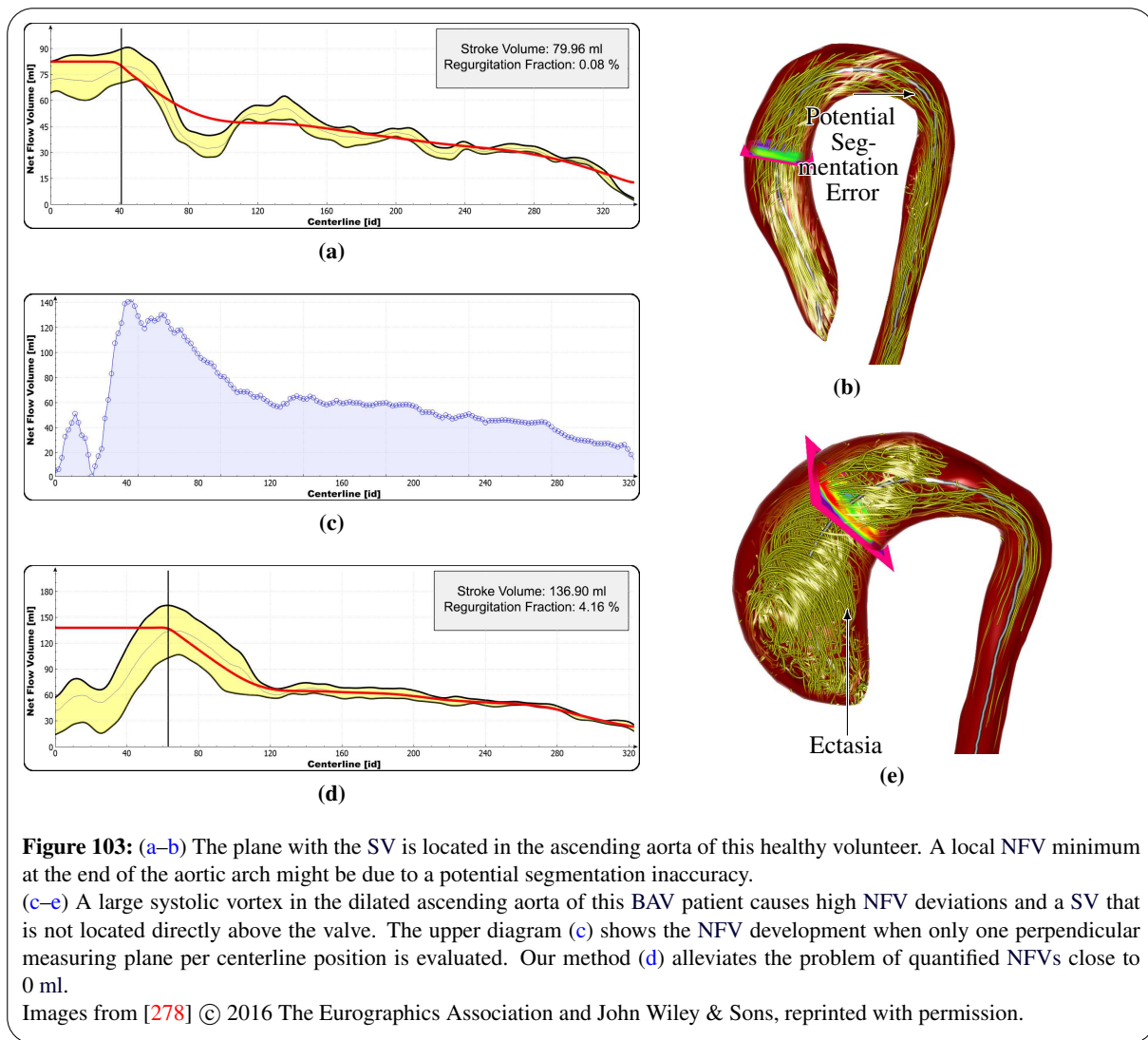
This section contains an informal evaluation based on selected datasets and a subsequent discussion that includes a justification of employed default parameters.

9.1.3.1. INFORMAL EVALUATION

We present six selected, anonymized datasets that were discussed with each two collaborating radiologists and cardiologists. The evaluation was performed informally, i.e., no specific tasks had to be solved. The robust NFV quantification for the whole centerline, SV and RF determination as well as monotonous function fitting took about 30 s on average per dataset on a GeForce GTX 680 and Intel i7-3930K. All images were directly captured from our software (recall Chapter 7) which is used by our clinical collaborators for research purposes.

HEALTHY VOLUNTEER: The first dataset shows a healthy volunteer. Figure 103a illustrates the result of our procedure. The highest NFV deviations and thus sensitivity to different plane angulations were detected in the ascending aorta and at the beginning of the aortic arch. Two likely reasons can be identified from the discussion with the experts. On the one hand, there is a physiological helix during systole. Regions with laminar flow seem to be less susceptible. On the other hand, different angulations of planes close to the valve have, from the outset, higher potential to cause deviations since the highest flow rates are present in this vessel section.

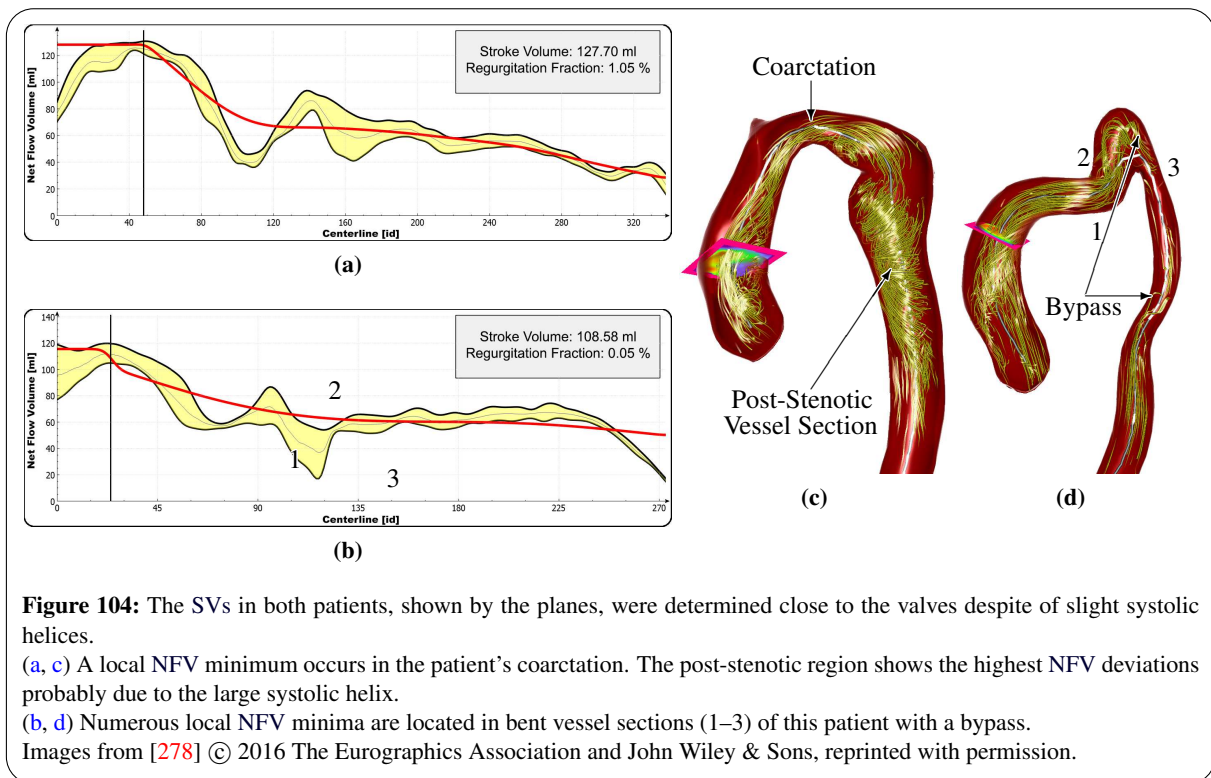
The NFVs show a physiologically implausible local minimum at about one third of the centerline, where the aortic arch ends. A possible explanation is a small segmentation error. The vessel diameter in and after the aortic arch is 1.5 cm but decreases to 1.24 cm at the transition. Figure 103b shows the systolic flow and a measuring plane close to the valve, where our method determined 79.96 ml SV. A RF of 0.08 % indicates a properly functioning aortic valve.



BAV PATIENT WITH DILATED ASCENDING AORTA: This patient has a bicuspid aortic valve (BAV). The upper diagram in Figure 103c shows the NFVs along the vessel course when one orthogonally aligned measuring plane per centerline position is evaluated. A nearly vanishing value at the beginning is conspicuous. Qualitative flow analysis reveals prominent systolic vortex flow in the abnormally widened ascending aorta. This is likely the cause for the enormous deviations in this vessel section. Our robust NFV procedure alleviates the problem, as shown in the lower diagram of Figure 103d. Figure 103e shows the systolic vortex flow and the location of the plane where 136.9 ml SV were determined. Contrary to the employed heuristic, this is not located directly above the valve but rather at the end of the vortex. The conventionally quantified RF ranges from 3–47%. The experts did agree on an increased amount of retrograde flow, but struggled to specify a concrete value. Our method determined 4.16% RF, which lies within the physiological range.

Figure 101 shows a similar patient with vortex flow in the ectatic ascending aorta. The same high sensitivity to different plane angulations was observed. Figure 105 shows the patient's healthy pulmonary artery. The determined SVs of 80.05 ml and 84.33 ml in the pulmonary artery and aorta, respectively, are physiologically plausible since both values are approximately equal.

COARCTATION PATIENT: The next patient has an aortic coarctation. Qualitative flow analysis shows three systolic vortices: A slight helix above the aortic valve, a small vortex before the narrowing, and one large helix in the post-stenotic vessel section, illustrated in Figure 104c. Figure 104a shows the NFV deviations along the centerline. There is a local NFV minimum in the coarctation at about one



third of the centerline, which again is considered as physiologically implausible. In addition to potential segmentation inaccuracies like in the healthy volunteer, this might be due to the low data resolution. The vessel diameter shrinks about 50 % in the narrowed region. Consequently, it is represented by far less voxels, which enhances partial volume effects.

The highest NFV deviations occur in the post-stenotic vessel section, approximately in the middle of the centerline, directly behind the local maximum. This is where the largest vortex is present. The collaborating experts agree that this is the likely cause for the quantification uncertainties. In contrast to the previous BAV patient, the location of the determined 127.7 ml SV is close to the aortic valve despite of the slight helix.

BYPASS PATIENT: An extraanatomic bypass surgery was performed to treat this patient's former coarctation. The altered vessel shape promotes the formation of systolic vortex flow in the ascending aorta, shown in Figure 104d. The obtained diagram is presented in Figure 104b. The SV is located close to the valve despite of the slight helix, like in the previous patient. Moreover, a number of local NFV minima and maxima is noticeable especially at the beginning of the bypass. The numbers 1–3 help to connect the diagram with centerline positions. A possible explanation is that partial volume effects make it difficult to capture the quickly changing flow directions in curved vessel sections. However, our monotonous function fitting produces a physiologically plausible NFV development along the centerline.

TETRALOGY OF FALLOT PATIENT: A surgical correction was performed in this patient with tetralogy of Fallot. The pulmonary insufficiency progressed to a severe state with nearly 25 % RF. Figure 102a illustrates the diastolic backward flow in the pulmonary artery. Vortex flow is present in the pulmonary trunk and right pulmonary artery during systole as well as diastole. Our robust quantification for bifurcations, shown in Figure 102b, determined 83.42 ml SV that splits into 52.39 ml and 31.03 ml for the right and left pulmonary artery, respectively. This is physiologically plausible since the right half of the lung consists of three lobes, whereas the left half of the lung with two lobes is smaller due to the neighboring heart.

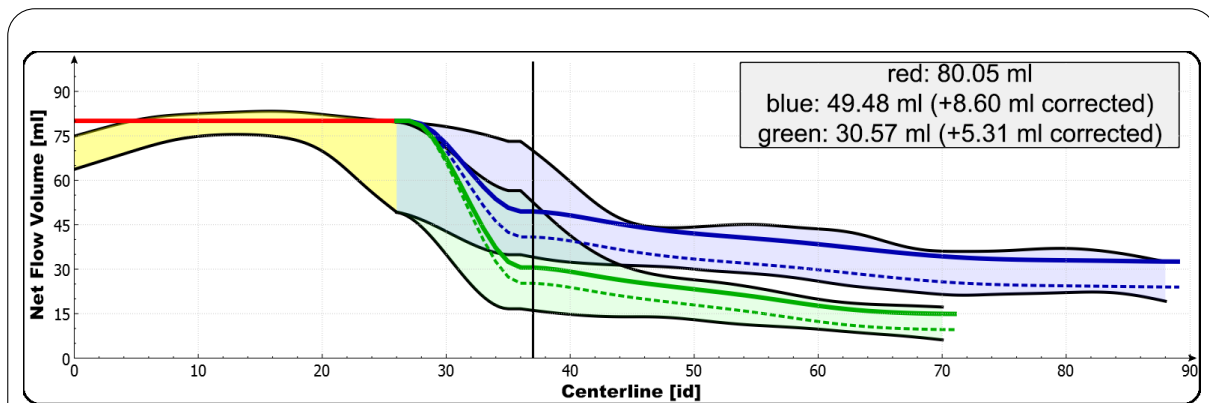


Figure 105: Healthy pulmonary artery of a patient with dilated ascending aorta (see Figure 101). 49.48 ml and 30.57 ml of the 80.05 ml **stroke volume** (red) flow into the **right** (blue) and **left pulmonary artery** (green), respectively. Image from [278] © 2016 The Eurographics Association and John Wiley & Sons, reprinted with permission.

9.1.3.2. DISCUSSION

The user's responsibility is to generate a valid segmentation and centerline. For bifurcations, three planes are required which are located in the origin and the two branches. Reasonable default values for other parameters are investigated at the end of this section.

The sensitivity to different plane angulations was visualized as area graphs that represent the middle 50 % (interquartile range, IQR) of box plots. Especially prominent vortex flow seems to cause high uncertainties since corresponding vessel sections show large IQRs. High variations led to careful result interpretations, whereas small deviations created trust.

Contrary to the assumptions, the SVs were not always determined directly above the valve. This is a serious error potential for the common 2D PC-MRI standard in addition to the plane angulation that is required before the acquisition. Though, the automatically obtained SVs show good correspondence with the expected results estimated by our collaborating experts using conventional methods. The SVs are expected between the aortic or pulmonary valve and the location where the first vessel branches off. In the pulmonary artery this is the junction where it splits into left and right. In the aorta, the small coronary arteries close behind the valve are neglected since they receive only a marginal amount of blood (about 5 %). Thus, the location is shortly after the beginning of the aortic arch, where the brachiocephalic artery is located. If solely the SV or RF is of interest, a priori knowledge can speed up our robust quantification method by restricting the calculations to the corresponding vessel sections. The user can specify two planes as start and end position for this purpose.

We described a method to analyze bifurcations. The algorithmic adaption to three or more branches is simple. Yet, the resulting plot visualization may become cluttered if two or more branches receive approximately the same volume of blood. In this case, the subgraphs, especially the IQR areas, would overlap. Fortunately, this problem is of minor relevance for the pulmonary artery since the right pulmonary artery normally receives more blood due to the larger right half of the lung.

SAMPLE GENERATION PARAMETER EVALUATION: Reasonable default values increase the practical applicability of our method. We experimentally determined an appropriate standard configuration during the development process, which is a grid size of $\vec{g} = 50 \times 50$, an angulation tolerance $\alpha = \pi/4 \hat{=} 45^\circ$, and Poisson-distributed angulation samples with a minimum distance of $d_{\min} = 0.075$ on the unit sphere surface (recall Section 9.1.2.2). The validation of these parameters is shown exemplary for the SV determination in the BAV patient (recall Section 9.1.3.1), which represents our experiences for all datasets.

New angulation samples are generated for each plane evaluation. Thus, every SV analysis is repeated 100 times per parameter set. The defaults produce 136.9 ± 0.87 ml, which is the samples' mean plus minus the standard deviation (σ).

Modifications of α produced 146.48 ± 1.27 ml for 15° , 143.24 ± 1.35 ml for 30° , 136.9 ± 0.87 ml for the default 45° , 136.61 ± 0.87 ml for 60° , 150.64 ± 1.18 ml for 75° , and 163.48 ± 1.1 ml for 90° . The σ were lowest for 45° and 60° and the best agreement with 140 ml SV estimated by the experts was achieved with $\alpha \in [30^\circ, 60^\circ]$. As a consequence, $\alpha = \pi/4 = 45^\circ$, the middle of this range, seems appropriate as default value.

Altered grid sizes produced 130.08 ± 0.53 ml for 5×5 , 136.75 ± 1.52 ml for 25×25 , 136.9 ± 0.87 ml for the default 50×50 , 136.66 ± 0.36 ml for 75×75 , and 135.47 ± 0.92 ml for 100×100 . There were no significant changes above grid sizes of 25×25 . Though, planes that are fitted to large aneurysms, e.g., with 55 mm vessel diameter, have isotropic rectangle sizes of $55/25 = 2.2$ mm in 25×25 grids. To ensure that the rectangles are smaller than our data's finest resolution of 1.77 mm in one dimension, we use 50×50 grids as default.

Altered d_{\min} of the Poisson distribution produce 138.73 ± 2.84 ml for 0.165 (≈ 50 samples), 136.65 ± 1.51 ml for 0.1 (≈ 125 samples), 136.9 ± 0.87 ml for the default 0.075 (≈ 200 samples), and 135.76 ± 0.64 ml for 0.05 (≈ 500 samples). Standard uniform distribution (recall Section 9.1.2.2) yields 140.19 ± 10.81 ml for 50 samples, 137.35 ± 6.38 ml for 125 samples, 137.66 ± 5.32 ml for 200 samples and 135.06 ± 3.18 ml for 500 samples. The σ from Poisson distribution are significantly lower than from uniform distribution. It was below 1 ml for $d_{\min} = 0.075$ and reduced only marginally with more samples. The difference between both distributions decreases with an increasing number of samples. However, Poisson distribution requires fewer samples to achieve sufficient results. The higher costs for angulation generation are not substantial. Summarizing, the sample distribution has the highest influence on the results.

9.1.4. CONCLUSION AND FUTURE WORK

We presented a method to robustly determine net flow (NFV) and stroke volumes (SV) as well as percentaged backward flow volumes (PBFV) and regurgitation fractions (RF) in cardiac 4D PC-MRI data of the aorta and pulmonary artery. The procedure was developed in close collaboration with cardiologists and radiologists and represents an automation of their manual approach. Statistical information and uncertainties were presented as area graphs which were derived from common box plots. The experts' expectations were employed as heuristics to establish a procedure that creates physiologically plausible NFV developments along the vessel course. The GPU's computing power was exploited to achieve average calculation times of 30 s.

In addition to partial volume effects, prominent vortex flow was identified as main cause for uncertainties. This seems plausible for two reasons:

1. 4D flow MRI sequences assume a constant velocity at the time of the measurement. Thus, acquisitions are more and less accurate in laminar and accelerated flows, respectively. The latter can be found, among others, in regions with turbulences.
2. Turbulent flow can cause *flow voids* if the spatial image resolution is limited. This means that the emitted signal, which is measured (recall Section 3.1.1), is averaged to zero.

Against the assumption, the SV could not be obtained directly above the aortic or pulmonary valve in all cases. This is a source of potential errors for the current 2D PC-MRI standard since the default is to use a plane above the valve that is orthogonal to the vessel's centerline. However, an advantage of 2D PC-MRI is that the measured slice lies directly in the cross-section and thus has a comparably high resolution, since distances of data points within a MRI slice are usually lower than distances between slices. In contrast, measuring planes in 4D PC-MRI are often aligned with the slice direction. Isotropic resolution is often not used to keep scan times low.

The robust determination of PBFVs and RFs is of particular importance for the discussion of appropriate treatments. The monotonous function fitting for both junction-free and branching vessels was able to generate physiologically plausible NFV developments. Something that needs to be considered in the future is that two digits after the comma suggest a result precision that is simply not given. This might be misleading and thus should be replaced with rounded values.

Due to reasonable default parameters the only required user input is a vessel segmentation and centerline, which both exploit expert knowledge. Hence, our procedure is eligible to be part of an automatic data evaluation procedure in the future that supports clinical report generation. Branching vessels additionally need a specification of the main vessels as well as the branches by placing planes inside each vessel section.

Until now, SV and RF quantification requires knowledge of highly specialized experts on the cardiovascular system and its hemodynamics. Our method reduces this to mainly anatomical knowledge. However, the newly enabled uncertainty assessment still needs experience. More sophisticated visualizations might support the interpretation in the future.

Another future topic might be to investigate the suitability of curved surfaces for the quantification of flow rates and related measures. For this purpose, the technique by Schulze et al. [461] is a good starting point. They proposed the generation of surfaces that are *as-perpendicular-as-possible* to the flow field. This could be adapted so that cross-sectional planes, which are normally used, become curved cross-sectional surfaces.

9.2. MOTION-AWARE STROKE VOLUME QUANTIFICATION

THIS SECTION IS BASED ON:

- [277]: B. KÖHLER, U. PREIM, M. GROTHOFF, M. GUTBERLET, K. FISCHBACH, AND B. PREIM. “MOTION-AWARE STROKE VOLUME QUANTIFICATION IN 4D PC-MRI DATA OF THE HUMAN AORTA”. IN: *International Journal for Computer Assisted Radiology and Surgery* 11.2 (2016), PP. 169–79. DOI: [10.1007/s11548-015-1256-4](https://doi.org/10.1007/s11548-015-1256-4)

SEE SECTION [PUBLICATIONS](#) IN THE APPENDIX FOR THE DIVISION OF WORK.

Stroke volumes (SVs) help to assess the cardiac function and monitor progression of various CVDs, such as BAV and heart insufficiencies. Static 3D approximations of the dynamic vessel wall are widely used to calculate this measure. There is a trade-off between easier, faster pre-processing and accurate information about the heart’s cyclic movement. Techniques with an enhanced level of automation could overcome this issue by speeding up data processing. However, the accurate definition of intravascular hemodynamics requires the determination of the time-dependent wall position, wall orientation, and vessel diameter. Approaches that neglect these components are error-prone. We investigate the reliability of such methods by extracting motion information of the aorta, incorporating them in the SV quantification and examining deviations.

The segmentation of time-varying cardiac image data was aimed at by several research groups from the image processing community (recall Section 4.2.3). Zhao et al. [578] and Abufadel [1] used level sets and deformable models for this purpose, respectively. GPU-accelerated time-varying direct volume rendering was used to display measured anatomical data [531, 577]. Algorithms such as graph cuts [107, 322, 332] only require the specification of areas inside and outside the target structure, which is convenient for physicians since it exploits their anatomical expert knowledge. Based on heuristics that were derived from discussions with collaborating radiologists, we automatically initialize a 3D graph cut for each temporal position of the dataset and obtain a time-dependent binary mask of the aorta.

A mesh model is described that contains motion information as vectorial displacement list per vertex. Displacement vectors are projections from a static vessel surface approximation onto the meshes of each time step. The latter were extracted from the 4D segmentation. This facilitates post-processing of the movement information. We incorporate the vessel dynamics in a motion-aware stroke volume quantification and investigate the reliability of the conventional quantification using static vessels by examining deviations. Various healthy volunteer and patient datasets were used in the evaluation.

9.2.1. METHOD

In the following, we describe the 4D segmentation of the aorta and the steps to obtain and post-process movement information. After the adjustment of centerlines and measuring planes, the stroke volume

quantification is adapted. We aim at a parameterization that medical doctors can easily adjust based on their expert knowledge. Carefully selected default values are provided for all parameters to ensure feasibility of our method for the clinical routine. Please recall Sections 7.1.1–7.1.2 for the graph cut-based extraction of an initial 3D vessel surface mesh.

9.2.1.1. STROKE VOLUME QUANTIFICATION IN STATIC (3D) VESSELS

The SV calculation in static vessels using a 3D segmentation S_3 is the same as described previously in Section 9.1.2.2. $S_3(P(x,y))$ describes the check whether or not a position is inside the vessel. When applied to each grid element of the measuring plane, it yields a 2D segmentation of the cross-section. The segmentation's resolution is given by the plane's grid size \vec{g} . $S_3(P(x,y))$ can be realized using the voxel-based 3D segmentation, which is rather coarse compared to the resolution of the plane's grid elements. However, it facilitates usage of the GPU, since it can be employed as 3D texture. A smoother result can be obtained by rasterizing the 3D mesh, as depicted in Figure 106. This is what we use for this work.

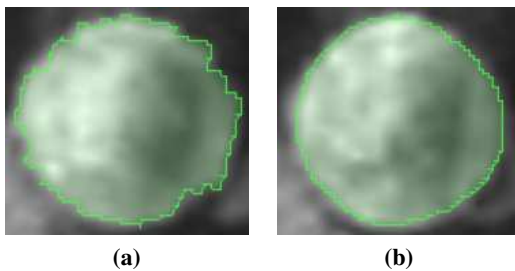


Figure 106: Mask of an aorta's cross-section obtained from rasterization of (a) the 3D vessel segmentation and (b) the extracted corresponding triangular surface. Images from [277] © 2016 Springer-Verlag Berlin Heidelberg, reprinted with permission.

9.2.1.2. FOUR-DIMENSIONAL VESSEL SEGMENTATION

Performing a manual vessel segmentation in every temporal position is too time-consuming for the clinical routine. Therefore, we automatically determine regions inside and outside the aorta for each time step based on the 3D segmentation and employ this to initialize graph cuts. Other segmentation algorithms that require the same kind of input are also suitable. We perform one 3D graph cut for each time step in the 4D anatomical image A .

The 3D segmentation, based on the magnitude images' TMIP, represents blood-filled vessels during systole and therefore the maximum extent – like an upper boundary. Thus, we assume that voxels outside this segmentation are also outside the segmentation of each temporal position. A safety margin is incorporated to consider inaccuracies. We subtract a kernel size 5 from a kernel size 8 dilated segmentation to obtain a dilated vessel hull. This is about 1–2 cm away from the vessel surface for the data's spatial resolution of $1.77 \times 1.77 \times 3.5 \text{ mm}^3$. We observed that a smaller margin does not improve the results of the employed graph cut. Based on discussions with radiologists, a second assumption is made that the vessel diameter does not shrink more than 50 % during diastole. Hence, all voxels are specified as inside the vessel that are closer to the centerline than to the wall. The same initialization is used for all time steps and graph cuts are performed separately for each of them.

Image quality, in particular the signal-to-noise ratio, depends on the acquisition time. In patients with severe heart diseases, acquisitions need to be performed in limited time with a quality that is just sufficient for diagnosis. As a consequence, the graph cut tolerance parameter α (recall Section 7.1.1) is increased by a factor of ten. The resulting segmentations for each temporal position are post-processed in the same manner as described in Section 7.1.1. The same applies to the extraction and post-processing of the polygonal 3D meshes. Figure 107 depicts the process.

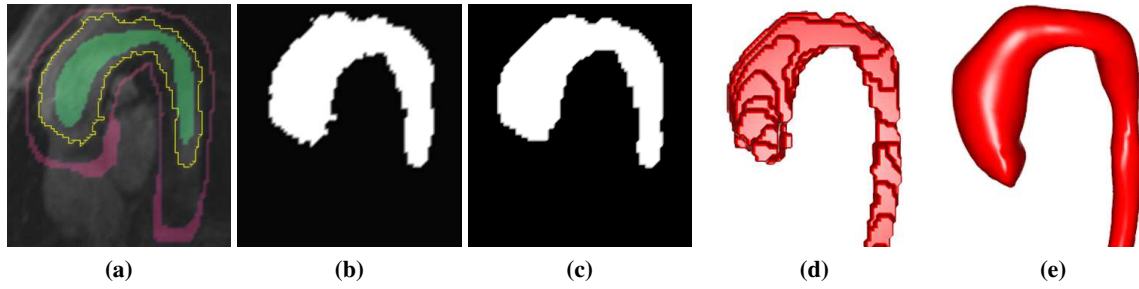


Figure 107: Extraction procedure for each temporal position.

- (a) Automatic specification of regions **inside** (green) and **outside the aorta** (red) as graph cut initialization.
- (b) Resulting 3D segmentation.
- (c) Post-processed segmentation.
- (d) Extracted triangular surface.
- (e) Postprocessed vessel mesh.

Images from [277] © 2016 Springer-Verlag Berlin Heidelberg, reprinted with permission.

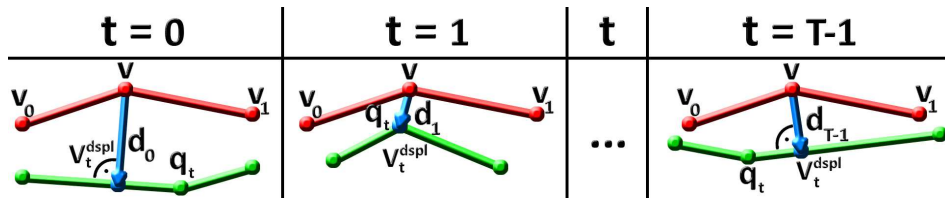
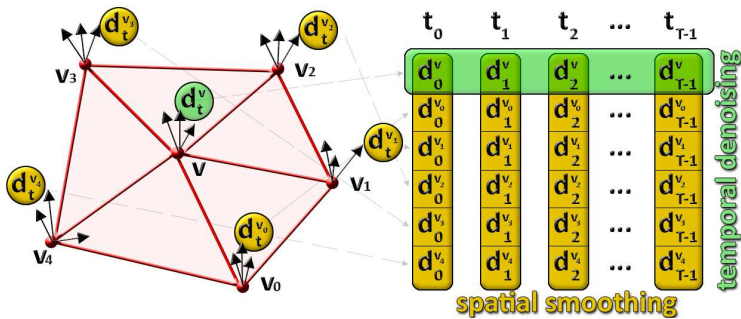


Figure 108: The projection \vec{v}_t^{dspl} of a **base mesh vertex** \vec{v} (red) onto the one-ring neighborhood of the **closest vertex** \vec{q}_t in the mesh M_t (green) of a temporal position t is determined to obtain the **displacement vector** \vec{d}_t (blue) as $\vec{v}_t^{\text{dspl}} - \vec{v}$.

Images from [277] © 2016 Springer-Verlag Berlin Heidelberg, reprinted with permission.

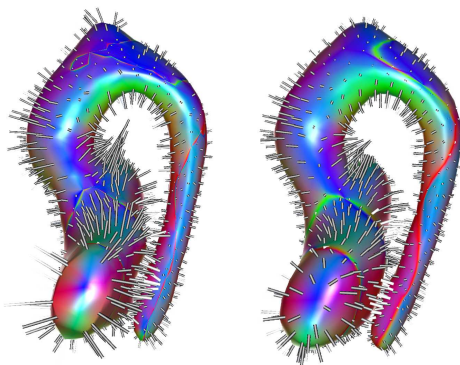


(a)

Figure 109: (a) Displacement post-processing. The **spatial smoothing** (orange) is a low-pass filter applied to the displacements $\{\vec{d}_t^v, \vec{d}_t^{v_i}\}$ of the one-ring neighborhood \vec{v}_i of the mesh vertex \vec{v} in each temporal position $t = 0 \dots T - 1$. The **temporal denoising** (green) smooths the displacement list \vec{d}_t^v of \vec{v} .

(b) Displacement vectors (white lines) of one temporal position without (left) and with (right) noise reduction. The surface is colored according to the displacements.

Images from [277] © 2016 Springer-Verlag Berlin Heidelberg, reprinted with permission.



(b)

9.2.1.3. DYNAMIC (4D) VESSELS

DISPLACEMENT VECTORS: We aim at extracting motion information that can be post-processed in order to reduce noise. Until now, we obtained independent 3D meshes M_t for each of the T temporal positions $t = 0 \dots T - 1$ in the dataset. Unfortunately, the meshes may differ in their number of vertices and topology. Thus, a vertex' time-dependent position \vec{v}_t^{dspl} cannot be derived implicitly. For the association of points on the surfaces with each other, a correspondence problem has to be solved.

A 4D mesh model requires a certain flexibility to capture pathologic vessel morphologies. We employ a 3D triangular surface mesh M with a constant topology as basis. It is the one extracted from the 3D segmentation that was performed on the magnitude images' TMIP. Every vertex $\vec{v} \in M$ stores a list of T 3D vectors \vec{d}_t , in the following referred to as displacement vectors. A vertex' position \vec{v}_t^{dspl} at time t is $\vec{v} + \vec{d}_t$.

Displacements \vec{v}_t^{dspl} are calculated as closest projection of a vertex $\vec{v} \in M$ onto M_t . To do so, the nearest vertex $\vec{q}_t \in M_t$ to \vec{v} is determined. Then, \vec{v} is projected onto each plane spanned by the triangles that \vec{q}_t is part of. If a projection lies outside a triangle, the closest projection onto one of the triangle's edges is used as result. The displacement vector \vec{d}_t results as $\vec{v}_t^{\text{dspl}} - \vec{v}$ (see Figure 108).

DISPLACEMENT POSTPROCESSING: For noise reduction of the displacement vector lists, two post-processing steps are applied, as depicted in Figure 109:

- The *spatial smoothing* aligns displacement vectors in a vertex' one-ring neighborhood in each temporal position separately. The same low-pass filter [500] as for the mesh smoothing is used for this purpose.
- The *temporal denoising* smoothes the displacement list of each vertex, i.e., the displacements along the temporal dimension. It is realized by fitting a [cubic penalized regression spline \(ALGLIB\)](#).

MOTION VISUALIZATION: A real-time capable visualization of the 4D mesh can be obtained using the GPU, or more precisely the OpenGL shader pipeline. A displaced vertex position \vec{v}_t^{dspl} at $t \in \mathbb{R}$ is calculated as linear interpolation between $v_{[t]}^{\text{dspl}}$ and $v_{[t]}^{\text{dspl}}$. Each vertex is uploaded to the GPU with:

- its position,
- its normal, and
- an index to access additional information, which are:
 - a list of all triangles,
 - the triangle count per vertex,
 - the corresponding triangle indices, and
 - the displacement list per vertex.

A dataset has about 15 temporal positions. Thus, there are 15 displacement vectors in the list. Linear interpolation of these few samples would not lead to a fluent motion visualization. Therefore, ten times as much displacement vectors are resampled from the spline during the temporal denoising. Figure 110 shows a result of the motion visualization.

MOVING MEASURING PLANES: Measuring planes, orthogonal to the centerline and freely movable along it, are a standard to quantify SVs (recall Section 6.1). To ensure that a plane remains perpendicular to the moving centerline C_t and fits the vessel at every temporal position M_t , the plane's center, normal and scale are modified to a list of size T – analogous to the displacement lists. The centers are derived from the centerline positions and the normals from the tangents. The scales are determined so that the plane fits the diameter of the corresponding vessel section in M_t . Oversampling for visualization purposes via spline approximation is performed as explained in Section 9.2.1.3. The lists are used in the geometry shader to span the plane at the current time of the heart cycle. Figure 111a shows a measuring plane that fits the vessel at any time and follows the moving centerline, i.e., stays orthogonal.

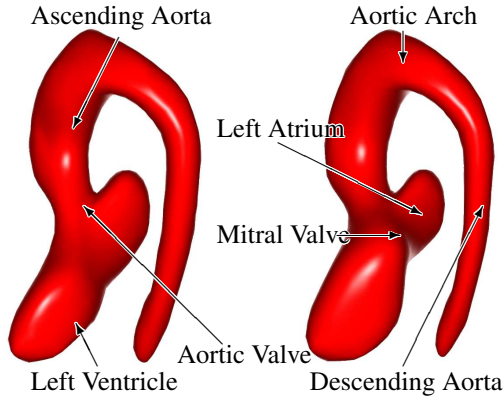


Figure 110: Cardiac motion visualization. The left ventricle contracts during systole (left) to pump blood into the aorta, resulting in a slightly increased vessel diameter. In the meantime, the left atrium fills and then supplies the left ventricle with new oxygenated blood during diastole (right).

Images from [277] © 2016 Springer-Verlag Berlin Heidelberg, reprinted with permission.

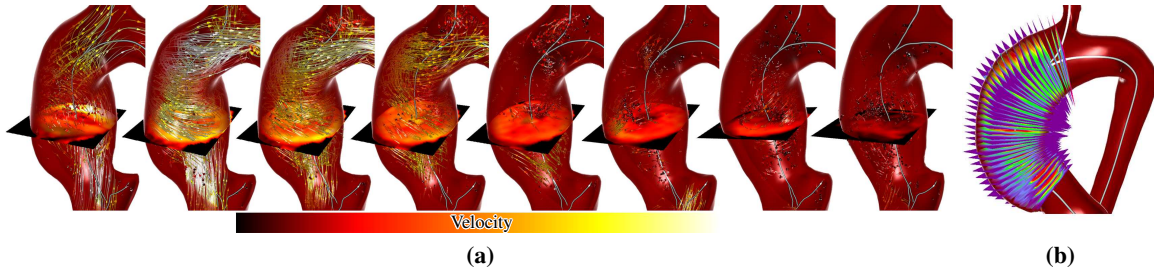


Figure 111: (a) A measuring plane inside the ascending aorta follows the vessel movement during the cardiac cycle by changing its size and orientation. An adapted stroke volume quantification incorporates the motion information.

(b) Equidistant measuring planes in the ascending aorta between the approximate coronary arteries' location and the brachiocephalic artery.

Images from [277] © 2016 Springer-Verlag Berlin Heidelberg, reprinted with permission.

STROKE VOLUMES IN DYNAMIC (4D) VESSELS: The incorporation of motion into the SV quantification requires a slight adaption of the calculation. The check $S_3(\cdot)$, whether or not a position is inside the vessel, becomes a dynamic counterpart $S_4(\cdot)$. In addition, planes have a list of T orthonormal systems $(\vec{n}^t, \vec{n}_x^t, \vec{n}_y^t)$, scales $\vec{s}^t = (s_x^t, s_y^t)$, and center positions $\vec{c}^t, t = 0 \dots T - 1$. The grid size \vec{g} remains constant. Following this, the flow rate calculation $\text{fr}(t)$ and transformation to world coordinates $P(x, y, t)$ have to be adjusted to:

$$\begin{aligned} \text{fr}(t) &= s_x^t \cdot s_y^t \cdot \vec{n}^t \cdot \sum_{x=0}^{g_x-1} \sum_{y=0}^{g_y-1} S_4(P(x, y, t), t) \cdot \mathbf{V}(P(x, y, t), t) \\ \text{with } S_4(P(x, y, t), t) &= \begin{cases} 1, & (P(x, y, t)) \text{ inside vessel} \\ 0, & \text{else} \end{cases} \\ \text{and } P(x, y, t) &= \vec{c}^t + s_x^t \cdot \left(x - \frac{g_x}{2}\right) \cdot \vec{n}_x^t + s_y^t \cdot \left(y - \frac{g_y}{2}\right) \cdot \vec{n}_y^t \end{aligned} \quad (51)$$

Analogous to the static version, $S_4(P(x, y, t), t)$ is realized with the dynamic triangular surface (see Figure 112).

9.2.2. RESULTS

In this section, we present a validation of the 4D segmentations, an overview of the seven datasets, and a discussion. In the implementation, the user is allowed to manually refine the 4D segmentations if desired. However, solely the automatically specified input, as described in Section 9.2.1, was used for this evaluation. The 4D segmentation including the motion extraction were performed in less than 15

seconds per case on an Intel i7-3930K. The stroke volume (SV) quantifications run in interactive speed. All presented images of vessels and flow were directly captured from our software (recall Chapter 7) which is used for research purposes by the clinical collaborators.¹¹ Plots were created with MATLAB. The first vessels that branch off the aorta are the coronary arteries (CAs) directly behind the valve. They receive about 5 % of the SV. The next branching vessel is the brachiocephalic artery (BA) in the aortic arch. In order to have a larger range of sample positions to compare the static and motion-aware quantification, we use the constant net flow volume in the ascending aorta after the CAs and before the BA as SV. Figure 111b depicts the evaluated planes in 1 mm steps on the centerline.

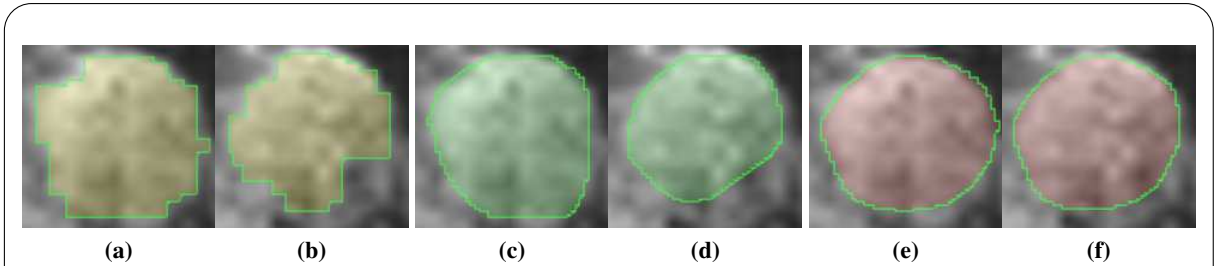


Figure 112: Binary mask of the ascending aorta’s cross-section for two of 15 temporal positions of the dataset obtained by rasterization of (a–b) the 4D segmentation, (c–d) the independent 3D meshes for each time step, and (e–f) the 4D mesh with post-processed motion information.

Images from [277] © 2016 Springer-Verlag Berlin Heidelberg, reprinted with permission.

		<i>Static</i>	<i>Dyn. (indep.)</i>	<i>Dynamic</i>
$(A - M) / M$ (%)		- 10.64	- 4.36	2.44
$(A \cap M) / (A \cup M)$ (%)		86.35	85.23	86.27
$(A \Delta M) / (A \cup M)$ (%)		13.65	14.77	13.73

Table 9: See Figure 113 for a depiction of the areas.

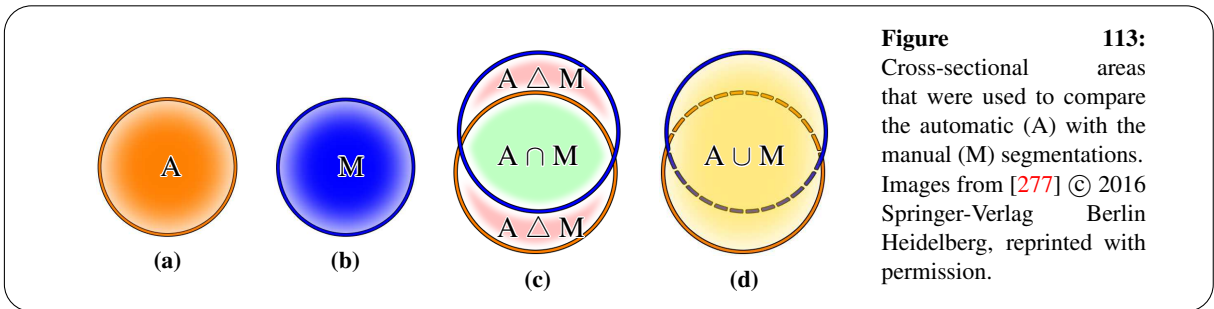


Figure 113: Cross-sectional areas that were used to compare the automatic (A) with the manual (M) segmentations. Images from [277] © 2016 Springer-Verlag Berlin Heidelberg, reprinted with permission.

9.2.2.1. ACCURACY OF 4D SEGMENTATIONS

For one dataset (see Figures 111b and 115), we generated vessel segmentations for all 43 equidistant planes in the ascending aorta manually by drawing contours. Randomly selected samples were validated by the collaborating experts. On the one hand, we performed this on the TMIP of the magnitude images and compared it to the rasterization of the static (3D) vessel surface (“*Static*”). On the other hand, this was done in the anatomical images A for each of the 18 temporal positions and compared to the rasterized independent 3D meshes for each temporal position (“*Dyn. (indep.)*”) as well as the rasterized dynamic vessel with post-processed motion information (“*Dynamic*”). Planes were always perpendicular to the vessel’s centerline. Each value in Table 9 is an average of all planes. The manual and automatic segmentations overlap by 85.95 ± 0.62 %. Cross-sections derived from the static mesh are 10.64 % smaller than the manual segmentations. This is the main cause for the 13.65 % difference. In the

¹¹A video is available at <https://www.youtube.com/watch?v=sozt3TFwWPE> (accessed 03/2016)

dynamic variant, these sizes differ less. Consequently, large parts of the about 14 % discrepancy are caused by the positioning. The 4D mesh with post-processed motion information directly depends on the independent 3D meshes of each temporal position. Thus, the results of both are similar.

9.2.2.2. CASES

The constant SV between the coronary arteries' location and the brachiocephalic artery was estimated by the collaborating experts for each case and used as a reference. For this purpose, they were allowed to freely move and rotate a measuring plane, obtain multiple SV samples and then estimate a result. In our experiments, the SV was calculated in three different variants "S", "D", and "D2":

- *S* uses the rasterized 3D vessel surface (see Figure 106b) that was extracted from the segmentation, which is based on the magnitude images' TMIP.
- *D* employs the rasterized dynamic (4D) surface with post-processed motion information from our proposed method (see Figures 112e–f).
- *D2* is a simulation of the common 2D PC-MRI. Here, planes are fix (constant angulation, size, center) per centerline position, but the segmentation is time-dependent. The 4D segmentation of the cross-sections is derived from rasterization of the 4D mesh (same as in *D*).

For each variant, the mean of the absolute deviation $\odot E_{\{S,D,D2\}}$ per centerline position from the reference was calculated. The following plots in (see Figures 114–120) show the reference in red, *S* in blue, *D* in green, and *D2* in orange. The x-axis shows the centerline positions in 1 mm steps, starting from the approximate coronary arteries' location on the left.

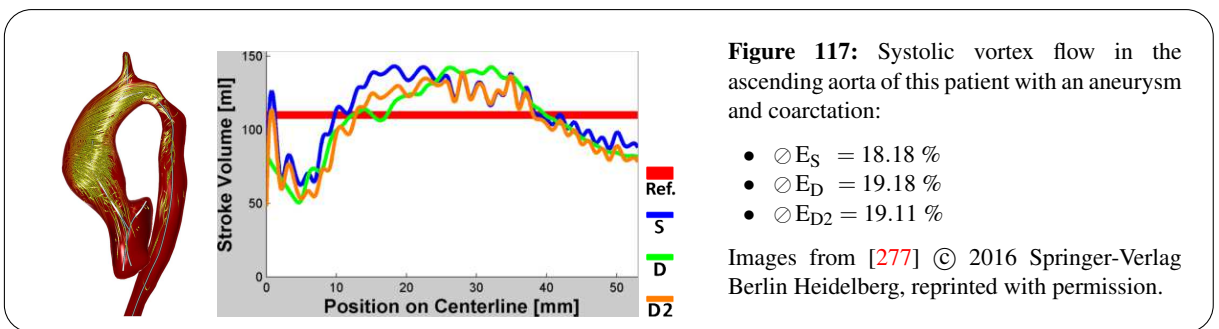
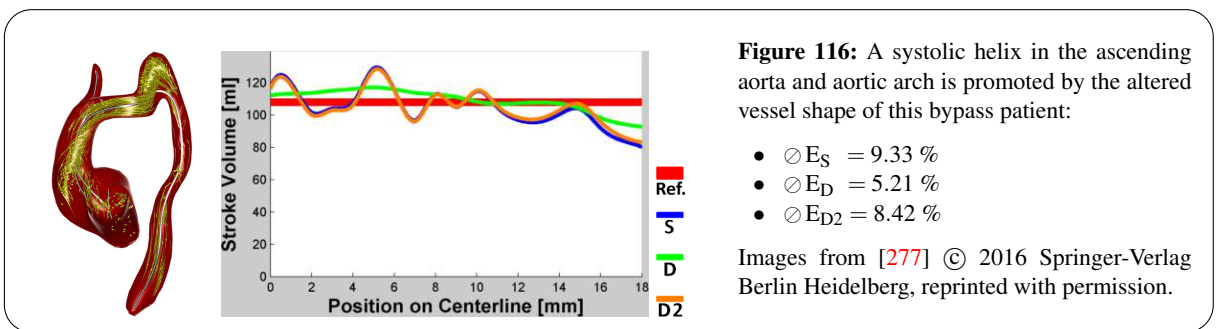
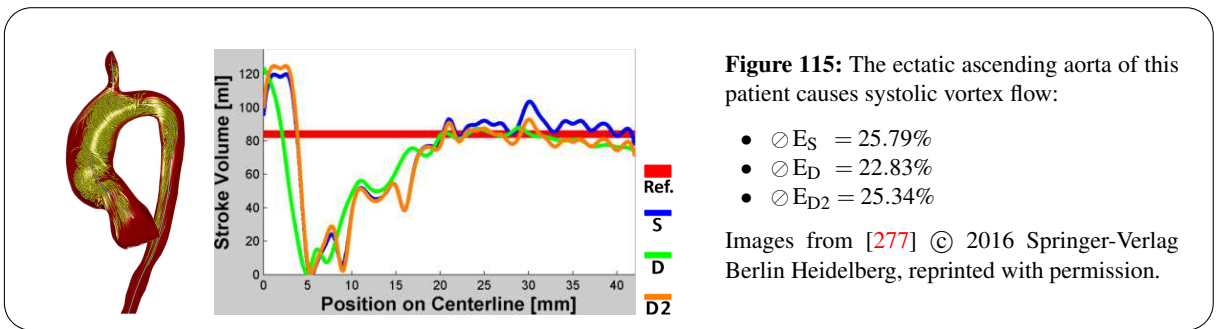
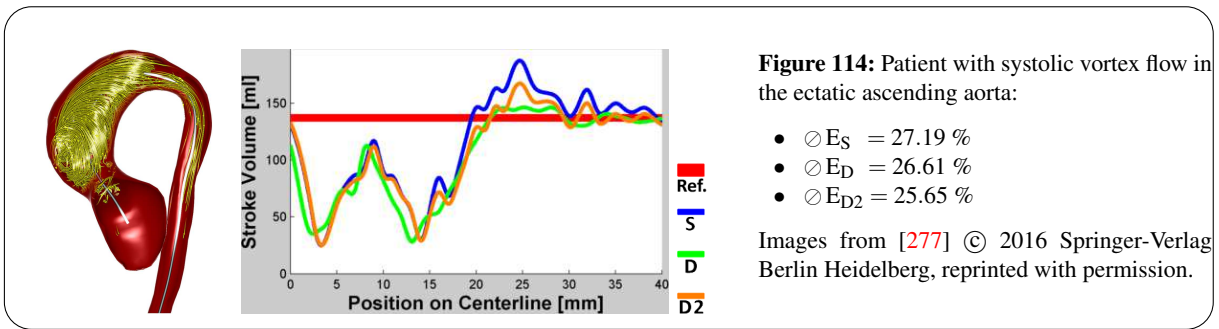
D performed, on average, 1.57 % better than *S* and *D2*. The improvements ranged from –1.0 % to 4.12 %. *D* was best in four cases, *S* in two and *D2* in one.

ECTASIA 1: The first patient has a pathologically dilated ascending aorta. Figure 114 shows emerging vortex flow during systole. All SV quantifications are most error-prone in the first half of the examined vessel section, where the vortex is most prominent. The 2D PC-MRI simulation *D2* performs marginally better than *S* and *D* with $\odot E_{D2} = 25.65$ %.

ECTASIA 2: In addition to an ectatic ascending aorta, the second patient has an improperly closing aortic valve which causes an abnormal amount of blood swirling back into the left ventricle during diastole. Figure 115 shows the systolic vortex flow. The diagram depicts the 2.96 % improvement of *D* compared to *S*. Like in the previous patient, the heavy vortex flow causes high quantification uncertainties in the first half of the examined vessel section.

BYPASS: Extra-anatomic bypass surgery was performed in this patient due to a severe coarctation. The motion extraction shows plausible results: There is a strong movement in the aortic root, no noticeable contraction in the vascular replacement, and then again a pulsating wall motion. The altered vessel shape promotes systolic vortex flow in the ascending aorta, shown in Figure 116. Dynamic quantification (*D*) is, on average, 4.12 % closer to the reference SV than *S*.

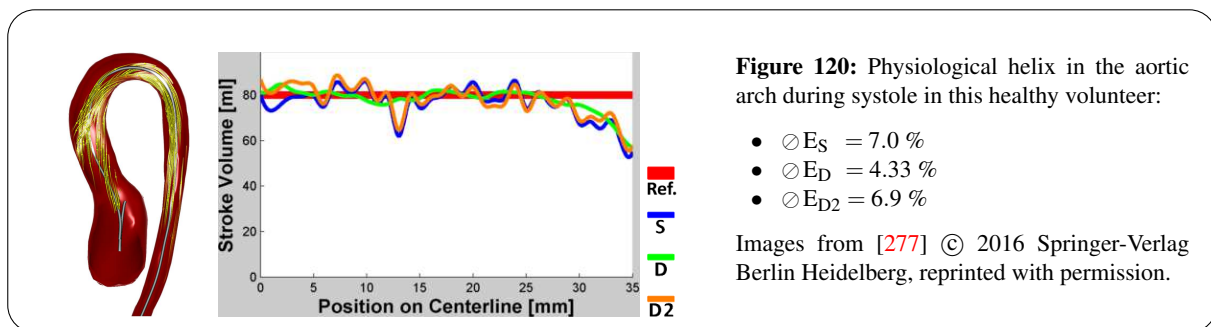
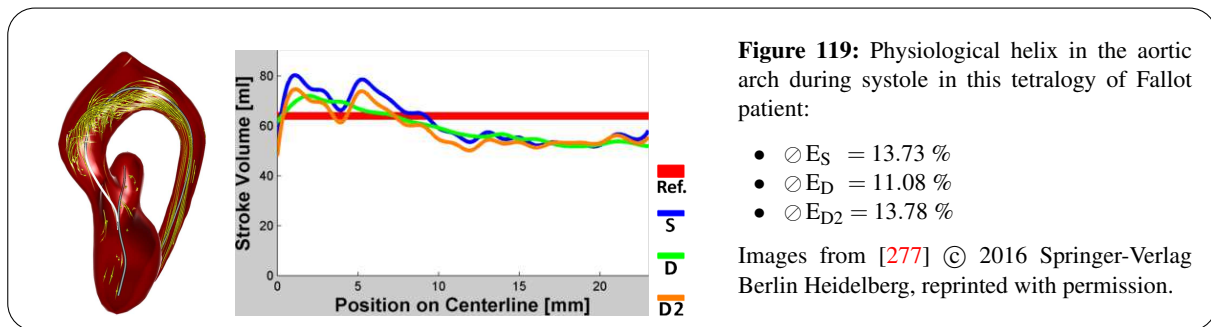
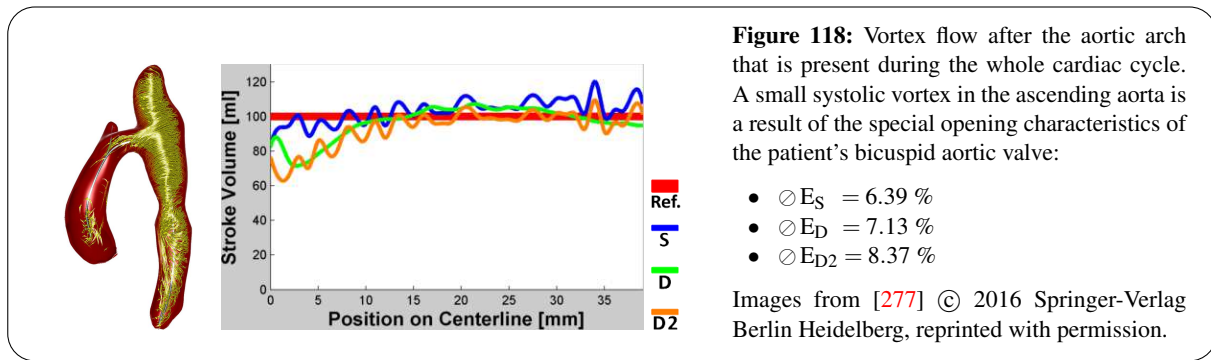
ANEURYSM AND COARCTATION (ANEUCO): This patient has an aneurysm in the ascending aorta and a coarctation. As illustrated in Figure 111a, there is a heavy movement in the ascending aorta that causes a high variation of the plane angulation. *S* performs slightly better (0.93 %) than the dynamic counterparts, shown in Figure 117. However, the SV quantification seems to be uncertain due to the present vortex flow.



ANEURYSM AND BAV (ANEUBAV): High velocity blood flow passes this patient’s aortic arch and impinges on the wall. A huge vortex emerges that is present during the whole cardiac cycle, shown in Figure 118. Progression for years probably caused the significant dilation of the left subclavian artery. The patient’s bicuspid aortic valve is likely responsible for a smaller systolic vortex in the ascending aorta. The resulting plot illustrates the 0.74 % and 1.98 % worse performance of D and $D2$ compared to S , respectively.

FALLOT: This patient has a pulmonary valve defect as consequence of a surgical tetralogy of Fallot correction. The aorta, however, is free of abnormal flow patterns – only a physiological systolic helix in the aortic arch occurs, as shown in Figure 119. All quantifications achieve similar results. Yet, D with $\odot E_D = 11.08\%$ is, on average, 2.7 % closer to the reference than the others.

HEALTHY VOLUNTEER: The last dataset is from a healthy volunteer with a slight physiological helix in the aortic arch during systole (see Figure 120). All SV curves match the reference relatively well and show only small average deviations. Yet, with $\odot E_D = 4.33\%$, D performs about 2.7 % better than the rest.



9.2.2.3. INFLUENCES

We analyzed influences on the result deviations by correlating the standard deviation (σ) of the three obtained SVs from S , D , and $D2$ per centerline position i to measures that describe differences between the static and dynamic vessels or measuring planes:

- $\Delta Area$ is the standard deviation (σ) of minimum and maximum plane areas A_S^i , A_D^i , and A_{D2}^i . High values indicate a strong vessel pulsation.
- $\Delta Normal$ refers to angulation changes of measuring planes in D . It is calculated as mean of angles between the average plane normal vector $\vec{o}\vec{n}^i$ and the time-varying plane angulations \vec{n}_t^i . High values indicate a strong movement of the dynamic centerline.
- $\Delta Center$ is the mean distance of the time-dependent dynamic measuring plane centers \vec{c}_t^i in D from the average plane center $\vec{o}\vec{c}^i$. Analogous to $\Delta Normal$, high values indicate a strong movement of the dynamic centerline.
- $\Delta Velocity$ is the σ of average velocities $\|\vec{o}\vec{u}_S^i\|$, $\|\vec{o}\vec{u}_D^i\|$ and $\|\vec{o}\vec{u}_{D2}^i\|$ that were sampled on the corresponding planes in S , D and $D2$. Different velocity vectors are the result of the deviating sample positions on the measuring planes.

Table 10 shows **no** ($\rho < 0.25$), **low** ($0.25 \leq \rho < 0.5$), **medium** ($0.5 \leq \rho < 0.75$), and **high** ($0.75 \leq \rho$) Pearson correlation coefficients. The normal ($\Delta Normal$) and plane center variation ($\Delta Center$) are the highest influence on deviations of the resulting SVs. Three high and five medium correlations were found in the datasets for these two measures. This seems plausible because both indicate a strong movement of the vessel or, more precisely, the centerline. The sampled average velocities ($\Delta Velocity$) in the cross-sections are the direct consequence of the resulting different plane configurations and rank third. The differences of the measuring plane sizes ($\Delta Area$) rank fourth. An interpretation could be that there is only a moderate amount of vessel pulsation in many cases. Exclusively no or low correlations were detected in the *Ectasia 1* patient. This might indicate that there are other, more complex influences or simply that the differences between the three SVs are not distinctive enough.

Measure	Dataset	Ectasia 1	Ectasia 2	Bypass	AneuCo	AneuBAV	Fallot	Healthy V.	Average
$\Delta Area$		0.19	0.16	0.24	0.14	0.3	0.69	0.64	0.4
$\Delta Normal$		0.43	0.02	0.63	0.5	0.84	0.18	0.53	0.45
$\Delta Center$		0.03	0.74	0.08	0.77	0.56	0.94	0.22	0.48
$\Delta Velocity$		0.23	0.71	0.03	0.69	0.34	0.96	0.11	0.44

Table 10: Pearson correlation of different measures to the standard deviation of SVs obtained with S , D , and $D2$ per centerline position. Table from [277] © 2016 Springer-Verlag Berlin Heidelberg, reprinted with permission.

9.2.3. DISCUSSION

The overall deviations from the reference SV were smallest if there was no prominent vortex flow (Healthy V., AneuBAV, Bypass, Fallot). This coincides with our previous findings [278] (recall Section 9.1).

The differences between the 2D PC-MRI simulation $D2$ and S were, on average, smaller than the differences between S and D – especially if there was just a moderate movement of the dynamic centerline. A possible explanation is as follows: The dynamic aorta has its minimum diameter during diastole. During systole, when the maximum diameter is reached due to the pumped blood, the aorta has approximately the same size as the static vessel approximation. Consequently, the difference between flow rates in S and $D2$ is smallest at this time of the cardiac cycle. The changing diameter causes exclusion of peripheral plane regions from the $D2$ quantification during diastole and during the transition from maximum to minimum vessel diameter. Nevertheless, differences between S and $D2$ remain small because of the low diastolic blood flow velocities with little contribution to the SV. In addition, the aorta

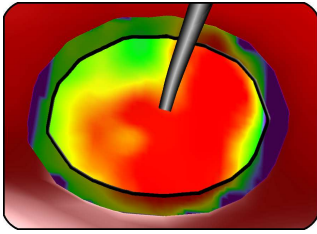


Figure 121: A plane, color-coded by velocity, orthogonal to the centerline (gray) inside the vessel (red surrounding). Motion-aware stroke volume quantification excludes peripheral regions (darkened) while the vessel diameter is below maximum. Yet, the difference using static vessels is relatively small since high velocities with most influence on the stroke volume quantification are often located in the center. Image from [277] © 2016 Springer-Verlag Berlin Heidelberg, reprinted with permission.

usually shows a parabolic velocity profile, i.e., the main blood flow jet with highest influence on the SV calculation is located in the center, as depicted in Figure 121.

LIMITATIONS: Contrast in the anatomical images strongly varies due to the pulsatile flow, making the automatic segmentation challenging during diastole. Correcting intensity inhomogeneities [440] might increase the robustness. Divergence-free filters [389] may be applied as further phase image pre-processing. The effect of phase dispersion [561] was not considered, but could introduce errors at the vessel boundaries. Scans with retrospective gating could produce different results, since early-systolic values are better captured. Generally, image data with a higher spatio-temporal resolution might generate more significant SV differences.

9.2.4. CONCLUSION AND FUTURE WORK

We have presented a cardiac motion extraction that is feasible for the clinical routine due to minimal required interaction. We focused on the aorta, but the application of our method to other vessels, such as the pulmonary artery, is possible. A carefully designed visualization of the results was established. Graph cuts were employed to support segmentation tasks and showed a high level of acceptance among the consulted radiologists because of the intuitive task of specifying regions inside and outside the vessel. Such regions were automatically determined for each temporal position and can be used for other segmentation algorithms as well.

We incorporated vessel dynamics to adjust stroke volume calculation and quantified differences to conventional methods using static vessels and a simulation of 2D PC-MRI. On average, the results differed by 7.82 %. Unfortunately, the incorporation of motion information does not achieve improvements for each position of the centerline and thus is no guarantee for more accurate results. Yet, it performed on average 1.57 % better by having lower differences to the reference stroke volumes estimated by the clinical collaborators. Limitations were pointed out. Variations of the planes' normal vectors and centers had the highest correlations to differences of the SVs obtained with the different methods. This is plausible since both indicate a strong vessel movement. The limited improvements imply that it is reasonable to employ static 3D vessel approximations to quantify stroke volumes and avoid the additional effort. Yet, the use of robust methods (recall Section 9.1) is recommended due to the calculations' high sensitivity to the measuring plane angulation [278].

OUTLOOK: Motion information open up various opportunities. Wall shear stress is another important measure that strongly depends on the accurate wall position and orientation. Possible improvements by incorporating vessel dynamics should be investigated. Models of the aortic valve facilitate further understanding of vortex formation in, e.g., bicuspid aortic valve patients. The extracted movement could support the determination of the valve's exact position and location. Finally, the wall movement allows conclusions regarding vessel elasticity, which is important for the risk assessment of aneurysm rupture and thus supports treatment decisions. The derivation of a vascular wall model was a major interest of the consulted experts.

Further research to assess the reliability of the obtained results is necessary. In the future, standardized and (semi-)automatic evaluation methods will enable the fast processing of large studies that are performed for statistical analysis of gender- and age-specific norm values. The derived physiological variations of different flow parameters will support the assessment of disease severity.

This concluding chapter starts with a brief summary of the main contributions of this thesis in Section 10.1. This is followed by a description of potential future topics and research fields in Section 10.2. The last Section 10.3 puts 4D PC-MRI in a bigger picture and points out the potential that the evaluation of such data offers.

10.1. SUMMARY OF CONTRIBUTIONS

This section briefly summarizes the main contributions of this thesis.

OVERVIEW: A comprehensive overview of 4D PC-MRI data measurement, pre-processing, state-of-the-art of quantitative and qualitative data analysis, and visualization was provided. This gives future researchers in the field of 4D flow CMR a strong starting point for further advancements.

GUIDED EVALUATION: The research prototype *Bloodline* was described. It provides a guided analysis pipeline that facilitates a basic dataset evaluation within ten minutes. This comprises the extraction of a vessel, the corresponding flow calculation as well as vortex extraction, and the quantification of cardiac function parameters, such as the stroke volume (SV) and regurgitation fraction (RF). Reasonable default values limit the amount of parameters that need to be adjusted. Results can comfortably be shared with screenshots or with videos of the flow.

VORTEX FLOW: The assessment of vortex flow is a major interest in the cardiac flow analysis. In this thesis, several methods were presented that support this task, starting with a recap of a semi-automatic extraction of vortex flow-representing path lines of high visual quality. This forms the basis for three subsequent methods:

1. A 2D polar plot was established as overview visualization of aortic vortex flow. A grid view facilitates the quick comparison of datasets within a study regarding the occurrence of pathological vortex flow.
2. Videos with adaptive speed were proposed that optimize the display time of extracted vortex flow. This was made to support offline case discussions and presentations.
3. A suitable clustering method was determined to group single vortex entities. A subsequent classification, which is based on characteristics that were described in recent medical publications, was proposed to minimize inter-observer variabilities and increase the objective comparability of datasets.

FLOW RATE AND STROKE VOLUME QUANTIFICATION: 4D PC-MRI data allow to evaluate arbitrary measuring planes. However, results strongly vary with different plane configurations (position and angulation). A method was presented that automates the manual trial-and-error process to determine reasonable SV results. An initial visualization of the quantification uncertainty was established from the statistical analysis.

Usually, static approximations of the actually dynamic vessel are employed in the quantification of flow rates. This is inherently inaccurate. A method was described to obtain 4D segmentations and dynamic vessels solely from the 4D PC-MRI data. This was incorporated in the SV quantification. Result deviations were analyzed compared to static vessels.

10.2. FUTURE WORK

The field of 4D PC-MRI provides a vast amount of potential future topics. This section presents only selected ideas.

COUPLING WITH CFD: Besides MRI-based measurements, flow data can be obtained using *computational fluid dynamics* (CFD). Numerical flow simulations require the specification of various boundary conditions [299], which is often based on assumptions. For example, it is assumed that flow at the vessel wall is at 0 m/s. In addition, information about the inflow and outflow velocity profile are necessary. Among others, CFD simulations are useful to predict the potential outcome of a treatment like valve replacement or stenting [381]. CFD simulations have already been used to verify various measures, e.g., WSS (recall Section 6.2.1) peak locations by Petersson et al. [408], TKE (recall Section 6.3.2) by Arzani et al. [14], systolic pressure drops (recall Section 6.3.1) by Goubergrits et al. [188], and TKE in combination with flow displacements (recall Section 6.1.3) by Andersson et al. [7].

While 4D PC-MRI data suffer from a limited spatio-temporal resolution, noise, and different image artifacts, it is not clear to what extent CFD data truly represent a patient's situation, since the simulations rely on various model assumptions. However, *data assimilation* allows to link the methods and taking advantages of both. A combined approach can be seen as patient-specific simulation, where the measured data are employed as input, or as 4D PC-MRI data with enforced model assumptions, such as zero-divergence. De Hoon et al. [114] presented a fluid simulation where MRI and CFD are coupled in order to exploit the benefits of both methods and improve the visual analysis of hemodynamics. This is a promising approach that should be further investigated in the future. For example it should be determined to what extent quantification results are influenced.

UNCERTAINTY: During this thesis it became clear that the flow data, and consequently the results, are prone to various errors. Spatio-temporal image resolutions are improving as well as the employed MRI sequences in general. In addition, more elaborated post-processing methods, such as divergence filtering (recall Section 4.1.4), are being developed. Though, obtained qualitative and quantitative results should always be interpreted with care.

Uncertainties in the flow trajectory calculation have already been investigated [162, 463] (recall Section 6.3.5). However, such an analysis is usually not performed in a standard data evaluation. This might be due to the high computational effort and the huge amount of resulting information of probabilistic methods. The latter are well-known from *diffusion tensor imaging* and the related *fiber tracking* [372]. Future works could investigate to what extent corresponding methods could be a benefit to the analysis of 4D PC-MRI data, although the situation is slightly different. While fiber tracking has to handle multiple direction within one voxel in a 3D grid, blood flow analysis deals with one direction per voxel in 4D data.

Uncertainty might be even more important in the quantitative data analysis. It has been shown in this thesis how sensitive flow rate calculations are to different measuring plane configurations, and a first uncertainty visualization for stroke volume quantifications has been proposed (recall Section 9.1). With more experience on what are relatively high and low deviations and a better understanding of where the highest uncertainties occur aside from vessel sections with vortex flow, this could be incorporated in a way that the user receives a warning if an analysis is performed in an uncertain region. Other measures, such as WSS, are likely to show a similar uncertainty behavior, since they directly depend on vessel wall position and orientation. The proposed approach of systematically evaluating slightly different configurations could be adapted to the WSS quantification in the future. The same yields for incorporating the vessel's motion information.

VENTRICULAR CONTRAST ENHANCEMENT: 4D PC-MRI image contrast strongly depends on the expected maximum velocities, which are configured prior to the scan with the V_{ENC} parameter (recall Section 3.1.2). Too low V_{ENC} estimations produce phase wraps (recall Section 4.1.1), whereas too high estimations result in poor contrast that impedes a subsequent segmentation process.

An appropriate choice is difficult for the ventricles since one usually also wants to measure the left-(LVOT) or right-ventricular outflow tract (RVOT) correctly. This means: Either a low V_{ENC} is set so that the relatively slow intraventricular flow velocities can be obtained with a decent contrast. In this case, phase wraps in the LVOT / RVOT are likely to occur. Or the V_{ENC} is adjusted with regard to the LVOT /

RVOT, which yields a limited contrast within the ventricles. Mostly, the latter approach is applied. Here, contrast enhancement would be a beneficial tool. An idea is outlined in the following.

First, the LVOT / RVOT, which should be clearly visible in the data, is segmented by the user. Assuming that blood in a ventricle has to pass the corresponding outflow tract, the flow connectivity could be exploited by performing a backward flow integration starting from the outflow tract. Aforementioned probabilistic approaches might be suitable here to increase the chance that every voxel in the ventricle is reached. Then, image intensities along the path line courses are increased, depending on properties regarding the path lines' appearance (e.g. curvature). The "nicer" a trajectory is, the more contrast enhancement is applied.

PERCEPTION AND VISUALIZATION: Other future topics could deal with more perception-based visualization approaches. There is a good understanding of separate *visual channels*, such as color and motion, that are processed relatively independently from one another [543] as well as the visual perception of flow directions and velocities [542]. This could be exploited to further refine blood flow visualization techniques, especially the visual assessment of quantitative measures color-mapped to the flow trajectories. Existing research on the human visual perception is often focused on simple shapes, such as T and L junctions, and on static images [207]. Further research could put emphasis on accentuating dynamic scenes, e.g., blood flow animations.

Pilar and Ware [411] used special glyphs to convey additional information in 2D meteorological data. Generally, the literature on perception-based visualization techniques in meteorology and oceanology seems to be a good starting point. Such approaches may be customized to the cardiac context. This requires a careful adaptation, evaluation, further refinement, and finally, task-based experiments that compare different visualizations in order to better understand how the design choices affect the accuracy and efficiency of the result interpretation.

Eichelbaum et al. [140] proposed an ambient occlusion method for 3D stream line bundles. Due to its real-time capability, an adaption to path line animations is conceivable. Global illumination has been shown to be effective for the display of dense 3D streamtubes [547]. It should be investigated if ambient occlusion is superior to commonly employed halos regarding the depiction of depth relations during animations. The same questions applies to illustrative techniques for line bundles, as summarized by Isenberg [242]. An overview of further open visualization challenges was given by Van Pelt and Vilanova [523].

STUDY EVALUATION: Another goal is to support the evaluation of potentially large studies. This requires the generation of comprehensive reports with standardized, qualitative and quantitative results.

The automatic generation of 3D and 4D visualizations (screenshots and videos of the scene) makes finding suitable viewing perspectives necessary that ensures the visibility of all relevant features and structures. Corresponding earlier works, such as by Mühler et al. [374], could be adapted for this purpose.

Dataset comparison is another highly important topic. Verma and Pang [532] proposed tools for general flow fields, Van Pelt et al. [529] specifically for the pairwise comparison of simulated (CFD) datasets of patients with cerebral aneurysms. An investigation should be performed to what extent such methods are suitable for the cardiac context. However, when it comes to evaluating whole studies and finding meaningful correlations, statistical methods are inevitable. Here, the wide field of epidemiology [302, 435] and corresponding analysis methods [267] provide a rich pool of ideas and concepts that might be adapted to blood flow measured with 4D PC-MRI. Moreover, the comparability of datasets acquired with different scanners and / or MR sequences has to be analyzed in a future work.

CLASSIFICATION: Vortex classification criteria that are based on recent medical studies were described in this thesis (recall Section 8.4.2). However, there is still room for improvements. For example, proximity to the vessel wall was not considered so far. Also, the size of a vortex can be varying over time. This temporal component was neglected in our initial approach. A corresponding extension also entails the adaption of the proposed glyph visualization.

Moreover, the vessel morphology should be further incorporated to achieve more comprehensive descriptions of a patient's situation. For example, the extent and length of a stenosis could improve the understanding of the potential post-stenotic vortex formation. Both together could be linked to the often developing post-stenotic vessel dilation.

10.3. 4D PC-MRI POTENTIAL

4D PC-MRI enables the measurement of 3D blood flow and its change over the heart cycle. Medical researchers start using these data to develop an increased understanding of healthy cardiovascular systems and to find indicators for the genesis and evolution of cardiovascular diseases.

4D flow CMR is expected to significantly improve patient treatment, which was confirmed by recent medical studies [83, 226, 488, 530]. One goal is, e.g., that it can replace right-heart catheterizations for pressure estimations. This is not only less stress for the patient, it is also considerably less dangerous.

The clinical feasibility of 4D PC-MRI is increasing constantly. Many research groups are working on improvements of the employed MR sequences and already achieved a reduction of the acquisition times to 10–20 min from originally about 45 min. In combination with the development of standardized, easy-to-use software with guided workflows, report generation, and elaborate dataset comparison as well as statistical analysis, the evaluation of large studies including follow-up acquisitions becomes possible and feasible. Then, a long-term goal is to obtain age and gender-specific normative values for different flow parameters, which could help to refine current treatment guidelines.

D

APPENDIX

- [1] A. Abufadel. “4D segmentation of cardiac MRI data using active surfaces with spatiotemporal shape priors”. PhD thesis. Georgia Institute of Technology, USA, 2006. Link: hdl.handle.net (accessed at 02/2016) (cited on page 148).
- [2] R. J. Adrian. “Particle-imaging techniques for experimental fluid mechanics”. In: *Annual Review of Fluid Mechanics* 23.1 (1991), pp. 261–304. DOI: [10.1146/annurev.fl.23.010191.001401](https://doi.org/10.1146/annurev.fl.23.010191.001401) (cited on page 29).
- [3] C. W. Akins, B. Travis, and A. P. Yoganathan. “Energy loss for evaluating heart valve performance”. In: *The Journal of Thoracic and Cardiovascular Surgery* 136.4 (2008), pp. 820–33. DOI: [10.1016/j.jtcvs.2007.12.059](https://doi.org/10.1016/j.jtcvs.2007.12.059) (cited on page 75).
- [4] B. D. Allen, A. J. Barker, K. Parekh, L. C. Sommerville, S. Schnell, K. B. Jarvis, M. Carr, J. C. Carr, J. Collins, and M. Markl. “Incorporating time-resolved three-dimensional phase contrast (4D flow) MRI in clinical workflow: Initial experiences at a large tertiary care medical center”. In: *Journal of Cardiovascular Magnetic Resonance* 15.Suppl 1 (2013), P32. DOI: [10.1186/1532-429X-15-S1-P32](https://doi.org/10.1186/1532-429X-15-S1-P32) (cited on page 8).
- [5] Y. Amano, T. Sekine, Y. Suzuki, K. Tanaka, R. Takagi, and S. Kumita. “Time-resolved three-dimensional magnetic resonance velocity mapping of chronic thoracic aortic dissection: A preliminary investigation”. In: *Magnetic Resonance in Medical Sciences* 10.2 (2011), pp. 93–9. DOI: [10.2463/mrms.10.93](https://doi.org/10.2463/mrms.10.93) (cited on page 16).
- [6] A. F. S. Amaral, J. Patel, L. Gnatiuc, M. Jones, and P. G. J. Burney. “Association of pulse wave velocity with total lung capacity: A cross-sectional analysis of the BOLD London study”. In: *Respiratory Medicine* 109.12 (2015), pp. 1569–75. DOI: [10.1016/j.rmed.2015.10.016](https://doi.org/10.1016/j.rmed.2015.10.016) (cited on page 67).
- [7] M. Andersson, J. Lantz, T. Ebberts, and M. Karlsson. “Quantitative assessment of turbulence and flow eccentricity in an aortic coarctation: Impact of virtual interventions”. In: *Cardiovascular Engineering and Technology* 6.3 (2015), pp. 281–93. DOI: [10.1007/s13239-015-0218-x](https://doi.org/10.1007/s13239-015-0218-x) (cited on page 160).
- [8] P. Angelelli and H. Hauser. “Straightening tubular flow for side-by-side visualization”. In: *IEEE Transactions on Visualization and Computer Graphics* 17.12 (2011), pp. 2063–70. DOI: [10.1109/TVCG.2011.235](https://doi.org/10.1109/TVCG.2011.235) (cited on pages 50, 108, 120, 132).
- [9] L. Antiga and D. A. Steinman. “Robust and objective decomposition and mapping of bifurcating vessels”. In: *IEEE Transactions on Medical Imaging* 23.6 (2004), pp. 704–13. DOI: [10.1109/TMI.2004.826946](https://doi.org/10.1109/TMI.2004.826946) (cited on pages 86, 142).
- [10] L. Antiga, E. B. Iordache, and A. Remuzzi. “Computational geometry for patient-specific reconstruction and meshing of blood vessels from MR and CT angiography”. In: *IEEE Transactions on Medical Imaging* 22.5 (2003), pp. 674–84. DOI: [10.1109/TMI.2003.812261](https://doi.org/10.1109/TMI.2003.812261) (cited on pages 38, 85, 118, 125).
- [11] A. Appel, F. J. Rohlf, and A. J. Stein. “The haloed line effect for hidden line elimination”. In: *SIGGRAPH Computer Graphics* 13.2 (1979), pp. 151–7. DOI: [10.1145/965103.807437](https://doi.org/10.1145/965103.807437) (cited on page 48).
- [12] M. Arevalillo-Herráez, M. A. Gdeisat, and D. R. Burton. “Hybrid robust and fast algorithm for three-dimensional phase unwrapping”. In: *Applied Optics* 48.32 (2009), pp. 6313–23. DOI: [10.1364/AO.48.006313](https://doi.org/10.1364/AO.48.006313) (cited on page 34).
- [13] H. Arheden, M. Saeed, E. Törnqvist, G. Lund, M. F. Wendland, C. B. Higgins, and F. Ståhlberg. “Accuracy of segmented MR velocity mapping to measure small vessel pulsatile flow in a phantom simulating cardiac motion”. In: *Journal of Magnetic Resonance Imaging* 13.5 (2001), pp. 722–8. DOI: [10.1002/jmri.1100](https://doi.org/10.1002/jmri.1100) (cited on page 33).
- [14] A. Arzani, P. Dyverfeldt, T. Ebberts, and S. C. Shadden. “In vivo validation of numerical prediction for turbulence intensity in an aortic coarctation”. In: *Annals of Biomedical Engineering* 40.4 (2012), pp. 860–70. DOI: [10.1007/s10439-011-0447-6](https://doi.org/10.1007/s10439-011-0447-6) (cited on page 160).
- [15] R. Asmar, A. Benetos, J. Topouchian, P. Laurent, B. Pannier, A. M. Brisac, R. Target, and B. I. Levy. “Assessment of arterial distensibility by automatic pulse wave velocity measurement. Validation and clinical application studies”. In: *Hypertension* 26.3 (1995), pp. 485–90. DOI: [10.1161/01.HYP.26.3.485](https://doi.org/10.1161/01.HYP.26.3.485) (cited on page 68).
- [16] P. Bächler, N. Pinochet, J. Sotelo, G. Crelier, P. Irrazaval, C. Tejos, and S. Uribe. “Assessment of normal flow patterns in the pulmonary circulation by using 4D magnetic resonance velocity mapping”. In: *Journal of Magnetic Resonance Imaging* 31.2 (2013), pp. 178–88. DOI: [10.1016/j.mri.2012.06.036](https://doi.org/10.1016/j.mri.2012.06.036) (cited on pages 58, 76).
- [17] R. Bade, J. Haase, and B. Preim. “Comparison of fundamental mesh smoothing algorithms for medical surface models”. In: *Simulation und Visualisierung*. 2006, pp. 289–304. Link: citeseerx.ist.psu.edu (accessed at 02/2016) (cited on page 85).
- [18] H. Bagher-Ebadian, Q. Jiang, and J. R. Ewing. “A modified Fourier-based phase unwrapping algorithm with an application to MRI venography”. In: *Journal of Magnetic Resonance Imaging* 27.3 (2008), pp. 649–52. DOI: [10.1002/jmri.21230](https://doi.org/10.1002/jmri.21230) (cited on page 34).

- [19] C. J. Bakker, R. M. Hoogeveen, and M. A. Viergever. “Construction of a protocol for measuring blood flow by two-dimensional phase-contrast MRI”. In: *Journal of Magnetic Resonance Imaging* 9.1 (1999), pp. 119–27. DOI: [10.1002/\(SICI\)1522-2586\(199901\)9:1\(119::AID-JMRI16\)3.0.CO;2-F](https://doi.org/10.1002/(SICI)1522-2586(199901)9:1(119::AID-JMRI16)3.0.CO;2-F) (cited on pages 33, 67).
- [20] R. Bammer, T. A. Hope, M. Aksoy, and M. T. Alley. “Time-resolved 3D quantitative flow MRI of the major intracranial vessels: Initial experience and comparative evaluation at 1.5 T and 3.0 T in combination with parallel imaging”. In: *Magnetic Resonance in Medicine* 57.1 (2007), pp. 127–40. DOI: [10.1002/mrm.21109](https://doi.org/10.1002/mrm.21109) (cited on page 21).
- [21] D. C. Banks and B. A. Singer. “Vortex tubes in turbulent flows: Identification, representation, reconstruction”. In: *Proceedings: IEEE Conference on Visualization (Vis)*. 1994, pp. 132–9. DOI: [10.1109/VISUAL.1994.346327](https://doi.org/10.1109/VISUAL.1994.346327) (cited on pages 53, 76).
- [22] A. J. Barker and M. Markl. “The role of hemodynamics in bicuspid aortic valve disease”. In: *European Journal of Cardio-Thoracic Surgery* 39.6 (2011), pp. 805–6. DOI: [10.1016/j.ejcts.2011.01.006](https://doi.org/10.1016/j.ejcts.2011.01.006) (cited on page 60).
- [23] A. J. Barker, J. Bock, R. Lorenz, and M. Markl. *4D flow MR imaging*. Tech. rep. Siemens Healthcare, 2010. Link: [researchgate.net](https://www.researchgate.net) (accessed at 02/2016) (cited on page 91).
- [24] A. J. Barker, M. Markl, J. Bürk, R. Lorenz, J. Bock, S. Bauer, J. Schulz-Menger, and F. von Knobelsdorff-Brenkenhoff. “Bicuspid aortic valve is associated with altered wall shear stress in the ascending aorta”. In: *Circulation. Cardiovascular Imaging* 5.4 (2012), pp. 457–66. DOI: [10.1161/CIRCIMAGING.112.973370](https://doi.org/10.1161/CIRCIMAGING.112.973370) (cited on page 60).
- [25] A. J. Barker, J. D. Robinson, and M. Markl. “Bicuspid aortic valve phenotype and aortopathy: Nomenclature and role of aortic hemodynamics”. In: *JACC: Cardiovascular Imaging* 6.8 (2013), p. 921. DOI: [10.1016/j.jcmg.2013.03.006](https://doi.org/10.1016/j.jcmg.2013.03.006) (cited on pages 60, 116).
- [26] A. J. Barker, P. Van Ooij, K. Bandi, J. Garcia, M. Albaghdadi, P. McCarthy, R. O. Bonow, J. C. Carr, J. Collins, S. C. Malaisrie, and M. Markl. “Viscous energy loss in the presence of abnormal aortic flow”. In: *Journal of Magnetic Resonance in Medicine* 72.3 (2014), pp. 620–8. DOI: [10.1002/mrm.24962](https://doi.org/10.1002/mrm.24962) (cited on page 75).
- [27] H. Baumgartner. “Aortic stenosis: Medical and surgical management”. In: *Heart* 91.11 (2005), pp. 1483–8. DOI: [10.1136/hrt.2004.056176](https://doi.org/10.1136/hrt.2004.056176) (cited on page 16).
- [28] B. Behrendt. “Vollautomatische Visualisierung von kardialen 4D PC-MRI Blutflussdaten mit intelligenter Fokussierung auf Features”. MA thesis. Otto-von-Guericke-University, Magdeburg, Germany, 2015. Link: [vismd.de](https://www.vismd.de) (accessed at 02/2016) (cited on pages 206, 209).
- [29] B. Behrendt, B. Köhler, and B. Preim. “Enhancing visibility of blood flow in volume rendered cardiac 4D PC-MRI data”. In: *Proceedings: Bildverarbeitung für die Medizin*. 2016, pp. 188–93 (cited on pages 45, 206).
- [30] M. Belohlavek. “Vortex formation time: An emerging echocardiographic index of left ventricular filling efficiency?” In: *European Heart Journal - Cardiovascular Imaging* 13.5 (2012), pp. 367–9. DOI: [10.1093/ejehocard/jer311](https://doi.org/10.1093/ejehocard/jer311) (cited on page 61).
- [31] R. V. Bergen, H. Y. Lin, M. E. Alexander, and C. P. Bidinosti. “4D MR phase and magnitude segmentations with GPU parallel computing”. In: *Journal of Magnetic Resonance Imaging* 33.1 (2015), pp. 134–45. DOI: [10.1016/j.mri.2014.08.019](https://doi.org/10.1016/j.mri.2014.08.019) (cited on pages 39, 40).
- [32] M. A. Bernstein, X. J. Zhou, J. A. Polzin, K. F. King, A. Ganin, N. J. Pelc, and G. H. Glover. “Concomitant gradient terms in phase contrast MR: Analysis and correction”. In: *Journal of Magnetic Resonance in Medicine* 39.2 (1998), pp. 300–8. DOI: [10.1002/mrm.1910390218](https://doi.org/10.1002/mrm.1910390218) (cited on page 35).
- [33] M. A. Bernstein, K. F. King, and X. J. Zhou. *Handbook of MRI pulse sequences*. Elsevier, 2004. ISBN: 978-0120928613 (cited on page 23).
- [34] A. Bhalerao, C.-F. Westin, and R. Kikinis. “Unwrapping phase in 3D MR phase contrast angiograms”. In: *Proceedings: First Joint Conference on Computer Vision, Virtual Reality and Robotics in Medicine and Medial Robotics and Computer-Assisted Surgery*. 1997, pp. 193–202. DOI: [10.1007/BFb0029238](https://doi.org/10.1007/BFb0029238) (cited on page 34).
- [35] E. T. Biegging, A. Frydrychowicz, A. L. Wentland, B. R. Landgraf, K. M. Johnson, O. Wieben, and C. J. François. “In vivo three-dimensional MR wall shear stress estimation in ascending aortic dilatation”. In: *Journal of Magnetic Resonance Imaging* 33.3 (2011), pp. 589–97. DOI: [10.1002/jmri.22485](https://doi.org/10.1002/jmri.22485) (cited on page 73).
- [36] E. A. Bier, M. C. Stone, K. Pier, W. Buxton, and T. D. DeRose. “Toolglass and magic lenses: The see-through interface”. In: *Proceedings: 20th Annual Conference on Computer Graphics and Interactive Techniques (SIGGRAPH)*. 1993, pp. 73–80. DOI: [10.1145/166117.166126](https://doi.org/10.1145/166117.166126) (cited on page 50).
- [37] C. Binter, V. Knobloch, R. Manka, A. Sigfridsson, and S. Kozerke. “Bayesian multipoint velocity encoding for concurrent flow and turbulence mapping”. In: *Journal of Magnetic Resonance Imaging* 69.5 (2013), pp. 1337–45. DOI: [10.1002/mrm.24370](https://doi.org/10.1002/mrm.24370) (cited on page 76).
- [38] C. Binter, U. Gülan, M. Holzner, and S. Kozerke. “On the accuracy of viscous and turbulent loss quantification in stenotic aortic flow using phase-contrast MRI”. In: *Journal of Magnetic Resonance in Medicine* 76.1 (2016), pp. 191–6. DOI: [10.1002/mrm.25862](https://doi.org/10.1002/mrm.25862) (cited on page 76).

- [39] J. M. Bioucas-Dias and G. Valadão. “Phase unwrapping via graph cuts”. In: *IEEE Transactions on Image Processing* 16.3 (2007), pp. 698–709. DOI: [10.1109/TIP.2006.888351](https://doi.org/10.1109/TIP.2006.888351) (cited on page 33).
- [40] M. M. Bissell, A. T. Hess, L. Biasioli, S. J. Glaze, M. Loudon, A. Pitcher, A. Davis, B. Prendergast, M. Markl, A. J. Barker, S. Neubauer, and S. G. Myerson. “Aortic dilation in bicuspid aortic valve disease: Flow pattern is a major contributor and differs with valve fusion type”. In: *Circulation: Cardiovascular Imaging* 6.4 (2013), pp. 499–507. DOI: [10.1161/CIRCIMAGING.113.000528](https://doi.org/10.1161/CIRCIMAGING.113.000528) (cited on pages 7, 60, 116).
- [41] M. M. Bissell, A. T. Hess, S. J. Glaze, A. Pitcher, M. D. Robson, A. J. Barker, S. Myerson, and S. Neubauer. “Cusp fusion pattern in bicuspid aortic valve disease predicts severity of aortic flow abnormalities”. In: *Journal of Cardiovascular Magnetic Resonance* 15.Suppl 1 (2013), O69. DOI: [10.1186/1532-429X-15-S1-O69](https://doi.org/10.1186/1532-429X-15-S1-O69) (cited on pages 60, 116).
- [42] A. Biswas, W. He, Q. Deng, C.-M. Chen, H.-W. Shen, R. Machiraju, and A. Rangarajan. “An uncertainty-driven approach to vortex analysis using oracle consensus and spatial proximity”. In: *Proceedings: IEEE Pacific Visualization Symposium (PacificVis)*. 2015, pp. 223–30. DOI: [10.1109/PACIFICVIS.2015.7156381](https://doi.org/10.1109/PACIFICVIS.2015.7156381) (cited on page 55).
- [43] J. Blacher, R. Asmar, S. Djane, G. M. London, and Safar. M. E. “Aortic pulse wave velocity as a marker of cardiovascular risk in hypertensive patients”. In: *Hypertension* 33.5 (1999), pp. 1111–7. DOI: [10.1161/01.HYP.33.5.1111](https://doi.org/10.1161/01.HYP.33.5.1111) (cited on page 67).
- [44] Blausen.com staff. “Blausen gallery 2014”. In: *Wikiversity Journal of Medicine* (2014). DOI: [10.15347/wjm/2014.010](https://doi.org/10.15347/wjm/2014.010). Link: en.wikiversity.org (accessed at 02/2016) (cited on pages 13, 15, 16).
- [45] J. Bock. “Development and testing of new strategies for pre-processing and analysis of 4D flow-sensitive MRI data”. PhD thesis. Albert-Ludwigs-University, Freiburg, Germany, 2012. Link: [urn:nbn:de:bsz:25-opus-90260](https://nbn-resolving.org/urn:nbn:de:bsz:25-opus-90260) (accessed at 02/2016) (cited on page 35).
- [46] J. Bock, B. Kreher, J. Henning, and M. Markl. “Optimized pre-processing of time-resolved 2D and 3D phase contrast MRI data”. In: *Proceedings: International Society for Magnetic Resonance in Medicine*. 2007, p. 3138. Link: cds.ismrm.org (accessed at 02/2016) (cited on pages 33, 35).
- [47] J. Bock, O. Wieben, K. Johnson, J. Hennig, and M. Markl. “Optimal processing to derive static PC-MRA from time-resolved 3D PC-MRI data”. In: *Proceedings: International Society for Magnetic Resonance in Medicine*. 2008, p. 3053. Link: cds.ismrm.org (accessed at 02/2016) (cited on page 37).
- [48] J. Bock, A. Frydrychowicz, R. Lorenz, D. Hirtler, A. J. Barker, K. M. Johnson, R. Arnold, H. Burkhardt, J. Hennig, and M. Markl. “In vivo noninvasive 4D pressure difference mapping in the human aorta: Phantom comparison and application in healthy volunteers and patients”. In: *Journal of Magnetic Resonance Imaging* 66.4 (2011), pp. 1079–88. DOI: [10.1002/mrm.22907](https://doi.org/10.1002/mrm.22907) (cited on page 75).
- [49] T. Boerma, C. Mathers, C. AbouZahr, S. Chatterji, D. Hogan, G. Stevens, R. W. Mahanani, J. Ho, F. Rusciano, G. Humphreys, and World Health Organization. *Health in 2015: From millenium development goals to sustainable development goals*. 2015. Link: apps.who.int (accessed at 02/2016) (cited on page 14).
- [50] J. M. Boese, M. Bock, S. O. Schoenberg, and L. R. Schad. “Estimation of aortic compliance using magnetic resonance pulse wave velocity measurement”. In: *Physics in Medicine and Biology* 45.6 (2000), pp. 1703–13. DOI: [10.1088/0031-9155/45/6/320](https://doi.org/10.1088/0031-9155/45/6/320) (cited on page 67).
- [51] H. G. Bogren and M. H. Buonocore. “Blood flow measurements in the aorta and major arteries with MR velocity mapping”. In: *Journal of Magnetic Resonance Imaging* 4.2 (1994), pp. 119–30. DOI: [10.1002/jmri.1880040204](https://doi.org/10.1002/jmri.1880040204) (cited on page 66).
- [52] H. G. Bogren and M. H. Buonocore. “4D magnetic resonance velocity mapping of blood flow patterns in the aorta in young vs. elderly normal subjects”. In: *Journal of Magnetic Resonance Imaging* 10.5 (1999), pp. 861–9. DOI: [10.1002/\(SICI\)1522-2586\(199911\)10:5<861::AID-JMRI35>3.0.CO;2-E](https://doi.org/10.1002/(SICI)1522-2586(199911)10:5<861::AID-JMRI35>3.0.CO;2-E) (cited on page 57).
- [53] H. G. Bogren and M. H. Buonocore. “Complex flow patterns in the great vessels: A review”. In: *International Journal of Cardiac Imaging* 15.2 (1999), pp. 105–13. DOI: [10.1023/A:1006281923372](https://doi.org/10.1023/A:1006281923372) (cited on page 56).
- [54] H. G. Bogren, R. H. Klipstein, R. H. Mohiaddin, D. N. Firmin, S. R. Underwood, R. S. O. Rees, and D. B. Longmore. “Pulmonary artery distensibility and blood flow patterns: A magnetic resonance study of normal subjects and of patients with pulmonary arterial hypertension”. In: *American Heart Journal* 118.5 Pt. 1 (1989), pp. 990–9. DOI: [10.1016/0002-8703\(89\)90235-4](https://doi.org/10.1016/0002-8703(89)90235-4) (cited on page 58).
- [55] H. G. Bogren, R. H. Mohiaddin, G. Z. Yang, P. J. Kilner, and D. N. Firmin. “Magnetic resonance velocity vector mapping of blood flow in thoracic aortic aneurysms and grafts”. In: *The Journal of Thoracic and Cardiovascular Surgery* 110.3 (1995), pp. 704–14. DOI: [10.1016/S0022-5223\(95\)70102-8](https://doi.org/10.1016/S0022-5223(95)70102-8) (cited on page 61).
- [56] H. G. Bogren, R. H. Mohiaddin, P. J. Kilner, L. J. Jimenez-Borreguero, G. Z. Yang, and D. N. Firmin. “Blood flow patterns in the thoracic aorta studied with three-directional MR velocity mapping: The effects of age and coronary artery disease”. In: *Journal of Magnetic Resonance Imaging* 7.5 (1997), pp. 784–93. DOI: [10.1002/jmri.1880070504](https://doi.org/10.1002/jmri.1880070504) (cited on pages 57, 58).

- [57] R. O. Bonow, B. Carabello, A. C. de Leon Jr., L. H. Edmunds Jr., B. J. Fedderly, M. D. Freed, W. H. Gaasch, C. R. McKay, R. A. Nishimura, P. T. O’Gara, R. A. O’Rourke, S. H. Rahimtoola, J. L. Ritchie, M. D. Cheitlin, K. A. Eagle, T. J. Gardner, A. Garson Jr., R. J. Gibbons, R. O. Russell, T. J. Ryan, and S. C. Smith Jr. “Guidelines for the management of patients with valvular heart disease. Executive summary. A report of the American College of Cardiology / American Heart Association task force on practice guidelines (Committee on management of patients with valvular heart disease)”. In: *Circulation* 98.18 (1998), pp. 1949–84. DOI: [10.1161/01.CIR.98.18.1949](https://doi.org/10.1161/01.CIR.98.18.1949) (cited on page 16).
- [58] A. O. Borisyuk. “Experimental study of noise produced by steady flow through a simulated vascular stenosis”. In: *Journal of Sound and Vibration* 256.3 (2002), pp. 475–98. DOI: [10.1006/jsvi.2002.5001](https://doi.org/10.1006/jsvi.2002.5001) (cited on page 70).
- [59] D. Borland and R. M. Taylor. “Rainbow color map (still) considered harmful”. In: *IEEE Computer Graphics and Applications* 27.2 (2007), pp. 14–7. DOI: [10.1109/MCG.2007.323435](https://doi.org/10.1109/MCG.2007.323435) (cited on page 46).
- [60] S. Born. “Illustrative flow visualization of 4D PC-MRI blood flow and CFD data”. PhD thesis. University of Leipzig, Germany, 2014. Link: [urn:nbn:de:bsz:15-qucosa-154354](https://nbn-resolving.org/urn:nbn:de:bsz:15-qucosa-154354) (accessed at 02/2016) (cited on pages 48–51, 53).
- [61] S. Born, A. Wiebel, J. Friedrich, G. Scheuermann, and D. Bartz. “Illustrative stream surfaces”. In: *IEEE Transactions on Visualization and Computer Graphics* 16.6 (2010), pp. 1329–38. DOI: [10.1109/TVCG.2010.166](https://doi.org/10.1109/TVCG.2010.166) (cited on page 50).
- [62] S. Born, M. Markl, M. Gutberlet, and G. Scheuermann. “Illustrative visualization of cardiac and aortic blood flow from 4D MRI Data”. In: *Proceedings: IEEE Pacific Visualization Symposium (PacificVis)*. 2013, pp. 129–36. DOI: [10.1109/PacificVis.2013.6596137](https://doi.org/10.1109/PacificVis.2013.6596137) (cited on pages 51, 117).
- [63] S. Born, M. Pfeifle, M. Markl, M. Gutberlet, and G. Scheuermann. “Visual analysis of cardiac 4D MRI blood flow using line predicates”. In: *IEEE Transactions on Visualization and Computer Graphics* 19 (2013), pp. 900–12. DOI: [10.1109/TVCG.2012.318](https://doi.org/10.1109/TVCG.2012.318) (cited on pages 49, 51, 53, 97, 102, 108).
- [64] E. Bostan, O. Vardoulis, D. Piccini, P. D. Tafti, N. Stergiopoulos, and M. Unser. “Spatio-temporal regularization of flow-fields”. In: *Proceedings: IEEE International Symposium on Biomedical Imaging*. 2013, pp. 824–7. DOI: [10.1109/ISBI.2013.6556605](https://doi.org/10.1109/ISBI.2013.6556605) (cited on page 36).
- [65] E. Bostan, S. Lefkimmiatis, O. Vardoulis, N. Stergiopoulos, and M. Unser. “Improved variational denoising of flow fields with application to phase-contrast MRI data”. In: *IEEE Signal Processing Letters* 22.6 (2015), pp. 762–6. DOI: [10.1109/LSP.2014.2369212](https://doi.org/10.1109/LSP.2014.2369212) (cited on page 37).
- [66] N. Boukhelifa and D. J. Duke. “Uncertainty visualization – Why might it fail?” In: *Proceedings: ACM Conference on Human Factors in Computing Systems (CHI)*. 2009, pp. 4051–6. Link: [delivery.acm.org](https://dl.acm.org/) (accessed at 03/2016) (cited on page 48).
- [67] L. Boussel, V. Rayz, C. McCulloch, A. Martin, G. Acevedo-Bolton, M. Lawton, R. Higashida, W. S. Smith, W. L. Young, and D. Saloner. “Aneurysm growth occurs at region of low wall shear stress patient-specific correlation of hemodynamics and growth in a longitudinal study”. In: *Stroke* 39.11 (2008), pp. 2997–3002. DOI: [10.1161/STROKEAHA.108.521617](https://doi.org/10.1161/STROKEAHA.108.521617) (cited on page 73).
- [68] Y. Boykov and V. Kolmogorov. “An experimental comparison of min-cut / max-flow algorithms for energy minimization in vision”. In: *IEEE Transactions on Pattern Analysis and Machine Intelligence* 26.9 (2004), pp. 1124–37. DOI: [10.1109/TPAMI.2004.60](https://doi.org/10.1109/TPAMI.2004.60) (cited on pages 39, 84).
- [69] A. Brambilla and H. Hauser. “Expressive seeding of multiple stream surfaces for interactive flow exploration”. In: *Computers & Graphics* 47.C (2015), pp. 123–34. DOI: [10.1016/j.cag.2015.01.002](https://doi.org/10.1016/j.cag.2015.01.002) (cited on page 50).
- [70] A. Brambilla, R. Carnecky, R. Peikert, I. Viola, and H. Hauser. “Illustrative flow visualization: State of the art, trends and challenges”. In: *Proceedings: Eurographics - State of the Art Reports*. 2012. DOI: [10.2312/conf/EG2012/stars/075-094](https://doi.org/10.2312/conf/EG2012/stars/075-094) (cited on page 48).
- [71] J. C. Bramwell and A. V. Hill. “The velocity of the pulse wave in man”. In: *Proceedings of the Royal Society of London B: Biological Sciences* 93.652 (1922), pp. 298–306. DOI: [10.1098/rspb.1922.0022](https://doi.org/10.1098/rspb.1922.0022) (cited on page 67).
- [72] A. Brandts, S. G. van Elderen, J. J. M. Westenberg, J. van der Grond, M. A. van Buchem, M. V. Huisman, L. J. Kroft, J. T. Tamsma, and A. de Roos. “Association of aortic arch pulse wave velocity with left ventricular mass and lacunar brain infarcts in hypertensive patients: Assessment with MR imaging”. In: *Radiology* 253.3 (2009), pp. 681–8. DOI: [10.1148/radiol.2533082264](https://doi.org/10.1148/radiol.2533082264) (cited on page 67).
- [73] S. L. Brunton and C. W. Rowley. “Fast computation of finite-time Lyapunov exponent fields for unsteady flows”. In: *Chaos: An Interdisciplinary Journal of Nonlinear Science* 20.1 (2010), p. 017503. DOI: [10.1063/1.3270044](https://doi.org/10.1063/1.3270044) (cited on page 77).
- [74] D. J. Bryant, J. A. Payne, D. N. Firmin, and D. B. Longmore. “Measurement of flow with NMR imaging using a gradient pulse and phase difference technique”. In: *Journal of Computer Assisted Tomography* 8.4 (1984), pp. 588–93. DOI: [10.1097/00004728-198408000-00002](https://doi.org/10.1097/00004728-198408000-00002) (cited on page 7).
- [75] M. H. Buonocore. “Blood flow measurement using variable velocity encoding in the RR interval”. In: *Journal of Magnetic Resonance in Medicine* 29.6 (1993), pp. 790–5. DOI: [10.1002/mrm.1910290611](https://doi.org/10.1002/mrm.1910290611) (cited on page 26).

- [76] M. H. Buonocore. “Visualizing blood flow patterns using streamlines, arrows, and particle paths”. In: *Journal of Magnetic Resonance in Medicine* 40.2 (1998), pp. 210–26. DOI: [10.1002/mrm.1910400207](https://doi.org/10.1002/mrm.1910400207) (cited on page 47).
- [77] K. Bürger, J. Schneider, P. Kondratieva, J. Krüger, and R. Westermann. “Interactive visual exploration of instationary 3D-flows”. In: *Proceedings: Eurographics Conference on Visualization (EuroVis)*. 2007, pp. 251–8. DOI: [10.2312/VisSym/EuroVis07/251-258](https://doi.org/10.2312/VisSym/EuroVis07/251-258) (cited on page 50).
- [78] J. Bürk, P. Blanke, Z. Stankovic, A. J. Barker, M. Russe, J. Geiger, A. Frydrychowicz, M. Langer, and M. Markl. “Evaluation of 3D blood flow patterns and wall shear stress in the normal and dilated thoracic aorta using flow-sensitive 4D CMR”. In: *Journal of Cardiovascular Magnetic Resonance* 14.84 (2012). DOI: [10.1186/1532-429X-14-84](https://doi.org/10.1186/1532-429X-14-84) (cited on pages 60, 65).
- [79] N. S. Burris, M. Sigovan, H. A. Knauer, E. E. Tseng, D. Saloner, and M. D. Hope. “Systolic flow displacement correlates with future ascending aortic growth in patients with bicuspid aortic valves undergoing magnetic resonance surveillance”. In: *Investigative Radiology* 49.10 (2014), pp. 635–9. DOI: [10.1097/RLI.000000000000064](https://doi.org/10.1097/RLI.000000000000064) (cited on pages 7, 71).
- [80] M. Bußler, T. Rick, A. Kelle-Emden, B. Hentschel, and T. Kuhlen. “Interactive particle tracing in time-varying tetrahedral grids”. In: *Proceedings: 11th Eurographics Conference on Parallel Graphics and Visualization*. 2011, pp. 71–80. DOI: [10.2312/EGPGV/EGPGV11/071-080](https://doi.org/10.2312/EGPGV/EGPGV11/071-080) (cited on page 50).
- [81] M. Bustamante, S. Petersson, J. Eriksson, U. Alehagen, P. Dyverfeldt, C. J. Carlhäll, and T. Ebbers. “Atlas-based analysis of 4D flow CMR: Automated vessel segmentation and flow quantification”. In: *Journal of Cardiovascular Magnetic Resonance* 17.87 (2015), Epub. DOI: [10.1186/s12968-015-0190-5](https://doi.org/10.1186/s12968-015-0190-5) (cited on page 40).
- [82] B. Cabral and L. C. Leedom. “Imaging vector fields using line integral convolution”. In: *Proceedings: 20th Annual Conference on Computer Graphics and Interactive Techniques (SIGGRAPH)*. 1993, pp. 263–70. DOI: [10.1145/166117.166151](https://doi.org/10.1145/166117.166151) (cited on page 46).
- [83] E. E. Calkoen, A. A. W. Roest, R. J. Van der Geest, A. De Roos, and J. J. M. Westenberg. “Cardiovascular function and flow by 4-dimensional magnetic resonance imaging techniques: New applications”. In: *Journal of Thoracic Imaging* 29.3 (2014), pp. 185–96. DOI: [10.1097/RTI.000000000000068](https://doi.org/10.1097/RTI.000000000000068) (cited on pages 8, 162).
- [84] E. E. Calkoen, A. A. W. Roest, L. J. Kroft, P. J. Van den Boogaard, M. R. Jongbloed, R. J. Van der Geest, A. De Roos, and J. J. M. Westenberg. “The added value of streamline visualization in the evaluation of left atrioventricular valve flow and left ventricular diastolic function with 4D flow MRI”. In: *Journal of Cardiovascular Magnetic Resonance* 16.Suppl 1 (2014), P353. DOI: [10.1186/1532-429X-16-S1-P353](https://doi.org/10.1186/1532-429X-16-S1-P353) (cited on page 56).
- [85] E. E. Calkoen, J. J. M. Westenberg, L. J. M. Kroft, N. A. Blom, M. G. Hazekamp, M. E. Rijlaarsdam, M. R. M. Jongbloed, A. de Roos, and A. A. W. Roest. “Characterization and quantification of dynamic eccentric regurgitation of the left atrioventricular valve after atrioventricular septal defect correction with 4D flow cardiovascular magnetic resonance and retrospective valve tracking”. In: *Journal of Cardiovascular Magnetic Resonance* 17.1 (2015), p. 18. DOI: [10.1186/s12968-015-0122-4](https://doi.org/10.1186/s12968-015-0122-4) (cited on page 56).
- [86] J. Canny. “A computational approach to edge detection”. In: *IEEE Transactions on Pattern Analysis and Machine Intelligence* 8.6 (1986), pp. 679–98. DOI: [10.1109/TPAMI.1986.4767851](https://doi.org/10.1109/TPAMI.1986.4767851) (cited on page 40).
- [87] L. Cardamone and J. D. Humphrey. “Arterial growth and remodelling is driven by hemodynamics”. In: *Modeling of Physiological Flows*. Vol. 5. 2012, pp. 187–203. DOI: [10.1007/978-88-470-1935-5_7](https://doi.org/10.1007/978-88-470-1935-5_7) (cited on page 73).
- [88] C. J. Carlhäll and A. F. Bolger. “Passing strange flow in the failing ventricle”. In: *Circulation: Heart Failure* 3.2 (2010), pp. 326–31. DOI: [10.1161/CIRCHEARTFAILURE.109.911867](https://doi.org/10.1161/CIRCHEARTFAILURE.109.911867) (cited on page 56).
- [89] C. J. Carlhäll, A. G. Fredriksson, J. Zajac, J. Eriksson, P. Dyverfeldt, J. Engvall, A. F. Bolger, and T. Ebbers. “Visualization and quantification of 4D blood flow distribution and energetics in the right ventricle”. In: *Journal of Cardiovascular Magnetic Resonance* 13.Suppl 1 (2011), O83. DOI: [10.1186/1532-429X-13-S1-O83](https://doi.org/10.1186/1532-429X-13-S1-O83) (cited on page 57).
- [90] M. Carlsson, E. Heiberg, J. Töger, K. Markenroth, F. Ståhlberg, and H. Arheden. “Quantification of left and right ventricular kinetic energy using four dimensional intracardiac magnetic resonance imaging flow measurements”. In: *Proceedings: International Society for Magnetic Resonance in Medicine*. 2010, p. 1358. DOI: [10.1152/ajpheart.00942.2011](https://doi.org/10.1152/ajpheart.00942.2011) (cited on page 76).
- [91] M. Carlsson, E. Heiberg, J. Töger, and H. Arheden. “Quantification of left and right ventricular kinetic energy using four-dimensional intracardiac magnetic resonance imaging flow measurements”. In: *American Journal of Physiology - Heart and Circulatory Physiology* 302.4 (2012), H893–H900. DOI: [10.1152/ajpheart.00942.2011](https://doi.org/10.1152/ajpheart.00942.2011) (cited on page 76).
- [92] B. S. Carmo, Y. H. P. Ng, A. Prügel-Bennett, and G.-Z. Yang. “A data clustering and streamline reduction method for 3D MR flow vector field simplification”. In: *Proceedings: Medical Image Computing and Computer Assisted Intervention*. 2004, pp. 451–8. DOI: [10.1007/978-3-540-30135-6_55](https://doi.org/10.1007/978-3-540-30135-6_55) (cited on page 51).
- [93] R. Carnecky, R. Fuchs, S. Mehl, Y. Jang, and R. Peikert. “Smart transparency for illustrative visualization of complex flow surfaces”. In: *IEEE Transactions on Visualization and Computer Graphics* 19.5 (2013), pp. 838–51. DOI: [10.1109/TVCG.2012.159](https://doi.org/10.1109/TVCG.2012.159) (cited on page 50).

- [94] R. Carnecky, S. Brunner T. Born, J. Waser, C. Heine, and R. Peikert. "Vortex detection in 4D MRI data: Using the proper orthogonal decomposition for improved noise-robustness". In: *Proceedings: Eurographics Conference on Visualization (EuroVis) - Short Papers*. 2014, pp. 127–31. DOI: [10.2312/eurovisshort.20141169](https://doi.org/10.2312/eurovisshort.20141169) (cited on page 108).
- [95] V. Caselles, R. Kimmel, and G. Sapiro. "Geodesic active contours". In: *International Journal of Computer Vision* 22.1 (1997), pp. 61–79. DOI: [10.1023/A:1007979827043](https://doi.org/10.1023/A:1007979827043) (cited on page 39).
- [96] M. A. Castro, M. C. Ahumada Olivares, C. M. Putman, and J. R. Cebal. "Intracranial aneurysm wall motion and wall shear stress from 4D computerized tomographic angiography images". In: *Proceedings: International Society for Optics and Photonics (SPIE)*. 2013, p. 8672. DOI: [10.1117/12.2005982](https://doi.org/10.1117/12.2005982) (cited on pages 73, 112).
- [97] E. Cecchi, C. Giglioli, S. Valente, C. Lazzeri, G. F. Gensini, R. Abbate, and L. Mannini. "Role of hemodynamic shear stress in cardiovascular disease". In: *Atherosclerosis* 214.2 (2011), pp. 249–56. DOI: [10.1016/j.atherosclerosis.2010.09.008](https://doi.org/10.1016/j.atherosclerosis.2010.09.008) (cited on page 73).
- [98] M. D. Cerqueira, N. J. Weissman, V. Dilsizian, A. K. Jacobs, S. Kaul, W. K. Laskey, D. J. Pennell, J. A. Rumberger, T. Ryan, and M. S. Verani. "Standardized myocardial segmentation and nomenclature for tomographic imaging of the heart: A statement for healthcare professionals from the cardiac imaging committee of the council on clinical cardiology of the American Heart Association". In: *Circulation* 105.4 (2002), pp. 539–42. DOI: [10.1161/hc0402.102975](https://doi.org/10.1161/hc0402.102975) (cited on page 108).
- [99] P. Chakraborty, S. Balachandrar, and R. J. Adrian. "On the relationships between local vortex identification schemes". In: *Journal of Fluid Mechanics* 535 (2005), pp. 189–214. DOI: [10.1017/S0022112005004726](https://doi.org/10.1017/S0022112005004726) (cited on page 53).
- [100] Y. Chen, J. Cohen, and J. Krolík. "Similarity-guided streamline placement with error evaluation". In: *IEEE Transactions on Visualization and Computer Graphics* 13.6 (2007), pp. 1448–55. DOI: [10.1109/TVCG.2007.70595](https://doi.org/10.1109/TVCG.2007.70595) (cited on page 47).
- [101] C. P. Cheng, D. Parker, and C. A. Taylor. "Quantification of wall shear stress in large blood vessels using Lagrangian interpolation functions with cine phase-contrast magnetic resonance imaging". In: *Annals of Biomedical Engineering* 30.8 (2002), pp. 1020–32. DOI: [10.1114/1.1511239](https://doi.org/10.1114/1.1511239) (cited on page 72).
- [102] A. Chernobelsky, O. Shubayev, C. R. Comeau, and S. D. Wolff. "Baseline correction of phase contrast images improves quantification of blood flow in the great vessels". In: *Journal of Cardiovascular Magnetic Resonance* 9.4 (2007), pp. 681–5. Link: tandfonline.com (accessed at 02/2016) (cited on page 35).
- [103] A. C. S. Chung, J. A. Noble, and P. Summers. "Vascular segmentation of phase contrast magnetic resonance angiograms based on statistical mixture modeling and local phase coherence". In: *IEEE Transactions on Medical Imaging* 23.12 (2004), pp. 1490–507. DOI: [10.1109/TMI.2004.836877](https://doi.org/10.1109/TMI.2004.836877) (cited on page 38).
- [104] C. Clark. "Turbulent velocity measurements in a model of aortic stenosis". In: *Journal of Biomechanics* 9.11 (1976), pp. 677–87. DOI: [10.1016/0021-9290\(76\)90169-X](https://doi.org/10.1016/0021-9290(76)90169-X) (cited on page 75).
- [105] A. Cockburn, A. Karlson, and B. B. Bederson. "A review of overview+detail, zooming, and focus+context interfaces". In: *ACM Computing Surveys* 41.1 (2009), 2:1–31. DOI: [10.1145/1456650.1456652](https://doi.org/10.1145/1456650.1456652) (cited on page 50).
- [106] I. Corouge, S. Gouttard, and G. Gerig. "Towards a shape model of white matter fiber bundles using diffusion tensor MRI". In: *Proceedings: IEEE International Symposium on Biomedical Imaging: Nano to Macro*. 2004, pp. 344–7. DOI: [10.1109/ISBI.2004.1398545](https://doi.org/10.1109/ISBI.2004.1398545) (cited on page 52).
- [107] J. Cousty, L. Najman, M. Couprie, S. C. Guinaudeau, T. Goissen, and J. Garot. "Segmentation of 4D cardiac MRI: Automated method based on spatio-temporal watershed cuts". In: *Image and Vision Computing* 28.8 (2010), pp. 1229–43. DOI: [10.1016/j.imavis.2010.01.001](https://doi.org/10.1016/j.imavis.2010.01.001) (cited on page 148).
- [108] M. Crapper, T. Bruce, and C. Gouble. "Flow field visualization of sediment-laden flow using ultrasonic imaging". In: *Dynamics of Atmospheres and Oceans* 31.1-4 (2000), pp. 233–45. DOI: [10.1016/S0377-0265\(99\)00035-4](https://doi.org/10.1016/S0377-0265(99)00035-4) (cited on page 29).
- [109] S. J. Crick, M. N. Shepard, S. Y. Ho, L. Gebstein, and R. H. Anderson. "Anatomy of the pig heart: Comparisons with normal human cardiac structure". In: *Journal of Anatomy* 193.1 (1998), pp. 105–19. DOI: [10.1046/j.1469-7580.1998.19310105.x](https://doi.org/10.1046/j.1469-7580.1998.19310105.x) (cited on page 107).
- [110] S. E. Crook and M. D. Hope. "Arch hypoplasia and aneurysm after aortic coarctation repair: Abnormal flow may be the link". In: *JACC: Cardiovascular Imaging* 4.6 (2011), pp. 685–6. DOI: [10.1016/j.jcmg.2011.02.016](https://doi.org/10.1016/j.jcmg.2011.02.016) (cited on page 59).
- [111] R. Cusack and N. Papadakis. "New robust 3-D phase unwrapping algorithms: Application to magnetic field mapping and undistorting echoplanar images". In: *Neuroimage* 16.3 (2002), pp. 754–64. DOI: [10.1006/nimg.2002.1092](https://doi.org/10.1006/nimg.2002.1092) (cited on page 33).
- [112] T. E. David. "Aortic valve sparing operations: A review". In: *The Korean Journal of Thoracic and Cardiovascular Surgery* 45.4 (2012), pp. 205–12. DOI: [10.5090/kjtc.2012.45.4.205](https://doi.org/10.5090/kjtc.2012.45.4.205) (cited on page 16).
- [113] W. H. E. Day and H. Edelsbrunner. "Efficient algorithms for agglomerative hierarchical clustering methods". In: *Journal of Classification* 1.1 (1984), pp. 7–24. DOI: [10.1007/BF01890115](https://doi.org/10.1007/BF01890115) (cited on page 118).

- [114] N. De Hoon, R. F. P. Van Pelt, A. Jalba, and A. Vilanova. “4D MRI flow coupled to physics-based fluid simulation for blood-flow visualization”. In: *Computer Graphics Forum* 33.3 (2014), pp. 121–30. DOI: [10.1111/cgf.12368](https://doi.org/10.1111/cgf.12368) (cited on page 160).
- [115] D. DeCarlo, A. Finkelstein, S. Rusinkiewicz, and A. Santella. “Suggestive contours for conveying shape”. In: *ACM Transactions on Graphics* 22.3 (2003), pp. 848–55. DOI: [10.1145/882262.882354](https://doi.org/10.1145/882262.882354) (cited on page 44).
- [116] P. Decaudin. *Cartoon looking rendering of 3D scenes*. Research Report 2919. INRIA, 1996. Link: phildec.users.sf.net (accessed at 03/2016) (cited on page 44).
- [117] P. M. den Reijer, D. Sallee, P. van der Velden, E. R. Zaaijer, W. J. Parks, S. Ramamurthy, T. Q. Robbie, G. Donati, C. Lamphier, R. P. Beekman, and M. E. Brummer. “Hemodynamic predictors of aortic dilatation in bicuspid aortic valve by velocity-encoded cardiovascular magnetic resonance”. In: *Journal of Cardiovascular Magnetic Resonance* 12.4 (2010). DOI: [10.1186/1532-429X-12-4](https://doi.org/10.1186/1532-429X-12-4) (cited on page 70).
- [118] C. Díaz and L. A. Robles. “Fast noncontinuous path phase-unwrapping algorithm based on gradients and mask”. In: *Proceedings: Iberoamerican Congress on Pattern Recognition (CIARP)*. 2004, pp. 116–23. DOI: [10.1007/978-3-540-30463-0_14](https://doi.org/10.1007/978-3-540-30463-0_14) (cited on page 85).
- [119] A. Dogui, A. Redheuil, M. Lefort, A. DeCesare, N. Kachenoura, A. Herment, and E. Mousseaux. “Measurement of aortic arch pulse wave velocity in cardiovascular MR: Comparison of transit time estimators and description of a new approach”. In: *Journal of Magnetic Resonance Imaging* 33.6 (2011), pp. 1321–9. DOI: [10.1002/jmri.22570](https://doi.org/10.1002/jmri.22570) (cited on page 68).
- [120] E. Donal, G. M. Novaro, D. Deserrano, Z. B. Popovic, N. L. Greenberg, K. E. Richards, J. D. Thomas, and M. J. Garcia. “Planimetric assessment of anatomic valve area overestimates effective orifice area in bicuspid aortic stenosis”. In: *Journal of the American Society of Echocardiography* 18.12 (2005), pp. 1392–8. DOI: [10.1016/j.echo.2005.04.005](https://doi.org/10.1016/j.echo.2005.04.005) (cited on page 70).
- [121] F. Donati, D. A. Nordsletten, N. P. Smith, and P. Lamata. “Pressure mapping from flow imaging: Enhancing computation of the viscous term through velocity reconstruction in near-wall regions”. In: *Proceedings: IEEE Engineering in Medicine and Biology*. 2014, pp. 5097–100. DOI: [10.1109/EMBC.2014.6944771](https://doi.org/10.1109/EMBC.2014.6944771) (cited on page 75).
- [122] F. Donati, C. A. Figueroa, N. P. Smith, P. Lamata, and D. A. Nordsletten. “Non-invasive pressure difference estimation from PC-MRI using the work-energy equation”. In: *Medical Image Analysis* 26.1 (2015), pp. 159–72. DOI: [10.1016/j.media.2015.08.012](https://doi.org/10.1016/j.media.2015.08.012) (cited on page 75).
- [123] H. Dormand and R. H. Mohiaddin. “Cardiovascular magnetic resonance in Marfan syndrome”. In: *Journal of Cardiovascular Magnetic Resonance* 15.33 (2013). DOI: [10.1186/1532-429X-15-33](https://doi.org/10.1186/1532-429X-15-33) (cited on pages 17, 18).
- [124] J. R. Dormand and P. J. Prince. “A family of embedded Runge-Kutta formulae”. In: *Journal of Computational and Applied Mathematics* 6.1 (1980), pp. 19–26. DOI: [10.1016/0771-050X\(80\)90013-3](https://doi.org/10.1016/0771-050X(80)90013-3) (cited on pages 47, 86).
- [125] O. Dössel. *Bildgebende Verfahren in der Medizin – Von der Technik zur medizinischen Anwendung*. Springer, 2000. ISBN: 978-3-662-06046-9 (cited on page 28).
- [126] J. Drexler, H. Mirzaee, A. Harloff, M. Hüllebrand, A. Hennemuth, and H. K. Hahn. “A software tool for the computation of arterial pulse wave velocity from flow-sensitive 4D MRI data”. In: *Proceedings: Computing in Cardiology*. 2013, pp. 559–62. Link: publica.fraunhofer.de (accessed at 02/2016) (cited on page 68).
- [127] J. Drexler, H. Khan, M. Markl, A. Hennemuth, S. Meier, R. Lorenz, and H. K. Hahn. “Detection of vortical structures in 4D velocity encoded phase contrast MRI data using vector template matching”. In: *Proceedings: Functional Imaging and Modeling of the Heart*. 2013, pp. 276–83. DOI: [10.1007/978-3-642-38899-6_33](https://doi.org/10.1007/978-3-642-38899-6_33) (cited on pages 54, 55).
- [128] C. L. Dumoulin and H. R. Hart Jr. “Magnetic resonance angiography”. In: *Radiology* 161.3 (1986), pp. 717–20. DOI: [10.1148/radiology.161.3.3786721](https://doi.org/10.1148/radiology.161.3.3786721) (cited on page 37).
- [129] P. Dyverfeldt, A. Sigfridsson, J.-P. E. Kvitting, and T. Ebbers. “Quantification of intravoxel velocity standard deviation and turbulence intensity by generalizing phase-contrast MRI”. In: *Journal of Magnetic Resonance in Medicine* 56.4 (2006), pp. 850–8. DOI: [10.1002/mrm.21022](https://doi.org/10.1002/mrm.21022) (cited on page 75).
- [130] P. Dyverfeldt, J.-P. E. Kvitting, A. Sigfridsson, J. Engvall, A. F. Bolger, and T. Ebbers. “Assessment of fluctuating velocities in disturbed cardiovascular blood flow: In vivo feasibility of generalized phase-contrast MRI”. In: *Journal of Magnetic Resonance Imaging* 28.3 (2008), pp. 655–63. DOI: [10.1002/jmri.21475](https://doi.org/10.1002/jmri.21475) (cited on page 75).
- [131] P. Dyverfeldt, J. Eriksson, A. Sigfridsson, J.-P. E. Kvitting, C. Carlhäll, J. Engvall, A. F. Bolger, and T. Ebbers. “Extending 4D flow visualization to the human right ventricle”. In: *Proceedings: International Society for Magnetic Resonance in Medicine*. 2009, p. 3860. Link: diva2:331963 (accessed at 02/2016) (cited on page 56).
- [132] P. Dyverfeldt, J. P. Kvitting, C.-J. Carlhäll, G. Boano, A. Sigfridsson, U. Hermansson, A. F. Bolger, J. Engvall, and T. Ebbers. “Hemodynamic aspects of mitral regurgitation assessed by generalized phase-contrast MRI”. In: *Journal of Magnetic Resonance Imaging* 33.3 (2011), pp. 582–8. DOI: [10.1002/jmri.22407](https://doi.org/10.1002/jmri.22407) (cited on page 76).
- [133] P. Dyverfeldt, M. D. Hope, M. Sigovan, J. Wrenn, and D. Saloner. “Reproducibility of quantitative analysis of aortic 4D flow data”. In: *Journal of Cardiovascular Magnetic Resonance* 15.Suppl 1 (2013), P126. DOI: [10.1186/1532-429X-15-S1-P126](https://doi.org/10.1186/1532-429X-15-S1-P126) (cited on page 70).

- [134] P. Dyverfeldt, T. Ebberts, and T. Länne. “Pulse wave velocity with 4D flow MRI: Systematic differences and age-related regional vascular stiffness”. In: *Journal of Magnetic Resonance Imaging* 32.10 (2014), pp. 1266–71. DOI: [10.1016/j.mri.2014.08.021](https://doi.org/10.1016/j.mri.2014.08.021) (cited on pages 67–69).
- [135] P. Dyverfeldt, M. Bissell, A. J. Barker, A. F. Bolger, C.-J. Carlhäll, T. Ebberts, C. J. François, A. Frydrychowicz, J. Geiger, D. Giese, M. D. Hope, P. J. Kilner, S. Kozerke, S. Myerson, S. Neubauer, O. Wieben, and M. Markl. “4D flow cardiovascular magnetic resonance consensus statement”. In: *Journal of Cardiovascular Magnetic Resonance* 17.1 (2015), pp. 1–19. DOI: [10.1186/s12968-015-0174-5](https://doi.org/10.1186/s12968-015-0174-5) (cited on page 8).
- [136] T. Ebberts. “Flow imaging: Cardiac applications of 3D cine phase-contrast MRI”. In: *Current Cardiovascular Imaging Reports* 4.2 (2011), pp. 127–33. DOI: [10.1007/s12410-011-9065-9](https://doi.org/10.1007/s12410-011-9065-9) (cited on page 8).
- [137] T. Ebberts and G. Farnebäck. “Improving computation of cardiovascular relative pressure fields from velocity MRI”. In: *Journal of Magnetic Resonance Imaging* 30.1 (2009), pp. 54–61. DOI: [10.1002/jmri.21775](https://doi.org/10.1002/jmri.21775) (cited on page 75).
- [138] T. Ebberts, L. Wigström, A. F. Bolger, J. Engvall, and M. Karlsson. “Estimation of relative cardiovascular pressures using time-resolved three-dimensional phase contrast MRI”. In: *Journal of Magnetic Resonance in Medicine* 45.5 (2001), pp. 872–9. DOI: [10.1002/mrm.1116](https://doi.org/10.1002/mrm.1116) (cited on page 75).
- [139] H. Eggebrecht, U. Herold, O. Kuhnt, A. Schmermund, T. Bartel, S. Martini, A. Lind, C. K. Naber, P. Kienbaum, H. Köhl, J. Peters, H. Jakob, R. Erbel, and D. Baumgart. “Endovascular stent-graft treatment of aortic dissection: Determinants of post-interventional outcome”. In: *European Heart Journal* 26.5 (2005), pp. 489–97. DOI: [10.1093/eurheartj/ehi099](https://doi.org/10.1093/eurheartj/ehi099) (cited on page 16).
- [140] S. Eichelbaum, M. Hlawitschka, and G. Scheuermann. “LineAO – Improved three-dimensional line rendering”. In: *IEEE Transactions on Visualization and Computer Graphics* 19.3 (2013), pp. 433–45. DOI: [10.1109/TVCG.2012.142](https://doi.org/10.1109/TVCG.2012.142) (cited on page 161).
- [141] M. S. M. Elbaz, E. E. Calkoen, J. J. M. Westenberg, B. P. F. Lelieveldt, A. A. W. Roest, and R. J. van der Geest. “Three dimensional right ventricular diastolic vortex rings: Characterization and comparison with left ventricular diastolic vortex rings from 4D flow MRI”. In: *Journal of Cardiovascular Magnetic Resonance* 16.Suppl 1 (2014), P42. DOI: [10.1186/1532-429X-16-S1-P42](https://doi.org/10.1186/1532-429X-16-S1-P42) (cited on pages 58, 59).
- [142] M. S. M. Elbaz, E. E. Calkoen, J. J. M. Westenberg, B. P. F. Lelieveldt, A. A. W. Roest, and R. J. Van der Geest. “Vortex flow during early and late left ventricular filling in normal subjects: Quantitative characterization using retrospectively-gated 4D flow cardiovascular magnetic resonance and three-dimensional vortex core analysis”. In: *Journal of Cardiovascular Magnetic Resonance* 16.78 (2014), p. 12. DOI: [10.1186/s12968-014-0078-9](https://doi.org/10.1186/s12968-014-0078-9) (cited on pages 55, 58).
- [143] M. S. M. Elbaz, E. E. Calkoen, A. A. W. Roest, J. J. M. Westenberg, and R. J. van der Geest. “Disturbed diastolic left ventricular inflow vortex ring formation in patients with corrected atrioventricular septal defect: Quantitative three-dimensional vortex core analysis from 4D flow MRI”. In: *Journal of Cardiovascular Magnetic Resonance* 17.Suppl 1 (2015), O4. DOI: [10.1186/1532-429X-17-S1-O4](https://doi.org/10.1186/1532-429X-17-S1-O4) (cited on page 61).
- [144] M. S. M. Elbaz, B. P. F. Lelieveldt, and R. J. Van der Geest. “Hierarchical shape distributions for automatic identification of 3D diastolic vortex rings from 4D flow MRI”. In: *Proceedings: Medical Image Computing and Computer-Assisted Intervention*. 2015, pp. 467–75. DOI: [10.1007/978-3-319-24571-3_56](https://doi.org/10.1007/978-3-319-24571-3_56) (cited on pages 55, 58).
- [145] J. A. Elefteriades, C. J. Lovoulos, M. A. Coady, G. Tellides, G. S. Kopf, and J. A. Rizzo. “Management of descending aortic dissection”. In: *The Annals of Thoracic Surgery* 67.6 (1999), pp. 2002–5. DOI: [10.1016/S0003-4975\(99\)00428-2](https://doi.org/10.1016/S0003-4975(99)00428-2) (cited on page 16).
- [146] P. Entezari, S. Schnell, R. Mahadevia, C. Malaisrie, P. McCarthy, M. Mendelson, J. Collins, J. C. Carr, M. Markl, and A. J. Barker. “From unicuspid to quadricuspid: Influence of aortic valve morphology on aortic three-dimensional hemodynamics”. In: *Journal of Magnetic Resonance Imaging* 40.6 (2014), pp. 1342–6. DOI: [10.1002/jmri.24498](https://doi.org/10.1002/jmri.24498) (cited on page 60).
- [147] J. Eriksson, C. J. Carlhäll, P. Dyverfeldt, J. Engvall, A. F. Bolger, and T. Ebberts. “Semi-automatic quantification of 4D left ventricular blood flow”. In: *Journal of Cardiovascular Magnetic Resonance* 12.9 (2010). DOI: [10.1186/1532-429X-12-9](https://doi.org/10.1186/1532-429X-12-9) (cited on pages 14, 56, 57).
- [148] J. Eriksson, A. F. Bolger, T. Ebberts, and C. J. Carlhäll. “Equal stroke volumes, different costs – Left ventricular 4D flow in normal and failing hearts”. In: *Journal of Cardiovascular Magnetic Resonance* 14.Suppl 1 (2012), W22. DOI: [10.1186/1532-429X-14-S1-W22](https://doi.org/10.1186/1532-429X-14-S1-W22) (cited on page 66).
- [149] J. Eriksson, A. F. Bolger, T. Ebberts, and C.-J. Carlhäll. “Spatial heterogeneity of intracardiac 4D relative pressure fields during diastole”. In: *Journal of Cardiovascular Magnetic Resonance* 15.Suppl 1 (2013), p. M13. DOI: [10.1186/1532-429X-15-S1-M13](https://doi.org/10.1186/1532-429X-15-S1-M13) (cited on page 74).
- [150] J. Eriksson, A. F. Bolger, C.-J. Carlhäll, and T. Ebberts. “Spatial heterogeneity of four-dimensional relative pressure fields in the human left ventricle”. In: *Magnetic Resonance in Medicine* 74.6 (2015), pp. 1716–25. DOI: [10.1002/mrm.25539](https://doi.org/10.1002/mrm.25539) (cited on page 74).

- [151] M. H. Everts. “Visualization of dense line data”. PhD thesis. University of Groningen, Netherlands, 2011. Link: irs.ub.rug.nl (accessed at 03/2016) (cited on page 48).
- [152] M. H. Everts, H. Bekker, J. B. T. M. Roerdink, and T. Isenberg. “Depth-dependent halos: Illustrative rendering of dense line data”. In: *IEEE Transactions on Visualization and Computer Graphics* 15.6 (2009), pp. 1299–306. DOI: [10.1109/TVCG.2009.138](https://doi.org/10.1109/TVCG.2009.138) (cited on page 48).
- [153] M. H. Everts, H. Bekker, J. B. T. M. Roerdink, and T. Isenberg. “Interactive illustrative line styles and line style transfer functions for flow visualization”. In: *Computing Research Repository* (2015). Link: arxiv.org (accessed at 02/2016) (cited on page 48).
- [154] M. Fair, P. D. Gatehouse, A. Greiser, P. Drivas, and D. N. Firmin. “A novel approach to phase-contrast velocity offset correction by in vivo high-SNR acquisitions”. In: *Journal of Cardiovascular Magnetic Resonance* 15.Suppl 1 (2013), P56. Link: biomedcentral.com (accessed at 02/2016) (cited on page 35).
- [155] P. W. Fedak, S. Verma, T. E. David, R. L. Leask, R. D. Weisel, and J. Butany. “Clinical and pathophysiological implications of a bicuspid aortic valve”. In: *Circulation* 106.8 (2002), pp. 900–4. DOI: [10.1161/01.CIR.0000027905.26586.E8](https://doi.org/10.1161/01.CIR.0000027905.26586.E8) (cited on page 17).
- [156] S. W. Fielden, B. K. Fornwalt, M. Jerosch-Herold, R. L. Eisner, A. E. Stillman, and J. N. Oshinski. “A new method for the determination of aortic pulse wave velocity using cross-correlation on 2D PCMR velocity data”. In: *Journal of Magnetic Resonance Imaging* 27.6 (2008), pp. 1382–7. DOI: [10.1002/jmri.21387](https://doi.org/10.1002/jmri.21387) (cited on page 68).
- [157] A. S. Forsberg, J. Chen, and D. H. Laidlaw. “Comparing 3D vector field visualization methods: A user study”. In: *IEEE Transactions on Visualization and Computer Graphics* 15.6 (2009), pp. 1219–26. DOI: [10.1109/TVCG.2009.126](https://doi.org/10.1109/TVCG.2009.126) (cited on page 48).
- [158] K. M. Fox, R. G. Patel, G. R. Graham, J. F. Taylor, J. Stark, M. R. De Leval, and F. J. Macartney. “Multiple and single ventricular septal defect. A clinical and haemodynamic comparison”. In: *British Heart Journal* 40.2 (1978), pp. 141–46. DOI: [10.1136/hrt.40.2.141](https://doi.org/10.1136/hrt.40.2.141) (cited on page 29).
- [159] C. J. François, S. Srinivasan, M. L. Schiebler, S. B. Reeder, E. Niespodzany, B. R. Landgraf, O. Wieben, and A. Frydrychowicz. “4D cardiovascular magnetic resonance velocity mapping of alterations of right heart flow patterns and main pulmonary artery hemodynamics in tetralogy of Fallot”. In: *Journal of Cardiovascular Magnetic Resonance* 14.16 (2012). DOI: [10.1186/1532-429X-14-16](https://doi.org/10.1186/1532-429X-14-16) (cited on pages 58, 135).
- [160] C. J. François, M. Markl, M. L. Schiebler, E. Niespodzany, B. R. Landgraf, C. Schlensak, and A. Frydrychowicz. “Four-dimensional, flow-sensitive magnetic resonance imaging of blood flow patterns in thoracic aortic dissections”. In: *The Journal of Thoracic and Cardiovascular Surgery* 145.5 (2013), pp. 1359–66. DOI: [10.1016/j.jtcvs.2012.07.019](https://doi.org/10.1016/j.jtcvs.2012.07.019) (cited on page 59).
- [161] A. G. Fredriksson, E. Svalbring, J. Eriksson, P. Dyverfeldt, U. Alehagen, J. E. Engvall, T. Ebbers, and C. J. Carlhäll. “4D flow CMR can detect subtle right ventricular dysfunction in primary left ventricular disease”. In: *Journal of Cardiovascular Magnetic Resonance* 17.Suppl 1 (2015), Q4. DOI: [10.1186/1532-429X-17-S1-Q4](https://doi.org/10.1186/1532-429X-17-S1-Q4) (cited on pages 56, 57).
- [162] O. Friman, A. Hennemuth, A. Harloff, J. Bock, M. Markl, and H.-O. Peitgen. “Probabilistic 4D blood flow mapping”. In: *Proceedings: Medical Image Computing and Computer Assisted Intervention*. 2010, pp. 416–23. DOI: [10.1007/978-3-642-15711-0_52](https://doi.org/10.1007/978-3-642-15711-0_52) (cited on pages 78, 160).
- [163] K. J. Friston, P. Fletcher, O. Josephs, A. Holmes, M. D. Rugg, and R. Turner. “Event-related fMRI: Characterizing differential responses”. In: *NeuroImage* 7.1 (1998), pp. 30–40. DOI: [10.1006/nimg.1997.0306](https://doi.org/10.1006/nimg.1997.0306) (cited on page 21).
- [164] A. Frydrychowicz, A. Harloff, B. Jung, M. Zaitsev, E. Weigang, T. A. Bley, M. Langer, J. Hennig, and M. Markl. “Time-resolved, 3-dimensional magnetic resonance flow analysis at 3 T: Visualization of normal and pathological aortic vascular hemodynamics”. In: *Journal of Computer Assisted Tomography* 31.1 (2007), pp. 9–15. DOI: [10.1097/01.rct.0000232918.45158.c9](https://doi.org/10.1097/01.rct.0000232918.45158.c9) (cited on page 60).
- [165] A. Frydrychowicz, R. Arnold, D. Hirtler, C. Schlensak, A. F. Stalder, J. Hennig, M. Langer, and M. Markl. “Multidirectional flow analysis by cardiovascular magnetic resonance in aneurysm development following repair of aortic coarctation”. In: *Journal of Cardiovascular Magnetic Resonance* 10.30 (2008). DOI: [10.1186/1532-429X-10-30](https://doi.org/10.1186/1532-429X-10-30) (cited on page 59).
- [166] A. Frydrychowicz, M. Markl, D. Hirtler, A. Harloff, C. Schlensak, J. Geiger, B. Stiller, and R. Arnold. “Aortic hemodynamics in patients with and without repair of aortic coarctation: In vivo analysis by 4D flow-sensitive magnetic resonance imaging”. In: *Investigative Radiology* 46.5 (2011), pp. 317–25. DOI: [10.1097/RLI.0b013e3182034fc2](https://doi.org/10.1097/RLI.0b013e3182034fc2) (cited on page 59).
- [167] A. Frydrychowicz, A. Berger, A. M. del Rio, M. F. Russe, J. Bock, A. Harloff, and M. Markl. “Interdependencies of aortic arch secondary flow patterns, geometry, and age analysed by 4-dimensional phase contrast magnetic resonance imaging at 3 Tesla”. In: *European Radiology* 22.5 (2012), pp. 1122–30. DOI: [10.1007/s00330-011-2353-6](https://doi.org/10.1007/s00330-011-2353-6) (cited on pages 57, 58).

- [168] R. Fuchs, R. Peikert, H. Hauser, F. Sadlo, and P. Muigg. “Parallel vectors criteria for unsteady flow vortices”. In: *IEEE Transactions on Visualization and Computer Graphics* 14.3 (2008), pp. 615–26. DOI: [10.1109/TVCG.2007.70633](https://doi.org/10.1109/TVCG.2007.70633) (cited on page 53).
- [169] A. Fuhrmann and M. E. Gröller. “Real-time techniques for 3D flow visualization”. In: *Proceedings: IEEE Conference on Visualization (Vis)*. 1998, pp. 305–12. DOI: [10.1109/VISUAL.1998.745317](https://doi.org/10.1109/VISUAL.1998.745317) (cited on page 50).
- [170] N. Galiè, M. M. Hoepfer, M. Humbert, A. Torbicki, J.-L. Vachiery, J. A. Barbera, M. Beghetti, P. Corris, S. Gaine, J. S. Gibbs, M. A. Gomez-Sanchez, G. Jondeau, W. Klepetko, C. Opitz, A. Peacock, L. Rubin, M. Zellweger, G. Simonneau, A. Vahanian, A. Auricchio, J. Bax, C. Ceconi, V. Dean, G. Filippatos, C. Funck-Brentano, R. Hobbs, P. Kearney, T. McDonagh, K. McGregor, B. A. Popescu, Z. Reiner, U. Sechtem, P. A. Sirnes, M. Tendera, P. Vardas, P. Widimsky, U. Sechtem, N. Al Attar, F. Andreotti, M. Aschermann, R. Asteggiano, R. Benza, R. Berger, D. Bonnet, M. Delcroix, L. Howard, A. N. Kitsiou, I. Lang, A. Maggioni, J. E. Nielsen-Kudsk, M. Park, P. Perrone-Filardi, S. Price, M. T. S. Domenech, A. Vonk-Noordegraaf, and J. L. Zamorano. “Guidelines for the diagnosis and treatment of pulmonary hypertension: The task force for the diagnosis and treatment of pulmonary hypertension of the European Society of Cardiology (ESC) and the European Respiratory Society (ERS), endorsed by the International Society of Heart and Lung Transplantation (ISHLT)”. In: *European Heart Journal* 30.20 (2009), pp. 2493–537. DOI: [10.1093/eurheartj/ehp297](https://doi.org/10.1093/eurheartj/ehp297) (cited on page 16).
- [171] D. Garcia and L. Kadem. “What do you mean by aortic valve area: Geometric orifice area, effective orifice area, or Gorlin area?”. In: *The Journal of Heart Valve Disease* 15.5 (2006), pp. 601–8. Link: biomecardio.com (accessed at 02/2016) (cited on pages 16, 70).
- [172] J. Garcia, O. R. Marrufo, A. O. Rodriguez, E. Larose, P. Pibarot, and L. Kadem. “Cardiovascular magnetic resonance evaluation of aortic stenosis severity using single plane measurement of effective orifice area”. In: *Journal of Cardiovascular Magnetic Resonance* 14.23 (2012). DOI: [10.1186/1532-429X-14-23](https://doi.org/10.1186/1532-429X-14-23) (cited on pages 70, 71).
- [173] J. Garcia, M. Markl, S. Schnell, B. Allen, P. Entezari, R. Mahadevia, S. C. Malaisrie, P. Pibarot, J. C. Carr, and A. J. Barker. “Evaluation of aortic stenosis severity using 4D flow jet shear layer detection for the measurement of valve effective orifice area”. In: *Journal of Magnetic Resonance Imaging* 32.7 (2014), pp. 891–8. DOI: [10.1016/j.mri.2014.04.017](https://doi.org/10.1016/j.mri.2014.04.017) (cited on page 71).
- [174] C. Garth, X. Tricoche, T. Salzbrunn, T. Bobach, and G. Scheuermann. “Surface techniques for vortex visualization”. In: *Proceedings: Sixth Joint Eurographics - IEEE TCVG Conference on Visualization (VisSym)*. 2004, pp. 155–64. DOI: [10.2312/VisSym/VisSym04/155-164](https://doi.org/10.2312/VisSym/VisSym04/155-164) (cited on page 50).
- [175] C. Garth, X. Tricoche, and G. Scheuermann. “Tracking of vector field singularities in unstructured 3D time-dependent datasets”. In: *Proceedings: IEEE Conference on Visualization (Vis)*. 2004, pp. 329–36. DOI: [10.1109/VISUAL.2004.107](https://doi.org/10.1109/VISUAL.2004.107) (cited on page 53).
- [176] C. Garth, H. Krishnan, X. Tricoche, T. Bobach, and K. I. Joy. “Generation of accurate integral surfaces in time-dependent vector fields”. In: *IEEE Transactions on Visualization and Computer Graphics* 14.6 (2008), pp. 1404–11. DOI: [10.1109/TVCG.2008.133](https://doi.org/10.1109/TVCG.2008.133) (cited on page 50).
- [177] R. Gasteiger. “Visual exploration of cardiovascular hemodynamics”. PhD thesis. Otto-von-Guericke-University, Magdeburg, Germany, 2014. Link: diglib.eg.org (accessed at 03/2016) (cited on pages 44, 53).
- [178] R. Gasteiger, M. Neugebauer, C. Kubisch, and B. Preim. “Adapted surface visualization of cerebral aneurysms with embedded blood flow information”. In: *Proceedings: Eurographics Workshop on Visual Computing for Biology and Medicine*. 2010, pp. 25–32. DOI: [10.2312/VCBM/VCBM10/025-032](https://doi.org/10.2312/VCBM/VCBM10/025-032) (cited on pages 44, 88).
- [179] R. Gasteiger, M. Neugebauer, O. Beuing, and B. Preim. “The FLOWLENS: A focus-and-context visualization approach for exploration of blood flow in cerebral aneurysms”. In: *IEEE Transactions on Visualization and Computer Graphics* 17.12 (2011), pp. 2183–92. DOI: [10.1109/TVCG.2011.243](https://doi.org/10.1109/TVCG.2011.243) (cited on page 50).
- [180] R. Gasteiger, D. J. Lehmann, R. F. P. Van Pelt, G. Janiga, O. Beuing, A. Vilanova, H. Theisel, and B. Preim. “Automatic detection and visualization of qualitative hemodynamic characteristics in cerebral aneurysms”. In: *IEEE Transactions on Visualization and Computer Graphics* 18.12 (2012), pp. 2178–87. DOI: [10.1109/TVCG.2012.202](https://doi.org/10.1109/TVCG.2012.202) (cited on page 53).
- [181] J. Geiger, M. Markl, L. Herzer, D. Hirtler, F. Loeffelbein, B. Stiller, M. Langer, and R. Arnold. “Aortic flow patterns in patients with Marfan syndrome assessed by flow-sensitive four-dimensional MRI”. In: *Journal of Magnetic Resonance Imaging* 35.3 (2012), pp. 594–600. DOI: [10.1002/jmri.23500](https://doi.org/10.1002/jmri.23500) (cited on pages 17, 60–62).
- [182] J. Geiger, R. Arnold, L. Herzer, D. Hirtler, Z. Stankovic, M. Russe, M. Langer, and M. Markl. “Aortic wall shear stress in Marfan syndrome”. In: *Journal of Magnetic Resonance in Medicine* 70.4 (2013), pp. 1137–44. DOI: [10.1002/mrm.24562](https://doi.org/10.1002/mrm.24562) (cited on page 71).
- [183] M. Gharib, E. Rambod, A. Kheradvar, D. J. Sahn, and J. O. Dabiri. “Optimal vortex formation as an index of cardiac health”. In: *Proceedings of the National Academy of Sciences of the United States of America* 103.16 (2006), pp. 6305–8. DOI: [10.1073/pnas.0600520103](https://doi.org/10.1073/pnas.0600520103) (cited on page 61).
- [184] V. Gibbs, D. Cole, and A. Sassano. *Ultrasound physics and technology: How, why, and when*. Churchill Livingstone Elsevier, 2009. ISBN: 978-0702030413 (cited on page 28).

- [185] S. F. F. Gibson. “Constrained elastic surface nets: Generating smooth surfaces from binary segmented data”. In: *Proceedings: Conference on Medical Image Computing and Computer-Assisted Intervention*. 1998, pp. 888–98. DOI: [10.1007/BFb0056277](https://doi.org/10.1007/BFb0056277) (cited on page 43).
- [186] S. Glaßer, S. Oeltze, A. Hennemuth, C. Kubisch, A. Mahnken, S. Wilhelmsen, and B. Preim. “Automatic transfer function specification for visual emphasis of coronary artery plaque”. In: *Computer Graphics Forum* 29.1 (2010), pp. 191–201. DOI: [10.1111/j.1467-8659.2009.01590.x](https://doi.org/10.1111/j.1467-8659.2009.01590.x) (cited on page 15).
- [187] A. Goel, R. McColl, K. S. King, A. Whittemore, and R. M. Peshock. “Fully automated tool to identify the aorta and compute flow using phase-contrast MRI: Validation and application in a large population based study”. In: *Journal of Magnetic Resonance Imaging* 40.1 (2014), pp. 221–8. DOI: [10.1002/jmri.24338](https://doi.org/10.1002/jmri.24338) (cited on page 41).
- [188] L. Goubergrits, E. Riesenkampff, P. Yevtushenko, J. Schaller, U. Kertzscher, A. Hennemuth, F. Berger, S. Schubert, and T. Kühne. “MRI-based computational fluid dynamics for diagnosis and treatment prediction: Clinical validation study in patients with coarctation of aorta”. In: *Journal of Magnetic Resonance Imaging* 41.4 (2015), pp. 909–16. DOI: [10.1002/jmri.24639](https://doi.org/10.1002/jmri.24639) (cited on page 160).
- [189] G. Greil, T. Geva, S. E. Maier, and A. J. Powell. “Effect of acquisition parameters on the accuracy of velocity encoded cine magnetic resonance imaging blood flow measurements”. In: *Journal of Magnetic Resonance Imaging* 15.1 (2002), pp. 47–54. DOI: [10.1002/jmri.10029](https://doi.org/10.1002/jmri.10029) (cited on page 26).
- [190] M. A. Griswold, P. M. Jakob, R. M. Heidemann, M. Nittka, V. Jellus, J. Wang, B. Kiefer, and A. Haase. “Generalized autocalibrating partially parallel acquisitions (GRAPPA)”. In: *Journal of Magnetic Resonance in Medicine* 47.6 (2002), pp. 1202–10. DOI: [10.1002/mrm.10171](https://doi.org/10.1002/mrm.10171) (cited on page 26).
- [191] M. Grothoff, B. Spors, H. Abdul-Khaliq, and M. Gutberlet. “Evaluation of postoperative pulmonary regurgitation after surgical repair of tetralogy of Fallot: Comparison between Doppler echocardiography and MR velocity mapping”. In: *Pediatric Radiology* 38.2 (2008), pp. 186–91. DOI: [10.1007/s00247-007-0691-y](https://doi.org/10.1007/s00247-007-0691-y) (cited on page 29).
- [192] M. Grothoff, C. D. Etz, B. Preim, **B. Köhler**, and M. Gutberlet. “Phase contrast 4D flow in bicuspid aortic valve in a porcine model”. In: *Journal of Cardiovascular Magnetic Resonance* 17.Suppl 1 (2015), P416. DOI: [10.1186/1532-429X-17-S1-P416](https://doi.org/10.1186/1532-429X-17-S1-P416) (cited on pages 107, 206).
- [193] M. A. Gülsün and H. Tek. “Segmentation of carotid arteries by graph-cuts using centerline models”. In: *Proceedings: International Society for Optics and Photonics (SPIE)*. 2010, p. 762530. Link: hdl.handle.net (accessed at 02/2016) (cited on page 39).
- [194] T. Günther, C. Rössl, and H. Theisel. “Opacity optimization for 3D line fields”. In: *ACM Transactions on Graphics* 32.4 (2013), 120:1–8. DOI: [10.1145/2461912.2461930](https://doi.org/10.1145/2461912.2461930) (cited on page 49).
- [195] T. Günther, C. Rössl, and H. Theisel. “Hierarchical opacity optimization for sets of 3D line fields”. In: *Computer Graphics Forum* 33.2 (2014), pp. 507–16. DOI: [10.1111/cgf.12336](https://doi.org/10.1111/cgf.12336) (cited on page 49).
- [196] M. R. Gupta and Y. Chen. “Theory and use of the EM algorithm”. In: *Foundations and Trends in Signal Processing* 4.3 (2010), pp. 223–96. DOI: [10.1561/20000000034](https://doi.org/10.1561/20000000034) (cited on page 39).
- [197] D. G. Guzzardi, A. J. Barker, P. Van Ooij, S. C. Malaisrie, J. J. Puthumana, D. D. Belke, H. E. Mewhort, D. A. Svystonyuk, S. Kang, S. Verma, J. Collins, J. C. Carr, R. O. Bonow, M. Markl, J. D. Thomas, P. M. McCarthy, and P. W. Fedak. “Valve-related hemodynamics mediate human bicuspid aortopathy: Insights from wall shear stress mapping”. In: *Journal of the American College of Cardiology* 66.8 (2015), pp. 892–900. DOI: [10.1016/j.jacc.2015.06.1310](https://doi.org/10.1016/j.jacc.2015.06.1310) (cited on pages 7, 73).
- [198] E. L. Hahn. “Spin echoes”. In: *Physical Review* 80.4 (1950), pp. 580–94. DOI: [10.1103/PhysRev.80.580](https://doi.org/10.1103/PhysRev.80.580) (cited on page 24).
- [199] G. Haller. “Lagrangian coherent structures from approximate velocity data”. In: *Physics of Fluids* 14.6 (2002), pp. 1851–61. DOI: [10.1063/1.1477449](https://doi.org/10.1063/1.1477449) (cited on page 77).
- [200] J. Han, M. Kamber, and J. Pei. *Data mining: Concepts and techniques*. Morgan Kaufmann, 2011. ISBN: 978-0123814791 (cited on page 52).
- [201] L. G. Hanson. “Is quantum mechanics necessary for understanding magnetic resonance?” In: *Concepts in Magnetic Resonance* 32A.5 (2008), pp. 329–40. DOI: [10.1002/cmr.a.20123](https://doi.org/10.1002/cmr.a.20123) (cited on page 21).
- [202] R. H. Hashemi, W. G. Bradley, and C. J. Lisanti. *MRI: The basics*. Wolters Kluwer Health, 2012. ISBN: 978-1608311156 (cited on page 21).
- [203] T. Hastie, R. Tibshirani, and J. Freidman. *The elements of statistical learning: Data mining, inference, and prediction*. Springer, 2001. ISBN: 978-0-387-84857-0. DOI: [10.1007/978-0-387-84858-7](https://doi.org/10.1007/978-0-387-84858-7) (cited on page 52).
- [204] L. Hatle and B. Angelsen. *Doppler ultrasound in cardiology: Physical principles and clinical applications*. 3rd ed. Lea & Febiger, 1993. ISBN: 978-0812112672 (cited on page 28).
- [205] L. Hatle, A. Brubakk, A. Tromsdal, and B. Angelsen. “Noninvasive assessment of pressure drop in mitral stenosis by Doppler ultrasound”. In: *British Heart Journal* 40.2 (1978), pp. 131–40. Link: [PMC482788](https://pubmed.ncbi.nlm.nih.gov/482788/) (accessed at 02/2016) (cited on page 75).

- [206] F. Hausdorff. *Set theory*. Translated by J. R. Aumann et al. Chelsea Publishing Company, 1957 (cited on page 51).
- [207] C. G. Healey and J. T. Enns. “Attention and visual memory in visualization and computer graphics”. In: *IEEE Transactions on Visualization and Computer Graphics* 18.7 (2012), pp. 1170–88. DOI: [10.1109/TVCG.2011.127](https://doi.org/10.1109/TVCG.2011.127) (cited on page 161).
- [208] E. Heiberg, T. Ebbens, L. Wigström, and M. Karlsson. “Three-dimensional flow characterization using vector pattern matching”. In: *IEEE Transactions on Visualization and Computer Graphics* 9.3 (2003), pp. 313–9. DOI: [10.1109/TVCG.2003.1207439](https://doi.org/10.1109/TVCG.2003.1207439) (cited on pages 55, 56).
- [209] E. Heiberg, J. Sjögren, M. Ugander, M. Carlsson, H. Engblom, and H. Arheden. “Design and validation of Segment – Freely available software for cardiovascular image analysis”. In: *BioMedCentral (BMC) Medical Imaging* 10.1 (2010). DOI: [10.1186/1471-2342-10-1](https://doi.org/10.1186/1471-2342-10-1) (cited on pages 44, 46, 92).
- [210] E. Heiberg, C. Green, J. Töger, A. M. Andersson, M. Carlsson, and H. Arheden. “FourFlow – Open source code software for quantification and visualization of time-resolved three-directional phase contrast magnetic resonance velocity mapping”. In: *Journal of Cardiovascular Magnetic Resonance* 14.Suppl 1 (2012), W14. DOI: [10.1186/1532-429X-14-S1-W14](https://doi.org/10.1186/1532-429X-14-S1-W14) (cited on page 91).
- [211] F. Helderma, G. J. Mauritz, K. E. Andringa, A. Vonk-Noordegraaf, and J. T. Marcus. “Early onset of retrograde flow in the main pulmonary artery is a characteristic of pulmonary arterial hypertension”. In: *Journal of Magnetic Resonance Imaging* 33.6 (2011), pp. 1362–8. DOI: [10.1002/jmri.22581](https://doi.org/10.1002/jmri.22581) (cited on page 60).
- [212] J. L. Helman and L. Hesselink. “Visualizing vector field topology in fluid flows”. In: *IEEE Computer Graphics and Applications* 11.3 (1991), pp. 36–46. DOI: [10.1109/38.79452](https://doi.org/10.1109/38.79452) (cited on page 52).
- [213] A. Hennemuth, O. Friman, C. Schumann, J. Bock, J. Drexl, M. Huellebrand, M. Markl, and H.-O. Peitgen. “Fast interactive exploration of 4D MRI flow data”. In: *Proceedings: International Society for Optics and Photonics (SPIE)*. 2011, 79640E–11. DOI: [10.1117/12.878202](https://doi.org/10.1117/12.878202) (cited on pages 37, 39, 53, 78, 91).
- [214] A. T. Hess, M. M. Bissell, S. J. Glaze, A. Pitcher, S. Myerson, S. Neubauer, and M. D. Robson. “Evaluation of circulation, Γ , as a quantifying metric in 4D flow MRI”. In: *Journal of Cardiovascular Magnetic Resonance* 15.Suppl 1 (2013), E36. DOI: [10.1186/1532-429X-15-S1-E36](https://doi.org/10.1186/1532-429X-15-S1-E36) (cited on page 76).
- [215] A. T. Hess, M. M. Bissell, N. A. B. Ntusi, A. J. M. Lewis, E. M. Tunnicliffe, A. Greiser, A. F. Stalder, J. M. Francis, S. G. Myerson, S. Neubauer, and M. D. Robson. “Aortic 4D flow: Quantification of signal-to-noise ratio as a function of field strength and contrast enhancement for 1.5T, 3T, and 7T”. In: *Journal of Magnetic Resonance in Medicine* 73.5 (2015), pp. 1864–71. DOI: [10.1002/mrm.25317](https://doi.org/10.1002/mrm.25317) (cited on page 26).
- [216] J. Hettig. *Kontrastverstärkung des rechten Ventrikels in 4D PC-MRI Daten*. Scientific Project, Otto-von-Guericke-University, Magdeburg, Germany. 2014 (cited on page 209).
- [217] M. Hlawatsch, P. Leube, W. Nowak, and D. Weiskopf. “Flow radar glyphs – Static visualization of unsteady flow with uncertainty”. In: *IEEE Transactions on Visualization and Computer Graphics* 17.12 (2011), pp. 1949–58. DOI: [10.1109/TVCG.2011.203](https://doi.org/10.1109/TVCG.2011.203) (cited on page 48).
- [218] G. R. Hong, G. Pedrizzetti, G. Tonti, P. Li, Z. Wei, J. K. Kim, A. Baweja, S. Liu, N. Chung, H. Houle, J. Narula, and M. A. Vannan. “Characterization and quantification of vortex flow in the human left ventricle by contrast echocardiography using vector particle image velocimetry”. In: *JACC: Cardiovascular Imaging* 1.6 (2008), pp. 705–17. DOI: [10.1016/j.jcmg.2008.06.008](https://doi.org/10.1016/j.jcmg.2008.06.008) (cited on page 29).
- [219] R. M. Hoogeveen, C. J. Bakker, and M. A. Viergever. “MR phase-contrast flow measurement with limited spatial resolution in small vessels: Value of model-based image analysis”. In: *Journal of Magnetic Resonance Imaging* 41.3 (1999), pp. 520–8. DOI: [10.1002/\(SICI\)1522-2594\(199903\)41:3<520::AID-MRM14>3.0.CO;2-A](https://doi.org/10.1002/(SICI)1522-2594(199903)41:3<520::AID-MRM14>3.0.CO;2-A) (cited on pages 67, 137).
- [220] M. D. Hope, A. K. Meadows, T. A. Hope, K. G. Ordovas, G. P. Reddy, M. T. Alley, and C. B. Higgins. “Evaluation of bicuspid aortic valve and aortic coarctation with 4D flow magnetic resonance imaging”. In: *Circulation*, 117.21 (2008), pp. 2818–9. DOI: [10.1161/CIRCULATIONAHA.107.760124](https://doi.org/10.1161/CIRCULATIONAHA.107.760124) (cited on page 17).
- [221] M. D. Hope, T. A. Hope, A. K. Meadows, K. G. Ordovas, T. H. Urbania, M. T. Alley, and C. B. Higgins. “Bicuspid aortic valve: Four-dimensional MR evaluation of ascending aortic systolic flow patterns”. In: *Radiology* 255.1 (2010), pp. 53–61. DOI: [10.1148/radiol.09091437](https://doi.org/10.1148/radiol.09091437) (cited on pages 60, 62, 104, 116, 135).
- [222] M. D. Hope, A. K. Meadows, T. A. Hope, K. G. Ordovas, D. Saloner, G. P. Reddy, M. T. Alley, and C. B. Higgins. “Clinical evaluation of aortic coarctation with 4D flow MR imaging”. In: *Journal of Magnetic Resonance Imaging* 31.3 (2010), pp. 711–8. DOI: [10.1002/jmri.22083](https://doi.org/10.1002/jmri.22083) (cited on page 59).
- [223] M. D. Hope, T. A. Hope, S. E. Crook, K. G. Ordovas, T. H. Urbania, M. T. Alley, and C. B. Higgins. “4D flow CMR in assessment of valve-related ascending aortic disease”. In: *JACC: Cardiovascular Imaging* 4.7 (2011), pp. 781–7. DOI: [10.1016/j.jcmg.2011.05.004](https://doi.org/10.1016/j.jcmg.2011.05.004) (cited on page 60).
- [224] M. D. Hope, J. Wrenn, M. Sigovan, E. Foster, E. E. Tseng, and D. Saloner. “Imaging biomarkers of aortic disease: Increased growth rates with eccentric systolic flow”. In: *Journal of the American College of Cardiology* 60.4 (2012), pp. 356–7. DOI: [10.1016/j.jacc.2012.01.072](https://doi.org/10.1016/j.jacc.2012.01.072) (cited on page 60).

- [225] M. D. Hope, P. Dyverfeldt, G. Acevedo-Bolton, J. Wrenn, E. Foster, E. Tseng, and D. Saloner. “Post-stenotic dilation: Evaluation of ascending aortic dilation with 4D flow MR imaging”. In: *International Journal of Cardiology* 156.2 (2012), e40–2. DOI: [10.1016/j.ijcard.2011.08.018](https://doi.org/10.1016/j.ijcard.2011.08.018) (cited on page 59).
- [226] M. D. Hope, T. Sedlic, and P. Dyverfeldt. “Cardiothoracic magnetic resonance flow imaging”. In: *Journal of Thoracic Imaging* 28.4 (2013), pp. 217–30. DOI: [10.1097/RTI.0b013e31829192a1](https://doi.org/10.1097/RTI.0b013e31829192a1) (cited on pages 8, 65, 67, 162).
- [227] T. A. Hope and R. J. Herfkens. “Imaging of the thoracic aorta with time-resolved three-dimensional phase-contrast MRI: A review”. In: *The Journal of Thoracic and Cardiovascular Surgery* 20.4 (2008), pp. 358–64. DOI: [10.1053/j.semtevs.2008.11.013](https://doi.org/10.1053/j.semtevs.2008.11.013) (cited on page 8).
- [228] T. A. Hope, M. Markl, L. Wigström, M. T. Alley, D. C. Miller, and R. J. Herfkens. “Comparison of flow patterns in ascending aortic aneurysms and volunteers using four-dimensional magnetic resonance velocity mapping”. In: *Journal of Magnetic Resonance Imaging* 26.6 (2007), pp. 1471–9. DOI: [10.1002/jmri.21082](https://doi.org/10.1002/jmri.21082) (cited on pages 59, 62).
- [229] H. Hoppe. “New quadric metric for simplifying meshes with appearance attributes”. In: *Proceedings: IEEE Conference on Visualization (Vis)*. 1999, pp. 59–66. DOI: [10.1109/VISUAL.1999.809869](https://doi.org/10.1109/VISUAL.1999.809869) (cited on page 85).
- [230] J. P. Hornak. *The basics of MRI*. 1996. Link: cis.rit.edu (accessed at 03/2016) (cited on page 21).
- [231] P. V. C. Hough. “Machine analysis of bubble chamber pictures”. In: *Proceedings: International Conference on High-Energy Accelerators and Instrumentation*. 1959, pp. 554–8. Link: inspirehep.net (accessed at 04/2016) (cited on page 41).
- [232] C. M. House, K. A. Moriarty, and W. B. Nelson. “Anatomic versus effective orifice area in a bicuspid aortic valve”. In: *Echocardiography* 31.8 (2014), pp. 1023–7. DOI: [10.1111/echo.12619](https://doi.org/10.1111/echo.12619) (cited on page 70).
- [233] M. Howe. *Theory of vortex sound*. Cambridge University Press, 2002. ISBN: 9780521012232 (cited on page 70).
- [234] A. Hsiao, M. Lustig, M. T. Alley, M. Murphy, F. P. Chan, R. J. Herfkens, and S. S. Vasanawala. “Rapid pediatric cardiac assessment of flow and ventricular volume with compressed sensing parallel imaging volumetric cine phase-contrast MRI”. In: *American Journal of Roentgenology* 198.3 (2012), W250–9. DOI: [10.2214/AJR.11.6969](https://doi.org/10.2214/AJR.11.6969) (cited on page 66).
- [235] W.-H. Hsu, J. Mei, C. D. Correa, and K.-L. Ma. “Depicting time evolving flow with illustrative visualization techniques”. In: *Arts and Technology*. 2010, pp. 136–47. DOI: [10.1007/978-3-642-11577-6_18](https://doi.org/10.1007/978-3-642-11577-6_18) (cited on page 48).
- [236] M. Hüllebrand, A. Hennemuth, D. Messrogli, and T. Kühne. “An OsiriX plugin for integrated cardiac image processing research”. In: *Proceedings: International Society for Optics and Photonics (SPIE)*. 2014, p. 90390D. DOI: [10.1117/12.2043735](https://doi.org/10.1117/12.2043735) (cited on page 91).
- [237] J. P. M. Hultquist. “Interactive numerical flow visualization using stream surfaces”. In: *Computing Systems in Engineering* 1.2-4 (1990), pp. 349–53. DOI: [10.1016/0956-0521\(90\)90021-C](https://doi.org/10.1016/0956-0521(90)90021-C) (cited on page 50).
- [238] M. Hummel, C. Garth, B. Hamann, H. Hagen, and K. I. Joy. “IRIS: Illustrative rendering for integral surfaces”. In: *IEEE Transactions on Visualization and Computer Graphics* 16.6 (2010), pp. 1319–28. DOI: [10.1109/TVCG.2010.173](https://doi.org/10.1109/TVCG.2010.173) (cited on page 50).
- [239] J. Hunt. “Vorticity and vortex dynamics in complex turbulent flows”. In: *Transactions of the Canadian Society for Mechanical Engineering* 11.1 (1987), pp. 21–35 (cited on pages 54, 99).
- [240] W. Insull Jr. “The pathology of atherosclerosis: Plaque development and plaque responses to medical treatment”. In: *The American Journal of Medicine* 122.Suppl 1 (2009), S3–14. DOI: [10.1016/j.amjmed.2008.10.013](https://doi.org/10.1016/j.amjmed.2008.10.013) (cited on page 15).
- [241] V. Interrante and C. Grosch. “Strategies for effectively visualizing 3D flow with volume LIC”. In: *Proceedings: IEEE Conference on Visualization (Vis)*. 1997, pp. 421–4. DOI: [10.1109/VISUAL.1997.663912](https://doi.org/10.1109/VISUAL.1997.663912) (cited on page 48).
- [242] T. Isenberg. “A survey of illustrative visualization techniques for diffusion-weighted MRI tractography”. In: *Visualization and Processing of Higher Order Descriptors for Multi-Valued Data*. 2015, pp. 235–56. DOI: [10.1007/978-3-319-15090-1_12](https://doi.org/10.1007/978-3-319-15090-1_12) (cited on page 161).
- [243] L. M. Itu, P. Sharma, M. A. Gülsün, V. Mihalef, A. Kamen, and A. Greiser. “Determination of time-varying pressure field from phase contrast MRI data”. In: *Journal of Cardiovascular Magnetic Resonance* 14.Suppl 1 (2012), W36. DOI: [10.1186/1532-429X-14-S1-W36](https://doi.org/10.1186/1532-429X-14-S1-W36) (cited on page 75).
- [244] O. Jamriška, D. Sýkora, and A. Hornung. “Cache-efficient graph cuts on structured grids”. In: *Proceedings: IEEE Conference on Computer Vision and Pattern Recognition*. 2012, pp. 3673–80. DOI: [10.1109/CVPR.2012.6248113](https://doi.org/10.1109/CVPR.2012.6248113) (cited on pages 39, 84).
- [245] M. Jenkinson. “Fast, automated, N-dimensional phase-unwrapping algorithm”. In: *Journal of Magnetic Resonance in Medicine* 49.1 (2003), pp. 193–7. DOI: [10.1002/mrm.10354](https://doi.org/10.1002/mrm.10354) (cited on page 33).
- [246] D. Jeong, P. V. Anagnostopoulos, A. Roldán-Alzate, S. Srinivasan, M. L. Schiebler, O. Wieben, and C. J. François. “Ventricular kinetic energy may provide a novel noninvasive way to assess ventricular performance in patients with repaired tetralogy of Fallot”. In: *The Journal of Thoracic and Cardiovascular Surgery* 149.5 (2015), pp. 1339–47. DOI: [10.1016/j.jtcvs.2014.11.085](https://doi.org/10.1016/j.jtcvs.2014.11.085) (cited on page 76).

- [247] J. Jeong and F. Hussain. “On the identification of a vortex”. In: *Journal of Fluid Mechanics* 285 (1995), pp. 69–94. DOI: [10.1017/S0022112095000462](https://doi.org/10.1017/S0022112095000462) (cited on pages 54, 99).
- [248] M. Jiang, R. Machiraju, and D. Thompson. “A novel approach to vortex core region detection”. In: *Proceedings: Symposium on Data Visualization*. 2002, pp. 217–25. DOI: [10.2312/VisSym/VisSym02/217-225](https://doi.org/10.2312/VisSym/VisSym02/217-225) (cited on page 53).
- [249] M. Jiang, R. Machiraju, and D. Thompson. “Geometric verification of swirling features in flow fields”. In: *Proceedings: IEEE Conference on Visualization (Vis)*. 2002, pp. 307–14. DOI: [10.1109/VISUAL.2002.1183789](https://doi.org/10.1109/VISUAL.2002.1183789) (cited on page 53).
- [250] M. Jiang, R. Machiraju, and D. Thompson. “Detection and visualization of vortices”. In: *The Visualization Handbook*. 2005, pp. 295–309. DOI: [10.1016/B978-012387582-2/50016-2](https://doi.org/10.1016/B978-012387582-2/50016-2) (cited on pages 53–55).
- [251] S. Jin, J. Oshinski, and D. P. Giddens. “Effects of wall motion and compliance on flow patterns in the ascending aorta”. In: *Journal of Biomechanical Engineering* 125.3 (2003), pp. 347–54. DOI: [10.1115/1.1574332](https://doi.org/10.1115/1.1574332) (cited on page 57).
- [252] B. Jobard and W. Lefer. “Creating evenly-spaced streamlines of arbitrary density”. In: *Visualization in Scientific Computing*. 1997, pp. 43–55. DOI: [10.1007/978-3-7091-6876-9_5](https://doi.org/10.1007/978-3-7091-6876-9_5) (cited on page 47).
- [253] C. Jones and K.-L. Ma. “Visualizing flow trajectories using locality-based rendering and warped curve plots”. In: *IEEE Transactions on Visualization and Computer Graphics* 16.6 (2010), pp. 1587–94. DOI: [10.1109/TVCG.2010.218](https://doi.org/10.1109/TVCG.2010.218) (cited on page 50).
- [254] T. R. Jones. “Efficient generation of Poisson-disk sampling patterns”. In: *Journal of Graphics, GPU, and Game Tools* 11.2 (2006), pp. 27–36. DOI: [10.1080/2151237X.2006.10129217](https://doi.org/10.1080/2151237X.2006.10129217) (cited on page 138).
- [255] L. Kadem, Y. Knapp, P. Pibarot, E. Bertrand, D. Garcia, L. G. Durand, and R. Rieu. “A new experimental method for the determination of the effective orifice area based on the acoustical source term”. In: *Experiments in Fluids* 39.6 (2005), pp. 1051–60. DOI: [10.1007/s00348-005-0038-0](https://doi.org/10.1007/s00348-005-0038-0) (cited on page 71).
- [256] L. Kadem, R. Rieu, J. G. Dumesnil, L.-G. Durand, and P. Pibarot. “Flow-dependent changes in Doppler-derived aortic valve effective orifice area are real and not due to artifact”. In: *Journal of the American College of Cardiology* 47.1 (2006), pp. 131–7. DOI: [10.1016/j.jacc.2005.05.100](https://doi.org/10.1016/j.jacc.2005.05.100) (cited on page 71).
- [257] D. Kainmüller, R. Unterhinninghofen, S. Ley, and R. Dillmann. “Level set segmentation of the heart from 4D phase contrast MRI”. In: *Proceedings: International Society for Optics and Photonics (SPIE)*. 2008, pp. 691414–1–8. DOI: [10.1117/12.769435](https://doi.org/10.1117/12.769435) (cited on page 40).
- [258] M. Kanski, J. Töger, K. Steding-Ehrenborg, C. Xanthis, K. Markenroth Bloch, E. Heiberg, M. Carlsson, and H. Arheden. “Whole-heart four-dimensional flow can be acquired with preserved quality without respiratory gating, facilitating clinical use: A head-to-head comparison”. In: *BioMedCentral (BMC) Medical Imaging* 15.1 (2015), p. 20. DOI: [10.1186/s12880-015-0061-4](https://doi.org/10.1186/s12880-015-0061-4) (cited on page 30).
- [259] F. A. Kari, N. Kocher, F. Beyersdorf, A. Tscheuschler, P. Meffert, B. Rylski, M. Siepe, M. F. Russe, and M. D. Hope. “Four-dimensional magnetic resonance imaging-derived ascending aortic flow eccentricity and flow compression are linked to aneurysm morphology”. In: *Interactive Cardiovascular and Thoracic Surgery* 20.5 (2015), pp. 582–7. DOI: [10.1093/icvts/ivv446](https://doi.org/10.1093/icvts/ivv446) (cited on page 69).
- [260] A. Karthikesalingam, P. J. Holt, R. J. Hinchliffe, M. M. Thompson, and I. M. Loftus. “The diagnosis and management of aortic dissection”. In: *Vascular and Endovascular Surgery* 44.3 (2010), pp. 165–9. DOI: [10.1177/1538574410362118](https://doi.org/10.1177/1538574410362118) (cited on page 16).
- [261] J. Kasten, C. Petz, I. Hotz, B. R. Noack, and H.-C. Hege. “Localized finite-time Lyapunov exponent for unsteady flow analysis”. In: *Proceedings: Vision Modeling and Visualization*. 2009, pp. 265–74. Link: zib.de (accessed at 03/2016) (cited on page 77).
- [262] A. Kheradvar, R. Assadi, A. Falahatpisheh, and P. P. Sengupta. “Assessment of transmitral vortex formation in patients with diastolic dysfunction”. In: *Journal of the American Society of Echocardiography* 25.2 (2012), pp. 220–7. DOI: [10.1016/j.echo.2011.10.003](https://doi.org/10.1016/j.echo.2011.10.003) (cited on page 61).
- [263] P. J. Kilner, G. Z. Yang, R. H. Mohiaddin, D. N. Firmin, and D. B. Longmore. “Helical and retrograde secondary flow patterns in the aortic arch studied by three-directional magnetic resonance velocity mapping”. In: *Circulation* 88.5 Pt. 1 (1993), pp. 2235–47. DOI: [10.1161/01.CIR.88.5.2235](https://doi.org/10.1161/01.CIR.88.5.2235) (cited on page 57).
- [264] P. J. Kilner, G. Z. Yang, A. J. Wilkes, R. H. Mohiaddin, D. N. Firmin, and M. H. Yacoub. “Asymmetric redirection of flow through the heart”. In: *Nature* 404.6779 (2000), pp. 759–61. DOI: [10.1038/35008075](https://doi.org/10.1038/35008075) (cited on page 14).
- [265] W. Y. Kim, P. G. Walker, E. M. Pedersen, J. K. Poulsen, S. Oyre, K. Houliind, and A. P. Yoganathan. “Left ventricular blood flow patterns in normal subjects: A quantitative analysis by three-dimensional magnetic resonance velocity mapping”. In: *Journal of the American College of Cardiology* 26.1 (1995), pp. 224–38. DOI: [10.1016/0735-1097\(95\)00141-L](https://doi.org/10.1016/0735-1097(95)00141-L) (cited on page 58).
- [266] P. Kipfer, M. Segal, and R. Westermann. “UberFlow: A GPU-based particle engine”. In: *Proceedings: ACM SIGGRAPH/EUROGRAPHICS Conference on Graphics Hardware*. 2004, pp. 115–22. DOI: [10.1145/1058129.1058146](https://doi.org/10.1145/1058129.1058146) (cited on page 47).

- [267] P. Klemm, K. Lawonn, S. Glaßer, U. Niemann, K. Hegenscheid, H. Völzke, and B. Preim. “3D regression heat map analysis of population study data”. In: *IEEE Transactions on Visualization and Computer Graphics* 22.1 (2015), pp. 81–90. DOI: [10.1109/TVCG.2015.2468291](https://doi.org/10.1109/TVCG.2015.2468291) (cited on page 161).
- [268] R. H. Klipstein, D. N. Firmin, S. R. Underwood, R. S. O. Rees, and D. B. Longmore. “Blood flow patterns in the human aorta studied by magnetic resonance”. In: *British Heart Journal* 58.4 (1987), pp. 316–23. DOI: [10.1136/hrt.58.4.316](https://doi.org/10.1136/hrt.58.4.316) (cited on pages 7, 66).
- [269] **B. Köhler**. “Wirbelextraktion in 4D PC-MRI Blutflussdaten der Aorta”. MA thesis. Otto-von-Guericke-University, Magdeburg, Germany, 2012. Link: vismd.de (accessed at 02/2016) (cited on pages 48, 53, 95, 97–99, 103, 107, 205, 206).
- [270] **B. Köhler**, R. Gasteiger, U. Preim, H. Theisel, M. Gutberlet, and B. Preim. “Semi-automatic vortex extraction in 4D PC-MRI cardiac blood flow data using line predicates”. In: *IEEE Transactions on Visualization and Computer Graphics* 19.12 (2013), pp. 2773–82. DOI: [10.1109/TVCG.2013.189](https://doi.org/10.1109/TVCG.2013.189) (cited on pages 7, 14, 48, 55, 83, 87, 95, 96, 98, 99, 101, 103–106, 110, 112, 205, 209).
- [271] **B. Köhler**, U. Preim, M. Gutberlet, K. Fischbach, and B. Preim. “Robust cardiac function assessment in 4D PC-MRI data”. In: *Proceedings: Eurographics Workshop on Visual Computing for Biology and Medicine*. 2014, pp. 1–9. DOI: [10.2312/vcbm.20141179](https://doi.org/10.2312/vcbm.20141179) (cited on pages 205, 206, 209).
- [272] **B. Köhler**, S. Born, R. F. P. Van Pelt, U. Preim, and B. Preim. “A survey of cardiac 4D PC-MRI data processing”. In: *Proceedings: Eurographics Workshop on Visual Computing for Biology and Medicine*. 2015, pp. 139–48. DOI: [10.2312/vcbm.20151217](https://doi.org/10.2312/vcbm.20151217) (cited on pages 205, 206, 209).
- [273] **B. Köhler**, U. Preim, M. Grothoff, M. Gutberlet, K. Fischbach, and B. Preim. “Guided analysis of cardiac 4D PC-MRI blood flow data”. In: *Proceedings: Eurographics Short Papers and Medical Prize Awards*. 2015, Epub. DOI: [10.2312/egm.20151029](https://doi.org/10.2312/egm.20151029) (cited on pages 9, 83, 85, 87, 89, 206, 209).
- [274] **B. Köhler**, M. Meuschke, U. Preim, K. Fischbach, M. Gutberlet, and B. Preim. “Two-dimensional plot visualization of aortic vortex flow in cardiac 4D PC-MRI data”. In: *Proceedings: Bildverarbeitung für die Medizin*. 2015, pp. 257–61. DOI: [10.1007/978-3-662-46224-9_45](https://doi.org/10.1007/978-3-662-46224-9_45) (cited on pages 50, 87, 108–111, 205, 206, 209).
- [275] **B. Köhler**, S. Born, R. F. P. Van Pelt, A. Hennemuth, U. Preim, and B. Preim. “A survey of cardiac 4D PC-MRI data processing”. In: *Computer Graphics Forum* (2016), Epub. DOI: [10.1111/cgf.12803](https://doi.org/10.1111/cgf.12803) (cited on pages 7, 9, 10, 25–27, 33–36, 38, 40, 43–46, 49, 52, 53, 56, 65, 66, 68, 69, 72, 74, 76–78, 112, 205).
- [276] **B. Köhler**, U. Preim, M. Grothoff, M. Gutberlet, and B. Preim. “Adaptive animations of vortex flow extracted from cardiac 4D PC-MRI data”. In: *Proceedings: Bildverarbeitung für die Medizin*. 2016, pp. 194–9 (cited on pages 49, 112, 113, 115, 116, 205, 209).
- [277] **B. Köhler**, U. Preim, M. Grothoff, M. Gutberlet, K. Fischbach, and B. Preim. “Motion-aware stroke volume quantification in 4D PC-MRI data of the human aorta”. In: *International Journal for Computer Assisted Radiology and Surgery* 11.2 (2016), pp. 169–79. DOI: [10.1007/s11548-015-1256-4](https://doi.org/10.1007/s11548-015-1256-4) (cited on pages 14, 44, 83, 148–150, 152, 153, 155–158, 205).
- [278] **B. Köhler**, U. Preim, M. Grothoff, M. Gutberlet, K. Fischbach, and B. Preim. “Robust cardiac function assessment in 4D PC-MRI data of the aorta and pulmonary artery”. In: *Computer Graphics Forum* 35.1 (2016), pp. 32–43. DOI: [10.1111/cgf.12669](https://doi.org/10.1111/cgf.12669) (cited on pages 14, 67, 69, 83, 88, 135–138, 140, 141, 143–146, 157, 158, 205).
- [279] U. Köhler, I. Marshall, M. B. Robertson, Q. Long, X. Y. Xu, and P. R. Hoskins. “MRI measurement of wall shear stress vectors in bifurcation models and comparison with CFD predictions”. In: *Journal of Magnetic Resonance Imaging* 14.5 (2001), pp. 563–73. DOI: [10.1002/jmri.1220](https://doi.org/10.1002/jmri.1220) (cited on page 72).
- [280] V. Kolář. “Vortex identification: New requirements and limitations”. In: *International Journal of Heat and Fluid Flow* 28.4 (2007), pp. 638–52. DOI: [10.1016/j.ijheatfluidflow.2007.03.004](https://doi.org/10.1016/j.ijheatfluidflow.2007.03.004) (cited on pages 53, 54).
- [281] J. Kopp. “Efficient numerical diagonalization of Hermitian 3×3 matrices”. In: *International Journal of Modern Physics* 19.3 (2008), pp. 523–48. DOI: [10.1142/S0129183108012303](https://doi.org/10.1142/S0129183108012303) (cited on pages 95, 102).
- [282] S. Kozerke, J. M. Hasenkam, E. M. Pedersen, and P. Boesiger. “Visualization of flow patterns distal to aortic valve prostheses in humans using a fast approach for cine 3D velocity mapping”. In: *Journal of Magnetic Resonance Imaging* 13.5 (2001), pp. 690–8. DOI: [10.1002/jmri.1097](https://doi.org/10.1002/jmri.1097) (cited on page 60).
- [283] G. E. Krasner and S. T. Pope. “A cookbook for using the model-view controller user interface paradigm in Smalltalk-80”. In: *Journal of Object-Oriented Programming* 1.3 (1988), pp. 26–49. Link: kanjiteacher.googlecode.com (accessed at 03/2016) (cited on page 89).
- [284] H. Krishnan, C. Garth, and K. I. Joy. “Time and streak surfaces for flow visualization in large time-varying data sets”. In: *IEEE Transactions on Visualization and Computer Graphics* 15.6 (2009), pp. 1267–74. DOI: [10.1109/TVCG.2009.190](https://doi.org/10.1109/TVCG.2009.190) (cited on page 50).
- [285] H. Krishnan, C. Garth, J. Gühring, M. A. Gülsün, A. Greiser, and K. I. Joy. “Analysis of time-dependent flow-sensitive PC-MRI data”. In: *IEEE Transactions on Visualization and Computer Graphics* 18.6 (2012), pp. 966–77. DOI: [10.1109/TVCG.2011.80](https://doi.org/10.1109/TVCG.2011.80) (cited on page 77).

- [286] S. B. S. Krittian, P. Lamata, C. Michler, D. A. Nordsletten, J. Bock, C. P. Bradley, A. Pitcher, P. J. Kilner, M. Markl, and N. P. Smith. “A finite-element approach to the direct computation of relative cardiovascular pressure from time-resolved MR velocity data”. In: *Medical Image Analysis* 16.5 (2012), pp. 1029–37. DOI: [10.1016/j.media.2012.04.003](https://doi.org/10.1016/j.media.2012.04.003) (cited on page 75).
- [287] E. S. J. Kröner, J. J. M. Westenberg, L. J. M. Kroft, N. J. Brouwer, P. J. van den Boogaard, and A. J. H. A. Scholte. “Coupling between MRI-assessed regional aortic pulse wave velocity and diameters in patients with thoracic aortic aneurysm: A feasibility study”. In: *Netherlands Heart Journal* 23.10 (2015), pp. 493–501. DOI: [10.1007/s12471-015-0735-0](https://doi.org/10.1007/s12471-015-0735-0) (cited on page 67).
- [288] J. Krüger and R. Westermann. “Acceleration techniques for GPU-based volume rendering”. In: *Proceedings: IEEE Conference on Visualization (Vis)*. 2003. DOI: [10.1109/VISUAL.2003.1250384](https://doi.org/10.1109/VISUAL.2003.1250384) (cited on page 44).
- [289] J. Krüger, P. Kipfer, P. Kondratieva, and R. Westermann. “A particle system for interactive visualization of 3D flows”. In: *IEEE Transactions on Visualization and Computer Graphics* 11.6 (2005), pp. 744–56. DOI: [10.1109/TVCG.2005.87](https://doi.org/10.1109/TVCG.2005.87) (cited on page 47).
- [290] A. Kuhn, D. J. Lehmann, R. Gaststeiger, M. Neugebauer, B. Preim, and H. Theisel. “A clustering-based visualization technique to emphasize meaningful regions of vector fields”. In: *Proceedings: Vision, Modeling, and Visualization*. 2011, pp. 191–8. Link: vc.cs.ovgu.de (accessed at 02/2016) (cited on page 51).
- [291] J. P. Kvitting, T. Ebbers, L. Wigström, J. Engvall, C. L. Olin, and A. F. Bolger. “Flow patterns in the aortic root and the aorta studied with time-resolved, 3-dimensional, phase-contrast magnetic resonance imaging: Implications for aortic valve-sparing surgery”. In: *The Journal of Thoracic and Cardiovascular Surgery* 127.6 (2004), pp. 1602–7. DOI: [10.1016/j.jtcvs.2003.10.042](https://doi.org/10.1016/j.jtcvs.2003.10.042) (cited on page 60).
- [292] D. H. Laidlaw, R. M. Kirby, C. D. Jackson, J. S. Davidson, T. S. Miller, M. da Silva, W. H. Warren, and M. J. Tarr. “Comparing 2D vector field visualization methods: A user study”. In: *IEEE Transactions on Visualization and Computer Graphics* 11.1 (2005), pp. 59–70. DOI: [10.1109/TVCG.2005.4](https://doi.org/10.1109/TVCG.2005.4) (cited on page 46).
- [293] P. Lamata, A. Pitcher, S. B. S. Krittian, D. Nordsletten, M. M. Bissell, T. Cassar, A. J. Barker, M. Markl, S. Neubauer, and N. P. Smith. “Aortic relative pressure components derived from four-dimensional flow cardiovascular magnetic resonance”. In: *Journal of Magnetic Resonance Imaging* 72.4 (2014), pp. 1162–9. DOI: [10.1002/mrm.25015](https://doi.org/10.1002/mrm.25015) (cited on page 75).
- [294] K. Lampropoulos, W. Budts, A. Van de Bruaene, E. Troost, and J. P. Van Melle. “Visualization of the intracavitary blood flow in systemic ventricles of Fontan patients by contrast echocardiography using particle image velocimetry”. In: *Cardiovascular Ultrasound* 10.5 (2012). DOI: [10.1186/1476-7120-10-5](https://doi.org/10.1186/1476-7120-10-5) (cited on page 29).
- [295] B. R. Landgraf, C. J. François, K. M. Johnson, E. T. Biegling, and O. Wieben. “Visualization and quantification of helical and vortical flow in ascending aortic aneurysms”. In: *Journal of Cardiovascular Magnetic Resonance* 12.Supp 1 (2010), P239. DOI: [10.1186/1532-429X-12-S1-P239](https://doi.org/10.1186/1532-429X-12-S1-P239) (cited on page 60).
- [296] J. Langley and Q. Zhao. “Unwrapping magnetic resonance phase maps with Chebyshev polynomials”. In: *Magnetic Resonance Imaging* 27.9 (2009), pp. 1293–301. DOI: [10.1016/j.mri.2009.05.013](https://doi.org/10.1016/j.mri.2009.05.013) (cited on page 33).
- [297] J.-W. Lankhaar, M. B. M. Hofman, J. T. Marcus, J. J. M. Zwanenburg, T. J. C. Faes, and A. Vonk-Noordegraaf. “Correction of phase offset errors in main pulmonary artery flow quantification”. In: *Journal of Magnetic Resonance Imaging* 22.1 (2005), pp. 73–9. DOI: [10.1002/jmri.20361](https://doi.org/10.1002/jmri.20361) (cited on page 35).
- [298] S. L. Lansman, J. N. McCullough, K. H. Nguyen, D. Spielvogel, J. J. Klein, J. D. Galla, M. A. Ergin, and R. B. Griepp. “Subtypes of acute aortic dissection”. In: *The Annals of Thoracic Surgery* 67.6 (1999), pp. 1975–8. DOI: [10.1016/S0003-4975\(99\)00419-1](https://doi.org/10.1016/S0003-4975(99)00419-1) (cited on page 15).
- [299] J. Lantz, R. Gårdhagen, and M. Karlsson. “Quantifying turbulent wall shear stress in a subject specific human aorta using large eddy simulation”. In: *Medical Engineering & Physics* 34.8 (2012), pp. 1139–48. DOI: [10.1016/j.medengphy.2011.12.002](https://doi.org/10.1016/j.medengphy.2011.12.002) (cited on page 160).
- [300] J. Lantz, P. Dyverfeldt, and T. Ebbers. “Improving blood flow simulations by incorporating measured subject-specific wall motion”. In: *Cardiovascular Engineering and Technology* 5.3 (2014), pp. 261–9. DOI: [10.1007/s13239-014-0187-5](https://doi.org/10.1007/s13239-014-0187-5) (cited on page 44).
- [301] G. Lapeyre. “Characterization of finite-time Lyapunov exponents and vectors in two-dimensional turbulence”. In: *Chaos: An Interdisciplinary Journal of Nonlinear Science* 12.3 (2002), p. 688. DOI: [10.1063/1.1499395](https://doi.org/10.1063/1.1499395) (cited on page 77).
- [302] J. M. Last and International Epidemiological Association. *A dictionary of epidemiology*. Vol. 141. Oxford University Press, 2001 (cited on page 161).
- [303] T. W. Latson, W. C. Hunter, N. Katoh, and K. Sagawa. “Effect of nitroglycerin on aortic impedance, diameter, and pulse-wave velocity”. In: *Circulation Research* 62.5 (1988), pp. 884–90. DOI: [10.1161/01.RES.62.5.884](https://doi.org/10.1161/01.RES.62.5.884) (cited on page 68).

- [304] S. Laurent, P. Boutouyrie, R. Asmar, I. Gautier, B. Laloux, L. Guize, P. Ducimetiere, and A. Benetos. “Aortic stiffness is an independent predictor of all-cause and cardiovascular mortality in hypertensive patients”. In: *Hypertension* 37.5 (2001), pp. 1236–41. DOI: [10.1161/01.HYP.37.5.1236](https://doi.org/10.1161/01.HYP.37.5.1236) (cited on page 67).
- [305] S. Laurent, J. Cockcroft, L. Van Bortel, P. Boutouyrie, C. Giannattasio, D. Hayoz, B. Pannier, C. Vlachopoulos, I. Wilkinson, H. Struijker-Boudier, and European Network for Non-invasive Investigation of Large Arteries. “Expert consensus document on arterial stiffness: Methodological issues and clinical applications”. In: *European Heart Journal* 27.21 (2006), pp. 2588–605. DOI: [10.1093/eurheartj/ehl254](https://doi.org/10.1093/eurheartj/ehl254) (cited on page 67).
- [306] K. Lawonn, R. Gasteiger, and B. Preim. “Adaptive surface visualization of vessels with animated blood flow”. In: *Computer Graphics Forum* 33.8 (2014), pp. 16–27. DOI: [10.1111/cgf.12355](https://doi.org/10.1111/cgf.12355) (cited on page 44).
- [307] K. Lawonn, S. Glaßer, A. Vilanova, B. Preim, and T. Isenberg. “Occlusion-free blood flow animation with wall thickness visualization”. In: *IEEE Transactions on Visualization and Computer Graphics* 22.1 (2016), pp. 728–37. DOI: [10.1109/TVCG.2015.2467961](https://doi.org/10.1109/TVCG.2015.2467961) (cited on page 127).
- [308] D. Lee and T. Carroll. *Practical signal and image processing in clinical cardiology*. Springer London, 2010. ISBN: 978-1-84882-514-7 (cited on page 21).
- [309] N. Lee, M. D. Taylor, K. N. Hor, and R. K. Banerjee. “Non-invasive evaluation of energy loss in the pulmonary arteries using 4D phase contrast MR measurement: A proof of concept”. In: *Biomedical Engineering Online* 12.93 (2013). DOI: [10.1186/1475-925X-12-93](https://doi.org/10.1186/1475-925X-12-93) (cited on page 76).
- [310] D. Lesage, E. D. Angelini, I. Bloch, and G. Funka-Lea. “A review of 3D vessel lumen segmentation techniques: Models, features and extraction schemes”. In: *Medical Image Analysis* 13.6 (2009), pp. 819–45. DOI: [10.1016/j.media.2009.07.011](https://doi.org/10.1016/j.media.2009.07.011) (cited on page 37).
- [311] Y. Levy, D. Degani, and A. Seginer. “Graphical visualization of vortical flows by means of helicity”. In: *The American Institute of Aeronautics and Astronautics Journal* 28.8 (1990), pp. 1347–52. DOI: [10.2514/3.25224](https://doi.org/10.2514/3.25224) (cited on pages 54, 99).
- [312] M. J. Lewis, D. S. O’Connor, A. Rozenshtien, S. Ye, A. J. Einstein, J. M. Ginns, and M. S. Rosenbaum. “Usefulness of magnetic resonance imaging to guide referral for pulmonary valve replacement in repaired tetralogy of Fallot”. In: *The American Journal of Cardiology* 114.9 (2014), pp. 1406–11. DOI: [10.1016/j.amjcard.2014.07.082](https://doi.org/10.1016/j.amjcard.2014.07.082) (cited on page 60).
- [313] W. Li, A. V. Avram, B. Wu, X. Xiao, and C. Liu. “Integrated Laplacian-based phase unwrapping and background phase removal for quantitative susceptibility mapping”. In: *NMR in Biomedicine* 27.2 (2014), pp. 219–27. DOI: [10.1002/nbm.3056](https://doi.org/10.1002/nbm.3056) (cited on page 34).
- [314] M. J. Lighthill. “On sound generated aerodynamically. I. General theory”. In: *Proceedings of the Royal Society A: Mathematical, Physical and Engineering Sciences* 211.1107 (1952), pp. 564–87. DOI: [10.1098/rspa.1952.0060](https://doi.org/10.1098/rspa.1952.0060) (cited on page 70).
- [315] J. Liu and J. Sun. “Parallel graph-cuts by adaptive bottom-up merging”. In: *Proceedings: IEEE Conference on Computer Vision and Pattern Recognition*. 2010, pp. 2181–8. DOI: [10.1109/CVPR.2010.5539898](https://doi.org/10.1109/CVPR.2010.5539898) (cited on pages 39, 84).
- [316] X. Liu, F. Pu, Y. Fan, X. Deng, D. Li, and S. Li. “A numerical study on the flow of blood and the transport of LDL in the human aorta: The physiological significance of the helical flow in the aortic arch”. In: *American Journal of Physiology. Heart and Circulatory Physiology* 297.1 (2009), H163–70. DOI: [10.1152/ajpheart.00266.2009](https://doi.org/10.1152/ajpheart.00266.2009) (cited on page 57).
- [317] S. K. Lodha, A. Pang, R. E. Sheehan, and C. M. Wittenbrink. “UFLOW: Visualizing uncertainty in fluid flow”. In: *Proceedings: IEEE Conference on Visualization (Vis)*. 1996, pp. 249–54. DOI: [10.1109/VISUAL.1996.568116](https://doi.org/10.1109/VISUAL.1996.568116) (cited on page 48).
- [318] M. Loecher, K. Johnson, B. Landgraf, and O. Wieben. “4D gradient based phase unwrapping for PC-MR flow data”. In: *Proceedings: International Society for Magnetic Resonance in Medicine*. 2011, p. 3284. Link: cds.ismrm.org (accessed at 02/2016) (cited on page 34).
- [319] M. Loecher, S. Kecskemeti, P. Turski, and O. Wieben. “Comparison of divergence-free algorithms for 3D MRI with three-directional velocity encoding”. In: *Journal of Cardiovascular Magnetic Resonance* 14.Suppl 1 (2012), W64. DOI: [10.1186/1532-429X-14-S1-W64](https://doi.org/10.1186/1532-429X-14-S1-W64) (cited on page 36).
- [320] M. Loecher, E. Schrauben, K. M. Johnson, and O. Wieben. “Phase unwrapping in 4D MR flow with a 4D single-step Laplacian algorithm”. In: *Journal of Magnetic Resonance Imaging* 43.4 (2015), pp. 833–42. DOI: [10.1002/jmri.25045](https://doi.org/10.1002/jmri.25045) (cited on pages 33, 34).
- [321] N. K. Logothetis, J. Pauls, M. Augath, T. Trinath, and A. Oeltermann. “Neurophysiological investigation of the basis of the fMRI signal”. In: *Nature* 412.6843 (2001), pp. 150–7. DOI: [10.1038/35084005](https://doi.org/10.1038/35084005) (cited on page 21).
- [322] H. Lombaert, Y. Sun, and F. Cheriet. “Fast 4D segmentation of large datasets using graph cuts”. In: *Proceedings: International Society for Optics and Photonics (SPIE)*. 2011, 79622H–79622H–7. DOI: [10.1117/12.877505](https://doi.org/10.1117/12.877505) (cited on page 148).

- [323] D. B. Longmore, D. N. Firmin, G. L. Nayler, S. R. Underwood, and R. H. Klipstein. "Cine magnetic resonance blood flow imaging in clinical use". In: *JMRI* 4.2 (1986), p. 157. DOI: [10.1016/0730-725X\(86\)90991-4](https://doi.org/10.1016/0730-725X(86)90991-4) (cited on page 7).
- [324] W. E. Lorensen and H. E. Cline. "Marching cubes: A high resolution 3D surface construction algorithm". In: *SIGGRAPH Computer Graphics* 21.4 (1987), pp. 163–9. DOI: [10.1145/37402.37422](https://doi.org/10.1145/37402.37422) (cited on pages 39, 43, 51, 85).
- [325] R. Lorenz, J. Bock, A. J. Barker, F. von Knobelsdorff-Brenkenhoff, W. Wallis, J. G. Korvink, M. M. Bissell, J. Schulz-Menger, and M. Markl. "4D flow magnetic resonance imaging in bicuspid aortic valve disease demonstrates altered distribution of aortic blood flow helicity". In: *Journal of Magnetic Resonance in Medicine* 71.4 (2014), pp. 1542–53. DOI: [10.1002/mrm.24802](https://doi.org/10.1002/mrm.24802) (cited on pages 7, 77).
- [326] R. Lorenz, J. Bock, J. Snyder, J. G. Korvink, B. A. Jung, and M. Markl. "Influence of eddy current, maxwell and gradient field corrections on 3D flow visualization of 3D cine PC-MRI data". In: *Journal of Magnetic Resonance in Medicine* 72.33 (2014), pp. 33–40. DOI: [10.1002/mrm.24885](https://doi.org/10.1002/mrm.24885) (cited on pages 34, 35).
- [327] J. Lotz, C. Meier, A. Leppert, and M. Galanski. "Cardiovascular flow measurement with phase-contrast MR imaging: Basic facts and implementation". In: *Radiographics* 22.3 (2002), pp. 651–71. DOI: [10.1148/radiographics.22.3.g02ma11651](https://doi.org/10.1148/radiographics.22.3.g02ma11651) (cited on pages 25, 26, 35).
- [328] M. Loudon, M. M. Bissell, P. Dyverfeldt, C.-J. Carlhäll, T. Ebbers, A. T. Hess, B. D. Prendergast, S. Neubauer, and S. G. Myerson. "Turbulent kinetic energy in the ascending aorta is greater in bicuspid than tricuspid aortic valve stenosis". In: *Journal of Cardiovascular Magnetic Resonance* 17.Suppl 1 (2015), O88. DOI: [10.1186/1532-429X-17-S1-O88](https://doi.org/10.1186/1532-429X-17-S1-O88) (cited on page 76).
- [329] J. B. MacQueen. "Some methods for classification and analysis of multivariate observations". In: *Proceedings: 5th Berkeley Symposium on Mathematical Statistics and Probability*. Vol. 1. 1967, pp. 281–97. Link: projecteuclid.org (accessed at 02/2016) (cited on page 52).
- [330] P. Magrath, M. Markl, A. F. Stalder, M. A. Gülsün, and B. Spottiswoode. "Improved semi-automated pulse wave velocity analysis in the thoracic aorta using 4D flow MRI". In: *Proceedings: International Society for Magnetic Resonance in Medicine*. 2014, p. 2482. Link: healthcare.siemens.com (accessed at 02/2016) (cited on page 68).
- [331] R. Mahadevia, A. J. Barker, S. Schnell, P. Entezari, P. Kansal, P. W. Fedak, S. C. Malaisrie, P. McCarthy, J. Collins, J. C. Carr, and M. Markl. "Bicuspid aortic cusp fusion morphology alters aortic three-dimensional outflow patterns, wall shear stress, and expression of aortopathy". In: *Circulation* 129.6 (2014), pp. 673–82. DOI: [10.1161/CIRCULATIONAHA.113.003026](https://doi.org/10.1161/CIRCULATIONAHA.113.003026) (cited on page 60).
- [332] M. Mahapatra and J. M. Buhmann. "Automatic cardiac RV segmentation using semantic information with graph cuts". In: *Proceedings: IEEE International Symposium on Biomedical Imaging*. 2013, pp. 1106–9. DOI: [10.1109/ISBI.2013.6556672](https://doi.org/10.1109/ISBI.2013.6556672) (cited on page 148).
- [333] A. M. Malek, S. L. Alper, and S. Izumo. "Hemodynamic shear stress and its role in atherosclerosis". In: *The Journal of the American Medical Association* 282.21 (1999), pp. 2035–42. DOI: [10.1001/jama.282.21.2035](https://doi.org/10.1001/jama.282.21.2035) (cited on page 72).
- [334] O. Mallo, R. Peikert, C. Sigg, and F. Sadlo. "Illuminated lines revisited". In: *Proceedings: IEEE Conference on Visualization (Vis)*. 2005, pp. 19–26. DOI: [10.1109/VISUAL.2005.1532772](https://doi.org/10.1109/VISUAL.2005.1532772) (cited on page 48).
- [335] A. J. Marelli, A. S. Mackie, R. Ionescu-Ittu, E. Rahme, and L. Pilote. "Congenital heart disease in the general population: Changing prevalence and age distribution". In: *Circulation* 115.2 (2007), pp. 163–72. DOI: [10.1161/CIRCULATIONAHA.106.627224](https://doi.org/10.1161/CIRCULATIONAHA.106.627224) (cited on page 18).
- [336] M. Markl. *Velocity encoding and flow imaging*. 2005. Link: ee-classes.usc.edu (accessed at 02/2016) (cited on page 26).
- [337] M. Markl, R. Bammer, M. T. Alley, C. J. Elkins, M. T. Draney, A. Barnett, M. E. Moseley, G. H. Glover, and N. J. Pelc. "Generalized reconstruction of phase contrast MRI: Analysis and correction of the effect of gradient field distortions". In: *Journal of Magnetic Resonance in Medicine* 50.4 (2003), pp. 791–801. DOI: [10.1002/mrm.10582](https://doi.org/10.1002/mrm.10582) (cited on page 35).
- [338] M. Markl, M. T. Draney, M. D. Hope, J. M. Levin, F. P. Chan, M. T. Alley, N. J. Pelc, and R. J. Herfkens. "Time-resolved 3-dimensional velocity mapping in the thoracic aorta: Visualization of 3-directional blood flow patterns in healthy volunteers and patients". In: *Journal of Computer Assisted Tomography* 28.4 (2004), pp. 459–69. DOI: [10.1097/00004728-200407000-00005](https://doi.org/10.1097/00004728-200407000-00005) (cited on page 60).
- [339] M. Markl, W. Wallis, S. Brendecke, J. Simon, A. Frydrychowicz, and A. Harloff. "Estimation of global aortic pulse wave velocity by flow-sensitive 4D MRI". In: *Journal of Magnetic Resonance Imaging* 63.6 (2010), pp. 1575–82. DOI: [10.1002/mrm.22353](https://doi.org/10.1002/mrm.22353) (cited on page 67).
- [340] M. Markl, J. Geiger, L. Herzer, B. Stiller, and R. Arnold. "3D aortic blood flow in patients with Marfan syndrome: Changes in hemodynamics and correlation with aortic geometry". In: *Proceedings: International Society for Magnetic Resonance in Medicine*. 2011, p. 725. Link: cds.ismrm.org (accessed at 02/2016) (cited on page 60).
- [341] M. Markl, P. J. Kilner, and T. Ebbers. "Comprehensive 4D velocity mapping of the heart and great vessels by cardiovascular magnetic resonance". In: *Journal of Cardiovascular Magnetic Resonance* 13.7 (2011). DOI: [10.1186/1532-429X-13-7](https://doi.org/10.1186/1532-429X-13-7) (cited on pages 8, 91).

- [342] M. Markl, A. Frydrychowicz, S. Kozerke, M. D. Hope, and O. Wieben. “4D flow MRI”. In: *Journal of Magnetic Resonance Imaging* 36.5 (2012), pp. 1015–36. DOI: [10.1002/jmri.23632](https://doi.org/10.1002/jmri.23632) (cited on pages 8, 26, 59).
- [343] M. Markl, S. Schnell, and A. J. Barker. “4D flow imaging: Current status to future clinical applications”. In: *Current Cardiology Reports* 16.5 (2014), p. 481. DOI: [10.1007/s11886-014-0481-8](https://doi.org/10.1007/s11886-014-0481-8) (cited on page 8).
- [344] P. S. Martin, B. Kloesel, R. A. Norris, M. Lindsay, D. Milan, and S. C. Body. “Embryonic development of the bicuspid aortic valve”. In: *Journal of Cardiovascular Development and Disease* 2.4 (2015), pp. 248–72. DOI: [10.3390/jcdd2040248](https://doi.org/10.3390/jcdd2040248) (cited on pages 17, 107).
- [345] J. Martinez Esturo, M. Schulze, C. Rössl, and H. Theisel. “Global selection of stream surfaces”. In: *Computer Graphics Forum* 32.2 (2013), pp. 113–22. DOI: [10.1111/cgf.12031](https://doi.org/10.1111/cgf.12031) (cited on page 50).
- [346] A. M. Masaryk, R. Frayne, O. Unal, E. Krupinski, and C. M. Strother. “In vitro and in vivo comparison of three MR measurement methods for calculating vascular shear stress in the internal carotid artery”. In: *American Journal of Neuroradiology* 20.2 (1999), pp. 237–45. Link: ajnr.org (accessed at 02/2016) (cited on page 72).
- [347] O. Mattausch, T. Theußl, H. Hauser, and M. E. Gröller. “Strategies for interactive exploration of 3D flow using evenly-spaced illuminated streamlines”. In: *Proceedings: 19th Spring Conference on Computer Graphics*. 2003, pp. 213–22. DOI: [10.1145/984952.984987](https://doi.org/10.1145/984952.984987) (cited on pages 48, 50).
- [348] G. J. Mauritz, J. T. Marcus, A. Boonstra, P. E. Postmus, N. Westerhof, and A. Vonk-Noordegraaf. “Non-invasive stroke volume assessment in patients with pulmonary arterial hypertension: Left-sided data mandatory”. In: *Journal of Cardiovascular Magnetic Resonance* 10.51 (2008). DOI: [10.1186/1532-429X-10-51](https://doi.org/10.1186/1532-429X-10-51) (cited on page 66).
- [349] D. A. McDonald. “Regional pulse-wave velocity in the arterial tree”. In: *Journal of Applied Physiology* 24.1 (1968), pp. 73–8. Link: jap.physiology.org (accessed at 02/2016) (cited on page 67).
- [350] V. V. McLaughlin, S. L. Archer, D. B. Badesch, R. J. Barst, H. W. Farber, J. R. Lindner, M. A. Mathier, M. D. McGoon, M. H. Park, R. S. Rosenson, L. J. Rubin, V. F. Tapson, and J. Varga. “ACCF/AHA 2009 expert consensus document on pulmonary hypertension: A report of the American College of Cardiology Foundation task force on expert consensus documents and the American Heart Association developed in collaboration with the American College of Chest Physicians; American Thoracic Society, Inc.; and the Pulmonary Hypertension Association”. In: *Journal of the American College of Cardiology* 53.17 (2009), pp. 1573–619. DOI: [10.1016/j.jacc.2009.01.004](https://doi.org/10.1016/j.jacc.2009.01.004) (cited on page 15).
- [351] T. McLoughlin, R. S. Laramée, R. Peikert, F. H. Post, and M. Chen. “Over two decades of integration-based, geometric flow”. In: *Computer Graphics Forum* 29.6 (2010), pp. 1807–29. DOI: [10.1111/j.1467-8659.2010.01650.x](https://doi.org/10.1111/j.1467-8659.2010.01650.x) (cited on pages 47, 48, 50, 112).
- [352] T. McLoughlin, M. W. Jones, R. S. Laramée, R. Malki, I. Masters, and C. D. Hansen. “Similarity measures for enhancing interactive streamline seeding”. In: *IEEE Transactions on Visualization and Computer Graphics* 19.8 (2013), pp. 1342–53. DOI: [10.1109/TVCG.2012.150](https://doi.org/10.1109/TVCG.2012.150) (cited on page 51).
- [353] D. W. McRobbie, E. A. Moore, M. J. Graves, and M. R. Prince. *MRI – From picture to proton*. Cambridge University Press, 2007. ISBN: 978-0521683845 (cited on page 23).
- [354] S. Meier, A. Hennemuth, O. Friman, J. Bock, M. Markl, and T. Preusser. “Non-invasive 4D blood flow and pressure quantification in central blood vessels via PC-MRI”. In: *Proceedings: Computing in Cardiology*. 2010, pp. 903–6. Link: publica.fraunhofer.de (accessed at 02/2016) (cited on page 75).
- [355] S. Meier, A. Hennemuth, J. Drexler, J. Bock, B. Jung, and T. Preusser. “A fast and noise-robust method for computation of intravascular pressure difference maps from 4D PC-MRI data”. In: *Proceedings: Statistical Atlases and Computational Models of the Heart. Imaging and Modelling Challenges (STACOM)*. 2013, pp. 215–24. DOI: [10.1007/978-3-642-36961-2_25](https://doi.org/10.1007/978-3-642-36961-2_25) (cited on pages 37, 75).
- [356] C. Meierhofer, E. P. Schneider, C. Lyko, A. Hutter, S. Martinoff, M. Markl, A. Hager, J. Hess, H. Stern, and S. Fratz. “Wall shear stress and flow patterns in the ascending aorta in patients with bicuspid aortic valves differ significantly from tricuspid aortic valves: A prospective study”. In: *European Heart Journal - Cardiovascular Imaging* 14.8 (2013), pp. 797–804. DOI: [10.1093/ehjci/jes273](https://doi.org/10.1093/ehjci/jes273) (cited on pages 60, 62, 116).
- [357] S. Mendis, P. Puska, and B. Norrving. *Global atlas on cardiovascular disease prevention and control*. World Health Organization, World Heart Federation and World Stroke Organization, 2011. Link: whqlibdoc.who.int (accessed at 02/2016) (cited on pages 7, 14).
- [358] H. Meng, V. Tutino, J. Xiang, and A. Siddiqui. “High WSS or low WSS? Complex interactions of hemodynamics with intracranial aneurysm initiation, growth, and rupture: Toward a unifying hypothesis”. In: *American Journal of Neuroradiology* 35.7 (2014), pp. 1254–62. DOI: [10.3174/ajnr.A3558](https://doi.org/10.3174/ajnr.A3558) (cited on page 73).
- [359] E. Metaxa, M. Tremmel, J. Xiang, J. Kolega, M. Mandelbaum, A. Siddiqui, J. Mocco, and H. Meng. “High wall shear stress and positive wall shear stress gradient trigger the initiation of intracranial aneurysms”. In: *Proceedings: Summer Bioengineering Conference*. 2009, pp. 523–24. DOI: [10.1115/SBC2009-206395](https://doi.org/10.1115/SBC2009-206395) (cited on page 73).
- [360] M. Meuschke. “Computergestützte Analyse von Verwirbelungen in 4D PC-MRI Blutflussdaten der Aorta”. MA thesis. Otto-von-Guericke-University, Magdeburg, Germany, 2015 (cited on pages 50, 117, 120, 121, 123, 124, 205, 206, 209).

- [361] M. Meuschke, J. Hettig, and S. Pauksch. *Entwicklung eines Polarplots zur Darstellung kardialer Blutflussdaten*. Scientific Team Project, Otto-von-Guericke-University, Magdeburg, Germany. 2014 (cited on pages 206, 209).
- [362] M. Meuschke, K. Lawonn, **B. Köhler**, U. Preim, and B. Preim. “Clustering of aortic vortex flow in cardiac 4D PC-MRI data”. In: *Proceedings: Bildverarbeitung für die Medizin*. 2016, pp. 182–7 (cited on pages 51, 117, 206).
- [363] M. Meuschke, **B. Köhler**, U. Preim, B. Preim, and K. Lawonn. “Semi-automatic vortex flow classification in 4D PC-MRI data of the aorta”. In: *Computer Graphics Forum* 35.3 (2016), pp. 351–60. DOI: [10.1111/cgf.12911](https://doi.org/10.1111/cgf.12911) (cited on pages 121, 122, 125, 128–132, 205).
- [364] V. Mihalef, S. Rapaka, M. A. Gülsün, A. Scorza, P. Sharma, L. M. Itu, A. Kamen, A. J. Barker, M. Markl, and D. Comaniciu. “Model-based estimation of 4D relative pressure map from 4D flow MR images”. In: *Proceedings: Statistical Atlases and Computational Models of the Heart. Imaging and Modelling Challenges (STACOM)*. 2014, pp. 236–43. DOI: [10.1007/978-3-642-54268-8_28](https://doi.org/10.1007/978-3-642-54268-8_28) (cited on page 75).
- [365] H. Mirzaee and A. Hennemuth. “Noninvasive measurement of intravascular pressure gradients based on 3D anatomy and 4D flow image fusion”. In: *Proceedings: International Society for Magnetic Resonance in Medicine*. 2015, p. 2753. Link: ismrm.org (accessed at 02/2016) (cited on page 37).
- [366] H. Mirzaee, J. Drexl, A. Hennemuth, and A. Harloff. “Investigation of arterial pulse wave velocity based on 4D phase contrast MR flow imaging (4D PC MRI)”. In: *Proceedings: Radiological Society of North America 2013 Scientific Assembly and Annual Meeting*. 2013. Link: archive.rsna.org (accessed at 02/2016) (cited on page 68).
- [367] R. H. Mohiaddin and D. B. Longmore. “MRI studies of atherosclerotic vascular disease: Structural evaluation and physiological measurements”. In: *British Medical Bulletin* 45.4 (1989), pp. 968–90. Link: bmb.oxfordjournals.org (accessed at 02/2016) (cited on page 67).
- [368] R. H. Mohiaddin, D. N. Firmin, and D. B. Longmore. “Age-related changes of human aortic flow wave velocity measured noninvasively by magnetic resonance imaging”. In: *Journal of Applied Physiology (1985)* 74.1 (1993), pp. 492–7. Link: jap.physiology.org (accessed at 02/2016) (cited on page 67).
- [369] S. Moltzahn and M. Zeydabadinejad. *Dopplerechokardiographie. CW, PW, Farbdoppler – Eine Einführung*. Georg Thieme Verlag, 2000. ISBN: 978-3131393029 (cited on page 28).
- [370] U. Morbiducci, R. Ponzini, G. Rizzo, M. Cadioli, A. Esposito, F. De Cobelli, A. Del Maschio, F. M. Montevecchi, and A. Redaelli. “In vivo quantification of helical blood flow in human aorta by time-resolved three-dimensional cine phase contrast magnetic resonance imaging”. In: *Annals of Biomedical Engineering* 37.3 (2009), pp. 516–31. DOI: [10.1007/s10439-008-9609-6](https://doi.org/10.1007/s10439-008-9609-6) (cited on page 77).
- [371] U. Morbiducci, R. Ponzini, G. Rizzo, M. Cadioli, A. Esposito, F. M. Montevecchi, and A. Redaelli. “Mechanistic insight into the physiological relevance of helical blood flow in the human aorta: An in vivo study”. In: *Biomechanics and Modeling in Mechanobiology* 10.3 (2011), pp. 339–55. DOI: [10.1007/s10237-010-0238-2](https://doi.org/10.1007/s10237-010-0238-2) (cited on page 57).
- [372] S. Mori and P. C. M. van Zijl. “Fiber tracking: Principles and strategies – A technical review”. In: *NMR in Biomedicine* 15.7-8 (2002), pp. 468–80. DOI: [10.1002/nbm.781](https://doi.org/10.1002/nbm.781) (cited on pages 21, 78, 160).
- [373] D. Mozaffarian, E. J. Benjamin, A. S. Go, D. K. Arnett, M. J. Blaha, M. Cushman, S. de Ferranti, J.-P. Després, H. J. Fullerton, V. J. Howard, M. D. Huffman, S. E. Judd, B. M. Kissela, D. T. Lackland, J. H. Lichtman, L. D. Lisabeth, S. Liu, R. H. Mackey, D. B. Matchar, D. K. McGuire, E. R. Mohler, C. S. Moy, P. Muntner, M. E. Mussolino, K. Nasir, R. W. Neumar, G. Nichol, L. Palaniappan, D. K. Pandey, M. J. Reeves, C. J. Rodriguez, P. D. Sorlie, J. Stein, A. Towfighi, T. N. Turan, S. S. Virani, D. Willey J. Z. Woo, R. W. Yeh, and M. B. Turner. “Heart disease and stroke statistics – 2015 update: A report from the American Heart Association”. In: *Circulation* 131.4 (2015), e29–e322. DOI: [10.1161/CIR.000000000000152](https://doi.org/10.1161/CIR.000000000000152) (cited on page 14).
- [374] K. Mühlner, M. Neugebauer, C. Tietjen, and B. Preim. “Viewpoint selection for intervention planning”. In: *Proceedings: 9th Joint Eurographics and IEEE VGTC Conference on Visualization*. 2007, pp. 267–74. DOI: [10.2312/VisSym/EuroVis07/267-274](https://doi.org/10.2312/VisSym/EuroVis07/267-274) (cited on page 161).
- [375] K. S. Nayak, J.-F. Nielsen, M. A. Bernstein, M. Markl, P. D. Gatehouse, R. M. Botnar, D. Saloner, C. Lorenz, H. Wen, B. S. Hu, F. H. Epstein, J. N. Oshinski, and S. V. Raman. “Cardiovascular magnetic resonance phase contrast imaging”. In: *Journal of Cardiovascular Magnetic Resonance* 17.71 (2015), pp. 1–26. DOI: [10.1186/s12968-015-0172-7](https://doi.org/10.1186/s12968-015-0172-7) (cited on pages 8, 26).
- [376] G. L. Nayler, D. N. Firmin, and D. B. Longmore. “Blood flow imaging by cine magnetic resonance”. In: *Journal of Computer Assisted Tomography* 10.5 (1986), pp. 715–22. DOI: [10.1097/00004728-198609000-00001](https://doi.org/10.1097/00004728-198609000-00001) (cited on page 7).
- [377] R. Nepomuceno, M. Zeglinski, J. Lerner, W. Czarnecki, I. D. C. Kirkpatrick, J. Strzelczyk, and D. S. Jassal. “Multimodality imaging of anomalous pulmonary veins”. In: *Cardiovascular Ultrasound* 9.3 (2011). DOI: [10.1186/1476-7120-9-3](https://doi.org/10.1186/1476-7120-9-3) (cited on page 29).
- [378] R. M. Nerem and W. A. Seed. “An in vivo study of aortic flow disturbances”. In: *Cardiovascular Research* 6.1 (1972), pp. 1–14. DOI: [10.1093/cvr/6.1.1](https://doi.org/10.1093/cvr/6.1.1) (cited on page 75).

- [379] E. J. Nett, K. M. Johnson, A. Frydrychowicz, A. M. Del Rio, E. Schrauben, C. J. François, and O. Wieben. “Four-dimensional phase contrast magnetic resonance imaging with accelerated dual velocity encoding”. In: *Journal of Magnetic Resonance Imaging* 35.6 (2012), pp. 1462–71. DOI: [10.1002/jmri.23588](https://doi.org/10.1002/jmri.23588) (cited on page 26).
- [380] E. J. Nett, J. C. Nguyen, K. Johnson, O. Wieben, and C. François. “Noninvasive pressure measurement with 4D phase contrast MRI in patients with aortic coarctations”. In: *Journal of Cardiovascular Magnetic Resonance* 14.Suppl 1 (2012), P106. DOI: [10.1186/1532-429X-14-S1-P106](https://doi.org/10.1186/1532-429X-14-S1-P106) (cited on page 74).
- [381] M. Neugebauer, M. Glöckler, L. Goubergrits, M. Kelm, T. Kühne, and A. Hennemuth. “Interactive virtual stent planning for the treatment of coarctation of the aorta”. In: *International Journal of Computer Assisted Radiology and Surgery* 11.1 (2015), pp. 133–44. DOI: [10.1007/s11548-015-1220-3](https://doi.org/10.1007/s11548-015-1220-3) (cited on page 160).
- [382] M. Nichols, N. Townsend, P. Scarborough, and M. Rayner. *European cardiovascular disease statistics*. 2012. Link: ehnheart.org (accessed at 02/2016) (cited on page 14).
- [383] R. Nishimura. “Aortic valve disease”. In: *Circulation* 106.7 (2002), pp. 770–2. DOI: [10.1161/01.CIR.0000027621.26167.5E](https://doi.org/10.1161/01.CIR.0000027621.26167.5E) (cited on page 16).
- [384] A. M. Nixon, M. Gunel, and B. E. Sumpio. “The critical role of hemodynamics in the development of cerebral vascular disease”. In: *Journal of Neurosurgery* 112.6 (2010), pp. 1240–53. DOI: [10.3171/2009.10.JNS09759](https://doi.org/10.3171/2009.10.JNS09759) (cited on page 104).
- [385] S. Nordmeyer, E. Riesenkampff, G. Crelier, A. Khasheei, B. Schnackenburg, F. Berger, and T. Kühne. “Flow-sensitive four-dimensional cine magnetic resonance imaging for offline blood flow quantification in multiple vessels: A validation study”. In: *Journal of Magnetic Resonance Imaging* 32.3 (2010), pp. 677–83. DOI: [10.1002/jmri.22280](https://doi.org/10.1002/jmri.22280) (cited on page 65).
- [386] H. Obermaier, J. Kuhnert, M. Hering-Bertram, and H. Hagen. “Stream volume segmentation of grid-less flow simulation”. In: *Topological Methods in Data Analysis and Visualization*. 2011, pp. 127–38. DOI: [10.1007/978-3-642-15014-2_11](https://doi.org/10.1007/978-3-642-15014-2_11) (cited on page 50).
- [387] S. Oeltze, D. J. Lehmann, A. Kuhn, G. Janiga, H. Theisel, and B. Preim. “Blood flow clustering and applications in virtual stenting of intracranial aneurysms”. In: *IEEE Transactions on Visualization and Computer Graphics* 20.5 (2014), pp. 686–701. DOI: [10.1109/TVCG.2013.2297914](https://doi.org/10.1109/TVCG.2013.2297914) (cited on pages 52, 118).
- [388] S. Oeltze-Jafra, J. R. Cebral, G. Janiga, and B. Preim. “Cluster analysis of vortical flow in simulations of cerebral aneurysm hemodynamics”. In: *IEEE Transactions on Visualization and Computer Graphics* 22.1 (2015), pp. 757–66. DOI: [10.1109/TVCG.2015.2467203](https://doi.org/10.1109/TVCG.2015.2467203) (cited on page 52).
- [389] F. Ong, M. Uecker, U. Tariq, A. Hsiao, M. T. Alley, S. S. Vasanawala, and M. Lustig. “Robust 4D flow denoising using divergence-free wavelet transform”. In: *Journal of Magnetic Resonance Imaging* 73.2 (2015), pp. 828–42. DOI: [10.1002/mrm.25176](https://doi.org/10.1002/mrm.25176) (cited on pages 36, 37, 158).
- [390] S. Osher and R. P. Fedkiw. “Level set methods: An overview and some recent results”. In: *Journal of Computational Physics* 169.2 (2001), pp. 463–502. DOI: [10.1006/jcph.2000.6636](https://doi.org/10.1006/jcph.2000.6636) (cited on page 39).
- [391] S. Osher and J. A. Sethian. “Fronts propagating with curvature dependent speed: Algorithms based on Hamilton-Jacobi formulations”. In: *Journal of Computational Physics* 79.1 (1988), pp. 12–49. DOI: [10.1016/0021-9991\(88\)90002-2](https://doi.org/10.1016/0021-9991(88)90002-2) (cited on page 39).
- [392] J. N. Oshinski, D. N. Ku, S. Mukundan Jr., F. Loth, and R. I. Pettigrew. “Determination of wall shear stress in the aorta with the use of MR phase velocity mapping”. In: *Journal of Magnetic Resonance Imaging* 5.6 (1995), pp. 640–7. DOI: [10.1002/jmri.1880050605](https://doi.org/10.1002/jmri.1880050605) (cited on page 72).
- [393] J. N. Oshinski, W. J. Parks, C. P. Markou, H. L. Bergman, B. E. Larson, D. N. Ku, S. Mukundan Jr., and R. I. Pettigrew. “Improved measurement of pressure gradients in aortic coarctation by magnetic resonance imaging”. In: *Journal of the American College of Cardiology* 28.7 (1996), pp. 1818–26. DOI: [10.1016/S0735-1097\(96\)00395-6](https://doi.org/10.1016/S0735-1097(96)00395-6) (cited on page 75).
- [394] M. Otto. “Topology of vector fields with uncertainty”. PhD thesis. Otto-von-Guericke-University, Magdeburg, Germany, 2015. Link: [urn:nbn:de:gbv:ma9:1-6895](https://nbn-resolving.org/urn:nbn:de:gbv:ma9:1-6895) (accessed at 03/2016) (cited on page 48).
- [395] S. Oyre, S. Ringgaard, S. Kozerke, W. P. Paaske, M. Erlandsen, P. Boesiger, and E. M. Pedersen. “Accurate noninvasive quantitation of blood flow, cross-sectional lumen vessel area and wall shear stress by three-dimensional paraboloid modeling of magnetic resonance imaging velocity data”. In: *Journal of the American College of Cardiology* 32.1 (1998), pp. 128–34. Link: [pubmed/9669260](https://pubmed.ncbi.nlm.nih.gov/9669260/) (accessed at 02/2016) (cited on page 72).
- [396] S. Oyre, W. P. Paaske, S. Ringgaard, S. Kozerke, M. Erlandsen, P. Boesiger, and E. M. Pedersen. “Automatic accurate non-invasive quantitation of blood flow, cross-sectional vessel area, and wall shear stress by modelling of magnetic resonance velocity data”. In: *European Journal of Vascular and Endovascular Surgery: The Official Journal of the European Society for Vascular Surgery* 16.6 (1998), pp. 517–24. Link: [pubmed/9894493](https://pubmed.ncbi.nlm.nih.gov/9894493/) (accessed at 02/2016) (cited on page 72).
- [397] S. Oyre, S. Ringgaard, S. Kozerke, W. P. Paaske, M. B. Scheidegger, P. Boesiger, and E. M. Pedersen. “Quantitation of circumferential subpixel vessel position and wall shear stress by multiple sectored three-dimensional paraboloid modeling of velocity encoded cine MR”. In: *Journal of Magnetic Resonance in Medicine* 40.5 (1998), pp. 645–55. Link: [pubmed/9797146](https://pubmed.ncbi.nlm.nih.gov/9797146/) (accessed at 02/2016) (cited on page 72).

- [398] H.-G. Pagendarm, B. Henne, and M. Rutten. “Detecting vortical phenomena in vector data by medium-scale correlation”. In: *Proceedings: IEEE Conference on Visualization (Vis)*. 1999, pp. 409–552. DOI: [10.1109/VISUAL.1999.809917](https://doi.org/10.1109/VISUAL.1999.809917) (cited on page 53).
- [399] K. Palágyi and A. Kuba. “A 3D 6-subiteration thinning algorithm for extracting medial lines”. In: *Pattern Recognition Letters* 19.7 (1998), pp. 613–27. DOI: [10.1016/S0167-8655\(98\)00031-2](https://doi.org/10.1016/S0167-8655(98)00031-2) (cited on page 51).
- [400] T. G. Papaioannou and C. Stefanadis. “Vascular wall shear stress: Basic principles and methods”. In: *Hellenic Journal of Cardiology* 46.1 (2005), pp. 9–15. Link: hellenicjcardiol.org (accessed at 02/2016) (cited on pages 71, 72).
- [401] P. Papathanasopoulou, S. Zhao, U. Köhler, M. B. Robertson, Q. Long, P. Hoskins, X. Y. Xu, and I. Marshall. “MRI measurement of time-resolved wall shear stress vectors in a carotid bifurcation model, and comparison with CFD predictions”. In: *Journal of Magnetic Resonance Imaging* 17.2 (2003), pp. 153–62. DOI: [10.1002/jmri.10243](https://doi.org/10.1002/jmri.10243) (cited on page 72).
- [402] P. M. Pattany and G. L. Nayler. “High velocity flow imaging by even echo rephasing”. In: *Proceedings: International Society for Magnetic Resonance in Medicine*. 1985, pp. 599–600. DOI: [10.1002/mrmp.22419850113](https://doi.org/10.1002/mrmp.22419850113) (cited on page 7).
- [403] P. K. Paulsen and J. M. Hasenkam. “Three-dimensional visualization of velocity profiles in the ascending aorta in dogs, measured with a hot-film anemometer”. In: *Journal of Biomechanics* 16.3 (1983), pp. 201–10. DOI: [10.1016/0021-9290\(83\)90127-6](https://doi.org/10.1016/0021-9290(83)90127-6) (cited on pages 7, 46).
- [404] G. Pedrizzetti, G. La Canna, O. Alfieri, and G. Tonti. “The vortex – An early predictor of cardiovascular outcome?” In: *Nature Reviews Cardiology* 11.9 (2014), pp. 545–53. DOI: [10.1038/nrcardio.2014.75](https://doi.org/10.1038/nrcardio.2014.75) (cited on page 61).
- [405] J. M. Peeters, C. Bos, and C. J. Bakker. “Analysis and correction of gradient nonlinearity and B0 inhomogeneity related scaling errors in two-dimensional phase contrast flow measurements”. In: *Journal of Magnetic Resonance in Medicine* 53.1 (2005), pp. 126–33. DOI: [10.1002/mrm.20309](https://doi.org/10.1002/mrm.20309) (cited on page 35).
- [406] R. Peikert and F. Sadlo. “Topologically relevant stream surfaces for flow visualization”. In: *Proceedings: 25th Spring Conference on Computer Graphics*. 2009, pp. 35–42. DOI: [10.1145/1980462.1980472](https://doi.org/10.1145/1980462.1980472) (cited on page 50).
- [407] M. Persson, J. E. Solem, K. Markenroth, J. Svensson, and A. Heyden. “Phase contrast MRI segmentation using velocity and intensity”. In: *Scale Space and PDE Methods in Computer Vision*. 2005, pp. 119–30. DOI: [10.1007/11408031_11](https://doi.org/10.1007/11408031_11) (cited on page 38).
- [408] S. Petersson, P. Dyverfeldt, and T. Ebbens. “Assessment of the accuracy of MRI wall shear stress estimation using numerical simulations”. In: *Journal of Magnetic Resonance Imaging* 36.1 (2012), pp. 128–38. DOI: [10.1002/jmri.23610](https://doi.org/10.1002/jmri.23610) (cited on page 160).
- [409] B. T. Phong. “Illumination for computer generated pictures”. In: *Communications of the ACM* 18.6 (1975), pp. 311–7. DOI: [10.1145/360825.360839](https://doi.org/10.1145/360825.360839) (cited on pages 43, 48, 88).
- [410] M. Piccinelli, A. Veneziani, D. A. Steinman, A. Remuzzi, and L. Antiga. “A framework for geometric analysis of vascular structures: Application to cerebral aneurysms”. In: *IEEE Transactions on Medical Imaging* 28.8 (2009), pp. 1141–55. DOI: [10.1109/TMI.2009.2021652](https://doi.org/10.1109/TMI.2009.2021652) (cited on pages 38, 85, 118, 125).
- [411] D. H. F. Pilar and C. Ware. “Representing flow patterns by using streamlines with glyphs”. In: *IEEE Transactions on Visualization and Computer Graphics* 19.8 (2013), pp. 1331–41. DOI: [10.1109/TVCG.2013.10](https://doi.org/10.1109/TVCG.2013.10) (cited on page 161).
- [412] A. Pitcher, P. Lamata, S. B. Krittan, D. A. Nordslettern, M. M. Bissell, J. M. Francis, T. E. Cassar, A. J. Barker, M. Markl, S. Neubauer, and N. P. Smith. “Towards a comprehensive description of relative aortic pressure: Insights from 4D flow CMR”. In: *Journal of Cardiovascular Magnetic Resonance* 15.Suppl 1 (2013), P243. DOI: [10.1186/1532-429X-15-S1-P243](https://doi.org/10.1186/1532-429X-15-S1-P243) (cited on page 74).
- [413] A. Pobitzer, R. Peikert, R. Fuchs, B. Schindler, A. Kuhn, H. Theisel, K. Matkovic, and H. Hauser. “On the way towards topology-based visualization of unsteady flow – The state of the art”. In: *Proceedings: EuroGraphics State of the Art Reports*. 2010, pp. 137–54. Link: scivis.ethz.ch (accessed at 03/2016) (cited on page 52).
- [414] K. K. Poh, L. C. Lee, L. Shen, E. Chong, Y. L. Tan, P. Chai, T. C. Yeo, and M. J. Wood. “Left ventricular fluid dynamics in heart failure: Echocardiographic measurement and utilities of vortex formation time”. In: *European Heart Journal - Cardiovascular Imaging* 13.5 (2012), pp. 385–93. DOI: [10.1093/ejehocard/jer288](https://doi.org/10.1093/ejehocard/jer288) (cited on page 61).
- [415] L. M. Portela. “Identification and characterization of vortices in the turbulent boundary layer”. PhD thesis. Stanford University, California, USA, 1998 (cited on page 53).
- [416] F. H. Post, B. Vrolijk, H. Hauser, R. S. Laramée, and H. Doleisch. “The state of the art in flow visualisation: Feature extraction and tracking”. In: *Computer Graphics Forum* 22.4 (2003), pp. 775–92. DOI: [10.1111/j.1467-8659.2003.00723.x](https://doi.org/10.1111/j.1467-8659.2003.00723.x) (cited on page 46).
- [417] W. V. Potters, P. Van Ooij, E. vanBavel, and A. Nederveen. “Vectorial wall shear stress calculations in vessel structures using 4D PC-MRI”. In: *Journal of Cardiovascular Magnetic Resonance* 14.1 (2012), W5. DOI: [10.1186/1532-429X-14-S1-W5](https://doi.org/10.1186/1532-429X-14-S1-W5) (cited on page 73).

- [418] W. V. Potters, H. A. Marquering, E. vanBavel, and A. J. Nederveen. “Measuring wall shear stress using velocity-encoded MRI”. In: *Current Cardiovascular Imaging Reports* 7.4 (2014), pp. 1–12. DOI: [10.1007/s12410-014-9257-1](https://doi.org/10.1007/s12410-014-9257-1) (cited on pages 71, 73).
- [419] W. V. Potters, P. Van Ooij, H. Marquering, E. vanBavel, and A. J. Nederveen. “Volumetric arterial wall shear stress calculation based on cine phase contrast MRI”. In: *Journal of Magnetic Resonance Imaging* 41.2 (2015), pp. 505–16. DOI: [10.1002/jmri.24560](https://doi.org/10.1002/jmri.24560) (cited on page 73).
- [420] A. Powell. “Theory of vortex sound”. In: *The Journal of the Acoustical Society of America* 36.1 (1964), pp. 177–95. DOI: [10.1121/1.1918931](https://doi.org/10.1121/1.1918931) (cited on page 70).
- [421] B. Preim and C. Botha. *Visual computing for medicine*. 2nd ed. Morgan Kaufmann Publishers, 2013. DOI: [10.1016/B978-0-12-415873-3.00005-5](https://doi.org/10.1016/B978-0-12-415873-3.00005-5) (cited on page 44).
- [422] K. P. Pruessmann, M. Weiger, M. B. Scheidegger, and P. Boesiger. “SENSE: Sensitivity encoding for fast MRI”. In: *Journal of Magnetic Resonance in Medicine* 42.5 (1999), pp. 952–62. DOI: [10.1002/\(SICI\)1522-2594\(199911\)42:5\(952::AID-MRM16\)3.0.CO;2-S](https://doi.org/10.1002/(SICI)1522-2594(199911)42:5(952::AID-MRM16)3.0.CO;2-S) (cited on page 26).
- [423] D. A. Redel. “Physiological flow velocity patterns in the cardiovascular system”. In: *Color Blood Flow Imaging of the Heart*. 1988, pp. 27–41. DOI: [10.1007/978-3-642-71172-5_6](https://doi.org/10.1007/978-3-642-71172-5_6) (cited on page 56).
- [424] M. Reiser and W. Semmler. *Magnetresonanztomographie*. Springer, Berlin, Heidelberg, 2002. ISBN: 3-540-66668-0 (cited on page 23).
- [425] G. Reiter, U. Reiter, G. Kovacs, B. Kainz, K. Schmidt, R. Maier, H. Olschewski, and R. Rienmueller. “Magnetic resonance-derived 3-dimensional blood flow patterns in the main pulmonary artery as a marker of pulmonary hypertension and a measure of elevated mean pulmonary arterial pressure”. In: *Circulation. Cardiovascular Imaging* 1.1 (2008), pp. 23–30. DOI: [10.1161/CIRCIMAGING.108.780247](https://doi.org/10.1161/CIRCIMAGING.108.780247) (cited on page 60).
- [426] G. Reiter, U. Reiter, G. Kovacs, H. Olschewski, and M. Fuchsjäger. “Blood flow vortices along the main pulmonary artery measured with MR imaging for diagnosis of pulmonary hypertension”. In: *Radiology* 275.2 (2015), pp. 71–9. DOI: [10.1148/radiol.14140849](https://doi.org/10.1148/radiol.14140849) (cited on page 60).
- [427] Y. Richter and E. R. Edelman. “Cardiology is flow”. In: *Circulation* 113.23 (2006), pp. 2679–82. DOI: [10.1161/CIRCULATIONAHA.106.632687](https://doi.org/10.1161/CIRCULATIONAHA.106.632687) (cited on page 13).
- [428] E. Riesenkampff, J. F. Fernandes, S. Meier, L. Goubergrits, S. Kropf, S. Schubert, F. Berger, A. Hennemuth, and T. Kühne. “Pressure fields by flow-sensitive, 4D, velocity-encoded CMR in patients with aortic coarctation”. In: *JACC: Cardiovascular Imaging* 7.9 (2014), pp. 920–6. DOI: [10.1016/j.jcmg.2014.03.017](https://doi.org/10.1016/j.jcmg.2014.03.017) (cited on page 73).
- [429] P. A. Rinck. *Magnetic resonance in medicine. The basic textbook of the European magnetic resonance forum*. 9th ed. E-version 9.1 beta. 2016. Link: magnetic-resonance.org (accessed at 02/2016) (cited on page 21).
- [430] J. Rodés-Cabau. “Transcatheter aortic valve implantation: Current and future approaches”. In: *Nature Reviews. Cardiology* 9.1 (2011), pp. 15–29. DOI: [10.1038/nrcardio.2011.164](https://doi.org/10.1038/nrcardio.2011.164) (cited on page 17).
- [431] A. Roldán-Alzate, A. Frydrychowicz, K. M. Johnson, H. Kellihan, N. C. Chesler, O. Wieben, and C. J. François. “Non-invasive assessment of cardiac function and pulmonary vascular resistance in a canine model of acute thromboembolic pulmonary hypertension using 4D flow cardiovascular magnetic resonance”. In: *Journal of Cardiovascular Magnetic Resonance* 16.1 (2014), p. 23. DOI: [10.1186/1532-429X-16-23](https://doi.org/10.1186/1532-429X-16-23) (cited on page 66).
- [432] C. Rössl and H. Theisel. “Streamline embedding for 3D vector field exploration”. In: *IEEE Transactions on Visualization and Computer Graphics* 18.3 (2012), pp. 407–20. DOI: [10.1109/TVCG.2011.78](https://doi.org/10.1109/TVCG.2011.78) (cited on page 51).
- [433] M. Roth. “Automatic extraction of vortex core lines and other line-type features for scientific visualization”. PhD thesis. ETH Zürich, Switzerland, 2000. Link: <ftp.inf.ethz.ch> (accessed at 02/2016) (cited on page 54).
- [434] M. Roth and R. Peikert. “A higher-order method for finding vortex core lines”. In: *Proceedings: IEEE Conference on Visualization (Vis)*. 1998, pp. 143–50. DOI: [10.1109/VISUAL.1998.745296](https://doi.org/10.1109/VISUAL.1998.745296) (cited on page 53).
- [435] K. J. Rothman, S. Greenland, and T. L. Lash. *Modern epidemiology*. Lippincott Williams & Wilkins, 2008 (cited on page 161).
- [436] I. A. Sadarjoen and F. H. Post. “Geometric methods for vortex extraction”. In: *Proceedings: Joint Eurographics and IEEE TVCG Symposium on Visualization*. 1999, pp. 53–62. DOI: [10.1007/978-3-7091-6803-5](https://doi.org/10.1007/978-3-7091-6803-5) (cited on page 53).
- [437] I. A. Sadarjoen and F. H. Post. “Detection, quantification, and tracking of vortices using streamline geometry”. In: *Computers & Graphics* 24.3 (2000), pp. 333–41. DOI: [10.1016/S0097-8493\(00\)00029-7](https://doi.org/10.1016/S0097-8493(00)00029-7) (cited on page 53).
- [438] J. Sahrner, T. Weinkauff, and H.-C. Hege. “Galilean invariant extraction and iconic representation of vortex core lines”. In: *Proceedings: Joint Eurographics and IEEE TVCG Symposium on Visualization*. 2005, pp. 151–60. DOI: [10.2312/VisSym/EuroVis05/151-160](https://doi.org/10.2312/VisSym/EuroVis05/151-160) (cited on pages 53, 102).
- [439] M. F. Salfity, J. M. Huntley, M. J. Graves, O. Marklund, R. Cusack, and D. A. Beauregard. “Extending the dynamic range of phase contrast magnetic resonance velocity imaging using advanced higher-dimensional phase unwrapping algorithms”. In: *Journal of The Royal Society Interface* 3.8 (2006), pp. 415–27. DOI: [10.1098/rsif.2005.0096](https://doi.org/10.1098/rsif.2005.0096) (cited on page 34).

- [440] O. Salvado, C. Hillenbrand, S. Zhang, and D. L. Wilson. “Method to correct intensity inhomogeneity in MR images for atherosclerosis characterization”. In: *IEEE Transactions on Medical Imaging* 25.5 (2006), pp. 539–52. DOI: [10.1109/TMI.2006.871418](https://doi.org/10.1109/TMI.2006.871418) (cited on page 158).
- [441] S. Salvador and P. Chan. “Determining the number of clusters / segments in hierarchical clustering / segmentation algorithms”. In: *Proceedings: IEEE International Conference on Tools with Artificial Intelligence*. 2004, pp. 576–84. DOI: [10.1109/ICTAI.2004.50](https://doi.org/10.1109/ICTAI.2004.50) (cited on page 118).
- [442] T. Salzbrunn. “Flow visualization and analysis based on integral line predicates”. PhD thesis. University of Leipzig, Germany, 2008 (cited on page 52).
- [443] T. Salzbrunn and G. Scheuermann. “Streamline predicates”. In: *IEEE Transactions on Visualization and Computer Graphics* 12.6 (2006), pp. 1601–12. DOI: [10.1109/TVCG.2006.104](https://doi.org/10.1109/TVCG.2006.104) (cited on page 52).
- [444] T. Salzbrunn, C. Garth, G. Scheuermann, and J. Meyer. “Pathline predicates and unsteady flow structures”. In: *The Visual Computer* 24.12 (2008), pp. 1039–51. DOI: [10.1007/s00371-007-0204-x](https://doi.org/10.1007/s00371-007-0204-x) (cited on page 52).
- [445] T. Salzbrunn, H. Jänicke, T. Wischgoll, and G. Scheuermann. “The state of the art in flow visualization: Partition-based techniques”. In: *Proceedings: Simulation and Visualization*. 2008, pp. 75–92. Link: informatik.uni-leipzig.de (accessed at 02/2016) (cited on page 50).
- [446] C. Santelli, M. Loecher, J. Busch, O. Wieben, T. Schaeffter, and S. Kozerke. “Accelerating 4D flow MRI by exploiting vector field divergence regularization”. In: *Journal of Magnetic Resonance in Medicine* 75.1 (2016), pp. 115–25. DOI: [10.1002/mrm.25563](https://doi.org/10.1002/mrm.25563) (cited on page 37).
- [447] S. Schäffler and S. Schmidt. *Mensch, Körper, Krankheit*. Gustav Fischer Publisher, 1997 (cited on page 13).
- [448] T. Schafhitzel, E. Tejada, D. Weiskopf, and T. Ertl. “Point-based stream surfaces and path surfaces”. In: *Proceedings: Graphics Interface*. 2007, pp. 289–96. DOI: [10.1145/1268517.1268564](https://doi.org/10.1145/1268517.1268564) (cited on page 50).
- [449] T. Schafhitzel, J. E. Vollrath, J. P. Gois, D. Weiskopf, A. Castelo, and T. Ertl. “Topology-preserving λ_2 -based vortex core line detection for flow visualization”. In: *Computer Graphics Forum* 27.3 (2008), pp. 1023–30. DOI: [10.1111/j.1467-8659.2008.01238.x](https://doi.org/10.1111/j.1467-8659.2008.01238.x) (cited on pages 54, 102).
- [450] H. Scharsach. “Advanced GPU raycasting”. In: *Proceedings: Central European Seminar on Computer Graphics*. 2005, pp. 69–76. Link: m.gpucomputing.net (accessed at 03/2016) (cited on page 44).
- [451] A. Schenk, G. Prause, and H.-O. Peitgen. “Efficient semiautomatic segmentation of 3D objects in medical images”. In: *Proceedings: Medical Image Computing and Computer Assisted Intervention*. 2000, pp. 186–95. DOI: [10.1007/978-3-540-40899-4_19](https://doi.org/10.1007/978-3-540-40899-4_19) (cited on page 84).
- [452] T. Schenkel, M. Malve, M. Reik, M. Markl, B. Jung, and H. Oertel. “MRI-based CFD analysis of flow in a human left ventricle: Methodology and application to a healthy heart”. In: *Annals of Biomedical Engineering* 37.3 (2009), pp. 503–15. DOI: [10.1007/s10439-008-9627-4](https://doi.org/10.1007/s10439-008-9627-4) (cited on page 58).
- [453] G. Scheuermann, T. Bobach, H. Hagen, K. Mahrous, B. Hamann, K. I. Joy, and W. Kollmann. “A tetrahedra-based stream surface algorithm”. In: *Proceedings: IEEE Conference on Visualization (Vis)*. 2001, pp. 151–8. DOI: [10.1109/VISUAL.2001.964506](https://doi.org/10.1109/VISUAL.2001.964506) (cited on page 50).
- [454] M. Schirski, C. Bischof, and T. Kuhlen. “Interactive particle tracing on tetrahedral grids using the GPU”. In: *Proceedings: Vision, Modeling, and Visualization*. 2006, pp. 153–60. Link: books.google.de (accessed at 03/2016) (cited on page 50).
- [455] C. Schlick. “A customizable reflectance model for everyday rendering”. In: *Proceedings: Fourth Eurographics Workshop on Rendering*. 1993, pp. 73–83. Link: google.de (accessed at 03/2016) (cited on page 44).
- [456] D. Schneider, A. Wiebel, and G. Scheuermann. “Smooth stream surfaces of fourth order precision”. In: *Computer Graphics Forum* 28.3 (2009), pp. 871–8. DOI: [10.1111/j.1467-8659.2009.01462.x](https://doi.org/10.1111/j.1467-8659.2009.01462.x) (cited on page 50).
- [457] D. Schneider, W. Reich, A. Wiebel, and G. Scheuermann. “Topology aware stream surfaces”. In: *Computer Graphics Forum* 29.3 (2010), pp. 1153–61. DOI: [10.1111/j.1467-8659.2009.01672.x](https://doi.org/10.1111/j.1467-8659.2009.01672.x) (cited on page 50).
- [458] S. Schnell, M. Markl, P. Entezari, R. J. Mahadewia, E. M. Semaan, Z. Stankovic, J. Collins, J. C. Carr, and B. Jung. “k-t GRAPPA accelerated four-dimensional flow MRI in the aorta: Effect on scan time, image quality, and quantification of flow and wall shear stress”. In: *Journal of Magnetic Resonance in Medicine* 72.2 (2014), pp. 522–33. DOI: [10.1002/mrm.24925](https://doi.org/10.1002/mrm.24925) (cited on page 26).
- [459] M. A. Schofield and Y. Zhu. “Fast phase unwrapping algorithm for interferometric applications”. In: *Optics Letters* 28.14 (2003), pp. 1194–6. DOI: [10.1364/OL.28.001194](https://doi.org/10.1364/OL.28.001194) (cited on page 34).
- [460] J. Schulz-Menger, D. A. Bluemke, J. Bremerich, S. D. Flamm, M. A. Fogel, M. G. Friedrich, R. J. Kim, F. von Knobelsdorff-Brenkenhoff, C. M. Kramer, D. J. Pennell, S. Plein, and E. Nagel. “Standardized image interpretation and post processing in cardiovascular magnetic resonance: Society for cardiovascular magnetic resonance (SCMR) board of trustees task force on standardized post processing”. In: *Journal of Cardiovascular Magnetic Resonance* 15.35 (2013). DOI: [10.1186/1532-429X-15-35](https://doi.org/10.1186/1532-429X-15-35) (cited on pages 65, 88, 94).

- [461] M. Schulze, C. Rössl, T. Germer, and H. Theisel. “As-perpendicular-as-possible surfaces for flow visualization”. In: *Proceedings: IEEE Pacific Visualization Symposium (PacificVis)*. 2012, pp. 153–60. DOI: [10.1109/PacificVis.2012.6183586](https://doi.org/10.1109/PacificVis.2012.6183586) (cited on page 148).
- [462] C. Schumann and A. Hennemuth. “Three-dimensional visualization of relative pressure in vascular structures”. In: *Proceedings: Computer and Robot Assisted Surgery (CURAC)*. 2015, pp. 337–41 (cited on page 74).
- [463] M. Schwenke, A. Hennemuth, B. Fischer, and O. Friman. “Blood flow computation in phase-contrast MRI by minimal paths in anisotropic media”. In: *Proceedings: Medical Image Computing and Computer Assisted Intervention*. 2011, pp. 436–43. DOI: [10.1007/978-3-642-23623-5_55](https://doi.org/10.1007/978-3-642-23623-5_55) (cited on pages 78, 160).
- [464] C. Seaman and P. Sucosky. “Anatomic versus effective orifice area in a bicuspid aortic valve”. In: *Echocardiography* 31.8 (2014). Letter to the Editor, p. 1028. DOI: [10.1111/echo.12720](https://doi.org/10.1111/echo.12720) (cited on page 70).
- [465] C. Seaman, A. G. Akingba, and P. Sucosky. “Steady flow hemodynamic and energy loss measurements in normal and simulated calcified tricuspid and bicuspid aortic valves”. In: *Journal of Biomechanical Engineering* 136.4 (2014). DOI: [10.1115/1.4026575](https://doi.org/10.1115/1.4026575) (cited on page 70).
- [466] W. A. Seed and N. B. Wood. “Velocity patterns in the aorta”. In: *Cardiovascular Research* 5.3 (1971), pp. 319–30. DOI: [10.1093/cvr/5.3.319](https://doi.org/10.1093/cvr/5.3.319) (cited on page 7).
- [467] E. M. Semaan, M. Carr, M. A. Gülsün, P. Van Ooij, A. F. Stalder, J. C. Carr, J. Collins, M. Markl, and B. Spottiswoode. “Evaluation of an optimized post-processing tool for 4D flow MRI data analysis in healthy volunteers and patients with aortic stenosis, aortic insufficiency, and aortic aneurysm”. In: *Proceedings: International Society for Magnetic Resonance in Medicine*. 2014, p. 3948. Link: healthcare.siemens.com (accessed at 02/2016) (cited on page 91).
- [468] P. P. Sengupta, G. Pedrizzetti, P. J. Kilner, A. Kheradvar, T. Ebbers, G. Tonti, A. G. Fraser, and J. Narula. “Emerging trends in CV flow visualization”. In: *JACC: Cardiovascular Imaging* 5.3 (2012), pp. 305–16. DOI: [10.1016/j.jcmg.2012.01.003](https://doi.org/10.1016/j.jcmg.2012.01.003) (cited on pages 8, 30).
- [469] D. M. Sforza, C. M. Putman, and J. R. Cebal. “Hemodynamics of cerebral aneurysms”. In: *Annual Review of Fluid Mechanics* 41 (2009), pp. 91–107. DOI: [10.1146/annurev.fluid.40.111406.102126](https://doi.org/10.1146/annurev.fluid.40.111406.102126) (cited on pages 73, 104).
- [470] Y. L. Shekhter. *Hot-wire and hot-film anemometers*. DOI: [10.1615/AtoZ.h.hot-wire.and.hot-film.anemometers](https://doi.org/10.1615/AtoZ.h.hot-wire.and.hot-film.anemometers) (cited on page 46).
- [471] K. Shi, H. Theisel, H. Hauser, T. Weinkauff, K. Matkovic, H.-C. Hege, and H.-P. Seidel. “Path line attributes – An information visualization approach to analyzing the dynamic behavior of 3D time-dependent flow fields”. In: *Topology-based Methods in Visualization II*. 2009, pp. 75–88. DOI: [10.1007/978-3-540-88606-8_6](https://doi.org/10.1007/978-3-540-88606-8_6) (cited on page 52).
- [472] H. H. Sievers and C. Schmidtke. “A classification system for the bicuspid aortic valve from 304 surgical specimens”. In: *The Journal of Thoracic and Cardiovascular Surgery* 133.5 (2007), pp. 1226–33. DOI: [10.1016/j.jtcvs.2007.01.039](https://doi.org/10.1016/j.jtcvs.2007.01.039) (cited on pages 7, 60, 107, 116).
- [473] M. Sigovan, M. D. Hope, P. Dyverfeldt, and D. Saloner. “Comparison of four-dimensional flow parameters for quantification of flow eccentricity in the ascending aorta”. In: *Journal of Magnetic Resonance Imaging* 34.5 (2011), pp. 1226–30. DOI: [10.1002/jmri.22800](https://doi.org/10.1002/jmri.22800) (cited on page 69).
- [474] M. Sigovan, M. D. Hope, J. Wrenn, P. Dyverfeldt, and D. Saloner. “Improved quantification of abnormal aortic flow in 3D compared to standard 2D approach”. In: *Journal of Cardiovascular Magnetic Resonance* 15.Suppl 1 (2013), P232. DOI: [10.1186/1532-429X-15-S1-P232](https://doi.org/10.1186/1532-429X-15-S1-P232) (cited on page 69).
- [475] M. Sigovan, P. Dyverfeldt, J. Wrenn, E. E. Tseng, D. Saloner, and M. D. Hope. “Extended 3D approach for quantification of abnormal ascending aortic flow”. In: *Journal of Magnetic Resonance Imaging* 33.5 (2015), pp. 695–700. DOI: [10.1016/j.mri.2015.02.020](https://doi.org/10.1016/j.mri.2015.02.020) (cited on page 69).
- [476] S. Silva, B. S. Santos, and J. Madeira. “Using color in visualization: A survey”. In: *Computers & Graphics* 35.2 (2011), pp. 320–33. DOI: [10.1016/j.cag.2010.11.015](https://doi.org/10.1016/j.cag.2010.11.015) (cited on page 46).
- [477] G. Simonneau, M. A. Gatzoulis, I. Adatia, D. Celermajer, C. Denton, A. Ghofrani, M. A. Gomez Sanchez, R. Krishna Kumar, M. Landzberg, R. F. Machado, H. Olschewski, I. M. Robbins, and R. Souza. “Updated clinical classification of pulmonary hypertension”. In: *Journal of the American College of Cardiology* 62.25 Suppl (2013), pp. D34–41. DOI: [10.1016/j.jacc.2013.10.029](https://doi.org/10.1016/j.jacc.2013.10.029) (cited on page 15).
- [478] E. Sloth, K. C. Houlind, S. Oyre, W. Y. Kim, E. M. Pedersen, H. S. Jørgensen, and J. M. Hasenkam. “Three-dimensional visualization of velocity profiles in the human main pulmonary artery with magnetic resonance phase-velocity mapping”. In: *American Heart Journal* 128.6 Pt. 1 (1994), pp. 1130–8. DOI: [10.1016/0002-8703\(94\)90743-9](https://doi.org/10.1016/0002-8703(94)90743-9) (cited on page 58).
- [479] J. E. Solem, M. Persson, and A. Heyden. “Velocity based segmentation in phase contrast MRI images”. In: *Proceedings: Medical Image Computing and Computer Assisted Intervention*. 2004, pp. 459–66. DOI: [10.1007/978-3-540-30135-6_56](https://doi.org/10.1007/978-3-540-30135-6_56) (cited on page 38).
- [480] S. M.-H. Song, S. Napel, N. J. Pelc, and G. H. Glover. “Phase unwrapping of MR phase images using Poisson equation”. In: *IEEE Transactions on Image Processing* 4.5 (1995), pp. 667–76. DOI: [10.1109/83.382500](https://doi.org/10.1109/83.382500) (cited on page 34).

- [481] J. Sotelo, J. Urbina, I. Valverde, C. Tejos, P. Irrarázaval, D. E. Hurtado, and S. Uribe. “Quantification of wall shear stress using a finite-element method in multidimensional phase-contrast MR data of the thoracic aorta”. In: *Journal of Biomechanics* 48.10 (2015), pp. 1817–27. DOI: [10.1016/j.jbiomech.2015.04.038](https://doi.org/10.1016/j.jbiomech.2015.04.038) (cited on page 72).
- [482] B. Spottiswoode, A. F. Stalder, M. A. Gülsün, K. F. Campione, M. Carr, M. Wasielewski, and M. Markl. “Fast semi-automated analysis of pulse wave velocity in the thoracic aorta using high temporal resolution 4D flow MRI”. In: *Journal of Cardiovascular Magnetic Resonance* 15.Suppl 1 (2013), P87. DOI: [10.1186/1532-429X-15-S1-P87](https://doi.org/10.1186/1532-429X-15-S1-P87) (cited on pages 68, 69).
- [483] M. B. Srichai, R. P. Lim, S. Wong, and V. S. Lee. “Cardiovascular applications of phase-contrast MRI”. In: *American Journal of Roentgenology* 192.3 (2009), pp. 662–75. DOI: [10.2214/AJR.07.3744](https://doi.org/10.2214/AJR.07.3744) (cited on page 8).
- [484] A. F. Stalder, M. F. Russe, A. Frydrychowicz, J. Bock, J. Hennig, and M. Markl. “Quantitative 2D and 3D phase contrast MRI: Optimized analysis of blood flow and vessel wall parameters”. In: *Journal of Magnetic Resonance in Medicine* 60.5 (2008), pp. 1218–31. DOI: [10.1002/mrm.21778](https://doi.org/10.1002/mrm.21778) (cited on page 72).
- [485] A. F. Stalder, A. Frydrychowicz, A. Harloff, Q. Yang, J. Bock, J. Hennig, K. C. Li, and M. Markl. “Vortex core detection and visualization using 4D flow-sensitive MRI”. In: *Proceedings: International Society for Magnetic Resonance in Medicine*. 2010, p. 3708. Link: cds.ismrm.org (accessed at 02/2016) (cited on pages 50, 55, 102).
- [486] A. F. Stalder, M. A. Gülsün, A. Greiser, and M.-P. Jolly. “Fully automatic visualization of 4D flow data”. In: *Proceedings: International Society for Magnetic Resonance in Medicine*. 2013, p. 1434. Link: healthcare.siemens.com (accessed at 02/2016) (cited on page 39).
- [487] Z. Stankovic, Z. Csatari, P. Deibert, W. Euringer, P. Blanke, W. Kreisel, Z. Abdullah Zadeh, F. Kallfass, M. Langer, and M. Markl. “Normal and altered three-dimensional portal venous hemodynamics in patients with liver cirrhosis”. In: *Radiology* 262.3 (2012), pp. 862–73. DOI: [10.1148/radiol.11110127](https://doi.org/10.1148/radiol.11110127) (cited on page 21).
- [488] Z. Stankovic, B. D. Allen, J. Garcia, K. B. Jarvis, and M. Markl. “4D flow imaging with MRI”. In: *Journal of Cardiovascular Diagnosis and Therapy* 4.2 (2014), pp. 173–92. DOI: [10.3978/j.issn.2223-3652.2014.01.02](https://doi.org/10.3978/j.issn.2223-3652.2014.01.02) (cited on pages 8, 26, 30, 35, 162).
- [489] P. D. Stein and H. N. Sabbah. “Turbulent blood flow in the ascending aorta of humans with normal and diseased aortic valves”. In: *Circulation Research* 39.1 (1976), pp. 58–65. DOI: [10.1161/01.RES.39.1.58](https://doi.org/10.1161/01.RES.39.1.58) (cited on page 75).
- [490] C. Stoll and H.-P. Gumhold S.and Seidel. “Visualization with stylized line primitives”. In: *Proceedings: IEEE Conference on Visualization (Vis)*. 2005, pp. 695–702. DOI: [10.1109/VISUAL.2005.1532859](https://doi.org/10.1109/VISUAL.2005.1532859) (cited on page 48).
- [491] R. C. Strawn, D. Kenwright, and R. Haines. “Computer visualization of vortex wake systems”. In: *The American Institute of Aeronautics and Astronautics Journal* 37.4 (1999), pp. 511–2. DOI: [10.2514/2.744](https://doi.org/10.2514/2.744) (cited on page 54).
- [492] A. Strehl and J. Ghosh. “Cluster ensembles – A knowledge reuse framework for combining multiple partitions”. In: *The Journal of Machine Learning Research* 3 (2002), pp. 583–617. Link: strehl.com (accessed at 02/2016) (cited on page 120).
- [493] D. Sujudi and R. Haines. *Identification of swirling flow in 3-D vector fields*. Tech. rep. Department of Aeronautics and Astronautics, MIT, Cambridge, 1995, pp. 792–9. DOI: [10.2514/6.1995-1715](https://doi.org/10.2514/6.1995-1715) (cited on pages 54, 99).
- [494] K. S. Sundareswaran, C. M. Haggerty, D. de Zélicourt, L. P. Dasi, K. Pekkan, D. H. Frakes, A. J. Powell, K. R. Kanter, M. A. Fogel, and A. P. Yoganathan. “Visualization of flow structures in Fontan patients using 3-dimensional phase contrast magnetic resonance imaging”. In: *The Journal of Thoracic and Cardiovascular Surgery* 143.5 (2012), pp. 1108–16. DOI: [10.1016/j.jtcvs.2011.09.067](https://doi.org/10.1016/j.jtcvs.2011.09.067) (cited on page 58).
- [495] A. Swillens, P. Segers, H. Torp, and L. Løvstakken. “Two-dimensional blood velocity estimation with ultrasound: Speckle tracking versus crossed-beam vector Doppler based on flow simulations in a carotid bifurcation model”. In: *IEEE Transactions on Ultrasonics, Ferroelectrics, and Frequency Control* 57.2 (2010), pp. 327–39. DOI: [10.1109/TUFFC.2010.1413](https://doi.org/10.1109/TUFFC.2010.1413) (cited on page 29).
- [496] P. D. Tafti and M. Unser. “On regularized reconstruction of vector fields”. In: *IEEE Transactions on Image Processing* 20.11 (2011), pp. 3163–78. DOI: [10.1109/TIP.2011.2159230](https://doi.org/10.1109/TIP.2011.2159230) (cited on page 36).
- [497] P. D. Tafti, R. Delgado-Gonzalo, A. F. Stalder, and M. Unser. “Variational enhancement and denoising of flow field images”. In: *Proceedings: IEEE International Symposium on Biomedical Imaging*. 2011, pp. 1061–4. DOI: [10.1109/ISBI.2011.5872584](https://doi.org/10.1109/ISBI.2011.5872584) (cited on page 36).
- [498] A. Tagliasacchi. *Skeletal representations and applications*. Tech. rep. School of Computing Science, Simon Fraser University, 2014. Link: arxiv.org (accessed at 02/2016) (cited on page 38).
- [499] P.-N. Tan, N. Steinbach, and V. Kumar. *Introduction to data mining*. Addison Wesley, 2005. ISBN: 978-0321321367 (cited on page 52).
- [500] G. Taubin, T. Zhang, and G. H. Golub. “Optimal surface smoothing as filter design”. In: *Proceedings: 4th European Conference on Computer Vision*. 1996, pp. 283–92. DOI: [10.1007/BFb0015544](https://doi.org/10.1007/BFb0015544) (cited on pages 85, 151).
- [501] A. Telea and J. J. Van Wijk. “Simplified representation of vector fields”. In: *Proceedings: IEEE Conference on Visualization (Vis)*. 1999, pp. 35–42. DOI: [10.1109/VISUAL.1999.809865](https://doi.org/10.1109/VISUAL.1999.809865) (cited on pages 50, 51).

- [502] M. Termeer, J. Oliván Bescós, M. Breeuwer, A. Vilanova, F. Gerritsen, and M. E. Gröller. “CoViCAD: Comprehensive visualization of coronary artery disease”. In: *IEEE Transactions on Visualization and Computer Graphics* 13.6 (2007), pp. 1632–9. DOI: [10.1109/TVCG.2007.70550](https://doi.org/10.1109/TVCG.2007.70550) (cited on page 108).
- [503] H. Theisel and H.-P. Seidel. “Feature flow fields”. In: *Proceedings: Joint Eurographics and IEEE TVCG Symposium on Visualization*. 2003, pp. 141–8. Link: www.wisg.cs.uni-magdeburg.de (accessed at 03/2016) (cited on page 53).
- [504] J. Therrien, Y. Provost, N. Merchant, W. Williams, J. Colman, and A. G. Webb. “Optimal timing for pulmonary valve replacement in adults after tetralogy of Fallot repair”. In: *The American Journal of Cardiology* 95.6 (2005), pp. 779–82. DOI: [10.1016/j.amjcard.2004.11.037](https://doi.org/10.1016/j.amjcard.2004.11.037) (cited on page 60).
- [505] S. G. Thrumurthy, A. Karthikesalingam, B. O. Patterson, P. J. E. Holt, and M. M. Thompson. “The diagnosis and management of aortic dissection”. In: *British Medical Journal (BMJ)* 344 (2012), Epub. DOI: [10.1136/bmj.d8290](https://doi.org/10.1136/bmj.d8290) (cited on page 16).
- [506] J. Töger, M. Kanski, M. Carlsson, S. J. Kovács, G. Söderlind, H. Arheden, and E. Heiberg. “Vortex ring formation in the left ventricle of the heart: Analysis by 4D flow MRI and Lagrangian coherent structures”. In: *Annals of Biomedical Engineering* 40.12 (2012), pp. 2652–62. DOI: [10.1007/s10439-012-0615-3](https://doi.org/10.1007/s10439-012-0615-3) (cited on pages 58, 61, 77).
- [507] J. Töger, M. Kanski, M. Carlsson, S. J. Kovács, G. Söderlind, H. Arheden, and E. Heiberg. “Vortex ring mixing in the left ventricle of the human heart”. In: *Journal of Cardiovascular Magnetic Resonance* 15.Suppl 1 (2013), E27. DOI: [10.1186/1532-429X-15-S1-E27](https://doi.org/10.1186/1532-429X-15-S1-E27) (cited on page 59).
- [508] C. Tropea, A. L. Yarin, and J. F. Foss. *Handbook of experimental fluid mechanics*. Springer, 2007. ISBN: 978-9087240554 (cited on page 29).
- [509] U. Truong, B. Fonseca, J. Dunning, S. Burgett, C. Lanning, D. D. Ivy, R. Shandas, K. Hunter, and A. J. Barker. “Wall shear stress measured by phase contrast cardiovascular magnetic resonance in children and adolescents with pulmonary arterial hypertension”. In: *Journal of Cardiovascular Magnetic Resonance* 15.81 (2013). DOI: [10.1186/1532-429X-15-81](https://doi.org/10.1186/1532-429X-15-81) (cited on page 71).
- [510] J. Tsao, B. Behnia, and A. G. Webb. “Unifying linear prior-information-driven methods for accelerated image acquisition”. In: *Journal of Magnetic Resonance in Medicine* 46.4 (2001), pp. 652–60. DOI: [10.1002/mrm.1242](https://doi.org/10.1002/mrm.1242) (cited on page 26).
- [511] G. Turk and D. Banks. “Image-guided streamline placement”. In: *Proceedings: 23rd Annual Conference on Computer Graphics and Interactive Techniques (SIGGRAPH)*. 1996, pp. 453–60. DOI: [10.1145/237170.237285](https://doi.org/10.1145/237170.237285) (cited on page 47).
- [512] J. M. Tyszka, D. H. Laidlaw, J. W. Asa, and J. M. Silverman. “Three-dimensional, time-resolved (4D) relative pressure mapping using magnetic resonance imaging”. In: *Journal of Magnetic Resonance Imaging* 12.2 (2000), pp. 321–9. DOI: [10.1002/1522-2586\(200008\)12:2\(321::AID-JMRI15\)3.0.CO;2-2](https://doi.org/10.1002/1522-2586(200008)12:2(321::AID-JMRI15)3.0.CO;2-2) (cited on page 75).
- [513] S. R. Underwood, D. N. Firmin, R. H. Klipstein, R. S. O. Rees, and D. B. Longmore. “Magnetic resonance velocity mapping: Clinical application of a new technique”. In: *British Heart Journal* 57.5 (1987), pp. 404–12. DOI: [10.1136/hrt.57.5.404](https://doi.org/10.1136/hrt.57.5.404) (cited on page 7).
- [514] M. Untenberger, M. Hüllebrand, L. Tautz, A. A. Joseph, D. Voit, K. D. Merboldt, and J. Frahm. “Spatiotemporal phase unwrapping for real-time phase-contrast flow MRI”. In: *Journal of Magnetic Resonance in Medicine* 74.4 (2015), pp. 964–70. DOI: [10.1002/mrm.25471](https://doi.org/10.1002/mrm.25471) (cited on page 34).
- [515] I. Valverde, S. Nordmeyer, S. Uribe, G. Greil, F. Berger, T. Kühne, and P. Beerbaum. “Systemic-to-pulmonary collateral flow in patients with palliated univentricular heart physiology: Measurement using cardiovascular magnetic resonance 4D velocity acquisition”. In: *Journal of Cardiovascular Magnetic Resonance* 14.1 (2012), Epub. DOI: [10.1186/1532-429X-14-25](https://doi.org/10.1186/1532-429X-14-25) (cited on page 91).
- [516] S. G. Van Elderen, A. Brandts, J. van der Grond, J. J. M. Westenberg, L. J. Kroft, M. A. van Buchem, J. W. Smit, and A. de Roos. “Cerebral perfusion and aortic stiffness are independent predictors of white matter brain atrophy in type 1 diabetic patients assessed with magnetic resonance imaging”. In: *Diabetes Care* 34.2 (2011), pp. 459–63. DOI: [10.2337/dc10-1446](https://doi.org/10.2337/dc10-1446) (cited on page 67).
- [517] A. Van Gelder. “Vortex core detection: Back to basics”. In: *Proceedings: International Society for Optics and Photonics (SPIE)*. 2012, pp. 829413–1. DOI: [10.1117/12.912301](https://doi.org/10.1117/12.912301) (cited on page 53).
- [518] P. Van Ooij, W. V. Potters, A. Guédon, J. J. Schneiders, H. A. Marquering, C. B. Majoie, E. vanBavel, and A. J. Nederveen. “Wall shear stress estimated with phase contrast MRI in an in vitro and in vivo intracranial aneurysm”. In: *Journal of Magnetic Resonance Imaging* 38.4 (2013), pp. 876–84. DOI: [10.1002/jmri.24051](https://doi.org/10.1002/jmri.24051) (cited on page 73).
- [519] P. Van Ooij, W. V. Potters, A. J. Nederveen, J. D. Collins, J. C. Carr, S. C. Malaisrie, M. Markl, and A. J. Barker. “Thoracic aortic wall shear stress atlases in patients with bicuspid aortic valves”. In: *Journal of Cardiovascular Magnetic Resonance* 16.Suppl 1 (2014), P161. DOI: [10.1186/1532-429X-16-S1-P161](https://doi.org/10.1186/1532-429X-16-S1-P161) (cited on page 71).
- [520] P. Van Ooij, W. V. Potters, J. Collins, M. Carr, J. C. Carr, S. C. Malaisrie, P. W. Fedak, P. M. McCarthy, M. Markl, and A. J. Barker. “Characterization of abnormal wall shear stress using 4D flow MRI in human bicuspid aortopathy”. In: *Annals of Biomedical Engineering* 43.6 (2015), pp. 1385–97. DOI: [10.1007/s10439-014-1092-7](https://doi.org/10.1007/s10439-014-1092-7) (cited on page 7).

- [521] P. Van Ooij, A. L. Powell, W. V. Potters, J. C. Carr, M. Markl, and A. J. Barker. “Reproducibility and interobserver variability of systolic blood flow velocity and 3D wall shear stress derived from 4D flow MRI in the healthy aorta”. In: *Journal of Magnetic Resonance Imaging* 43.1 (2015), pp. 236–48. DOI: [10.1002/jmri.24959](https://doi.org/10.1002/jmri.24959) (cited on page 26).
- [522] R. F. P. Van Pelt. “Real-time illustrative visualization of cardiovascular hemodynamics”. PhD thesis. Eindhoven University of Technology, Netherlands, 2012. DOI: [10.6100/IR732929](https://doi.org/10.6100/IR732929) (cited on pages 44, 47–49, 51).
- [523] R. F. P. Van Pelt and A. Vilanova. “Understanding blood-flow dynamics: New challenges for visualization”. In: *Computer* 46.12 (2013), pp. 60–7. DOI: [10.1109/MC.2013.121](https://doi.org/10.1109/MC.2013.121) (cited on page 161).
- [524] R. F. P. Van Pelt, J. Oliván Bescós, M. Breeuwer, R. E. Clough, M. E. Gröller, B. M. ter Haar Romeny, and A. Vilanova. “Exploration of 4D MRI blood flow using stylistic visualization”. In: *IEEE Transactions on Visualization and Computer Graphics* 16.6 (2010), pp. 1339–47. DOI: [10.1109/TVCG.2010.153](https://doi.org/10.1109/TVCG.2010.153) (cited on pages 37, 41, 44, 65, 91).
- [525] R. F. P. Van Pelt, J. Oliván Bescós, M. Breeuwer, R. E. Clough, M. E. Gröller, B. M. ter Haar Romeny, and A. Vilanova. “Interactive virtual probing of 4D MRI blood-flow”. In: *IEEE Transactions on Visualization and Computer Graphics* 17.12 (2011), pp. 2153–62. DOI: [10.1109/TVCG.2011.215](https://doi.org/10.1109/TVCG.2011.215) (cited on pages 47–49).
- [526] R. F. P. Van Pelt, H. Nguyen, B. M. ter Haar Romeny, and A. Vilanova. “Automated segmentation of blood-flow regions in large thoracic arteries using 3D-cine PC-MRI measurements”. In: *International Journal for Computer Assisted Radiology and Surgery* 7.2 (2012), pp. 217–24. DOI: [10.1007/s11548-011-0642-9](https://doi.org/10.1007/s11548-011-0642-9) (cited on page 39).
- [527] R. F. P. Van Pelt, S. S. A. M. Jacobs, B. M. ter Haar Romeny, and A. Vilanova. “Visualization of 4D blood-flow fields by spatiotemporal hierarchical clustering”. In: *Computer Graphics Forum* 31.3 (2012), pp. 1065–74. DOI: [10.1111/j.1467-8659.2012.03099.x](https://doi.org/10.1111/j.1467-8659.2012.03099.x) (cited on pages 51, 117).
- [528] R. F. P. Van Pelt, A. Fuster, G. G. H. Claassen, and A. Vilanova. “Characterization of blood-flow patterns from phase-contrast MRI velocity fields”. In: *Eurographics Conference on Visualization (EuroVis) - Short Papers*. 2014. DOI: [10.2312/eurovisshort.20141158](https://doi.org/10.2312/eurovisshort.20141158) (cited on page 56).
- [529] R. F. P. Van Pelt, R. Gasteiger, K. Lawonn, M. Meuschke, and B. Preim. “Comparative blood flow visualization for cerebral aneurysm treatment assessment”. In: *Computer Graphics Forum* 33.3 (2014), pp. 131–40. DOI: [10.1111/cgf.12369](https://doi.org/10.1111/cgf.12369) (cited on page 161).
- [530] S. S. Vasanawala, K. Hanneman, M. T. Alley, and A. Hsiao. “Congenital heart disease assessment with 4D flow MRI”. In: *Journal of Magnetic Resonance Imaging* 42.4 (2015), pp. 870–86. DOI: [10.1002/jmri.24856](https://doi.org/10.1002/jmri.24856) (cited on pages 18, 162).
- [531] S. Venkataraman. *4D visualization of cardiac flow*. NVIDIA GPU Technology Conference Talk. 2010. Link: nvidia.com (accessed at 02/2016) (cited on pages 45, 86, 148).
- [532] V. Verma and A. Pang. “Comparative flow visualization”. In: *IEEE Transactions on Visualization and Computer Graphics* 10.6 (2004), pp. 609–24. DOI: [10.1109/TVCG.2004.39](https://doi.org/10.1109/TVCG.2004.39) (cited on page 161).
- [533] J. Viega, M. J. Conway, G. Williams, and R. Pausch. “3D magic lenses”. In: *Proceedings: 9th Annual ACM Symposium on User Interface Software and Technology*. 1996, pp. 51–8. DOI: [10.1145/237091.237098](https://doi.org/10.1145/237091.237098) (cited on page 50).
- [534] A. Vilanova, B. Preim, R. F. P. Van Pelt, R. Gasteiger, M. Neugebauer, and T. Wischgoll. “Visual exploration of simulated and measured blood flow”. In: Springer-Verlag London, 2014. Chap. 25, pp. 305–20. DOI: [10.1007/978-1-4471-6497-5_25](https://doi.org/10.1007/978-1-4471-6497-5_25) (cited on page 50).
- [535] V. V. Volkov and Y. Zhu. “Deterministic phase unwrapping in the presence of noise”. In: *Optics Letters* 28.22 (2003), pp. 2156–8. DOI: [10.1364/OL.28.002156](https://doi.org/10.1364/OL.28.002156) (cited on page 34).
- [536] P. Volonghi, D. Tresoldi, M. Cadioli, A. M. Uselli, R. Ponzini, U. Morbiducci, A. Esposito, and G. Rizzo. “Automatic extraction of three-dimensional thoracic aorta geometric model from phase contrast MRI for morphometric and hemodynamic characterization”. In: *Journal of Magnetic Resonance in Medicine* 75.2 (2015), pp. 873–82. DOI: [10.1002/mrm.25630](https://doi.org/10.1002/mrm.25630) (cited on page 39).
- [537] F. Von Knobelsdorff-Brenkenhoff, R. F. Trauzeddel, A. J. Barker, H. Gruettner, M. Markl, and J. Schulz-Menger. “Blood flow characteristics in the ascending aorta after aortic valve replacement – A pilot study using 4D-flow MRI”. In: *International Journal of Cardiology* 170.3 (2014), pp. 426–33. DOI: [10.1016/j.ijcard.2013.11.034](https://doi.org/10.1016/j.ijcard.2013.11.034) (cited on page 60).
- [538] U. Von Luxburg. “A tutorial on spectral clustering”. In: *Statistics and Computing* 17.4 (2007), pp. 395–416. DOI: [10.1007/s11222-007-9033-z](https://doi.org/10.1007/s11222-007-9033-z) (cited on page 52).
- [539] J. von Spiczak, G. Crelier, D. Giese, S. Kozerke, D. Maintz, and A. C. Bunck. “Quantitative analysis of vortical blood flow in the thoracic aorta using 4D phase contrast MRI”. In: *PLoS ONE* 10.9 (2015). DOI: [10.1371/journal.pone.0139025](https://doi.org/10.1371/journal.pone.0139025) (cited on pages 76, 77).
- [540] P. G. Walker, G. B. Cranney, M. B. Scheidegger, G. Waseleski, G. M. Pohost, and A. P. Yoganathan. “Semiautomated method for noise reduction and background phase error correction in MR phase velocity data”. In: *Journal of Magnetic Resonance Imaging* 3.3 (1993), pp. 521–30. DOI: [10.1002/jmri.1880030315](https://doi.org/10.1002/jmri.1880030315) (cited on pages 35, 39, 83).

- [541] J. H. Ward Jr. “Hierarchical grouping to optimize an objective function”. In: *Journal of the American Statistical Association* 58.301 (1963), pp. 536–44. DOI: [10.1080/01621459.1963.10500845](https://doi.org/10.1080/01621459.1963.10500845) (cited on page 118).
- [542] C. Ware. “Toward a perceptual theory of flow visualization”. In: *IEEE Computer Graphics and Applications* 28.2 (2008), pp. 6–11. DOI: [10.1109/MCG.2008.39](https://doi.org/10.1109/MCG.2008.39) (cited on pages 48, 55, 96, 161).
- [543] C. Ware and M. Plumlee. “Designing a better weather display”. In: *Information Visualization* 12.3-4 (2013), pp. 221–39. DOI: [10.1177/1473871612465214](https://doi.org/10.1177/1473871612465214) (cited on page 161).
- [544] P. E. Watson, I. D. Watson, and R. D. Batt. “Total body water volumes for adult males and females estimated from simple anthropometric measurements”. In: *The American Journal of Clinical Nutrition* 33.1 (1980), pp. 27–39 (cited on page 21).
- [545] T. Wehrum, M. Kams, F. Günther, P. Beryl, W. Vach, I. Dragonu, and A. Harloff. “Quantification of retrograde blood flow in the descending aorta using transesophageal echocardiography in comparison to 4D flow MRI”. In: *Cerebrovascular Diseases* 39.5-6 (2015), pp. 287–92. DOI: [10.1159/000381682](https://doi.org/10.1159/000381682) (cited on page 30).
- [546] E. Weigang, F. A. Kari, F. Beyersdorf, M. Luehr, C. D. Etz, A. Frydrychowicz, A. Harloff, and M. Markl. “Flow-sensitive four-dimensional magnetic resonance imaging: Flow patterns in ascending aortic aneurysms”. In: *European Journal of Cardio-Thoracic Surgery* 34.1 (2008), pp. 11–6. DOI: [10.1016/j.ejcts.2008.03.047](https://doi.org/10.1016/j.ejcts.2008.03.047) (cited on page 60).
- [547] C. Weigle and D. C. Banks. “A comparison of the perceptual benefits of linear perspective and physically-based illumination for display of dense 3D streamtubes”. In: *IEEE Transactions on Visualization and Computer Graphics* 14.6 (2008), pp. 1723–30. DOI: [10.1109/TVCG.2008.108](https://doi.org/10.1109/TVCG.2008.108) (cited on page 161).
- [548] J. Weil, H. Bertram, and J. S. Sachweh. *Leitlinie pädiatrische Kardiologie: Fallot'sche Tetralogie, deutsche Gesellschaft für pädiatrische Kardiologie*. 2013. Link: kinderkardiologie.org (accessed at 02/2016) (cited on page 18).
- [549] T. Weinkauff. “Extraction of topological structures in 2D and 3D vector fields”. PhD thesis. Otto-von-Guericke-University, Magdeburg, Germany, 2008. Link: diglib.uni-magdeburg.de (accessed at 03/2016) (cited on page 55).
- [550] T. Weinkauff, J. Sahner, H. Theisel, and H.-C. Hege. “Cores of swirling particle motion in unsteady flows”. In: *IEEE Transactions on Visualization and Computer Graphics* 13.6 (2007), pp. 1759–66. DOI: [10.1109/TVCG.2007.70545](https://doi.org/10.1109/TVCG.2007.70545) (cited on pages 55, 96, 99).
- [551] A. L. Wentland, O. Wieben, C. J. François, C. Boncyk, A. Munoz Del Rio, K. M. Johnson, T. M. Grist, and A. Frydrychowicz. “Aortic pulse wave velocity measurements with undersampled 4D flow-sensitive MRI: Comparison with 2D and algorithm determination”. In: *Journal of Magnetic Resonance Imaging* 37.4 (2013), pp. 853–9. DOI: [10.1002/jmri.23877](https://doi.org/10.1002/jmri.23877) (cited on page 68).
- [552] A. L. Wentland, T. M. Grist, and O. Wieben. “Repeatability and internal consistency of abdominal 2D and 4D phase contrast MR flow measurements”. In: *Academic Radiology* 20.6 (2013), pp. 699–704. DOI: [10.1016/j.acra.2012.12.019](https://doi.org/10.1016/j.acra.2012.12.019) (cited on page 26).
- [553] A. L. Wentland, T. M. Grist, and O. Wieben. “Review of MRI-based measurements of pulse wave velocity: A biomarker of arterial stiffness”. In: *Journal of Cardiovascular Diagnosis and Therapy* 4.2 (2014), pp. 193–296. DOI: [10.3978/j.issn.2223-3652.2014.03.04](https://doi.org/10.3978/j.issn.2223-3652.2014.03.04) (cited on pages 67, 68).
- [554] J. J. M. Westenberg, M. G. Danilouchkine, J. Doornbos, J. J. Bax, R. J. van der Geest, G. Labadie, H. J. Lamb, M. I. M. Versteegh, A. de Roos, and J. H. C. Reiber. “Accurate and reproducible mitral valvular blood flow measurement with three-directional velocity-encoded magnetic resonance imaging”. In: *Journal of Cardiovascular Magnetic Resonance* 6.4 (2004), pp. 767–76. Link: scmr.org (accessed at 02/2016) (cited on page 66).
- [555] N. Westerhof, N. Stergiopoulos, and M. I. M. Noble. *Snapshots of hemodynamics: An aid for clinical research and graduate education*. Springer, 2010. DOI: [10.1007/b101305](https://doi.org/10.1007/b101305) (cited on page 71).
- [556] L. Wigström, L. Sjöqvist, and B. Wranne. “Temporally resolved 3D phase-contrast imaging”. In: *Journal of Magnetic Resonance Imaging* 36.5 (1996), pp. 800–3. DOI: [10.1002/mrm.1910360521](https://doi.org/10.1002/mrm.1910360521) (cited on pages 7, 10).
- [557] L. Wigström, T. Ebbens, A. Fyrenius, M. Karlsson, J. Engvall, B. Wranne, and A. F. Bolger. “Particle trace visualization of intracardiac flow using time-resolved 3D phase contrast MRI”. In: *Journal of Magnetic Resonance in Medicine* 41.4 (1999), pp. 793–9. DOI: [10.1002/\(SICI\)1522-2594\(199904\)41:4<793::AID-MRM19>3.0.CO;2-2](https://doi.org/10.1002/(SICI)1522-2594(199904)41:4<793::AID-MRM19>3.0.CO;2-2) (cited on page 47).
- [558] C. Willert and M. Gharib. “Digital particle image velocimetry”. In: *Experiments in Fluids* 10.4 (1991), pp. 181–93. DOI: [10.1007/BF00190388](https://doi.org/10.1007/BF00190388) (cited on page 29).
- [559] C. M. Wittenbrink, A. T. Pang, and S. K. Lodha. “Glyphs for visualizing uncertainty in vector fields”. In: *IEEE Transactions on Visualization and Computer Graphics* 2.3 (1996), pp. 266–79. DOI: [10.1109/2945.537309](https://doi.org/10.1109/2945.537309) (cited on page 48).
- [560] J. Wöhrle, M. Kochs, J. Spiess, T. Nusser, V. Hombach, and N. Merkle. “Impact of percutaneous device implantation for closure of patent foramen ovale on valve insufficiencies”. In: *Circulation* 119.23 (2009), pp. 3002–8. DOI: [10.1161/CIRCULATIONAHA.109.851014](https://doi.org/10.1161/CIRCULATIONAHA.109.851014) (cited on pages 18, 66).

- [561] R. L. Wolf, R. L. Ehman, S. J. Riederer, and P. J. Rossman. “Analysis of systematic and random error in MR volumetric flow measurements”. In: *Journal of Magnetic Resonance Imaging* 30.1 (1993), pp. 82–91. DOI: [10.1002/mrm.1910300113](https://doi.org/10.1002/mrm.1910300113) (cited on pages 33, 158).
- [562] K. K. L. Wong, R. M. Kelso, S. G. Worthley, P. Sanders, J. Mazumdar, and D. Abbott. “Cardiac flow analysis applied to phase contrast magnetic resonance imaging of the heart”. In: *Annals of Biomedical Engineering* 37.8 (2009), pp. 1495–515. DOI: [10.1007/s10439-009-9709-y](https://doi.org/10.1007/s10439-009-9709-y) (cited on page 76).
- [563] K. K. L. Wong, J. Tu, R. M. Kelso, S. G. Worthley, P. Sanders, J. Mazumdar, and D. Abbott. “Cardiac flow component analysis”. In: *Medical Engineering & Physics* 32.2 (2010), pp. 174–88. DOI: [10.1016/j.medengphy.2009.11.007](https://doi.org/10.1016/j.medengphy.2009.11.007) (cited on page 76).
- [564] World Health Organization. *Global status report on noncommunicable diseases*. 2014. Link: apps.who.int (accessed at 02/2016) (cited on page 14).
- [565] J.-Z. Wu, A.-K. Xiong, and Y.-T. Yang. “Axial stretching and vortex definition”. In: *Physics of Fluids* 17.3 (2005), pp. 038108–1–4. DOI: [10.1063/1.1863284](https://doi.org/10.1063/1.1863284) (cited on page 54).
- [566] K. Wu, Z. Liu, S. Zhang, and R. J. Moorhead II. “Topology-aware evenly spaced streamline placement”. In: *IEEE Transactions on Visualization and Computer Graphics* 16.5 (2010), pp. 791–801. DOI: [10.1109/TVCG.2009.206](https://doi.org/10.1109/TVCG.2009.206) (cited on page 47).
- [567] Q.-S. Xiang. “Temporal phase unwrapping for cine velocity imaging”. In: *Journal of Magnetic Resonance Imaging* 5.5 (1995), pp. 529–34. DOI: [10.1002/jmri.1880050509](https://doi.org/10.1002/jmri.1880050509) (cited on page 34).
- [568] G. Z. Yang, P. Burger, P. J. Kilner, and R. H. Mohiaddin. “In vivo blood flow visualization with magnetic resonance imaging”. In: *Proceedings: IEEE Conference on Visualization (Vis)*. 1991, pp. 202–9. DOI: [10.1109/VISUAL.1991.175801](https://doi.org/10.1109/VISUAL.1991.175801) (cited on page 46).
- [569] G. Z. Yang, P. J. Kilner, N. B. Wood, S. R. Underwood, and D. N. Firmin. “Computation of flow pressure fields from magnetic resonance velocity mapping”. In: *Journal of Magnetic Resonance in Medicine* 36.4 (1996), pp. 520–6. DOI: [10.1002/mrm.1910360404](https://doi.org/10.1002/mrm.1910360404) (cited on page 75).
- [570] G. Z. Yang, P. Burger, P. J. Kilner, S. P. Karwatowski, and D. N. Firmin. “Dynamic range extension of cine velocity measurements using motion-registered spatiotemporal phase unwrapping”. In: *Journal of Magnetic Resonance Imaging* 6.3 (1996), pp. 495–502. DOI: [10.1002/jmri.1880060313](https://doi.org/10.1002/jmri.1880060313) (cited on page 34).
- [571] J. C. Yang, J. Hensley, H. Grün, and N. Thibieroz. “Real-time concurrent linked list construction on the GPU”. In: *Computer Graphics Forum*. 2010, pp. 1297–304. DOI: [10.1111/j.1467-8659.2010.01725.x](https://doi.org/10.1111/j.1467-8659.2010.01725.x) (cited on pages 48, 114).
- [572] X. Ye, D. Kao, and A. Pang. “Strategy for seeding 3D streamlines”. In: *Proceedings: IEEE Conference on Visualization (Vis)*. 2005, pp. 471–8. DOI: [10.1109/VISUAL.2005.1532831](https://doi.org/10.1109/VISUAL.2005.1532831) (cited on page 47).
- [573] H. Yu, C. Wang, and K.-L. Ma. “Parallel hierarchical visualization of large time-varying 3D vector fields”. In: *Proceedings: IEEE Supercomputing*. 2007, pp. 1–12. DOI: [10.1145/1362622.1362655](https://doi.org/10.1145/1362622.1362655) (cited on page 51).
- [574] H. Y. Yu, H. H. Peng, J. L. Wang, C. Y. Wen, and W. Y. Tseng. “Quantification of the pulse wave velocity of the descending aorta using axial velocity profiles from phase-contrast magnetic resonance imaging”. In: *Journal of Magnetic Resonance in Medicine* 56.4 (2006), pp. 876–83. DOI: [10.1002/mrm.21034](https://doi.org/10.1002/mrm.21034) (cited on page 67).
- [575] J. Zajac, J. Eriksson, P. Dyverfeldt, A. F. Bolger, T. Ebberts, and C.-J. Carlhäll. “Turbulent kinetic energy in normal and myopathic left ventricles”. In: *Journal of Magnetic Resonance Imaging* 41.4 (2015), pp. 1021–9. DOI: [10.1002/jmri.24633](https://doi.org/10.1002/jmri.24633) (cited on page 76).
- [576] L. Zelnik-Manor and P. Perona. “Self-tuning spectral clustering”. In: *Proceedings: Advances in Neural Information Processing Systems 17*. 2004, pp. 1601–8. Link: citeseerx.ist.psu.edu (accessed at 02/2016) (cited on page 118).
- [577] Q. Zhang, R. Eagleson, and T. M. Peters. “Dynamic real-time 4D cardiac MDCT image display using GPU-accelerated volume rendering”. In: *Computerized Medical Imaging and Graphics* 33.6 (2009), pp. 461–76. DOI: [10.1016/j.compmedimag.2009.04.002](https://doi.org/10.1016/j.compmedimag.2009.04.002) (cited on page 148).
- [578] F. Zhao, H. Zhang, A. Wahle, T. D. Scholz, and M. Sonka. “Automated 4D segmentation of aortic magnetic resonance images”. In: *Proceedings: British Machine Vision Conference*. 2006, pp. 247–56. DOI: [10.5244/C.20.26](https://doi.org/10.5244/C.20.26) (cited on page 148).
- [579] M. Zöckler, D. Stalling, and H.-C. Hege. “Interactive visualization of 3D-vector fields using illuminated stream lines”. In: *Proceedings: IEEE Conference on Visualization (Vis)*. 1996, pp. 107–13. DOI: [10.1109/VISUAL.1996.567777](https://doi.org/10.1109/VISUAL.1996.567777) (cited on page 48).

ABBREVIATIONS

Symbols

1D	One-dimensional
2D	Two-dimensional
3D	Three-dimensional
4D	Four-dimensional

A

AABR	Axis-aligned bounding rectangle
AAo	Ascending aorta
AHC	Agglomerative hierarchical clustering
Ao	Aorta
AST	Acoustical source term
AV	Aortic valve
AVA	Aortic valve area

B

BA	Brachiocephalic artery
BAV	Bicuspid aortic valve
BEP	Bull's eye plot
BFV	Backward flow volume
BLAST	Broad-use linear speed-up technique

C

CA	Coronary artery
CDF	Cumulative distribution function
CFD	Computational fluid dynamics
CHD	Congenital heart disease
CHF	Congestive heart failure
CI	Cardiac index
cm	Centimeters
CMR	Cardiovascular magnetic resonance
CO	Cardiac output
COM	Center of mass
COSPM	Cores of swirling particle motion
CPU	Central processing unit
CT	Computerized tomography
CVD	Cardiovascular disease

D

DAo	Descending aorta
DBSCAN	Density-based spatial clustering of application with noise
DICOM	Digital imaging and communications in medicine
DOPRI5(4)	Dormand-Prince method
DTI	Diffusion tensor imaging
DVM	Differential velocity map
DVR	Direct volume rendering

E

ECG	Echocardiography or electrocardiography
EOA	Effective orifice area
EVC	Eigenvalue coherence

F

FA	Fourier analysis method
FFV	Forward flow volume
fMRI	Functional magnetic resonance imaging
FOV	Field of view
FPS	Frames per second
fr	flow rate
FTLE	Finite-time Lyapunov exponent

G

g	Grams
GAC	Geodesic active contours
Gb	Gigabyte
GHz	Gigahertz
GOA	Geometric orifice area
GPU	Graphics processing unit
GRAPPA	Generalized autocalibrating partially parallel acquisitions
GUI	Graphical user interface

H

h	Hours
Hz	Hertz

I

I/O	Input / output
IQR	Interquartile range
ISL	Illuminated streamlines
IVSD	Intravoxel velocity standard deviation

J

J	Joule
JSLD	Jet shear layer detection

K

KE	Kinetic energy
kg	Kilograms

L

l	Liters
LA	Left atrium
LCS	Lagrangian coherent structures
LoCoSys	Local coordinate system
LPA	Left pulmonary artery
LPC	Local phase coherence
LV	Left ventricle
LVOT	Left ventricular outflow tract

M

m	Meters
MATLAB	Matrix laboratory
MHz	Megahertz
min	Minutes
MIP	Maximum intensity projection

mJ	Millijoule	T	Tesla
ml	Milliliters	TAVI	Transcatheter aortic-valve implantation
mm	Millimeters	TE	Echo time
mmHg	Millimeters of mercury	TH	Threshold method
MR	Magnetic resonance	TKE	Turbulent kinetic energy
MRI	Magnetic resonance imaging	TMIP	Temporal maximum intensity projection
ms	Milliseconds	ToF	Tetralogy of Fallot
MV	Mitral valve	TR	Repetition time
MVC	Model-view-controller	TTF	Time-to-foot
N		TTP	Time-to-peak
NCD	Noncommunicable disease	TTU	Time-to-upstroke
ND	N-dimensional	U	
NFV	Net flow volume	USD	Unites States dollar
O		V	
OIT	Order-independent transparency	VAAS	Vortex animations with adaptive speed
OpenGL	Open graphics library	VMTK	The Vascular Modeling Toolkit
P		VPM	Vector pattern matching
PA	Pulmonary artery	VSD	Ventricular septal defect
Pa	Pascal	VTK	The Visualization Toolkit
PACS	Picture archiving and communication system	W	
PAH	Pulmonary hypertension	WHO	World Health Organization
PBFV	Percentaged back flow volume	WSS	Wall shear stress
PC	Phase-contrast	X	
PCA	Principal component analysis	XCorr	Cross-correlation
PCMR	Phase-contrast magnetic resonance angiography		
PIV	Particle image velocimetry		
PPE	Pressure Poisson equation		
PT	Pulmonary trunk		
PV	Pulmonary valve		
PWV	Pulse wave velocity		
Q			
QML	Qt meta / modeling language		
Qt	Qt		
R			
RAM	Random-access memory		
RF	Regurgitation fraction		
RF	Radio frequency		
RK4	Runge-Kutta-4		
ROI	Region of interest		
RPA	Right pulmonary artery		
RV	Right ventricle		
RVM	Reference velocity map		
RVOT	Right ventricular outflow tract		
S			
s	Seconds		
SC	Spectral clustering		
SDG	Sustainable development goals		
SENSE	Sensitive encoding		
SNR	Signal-to-noise ratio		
SPVT	Single plane velocity truncation		
SV	Stroke volume		
T			

SYMBOLS

A		P	
A	Anatomy image	P	Measuring plane
B		Δp	Pressure gradient
B_0	Main magnetic field	p	Relative pressure
\vec{B}_0	Direction of the B_0 main magnetic field	\vec{p}	3D position
C		\mathbb{P}	Pathline
C_{Π}	Characteristic set	Π	Line predicate
$C(t)$	Curve	Π_V	Line predicate (flow field)
D		Π_{Γ}	Line predicate (geometry)
d	Distance	Π_{ϕ}	Line predicate (mean)
D	Spatial domain	Π_M	Line predicate (mesh)
E		$\Pi_{\sigma,n}$	Line predicate (smooth)
E	Elastic (Young's) modulus	Π_{meta}	Line predicate (meta)
G		Π_{Ω}	Line predicate (stream)
$\dot{\gamma}$	Shear rate	Π_{Σ}	Line predicate (sum)
H		\vec{p}_t	4D position
h	Wall thickness	Q	
H_d	Helicity density	Q	Volumetric flow rate
H_n	Normalized helicity	R	
H_r	Relative helicity	\mathbb{R}	Euclidean space
J		r	Radius
J	Jacobian matrix	ρ	Density
L		S	
ℓ_1 -norm	L_1 distance / taxicab geometry	S_3	3D segmentation
λ	Eigenvalue	S_4	4D segmentation
λ_2	λ_2 vortex criterion	S	Segmentation
M		σ	Standard deviation
M	Magnitude image	T	
\vec{M}	Overall magnetization	T	Number of temporal positions
\vec{M}_{xy}	Transversal magnetization	T_1	T_1 relaxation time
\vec{M}_z	Longitudinal magnetization	T_2	T_2 relaxation time
m	Mass	$\vec{\tau}_{\text{WSS}}$	Shear stress
μ	Dynamic viscosity	τ	Torsion
N		t	Time
N	Number	V	
$\nabla \times$	Curl operator	V	Phase / flow / velocity image
\vec{n}	Normal vector	$\ \vec{v}\ $	Velocity magnitude
O		\vec{v}	Velocity vector
$\vec{\omega}$	Vorticity	V_{ENC}	Velocity encoding
		$\ \vec{\omega}\ $	Vorticity magnitude
		X	
		x,y,z	Spatial dimensions

1	Heart anatomy and flow circulation	13
2	Cardiovascular diseases: Vessel wall alterations	15
3	Cardiovascular diseases: Treatments for vessel wall alterations	16
4	Cardiovascular diseases: Bicuspid aortic valve	17
5	Cardiovascular diseases: Tetralogy of Fallot and Marfan syndrome	18
6	MRI basics: Protons and spins	21
7	MRI basics: Precessing protons in the B_0 main magnetic field	22
8	MRI basics: Proton excitation and relaxation	23
9	MRI basics: T1- and T2-weighted images of a brain	23
10	MRI basics: Spatial encoding within a slice	24
11	MRI basics: Image reconstruction from k-space via inverse Fourier transform	24
12	4D PC-MRI acquisition: Velocity encoding using bipolar gradients	25
13	4D PC-MRI acquisition: Obtained images	27
14	Echocardiography: Ultrasound examination of the aortic valve	28
15	Echocardiography: The Doppler effect	28
16	Echocardiography: Doppler ECG exploits the Doppler effect	29
17	Echocardiography: Echo particle image velocimetry	29
18	4D PC-MRI data pre-processing: Phase unwrapping	34
19	4D PC-MRI data pre-processing: Velocity offset correction	35
20	4D PC-MRI data pre-processing: Noise masking	36
21	4D PC-MRI data pre-processing: Flow field regularization	36
22	Vessel segmentation: High contrast images	38
23	Vessel segmentation: Graph cut explanation	39
24	Vessel segmentation: Flow curves per voxel	40
25	Anatomical context visualization: Overview I	44
26	Anatomical context visualization: Front face culling for direct volume rendering	45
27	Anatomical context visualization: Overview II	45
28	Qualitative analysis: Direct visualization techniques	46
29	Qualitative analysis: Stream and path lines in a space-time diagram	48
30	Qualitative analysis: Geometry-based methods	49
31	Qualitative analysis: AHC dendogram	51
32	Qualitative analysis: Flow simplification	52
33	Qualitative analysis: Feature extraction with the line predicates technique	53
34	Qualitative analysis: Vector pattern matching	56
35	Clinical flow pattern analysis: Flow in the right ventricle	57
36	Clinical flow pattern analysis: Laminar flow with an approximate parabolic velocity profile	57
37	Clinical flow pattern analysis: Physiological helix in the aortic arch and physiological aortic shapes	58
38	Clinical flow pattern analysis: Physiological flow in the pulmonary artery	58
39	Clinical flow pattern analysis: Left ventricular mixing of blood	59
40	Clinical flow pattern analysis: Comparison of left and right ventricular vortex rings	59
41	Clinical flow pattern analysis: Pathologic flow in the aorta of patients	60
42	Clinical flow pattern analysis: Left ventricular vortex rings	61
43	Quantitative analysis: Standardized measuring planes in the thoracic aorta	65
44	Quantitative analysis: Time-dependent flow rate through a measuring plane	66
45	Quantitative analysis: Pulse wave velocity I	68
46	Quantitative analysis: Pulse wave velocity II	69
47	Quantitative analysis: Flow displacement (eccentricity) and compression	69
48	Quantitative analysis: Aortic valve area	70
49	Quantitative analysis: Wall shear stress in patients with bicuspid aortic valves	71
50	Quantitative analysis: Wall shear stress	72
51	Quantitative analysis: Pressure gradients	74
52	Quantitative analysis: Aortic and left ventricular pressure	74
53	Quantitative analysis: Turbulent kinetic energy	76

54	Quantitative analysis: Vorticity quantification	77
55	Quantitative analysis: Lagrangian coherent structures employing finite-time Lyapunov exponents	78
56	Bloodline: Start screen	84
57	Bloodline: Dataset import	84
58	Bloodline: Graph cut-based segmentation	85
59	Bloodline: Centerline extraction	86
60	Bloodline: Qualitative analysis	87
61	Bloodline: Video rendering	88
62	Bloodline: Quantitative analysis	89
63	Alternative software: Siemens 4D Flow Demonstrator, Ensight, and GTFlow	91
64	Vortex extraction: Physiological vortex in the left ventricle during diastole	96
65	Vortex extraction: Influence of smoothing line predicates and successive extraction procedure	99
66	Vortex extraction: Comparison of local vortex criteria in combination with line predicates	101
67	Vortex extraction: Pulmonary artery of a tetralogy of Fallot patient	104
68	Vortex extraction: Aorta of a patient with aneurysm and BAV	105
69	Vortex extraction: Patient overview I	105
70	Vortex extraction: Patient overview II	106
71	Vortex extraction: Patient overview III	106
72	Vortex extraction: BAV study in pigs	107
73	Aortic vortex flow polar plot: Temporal mapping	109
74	Aortic vortex flow polar plot: Spatial mapping	109
75	Aortic vortex flow polar plot: Plot cell scaling	109
76	Aortic vortex flow polar plot: λ_2 mapping and smoothing	110
77	Aortic vortex flow polar plot: Colored plot	110
78	Aortic vortex flow polar plot: No fixed λ_2 minimum	110
79	Aortic vortex flow polar plot: Grid view	111
80	Vortex animation with adaptive speed: Principle	113
81	Vortex animation with adaptive speed: Construction of the adaptive speed function	114
82	Vortex animation with adaptive speed: Results I	115
83	Vortex animation with adaptive speed: Results II	116
84	Vortex clustering: Centerline distance	117
85	Vortex clustering: Results	120
86	Vortex classification: Different shapes of path lines	121
87	Vortex classification: Eigenvalue analysis (PCA) of different line shapes	122
88	Vortex classification: Post-processing of helical shapes using torsion I	123
89	Vortex classification: Post-processing of helical shapes using torsion II	123
90	Vortex classification: Temporal occurrence based on flow rates	124
91	Vortex classification: Definition of vessel sections in the aorta	124
92	Vortex classification: Rotation direction relative to the centerline	125
93	Vortex classification: Rotation direction in the cross-section	127
94	Vortex classification: 3D glyph visualization	128
95	Vortex classification: Comparison with the ground truth	129
96	Vortex classification: 2D plot and 3D glyph results	130
97	Robust cardiac function assessment: NFV variation for different measuring plane configurations	136
98	Robust cardiac function assessment: Flow rate in the ascending aorta of a healthy volunteer	137
99	Robust cardiac function assessment: Systematically generated angulation samples	138
100	Robust cardiac function assessment: Consistent measuring plane orientations	140
101	Robust cardiac function assessment: NFV distributions along the vessel course	141
102	Robust cardiac function assessment: Plausible NFV development for branching vessels	143
103	Robust cardiac function assessment: Results I	144
104	Robust cardiac function assessment: Results II	145
105	Robust cardiac function assessment: Result for branching vessel	146
106	Motion-aware SV: Cross-section segmentation via rasterization	149
107	Motion-aware SV: Mesh extraction procedure per temporal position	150
108	Motion-aware SV: Deriving displacement vectors from projections	150
109	Motion-aware SV: Postprocessing of motion information	150
110	Motion-aware SV: Motion visualization	152
111	Motion-aware SV: Dynamic measuring planes	152
112	Motion-aware SV: Time-dependent cross-section segmentation via rasterization	153
113	Motion-aware SV: Evaluation of cross-section segmentations	153
114	Motion-aware SV: Results I	155

115	Motion-aware SV: Results II	155
116	Motion-aware SV: Results III	155
117	Motion-aware SV: Results IV	155
118	Motion-aware SV: Results V	156
119	Motion-aware SV: Results VI	156
120	Motion-aware SV: Results VII	156
121	Motion-aware SV: Motion-induced errors in the peripheral regions of a cross-section	158
122	Research awards	208

1	Bloodline: Alternative software	93
2	Vortex clustering: Results	119
3	Vortex classification: Specification of the torsion threshold	123
4	Vortex classification: Comparison of manual vs. automatic classification	129
5	Vortex classification: User study task 1	131
6	Vortex classification: User study task 2	131
7	Vortex classification: User study task 3	132
8	Vortex classification: User study task 4	132
9	Motion-aware SV: Evaluation of cross-section segmentations	153
10	Motion-aware SV: Determination of causes for deviations	157

JOURNAL PAPERS

- [363] M. Meuschke, **B. Köhler**, U. Preim, B. Preim, and K. Lawonn. “Semi-automatic vortex flow classification in 4D PC-MRI data of the aorta”. In: *Computer Graphics Forum* 35.3 (2016), pp. 351–60. DOI: [10.1111/cgf.12911](https://doi.org/10.1111/cgf.12911)
- *Division of work*: I provided the extracted, vortex-representing pathlines, meshes with centerlines, and flow curves for all datasets as well as first classification attempts from my Master’s thesis [269]. I summarized potential classification criteria including rough implementation ideas for two grant proposals which I gave to M. Meuschke as a starting point for her Master’s thesis [360]. The text describes: Vortex sizes as percentage occupation of cross-sectional planes, the idea to detect the cusp in the aortic arch for a subsequent partitioning, and the basic idea how to determine systole and diastole by separating the flow curve. M. Meuschke designed and implemented a stand-alone software prototype, adapted the 2D polar plot [274], completely established the pathline shape classification, and designed and conducted the user study. I wrote MATLAB code to obtain the turning direction of a line segment in a cross-section, to create consistently oriented cross-sections along the centerline (described in [278]), and provided the basic idea to replace classified vortex clusters with a simplifying glyph, which was designed and realized by M. Meuschke. K. Lawonn provided valuable mathematical support. He and M. Meuschke wrote the paper, while I commented two versions. U. Preim provided feedback from a clinical perspective.
- [275] **B. Köhler**, S. Born, R. F. P. Van Pelt, A. Hennemuth, U. Preim, and B. Preim. “A survey of cardiac 4D PC-MRI data processing”. In: *Computer Graphics Forum* (2016), Epub. DOI: [10.1111/cgf.12803](https://doi.org/10.1111/cgf.12803)
- *Division of work*: I did the extended literature research and wrote the paper. The coauthors provided, as in the prior version [272], helpful comments. A. Hennemuth provided the suggestion to include divergence filters and Lagrangian coherent structures already in the original version, but joined the list of authors only for the work.
- [277] **B. Köhler**, U. Preim, M. Grothoff, M. Gutberlet, K. Fischbach, and B. Preim. “Motion-aware stroke volume quantification in 4D PC-MRI data of the human aorta”. In: *International Journal for Computer Assisted Radiology and Surgery* 11.2 (2016), pp. 169–79. DOI: [10.1007/s11548-015-1256-4](https://doi.org/10.1007/s11548-015-1256-4)
- *Division of work*: I had fruitful discussions with the clinical partners, especially when the first prototype of a moving vessel was established. The algorithmic design is based on my ideas. I did the implementation and writing of the paper. Each coauthor read the paper at least once and provided comments.
- [278] **B. Köhler**, U. Preim, M. Grothoff, M. Gutberlet, K. Fischbach, and B. Preim. “Robust cardiac function assessment in 4D PC-MRI data of the aorta and pulmonary artery”. In: *Computer Graphics Forum* 35.1 (2016), pp. 32–43. DOI: [10.1111/cgf.12669](https://doi.org/10.1111/cgf.12669)
- *Division of work*: The extension of the original paper [271] to branching vessels was my work. Each coauthor (M. Grothoff joined the team) proofread the paper again and provided feedback.
- [270] **B. Köhler**, R. Gasteiger, U. Preim, H. Theisel, M. Gutberlet, and B. Preim. “Semi-automatic vortex extraction in 4D PC-MRI cardiac blood flow data using line predicates”. In: *IEEE Transactions on Visualization and Computer Graphics* 19.12 (2013), pp. 2773–82. DOI: [10.1109/TVCG.2013.189](https://doi.org/10.1109/TVCG.2013.189)
- Winner of the Karl-Heinz Höhne Prize (MedVis Award), awarded at the Eurographics Workshop on Visual Computing for Biology and Medicine, 2014 (see Figure 122b).
 - This work is a continuation of my Master’s thesis [269]. The following extensions were made as PhD student. A GPU implementation increases the clinical feasibility. Instead of seeding N uniformly distributed pathlines, it is now ensured that each voxel is visited at least once in every temporal position. The λ_2 calculation is performed together with the pathline integration on the GPU. The extraction procedure was adapted so that now a single slider facilitates the vortex filtering. A detailed, qualitative case evaluation was performed in collaboration with the clinical partners.
 - *Division of work*: During the Master’s thesis: U. Preim provided feedback from a clinical perspective, and I had discussions with H. Theisel about vortex extraction methods and with R. Gasteiger who supervised me. For the paper: U. Preim provided background information for the patients and verified the text, R. Gasteiger provided detailed comments and tips for writing the paper, and M. Gutberlet, representative for the clinical partners, provided the 4D PC-MRI data and feedback.

CONFERENCE PAPERS (PROCEEDINGS)

- [276] **B. Köhler**, U. Preim, M. Grothoff, M. Gutberlet, and B. Preim. “Adaptive animations of vortex flow extracted from cardiac 4D PC-MRI data”. In: *Proceedings: Bildverarbeitung für die Medizin*. 2016, pp. 194–9

- *Division of work*: The idea was mine and discussed with B. Preim. I realized it and wrote the paper. Result feedback was provided by the clinical partners.
- [362] M. Meuschke, K. Lawonn, **B. Köhler**, U. Preim, and B. Preim. “Clustering of aortic vortex flow in cardiac 4D PC-MRI data”. In: *Proceedings: Bildverarbeitung für die Medizin*. 2016, pp. 182–7
 - *Division of work*: Initial ideas on distance measures and the results with DBSCAN were provided from my Master’s thesis [269] as starting point for M. Meuschke’s own Master’s thesis [360]. She refined the distance measures, composed a distance matrix, compared different clustering algorithms, and wrote the paper with K. Lawonn. I provided detailed feedback twice and the datasets including the extracted, vortex flow-representing path lines.
- [29] B. Behrendt, **B. Köhler**, and B. Preim. “Enhancing visibility of blood flow in volume rendered cardiac 4D PC-MRI data”. In: *Proceedings: Bildverarbeitung für die Medizin*. 2016, pp. 188–93
 - *Division of work*: B. Behrendt received flow data as starting point for his Master’s thesis [28] which is the basis for this paper. He developed the method, wrote the paper, and I gave detailed comments in multiple iterations.
- [274] **B. Köhler**, M. Meuschke, U. Preim, K. Fischbach, M. Gutberlet, and B. Preim. “Two-dimensional plot visualization of aortic vortex flow in cardiac 4D PC-MRI data”. In: *Proceedings: Bildverarbeitung für die Medizin*. 2015, pp. 257–61. DOI: [10.1007/978-3-662-46224-9_45](https://doi.org/10.1007/978-3-662-46224-9_45)
 - Best Talk Award (see Figure 122f).
 - *Division of work*: A scientific team project [361], which I supervised, was done. Prior to the project, I provided the plot mapping idea, i.e., the mapping of time and vessel section (centerline) to the plot angle and distance from the plot center, respectively, as well as the idea to map individual pathline points to the plot and employ the λ_2 values for color-coding. I provided the datasets include the vortex-representing path lines and their λ_2 values. The team established an implementation, tested different visualization styles and conducted a user study. After the project, I reimplemented the mapping, and established a continuous color visualization as well as the grid view to compare datasets. I wrote the paper and had the final version verified by the coauthors.
- [272] **B. Köhler**, S. Born, R. F. P. Van Pelt, U. Preim, and B. Preim. “A survey of cardiac 4D PC-MRI data processing”. In: *Proceedings: Eurographics Workshop on Visual Computing for Biology and Medicine*. 2015, pp. 139–48. DOI: [10.2312/vcbm.20151217](https://doi.org/10.2312/vcbm.20151217)
 - Paper awarded as Honorable Mention (see Figure 122a) and invited for an extended submission to the Computer Graphics Forum.
 - *Division of work*: The authors had a joint brainstorming on the rough content of the paper based on an initial draft that I wrote. S. Born, R. F. P. van Pelt, and B. Preim repeatedly provided feedback on the paper structure and suggestions to include specific works. I did the literature research and wrote the paper. U. Preim verified the final paper from a medical perspective.
- [273] **B. Köhler**, U. Preim, M. Grothoff, M. Gutberlet, K. Fischbach, and B. Preim. “Guided analysis of cardiac 4D PC-MRI blood flow data”. In: *Proceedings: Eurographics Short Papers and Medical Prize Awards*. 2015, Epub. DOI: [10.2312/egm.20151029](https://doi.org/10.2312/egm.20151029)
 - Second place of the Eurographics Medical Prize (Dirk Bartz Prize) (see Figures 122c–122d).
 - *Division of work*: This short paper summarizes my software prototype Bloodline. I wrote the paper, and B. Preim provided feedback. Including the clinical partners as coauthors points out the collaboration.
- [271] **B. Köhler**, U. Preim, M. Gutberlet, K. Fischbach, and B. Preim. “Robust cardiac function assessment in 4D PC-MRI data”. In: *Proceedings: Eurographics Workshop on Visual Computing for Biology and Medicine*. 2014, pp. 1–9. DOI: [10.2312/vcbm.20141179](https://doi.org/10.2312/vcbm.20141179)
 - Paper awarded as Honorable Mention (see Figure 122e) and invited for an extended submission to the Computer Graphics Forum.
 - *Division of work*: The idea for this work comes from joint dataset evaluations with U. Preim. I designed and implemented the automatic procedure, which was discussed with all coauthors. I wrote the paper, B. Preim repeatedly gave feedback, and the clinical partners verified the work from a medical perspective.

POSTERS

- [192] M. Grothoff, C. D. Etz, B. Preim, **B. Köhler**, and M. Gutberlet. “Phase contrast 4D flow in bicuspid aortic valve in a porcine model”. In: *Journal of Cardiovascular Magnetic Resonance* 17.Suppl 1 (2015), P416. DOI: [10.1186/1532-429X-17-S1-P416](https://doi.org/10.1186/1532-429X-17-S1-P416)
 - *Division of work*: The data were acquired by the clinical partners from the Heart Center in Leipzig, Germany, represented by M. Grothoff and M. Gutberlet. The subjects were prepared (BAV surgery) by C. D. Etz. The submitted paper (abstract) was written by M. Grothoff. I provided before and after screenshots and videos of the intra-aortic vortex flow.

AWARDS



**NVIDIA Best Paper Award
honorable mention**

is presented to

**B. Köhler
U. Preim
M. Gutberlet
K. Fischbach
B. Preim**

for their work in

**Robust Cardiac Function Assessment
in 4D PC-MRI Data**

Bernhard Kainz

Nigel John

Charles Hansen

(a) VCBM 2014: Honorable mention.

medvis-award
KARL-HEINZ-HÖHNE-PREIS

2014

Benjamin Köhler

erhält den **1. Preis** im Jahr 2014 für seine wissenschaftliche Arbeit auf dem Gebiet der biomedizinischen Bildverarbeitung und Visualisierung mit dem Titel:

“Semi-Automatic Vortex Extraction in 4D PC-MRI Cardiac Blood Flow Data Using Line Predicates”

Mit dem KARL-HEINZ-HÖHNE-PREIS werden innovative Arbeiten mit methodischem Schwerpunkt in der Visualisierung und einem klaren Bezug zu medizinischen Fragestellungen, z.B. in der medizinischen Ausbildung, Diagnostik oder Therapie ausgezeichnet.

Der Preis wird von der Firma Brainlab gesponsert und ist mit insgesamt 1000€ dotiert. Der Preis wird von der Fachgruppe „Visual Computing in Biologie und Medizin“ der Gesellschaft für Informatik ausgelobt.

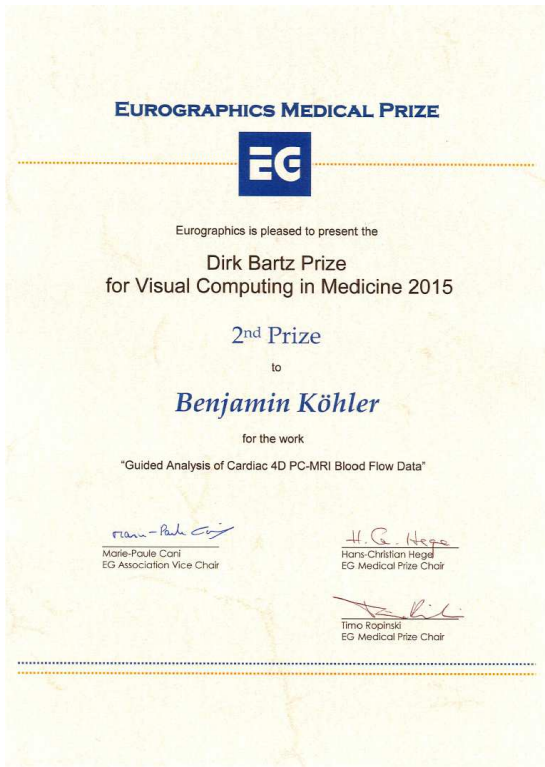
BRAINLAB

Dorit Merhof
Sprecherin der FG VCBM

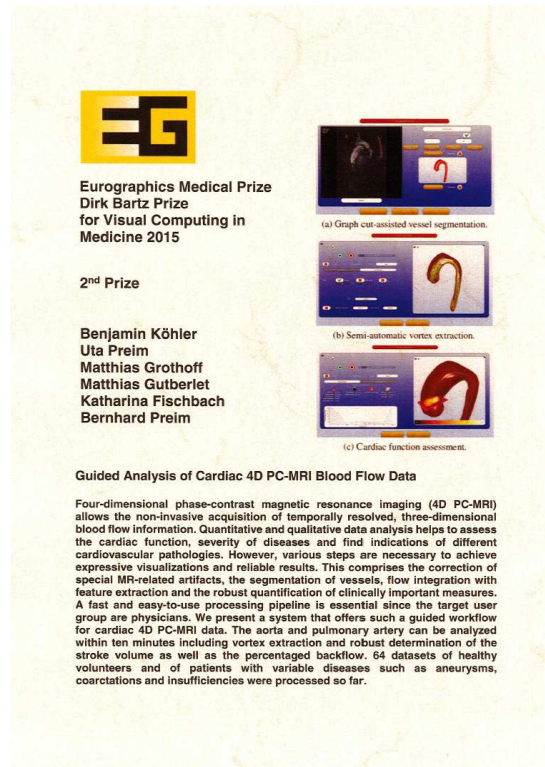
Rainer Birkenbach
BrainLAB Vorstand

Wolfgang Steinle
BrainLAB Abteilungsleiter Orthopädie

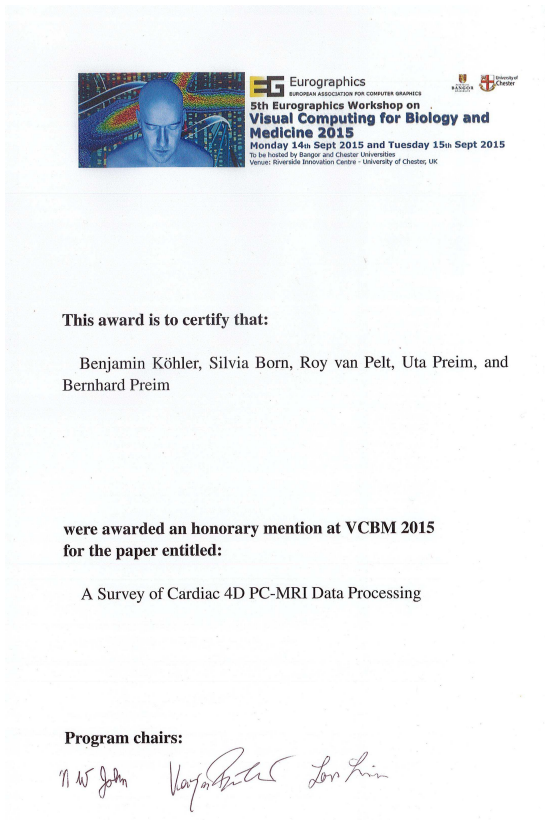
(b) VCBM 2014: Winner of the Karl-Heinz Höhne Prize (MedVis Award).



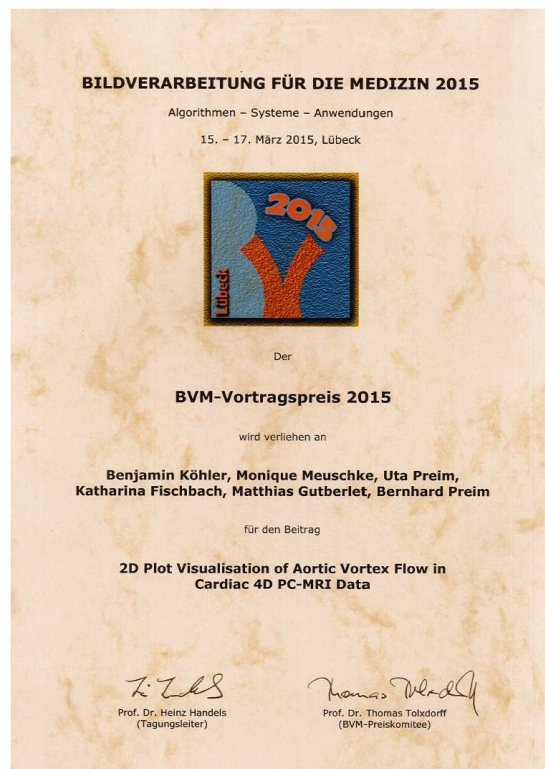
(c) EG 2015: Medical (Dirk Bartz) Prize page 1.



(d) EG 2015: Medical (Dirk Bartz) Prize page 2.



(e) VCBM 2015: Honorable mention.



(f) BVM 2015: Best talk.

Figure 122: Research awards.

PAPER PRESENTATIONS

03/2016	Workshop on Bildverarbeitung für die Medizin (BVM)	Berlin (GER)	[276]
09/2015	Eurographics Workshop on Visual Computing for Biology and Medicine (EG VCBM). Talk was given by Bernhard Preim	Chester (UK)	[272]
05/2015	The 36 th Annual Conference of the European Association for Computer Graphics (Eurographics). Talk was given via Skype	Zürich (CH)	[273]
03/2015	Workshop on Bildverarbeitung für die Medizin (BVM)	Lübeck (GER)	[274]
09/2014	Eurographics Workshop on Visual Computing for Biology and Medicine (EG VCBM)	Vienna (AT)	[271]
10/2013	IEEE Visualization Conference (VISweek)	Atlanta (USA)	[270]

INVITED TALKS

01/2015	7. Deutsche Kardiagnostik-Tage	Leipzig (GER)	4D PC-MRI data evaluation with <i>Bloodline</i>
---------	--------------------------------	---------------	---

SUPERVISED STUDENT PROJECTS

10/2014 – 07/2015	Master's thesis by Monique Meuschke	"Computer-aided analysis of vortex flow in 4D PC-MRI blood flow data of the aorta", original title: "Computergestützte Analyse von Verwirbelungen in 4D PC-MRI Blutflussdaten der Aorta" [360]
10/2014 – 04/2015	Master's thesis by Benjamin Behrendt	"Fully automatic visualization of cardiac 4D PC-MRI blood flow data with a smart focus on features", original title: "Vollautomatische Visualisierung von kardialen 4D PC-MRI Blutflussdaten mit intelligenter Fokussierung auf Features" [28]
04/2014 – 09/2014	Scientific Project by Julian Hettig	"Contrast-enhancement of the right ventricle in 4D PC-MRI data", original title: "Kontrastverstärkung des rechten Ventrikels in 4D PC-MRI Daten" [216]
10/2013 – 04/2014	Scientific Team Project by Monique Meuschke, Julian Hettig and Sarah Pauksch	"Development of a polar plot to depict cardiac blood flow", original title: "Entwicklung eines Polarplots zur Darstellung kardialer Blutflussdaten" [361]

TEACHING

04/2016 – 07/2016	Medical Visualization (ME), Interactive Systems (BE)
10/2015 – 01/2016	Visualization (BE), Computer-aided Diagnosis and Therapy (BS)
05/2015 – 07/2015	Interactive Systems (BE)
04/2015 – 07/2015	Medical Visualization (ME)
10/2015 – 01/2015	Visualization (BE)
04/2014 – 07/2014	Medical Visualization (ME)
10/2013 – 01/2014	Visualization (BE)
04/2013 – 07/2013	Medical Visualization (ME)

BE: Bachelor exercise ME: Master exercise BS: Bachelor seminar

GRANT PROPOSALS

- 07/2014 German Research Foundation
(rejected) (GRF) / Deutsche Forschungs-
gemeinschaft (DFG) *”Norm value generation and evaluation of pathological flow
patterns for different diseases of the semilunar valves using 4D
PC-MRF”, original title: ”Normwerterhebung und Evaluation
pathologischer Flussparameter bei verschiedenen Erkrank-
ungen der Semilunarklappen mittels 4D-Fluss”*
- 04/2016 German Research Foundation
(accepted) (GRF) / Deutsche Forschungs-
gemeinschaft (DFG) *”Norm value generation for well-established flow parameters in
a group of healthy volunteers and 1-year follow-up exam-
inations of patients with selected semilunar valve pathologies
using 4D PC-MRF”, original title: ”Normwerterhebung
etablierter Flussparameter bei einem gesunden Kollektiv und
1-Jahres Verlaufsevaluation ausgewählter Pathologien der
Semilunarklappen mittels 4D PC-MRF”*

PERSONAL DETAILS

Name: **Benjamin Köhler**
 Date of birth: 04.03.1988
 Place of birth: 98617 Meiningen
 Civil Status: Unmarried, no children
 Nationality: German
 Contact: ben.koehler@isg.cs.uni-magdeburg.de



EDUCATION

- 11/2012 – 06/2016: Otto-von-Guericke University Magdeburg, research assistant / PhD student
 – Teaching: Visualization, Interactive Systems, Computer-aided Diagnosis and Therapy (Bachelor courses), Medical Visualization (Master course)
 – Thesis topic: *”Guided qualitative and quantitative analysis of cardiac 4D PC-MRI blood flow data”*
 – Degree: **Doktoringenieur (Dr.-Ing.)**, grade: **summa cum laude**
- 04/2011 – 10/2012: Otto-von-Guericke University Magdeburg, studies of Computational Visualistics (Master):
 – Thesis title: *”Vortex extraction in 4D PC-MRI blood flow data of the aorta”*, original title: *”Wirbelextraktion in 4D PC-MRI Blutflussdaten der Aorta”*, grade: 1.0
 – Degree: **Master of Science (M. Sc.)**, grade: **1.0**
- 10/2007 – 03/2011: Otto-von-Guericke University Magdeburg, studies of Computational Visualistics (Bachelor):
 – Application subject: Medicine
 – Thesis title: *”Reconstruction of neuronal fiber bundles using global fiber tracking on an ODF-field derived from HARDI data”*, original title: *”Rekonstruktion neuronaler Faserbündel mittels globalem Fiber-Tracking ausgehend von einem aus HARDI-Daten erzeugten ODF-Feld”*, grade: 1.0
 – Degree: **Bachelor of Science (B. Sc.)**, grade: **1.6**
- 10/1998 – 06/2006: Henfling Gymnasium Meiningen:
 – Degree: **”Abitur”**, grade: **1.9**

WORK EXPERIENCE

- since 07/2016: Otto-von-Guericke University Magdeburg, research assistant
– GRF grant proposal title: *”Norm value generation for well-established flow parameters in a group of healthy volunteers and 1-year follow-up examinations of patients with selected semilunar valve pathologies using 4D PC-MRI”*, original title: *”Normwert-erhebung etablierter Flussparameter bei einem gesunden Kollektiv und 1-Jahres Verlaufsevaluation ausgewählter Pathologien der Semilunarklappen mittels 4D PC-MRI”*
- 11/2011 – 10/2012: Otto-von-Guericke University Magdeburg, student assistant
– Topic: Visualization of cardiac 4D PC-MRI blood flow data
- 03/2011 – 09/2011: Fraunhofer MeVis, Bremen, external student assistant
– Topic: Integration of the developed method during the Bachelor thesis as a module for MeVisLab
- 10/2010 – 02/2011: Fraunhofer MeVis, Bremen, combined internship and Bachelor thesis
– Topic: Global fiber tracking using HARDI data
- 11/2006 – 07/2007: Deutsches Rotes Kreuz (DRK), Meiningen, civilian service
- 2002 – 2006: Meiningen, deliverer of advertising leaflets

EXPERTISE

- Programming: C/C++, Qt, VTK, OpenGL, GLSL, MATLAB
- Applications: Microsoft Office, LibreOffice, MeVisLab, Visual Studio, CLion, QtCreator, QtDesigner, Adobe Photoshop, Gimp, ParaView, Meshlab, Camtasia Studio
- Typesetting: \LaTeX , Microsoft Word, LibreOffice Writer

ADDITIONAL SKILLS

- Languages: English (fluent in speech and writing)
- Driving License: B

”Ich versichere hiermit, dass ich die vorliegende Arbeit ohne unzulässige Hilfe Dritter und ohne Benutzung anderer als der angegebenen Hilfsmittel angefertigt habe; verwendete fremde und eigene Quellen sind als solche kenntlich gemacht. Insbesondere habe ich nicht die Hilfe eines kommerziellen Promotionsberaters in Anspruch genommen. Dritte haben von mir weder unmittelbar noch mittelbar geldwerte Leistungen für Arbeiten erhalten, die im Zusammenhang mit dem Inhalt der vorgelegten Dissertation stehen.

Ich habe insbesondere nicht wissentlich:

- Ergebnisse erfunden oder widersprüchliche Ergebnisse verschwiegen,
- statistische Verfahren absichtlich missbraucht, um Daten in ungerechtfertigter Weise zu interpretieren,
- fremde Ergebnisse oder Veröffentlichungen plagiiert,
- fremde Forschungsergebnisse verzerrt wiedergegeben.

Mir ist bekannt, dass Verstöße gegen das Urheberrecht Unterlassungs- und Schadensersatzansprüche des Urhebers sowie eine strafrechtliche Ahndung durch die Strafverfolgungsbehörden begründen kann. Die Arbeit wurde bisher weder im Inland noch im Ausland in gleicher oder ähnlicher Form als Dissertation eingereicht und ist als Ganzes auch noch nicht veröffentlicht.”

Magdeburg, den 10.10.2016

Benjamin Köhler

Zunächst einmal möchte ich meinem Doktorvater *Bernhard Preim* für die sehr gute Betreuung danken. In meinen Augen zeichnest du dich insbesondere dadurch aus, dass du dich flexibel auf deine Mitarbeiter einstellst, viele Freiheiten lässt, aber gleichzeitig immer intensiv mitdenkst und sehr kompetente Ratschläge gibst. Man hat bei dir immer das Gefühl, dass alles, was deine Mitarbeiter angeht, absolut oberste Priorität hat. Es ist alles andere als selbstverständlich, dass du dich mit so viel Engagement für uns einsetzt. Außerdem weiß ich dein stets offenes Ohr für Berufliches sowie Privates und deine lockere Art sehr zu schätzen.

Meiner gesamten Arbeitsgruppe bzw. meinen aktuellen und ehemaligen Kollegen möchte ich für die super angenehme Atmosphäre, die vielen lustigen Momente und die unzähligen Kaffeerunden danken. In willkürlicher Reihenfolge und womöglich unvollständig: *Benjamin Behrendt, Nico Merten, Steffen Oeltze-Jafra, Monique Meuschke, Kai Lawonn, Paul Klemm, Patrick Saalfeld, Sylvia Glaßer, Shiva Alemzadeh, Kai Nie, Alexandra Baer, Antje Hübler* und *Tobias Mönch*. So ein entspanntes Arbeitsumfeld kann man jedem nur wünschen. Einen besonderen Dank möchte ich *Rocco Gasteiger* und *Mathias Neugebauer* dafür aussprechen, dass ihr mich während des Masterstudiums so klasse als HiWi betreut habt und mir zudem aus dem Nähkästchen über das Leben als Doktorand erzählt habt. So konnte ich mir ein realistisches Bild machen, ob das überhaupt etwas für mich wäre – und offensichtlich war es das. Danke *Rocco*, dass du dann insbesondere in der Anfangszeit immer als Ansprechpartner für mich da warst. Das war wirklich Gold wert.

Außerdem möchte ich unser hilfsbereites Sekretariat erwähnen, das viele Dinge deutlich vereinfacht hat. Genauer gesagt: Vielen Dank an *Stefanie Quade* für das fleißige Korrekturlesen der Paper und an *Petra Specht* sowie *Petra Schumann* für eurer exzellentes Organisationstalent. Großes Lob gebührt auch unseren Technikern *Heiko Dorwarth* und *Thomas Rosenburg*, dafür, dass hier alles so reibungslos funktioniert.

Fachlich hatte ich mit einer Vielzahl von interessanten Persönlichkeiten die Ehre. Zunächst einmal möchte ich *Matthias Gutberlet, Matthias Grothoff, Franziska Reinhold, Barbara Brenneis, Huong Luu Thi Thanh* und *Daniel Gräfe* aus dem Leipziger Herzzentrum für die schöne und erfolgreiche Zusammenarbeit danken. Ein riesiges Dankeschön geht an *Uta Preim* dafür, dass du dir regelmäßig die Zeit genommen hast, um dir meine Prototypen anzuschauen, mir wertvolles Feedback sowie tiefere Einblicke aus klinischer Sicht gegeben hast und dich stets tapfer und geduldig mit meinem Tool Bloodline auseinandergesetzt hast. Aus dem Magdeburger Universitätsklinikum möchte ich *Katharina Fischbach, Alexander Schmeißer* und *Julian Jürgens* für einige spannende Gespräche danken. Dasselbe gilt für *Anja Hennemuth* vom Fraunhofer MeVis in Bremen. Außerdem vielen Dank an *Roy van Pelt* und *Silvia Born* für die tolle Zusammenarbeit bei dem Survey Paper. Das hat mir wirklich sehr viel Spaß bereitet. Des Weiteren möchte ich unsere Strömungsmechaniker *Gábor Janiga* und *Philipp Berg* für deren überaus freundliche Art hervorheben. Ein herzliches Dankeschön geht zudem an *Anna Vilanova* und *Gerik Scheuermann* für das Begutachten der vorliegenden Arbeit.

Zu guter Letzt möchte ich meinen Eltern *Heike* und *Klaus* sowie meinem Bruder *Steven* für die liebevolle seelische und moralische Unterstützung danken. Und das Allerwichtigste zum Schluss: Danke *Jenny* – für alles! Zwar stehst du auf keiner meiner Arbeiten, dafür bist du der bedeutendste Koautor meines Lebens.